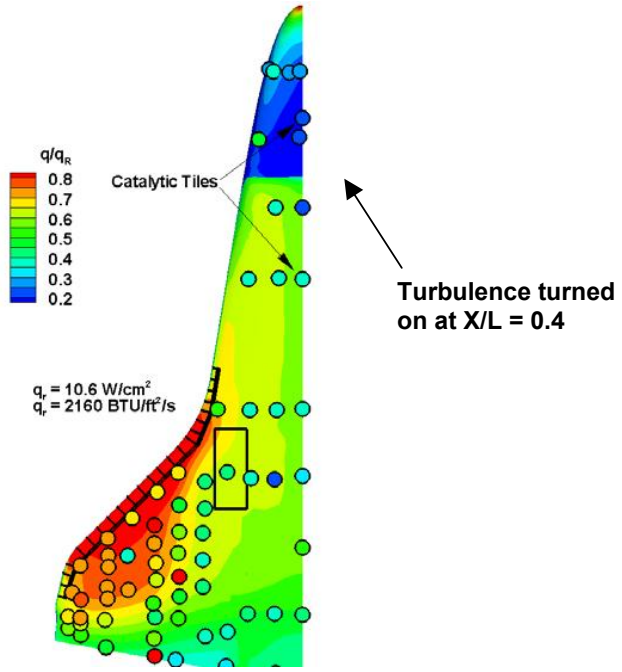

a) GASP

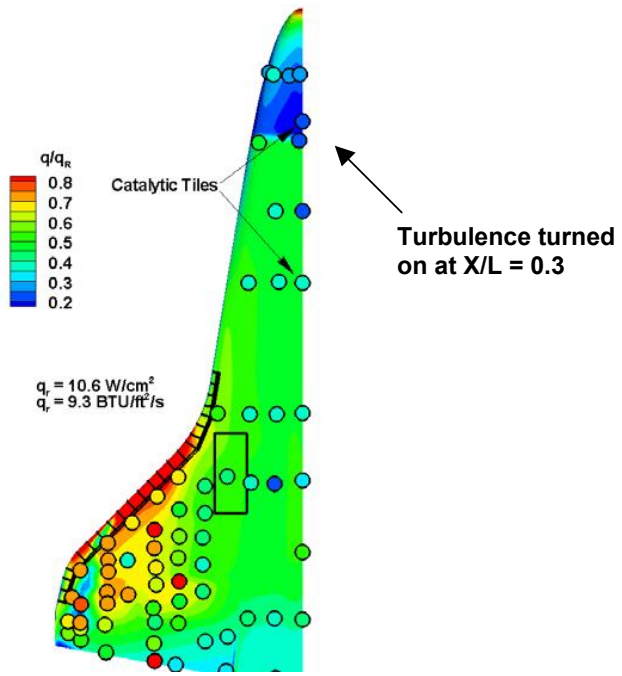

b) LAURA

Figure 5.2.4-20 Windward surface temperature predictions from GASP and LAURA compared with flight data at Mach 7. Experimental data are plotted inside the circular symbols. The symbol size is made larger than the measurement extent to aide visualization of the data.

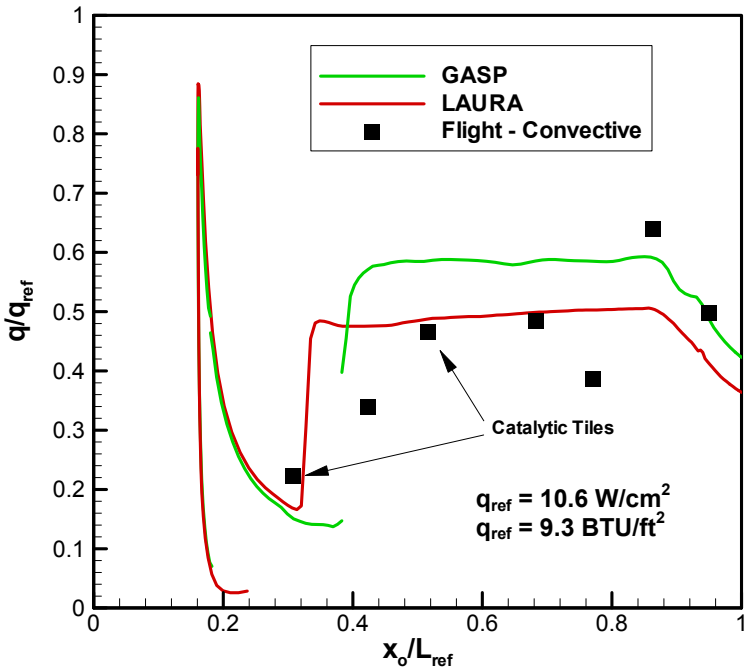

Figure 5.2.4-21 Windward centerline heat transfer rate for Mach 7. L_{ref} = 37.24 m = 1466 in.

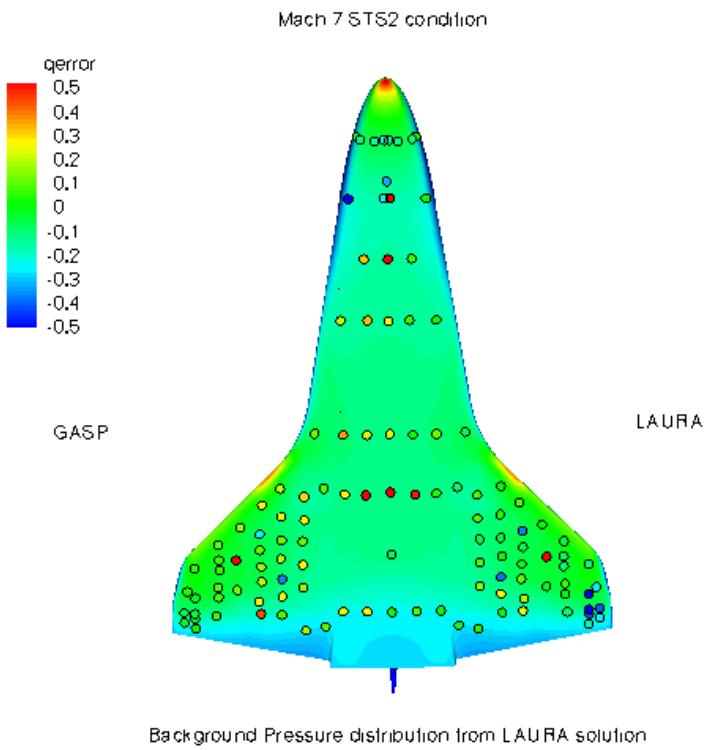

Figure 5.2.4-22 Windward heating rate uncertainty at Mach 7 plotted over pressure contours $q_{error} = (q_{cfd} - q_{flight})/q_{flight}$.

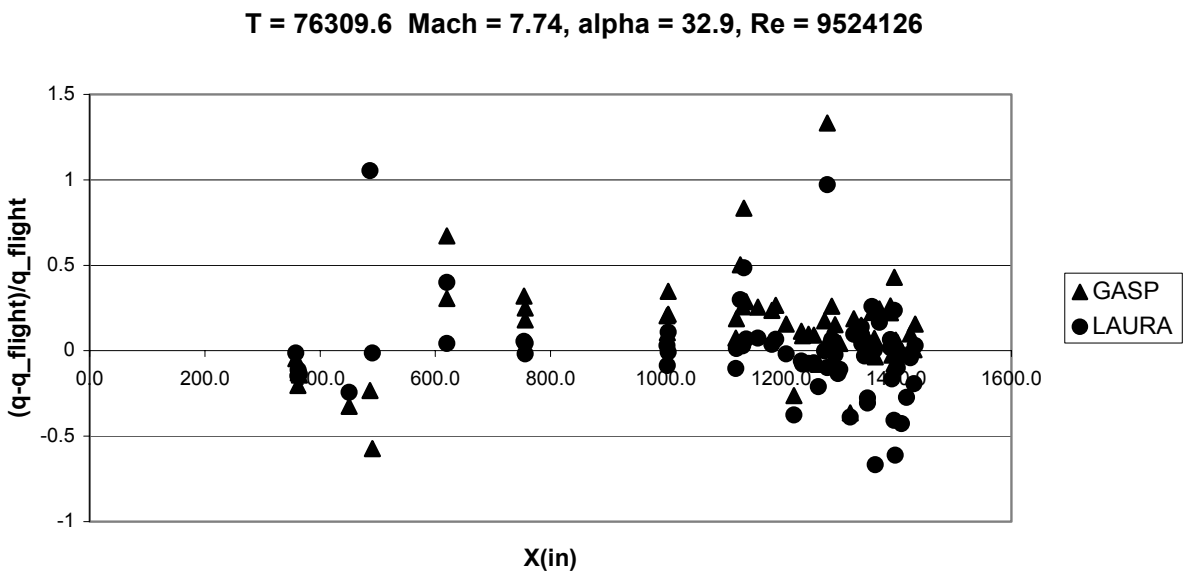

Figure 5.2.4-23 Heating rate uncertainty at Mach 7 as a function of axial distance along the orbiter

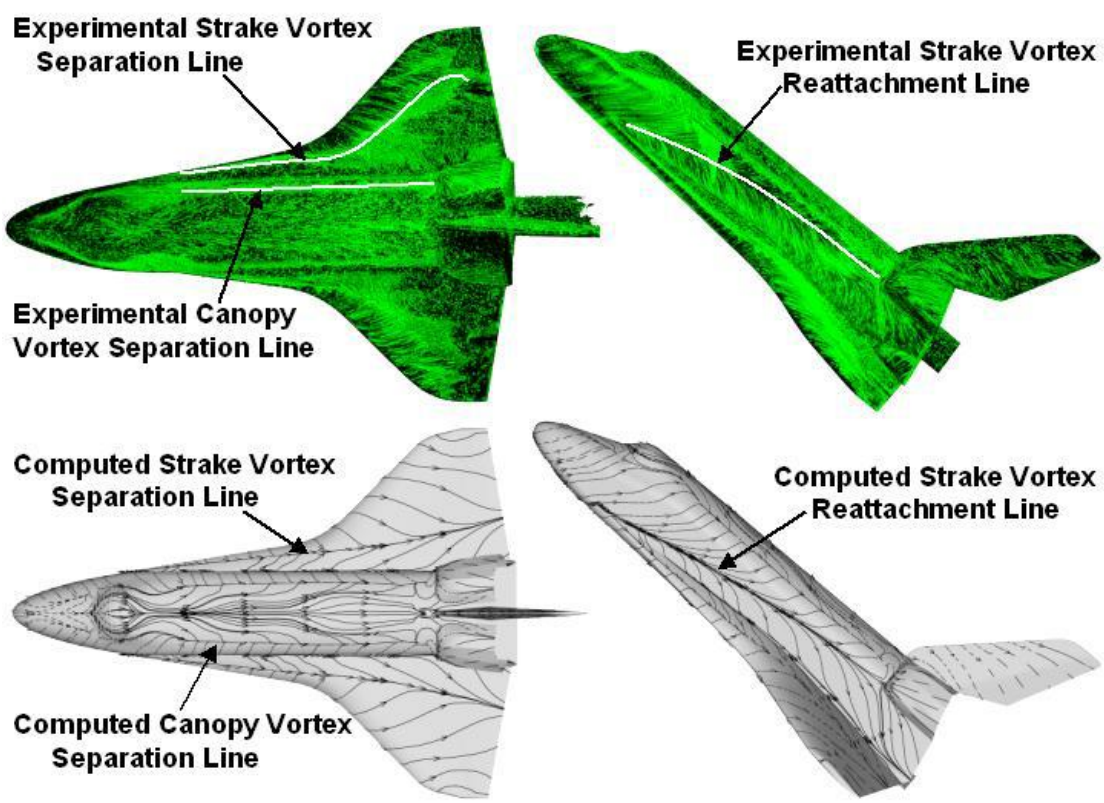

Figure 5.2.4-24 Comparison of Computed and Experimental Surface Streamlines on the Lee Side of the Baseline Orbiter in the CF_4 Wind Tunnel

5.2.4.4 Nominal Orbiter Configuration – Flight Environments

5.2.4.4.1 Introduction

The Orbiter re-entry environment exposes the vehicle to extreme high temperature gases, thus demanding as robust a thermal protection system as possible. The detailed physical features in the very complex Orbiter flow field during re-entry can be appreciated by examining high-fidelity CFD simulations calculated at the actual flight conditions. Thus, a need for understanding the details of local flow field features for the nominal Orbiter geometry led to the calculation of a suite of numerical solutions at STS-107-specific flight conditions. Details about the trajectory conditions identified to perform the simulations can be found in the Aerodynamics Section. The trajectory conditions cover the entire duration of the STS-107 entry trajectory, and as a whole provide a valuable database for the aero/aerothermal team. Because the Orbiter experiences conditions on re-entry that range from a very rarefied environment down to a fully continuum environment, the suite of nominal geometry solutions includes simulations appropriate to both regimes.

The external environment simulations along the STS-107 trajectory were performed by Boeing-Huntington Beach, NASA-ARC, NASA-JSC, NASA-LaRC and Sandia National Laboratories. The software tools used to perform these simulations included Navier-Stokes solvers (GASP, LAURA, SACCARA, USA) appropriate to the continuum regime, and DSMC software (DAC) appropriate to the rarefied regime. The database of solutions generated is provided in Table 5.2.4-4 , where the solutions obtained are listed by trajectory condition, grid basis, and software tool. The abbreviations for the entries correspond to 5-species chemical non-equilibrium using Reaction Cured Glass surface properties (Noneq), fully catalytic surface properties with 5-species non-equilibrium chemistry (FC), and equilibrium chemistry (Eq). The DAC solutions utilized a 6-species, non-equilibrium chemistry gas model, and a fully diffuse, non-catalytic surface with radiation equilibrium surface temperature boundary condition and an emissivity of 0.9. The Navier-Stokes simulations (GASP, LAURA, SACCARA and USA) all used laminar flow assumptions with a radiation equilibrium temperature boundary condition, and an emissivity of 0.9. Further details on the software tools can be found in the Appendices. As noted in the Grid Generation section, the initial nominal geometry grids mentioned in Table 5.2.4-4 were used to generate initial Navier-Stokes solutions immediately after the loss of Columbia. The common baseline grid was subsequently developed and was used to generate the additional solutions listed. The modified common baseline grid utilized for the SACCARA simulation used a grid system which had a resolution doubled in the streamwise and circumferential directions, and it encompassed only the front half of the Orbiter The DAC simulations utilized a surface definition already available at the time of the accident..

5.2.4.4.2 Description of the Nominal Orbiter Configuration Flow Field

Four of the flow field solutions shown in Table 5.2.4-4 were selected to present predicted surface pressure and thermal loads experienced by Columbia and to present the properties of the gas in close proximity to the Orbiter surface. The four solutions correspond to trajectory points with the following conditions:

CFD Point 1: EI+404 sec.; Mach = 24.9; Altitude = 243,000 ft; Alpha = 40°; Dyn. press. = 22.0 psf.
CFD Point 6: EI+921 sec.; Mach = 17.9; Altitude = 200,767 ft; Alpha = 40°; Dyn. press. = 83.5 psf.
DSMC Point A EI+197 sec.; Mach = 27.0; Altitude = 300,003 ft; Alpha = 40°; Dyn. press. = 1.6 psf.
DSMC Point AA EI+ 91 sec.; Mach = 25.1; Altitude = 350,274 ft; Alpha = 41°; Dyn. press. = 0.1 psf

Figure 5.2.4-25 presents the flow field Mach number distribution around the Orbiter as predicted by the LAURA code. Two views are shown – a pitch plane cut and a constant span cut through Panel 9. The first view shows that the bow shock is relatively close to the windward surface of the vehicle for the nominal 40-degree angle-of-attack re-entry. The second view shows that the distance between the Panel 9 wing leading edge surface and the shock is approximately 7 inches for a flight condition near Mach 25. Figure 5.2.4-26 and Figure 5.2.4-27 present the flow field number density distribution around the Orbiter for DSMC Points AA and A as predicted by the DAC code. The view shown is of the x-z plane down the centerline of the vehicle. Since the conditions of DSMC Points AA and A are more rarefied than the CFD points, the boundary layers shown in Figure 5.2.4-26 and Figure 5.2.4-27 merge with the shock layer,

creating a large compression region. This effect is more pronounced in Figure 5.2.4-26, with DSMC Point AA being the most rarefied.

Table 5.2.4-4 Nominal Geometry Hypersonic Orbiter Simulations at Flight Conditions

Trajectory Point		Common Baseline Grid			Modified Common Baseline Grid	Initial Grids	
	DAC	GASP	LAURA	USA	SACCARA	GASP	LAURA
AA	X	N/A	N/A	N/A		N/A	N/A
A	X	Noneq				Noneq & FC	Noneq
B		Noneq	Noneq	Eq		Noneq & FC	Noneq
1		Noneq	Noneq	Noneq & Eq		Noneq & FC	Noneq
2		Noneq				Noneq & FC	Noneq
3		Noneq	Noneq	Noneq & Eq		Noneq & FC	Noneq
4		Noneq				Noneq & FC	Noneq
5		Noneq				Noneq & FC	Noneq
6		Noneq				Noneq & FC	Noneq
VN					Eq		

Surface streamlines are presented in Figure 5.2.4-28 for the wing leading edge region at CFD point 1. An attachment line exists along the leading edge, which separates the flow that remains on the windward side from the flow that is swept over onto the leeward side of the vehicle. Note that the flow moves outboard along the attachment line. These streamlines provide an indication of where local disturbances on the surface will propagate downstream on the vehicle. Figure 5.2.4-29 through Figure 5.2.4-34 present the surface pressure distributions in the wing leading edge region for CFD Points 1 and 6 and DSMC Points AA and A, respectively. Absolute pressures in pounds per square foot (psf) are presented along with pressure coefficients. The pressure coefficient is defined as,

$$C_p = \frac{P_{local} - P_\infty}{\frac{1}{2}\rho_\infty V_\infty^2}$$

where P_{local} = local surface pressure, P_∞ = free stream atmospheric pressure, ρ_∞ = free stream atmospheric density, and V_∞ = relative velocity of vehicle. The pressure distributions for the CFD and DSMC flight conditions are very similar as depicted by the pressure coefficients. However, the wing leading edge peak pressure magnitudes change from ~0.001 psf at Mach 25.1 and 350,000 ft, ~0.01 psf at Mach 27.0 and 300,000 ft, ~35 psf at Mach 24.9 and 243,000 ft, and finally to ~140 psf at Mach 17.9 and 200,000 ft.

Figure 5.2.4-35 through Figure 5.2.4-40 present both the heat flux and Stanton number distributions on the wing leading edge region. The Stanton number is defined as,

$$St = \frac{q}{\rho_\infty V_\infty H_{total}}$$

where q = local heat flux, and H_{total} = total free stream enthalpy. The quantity $\rho_\infty V_\infty H_{total}$ is a measure of the total energy in the flow field and therefore the Stanton number provides an indication of how much of the total energy contained within the flow is transferred to the surface of the vehicle. Thus, a value of 1.0 for the Stanton number corresponds to complete energy accommodation to the surface. The results shown in Figure 5.2.4-35 Figure 5.2.4-36 , Figure 5.2.4-37 , and Figure 5.2.4-38 illustrate that the heating

distributions are very similar over the Mach 24.9 to 17.9 range, with the peak heat flux occurring along the attachment line of leading edge in the vicinity of RCC panels 8 and 9. Because the Orbiter GN&C attempts to guide the vehicle along a constant heat flux boundary between these Mach numbers, it should be expected that the peak heat flux remains fairly consistent in these illustrations. One additional observation is worthwhile. The Navier-Stokes results included here predict the magnitude of the peak heat flux in the region of leading edge panel 8 to be in the 38 to 40 Btu/ft^2-sec range. However, DeVenezia, et al. have shown that flight data typically indicate values of approximately 50 Btu/ft^2-sec for the same region. Clearly, the CFD results tend to under-predict the heating to this leading edge region of the vehicle. To date, no comprehensive Navier-Stokes calibration effort has ever been undertaken using the available Orbiter re-entry leading edge heating data.

However, an engineering code, XF0002, developed by Boeing and calibrated with Orbiter flight data can be used to predict peak heat fluxes to leading edge panel 9. The RCC panel 9 flight certified indicator in XF0002 is known as BP (Body Point) 5505. The XF0002 predicted heat flux and surface temperature histories are provided in Figure 5.2.4-41.

While the DSMC heating distributions at Mach 25.1 and Mach 27.0 are somewhat similar to those of the two CFD points, the area where the peak heat flux occurs along the attachment line of leading edge panels 8 and 9 is not as well defined, especially for DSMC Point AA. This lack of definition is due to the more diffuse nature of the flow under rarefied conditions. In addition, the significantly lower density at DSMC Points AA and A results in a peak wing leading edge heating rate of only about 2 Btu/ft^2-sec and 10 Btu/ft^2-sec, respectively. Note from Figure 5.2.4-35 and Figure 5.2.4-36 that the peak Stanton number for the continuum conditions is only 2 to 5%, while in Figure 5.2.4-38 and Figure 5.2.4-40 the peak Stanton number is approximately 25 to 50%. This is because at the rarefied high altitude conditions corresponding to DSMC Points AA and A, the flow is non-continuum. As a vehicle approaches completely rarefied conditions, where individual molecules do not interact, the Stanton number for a fully accommodated surface approaches 1 at the stagnation point. This rarefied flow effect is thus evident at the peak heating location on the wing leading edge, as illustrated in the DSMC heating figures.

Figure 5.2.4-42 presents radiation equilibrium surface temperature distributions for the wing leading edge region for CFD Points 1 and 6. The peak temperatures are along the leading edge attachment line and highest on Panels 8 and 9. As discussed previously, the peak temperatures predicted by the CFD codes are low and flight-calibrated values are presented in Figure 5.2.4-41. Figure 5.2.4-43 and Figure 5.2.4-44 show the radiation equilibrium surface temperature distribution for the wing leading edge region at DSMC Points AA and A. Note that no further discussion of the nominal geometry DSMC results will be included here, since the discussion to follow was important to the STS-107 investigation only for the continuum regime.

Another critical aspect of the flow environment experienced by the Orbiter during re-entry is the extreme gradients in flow field properties between the vehicle surface and the free stream. In order to illustrate these gradients, three locations in the leading edge (LE) region were selected to provide estimates of the local boundary-layer thickness, total enthalpy profiles, and static temperature profiles near the surface. Figure 5.2.4-45 provides a sketch describing the location of these three points – LE Panel 6, LE Panel 9 and Main Landing Gear Door forward outboard corner.

Figure 5.2.4-46 through Figure 5.2.4-51 provide predictions of the total enthalpy and static temperature variation of the gas near the surface of the Orbiter. These profiles for the CFD Point 1 flight condition, Mach 24.9 at an altitude of 243,000 feet, are provided in Figure 5.2.4-46 - Figure 5.2.4-48 for the locations shown in Figure 5.2.4-45 . On each of these plots the estimated boundary-layer thickness is noted. This estimate was obtained by locating the distance from the surface that the total enthalpy attains a value approximately 99% of the total free-stream value of 11,730 Btu/lb$_m$. For the 243,000 ft flight condition, the gas static temperatures are approximately 10,000 degrees Rankine at the boundary-layer edge. The thinnest boundary layer occurs at Panel 9. Figure 5.2.4-49 - Figure 5.2.4-51 provide the same information at the CFD Point 6 flight condition, Mach 17.9 and an altitude of 201,000 feet. For this flight condition, the boundary layer is considerably thinner at Panel 9 with a thickness of ~0.3 inches and the edge gas temperatures have decreased to about 7,000 degrees Rankine. This decrease in total enthalpy or total temperature corresponds to a decrease in kinetic energy of the Orbiter by approximately

40% between the conditions at CFD Point 1 and 6. Thus, roughly one-half the energy of the vehicle had been dissipated by the time Columbia reached LOS at about Mach 18.

Species concentration comparisons in the shock layer ahead of LE Panel 9 and the Orbiter nose stagnation point are provided in Figure 5.2.4-52 and Figure 5.2.4-53, respectively. These predictions were obtained from the LAURA solution at CFD Point 1. At the nose, the shock is approximately 2.5 inches from the surface and at Panel 9 it is about 7 inches from the surface. For both locations the oxygen is completely dissociated, thus only atomic oxygen is present in the shock layer. However, very near the surface some recombination occurs as the atomic oxygen mass fractions drop slightly. If the surface had been modeled as a fully catalytic surface instead of with the catalysis properties for the Reaction Cured Glass tile coating, full recombination of oxygen would have been predicted. For the nose shock layer, a significant amount of the nitrogen is dissociated with a peak atomic nitrogen mass fraction of about 0.38. This is in contrast to the Panel 9 shock layer, where the atomic nitrogen mass fraction is less than 0.1.

5.2.4.4.3 Orbiter Forebody CFD–Chin Panel / Vent Nozzle Cases

A focused set of simulations was conducted to investigate the anomalous chin panel and vent/dump nozzle instrumentation responses. See Section 5.2.1 for more information on the anomalous flight data characteristics. One theory to explain the increase in the temperature rise at the vent/dump nozzles is that an increase in sideslip angle moved the vortex at the wing body junction closer to the Orbiter fuselage, producing the increased heating. Thus, an effort to determine if the small changes in the angle of sideslip at those flight conditions could produce increased heating at the relevant vehicle OML locations was investigated. . In order to evaluate these anomalies, the common baseline grid of the nominal Orbiter was truncated at 50% of its length and additional grid, equivalent to what was removed by deleting the aft, was applied to the forebody. The resulting grid system had twice the resolution in the streamwise and circumferential directions compared with the baseline common mesh. The highly refined forebody grid were developed in order to provide the most accurate solution possible. In addition to flight simulations using the forward one-half of the Orbiter, a calibration was performed at wind tunnel conditions before attempting the flight simulations.

<u>OH109 Orbiter Wind Tunnel Test Overview</u>

Test OH109 was designed to investigate the effect of sideslip on heat transfer rate. The test was performed at Mach 8 for a range of Reynolds numbers and sideslip angles. A 0.04 scale thin-walled model of the shuttle was used in the experiment. The model was instrumented with thermocouples, and included thermocouples near the vent nozzles. These wind tunnel data provided a direct measurement of temperature rise rate near the vent nozzles and heat transfer data to benchmark the simulation tools.

The wind tunnel test measured the temperature rise rate on the surface of the model. The wind tunnel conditions were a Mach number of 8, side slip angle of –2.02°, -1.01°, -0.5°, 0.0°, angle of attack of 40.0, and a Reynolds number of $5x10^5$/ft. The flight vehicle was nominally at a Mach number of 24, angle of attack of 40°, a wind-corrected sideslip angle of 0.2°, and Reynolds number of $8x10^3$/ft when the instrumented vent nozzles recorded a doubling of the temperature rise rate. If the nominal temperature rise rate is measured at 0° sideslip, doubling the 0° sideslip temperature rise rate measured in the wind tunnel should produce a curve analogous to the off-nominal temperature rise rate observed in flight. In Figure 5.2.4-54 the white line near the wing-body junction is the vortex core location. Figure 5.2.4-55 shows the Orbiter forebody on the right and wind tunnel data comparisons on the left. The representative off-nominal curve shown in Figure 5.2.4-55 is the value the temperature rise rate would need to reach in order to match the increase observed in flight. The representative off-nominal curve is the dark line with no symbols. The arrow points to a line of thermocouples that are used for comparison in the image on the left. The red circles on the shuttle forebody are the location of the water dump, waste dump and vacuum nozzles. The plot on the left shows the temperature rise rate for sideslip angles from–2° to 0°. The wind tunnel data show only a moderate increase in temperature rise at a sideslip angle of –2°. The increase is approximately 20%, substantially less than the factor of two increase required to resemble the flight data. While the wind tunnel test did not match flight conditions and did not capture all the physical

phenomena that occurs in flight, the general data trend should be captured. Thus, the theory that the underlying cause of increased temperature rise rate is a sideslip effect is not supported by the available wind tunnel data. Even at an order of magnitude larger sideslip angle than the slip angle observed in flight, the increase in temperature rise rate from the wind tunnel data is only 20% of the flight observed increase.

Wind Tunnel Test OH109 Comparisons with Simulations

The experimental data taken in test OH109 provided an opportunity to benchmark the SACCARA prediction of heat transfer rates. A simulation was run on the truncated common baseline grid. The conditions computed matched the OH109 test: Mach number of 7.83, angle of attack of 40.04°, sideslip angle of -1.01°, Reynolds number of 4.938×10^5 and wall temperature of 505 °R. Figure 5.2.4-56 shows pressure contours along the centerline and the outflow boundary. Streamlines were placed near the wing-body junction vortex. Also, comparisons with the experimental data were made with a normalized heat transfer coefficient using the following definitions:

TT = tunnel total temperature, °R
QDOT = heat transfer rate, BTU/ft^2-sec
TW = wall temperature, °R
H(TT) = QDOT/(TT-TW), BTU/ ft^2-sec-°R
H(REF) = heat transfer coefficient derived from a Fay and Riddell based equilibrium stagnation point heating

Figure 5.2.4-57 shows the computed normalized heat transfer coefficient on both the in-wind side and the out-of-wind side, where the simulation results are co-plotted with the experimentally measured in-wind heat transfer coefficient. The Y- data were extracted from the simulation in-wind side and the Y+ data were extracted from the out-of-wind side. The comparisons are shown along the line of thermocouples indicated by the arrow shown in the right hand image. The diamonds depicted on the Orbiter fuselage represent the experimental data locations shown in the figure.

As illustrated in Figure 5.2.4-57, the in-wind and out-of-wind results have the same trends with a maximum change of approximately 20% in heat transfer coefficient. The simulation predicts a higher heat transfer coefficient that the experimental data. However, in comparison with the wind tunnel data, the predictions provide a conservative estimate of the heating rate. The in-wind and out-of-wind results show only modest differences in the heat transfer coefficient for the sideslip angle considered. An on-going study is under way to quantify the grid independence of the simulations. In addition, the experimental uncertainty in the OH109 data needs to be quantified before any conclusions can be drawn.

Simulation at flight conditions

One possible explanation for the flight observed temperature rise rate increase on the vent nozzles is that a gap or step located at the chin panel could have introduced a localized region of turbulent intermittency. The approach taken to examine this possible explanation was to run a simulation of the flight condition where the rise rate was observed, and to use the predicted surface quantities to determine where a disturbance would have to originate to affect the vent nozzles. Flight conditions for the simulation were selected based on the timesat which the vent nozzles were showing an increased rise rate, as in Section 5.1.2. The free stream conditions for this case use the VN (vent nozzle) identifier and are provided in the Aerodynamics section. Roughly, the conditions for the vent nozzle case are a Mach number of 24, altitude of 235,000 ft, with an angle of attack of approximately 40° and sideslip angle of -0.5°. The simulation was run on the same truncated common baseline grid used in the wind tunnel calibration study discussed above. Of particular interest in the flight simulation results is the behavior of the surface streamlines integrated from the surface shear stress vector. These streamlines should provide insight into the path a disturbance would follow. In Figure 5.2.4-58 , the water dump nozzle location and the vacuum vent location are indicated by the red circles, while the waste dump nozzle and thermocouple V07T9522A are shown in black. Figure 5.2.4-58 shows a number of streamlines on the Orbiter surface, along with colored contours of shear stress magnitude. The results show that the flight measurements are all located along the reattachment line. In relation to the attachment line, the vacuum nozzle is

located near its center, the waste dump nozzle is located below it, and the water dump nozzle and thermocouple are located above it. Figure 5.2.4-59 shows surface streamlines passing through the measurement locations for the vent/waste dump nozzle temperature instruments. The streamlines are tightly packed together until they reach the vacuum vent nozzle, where they begin diverging from one another. On the left of Figure 5.2.4-60 is an image of the front view, and on the right side is a close up of the nozzle. The front view shows that a disturbance in the chin panel region could propagate back to the nozzle locations. The close up of the nozzle locations shows that a disturbance could affect each nozzle differently, but with three streamlines passing the measurement locations, a clear case cannot be made. The simulation results do support the theory that a chin panel disturbance could have been the cause of the temperature rise rate. However, these results do not provide enough evidence to draw any conclusions. Since the temperature rise-rate returned to its nominal behavior after about 15 seconds of abnormality, it is very difficult to make any firm conclusions without additional data.

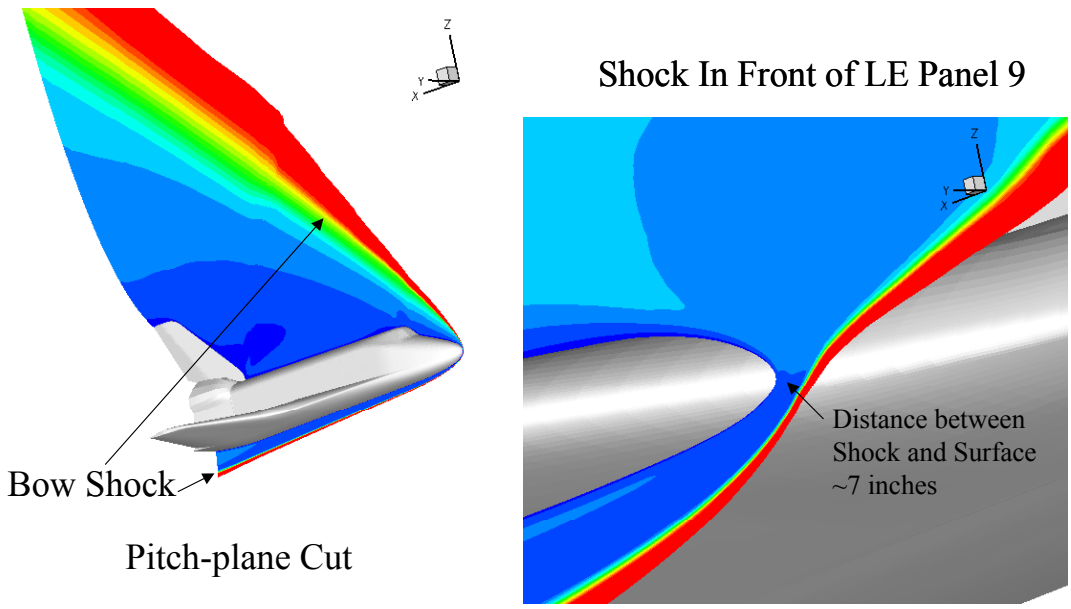

Figure 5.2.4-25 Shock Wave Structure around the undamaged Orbiter at CFD Point 1

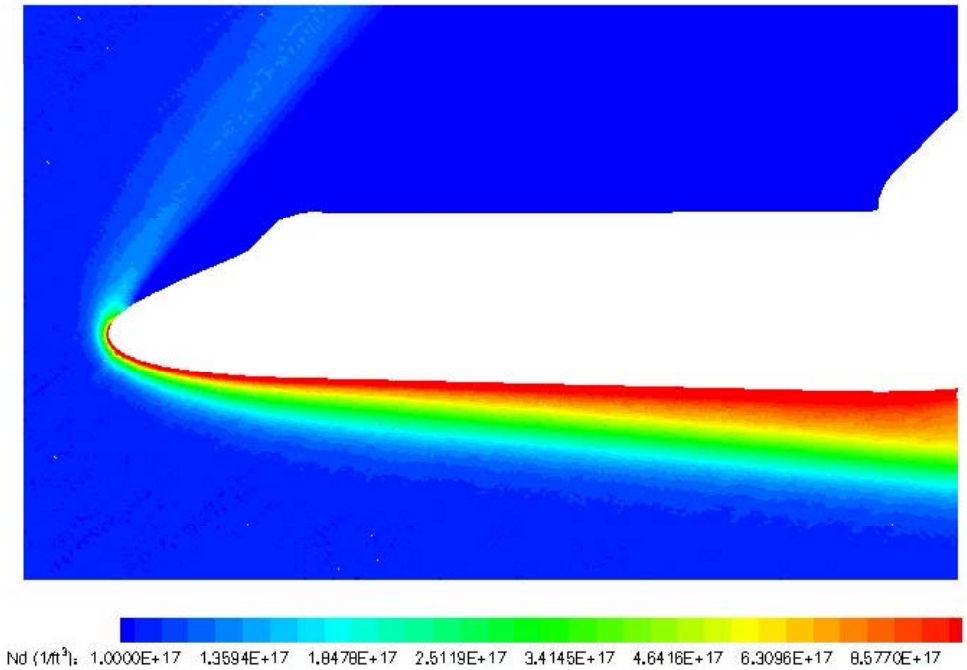

Figure 5.2.4-26 Number Density Distribution around Orbiter for DSMC Point AA

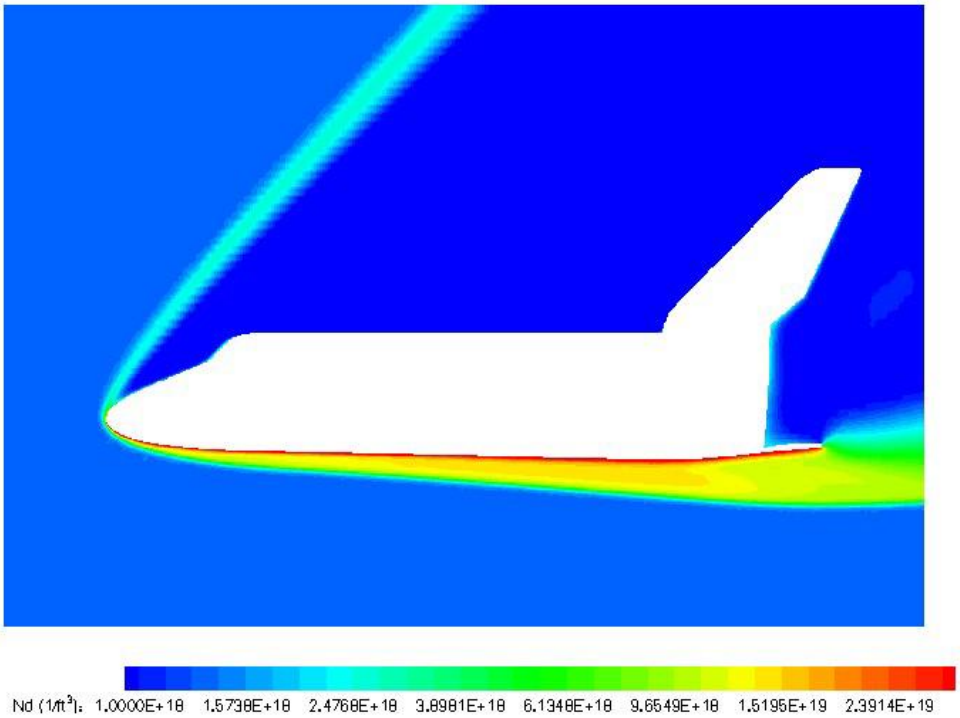

Figure 5.2.4-27 Number Density Distribution around Orbiter for DSMC Point A

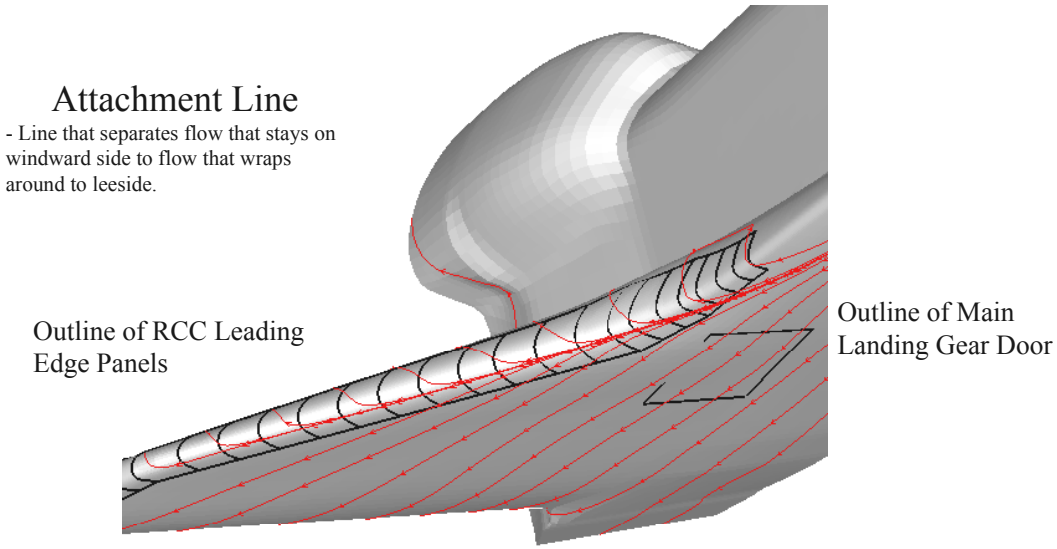

Figure 5.2.4-28 Surface Streamlines in the Wing Leading Edge Region

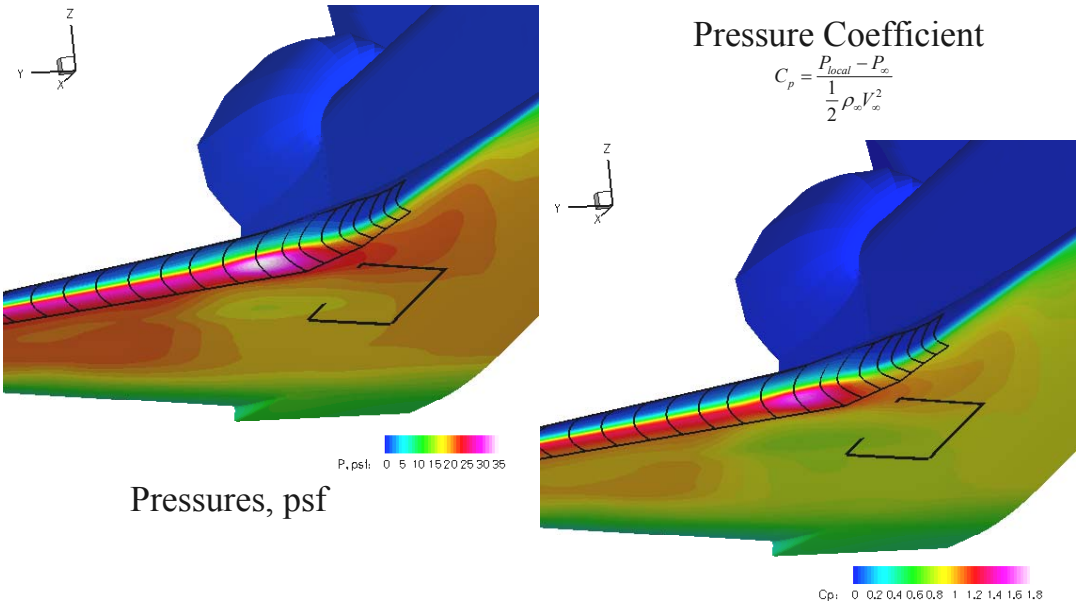

Figure 5.2.4-29 Surface Pressures for CFD Point 1, Mach 24.9

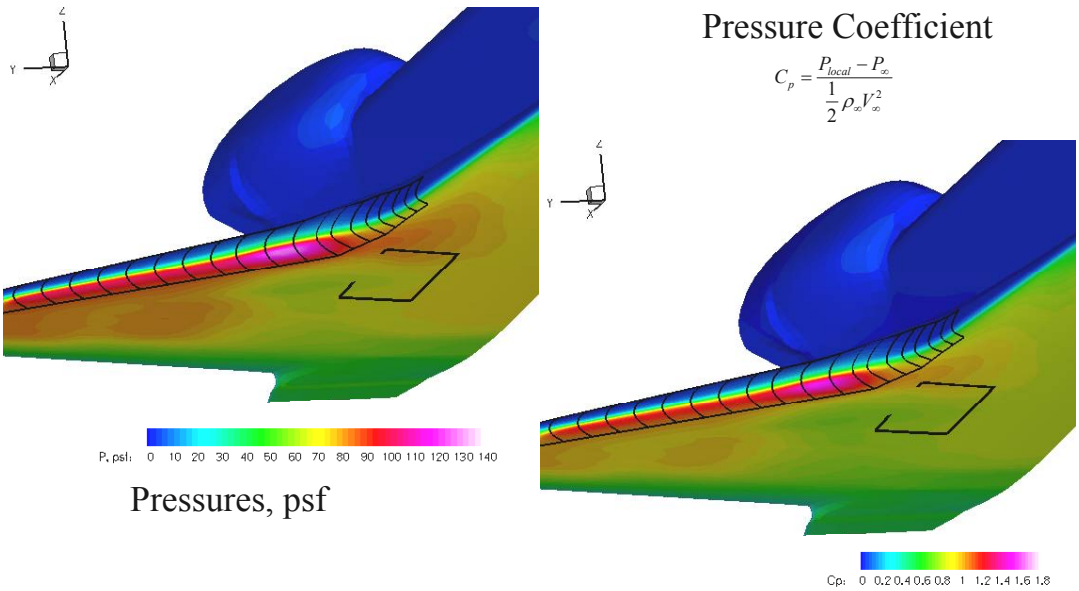

Figure 5.2.4-30 Surface Pressures for CFD Point 6, Mach 17.9

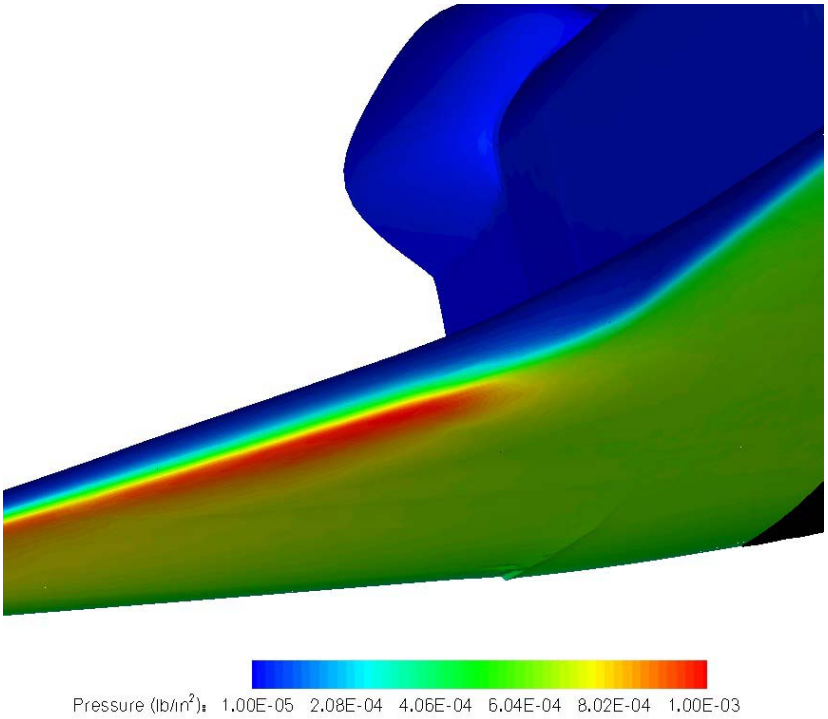

Figure 5.2.4-31 Surface Pressure for DSMC Point AA, Mach 25.1

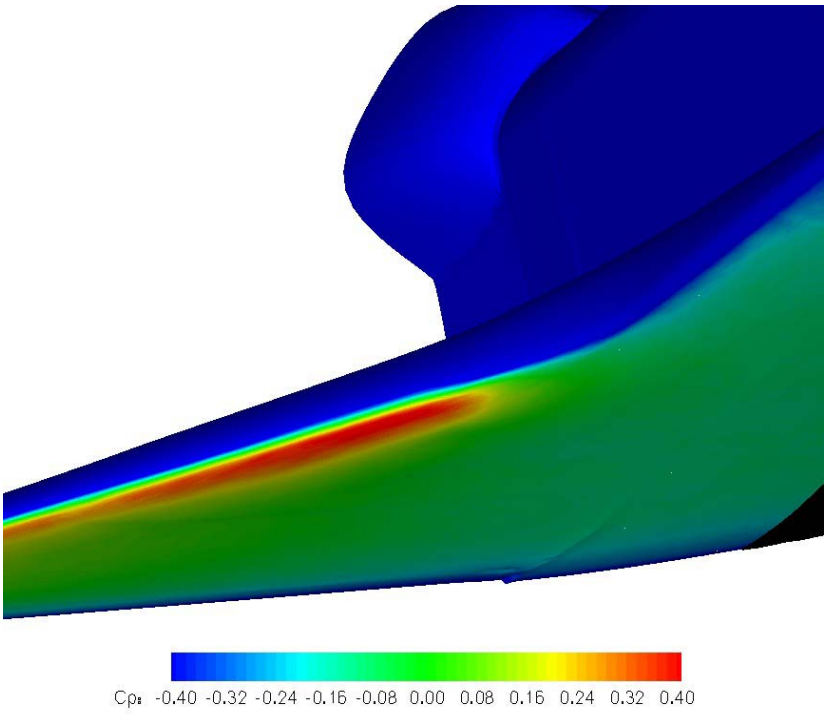

Figure 5.2.4-32 Surface Pressure Coefficient for DSMC Point AA, Mach 25.1

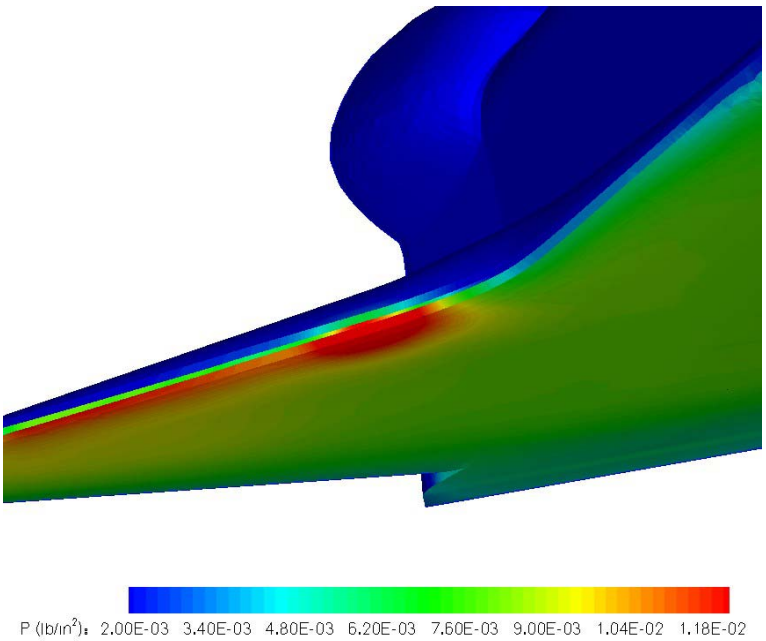

Figure 5.2.4-33 Surface Pressure for DSMC Point A, Mach 27.0

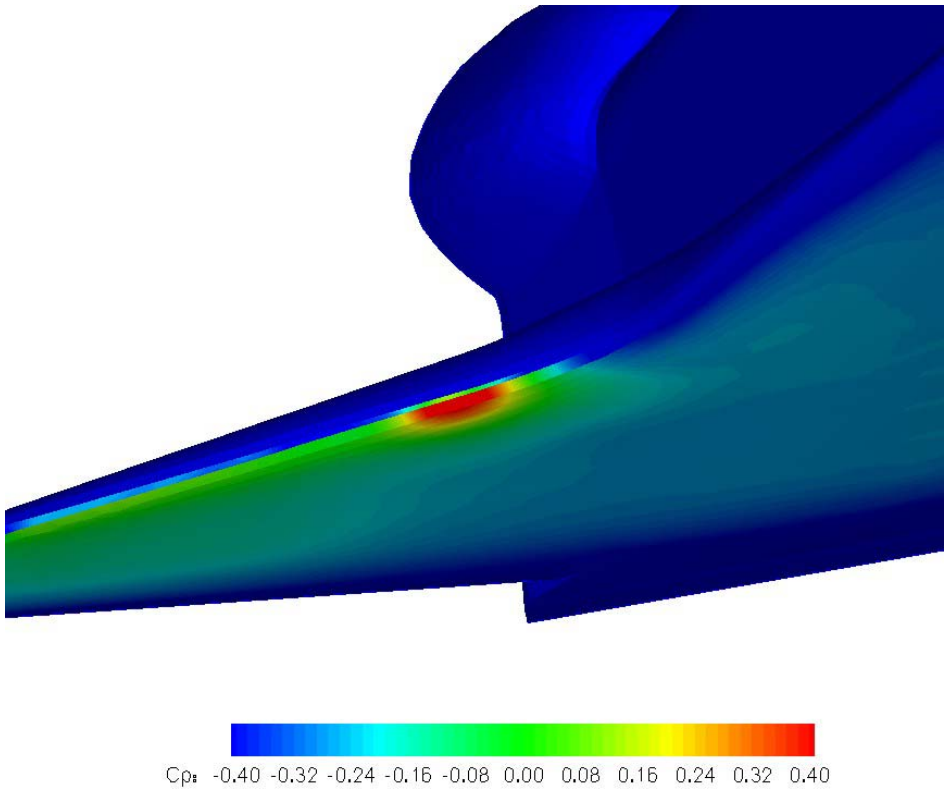

Figure 5.2.4-34 Surface Pressure Coefficient for DSMC Point A, Mach 27.0

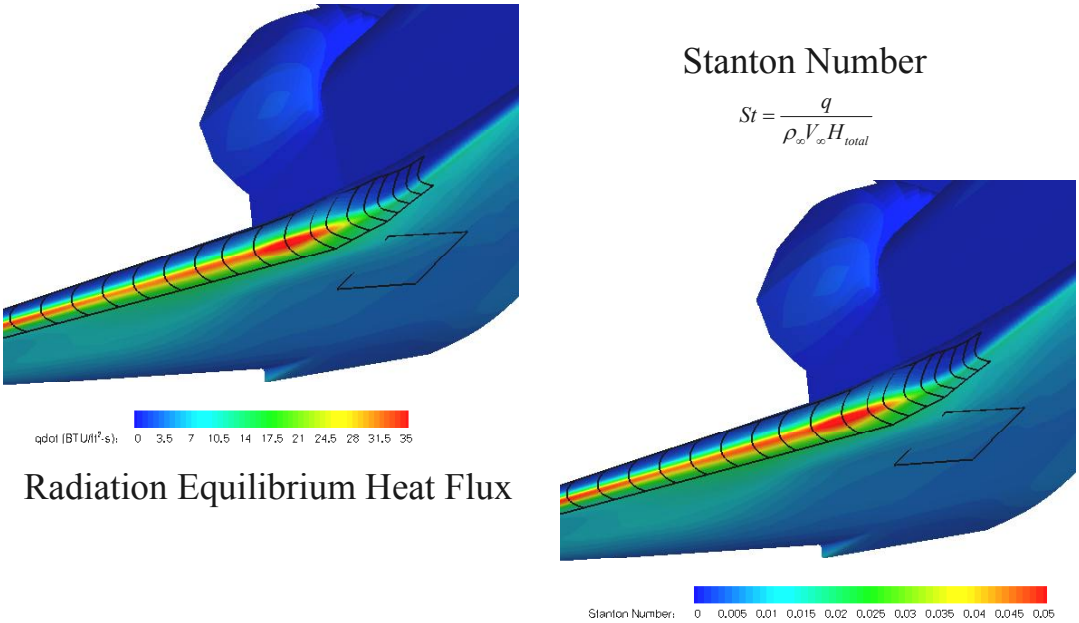

Figure 5.2.4-35 Surface Heat Flux Distributions for CFD Point 1, Mach 24.9

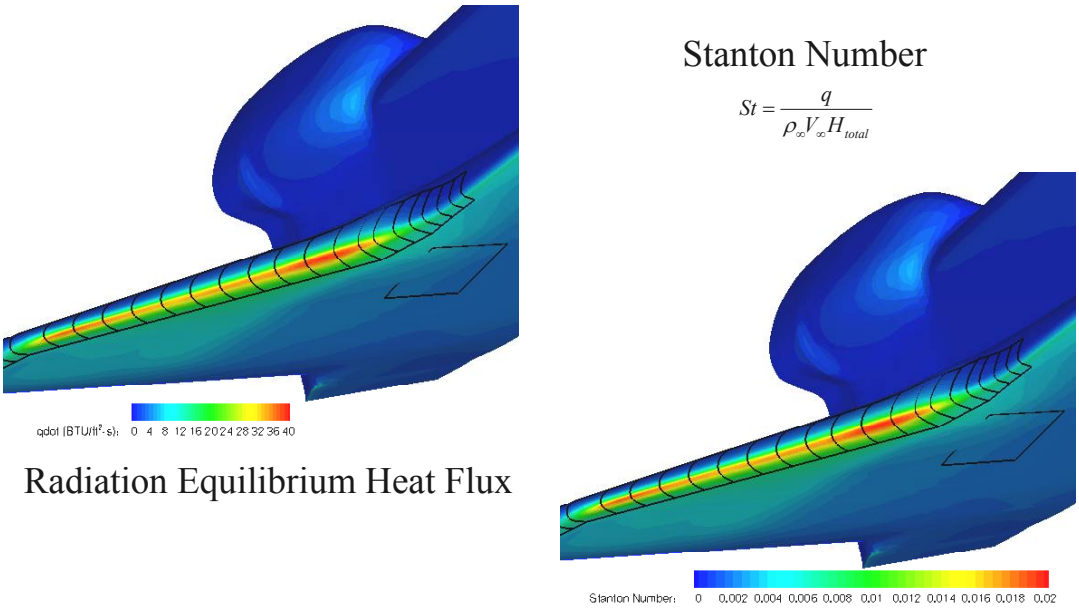

Figure 5.2.4-36 Surface Heat Flux Distributions for CFD Point 6, Mach 17.9

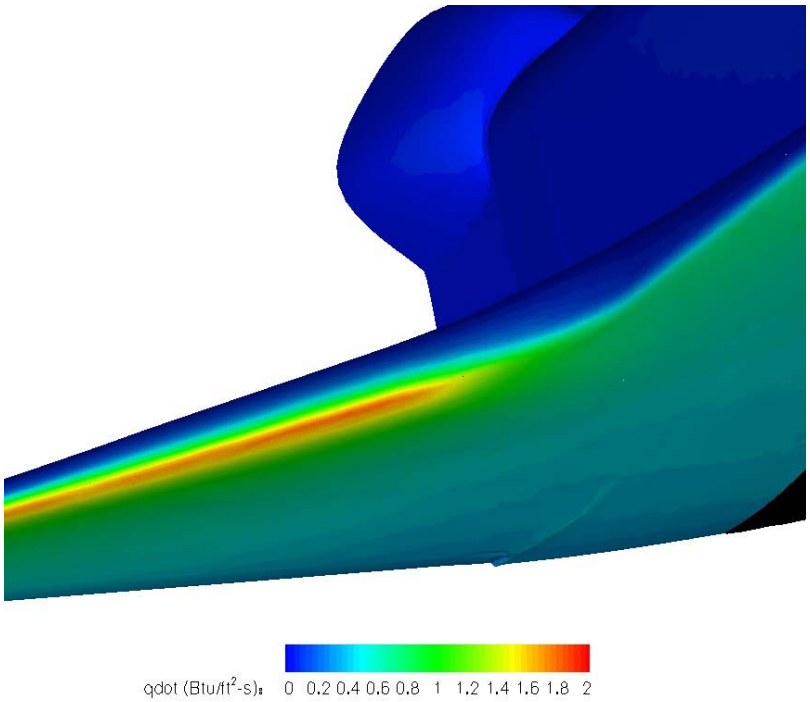

Figure 5.2.4-37 Surface Heat Flux Distribution for DSMC Point AA, Mach 25.1

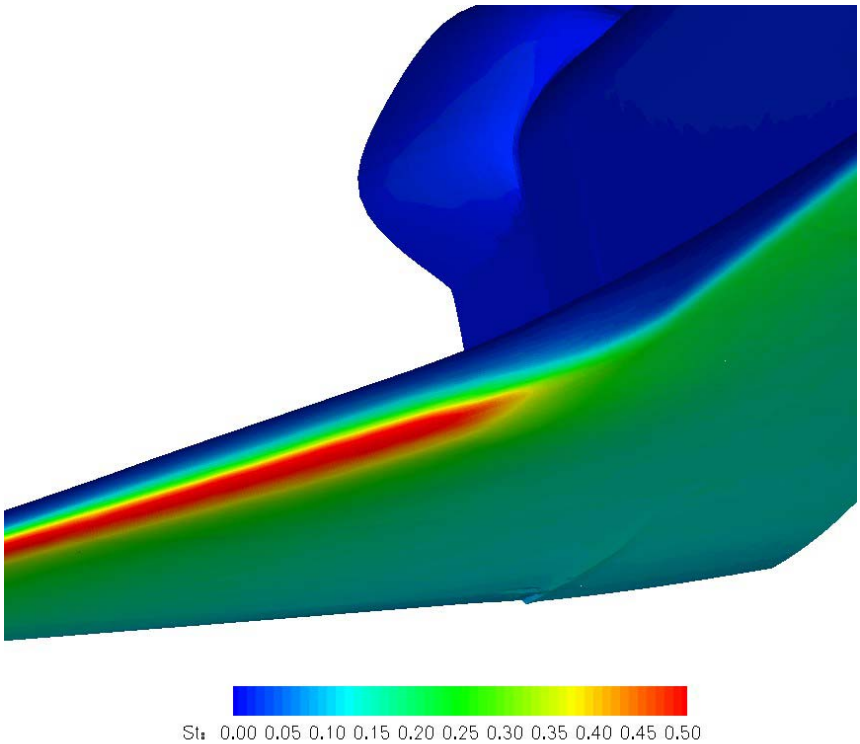

Figure 5.2.4-38 Stanton Number Distribution for DSMC Point AA, Mach 25.1

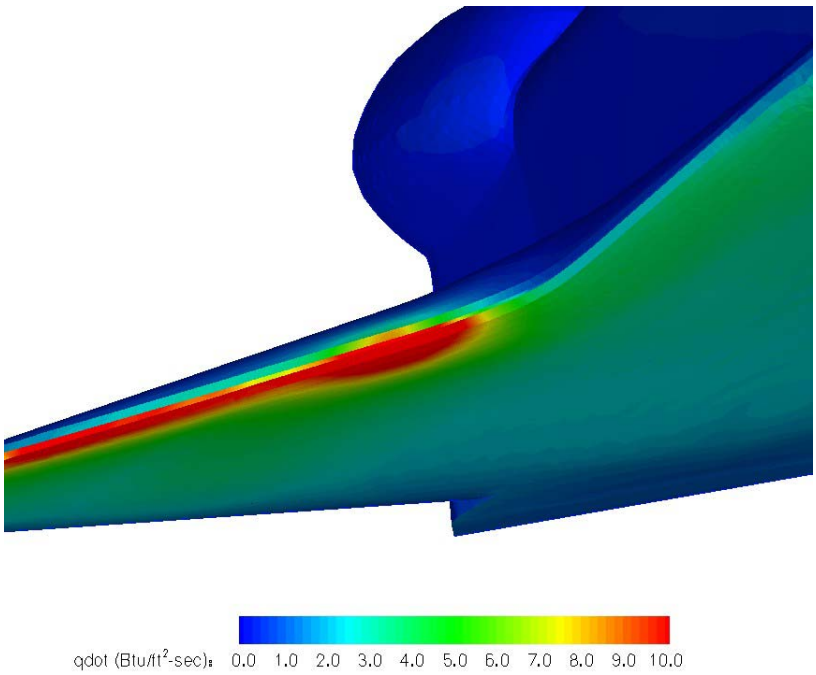

Figure 5.2.4-39 Surface Heat Flux Distribution for DSMC Point A, Mach 27.0

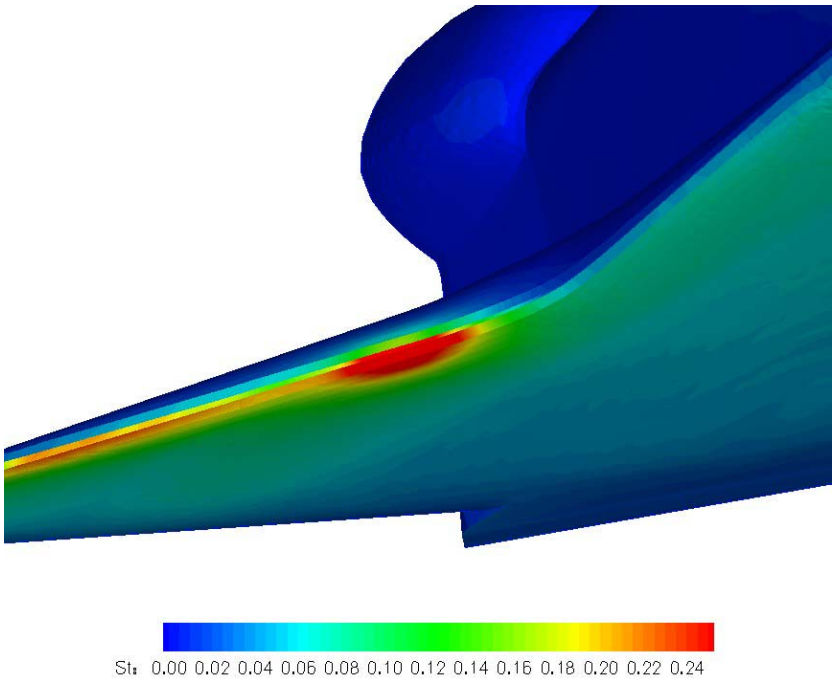

Figure 5.2.4-40 Stanton Number Distribution for DSMC Point A, Mach 27.0

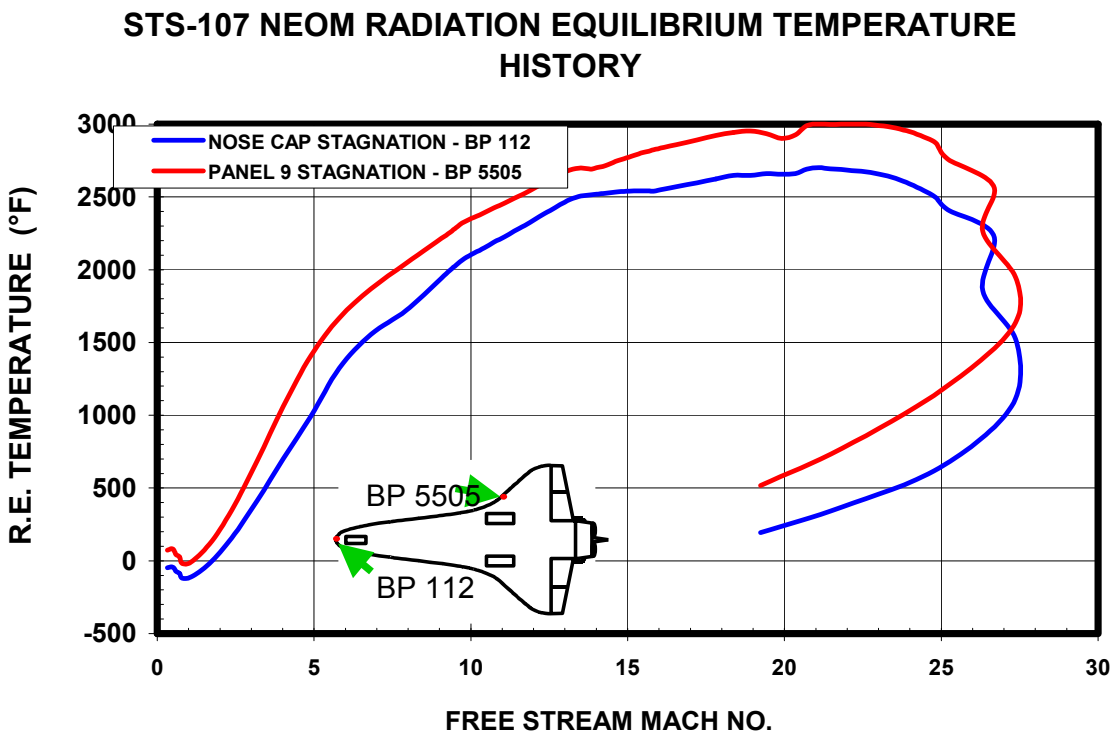

Figure 5.2.4-41 Flight Calibrated Estimate of Peak Heat Flux History on Panel 9

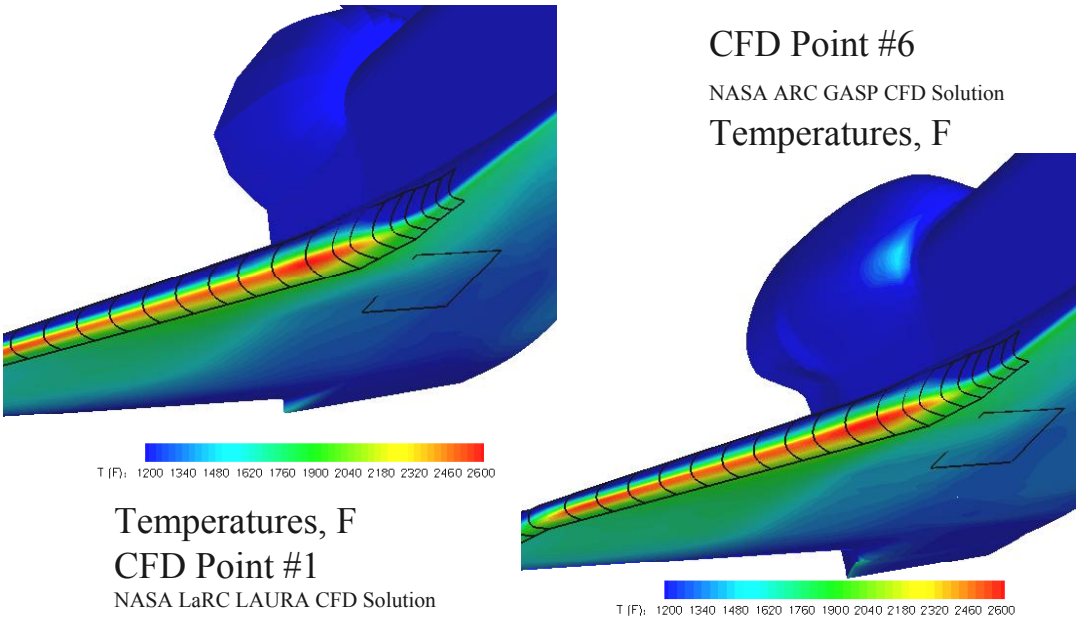

Figure 5.2.4-42 Radiation Equilibrium Surface Temperatures In the Wing Leading Edge Region

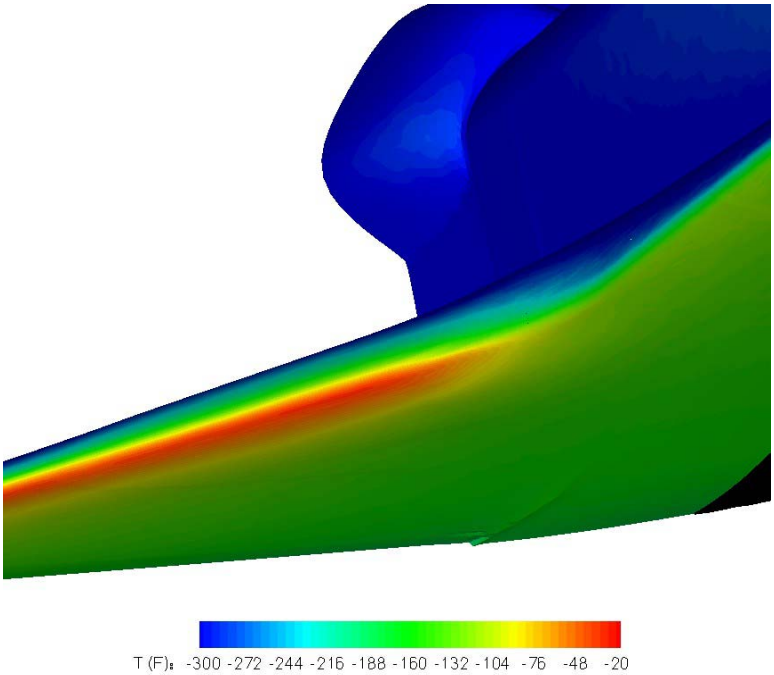

Figure 5.2.4-43 Radiation Equilibrium Surface Temperatures In the Wing Leading Edge Region for DSMC Point AA

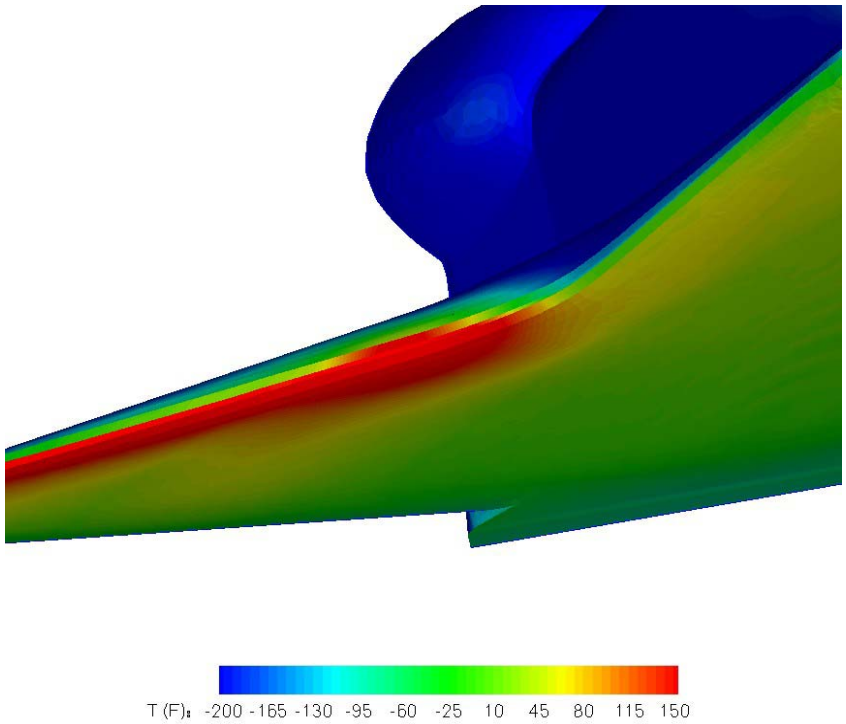

Figure 5.2.4-44 Radiation Equilibrium Surface Temperatures In the Wing Leading Edge Region for DSMC Point A

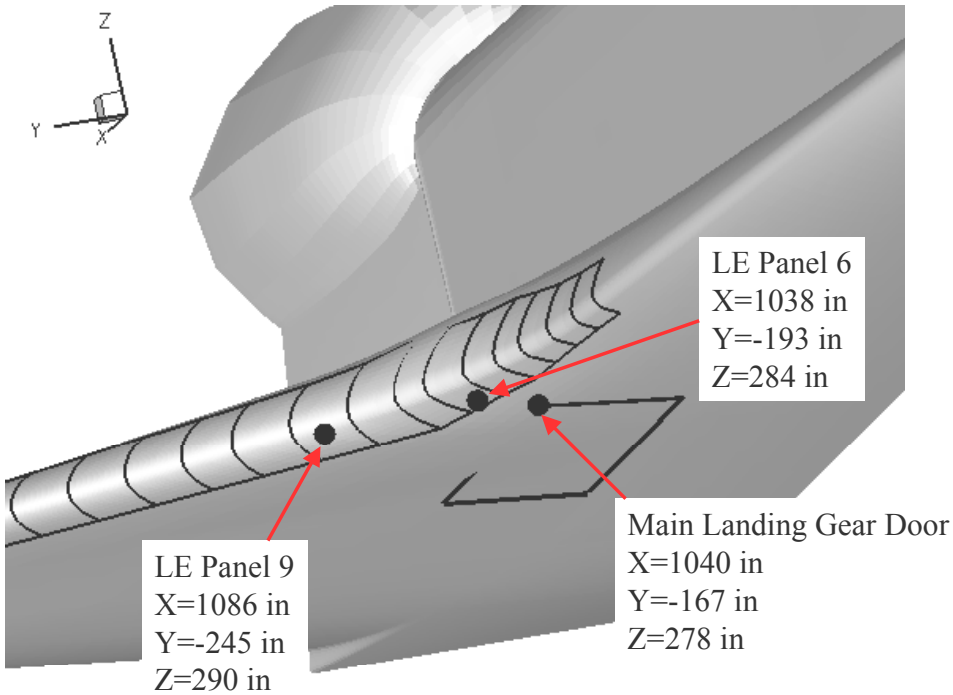

Figure 5.2.4-45 Boundary-layer Temperature and Enthalpy Profile Locations on Orbiter

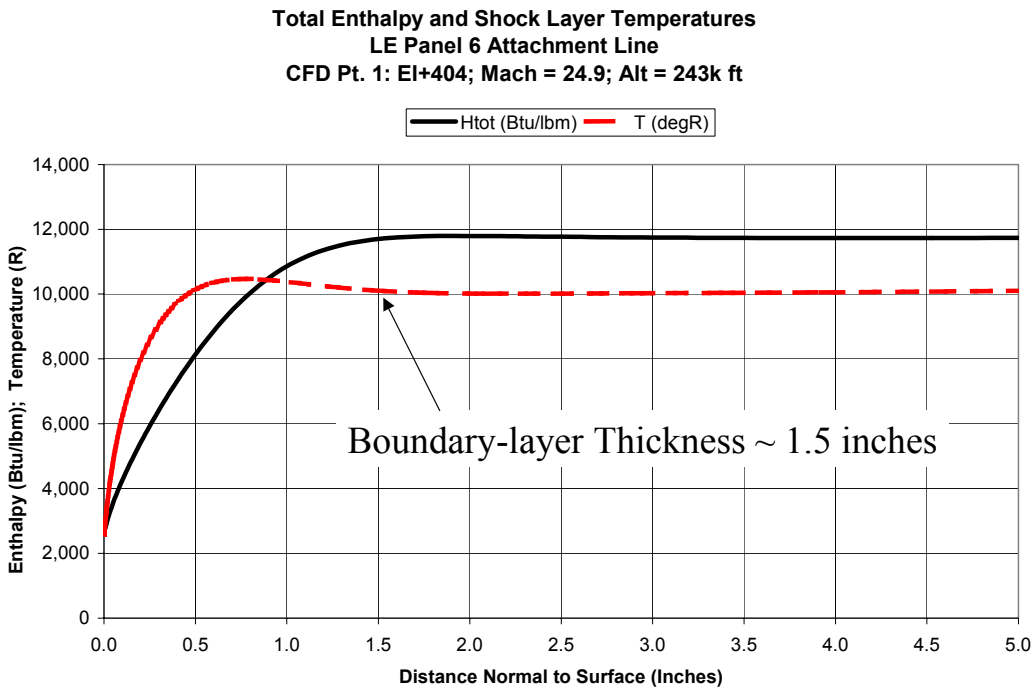

Figure 5.2.4-46 Total Enthalpy and Static Temperature Variation from LE Panel 6 Surface into Flow Field: CFD Point 1, Mach 24.9

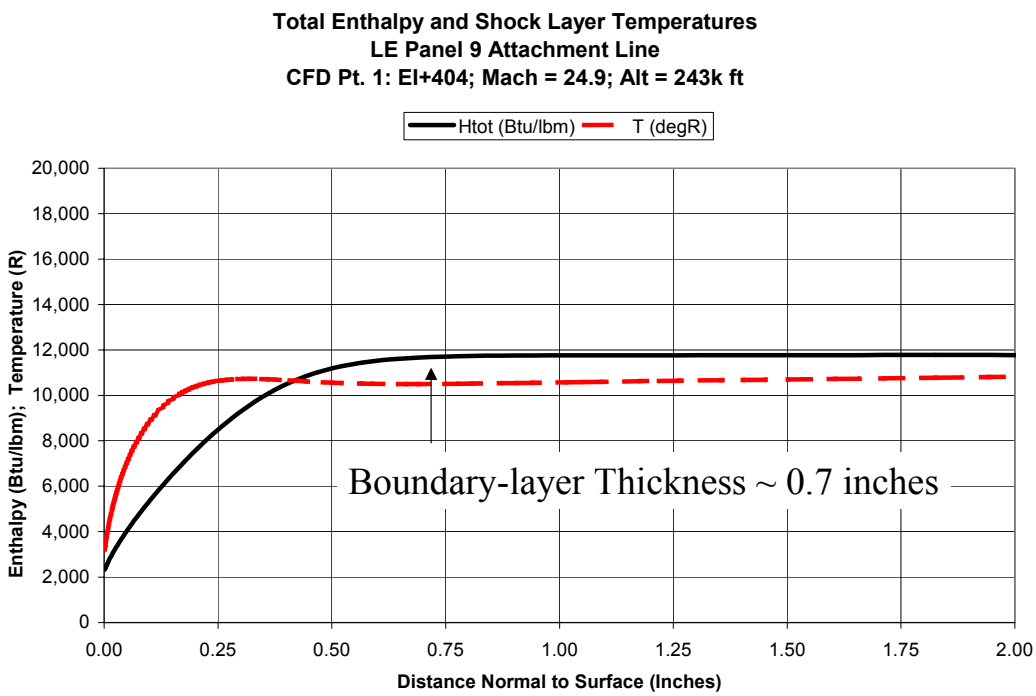

Figure 5.2.4-47 Total Enthalpy and Static Temperature Variation from LE Panel 9 Surface into Flow Field: CFD Point 1, Mach 24.9

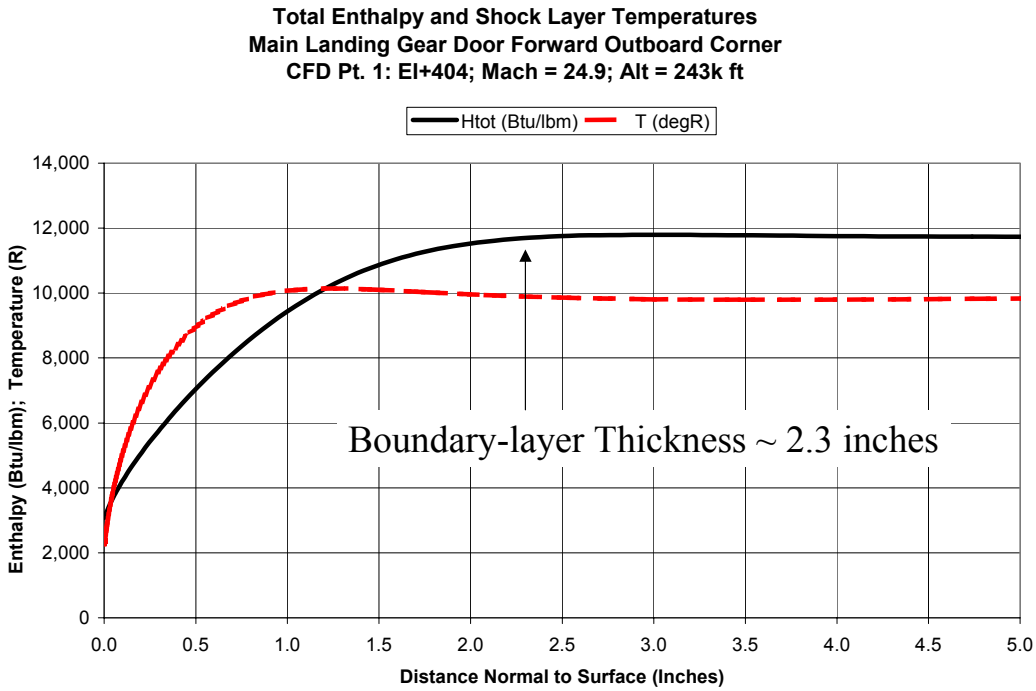

Figure 5.2.4-48 Total Enthalpy and Static Temperature Variation from Main LG Door Surface into Flow Field: CFD Point 1, Mach 24.9

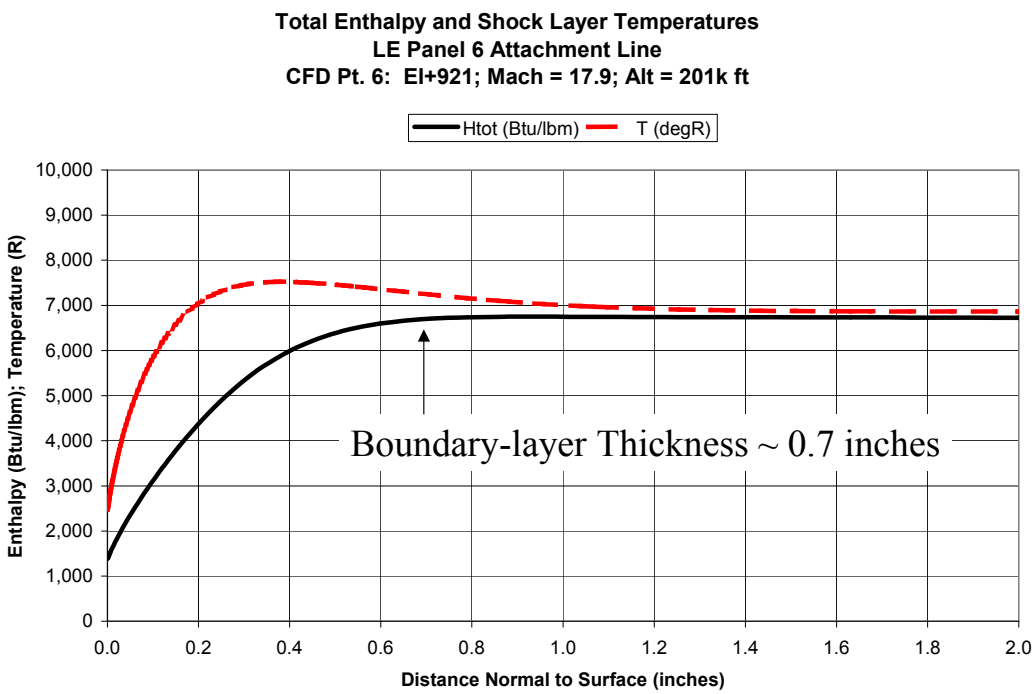

Figure 5.2.4-49 Total Enthalpy and Static Temperature Variation from LE Panel 6 Surface into Flow Field: CFD Point 6, Mach 17.9

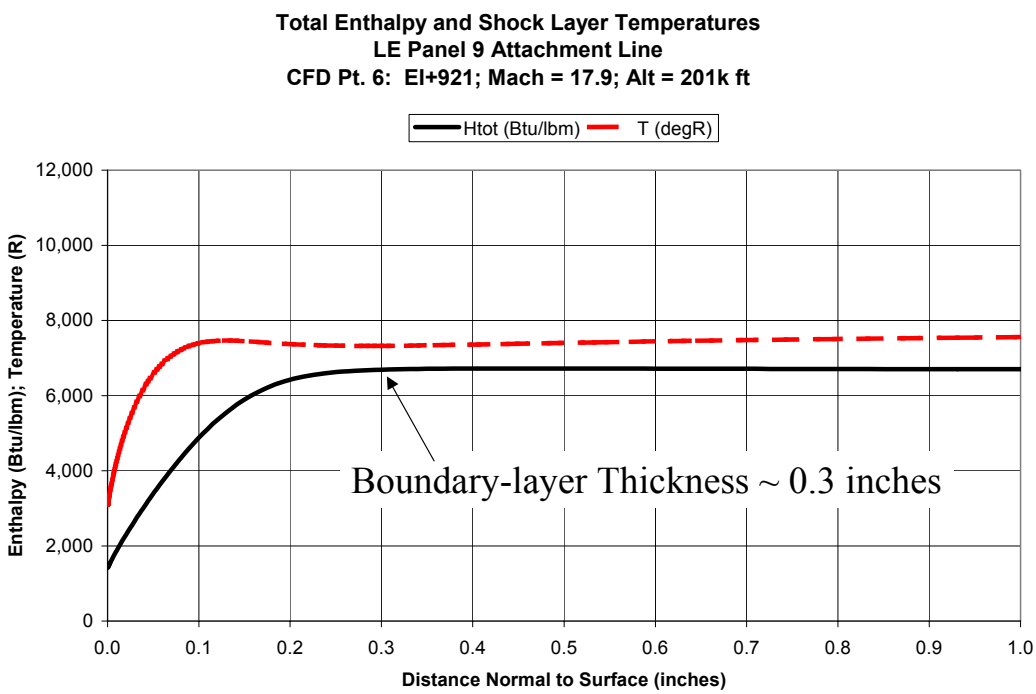

Figure 5.2.4-50 Total Enthalpy and Static Temperature Variation from LE Panel 9 Surface into Flow Field: CFD Point 6, Mach 17.9

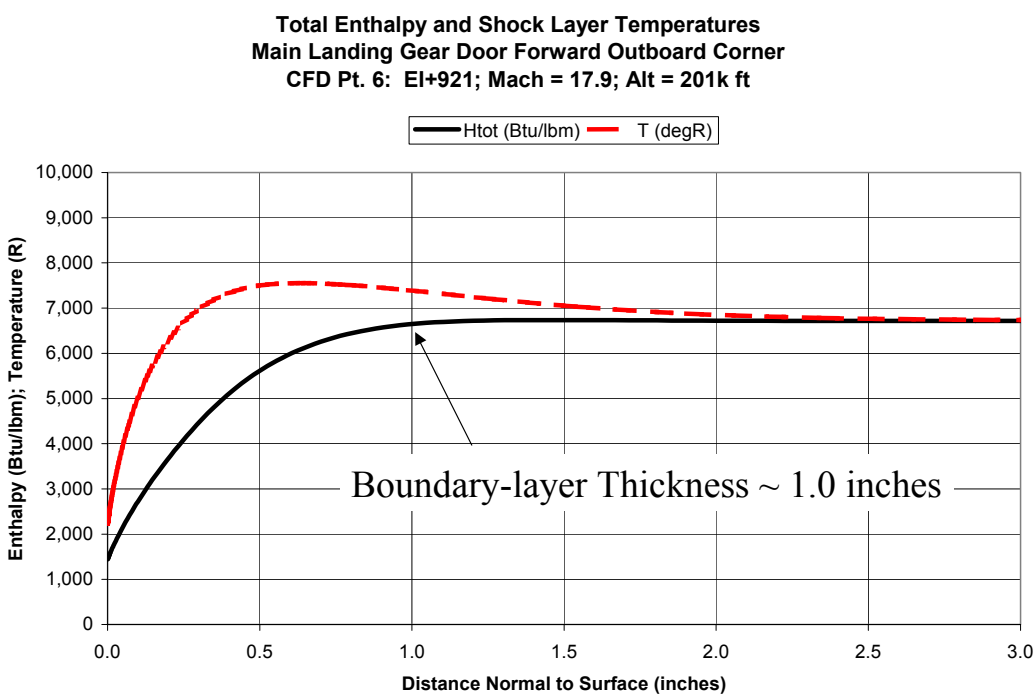

Figure 5.2.4-51 Total Enthalpy and Static Temperature Variation from Main LG Door Surface into Flow Field: CFD Point 6, Mach 17.9

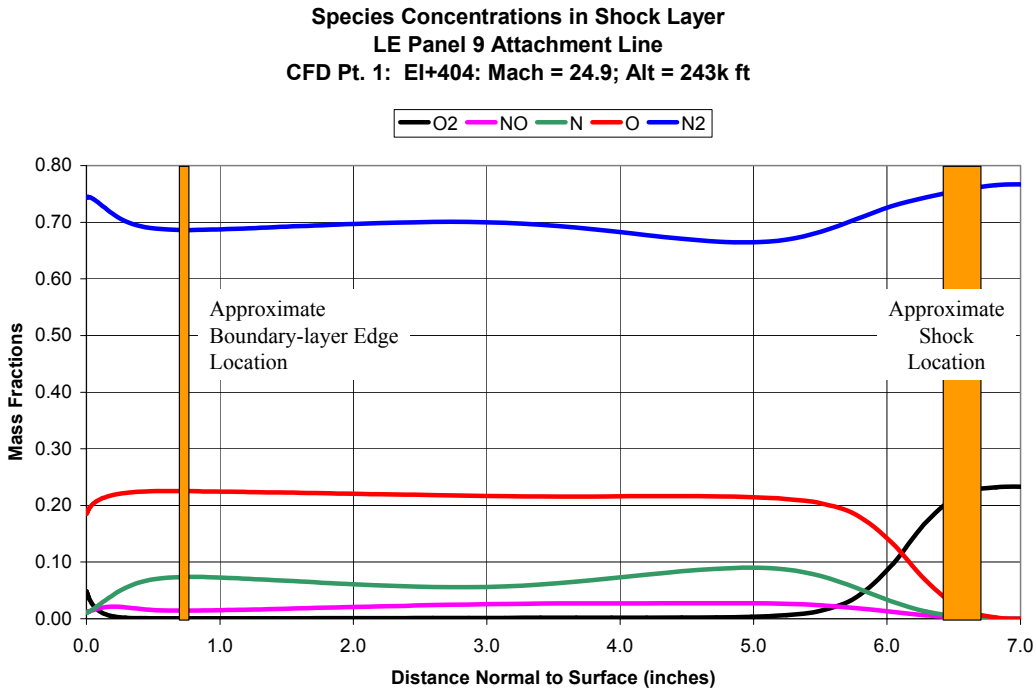

Figure 5.2.4-52 Predicted Species Mass Fractions in the LE Panel 9 Shock Layer: CFD Point 1, Mach 24.9

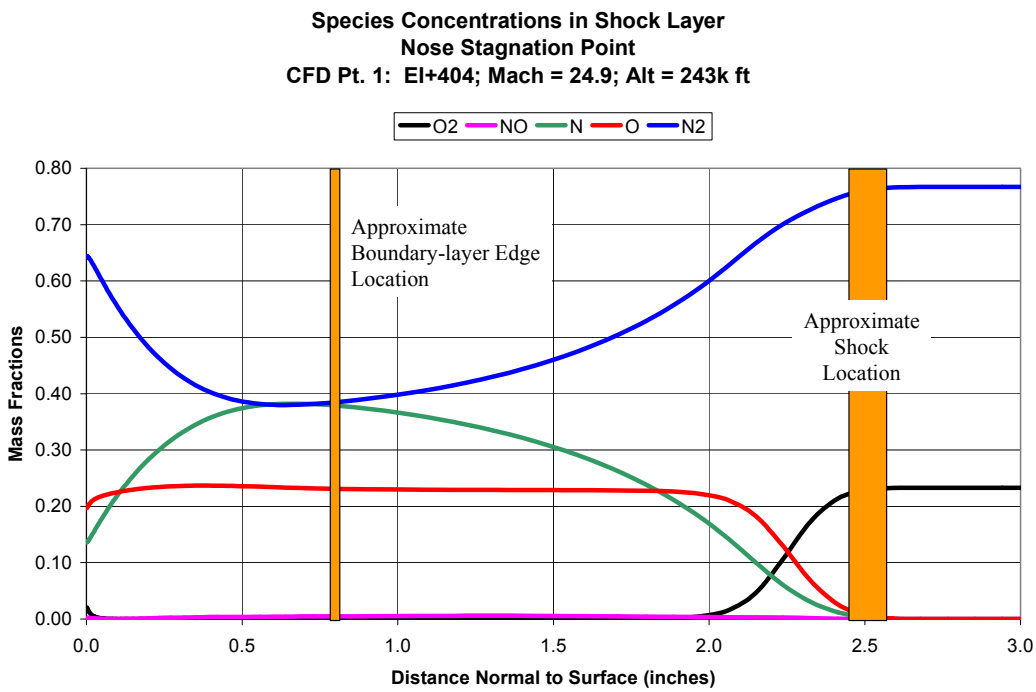

Figure 5.2.4-53 Predicted Species Mass Fractions in the Orbiter Nose Shock Layer: CFD Point 1, Mach 24.9

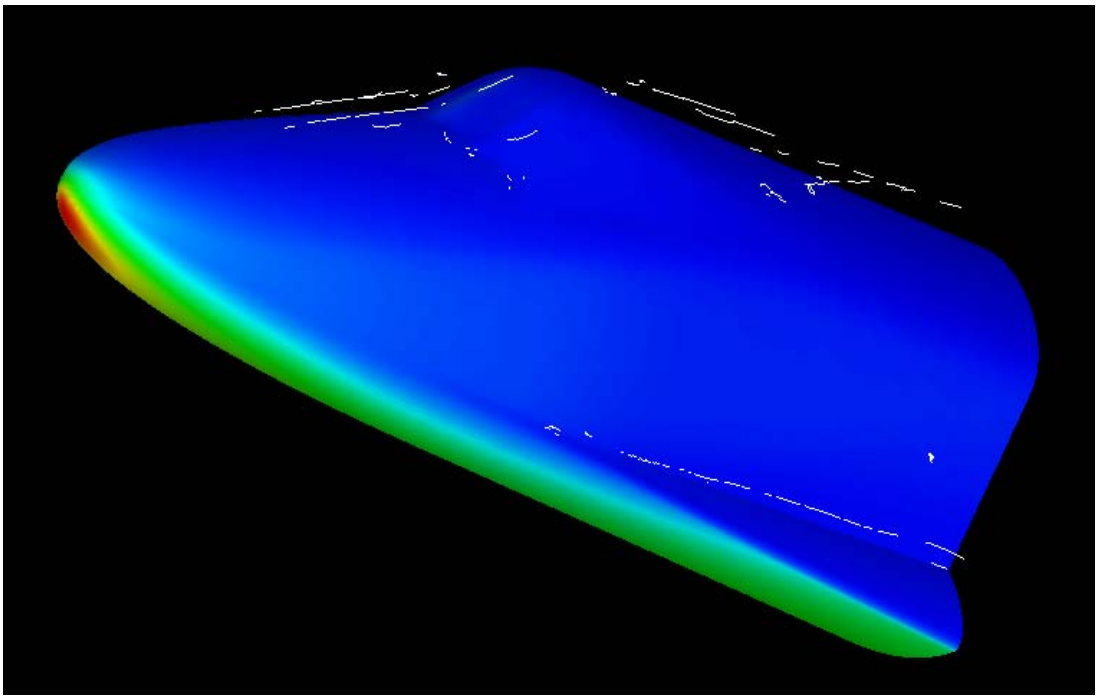

Figure 5.2.4-54 Pressure Contours and Vortex Location for wind tunnel conditions

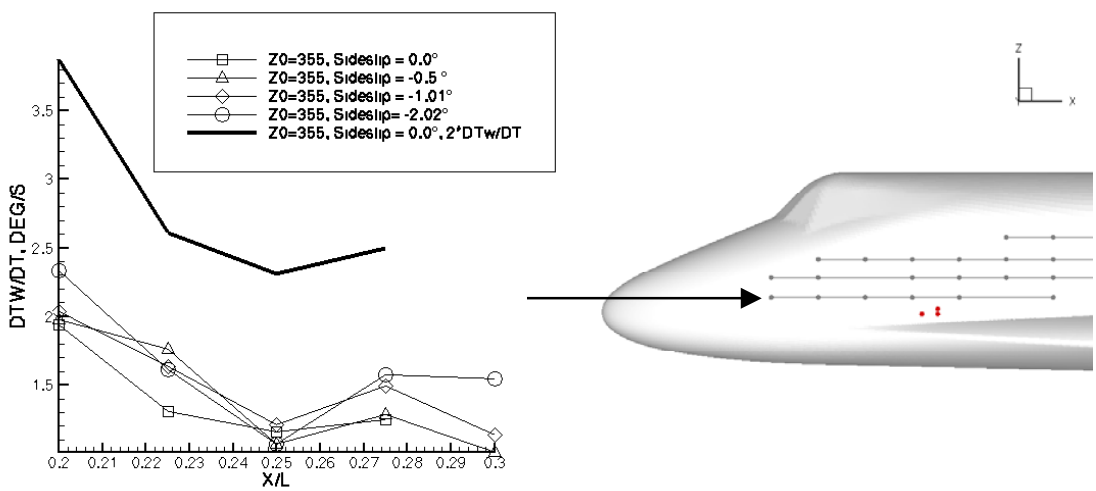

Figure 5.2.4-55 Wind Tunnel Measured Temperature Rise Rate

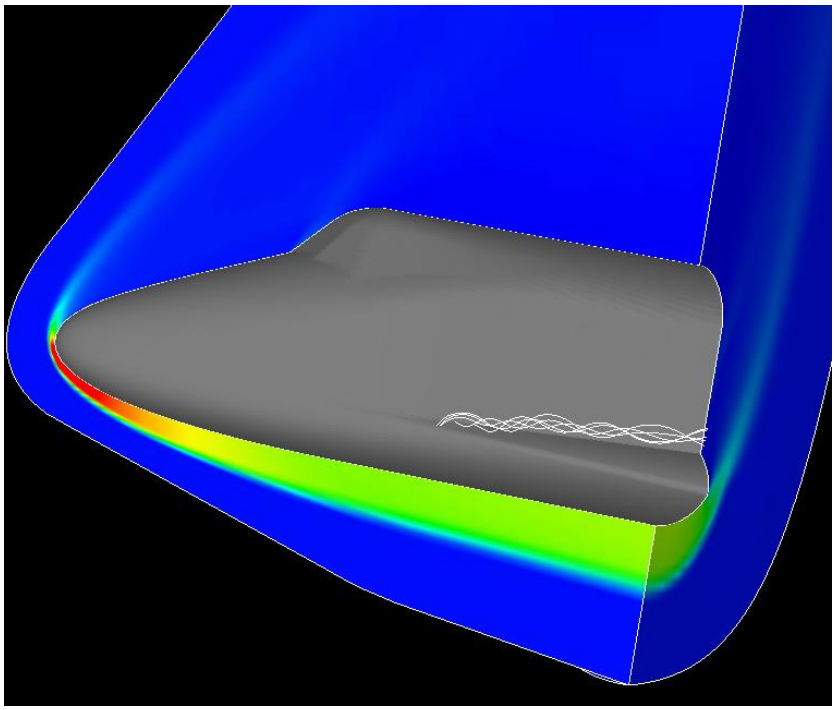

Figure 5.2.4-56 Pressure contour and vortex core location for wind tunnel conditions

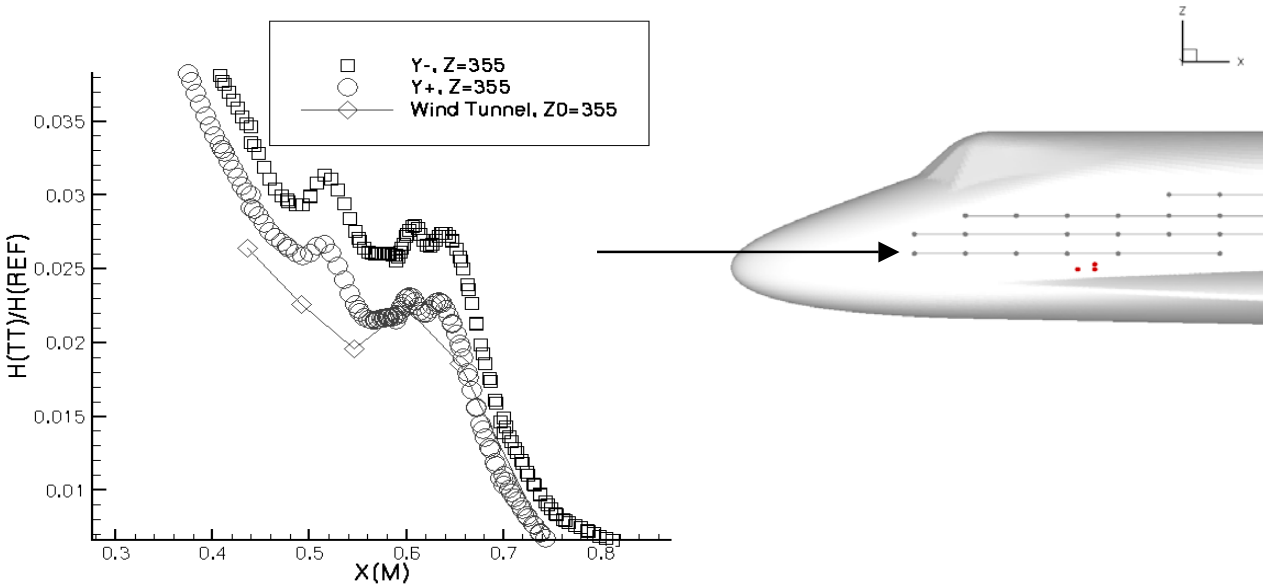

Figure 5.2.4-57 Comparisons with wind tunnel data

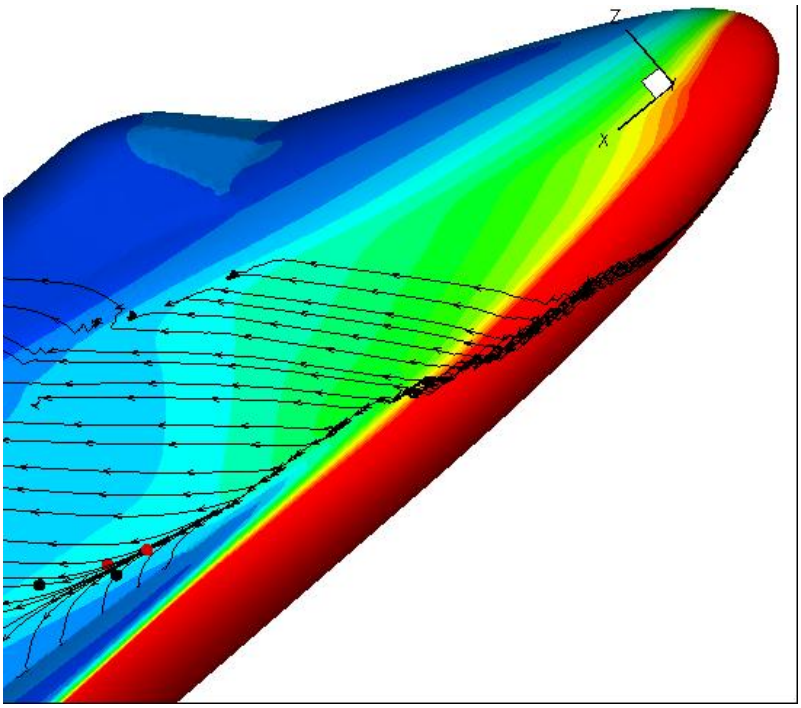

Figure 5.2.4-58 Shear stress contours and surface streamlines at flight conditions

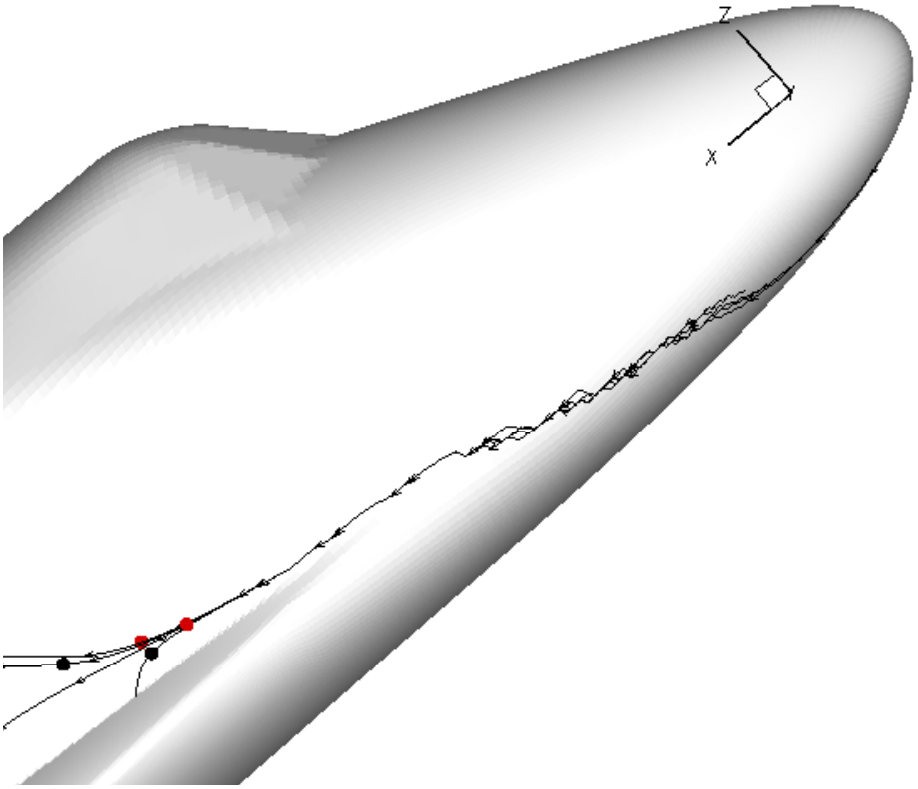

Figure 5.2.4-59 Nozzles and thermocouple streamlines at flight conditions

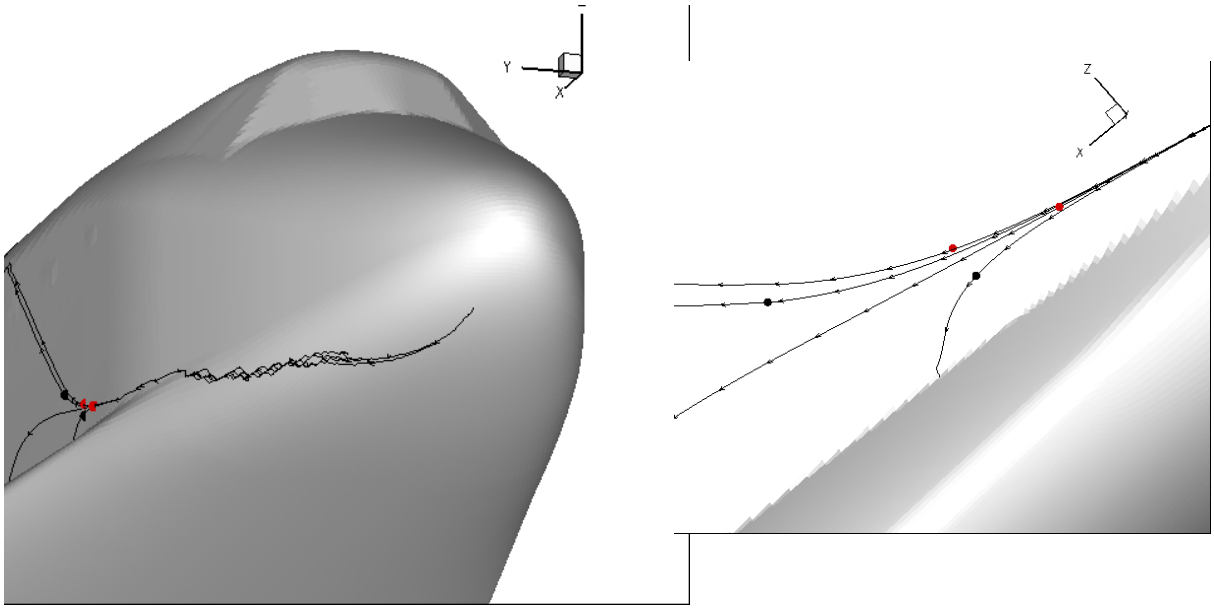

Figure 5.2.4-60 Front view and close-up of nozzles at flight conditions

5.2.4.5 *Damaged Orbiter Configurations Solutions*

5.2.4.5.1 Introduction

Computational aerothermodynamics was used to investigate the effects of damage to the Orbiter leading edge during Earth re-entry. The primary motivation in performing these RCC panel damage scenario CFD calculations was to gain a greater understanding of the detailed effects that various leading edge damage types and locations would have on overall vehicle dynamics and surface heating. Of particular interest in these CFD solutions was how the damage location and type would affect surface heating at the sensor locations on the side fuselage and OMS pod, where Columbia data were available. Another high priority aspect to be examined via the CFD solutions was the detailed off-body flow characteristics resulting from OML damage. Also, in order to aid the in the investigation of the delta aerodynamics (Section 4), these CFD solutions presented in this section were used to evaluate the damage effects on surface pressure and hence, on the integrated aerodynamic forces and moments. Obtaining a detailed understanding of RCC wing panel damage on the actual temperatures and heating for the wing spar, internal RCC channel insulation and other internal wing leading edge hardware was considered to be of secondary importance for these CFD computations. It is well understood that very small changes in damage topology or location will have very substantial effects on the actual heating values in the vicinity of the damage. The unknown nature of the actual STS-107 damage, combined with its likely rapid progression, makes quantitative internal cavity temperature and heating predictions virtually impossible. Furthermore, to attain even an engineering level of credibility on internal cavity heating, the cavity geometries would have to be more realistic and represent the actual internal wing leading edge hardware. Also, physically representative wall boundary conditions for the internal wing materials (emissivity and catalycity) and proper treatment of the internal radiative conditions would be necessary. Not only would these new kinds of boundary condition have to be implemented in our CFD codes, but they would have to be validated as well. Section 5.3 of this report focuses more on the interior heating details; thus this

section will not examine the physics or flow features within the cavities generated by removing RCC panels.

The studies described in this section were conducted at the start of peak heating where the external flow is characterized by high angle of attack, hypervelocity conditions: CFD case 1 condition (404 seconds from EI, free-stream Mach number = 24.83, angle of attack = 40.2 degrees, and altitude = 243,000 ft). Members of NASA-ARC Reacting Flow Environments (ASA) Branch and NASA-LaRC Aerothermodynamics Branch performed these computations using GASP (Appendix 5.6) and LAURA (Appendix 5.6), respectively. The entire flow field for these damage cases was assumed to be laminar and in a state of chemical nonequilibrium (5 reacting species), and in a state of thermal equilibrium. The boundary condition at all solid surfaces (both the OML and the internal cavity surfaces) used RCG catalysis assumptions developed by Stewart, radiative equilibrium, and an emissivity of 0.89. Complete details of the computational strategy and convergence acceptance and quality checking for both GASP and LAURA are provided in Appendix 5.6.

The damaged geometries considered in this work included an approximation of a complete missing panel 6 (herein referred to as the panel 6 “notch”), a fully removed and lower half removed panel 6, a lower half removed panel 9 with and without flow into the RCC channel, a complete missing panel 9 with and without flow into the RCC channel, and a lower half removed panel 9 with flow into the RCC channel and the upper carrier panel missing. These cases as well as the results observed from the computations are described more fully in the following sub-sections. A main point in considering the solutions below is that not all possible types of damage were explored nor were any thermal analyses performed to define in a precise way the actual damage experienced by STS-107. Rather the boundaries of a matrix of possible damage scenarios to the leading edge were explored. This matrix of damage solutions was used to establish the locations, extent and magnitude of associated temperature and heat flux anomalies that might credibly occur on the exterior surface of the Orbiter. Since special focus will later be placed on the effect that leading edge damage has on leeside heating of the fuselage side and the OMS pod, it is important to note the key parameters that appear to drive these effects: (1) the topology, size and location of any wind side wing leading edge damage, (2) the magnitude of venting into the interior wing, (3) the extent of venting to the lee side by hot gases within the RCC channel, and (4) the extent and nature of any breech that allows hot windside gases to pass directly to the leeward side of the vehicle. Thus, as mentioned in section 5.2.1.1, an engineering perspective is taken in the interpretation of these numerical results.

<u>RCC Panel 6, Baseline Smooth OML Solution with Embedded-O Mesh (ARC)</u>

The first in the series of GASP CFD computations for damaged RCC panel scenarios was that of the smooth OML panel 6 case. The computational mesh leaves both the upper and lower RCC half panels in place and therefore is simply another smooth OML solution. The main difference between this calculation at CFD condition 1 and the comparable GASP solution discussed in section 5.2.4.4.2 is the grid. The same forebody and aft body grids are used in the two GASP calculations, but the mid-body external grid for the current calculation uses an imbedded-O topology that focuses on the outer perimeter of RCC panel 6. Since this panel is left in place, the body surface face of the exterior H-grid that sits in the “eye” of the imbedded-O topology simply covers theRCC panel 6 OML. The calculation can be thought of as another comparison/validation case for the common baseline mesh solutions at CFD condition 1. Because of the use of the imbedded-O grid used in the earlier nominal GASP calculation (1.86 million for the current calculation, 1.06 million for the earlier nominal GASP calculation) its primary purpose here is to isolate possible solution problems related to the modified exterior grid or the complicated internal cavity grid. Also, when differences between the temperatures or heat fluxes of damaged and undamaged configurations are examined, the use of identical exterior meshes for both solutions greatly simplifies the differencing process.

Figure 5.2.4-68 and Figure 5.2.4-69 show side and top planform views of the normalized heating rates seen on the configuration for this nominal configuration case. These views shall be used repeatedly for all ARC-computed damage scenario CFD solutions presented later in this section. These images provide a viewpoint to understand changes in surface heating over regions of the vehicle where flight data were obtained during the STS-107 re-entry. The results of this computation are in very close agreement in

terms of temperature and heat flux compared with the corresponding solution obtained from the baseline common mesh discussed in section 5.2.4.4.2.

RCC Panel 6, Full "Notch" Out Solution with Solid Side Walls (LaRC)

For expediency in assessing the effects of leading edge damage, a grid approximating a missing RCC panel 6 was generated early in the investigation for the first damage scenario CFD case at flight conditions. Coordinates defining RCC panel 6 were estimated from existing literature since this work occurred prior to acceptance and distribution of a common CAD geometry within the investigation team. Subsequent comparison of the estimated panel 6 coordinates with the actual size and location revealed that the approximated missing panel was centered about the correct location but was roughly only 2/3 of the full panel. Figure 5.2.4-61 shows a planform view of the missing panel modeled in this work compared with the size and location of the actual RCC panels. The exterior grid for this "notched" panel 6 out case was developed at LaRC very early in the investigation before the common grid development had taken place. Details of the grid are presented in section 5.2.4.2. The grid uses an O-H topology to define the interiorof the missing RCC panel 6 cavity. This topology allows grid cells to be clustered against the solid side and back surfaces to capture viscous boundary-layer behavior. This current cavity grid can be thought of as a hybrid between two cavity grid alternatives described in section 5.2.4.2. The grid has an H topology in the spanwise direction and an O topology in the streamwise direction. The interior cavity grid was composed of 5 matching blocks, one in the center and four surrounding it with their outward faces forming the backplane and the matching faces to the RCC panel 6 OML. Each of the two spanwise faces of thesefive cavity blocks meets the side walls of the cavity. To construct the missing panel geometry, solid vertical surfaces were used to slice the nominal Orbiter geometry along the sidewalls and backplane, thereby forming the leading edge cavity. In reality, the sidewalls of a cavity formed by a missing RCC panel are hollow. This would allow flow into the channel on either side, but such venting was not modeled in the present computation. The backplane of the cavity is a rough approximation of the main wing spar in this simulation; however, no other internal geometry components (e.g., spanner bars, carrier panels, earmuffs) were modeled. The solution was obtained with LAURA using thin-layer Navier-Stokes equations on a grid that had been coarsened to one-half the available grid density in directions parallel to the surface, with full resolution normal to the Orbiter surface. This coarsened grid totaled approximately 8.5 million points, 2.5 million of them located within the missing RCC panel cavity.

Figure 5.2.4-62 shows one aspect of the resulting flow solution where a slice that crosses the RCC cavity has been extracted in the planform plane. The flooded contours on this figure show the flow field density levels for the case where the RCC panel is missing. It can be seen in the figure that shock waves are anchored at both the inboard and outboard leading-edge corners of the missing RCC panel. These embedded shocks are formed around the recirculating flow within the cavity at the inboard corner and from impingement of flow on the outboard corner. Both shocks form weak interactions with the wing bow-shock downstream of the cavity. Solid contour lines are overlaid on the figure to depict the density contours in this area for the case of a baseline geometry with no missing RCC panels. By comparison the presence of the cavity appears to have a very small effect on the outer bow shock and downstream flow in this plane. The only differences noted are the additional features described for the missing panel case. This observation regarding the downstream flow also held true for other planes around the leading edge.

While the missing RCC panel 6 "notch" effect was minimal along the wing leading edge, its impact was very evident in the wing leeside flow. Figure 5.2.4-63 through Figure 5.2.4-65 show temperature contours plotted in vertical planes that have been extracted from the flow field at three axial stations (at the missing RCC panel 6 "notch", midway between RCC panel 6 and the OMS pods, and at the front face of the OMS pods). These figures compare the flow fields of the nominal (i.e., undamaged) Orbiter geometry with the flow field predicted on the leeside with the RCC panel 6 "notch". The sequence of figures shows a jet flowing out of the cavity toward the side fuselage and then the subsequent flow development along the fuselage. In probing the computed flow field it can be ascertained that the jet flow leaves the cavity and travels across the wingspan toward the symmetry plane. Then, it impacts the fuselage at a nearly perpendicular angle. At the fuselage, the jet is turned abruptly downstream. The accompanying temperature increase in the flow field is due to both the hot gas flowing from the wind side and the impact of this jet on the fuselage.

The irregular flow effect on the Orbiter lee side is most evident in the surface pressure and heating experienced on the side fuselage. Figure 5.2.4-66 and Figure 5.2.4-67 illustrate these effects by showing contours of the increase in predicted surface pressure and heating rate over the nominal case. The pressure effect is computed as a difference in pressure coefficient and the effect on heat transfer is shown as a ratio of off-nominal to nominal heating. The area of pressure and heating increases are located almost directly transverse to the missing RCC panel 6. Both areas show an angled orientation sloping upward and aft. This result is in general agreement with wind-tunnel measurements of heating with missing RCC panel 6 geometry in terms of both location and orientation (Section 5.2.3). The maximum heating augmentation from the current prediction is ~5 times the nominal rate.

RCC Panel 6, Lower Half Panel Out Solution with Solid Side Walls (ARC)

The first damage scenario at flight conditions with an accurate definition of the RCC panels considered removing the lower half of RCC panel 6. A cavity was constructed into the wing leading edge by generating surfaces defining the spar, the inboard and outboard sides of RCC panel 6, and a constant waterline to define the vertical extent of panel loss. For the wing spar surface, a cutting plane was created that extends upward from the wing lower surface and parallel to the wing spar. The location of the vertical damage extent utilized a cutting plane that extends aft from the leading edge apex at a constant Z or waterline. Cutting planes between the edges that define the inboard and outboard RCC panel 6 side boundaries defined the width of the damage cavity. A pictorial representation of this geometry for a similar damage configuration at RCC Panel 9 is depicted in Figure 5.2.4-78. Solid wall RCG radiative equilibrium boundary conditions are applied along all of these interior cavity cut planes to fully define the boundary conditions.

The exterior mesh used for this calculation is the same as that used for the smooth OML RCC panel 6 case discussed above. It contained 1.86 million mesh points and 40 blocks, while the 7-block interior cavity mesh topology, which was described in detail in section 5.2.4.2 as the second alternative, contained 164 thousand points. Due to the short time frame allowed to complete this case and the long run times needed to converge a solution with leading edge damage, only a single CFD case was run. The conditions used for the GASP CFD code corresponded to point 1 in table 4.3-4 from section 4.3.2.2.

The cavity geometry is somewhat fictitious in that the inboard and outboard side walls should actually have vents into the RCC channel. Furthermore, the solid wall applied at the constant waterline cut plane actually has no physical basis. Finally, none of the internal RCC channel components such as the earmuffs, hardware insulation, or RCC panel attachment hardware were modeled. Instead, the interior of the RCC cavity was modeled with smooth straight walls. Nevertheless, to understand how significant windward RCC damage affects the leeside flow, this RCC half panel out cavity calculation was a helpful bounding case. In addition, an RCC half panel damage scenario solution at flight conditions helped to provide insight into differences between wind tunnel data and these flight simulations.

Figure 5.2.4-70 and Figure 5.2.4-71 show the analogous side and planform views of the damaged configuration with MADS (circles) and OI (boxes) sensors noted on the images. What is directly observable by comparing these images with the smooth OML images seen in Figure 5.2.4-68 and Figure 5.2.4-69, is that there is virtually no difference between the surface heating on the lee side, except for the region closest to the damage site. The conclusion from this solution is that having a lower half panel missing at the RCC panel 6 location has very little effect on the side fuselage or OMS pod heating. This result is consistent with the wind tunnel trends presented in Section 5.2.2. As a final note, the half RCC panel 6 out case calculation shows that there is some effect on the windward heating downstream of the damage region, although the images of this effect are not included in this report.

RCC Panel 6, Full Panel Out Solution with Solid Side Walls (ARC)

A follow-on to the RCC panel 6 half out case, simulated the loss of an entire RCC panel 6. Again cutting planes were constructed along the spar definition and at the RCC panel side boundaries. All of the new cavity-defining surfaces were specified as solid boundaries with RCG catalysis and radiative equilibrium. This cavity definition, as for the previous RCC half panel out case, was also somewhat flawed. No venting down the RCC channel was included, and hardware such as the insulating earmuffs and RCC panel retaining hardware was entirely missing. Both the backwall and the two side walls were modeled

as smooth featureless surfaces. Nevertheless, since our focus was on heating effects that occur away from the damage location, it provided a reasonable approximation of the loss of an entire RCC panel.

The mesh used for the exterior of the Orbiter was identical to that used for the two previous ARC RCC panel 6-related calculations. Inside the cavity, the 7-block interior mesh topology with 252 thousand points was used. CFD point 1 was used to define the conditions for GASP and only this single case was run.

Figure 5.2.4-72 and Figure 5.2.4-73 show the now familiar side and planform views of Orbiter leeside heating. Immediately evident from these images is that removal of the complete RCC panel 6 results in a rather significant heating change on the side fuselage and OMS pod. Figure 5.2.4-74 illustrates heat flux ratios on the side fuselage between the current complete-panel-removed solution and the smooth OML equivalent solution. Dramatic heat rate differences are indeed present. Very striking in the figure is the fact that locations of both significantly greater heating and moderate cooling relative to the undamaged OML solution are present on the vehicle. In particular, the OMS pod heating is dramatically reduced while a section on the side of the fuselage near the wing root and *ahead* of the actual damage location experiences heating levels that are dramatically higher than normal. Notice that the side fuselage region experiencing increased heating is quite large and that it is preceded upstream by a section of *reduced heating*. The increased heating of the side fuselage is due to impingement of the jet originating from the RCC cavity. The decreased heating on the OMS pod region may be due to changes in the position of the leeside wing-strake vortices, that normally run along paths that cause significant vortex scrubbing and hence heating effects on the OMS pod.

To illustrate the structure of the jet coming from the RCC cavity, Figure 5.2.4-75 through Figure 5.2.4-77 show temperature contours for cuts through the flow-field solution at three constant X locations. Side-by-side comparisons for both half RCC panel out and full RCC panel out with the smooth OML solutions are depicted. It is noted again that virtually no differences are seen in the leeside region for the half RCC panel out case. However, for the full panel out case, dramatic flow-field structures, not present in the smooth OML solution, are revealed. The very hot regions of these flow structures, which are especially evident at the X = 27 m and X = 30 m cuts, may be considered secondary shocks that are standing off the side of the fuselage. The shocks appear to be caused by an impinging jet hitting almost perpendicular to the side fuselage which emanates from the upper half of the RCC panel 6 removed cavity. The fact that the jet structure traverses the flow-field in the cross-stream direction while the free-stream flow is at Mach 25 emphasizes the strength of the jet. The removal of the panel can be thought of as creating a scoop down into the windside flow. The scoop turns the flow inward toward the body, and since on the leeside conditions are very nearly at a vacuum there is no resistance to this jet heading directly toward the side fuselage. Furthermore, once on the lee side, the jet must be traveling with considerable speed since it creates a secondary bow shock that stands off the side of fuselage. The temperature experienced by the flow as it traverses this secondary side-fuselage shock reaches levels that are near those present in the primary bow shock on the wind side of the vehicle. The cooler than normal region ahead of the jet impingement on the side of fuselage is a result of the jet flow moving aside the leeside flow that would normally be slowly accelerating along the side of body.

RCC Panel 9, Baseline Smooth OML Solution with Embedded-O Mesh (ARC)

In addition to the RCC panel 6 studies discussed above, studies at flight conditions focused on RCC panel number 9 were also conducted. Again an initial Ames solution using GASP for the smooth OML instance of the RCC panel 9 series was first conducted. The CFD case calculated was point 1 as defined in table 4.3-4. The mesh had an identical number of points to the equivalent RCC panel 6 case – 1.86 million points. For a comprehensive discussion on the motivation for running this case, the reader is referred to the RCC panel 6 equivalent case above. Figure 5.2.4-79 and Figure 5.2.4-80 show the side and planform views of the heating for this case. The images are very similar to those shown earlier for the smooth OML RCC panel 6 results, and thus will not be discussed in any more detail.

RCC Panel 9, Lower Half Panel Out Solution with Solid Side Walls (ARC)

The next case in the series of RCC panel 9 related CFD solutions, calculated with GASP at NASA Ames, follows the same sequence as that followed for the RCC panel 6 series. Specifically, the current case models a lower half RCC panel 9 out. A pictorial representation of the geometry for this damage

configuration at Panel 9 is shown in Figure 5.2.4-78. The construction of the lower half RCC panel out cavity used cutting planes just as in the corresponding half RCC panel 6 out case. The number of mesh points and the topological details of the mesh were also the same as those used for the RCC half panel 6 out case. A GASP simulation with the lower half RCC panel 9 removed and solid wall boundary conditions inside the resulting cavity is depicted in Figure 5.2.4-81 and Figure 5.2.4-82. Again, virtually nothing happens on the lee side, either on the upper wing surface or on the side of the body. A detailed examination showed that the differences in surface heating on the side fuselage and OMS pod, between the present case and the smooth OML RCC panel 9 case, are of the same order as the solution noise present for any calculation with the convergence tolerance used for this study. Thus, it can be concluded that the lower half RCC panel 9 damage case, at CFD flight condition 1, shows no leeside heating effect, within the tolerance of the CFD simulation. Note that the equivalent lower RCC half panel 6 out case discussed above showed slight but not negligible heating differences. The observation is that the attachment line along the leading edge that separates flow traveling to the lee side and the wind side moves higher with increasing span position. It is therefore expected that lower panel damage to the higher panel numbers will show less and less leeside influence. By the time lower RCC panel 9 is reached, essentially no leeside effects can be observed. Wind tunnel tests discussed earlier confirm this trend and demonstrate that rather sizeable leeside effects can be seen if the lower panel damage is as far inboard as RCC panel 3. Although it is not presented pictorially in this report, the RCC lower half panel 9 out does cause significant changes to the windside heating on the wing lower surface. However, these effects are well within the limits that can be tolerated by the RCG coated tiles.

RCC Panel 9, Lower Half Panel Out Solution with Vented Side Walls into the RCC Channel (ARC)

Solid sidewalls within the RCC cavity were used in the flight simulations discussed above, and it was recognized that those solutions could produce misleading results. Thus, an alternate CFD simulation of the lower half RCC panel 9 out scenario was conducted. There is one primary difference between this simulation and the previous RCC lower half panel 9 out case. Instead of the lower half panel out cavity being confined to the lower portion of the wing leading edge section, the entire extent of the RCC cavity bounded by the local RCC panel definition is modeled. This cavity modeling leaves the upper RCC half panel 9 hanging in space; its exterior OML side is exposed to the external flow and its interior cavity side is exposed to the interior flow. The actual RCC panel in this calculation is modeled as a zero thickness surface for the remaining upper section of RCC panel 9. The zero thickness approximation may not be appropriate to capture details of the internal cavity flow, but should suffice to model the leeside effects. In the actual case of a removal of just a lower half panel, a detached bow shock would form on the lip of what remains of the panel and disturb the flow inside the cavity in a way that is different from an attached shock caused by the infinitely thin edge used for the present calculation. This case also differs from the previous solutions in that the location of the RCC channel is defined, or scribed, on the sidewall mesh faces. The sidewall boundary conditions within the RCC channel regions are switched from being modeled as solid to being modeled as exit flow, with a (very low) fixed back pressure. By changing the sidewall boundary condition, we attempted to model the venting relief that occurs down the RCC channel in both spanwise directions. The upper left hand corner inset in Figure 5.2.4-91 shows details of the channel definition across which the exit/venting boundary condition is applied. The back pressure specified for these RCC channel vents was set to 0.1 lbf per ft^2.

The exterior mesh used for this case was identical to that used in the immediately preceding case. Again, only CFD point 1 was computed due to time and resource constraints. The interior mesh was actually identical to the next two full panel 9 out cases, using the 7-block internal topology with 252 thousand grid points. The side walls outside the vented regions, the back wall and the interior surface of the RCC 9 upper half panel were all model as solid walls with RCG catalysis, radiative equilibrium and an emissivity of 0.89.

The side and planform views of heating shown in Figure 5.2.4-83 and Figure 5.2.4-84 are indistinguishable from those shown in Figure 5.2.4-81 and Figure 5.2.4-82. The conclusion is that for the lower half RCC panel out case presented thus far, the details of the cavity modeling seem to have little leeside flow field influence. In general, for RCC panel 9, removal of the lower half does not propagate effects into the leeside flow. As noted previously leeside effects resulting from having a lower half panel out seem to increase as the removed half panel location is moved forward along the wing leading edge.

This result is consistent with experimental leeside heating data presented in Section 4.3.1 and 5.2.3. Lower wing heating differences were again observed but not examined in detail.

RCC Panel 9, Full Panel Out Solution with Solid Side Walls (ARC)

A damage scenario with all of RCC panel 9 removed, and the sidewall boundary conditions within the cavity returned to solid walls with RCG catalysis and radiative equilibrium, is considered next. The case is analogous to the simulation computed for the RCC panel 6 study at Ames. The grid was identical to that used in the preceding case. Figure 5.2.4-85 and Figure 5.2.4-86 show the heating levels from a side view and a planform view. Immediately clear from these figures is the presence of significant side fuselage heating. To reveal the details of this heating pattern more clearly, the heat flux ratio between this solution and the smooth OML panel 9 solution is depicted in Figure 5.2.4-87. Significantly increased heating levels are seen across a wide range of the lower part of the side fuselage, extending substantially upstream of the damage location. The peak heating increase shows a ratio of heating relative to the smooth OML case of above 50. Ahead of this increased heating region is a prominent section of reduced heating extending up and onto the payload bay doors. Unlike the full RCC panel 6 out with solid side walls solution that showed a decreased heating on the OMS pod, this full RCC panel 9 out solution shows a significant heating increase on the OMS pod. The differences in heating effects for RCC panel 6 missing and a RCC panel 9 missing show that leeside heating effects depend upon the actual leading edge damage location. Further information regarding leading edge panel parametrics with a much larger series of RCC panels removed can be found in the wind tunnel discussion of Section 5.2.3.

Figure 5.2.4-88 through Figure 5.2.4-90 show temperature contours across cuts through the solutions for the half and full panel solid sidewall RCC panel 9 damage scenarios. As in the RCC panel 6 equivalent images, the half RCC panel out case is virtually identical to the smooth OML solution. The solution with the full RCC panel 9 out shows very complex flow structures on the lee side above the wing. These “hot” flow structures interact with the side fuselage, resulting in surface heating similar to that seen in the Panel 6 plots of Figure 5.2.4-72 - Figure 5.2.4-77. The reader is referred back to the detailed discussion for the Ames full panel 6 out calculation to gather an understanding of the off body flow phenomena.

RCC Panel 9, Full Panel Out Solution with Vented Side Walls into the RCC Channel (ARC)

The next in the ARC series of panel 9 damage scenarios was the vented side wall version of the above RCC full panel 9 out calculation. In this computation the solid inboard and outboard sidewalls have been changed to the vented sidewalls boundary conditions. This boundary condition was analogous to what was already discussed above for the half RCC panel out cases. The mesh used in the previous computation was recycled for this case to compute CFD point 1. The objective of this simulation was to better understand the differences that RCC channel venting might have on the leeside flow field and surface heating.

Figure 5.2.4-101 and Figure 5.2.4-102 display the side and top planform views of surface heating. The figures show that a geometry with RCC channel venting also has very large heating increases on the lower part of the side fuselage, similar to the unvented full RCC panel 9 out case. Figure 5.2.4-103, illustrates the ratio of heat fluxes between the current case and the smooth OML case. A comparison with Figure 5.2.4-87 (RCC Panel 9 out unvented) leads to the observation that approximately the same side fuselage region experiences increased heating with or without RCC channel venting. However, the level of heating augmentation and the forward extent of the heating footprint are both somewhat reduced for the vented case compared with the unvented case. In addition, the vented RCC channel case experiences very significant cooling on the OMS pod region compared with the slight heating that was present in same location for the solid wall case. The conclusion is that venting down the RCC channel reduces the strength of the high-pressure jet emanating from the full RCC panel out cavity region. As a result, the effects on the side fuselage are less extreme than without the venting.

RCC Panel 9, Full Panel Out Solution with Vented Side Walls into the RCC Channel (LaRC)

A computational analysis of the flow field effects due to RCC panel 9 loss on the Orbiter was performed using the LAURA code. For this analysis, gas entering the cavity formed by the missing RCC panel was

allowed to flow into the outboard RCC channel by imposing vacuum conditions on the sidewall. Note that the previous GASP-calculated full RCC panel 9 out case used 0.1 psf back pressure instead of a hard vacuum. The inboard side of the cavity was modeled as a solid wall. For the vented outboard cavity surface, the solution remains independent of RCC channel back pressure as long as the back pressure is low enough to produce supersonic flow. This stipulation is true for all the vented cavity sidewall solutions. This is the only boundary condition that can be applied for a well-posed computation of flow through a sidewall without interior RCC channel modeling. The full scale computation at flight conditions was performed on a grid with 2 million cells where over half a million cells were located in the cavity.

An approximation of the RCC channel geometry was made for hardware exposed to the external flow by a missing panel 9. These features are shown in Figure 5.2.4-91. As noted in the illustration, the geometry modeled in the cavity extended to the main wing spar. This approach allowed for an approximation of the spanner beam/earmuff blockage, as well as the windward and leeward carrier panels. An additional detail modeled by this simulation was to maintain the height of the RCC rib exposed on panel 9. A vent area of about 312 square inches resulted after this rib surface was included in the geometry.

Figure 5.2.4-92 shows a cross-section of the flow field density at a constant waterline through the wing for the region surrounding RCC panel 9. Results for both the smooth OML geometry and the case of missing RCC panel 9 are shown. The density contours approaching the cavity are identical between the two solutions as expected, and a complex shock structure is observed in the cavity of the missing panel. At the upstream edge of the cavity an expansion fan propagates into the shock layer, accelerating and turning the flow into the gap. A weak recompression wave, also emanating from the upstream edge of the cavity, processes the over-expanded flow. On the outboard RCC rib, an embedded bow shock forms with one-half of the wave ingested into the RCC channel and the other half forming a second interaction with the downstream wing shock. The effects of this interaction with the wing shock appear to be very minor since the intersection angles of this secondary interaction are small and the incident wing shock is already weakened by ingestion of flow into the RCC channel. The shock layer thickness is approximately 20% smaller over the wing downstream of the missing panel. This is due to flow ingestion into the missing panel region, which is then convected into the outboard RCC channel, or is spilled over to the leeside of the wing.

A view of the missing panel cavity presented in Figure 5.2.4-93 illustrates the major surface and flow field features in the cavity. Color contours in the figure represent surface pressures, while volume streamlines are plotted to indicate flow direction. The streamlines illustrate that a substantial part of the flow entering the missing panel cavity also continues directly into the RCC channel. An attachment line is formed on the outboard RCC rib that separates flow going into the RCC channel from flow continuing onto the wing upper surface. The interior cavity, formed by the presence of upper and lower carrier panels and the spanner bar, produced additional flow features of note. Streamlines that flow into this cavity region are deflected toward the wing spar by the spanner bar (away from the outboard RCC channel). A circulation is formed within the volume encompassed by the interior cavity and the inboard sidewall. This recirculating flow is “spun” out the top of the missing RCC cavity into the leeside flow field.

Predicted heating rates to surfaces in the interior of the missing RCC panel area are presented in Figure 5.2.4-94. The heating contours closely follow the pressure contours shown in the previous figure except on the exposed edge of the lower carrier panel. It appears that heating in this area is elevated due to a thin boundary layer and high shear stresses. These two effects, in combination, lead to the highest heating rate observed in this simulation.

A simple view of the streamlines emanating from the leeside of the missing RCC panel is shown in Figure 5.2.4-95. The streamline patterns illustrate that the flow leaving the gap corner nearest the inboard sidewall and spar is directed straight toward the fuselage. Flow leaving the gap from other locations along the spar and toward the outboard cavity area is increasingly turned downstream. The end result is a small area of flow diverted low along the upper wing and toward the side fuselage in this simulation.

Temperature contours normal to the vehicle axis are shown in Figure 5.2.4-96 to Figure 5.2.4-99 for both the smooth OML and the missing RCC panel 9 solutions. The first figure, Figure 5.2.4-96, shows the temperature contours at X = 1051 inches which is 40 inches upstream of the missing RCC cavity. The

contours are symmetrical, illustrating that the cavity has no effect on the flow at this upstream station. The location at X=1051 inches is within a region of the volume grid which was significantly modified from the original common baseline grid. The solution's similarity for the nominal OML and the Panel 9 cavity grid demonstrate that the cavity modifications did not result in noticeable flow field differences in the computations forward of the damage site. Figure 5.2.4-97 shows the temperature contours at X = 1091 inches, corresponding to the inboard corner of the cavity. The missing RCC panel 9 solution produces a jet of hot gas which exits the cavity and scrubs the leeside of the wing in the direction of the fuselage. At this station, however, the side of the fuselage appears unaffected by the jet. Figure 5.2.4-98 shows the temperature contours at X = 1204 inches, halfway between the cavity and the OMS pod. At this downstream station, the jet from the cavity has been turned downstream and is scrubbing the side of the fuselage with the highest temperature gas near the intersection of the fuselage and the wing. Figure 5.2.4-99 shows the temperature contours at X = 1316 inches at the beginning of the OMS pod. The increased temperatures along the side fuselage persist at this station, although they have decreased somewhat. A region of off-nominal low temperature is also evident on the leeside surface of the wing for this missing RCC panel 9 solution. The most predominant feature, however, is the high temperature gas near the OMS pod surface. While both the baseline smooth OML and the missing RCC panel 9 solutions show hot gases in this region, a higher temperature gas occurs for the baseline solution. This effect can be noted by the white levels in the contours for the smooth OML solution, as opposed to the magenta contours in the missing panel 9 solution.

The leeside flow field perturbation seen in Figure 5.2.4-95 to Figure 5.2.4-99 causes the surface heating effect illustrated in Figure 5.2.4-100. Here the amplification of heating rate relative to the nominal (undamaged geometry) is plotted to isolate missing RCC panel 9 effects. As would be expected from the streamline patterns, the fuselage heating is increased in the area where the flow diverted through the missing panel gap strikes the fuselage. In this damage scenario, the heating augmentation pattern assumes a horizontal orientation and is confined near the wing-fuselage juncture. Augmentation factors up to 2 over the nominal heating case are predicted on the side fuselage. The effect on the OMS Pod is lower heating (approximately 70%) for the missing panel solution relative to the baseline. The results of other CFD simulations presented in this section, as well as the wind tunnel results in Section 5.2.3 with missing RCC panels have shown similar trends, but quantitatively different heating patterns. In many of those cases, the side fuselage heating augmentation is higher up on the fuselage, occurs more upstream, and the pattern assumes an angled orientation. Also, heating to the OMS pod in those cases generally increased. Differences in leeside surface heating characteristics between this simulation and the other results are primarily believed to be due to the amount of flow venting into the RCC channel and to the presence of an embedded cavity behind the missing RCC panel. This simulation illustrates the sensitivity to venting effects down the RCC channel, as well as the geometry of hardware in the RCC cavity.

<u>RCC Panel 9, Half Panel Out Solution with Vented Side Walls into the RCC Channel and the Upper Carrier Panel Out (ARC)</u>

The damaged RCC panel configurations discussed up to this point all involved permutations on the location of damage on the RCC panel, and different extents of vertical damage (i.e.., half or full panel). Concurrent with the development of the grid systems and the understanding developed from those CFD simulations, as well as on-going wind tunnel studies and observations from the debris, our understanding of the parametrics involved in wing leading edge damage increased dramatically. Late in the investigation, it became apparent that the extent of the initial wing leading edge damage was not likely to include large leeside sections of the RCC panels missing. Wind tunnel testing was indicating that some windward damage, together with some leeward damage near the RCC, could produce signatures consistent with the surface instrumentation responses during the early part (i.e., < EI + 480 seconds) of the STS-107 trajectory. With these observations from the later stages of the investigation in hand, a final solution at flight conditions was pursued with the lower half of RCC panel 9 removed, and an approximation of upper carrier panel damage. This configuration was deemed to be more representative of potential early timeline damage to Columbia, and complements a similar geometry considered in the wind tunnel testing (see Section 4.3.1). Similar to the more complicated half panel 9 out case discussed previously (i.e., with vented side walls and the complete RCC cavity modeled), the current case modeled the full RCC cavity with a zero thickness RCC upper half panel 9 and venting down the RCC channel through the inboard and outboard sidewalls. However, to model the desired upper carrier panel removed configuration, the last 4 inches of upper RCC panel 9 along the wing spar was also removed. Flow-

through boundary conditions were applied across this gap at the top of the RCC panel, allowing communication of the flow from the RCC cavity to the wing lee side. A graphic depicting the geometry is shown in Figure 5.2.4-104.

CFD condition 1 was calculated using GASP with the mesh remaining consistent with the other panel 9 out ARC cases. Figure 5.2.4-105 and Figure 5.2.4-106 show side and top planform views of the leeside heating. While the visible effects in these images are mild compared with those seen for the full RCC panel 6 or 9 out cases, the surface heating effects are still substantial compared with those seen on the previous half RCC panel out cases. Figure 5.2.4-107 depicts the ratio of the heat fluxes between the present case and the smooth OML panel 9 case. The figure shows that the primary leeside fuselage influence is a cooling effect on the OMS pod region. There is also some local increased heating near the wing-body intersection aft of the damage location.

5.2.4.5.2 Concluding damage scenario comments.

Because the exact damage to the wing leading edge of Columbia will remain unknown, a limited matrix of damage configurations were examined using CFD and focusing on RCC panels 6 and 9. These solutions suggest that initial damage to only the windside leading edge coupled with significant venting to the interior of the WLE cavity (possibly also with some open vent paths from the RCC channel to the lee side via T-seal gaps and upper carrier panel gaps) would result in only minor temperature anomalies on the fuselage, and potentially, decreased heating on the OMS pod. Also, as the damage geometry changed during the re-entry of Columbia, the footprint on the side fuselage and OMS pod would also have changed. Furthermore, a breach from the windward side via lower RCC panel damage coupled with significant upper carrier panel damage would be associated with initial moderate heating anomalies on the side fuselage. To experience extensive heating anomalies on the fuselage would require additional damage including either more upper carrier panel damage (e.g., more than a single upper carrier panel removed), loss of an entire RCC panel, or an equivalently large wing breach allowing windside flow to feed directly to the lee side. Venting to the interior of the wing leading edge (through the RCC channel) delays the extent of leeside anomalies. This is due to reduced mass flow to the lee side associated with the jet from the wind side to the lee side, emanating from the leading edge damage cavity. The existence of this jet due to wing leading edge damage is shown conclusively in the CFD simulations presented in this section. The character of that jet is such that, with sufficient damage to the wing leading edge, high temperature gas is driven toward the side fuselage of the Orbiter which can propagate *upstream* of the damage site. The most dramatic heating increases and the largest extent of surface heating effects occur when the leading edge cavity jet is driven by wing leading edge stagnation pressure due to a significant breach in the wing leading edge on the wind side. As a final comment on the damaged leading edge CFD simulations, it must be pointed out again that the nature of these simulations, and the conclusions to be drawn from them, should be restricted to an engineering perspective. The CFD simulations conducted as part of the investigation were performed on representative geometries. The particular geometries that have been assessed were chosen in a very dynamic environment of wind tunnel, CFD, flight instrumentation, and recovered debris investigations. The fact that these geometries were chosen for investigation does not mean that the damaged geometry experienced by Columbia is exactly represented in this suite of simulations. In fact the dynamic/progressive nature of the actual Columbia data coupled with the time responses for the sensors will likely mean that a direct one-to-one match between CFD simulations and instrumentation flight data will never be achieved.

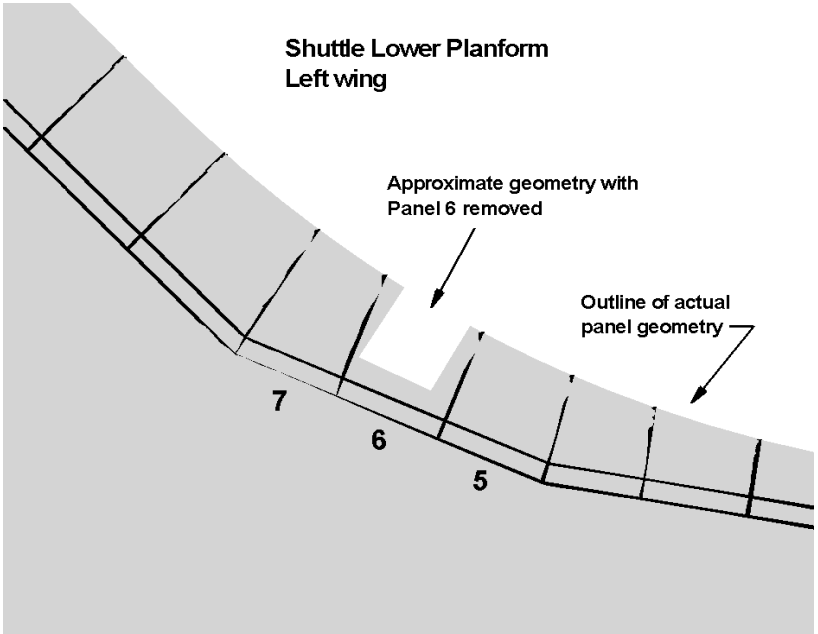

Figure 5.2.4-61 Planform view of missing panel 6 "notch"

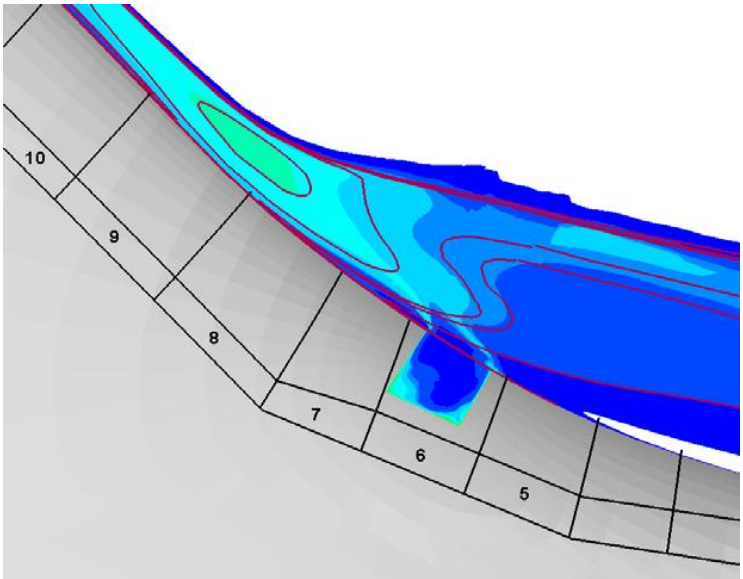

Figure 5.2.4-62 Planform view of flow field density contours for nominal geometry (contour lines) and for missing RCC panel 6 (flooded contours)

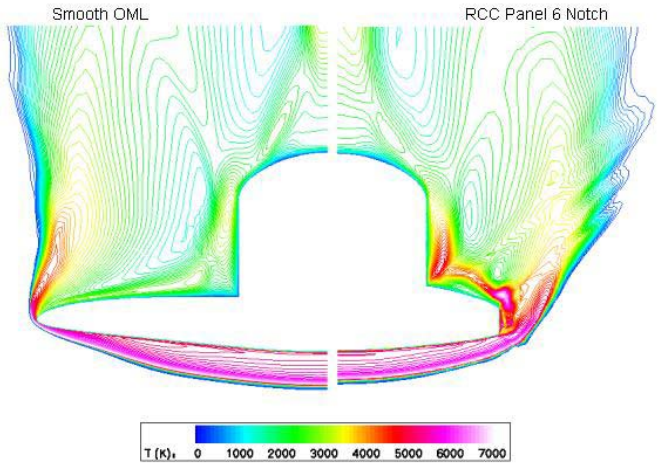

Figure 5.2.4-63 Temperature Contours at X = 1036 inches (through panel 6 notch)

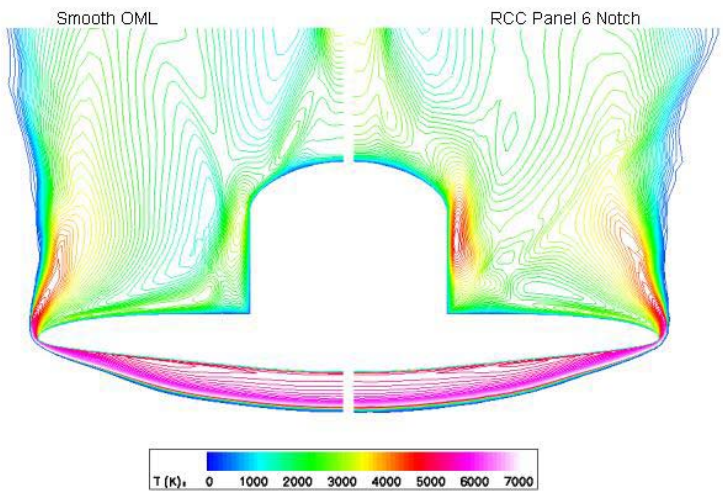

Figure 5.2.4-64 Temperature Contours at X = 1181 inches (halfway between notch and OMS pods)

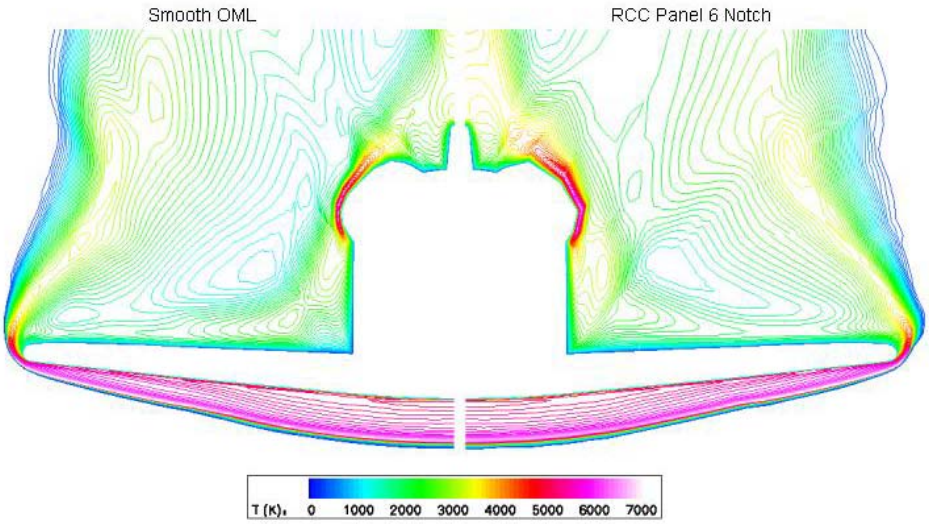

Figure 5.2.4-65 Temperature Contours at X = 1326 inches (forward face of OMS pod)

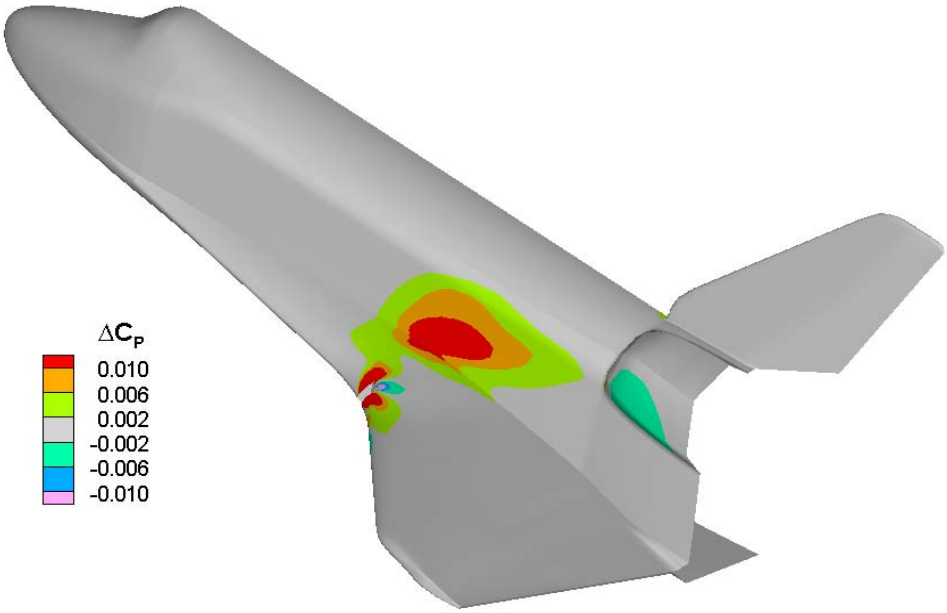

Figure 5.2.4-66 Difference in pressure coefficient due to missing RCC panel 6 "notch"

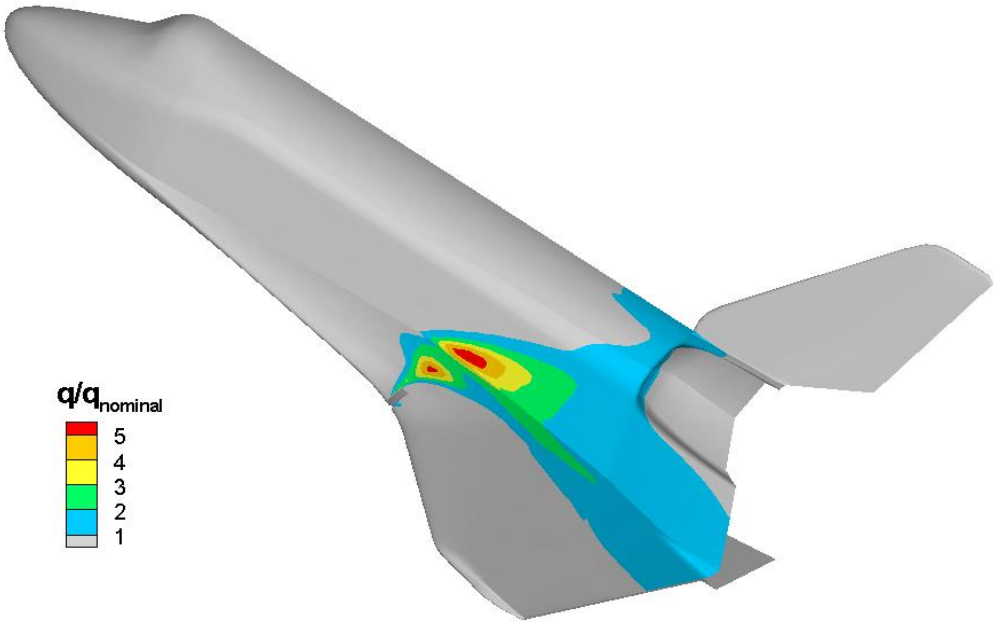

Figure 5.2.4-67 Heating augmentation due to missing RCC panel 6 "notch"

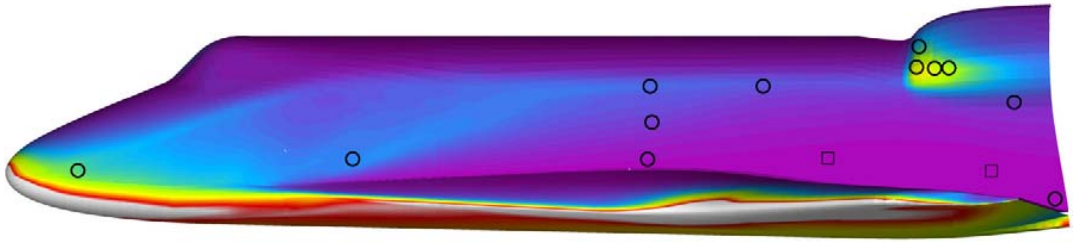

Figure 5.2.4-68 Smooth OML RCC Panel 6, Side View, Heating Rates

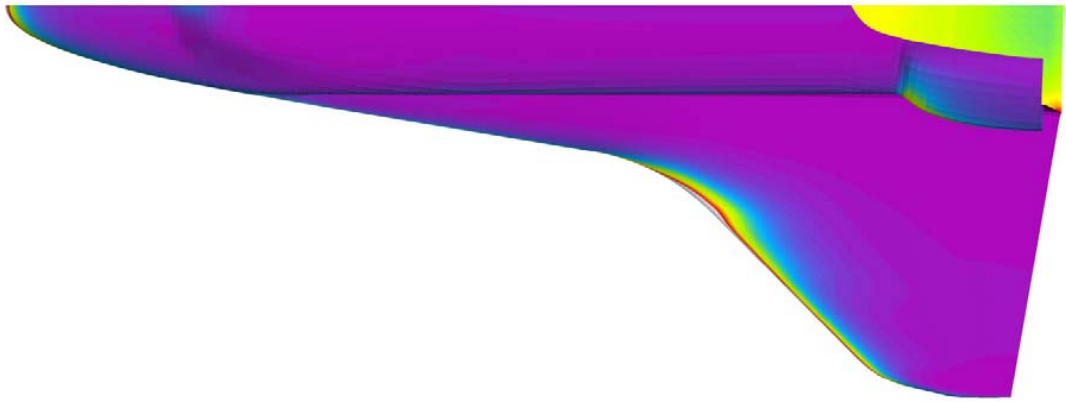

Figure 5.2.4-69 Smooth OML RCC Panel 6, Planform View, Heating Rates

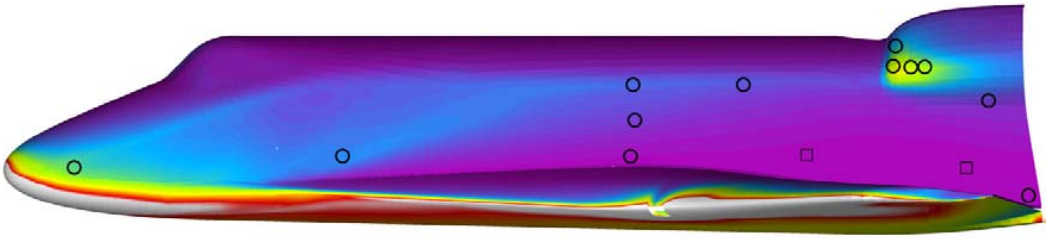

Figure 5.2.4-70 Lower Half RCC Panel 6 Out, Side View, Heating Rates

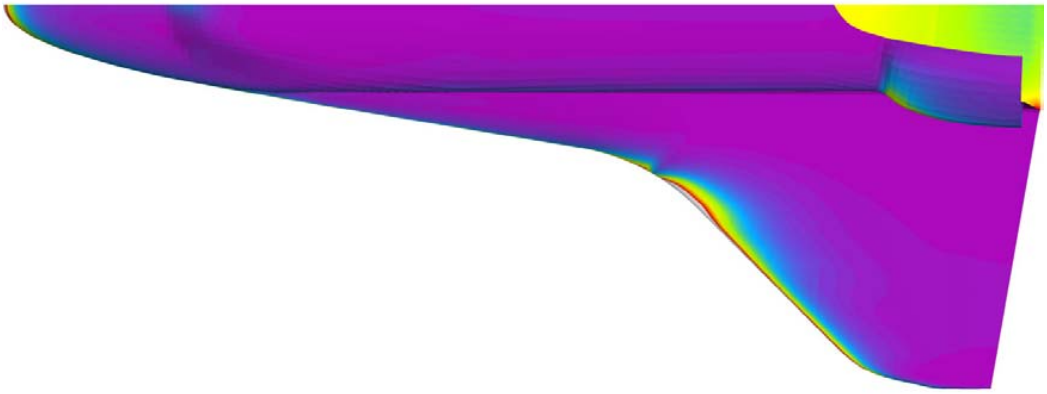

Figure 5.2.4-71 Lower Half RCC Panel 6 Out, Planform View, Heating Rates

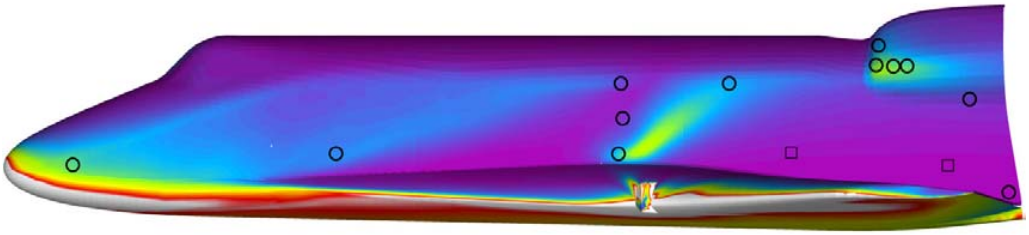

Figure 5.2.4-72 Full RCC Panel 6 Out, Side View, Heating Rates

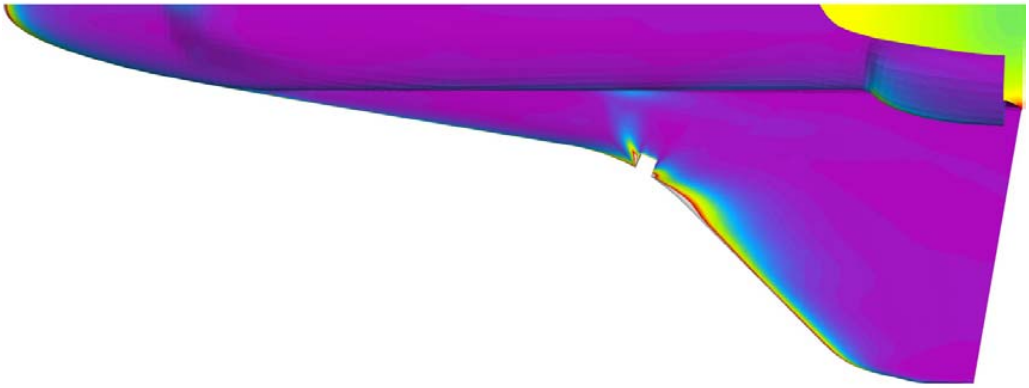

Figure 5.2.4-73 Full RCC Panel 6 Out, Planform View, Heating Rates

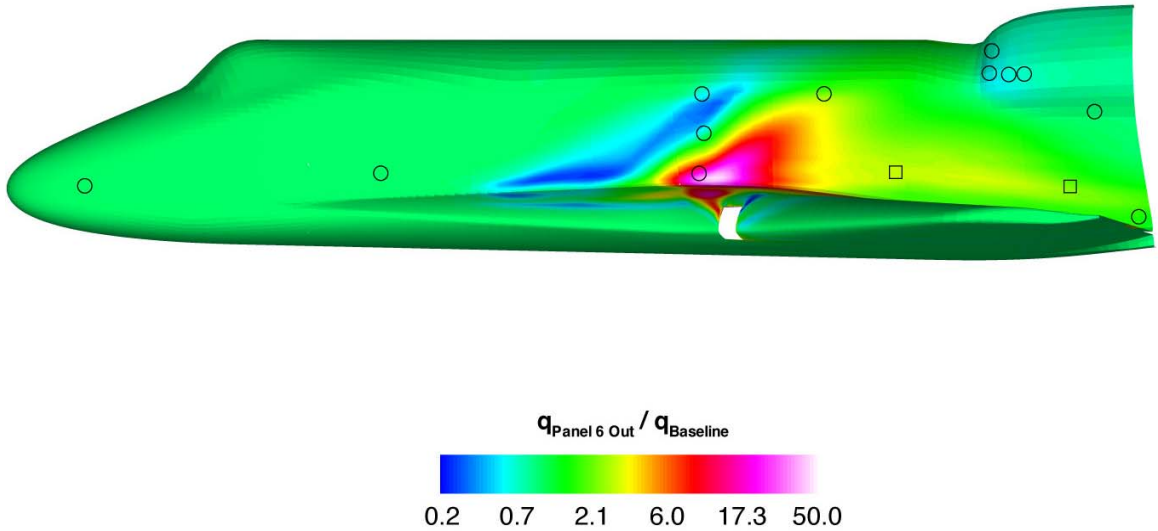

Figure 5.2.4-74 Full RCC Panel 6 Out, Side View, Ratio of Heat Fluxes

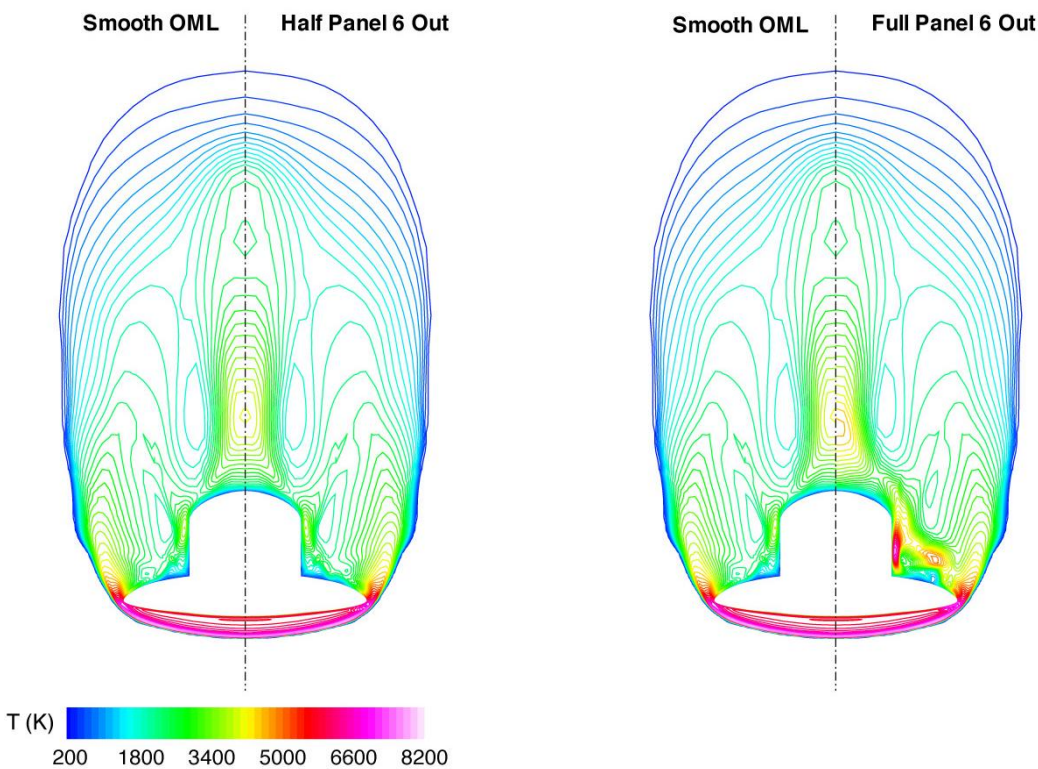

Figure 5.2.4-75 RCC Panel 6 Out, Y-Z Solution Cut at X = 27 m, Temperature Contours

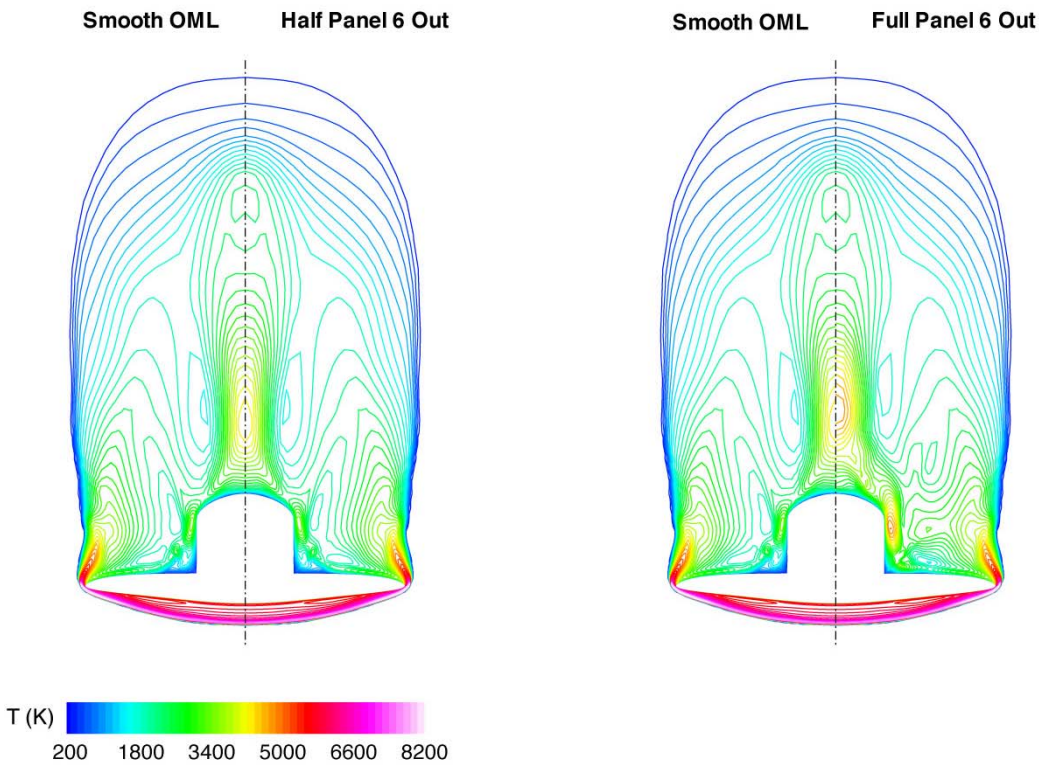

Figure 5.2.4-76 RCC Panel 6 Out, Y-Z Solution Cut at X = 30 m, Temperature Contours

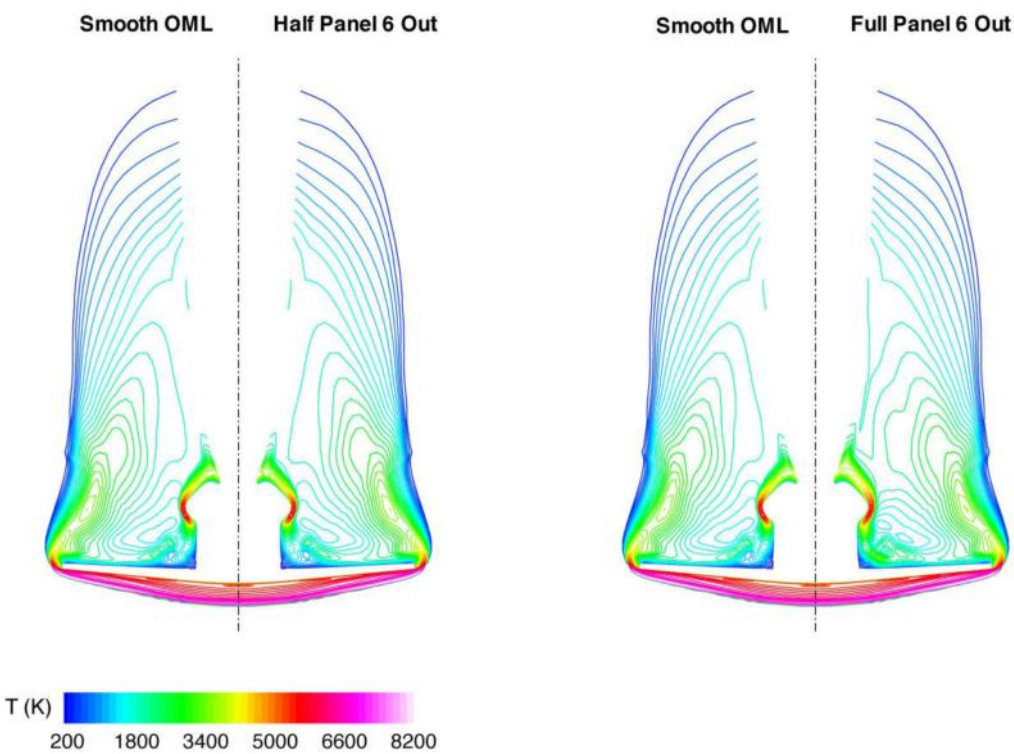

Figure 5.2.4-77 RCC Panel 6 Out, Y-Z Solution Cut at X = 35 m, Temperature Contours

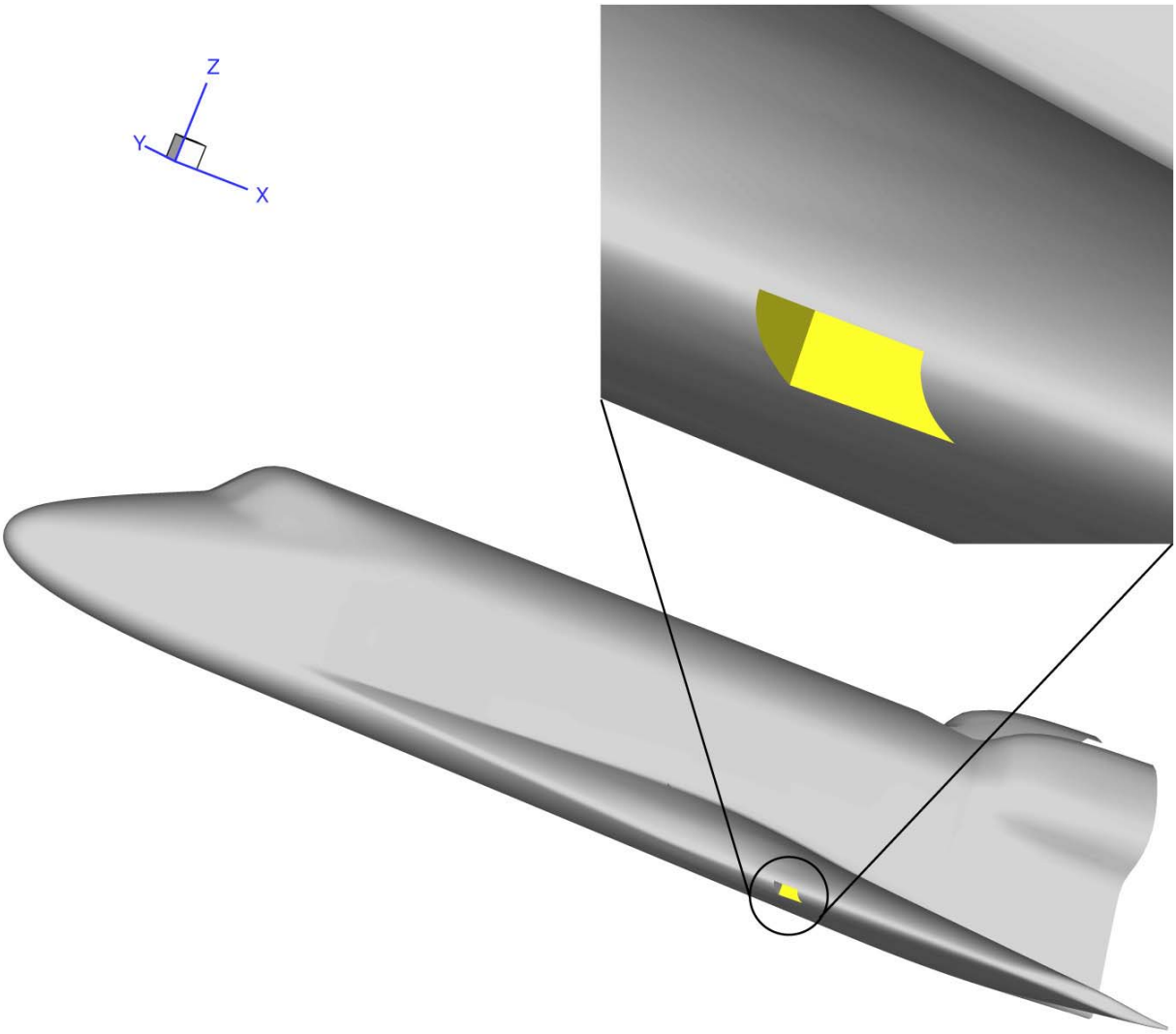

Figure 5.2.4-78 Lower Half RCC Panel 9 Out Geometry

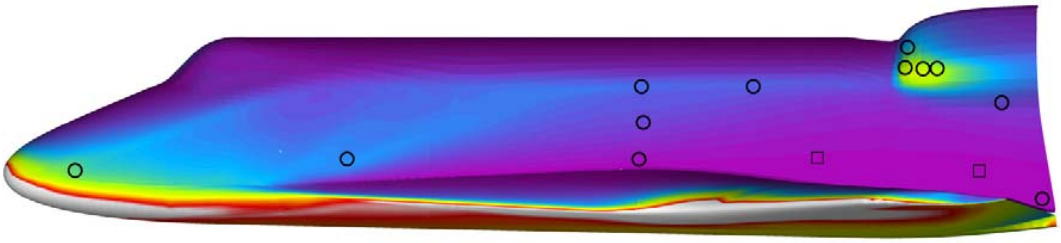

Figure 5.2.4-79 Smooth OML RCC Panel 9, Side View, Heating Rates

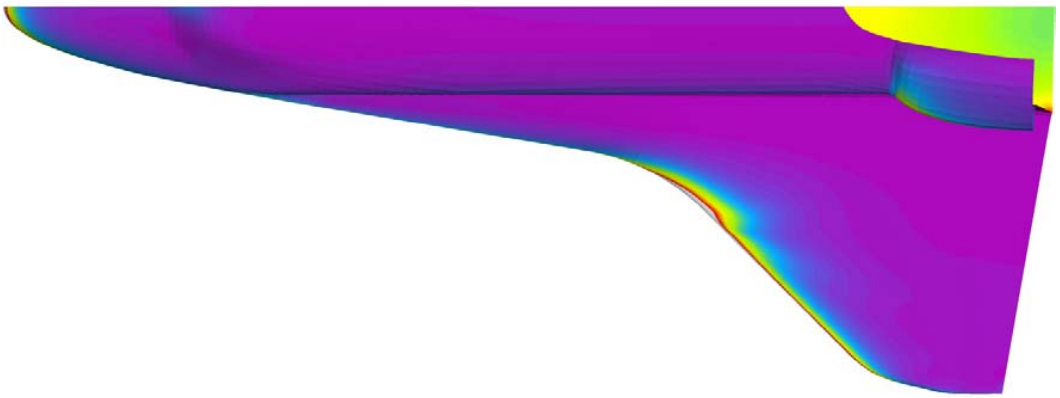

Figure 5.2.4-80 Smooth OML RCC Panel 9, Planform View, Heating Rates

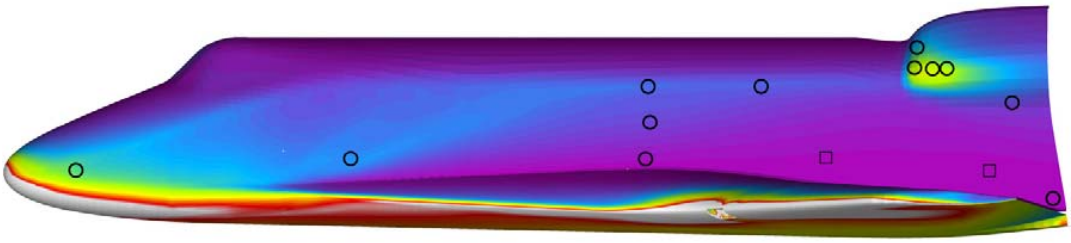

Figure 5.2.4-81 Lower Half RCC Panel 9 Out, with Solid Side Walls, Side View, Heating Rates

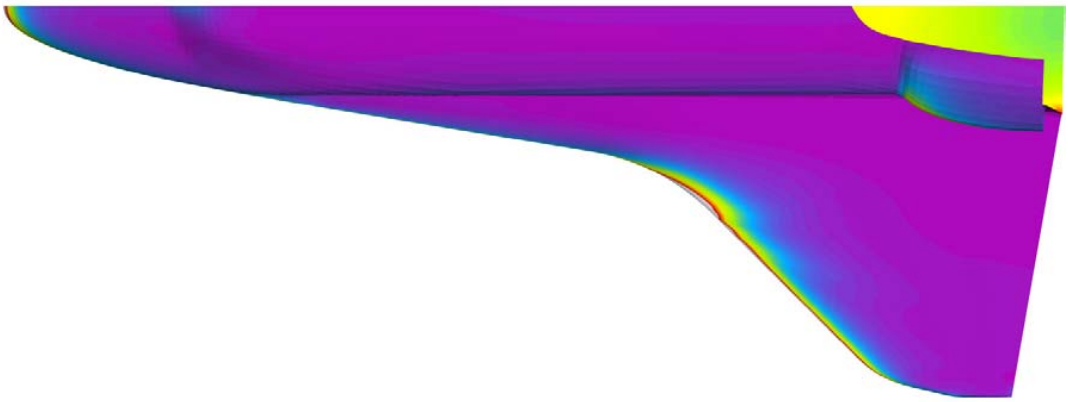

Figure 5.2.4-82 Lower Half RCC Panel 9 Out, with Solid Side Walls, Planform View, Heating Rates

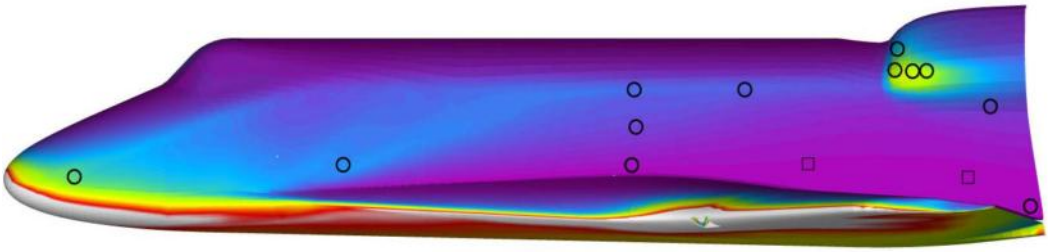

Figure 5.2.4-83 Lower Half RCC Panel 9 Out, with Vented Side Walls, Side View, Heating Rates

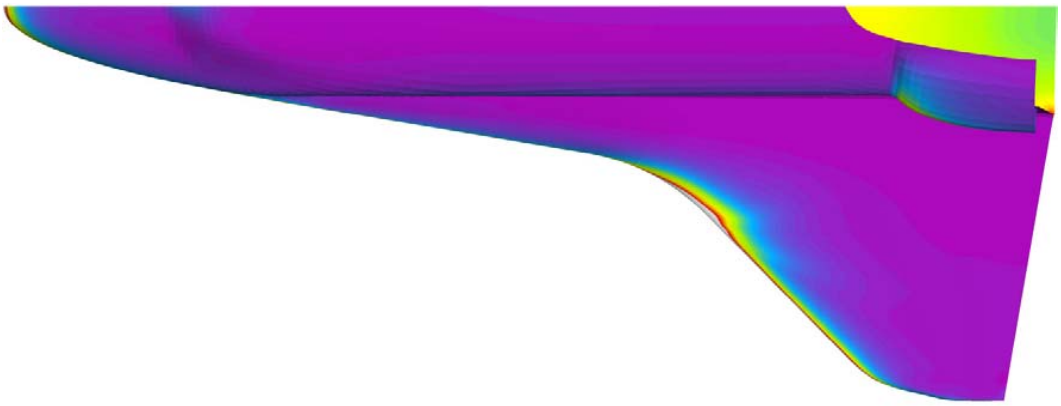

Figure 5.2.4-84 Lower Half RCC Panel 9 Out, with Vented Side Walls, Plan View, Heating Rates

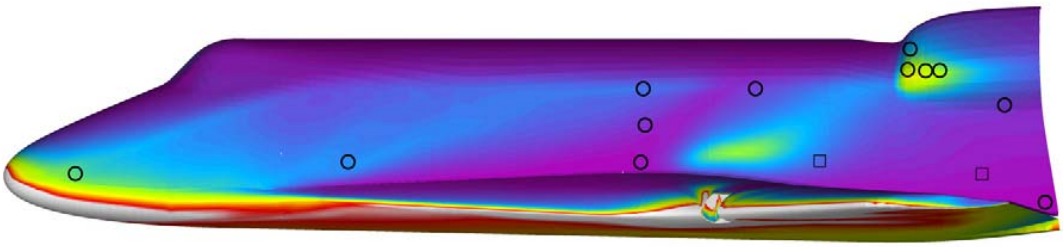

Figure 5.2.4-85 Full RCC Panel 9 Out, with Solid Side Walls, Side View, Heating Rate

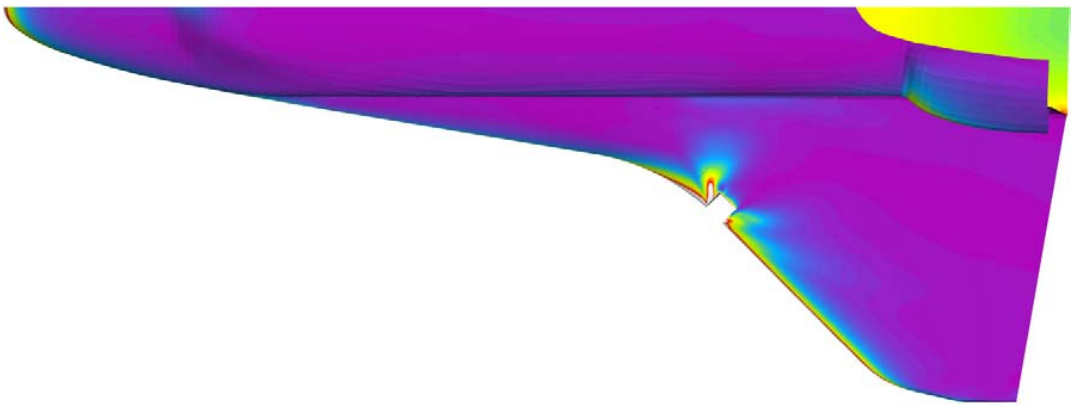

Figure 5.2.4-86 Full RCC Panel 9 Out, with Solid Side Walls, Planform View, Heating Rate

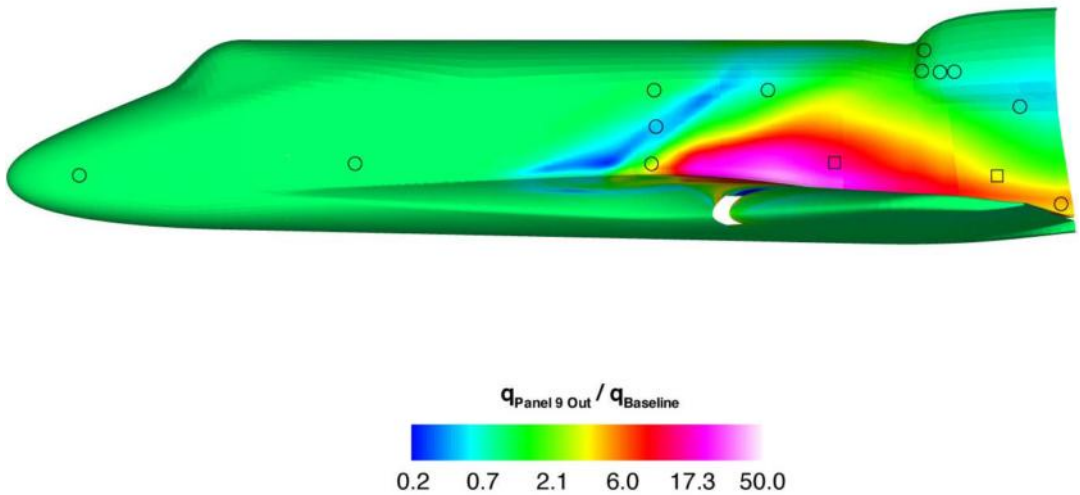

Figure 5.2.4-87 Full RCC Panel 9 Out, with Solid Side Walls, Side View, Ratio of Heat Fluxes

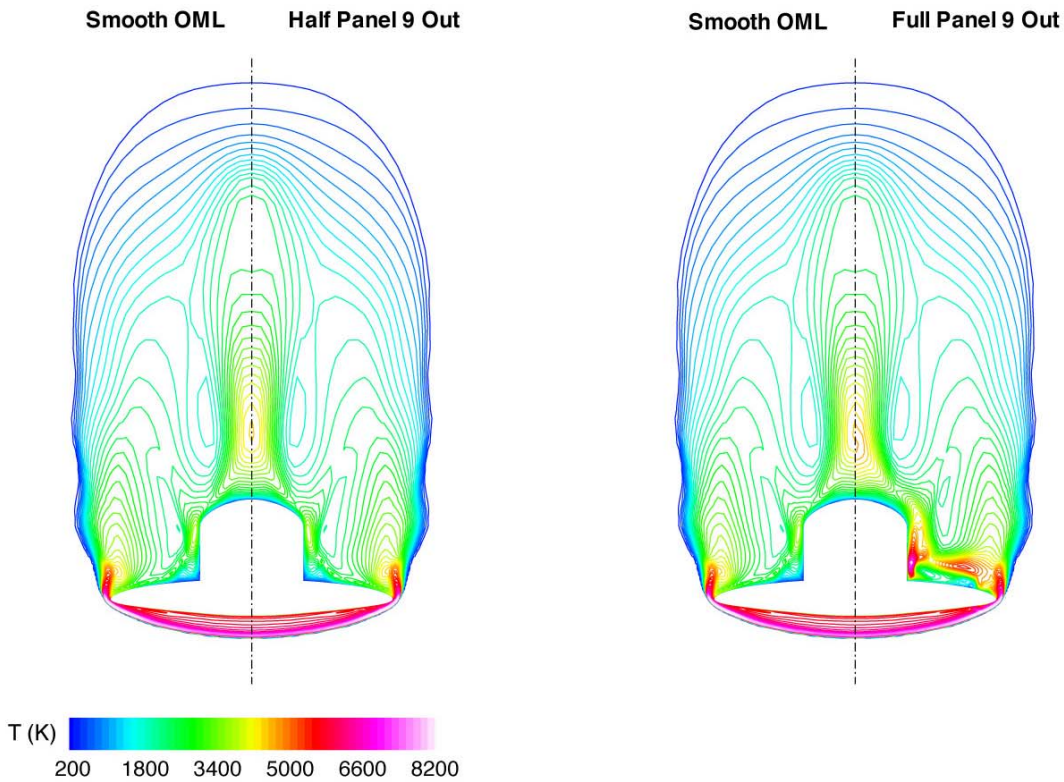

Figure 5.2.4-88 RCC Panel 9, Y-Z Solution Cut at X = 28.5 m, Temperature Contours

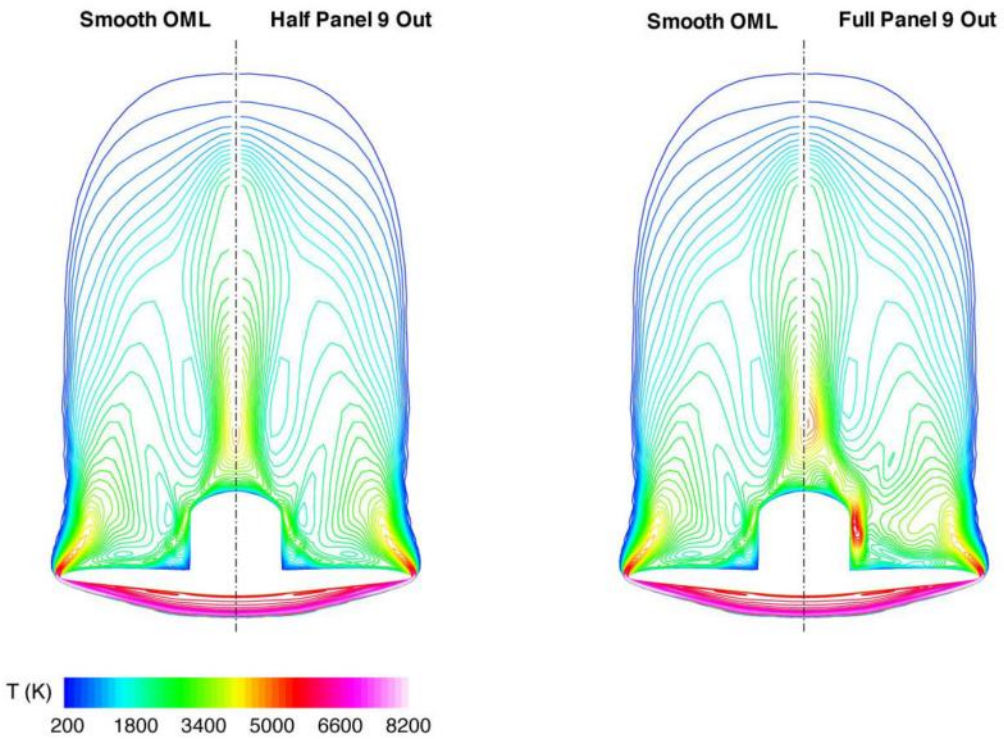

Figure 5.2.4-89 RCC Panel 9, Y-Z Solution Cut at X = 31.5 m, Temperature Contours

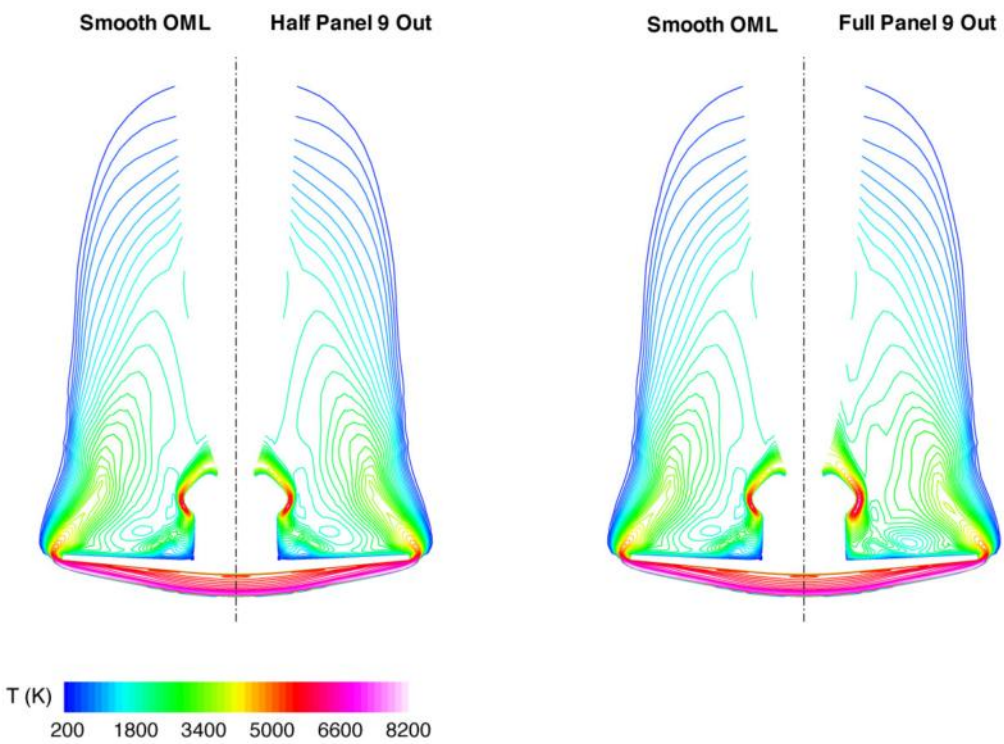

Figure 5.2.4-90 RCC Panel 9, Y-Z Solution Cut at X = 35.0 m, Temperature Contours

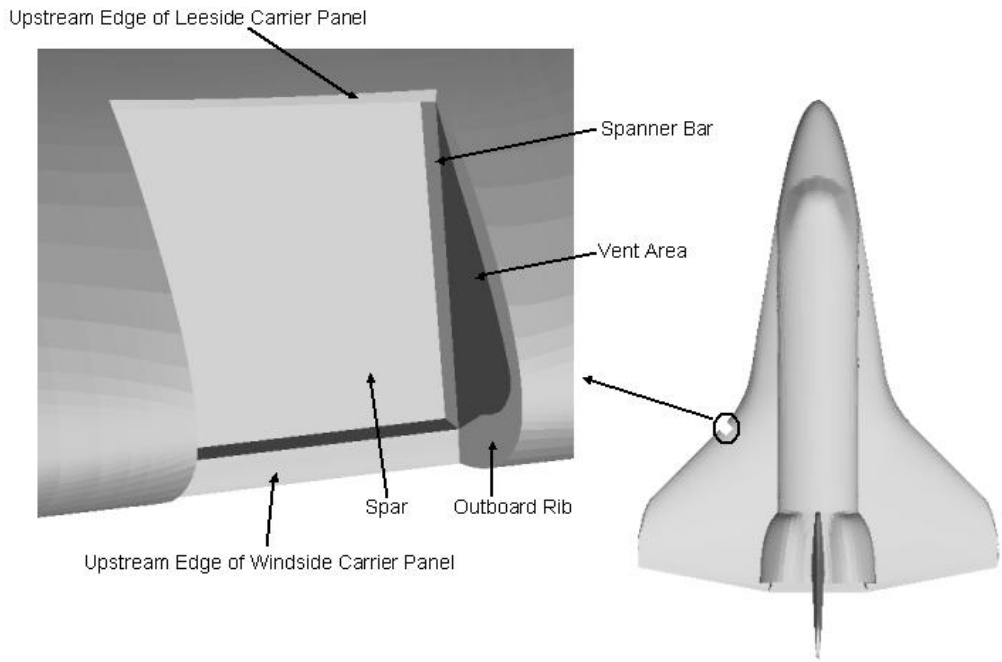

Figure 5.2.4-91 Geometry for Missing RCC Panel 9 with Venting in RCC Chamber

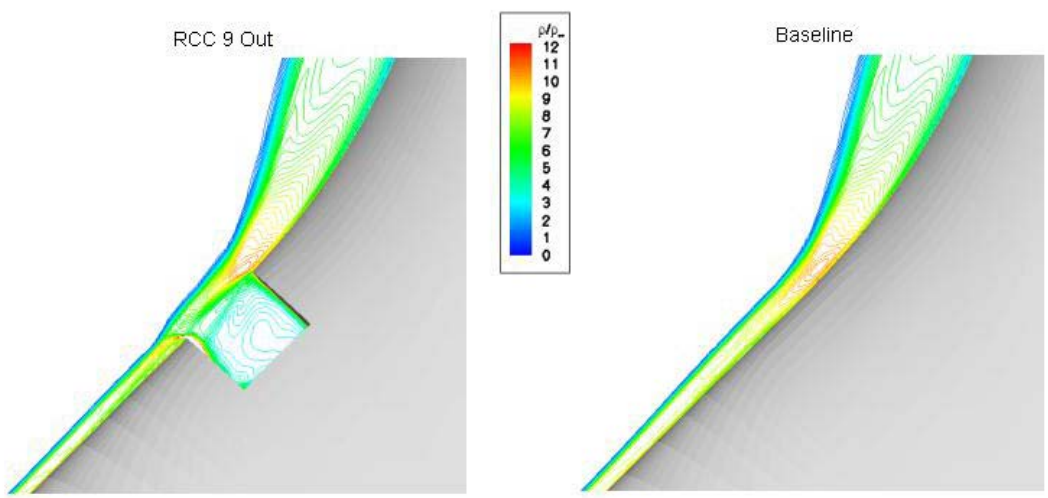

Figure 5.2.4-92 Comparison of Density Contours in Missing RCC Cavity and on Smooth OML Baseline Grid

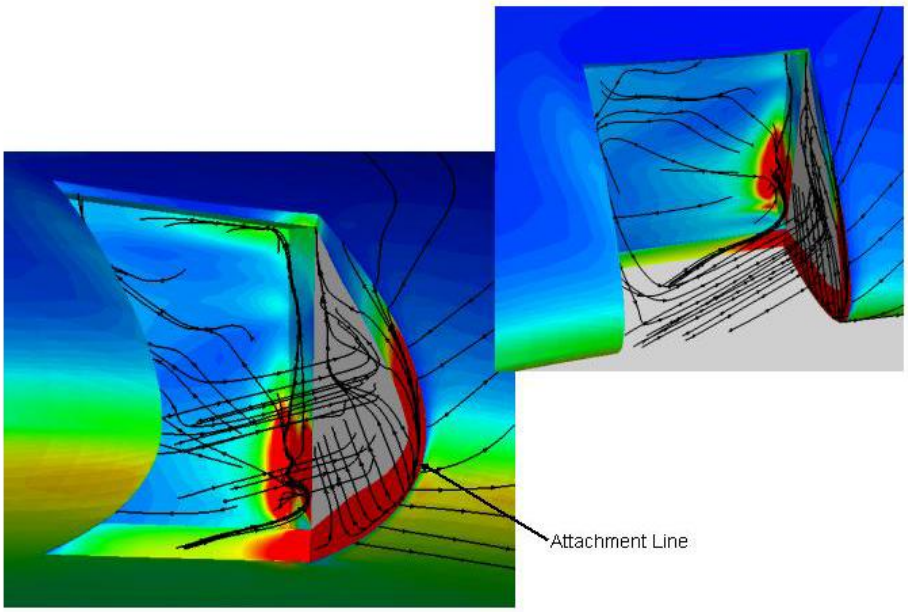

Figure 5.2.4-93 Pressure Contours, Volume Streamlines and Surface Streamlines in Vented RCC Panel 9 Cavity

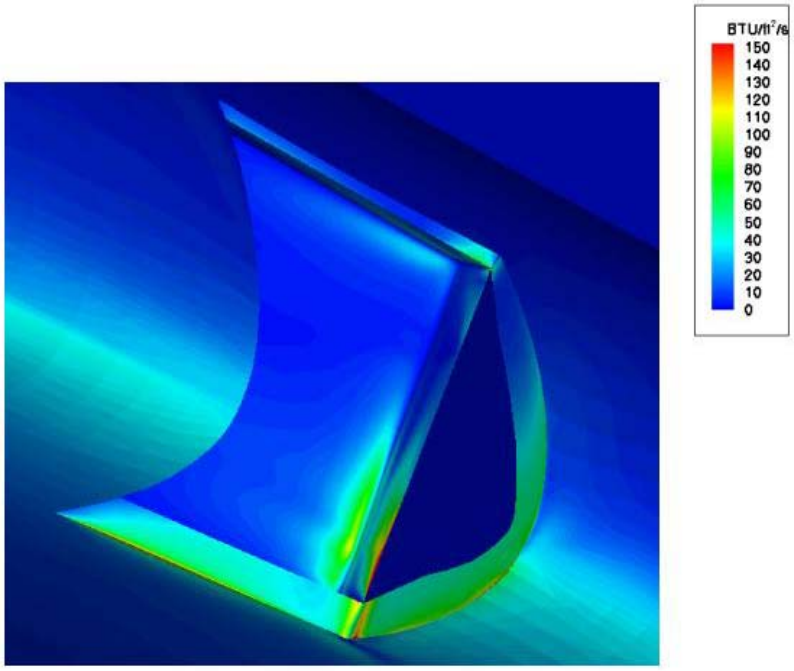

Figure 5.2.4-94 Heat Flux Contours in the Vented RCC Panel 9 Cavity

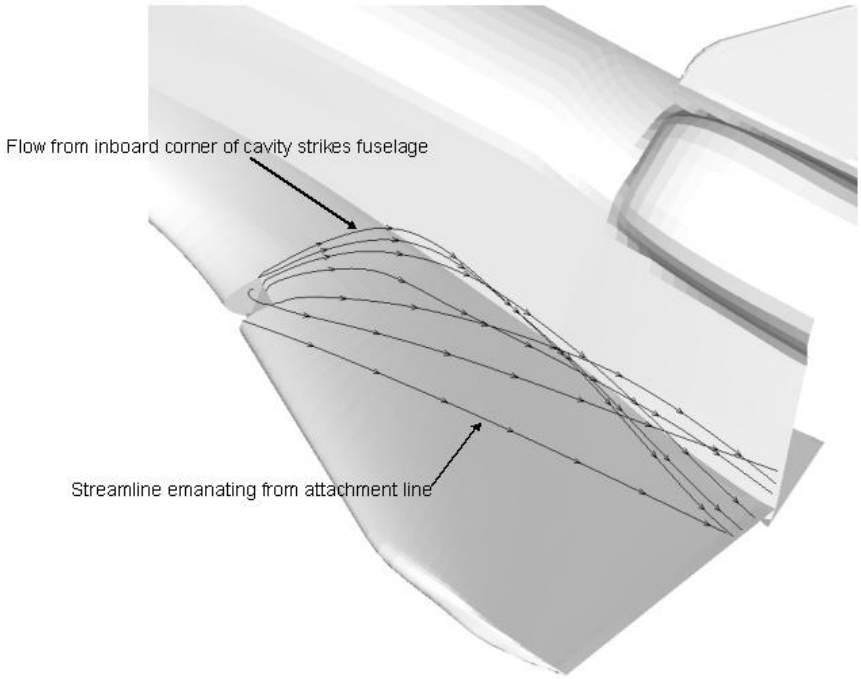

Figure 5.2.4-95 Streamlines on the Body Emanating from the RCC Panel 9 Cavity

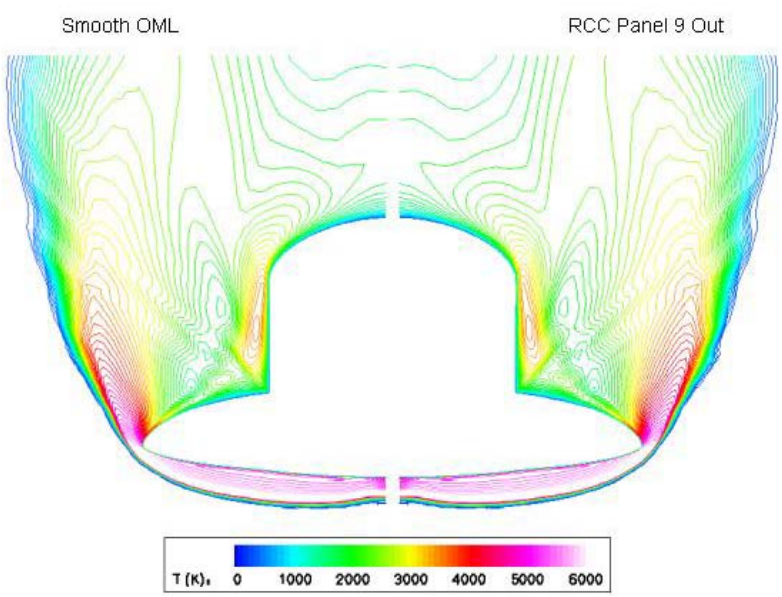

Figure 5.2.4-96 Temperature Contours at X = 1051 inches (40 inches upstream of RCC Panel 9 Cavity)

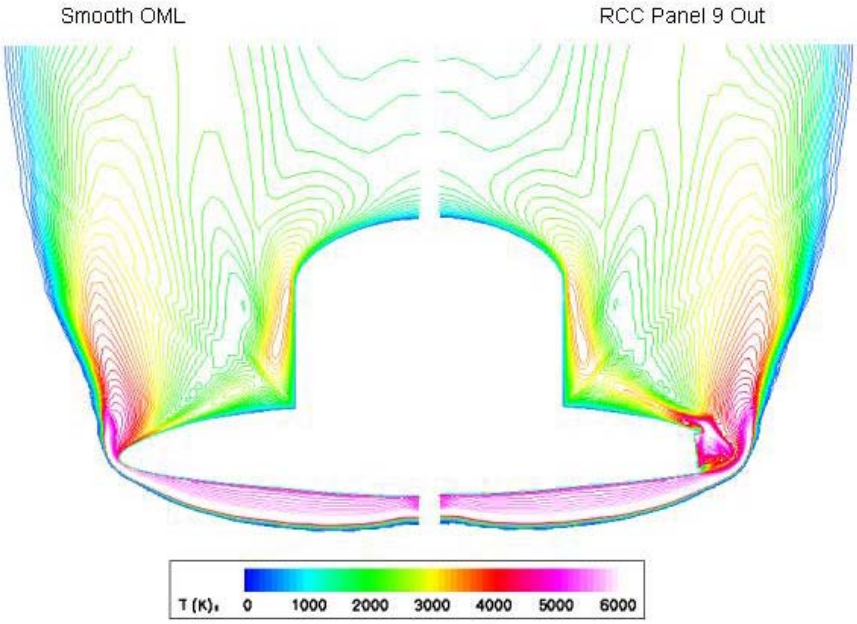

Figure 5.2.4-97 Temperature Contours at X = 1091 inches (at inboard corner of cavity)

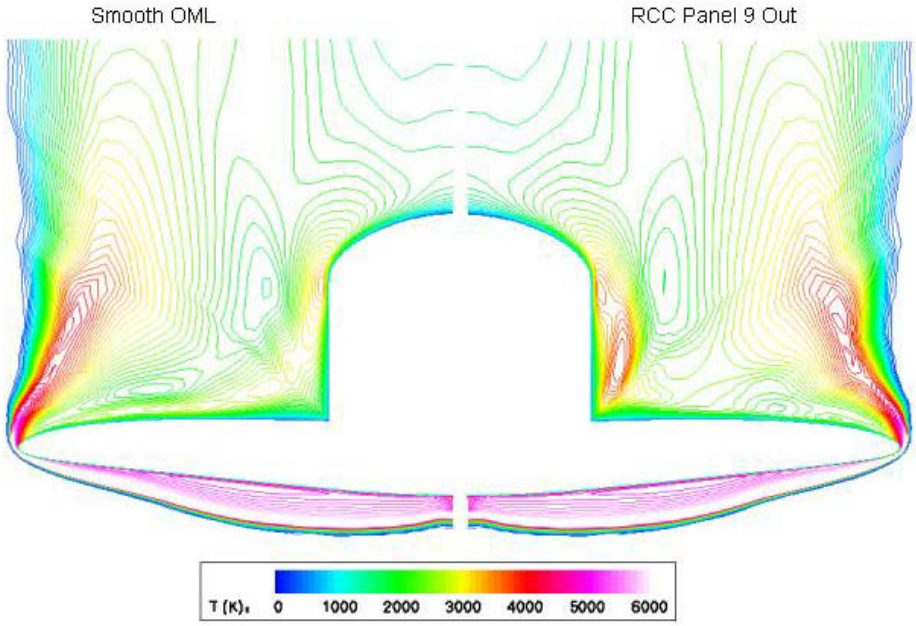

Figure 5.2.4-98 Temperature Contours at X = 1204 inches (halfway between cavity and OMS pods)

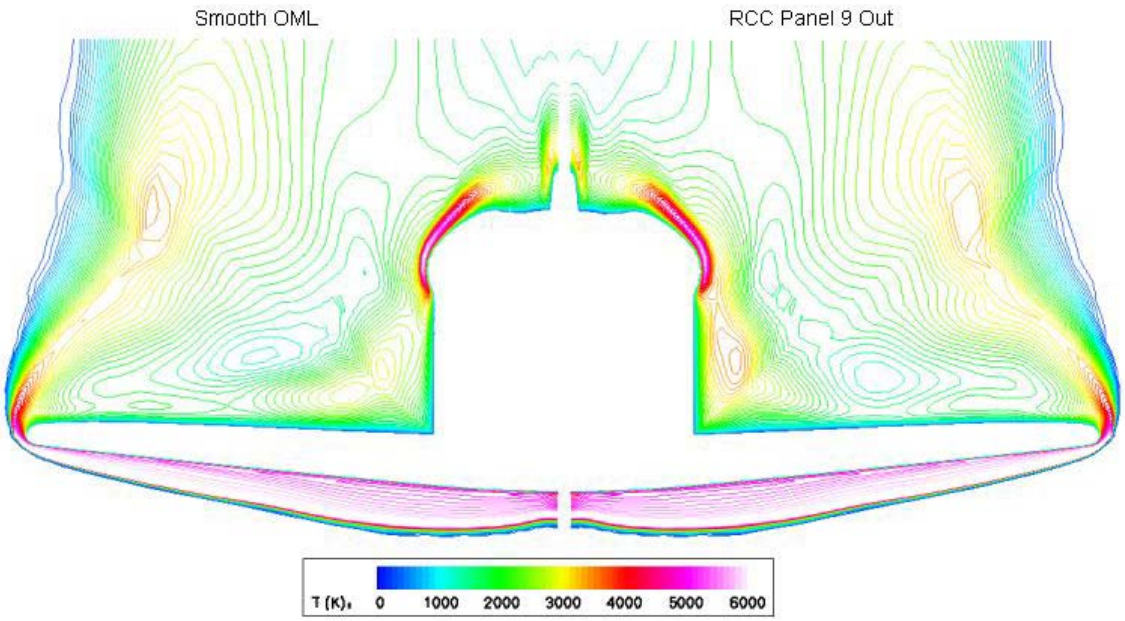

Figure 5.2.4-99 Temperature Contours at X = 1316 inches (at forward portions of OMS pods)

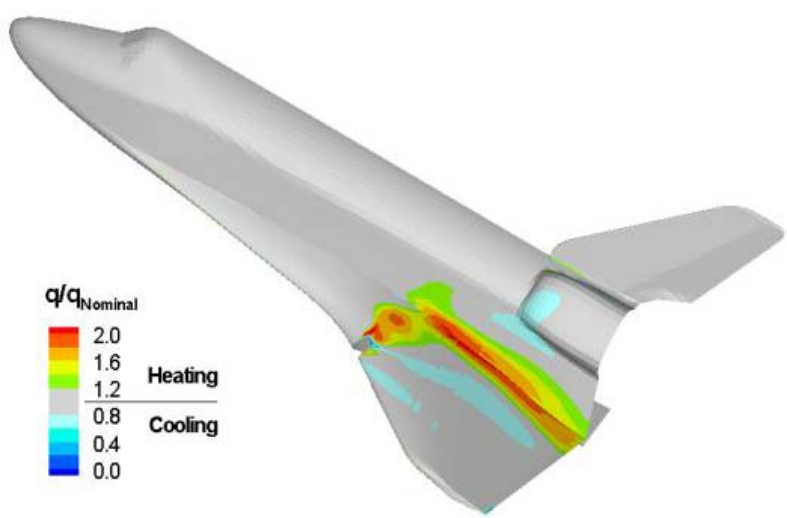

Figure 5.2.4-100 Magnification Factor for Missing RCC Panel 9 Heat Flux

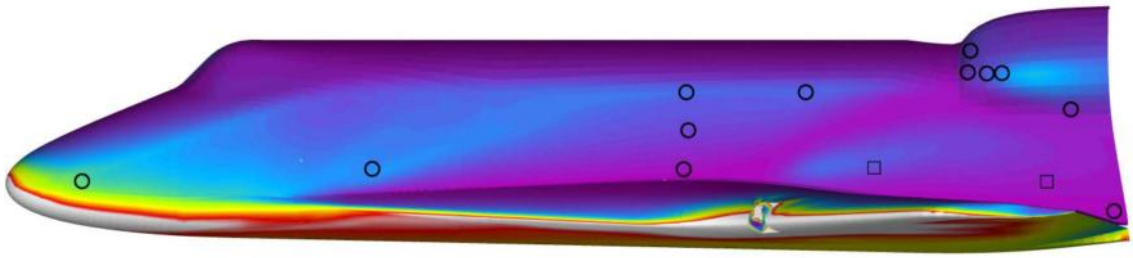

Figure 5.2.4-101 Full RCC Panel 9 Out, with Vented Side Walls, Side View, Heating Rate

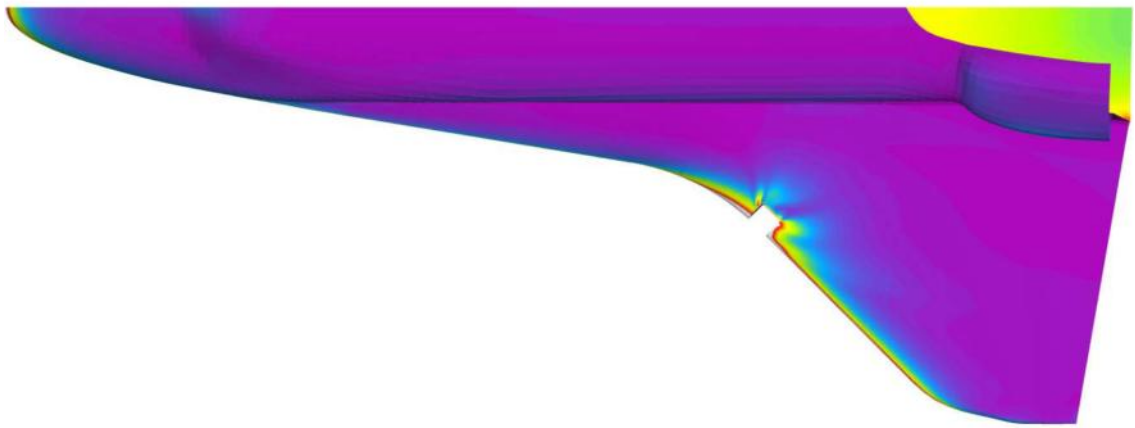

Figure 5.2.4-102 Full RCC Panel 9 Out, with Vented Side Walls, Planform View Heating Rate

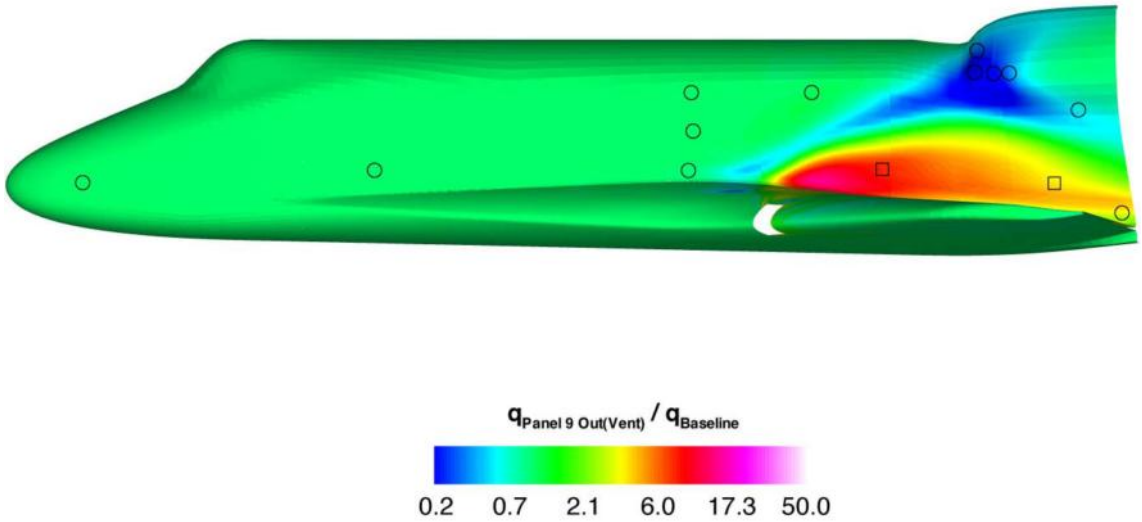

Figure 5.2.4-103 Full RCC Panel 9 Out, with Vented Side Walls, Side View, Ratio of Heat Fluxes

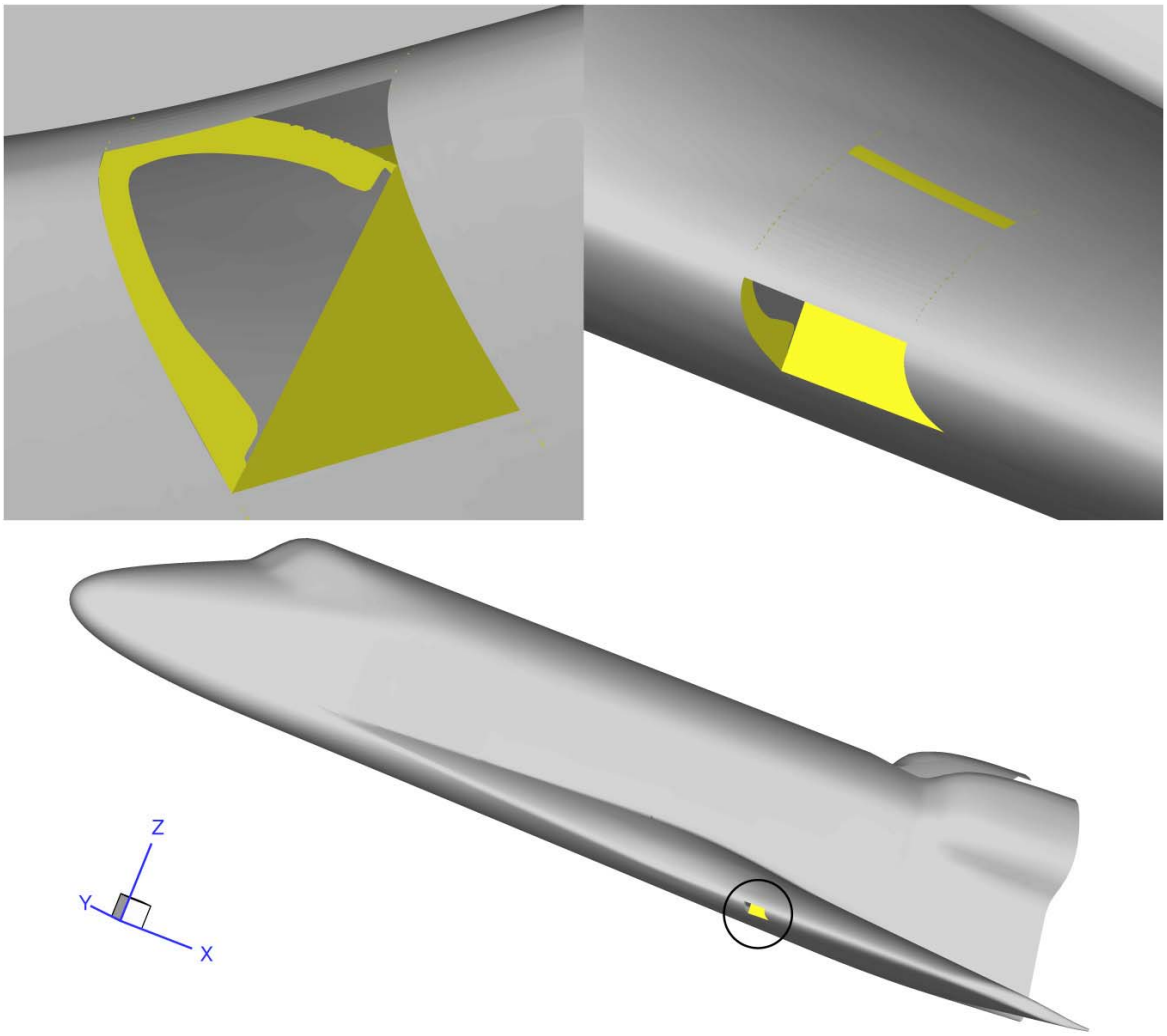

Figure 5.2.4-104 Lower Half RCC Panel 9 Out with Upper Carrier Panel Damage Geometry Used in GASP Simulations

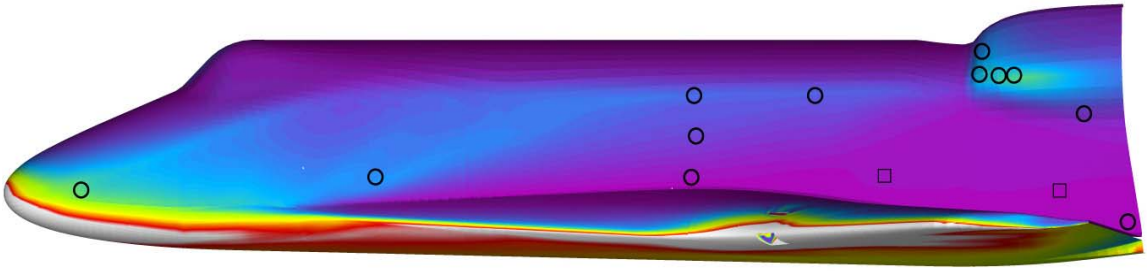

Figure 5.2.4-105 Lower Half RCC Panel 9 Out + Upper Carrier Panel 9 Out, with Vented Side Walls, Side View, Heating Rate

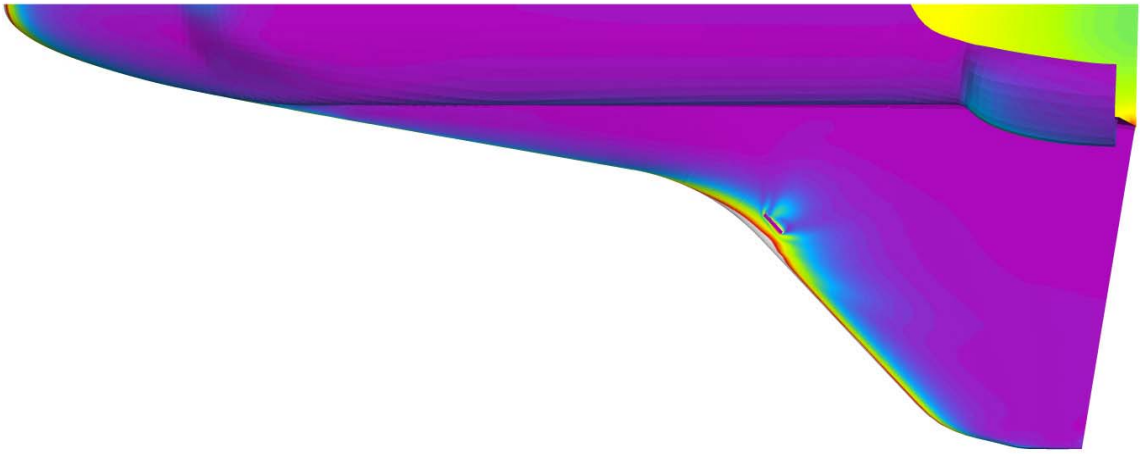

Figure 5.2.4-106 Lower Half RCC Panel 9 Out + Upper Carrier Panel 9 Out, with Vented Side Walls, Planform View, Heating Rate

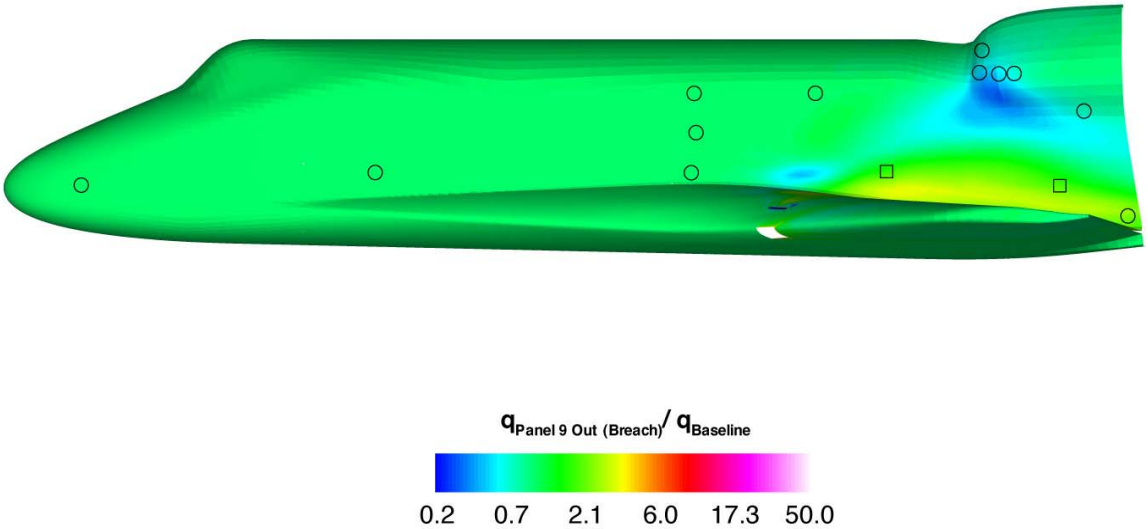

Figure 5.2.4-107 Lower Half RCC Panel 9 Out + Upper Carrier Panel 9 Out, with Vented Side Walls, Side View, Ratio of Heat Fluxes

5.2.5 Application of External Environments Data to the Working Scenario

The objective of this section is to provide a plausible explanation of the observed STS-107 flight data presented in Section 5.2.1 using the results from the various analyses and testing presented in sections 5.2.2 – 5.2.4 above or section 5.3 to follow.

5.2.5.1 Side Fuselage and OMS Pod

The decreased and increased temperature response on the side fuselage and OMS pod can be explained by the working scenario involving damage to the WLE, RCC panels 5 through 9. In Section 5.2.3, sufficient empirical evidence has been obtained to indicate that reduced heating exhibited early in flight (< EI + 480 sec) on the side fuselage and OMS pod sensors was due to changes in the leeside vortex field of the Orbiter, Figure 5.2.5-1, possibly coupled with the dynamics of flow emanating from the WLE damage which perturbs the WLE separation zone. For this reduced heating segment of the flight the most consistent result that matched the flight data was obtained by a case where there was flow through degraded RCC WLE cavity vents, Figure 5.2.3-22 through Figure 5.2.3-24. During this period of the flight, changes in the vortex field were likely caused by additional gas entering the leeside flow field through the vents designed into the upper RCC panel and T-seals, and in possible combination with small local upper carrier panel damage. The correlation of the vented flow to the lee side with flight data necessitates that there was a windside breach along the WLE in order to have the pressure necessary to drive the flow to the leeside with sufficient momentum. The momentum scaling, typically used for flows injected into a cross flow, was used to verify that a proper simulation of the flight environment was being performed and checked against various WLE breach CFD simulations, Figure 5.2.3-23. However, the slot in the wind tunnel model was an order of magnitude larger (1” width full scale, as opposed to 0.1” width full scale) than for the nominal Obiter WLE vent configuration. Therefore, local small damage to the vent area, which could easily occure where the RCC and upper carrier panels meet, has to be present to yield these leeside heating effects. The need for additional vent area was also confirmed using a coupled venting and thermal math model of the wing, Section 5.3.5, for a 10” diameter hole in the windward side of RCC panel 8. For this analysis, the hole existed at EI and the simulation was terminated at the estimated latest point of spar breach, Figure 5.2.5-2. Although mass flow rate is presented, the trend would be similar for momentum. The momentum scaling ratio is on the order of 0.6 from the coupled venting and thermal model. Venting of the RCC WLE cavity with a breach begins to increase significantly at the time the decreased temperature response is recorded on the Orbiter leeside instrumentation. However, the momentum ratio scaling parameter and the information from the wind tunnel tests and venting analyses allow the conclusion to be made, that the mass flow rates, and thus the momentum rates, out of the nominal 66 square inch leeside vent area would be too small to result in the initial side fuselage and OMS pod disturbance. Thus, before either the spar is breached or additional significant damage to the upper carrier panel occurs, the flow entering the WLE from the windward side was exiting through the leeside vents with locally damaged upper carrier panel(s), Figure 5.2.3-24.

The increase in side fuselage and OMS pod heating that occurred later in flight (> EI + 480 sec) can be explained by progressively worsening damage to the upper portion of the RCC panel, upper carrier, and eventually the upper wing skin. Although the increased side fuselage and OMS pod heating began as early as EI+510 seconds, significant changes in the off-nominal leeside temperature response can be attributed to the observed debris events. For instance, debris # 5 (considered to be more of a flash event than a debris event, as a result of ballistic coefficient and luminosity analyses) is closely tied to changes in the temperature response of gauges V07T9220, V07T9976, and V07T9978, Figure 5.2.1-6. Likewise, flash event 1/debris # 6 can be related to significant changes in slopes for gauges V07T9253 and V07T9925, Figure 5.2.1-5. It is important to note that debris # 5 is also closely correlated to the slope change in the delta rolling moment, discussed in Section 4. Therefore, significant changes in the increased heating signatures can be correlated to the observed debris events, which imply progressively worsening damage on the Orbiter.

During the increased heating period, the actual Orbiter configuration remains unknown; thus, multiple leading edge damage geometries, full and half panels, missing T-seal 8, and holes through the wing were evaluated in both the Mach 6 Air and CF_4 facilities. This information has been used to determine the

effect on side fuselage and OMS pod heating of different types of damage, Section 5.2.3. Since holes through the wing showed no evidence of sidewall and OMS pods heating augmentation, the focus turned towards some form of leading edge damage. Leading edge damage is required in order to provide the energy and pressure necessary to affect the leeside flow field. As can be seen in Figure 5.2.3-8 and Figure 5.2.3-16, the results from the Mach 6 air and CF_4 facilities show significant side fuselage and OMS pod disturbances for full RCC panel out cases 5 through 9 (Working Scenario). Overlaid on these figures are the MADS and OI measurement locations. As shown, the impingement footprint is dependent on the removed panel location and the facility. It was noted in the Mach 6 air results for panels 5 through 8 that although increased heating was indicated on the side fuselage, decreased heating was observed on the OMS pod. This combination is inconsistent with the flight data. However, when panel 9 was removed the results in the air facility were more consistent with the flight data. The results for the CF_4 facility showed that increased OMS pod heating was observed for all of the removed RCC panel cases. Setting aside the differences between the two facilities, there is substantial evidence that a damaged WLE will result in increased heating to the side fuselage and OMS pod. The testing results showed heating augmentation factors of from 2 to 10, whereas flight data indicated factors of 1.7 to 5.2 for the MADS data and up to 13 times for the OI V34T1106A gauge (Section 6).

However, the debris evidence indicates that most of the RCC panels were recovered with the exception of a majority of panel 9 and a large segment of panel 10. In addition, all the recovered RCC panel debris was found in Texas. It is believed that having substantial portions of the RCC missing as early as EI+510 seconds is not consistent with the vehicle flying all the way to Texas airspace. It is noted that the debris contains only a single interior tile for upper carrier panel 8 and that neither of upper carrier panels 9 and 10 was recovered. This lack of debris along with the above discussion on the reduced heating provides a consistent explanation for the initial cause of increased heating on the side fuselage and OMS pod. The explanation is that damage to the upper carrier panels became severe enough to allow substantial flow through the WLE vents, with at least a compromised vent path geometry. In order to demonstrate this, a half RCC panel 9 removed model configuration was modified to include the upper carrier panel missing. This geometry allows WLE damage to provide gas flow through the WLE and out the leeside venting location. The results of that wind tunnel test, shown in Section 4.3.1, indicated similar heating trends as the full panel out case.

As was stated above, a compromised upper surface geometry coupled with windward RCC damage was the most likely cause for the initial increased heating. Note that during this time the spar had already been breached and that significant damage was occurring to the wiring instrumentation along the spar and the wheel well. The analysis shown in the next section and the related results discussed in Section 6 will indicate that damage was also occurring to the intermediate wing structure. Since debris event 5 (flash 0) and flash event 1 / debris event 6 closely tie to changes in the side fuselage and OMS pod temperatures as well as the vehicle aerodynamics, it could be postulated that they are indications of upper wing skin breach in the intermediate wing area. The flash events are believed to be the release of small high temperature particles which rapidly decelerate in the Orbiter wake, as concluded from a ballistic coefficient. These particles, as will be shown, could have been combusting aluminum present in the intermediate wing interior, which was then vented to the exterior when the upper wing was breached.

A final question, that of determining which facility provides the more appropriate simulation of the Orbiter leeside flight environment for a damage configuration, may be addressed computationally Extensive aero/aerothermal calculations for the Orbiter with missing half and full RCC panels 6 and 9 were performed at CFD Case # 1 flight condition. Both the half panel out cases showed similar results to the wind tunnel in that no significant heating augmentation could be seen on the side fuselage and OMS Pod, although local disturbances do occur on the leeside of the WLE very near the damage location. The full RCC panel out cases with solid sidewall boundaries also showed side fuselage and OMS pod effects comparable to the wind tunnel results, and tend to favor the CF_4 measurements. However, because of uncertainties in grid resolution requirements and the physical modeling assumptions needed to simulate the leeside flow field accurately, it remains a judgment as to whether or not CFD solutions can be used to differentiate which facility best represents the Orbiter flight environment.

5.2.5.2 Wing Surface T/C V07T9666A

The response of V07T9666A is closely related to the events on the side fuselage and OMS Pod. As mentioned previously, the off-nominal trend for this T/C does not begin until after the indications of reduced side fuselage and OMS pod heating, off-nominal response of the spar temperature and strain gauge at RCC panel 9, and off-nominal clevis temperature response at the RCC panel 9/10 interface. There are two possible explanations for the V07T9666A measurement response. The first possibility is that an external flow disturbance caused by the damage site on the WLE propagated downstream to the measurement location via boundary layer transition. The second possibility is that disturbed flow came out of the WLE damage back onto the windward surface as a result of high temperature gas ingestion into the WLE cavity.

For the first possibility, a boundary layer transition analysis of the Orbiter near this point of the flight was performed. Figure 5.2.5-5 indicates that it would require a trip height of between 1.2" and 1.4" to result in an effective transition trip (see Appendix 5.6 for more information on effective trip calculation). At EI+370, the free stream Reynolds number for the Orbiter, presented in Figure 5.2.5-3, is approximately 5.0×10^5. Given a large enough damage site, a boundary layer disturbance could propagate downstream. No correlation is presented between the effectiveness of a protuberance versus that of a cavity, but a cavity would be more representative of a damaged WLE. However, protuberances are typically more effective at promoting boundary layer transition. For example, Figure 5.2.5-4 shows the limited downstream effect of a 6" diameter hole on the windward side of RCC panel 6. However, it will be shown that the damage necessary to cause the Columbia accident has been narrowed down to either a significant portion of a T-Seal, or RCC acreage damage on the order of 30 to 80 square inches. Moreover, this size of damage would be large enough to result in a locally disturbed flow extending from the damage site to this region of the wing given a high enough Reynolds number. Figure 5.2.5-6 presents a surface streamline plot of the Orbiter WLE region showing how the flow passes over the vehicle at EI+404 seconds. Since the working scenario addresses damage to the WLE in the area of RCC panels 5 through 9, this damage zone propagates streamwise effects which would pass over this gauge.

For the second possibility, the debris along with the above mentioned flight data provide a supporting rationale for the off-nominal temperature responses. As was noted, heating was already occurring in the WLE cavity at the time of leeside surface heating excursions. Therefore, flow was entering the cavity and exiting the WLE vent system (nominal configuration or damaged) prior to EI+370. Close inspection and reassembly of the debris in the RCC panel 8 and 9 area, Figure 5.2.5-7, indicated that flow out of the WLE cavity from a manufactured slot at the back corner of RCC panel 8 did occur. This flow is evidenced as well by the erosion on the RCC panel 9 lower carrier panel tiles. The answer for how flow can exit the WLE cavity to the lower surface of the wing is that the interior of the WLE cavity must be at a higher pressure than the local external pressure. At the high angle of attack during entry, the local pressure on the lower surface of the wing beyond the leading edge is approximately equal to the free stream dynamic pressure. In order to determine the relative pressure of the two regions given a damaged WLE condition, a coupled external / internal CFD of the Orbiter must be performed. This issue will be addressed in the section on internal aeroheating environments.

5.2.5.3 Chin Panel and Vacuum Vent / Water Supply Dump Nozzles

A possible explanation for the temperature responses of the chin panel and vacuum vent/water supply dump nozzles in flight is that a local disturbance to the flow, such as a protrusion, could have existed which then burned away over the period of time in question. For the chin panel gauge, the protrusion itself would have to be the gap between the nose cap and chin panel, exactly where the expansion seal resides. Preflight inspection of the gap, (see Boeing TM, ATA-TM-02-0009) indicated a small excursion of 0.002" beyond the equivalent roughness requirement of 0.120" just left of the vehicle centerline. Again referring to Figure 5.2.5-5, boundary layer transition analysis of the Orbiter at this point of the flight indicates that it would require a trip height of between 1" and 1.4" to result in an effective transition trip. Also, this trip had to be located at or outside the attachment line streamline such that the disturbance in the flow was swept overboard, because no disturbance was observed on any of the windward fuselage T/Cs downstream from the nose cap, see
Figure 5.2.5-8. Therefore, from an aerothermodynamic perspective, the response of the chin panel expansion seal gauge cannot be readily explained. Adding to that, as will be discussed in Section 6, is

the fact that the temperature response of the expansion seal gauge is non-physical with respect to how it recovers to the original slope of the curve.

For the vacuum vent and water supply dump nozzles, two possible explanations for the transient were proposed and investigated: (1) change in the vehicle orientation, and (2) a local flow disturbance just upstream from the two nozzles that flows along the same streamline. The nozzles are right above the beginning of the wing glove (forward wing extension). At this location the flow wraps around the chine of the wing glove, forming a vortex. This vortex is the source for the nominal heating in this region, Figure 5.2.5-9. Where the vortex scrubs the surface there is higher heating than where it does not; this can be seen in Figure 5.2.5-10. The location of this vortex is a function of the angle of attack and angle of sideslip, shown in Figure 5.2.5-11 and Figure 5.2.5-12, respectively. The variation in the angle of attack during this period is negligible with respect to the variation of the aeroheating environment. The variation of the angle of sideslip, although small, was investigated as a potential source for the off nominal events. As was seen in the aerodynamics section, this variation of sideslip was not outside previous flight experience of the Orbiter during this portion of the re-entry. CFD analysis of the Orbiter forebody showed insignificant changes in the heating due to variations in sideslip from 0 to –0.5 degrees.

From a local flow disturbance perspective, as can be seen in
Figure 5.2.5-9, the flow crossing both the vacuum vent nozzle and the water supply dump nozzle would also cross V07T9522, a surface T/C. Any disturbance strong enough to cause a change in the heating of the nozzle should have also disturbed the heating to this surface T/C. As was indicated previously, the only anomaly seen on this gauge is a sharp drop in temperature for one cycle during this time; otherwise, the response was determined to be nominal. Thus, again, from an aerothermodynamics perspective, the responses of the vent nozzle and water supply dump nozzle cannot be readily explained. Therefore, both the off-nominal events related to the chin panel and these nozzles should be listed as unexplained anomalies (UA).

5.2.5.4 Kirtland Photo

As was shown in Section 5.2.4, no dramatic changes to the windward and leading edge shock shapes could be discerned from the CFD solutions with RCC panel 6 or panel 9 removed. However, the source of the bulge in the light from the leading edge could have been either from embedded shocks in the damage zones or from additional particulates in the flow field as the damage progressed, or a combination thereof. No supporting evidence for the proposed particulate explanation exists. For the proposed imbedded shock explanation, Figure 5.2.5-13 is an example of the resultant embedded shocks due to WLE damage. The additional shocks would likely re-excite the N_2 first mode, which is the principle light source in the shock layer immediately around the vehicle. However, this explanation remains speculation, and thus there is no substantial evidence that can explain the Kirtland photo.

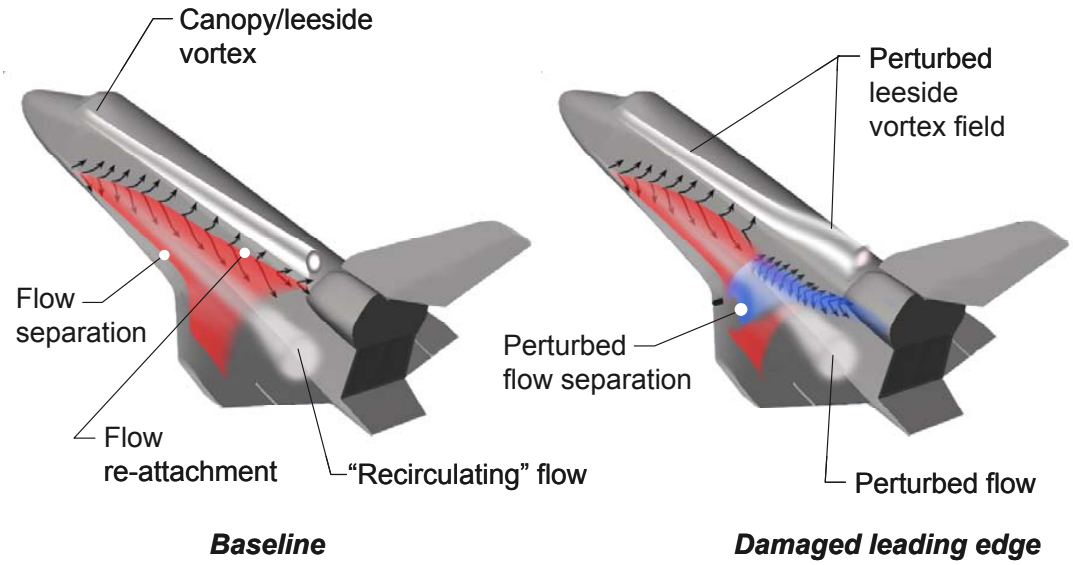

Figure 5.2.5-1 Postulated Orbiter Leeside Flowfield Associated With Wing Leading Edge Damage. Wing leading edge damage perturbs leeward flow separation and re-attachment locations as well as leeward embedded shocks (not shown).

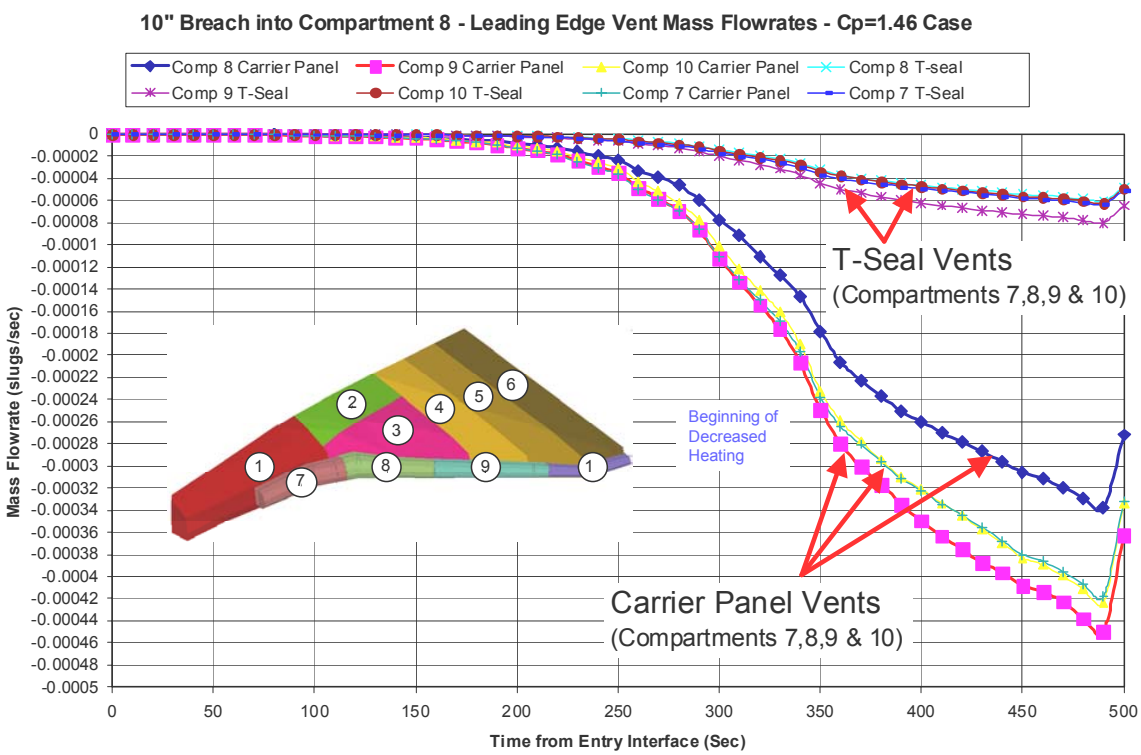

Figure 5.2.5-2 Leading Edge Vent Mass Flow-rate Summary - 10" Breach Cp=1.46. Results from MSFC-developed coupled venting and thermal wing model.

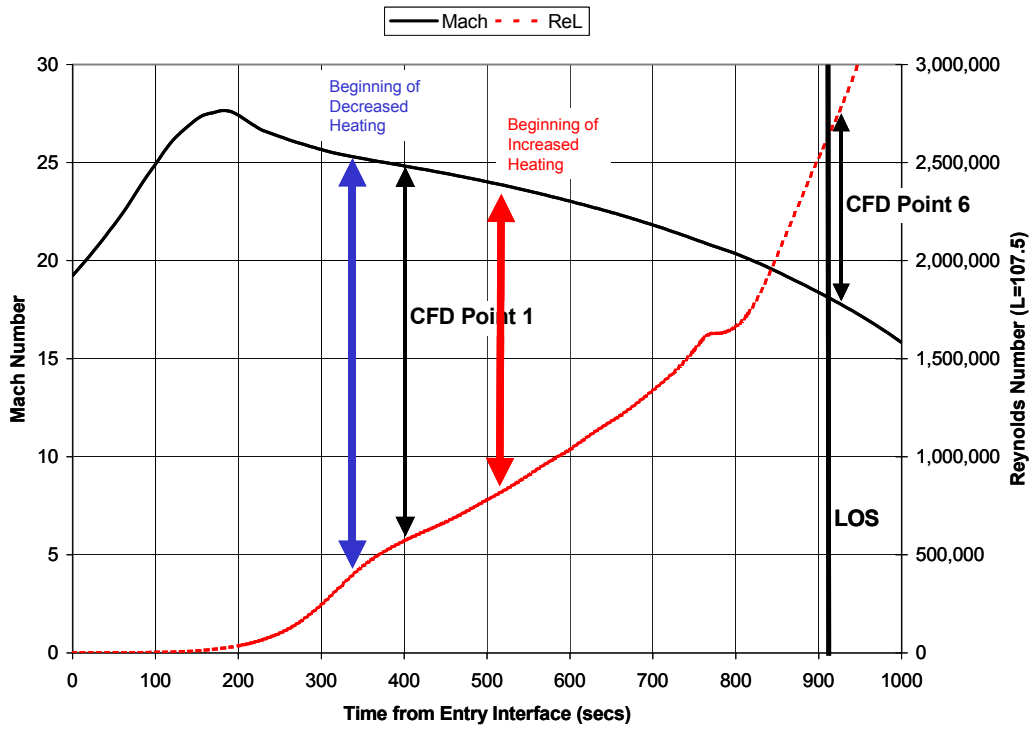

Figure 5.2.5-3 STS-107 entry trajectory, Mach No. and Reynolds No. from entry interface

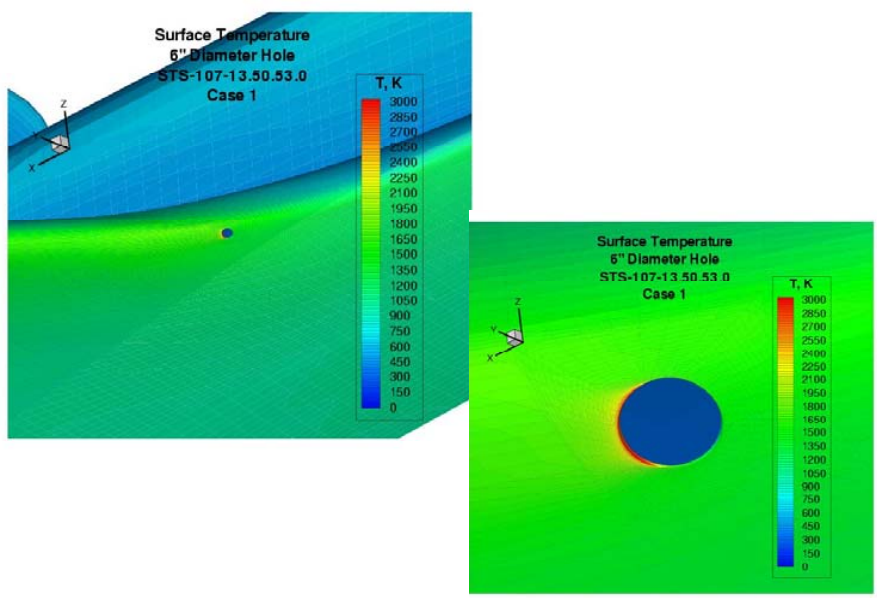

Figure 5.2.5-4 NASA LaRC LAURA CFD solution of a 6" hole on the windward side of Panel 6. Note the limited downstream disturbance of the flow.

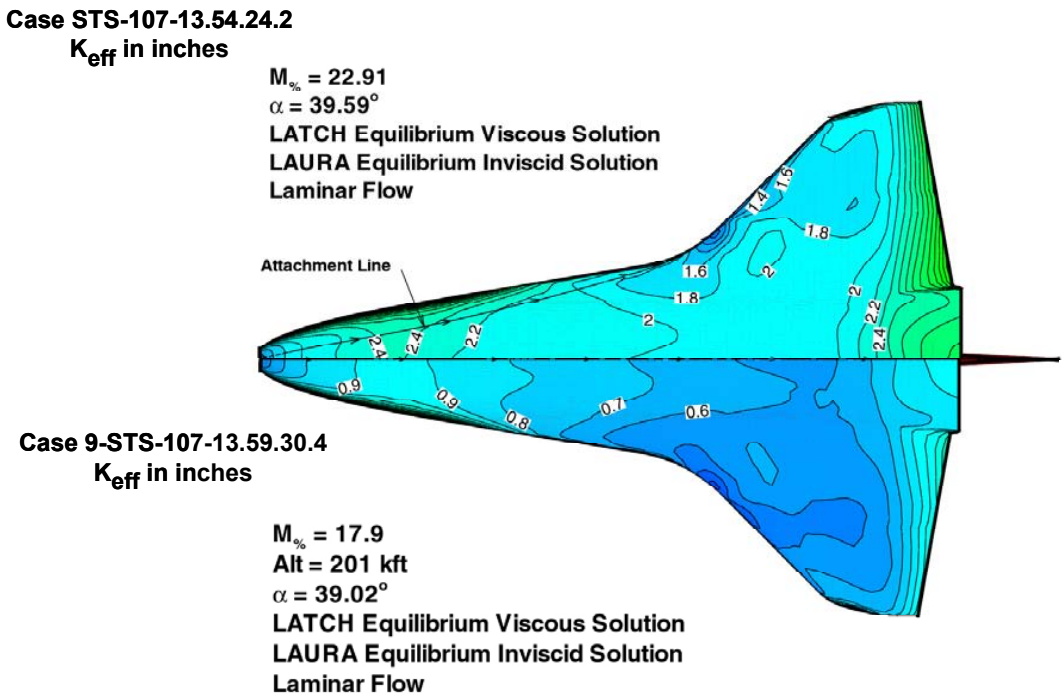

Figure 5.2.5-5 Effective Roughness Height for Transition

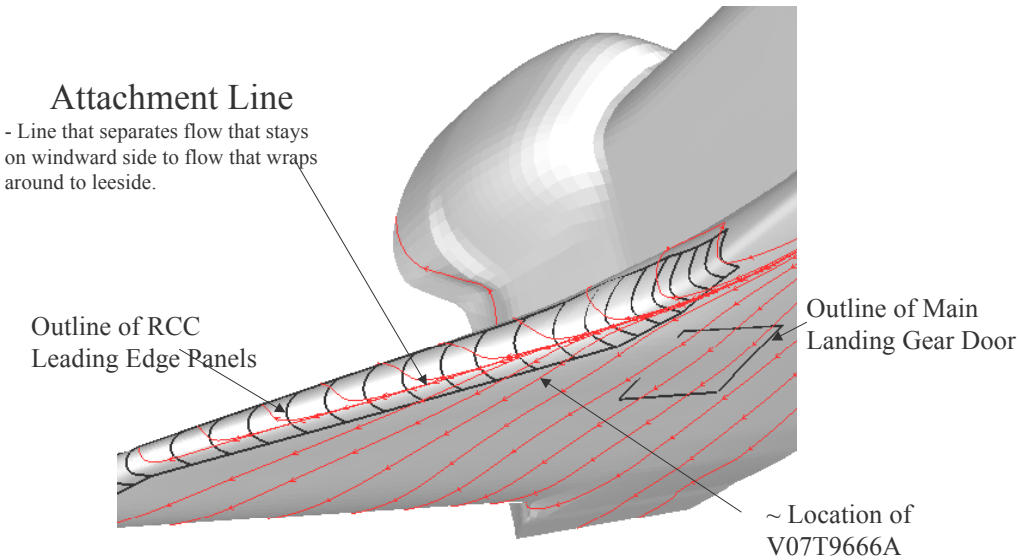

Figure 5.2.5-6 Orbiter surface streamlines. CFD Point 1, EI+404, Mach 24.9, 243 kft.

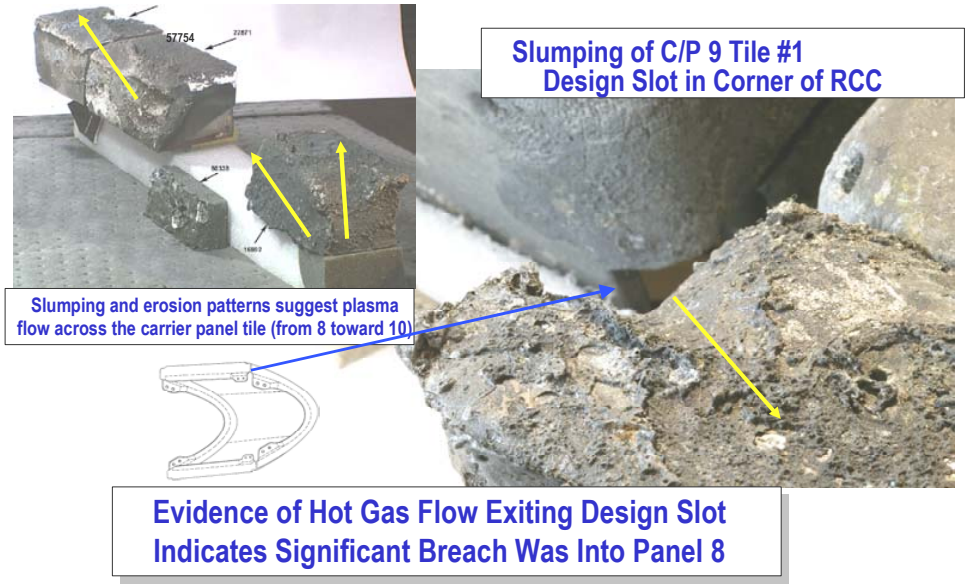

Figure 5.2.5-7 Hardware Forensics Team reassembly of RCC Panel 8 with RCC Panel 9 Lower Carrier Panel Tiles. April 28, 2003 presentation to the OVEWG.

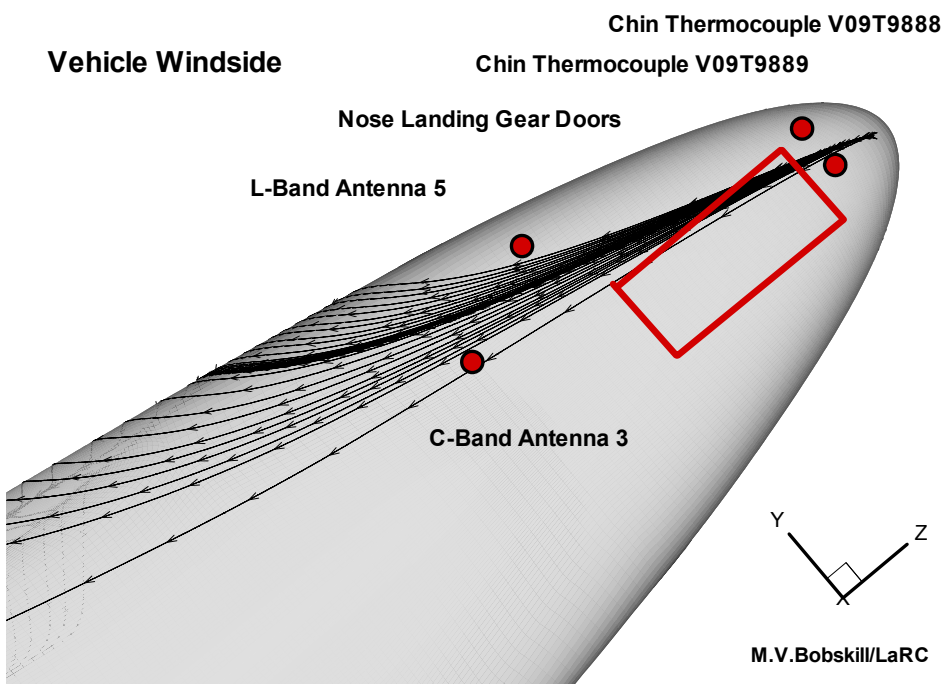

Figure 5.2.5-8 Orbiter surface streamlines crossing chin panel region.LaRC LAURA solution of CFD Case #1. CFD solution is of right side when angle of sideslip equals 0. Chin Panel gauges are in the correct relative position.

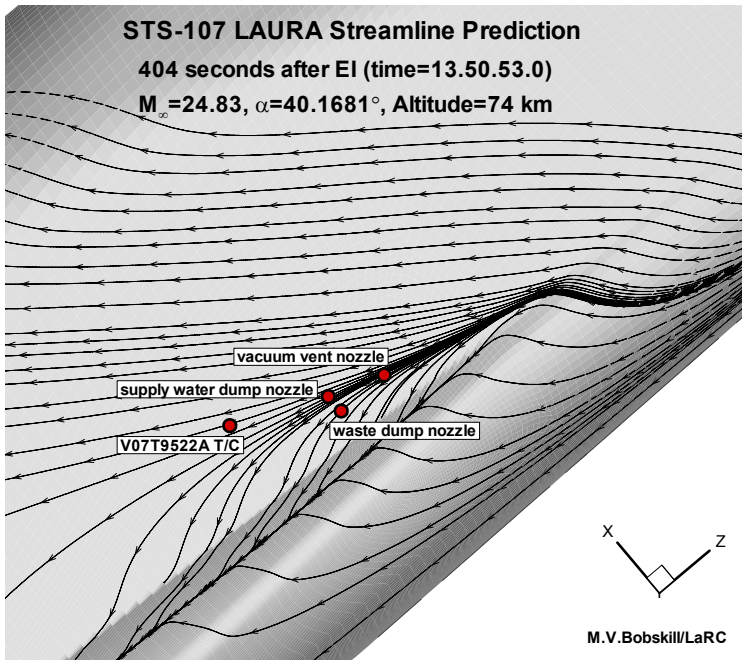

Figure 5.2.5-9 Orbiter surface streamlines in vent nozzle region. CFD solution is of right side when angle of sideslip equals 0. Nozzles are in the correct relative position.

.

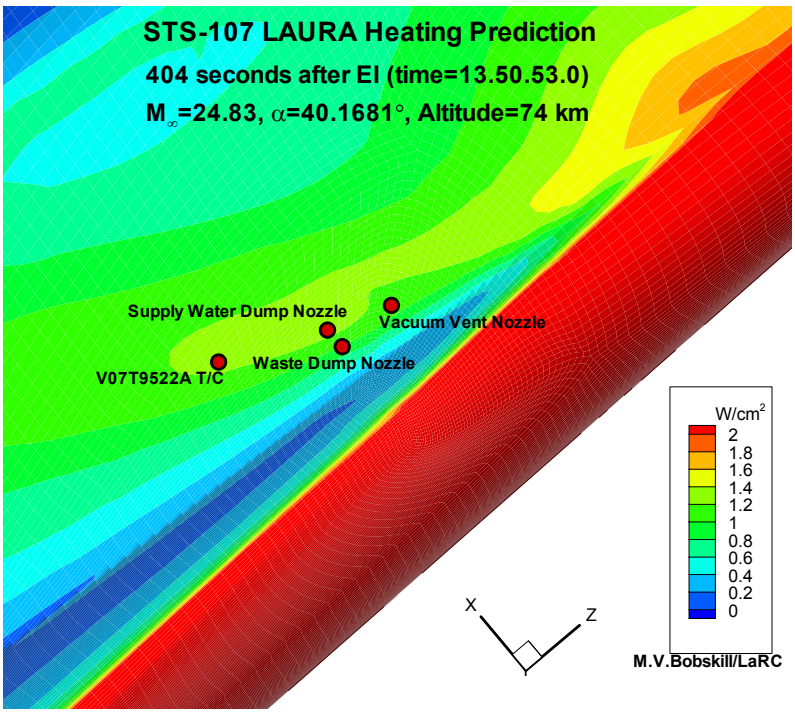

Figure 5.2.5-10 Orbiter surface heating in vent nozzle region. Note CFD solution is of right side when angle of sideslip = 0 deg. Nozzles are in the correct relative position.

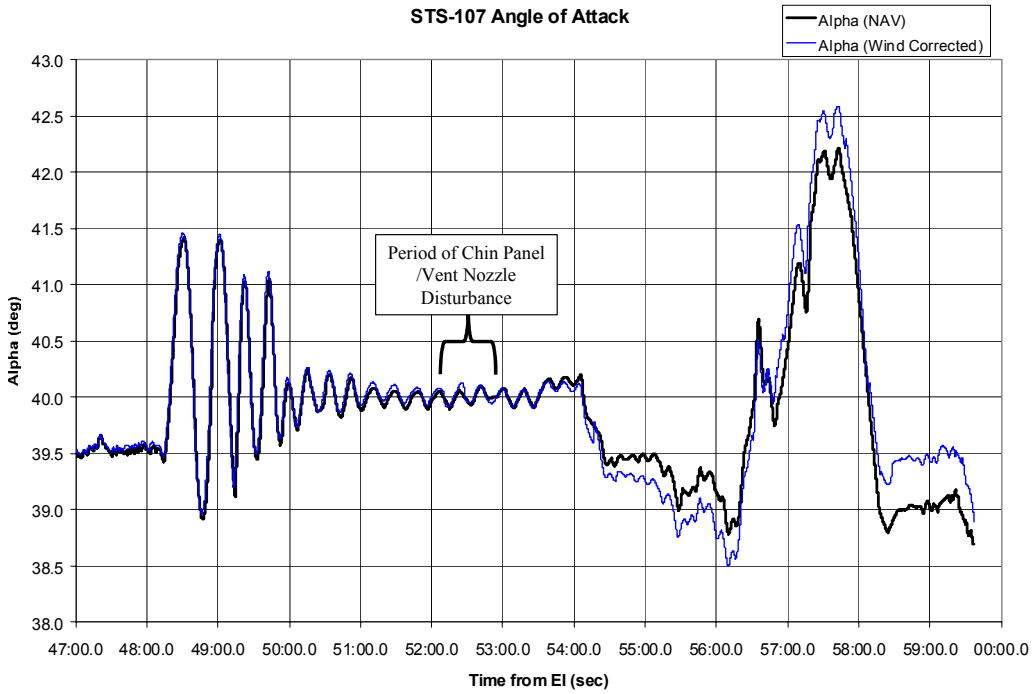

Figure 5.2.5-11 STS-107 Angle of Attack History with and without modeled winds. See Section 4.0 for further detail on model wind effects.

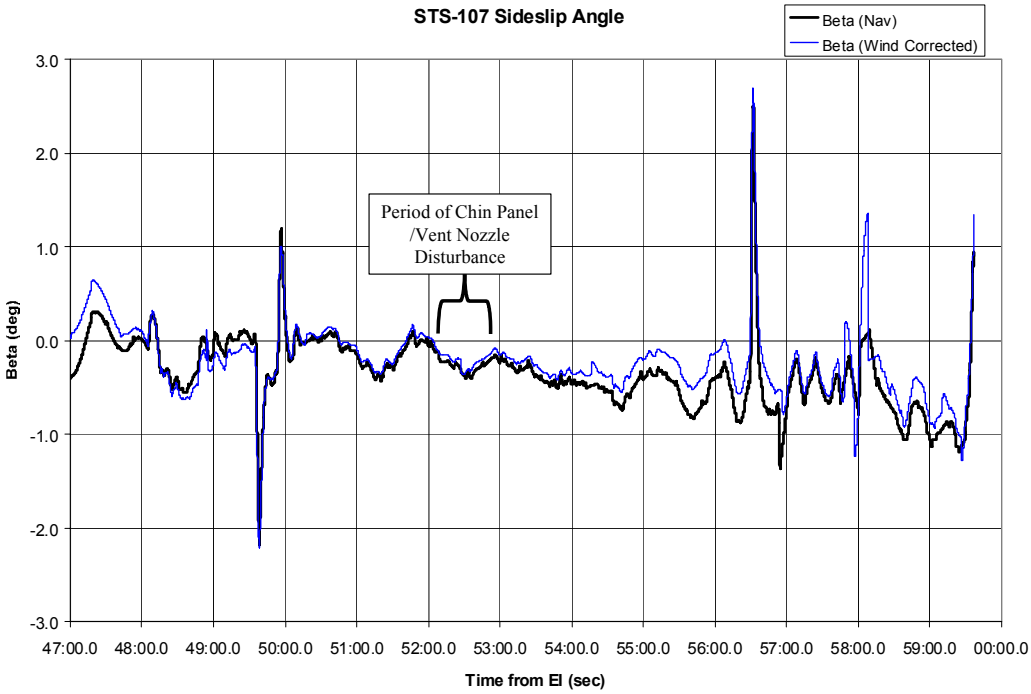

Figure 5.2.5-12 STS-107 Angle of Sideslip History with and without modeled winds. See Section 4.0 for further detail on model wind effects.

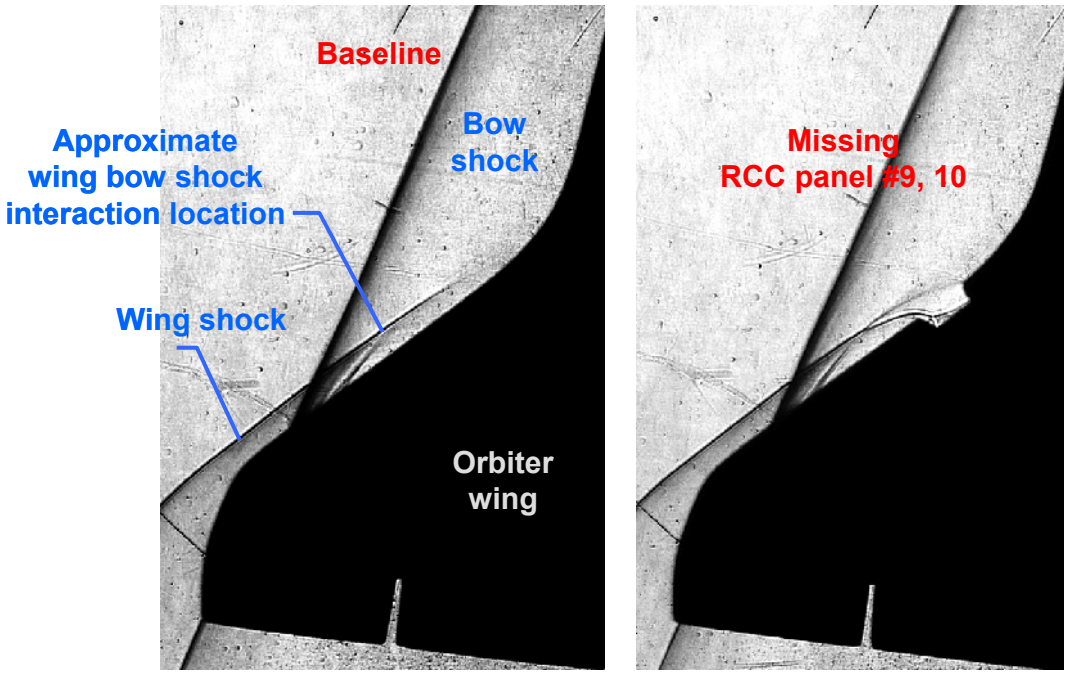

Shock patterns (path integrated)

Figure 5.2.5-13 An example of imbedded shocks along the wing leading edge as a result of wing damage. Schlieren images taken in the LaRC Mach 6 Air facility. Note, shock locations are freestream Mach No. dependent.

5.3 Damaged Orbiter Internal Aerothermodynamic Environments

This section of the report details Internal Aerothermodynamic team activities contributing to the STS107-investigation working scenario. Internal environment team members focused on the analysis, investigation, prediction, and understanding of the complex, high temperature gas dynamics environment within the Orbiter wing following a breach of the external thermal protection system. From this point of view, the internal environment interfaced to the external environment activities, previously discussed, at the undisturbed outer mold line of the vehicle. Preliminary assessments, assuming independence of the two separate environments, proved to be inadequate, however, and required the complete integration and coupling of the exterior flow field with the internal breach environments. This direction led to the development and application of new aerothermal tools and techniques, which are discussed in the following sections below.

Section 5.3.1 will discuss the overall process of developing the internal environments used for thermal analysis as detailed in Section 6. Sections 5.3.2 through 5.3.6 detail the individual activities and tool development efforts required to produce integrated environments. Finally Section 5.3.7 will pull together the lessons learned and insight provided by the studies as an application to the present working scenario.

By the very nature of internal flow environments (that a hole has to exist before they come into play), the results of all analysis are highly scenario dependent. While insight and general understanding of the dominant fluid dynamics can guide engineering analysis, one must keep in mind that a small change in hole location or diameter may produce entirely different results. Given the degree of uncertainty regarding the actual damage, internal engineering predictions of heating were generally characterized with +/- 50% levels of uncertainty. These models were most useful for matching trends and understanding major phenomena. Refined CFD analyses, discussed in Section 5.3.6, emerged late in the investigation that locally produced peak heating rates several factors larger than engineering model results. The large heating rates predicted result from extreme flowfield gradients picked up in the finer grid solutions. Comparisons with the engineering distributions are presented in Section 5.3.7.

5.3.1 Process of Determining Internal Aerothermodynamic Environments

The use of Computational Fluid Dynamic tools for high temperature gas dynamic environments has progressed significantly over the last decade in the development of external aerothermal environments. With experienced CFD personnel and baselined tools, the external Aerothermodynamic teams were primed to get started within a relatively short time. Internal environments, however, were a different story. The following process was developed from scratch specifically for the STS107 investigation and drew on tremendous talent from across the country. (Note: the work covered in this report represents only a fraction of the total effort put forth by the Internal Flow team. Much of the unique and cutting edge analysis did not have direct bearing on the present working scenario, and thus, was not reported here. The remaining work will be reported in the future.)

5.3.1.1 Process Development

Immediately following the demise of Columbia, the aerothermal community came together and brainstormed activities required for understanding fluid dynamics of the entry event timeline leading to the loss of vehicle. In the process, a framework for constructing the necessary information and toolsets emerged with clear delineation between external and internal aerothermodynamics. The internal team was given the challenge of developing insight and tools to understand an environment involving multiple penetrations of supersonic, high temperature gases into complex geometries with coupled heat transfer to structures. The starting point for the process was identification of the types of analyses that would be required, identification of personnel and tools to perform the analysis, and establishment of a plan to meet all objectives in a short few months. Table 5.3.1.1-1 displays the five major fields of analysis identified and how they play together to provide a clear picture of three early scenarios. Given the unique nature of the investigation it was clear to the team that the required expertise to complete the analysis did not presently exist within the aerothermal community and would have to be developed.

At the outset the team developed a series of Unit Physics benchmarks, see Table 5.3.1.1-2, that separated the fully coupled, complicated problem into smaller pieces that could be individually simulated and compared to

calibration quality test data to assure the tools and capabilities could accurately simulate the necessary phenomena. These pieces would then be built upon through a series of increasingly complicated, more flight-like cases, leading to the fully coupled external/ internal failure simulation at true flight conditions. This process, as developed, is summarized in Figure 5.3.1-1.

Implementing the entire process shown in Figure 5.3.1-1 proved to be untenable within the time constraints of the investigation. Therefore, the majority of the internal team's CFD analysis relied on current best practices. However, for three specific failure scenario analyses the CFD did proceed through the key steps of this process. The CFD tools implemented for the two and three-dimensional T-Seal damage and the RCC Panel 8 10" breach (Sections 5.3.6.2.2, 5.3.6.2.4, 5.3.6.1.2, respectively) were benchmarked to the key Unit Physics and Unit Physics Extension relevant for those failure scenarios.

Thermal analysts require heating distributions and histories to assess structural temperatures and hardware failure times. Engineering methodologies for predicting internal environments were developed in parallel with the CFD techniques for the full-scale problem to meet thermal analysts data and schedule requirements. In order to provide greater consistency and accuracy, the interface for all internal tools was always the latest, most complete CFD analyses available from the external environments team. These additional tools include boundary layer extraction and mass/energy balance tools, venting and coupled thermal/venting tools, engineering plume impingement heating tools, and basic engineering support CFD for tool assessments. Figure 5.3.1-2 presents the internal environments process and some of the interactions between components.

	A. MLGD Penetration	**B. Wing Leading Edge Damage**	**C. Acreage Tile Loss**
1. Venting Analysis	1. Mass flow analysis 2. Energy balance 3. Penetration parametrics	1. Mass flow analysis 2. Energy balance 3. Penetration parametrics	1. Penetration location parametrics
2. Fluid Thermal Coupling	1. Flow past seal 2. Flow through crack	1. Flow past seal 2. Energy loss to wing structure	
3. Engineering Model CFD Support	1. 2D/Axi Jet modeling 2. Flow into cavities 3. Simplified 3D	1. Swept cylinder with hole 2. 2D into RCC cavity	1. Flow over cavity with penetration
4. Penetration flow engineering models	1. Modeling of Jet 2. Impingement modeling	1. Spar Impingement 2. Attach Hardware	1. Test data analysis 2. 3D heating factors
5. Large Scale CFD	1. Wheel Well Penetration 2. Door Ajar/Seal Breach 3. Vent ingestion	1. RCC Leading Edge penetration 2. Lower Seal breach 3. Missing panel	1. Wing Box Flow

Table 5.3.1.1-1 Internal Flow Team Analysis Matrix

Unit Physics	Benchmark Dataset	POC and Consolidator	Location or Date Available
High Enthalpy Flow (HEF)	Sphere Flows. LAURA Cases	P. Gnofo, 757 864 4380 p.a.gnoffo@larc.nasa.gov	simak.jsc.nasa.gov/pub/from_hermes/LargeInternalFlow/Continuum/Benchmarks/HEF/
Underexpanded Jet (UEJ)	Donaldson & Snedeker '71	Joe Ruf, 256 544 4942 Joseph.h.ruf.nasa.gov	simak.jsc.nasa.gov/pub/from_hermes/LargeInternalFlow/Continuum/Benchmarks/UEJ/
Shock – Shock Interaction (SSI)	Glass's Material	Kim Bey, 757 864 1351 k.s.bey@larc.nasa.gov	
Cavity Flow (CF)	1) Laminar, Hahn '68, & Wyborney,AGARD 2) Turbulent, 3) Pressure Gradient	Kim Bey, 757 864 1351 k.s.bey@larc.nasa.gov	simak.jsc.nasa.gov/pub/CavityFlow_Bey/
Wall Bounded Jet (WBJ)	In work -	Chris Glass, 757 864 1350 c.e.glass@larc.nasa.gov	Experimental Data being generated

Table 5.3.1.1-2 Unit Physics Benchmarks

Large Scale Wing Internal CFD Roadmap Overview

- Multiple Failure Scenarios to be assessed
  - Many similarities, some uniqueness
  - Basic fluid physics broken down to several Unit Physics
- Unit Physics Problems
  - Each addresses a unique set of physics
  - Codes are compared to available test data for each unit physics
- Unit Physics Extensions
  - Extend the Unit Physics problems to flight fluid properties
- Bridging Problems
  - Combine all relevant physics together in a geometrically representative problem
- CFD of the Failure Scenario
  - Lessons learned from the process applied to improve the result of the 'Large Scale Wing Internal CFD'

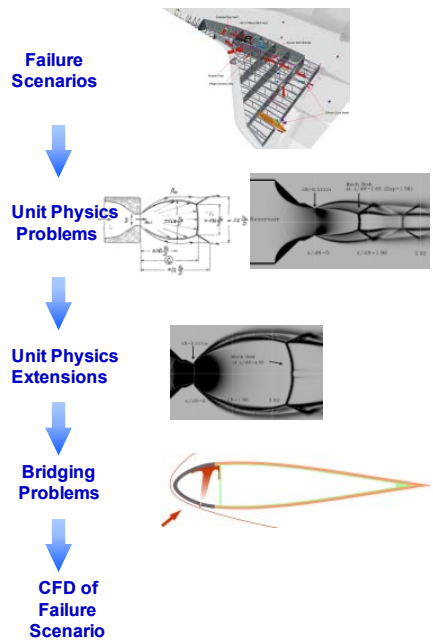

Figure 5.3.1-1 Large Scale Internal CFD Roadmap

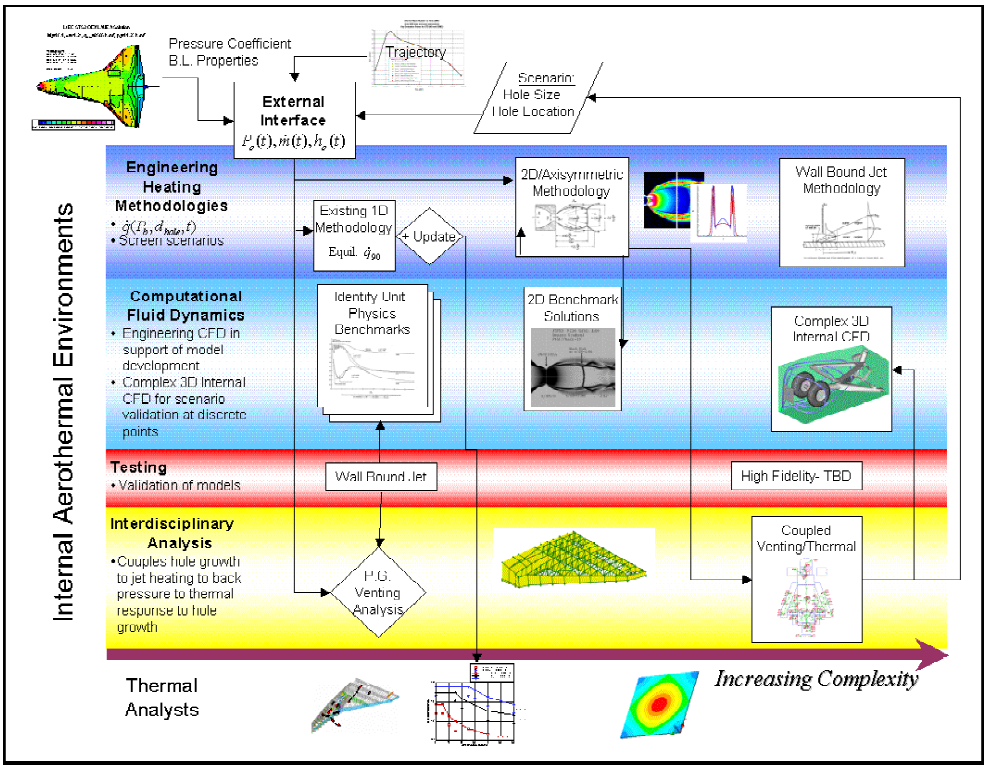

Figure 5.3.1-2 Internal Environments Flow

5.3.1.2 Tools

The unique application of aerothermodynamic analysis to the Orbiter internal environments required the development of a suite of unique capabilities and tools previously not available. A natural basis for much of the internal environment work involved the application of several CFD codes with diverse backgrounds. Each of the tools developed during this investigation for the assessment of the Orbiter, post breach, internal environment will be described in the following sections.

5.3.1.3 Integration

The original time-dependent, integrated analysis plan is given in Figure 5.3.1-3. In this original schematic, the intent was to fully assess a dynamic, multiple failure scenario leading to the STS-107 observed timeline. Within this schematic, the loop starts in the upper left with an assumed hole size, trajectory condition, and external properties from CFD solutions. This information is passed off to the external flow interface, which provides predictions of penetration mass and energy flux through the hole, as well as specifying fluid properties at the penetration. Fluid flow into the Orbiter through the penetration pressurizes the interior volume and transfers energy to the vehicle structure as modeled in the coupled venting thermal analysis loop. Once the quasi-steady internal properties are established, engineering predictions of jet impingement heating to internal structures are generated and fed to the detailed thermal models for local temperature predictions. Based on vehicle loads and material limits, breach and/or structural failure assessments are made and hole diameter/breach status is updated and the process starts the loop over again. The internal flow process, backed by the blue background, would be assessed at discrete time points by application of large-scale CFD solution methods and engineering validation for simplified jet impingement models.

This process was ultimately untenable within the time constraints of the investigation, given the distributed nature of the internal flow team. (Boeing Huntington Beach successfully implemented a similar process for their Progressive Failure Analysis as detailed in Section 6: provided a priori prediction for the hole diameter and internal heating distributions.) The present working scenarios are analyzed with fixed hole diameters up to

the point of structural failure, allowing specification of complete heating distribution histories to be computed and provided to thermal analysts for failure analysis.

Figure 5.3.1-4 presents the final integrated process for developing the internal heating environment for a breach into the wing leading edge RCC system. Starting in the upper left, the external team CFD solutions using LAURA are probed at the assumed hole location and values extracted as inputs to the external flow interface routines which generate bulk enthalpy values into the breach and into pressure inputs to the coupled thermal/venting methodology for the prediction of internal pressures and mass flow within the vehicle. Peter Gnoffo's LAURA calculations also serve as the basis for the fully coupled jet penetration calculations. *(Though larger holes were assessed later, the final environments produced utilized jet directions derived to match two-inch hole results.)* Potential penetration locations were screened along the predicted debris impact footprint to determine a worst-case penetration producing the peak impingement heating on the internal insulation surfaces. With the hole location specified, axisymmetric heating predictions are generated utilizing the previously calculated mass/energy flux and CFD predicted surface pressures. These results are then fed into the internal heating distribution methodology, which provides time histories of convective heating values over the internal volume of the RCC cavity. The final heating distributions and accompanying trajectory corrections are then provided to the thermal community. Use of large-scale CFD results is two-fold in this approach: 1) to independently assess the applicability of the final methodology, and 2) provide additional fluid insight in order to explain observed debris forensics.

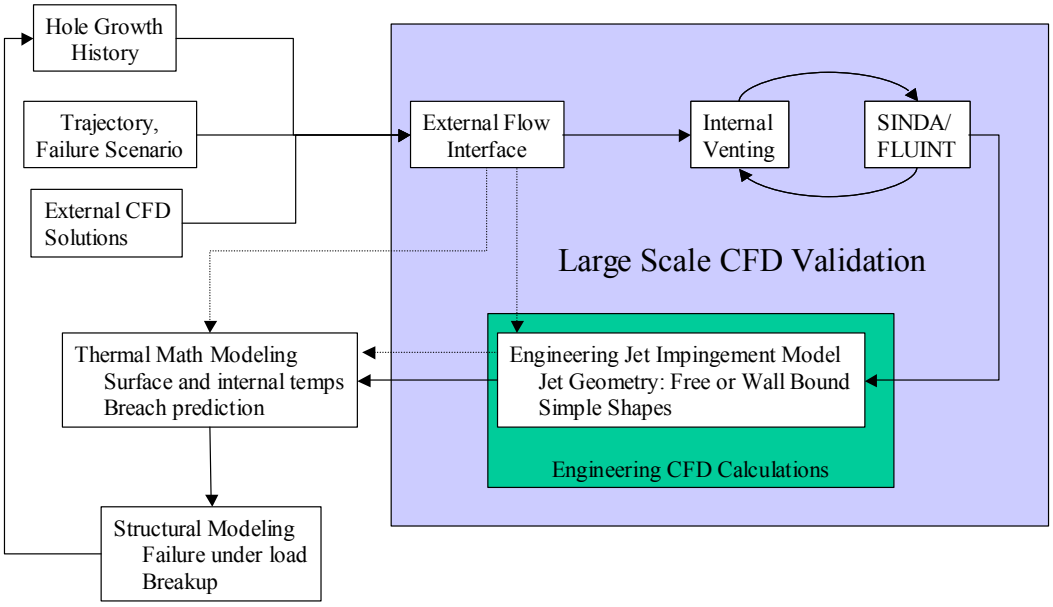

Figure 5.3.1-3 Closed Loop Integrated Analysis

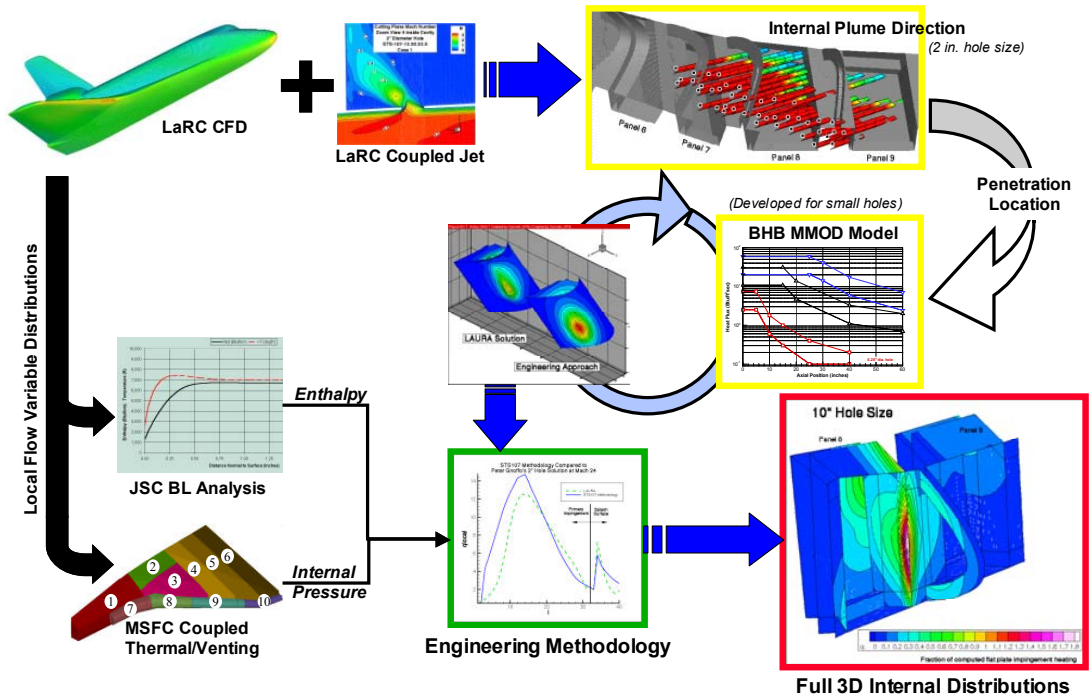

Figure 5.3.1-4 Integrated Internal Environments Schematic

5.3.2 External/Internal Environments – Engineering Analysis

In order to evaluate the effects of ingested reentry gases on the internal structure of the Orbiter wing, a method was needed that would provide the properties, e.g. mass flow rate and energy flux, of the ingested gas as a function of time through the trajectory. These values were needed as input to the 'plume' models that provided the local heating to internal hardware and as input to the coupled venting/thermal codes that modeled the flow and bulk heat transfer inside the wing. CFD solutions require significant resources to setup and then provide detailed data for only one or two free stream conditions. Therefore, selected CFD solutions were used to aid in the development of engineering tools that provided the histories of the ingested gas flow rate, bulk enthalpy and bulk temperature needed to evaluate the propagation of damage inside the vehicle.

5.3.2.1 Overview of Breach Hole Engineering Analysis Methodology

Figure 5.3.2-1 provides a sketch of the basic aspects of a breach flow field. Once a breach hole opens in the Orbiter aeroshell the pressure differential between the outside flow field and internal volume will cause reentry gases to enter the vehicle and generate a gas 'plume' that then impinges on internal structure. The flow rate and energy of the flow ingested depends on the size and shape of the hole and the properties of the gas just upstream of the hole. The gas properties in the external flow vary by location on the vehicle and by distance from the surface. For small breach holes, only a portion of the gas near the surface, as shown in Figure 5.3.2-1, is ingested. As the hole increases in size, more of the boundary-layer gas is ingested until the entire boundary layer is swallowed. Further increases in hole-size results in the boundary layer and a portion of the high enthalpy shock-layer gases to be ingested. The mass flow rate of gas through the breach hole is a function of the mass-averaged enthalpy of the boundary-layer gas that is ingested. Therefore, a mass balance between the gas flowing through the hole and that extracted from the external flow was used to obtain an engineering estimate of the mass flow rate and energy flux of the gas ingested.

The mass-flow rate through the hole was computed by the following isentropic relation from Shapiro:

$$\dot{m}_{hole} = Area\sqrt{\frac{\gamma}{R_{gas}}}\frac{P_o}{\sqrt{T_o}}\frac{M}{\left(1+\frac{\gamma-1}{2}M^2\right)^{\frac{\gamma+1}{2(\gamma-1)}}} \qquad (5.3.2\text{-}1)$$

where $\dot{m}_{hole}$ = mass flow rate through hole
Area = cross-sectional area of hole
γ = Ratio of specific heats
R_{gas} = Gas constant
P_o = External Pressure
T_o = Bulk temperature of ingested gas
M = Mach number at hole

The mass flow relation above has a maximum value when the Mach number is 1.0. The following isentropic relation was used to compute the Mach number as a function of the internal and external pressures, P_{int} and P_{ext}, respectively.

$$\frac{P_{ext}}{P_{\text{int}}} = \left(1+\frac{\gamma-1}{2}M^2\right)^{\frac{\gamma}{\gamma-1}} \qquad (5.3.2\text{-}2)$$

P_{ext} was used for the P_o value in Eqn. 5.3.2-1. The values γ, R_{gas}, *and* T_o are a function of the average gas properties of the flow extracted from the external flow field. To obtain these values it was assumed that chemical equilibrium air properties could be used given a pressure and an enthalpy. The average, or bulk, enthalpy of the ingested gas was obtained from the following relation:

$$H_{Bulk} = \frac{\int \rho u H dA}{\int \rho u dA} \qquad (5.3.2\text{-}3)$$

where H_{Bulk} = Bulk gas enthalpy
ρ = gas density in external flow field
u = gas velocity in external flow field
H = total gas enthalpy
dA = cross-sectional area of external flow ingested

The quantity ρudA is the mass flow rate through the cross-sectional area of the external flow streamtube that enters the hole. Therefore, to obtain the bulk enthalpy, the area of integration is enlarged until the quantity ρudA equals the mass flow rate through the hole, $\dot{m}_{hole}$. For this analysis, the local external flow properties were assumed to vary only in the y-direction normal to the surface. The area of integration was assumed to be

$$A_{st} = C\sqrt{A_{hole}}\int_0^y dy \qquad (5.3.2\text{-}4)$$

where A_{st} = cross-sectional area of external flow streamtube
C = constant derived from CFD solutions
A_{hole} = area of breach hole
y = normal distance from the surface

The value C was set to 0.4 to better match the ingested mass flow rate predicted by a CFD solution for a 2-inch diameter hole in Panel 6 (see Sec. 5.3.2.2). Therefore, the ingested streamtube had a rectangular cross-

sectional shape with a fraction of the square-root of the hole area defining the transverse dimension. The vertical distance was defined by integrating through the flow field until the value $C\sqrt{A_{hole}}\int_0^y \rho u dy$ equaled the hole mass flow rate, $\dot{m}_{hole}$.

Applying these assumptions for the ingested cross-sectional area, accounting for the enthalpy difference across the boundary layer, and non-dimensionalizing the values by the boundary-layer edge values, the bulk enthalpy relation used in the engineering analyses was obtained.

$$H_{Bulk} = \frac{\int_0^{y/y_e} \frac{\rho}{\rho_e}\frac{u}{u_e}\frac{(H - H_{wall})}{(H_e - H_{wall})} d\left(\frac{y}{y_e}\right)}{\int_0^{y/y_e} \frac{\rho}{\rho_e}\frac{u}{u_e} d\left(\frac{y}{y_e}\right)} + H_{wall} \qquad (5.3.2\text{-}5)$$

where the subscript *e* corresponds to the boundary-layer edge value and H_{wall} is the gas enthalpy at the wall temperature. As described in the next section, polynomial curve-fits for the quantities $\frac{\rho}{\rho_e}\frac{u}{u_e}$ and $\frac{\rho}{\rho_e}\frac{u}{u_e}\frac{(H - H_{wall})}{(H_e - H_{wall})}$ as a function of the non-dimensional distance, $\left(\frac{y}{y_e}\right)$, through the boundary layer were obtained from CFD solutions.

A FORTRAN computer code was used to solve for the breach hole gas mass flow rate, bulk enthalpy and bulk temperature using the relations above. The solution process included the following steps:

1) Compute the boundary-layer thickness and edge quantities as described in the next section.
2) Compute the bulk enthalpy and mass flux for the ingestion of the entire boundary layer and then compare the boundary-layer mass flux (denominator of Eqn. 5.3.2-5) to the hole flow rate (Eqn. 5.3.2-1). If the hole flow rate is greater than the boundary-layer mass flux, then it was assumed that more than the boundary layer was ingested into the hole. Outside of the boundary layer it was assumed that the gas properties are equal to the edge values. Increments of one-tenth of a boundary-layer thickness were used to find the vertical distance and therefore the external mass flux that best matched the flow rate through the hole.
3) If the hole-flow rate was less then the boundary-layer mass flux, then the vertical distance inside the boundary layer was varied by increments of one one-hundredth of a boundary-layer thickness to best match the flow rate through the hole.

5.3.2.2 Use of CFD Solutions

Two sets of CFD solutions were used to develop the engineering methods to estimate the ingested gas properties. The first set included two CFD solutions of the nominal undamaged Orbiter. These solutions were used to obtain curve-fits of flow field parameters just upstream of the assumed breach hole. The second set of CFD solutions were coupled external/internal flow field solutions for various size circular breach holes in the wing leading edge. These solutions were used to calibrate the engineering tool and to confirm its results.

5.3.2.3 External Flow Parameter Curve-fits

Two LAURA CFD solutions for the nominal Orbiter provided curve-fits for use in the breach hole gas ingestion engineering analysis. The CFD solutions for the following two flight conditions were chosen:

1) CFD Point 1: EI+404 secs.; Mach =24.9; Altitude = 243,000 ft; Angle-of-attack = 40 degs.; Dynamic pressure = 22.0 psf.
2) CFD Point 6: EI+921 secs.; Mach = 17.9; Altitude = 200,767 ft; Angle-of-attack = 40 degs.; Dynamic pressure = 83.5 psf.

For each of these 3-D flow field solutions, two points on the wing leading edge were selected – one on Panel 6 and one on Panel 8.

Panel	X (in)	Y (in)	Z (in)
6	1038	-193	284
8	1070	-211	294

At each of these points, predicted flow field properties were extracted from the CFD solutions as a function of the normal distance from the surface. Figure 5.3.2-2 presents the variation of gas temperature and enthalpy predicted by LAURA for the Panel 8 location at the CFD Point 1 flight condition. The boundary-layer thickness is 1.4 inches and was determined by selecting the first grid point from the wall where the total enthalpy value is approximately 99% of the free stream total enthalpy.

For use in the engineering analysis, curve fits of the quantities $\frac{\rho}{\rho_e}\frac{u}{u_e}$ and $\frac{\rho}{\rho_e}\frac{u}{u_e}\frac{(H-H_{wall})}{(H_e-H_{wall})}$ were defined using the extracted CFD values which were non-dimensionalized by the edge values. Figure 5.3.2-3 and Figure 5.3.2-4 present these curve-fits for the Panel 8 location. The extracted and curve-fit CFD values included both the CFD Point 1 and 6 data.

Since all of these values were non-dimensionalized by the boundary-layer edge values, relations also had to be developed to estimate the edge values as a function of nominal free stream parameters. Two values were needed – the boundary-layer thickness and the edge mass flux, $\rho_e u_e$. It was assumed that the boundary-layer thickness, δ, is a linear function of the square-root of the free stream Reynolds number, Re_L, based upon the length of the Orbiter (L=107.5 ft). Using the boundary-layer thickness values at the Panel 8 location from the two CFD solutions, the following relation was obtained.

$$\delta = \frac{1250}{\sqrt{\mathrm{Re}_L}} - 0.1617 \text{ (inches)} \qquad (5.3.2\text{-}6)$$

The edge mass flux , $\rho_e u_e$, was assumed to be a linear function of the free stream dynamic pressure, P_{dyn}, with the edge values for curve-fitting obtained from the two CFD solutions at the Panel 8 location.

$$\rho_e u_e = 1.0567E-03 P_{dyn} \text{ (slugs/ft}^2\text{-sec)} \qquad (5.3.2\text{-}7)$$

The relations and curve-fits presented are unique for the Panel 8 location. Additional relations of the same form were generated for the Panel 6 location.

5.3.2.4 Calibration of Engineering Tool

Several CFD solutions were generated for holes in the Orbiter wing leading edge. Four of these solutions described in Sec. 5.3.6.1.3 were used to calibrate and evaluate the engineering method for estimating the mass flow and energy flux of gas entering a leading edge breach hole. CFD solutions for 2, 4 and 6-inch diameter circular holes in Panel 6 and one for a 10-inch diameter hole in Panel 8 were reviewed and the predicted mass flow rate and energy flux flowing through the plane of the hole were computed. All of these values are for the same flight condition – CFD Point 1.

Case	Mass Flow Rate (lbm/sec)	Energy Flux (Btu/sec)
Panel 6: 2-in Dia. Hole	0.00152	9.4
Panel 6: 4-in Dia. Hole	0.00562	43.6
Panel 6: 6-in Dia. Hole	0.01247	110.9
Panel 8: 10-in Dia. Hole	0.04839	498.0

5.3.2.5 Properties of Flow into Breach Holes

The engineering method was exercised for four hole sizes in leading edge Panel 6 – 1, 2, 4, and 6 inches in diameter. Figure 5.3.2-5 presents the predicted fraction of the boundary layer that is ingested into the hole. Both the 4 and 6-inch diameter holes result in the ingestion of the entire boundary layer at later times in the trajectory. Figure 5.3.2-6 and Figure 5.3.2-7 present the predicted bulk gas temperature and enthalpy of the ingested gas. The gas temperatures are mostly between 9,000 and 10,000 R. Figure 5.3.2-8 and Figure 5.3.2-9 present the predicted mass flow rate and energy flux and compare the results to the values obtained from the CFD solutions for the holes in Panel 6. For the smaller holes – 2 and 4-inch diameter – the engineering method provides a very good estimate of the ingested flow rate and energy flux. However, as the hole is increased in size to the 6-inch diameter, the engineering methods tend to under predict the values.

Breach holes in Panel 8 were also analyzed with the engineering method. In this case, the external pressure used for the computation (C_p=1.46) was for a location slightly different from the location where the curve-fits were obtained. Figure 5.3.2-10 and Figure 5.3.2-11 present the predicted mass flux and energy flux into the holes. The values for the CFD solution with a 10-inch diameter hole are also plotted and indicate that the engineering method is under predicting the energy ingested into large breach holes.

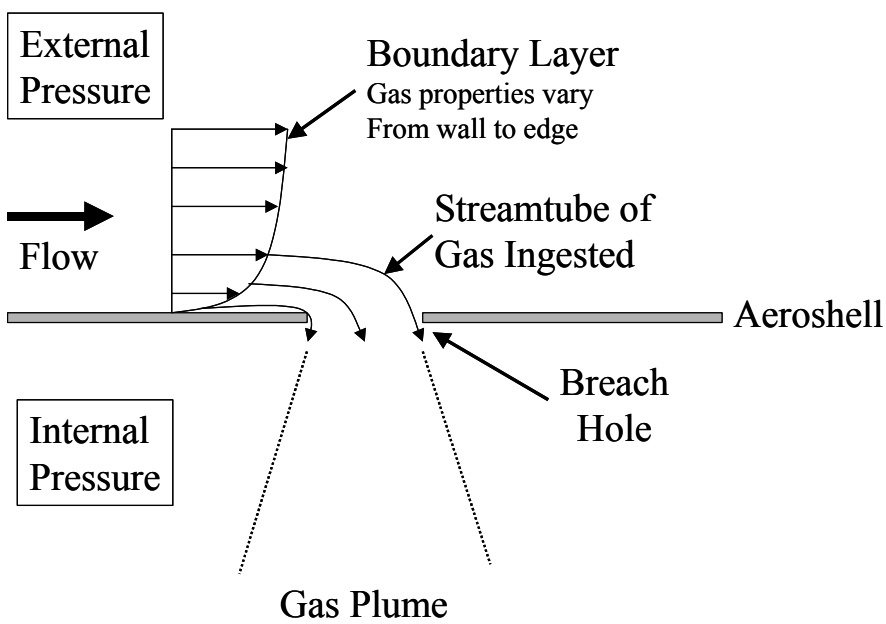

Figure 5.3.2-1 Sketch of Breach Flow Field

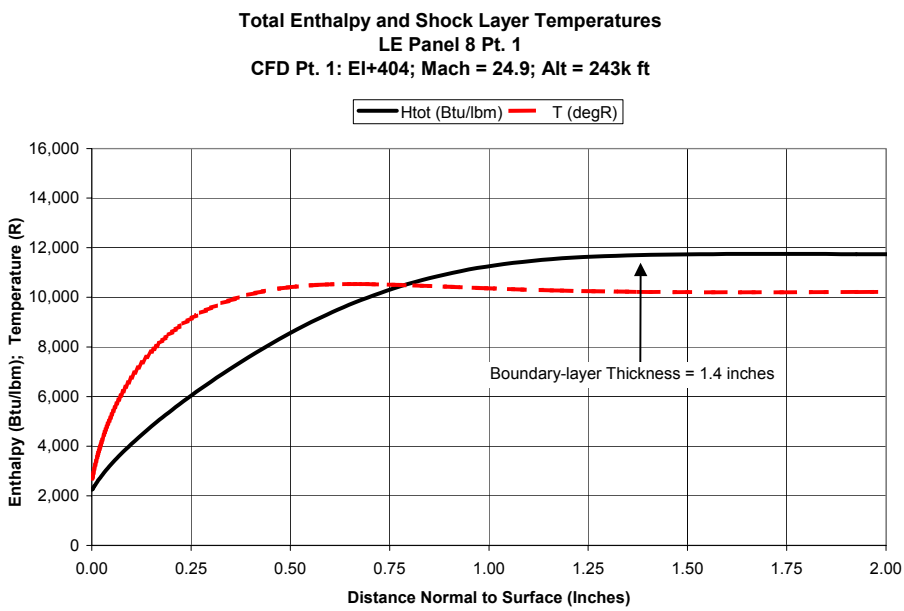

Figure 5.3.2-2 Total Enthalpy and Temperature Profiles at LE Panel 8 for Mach 24.9.

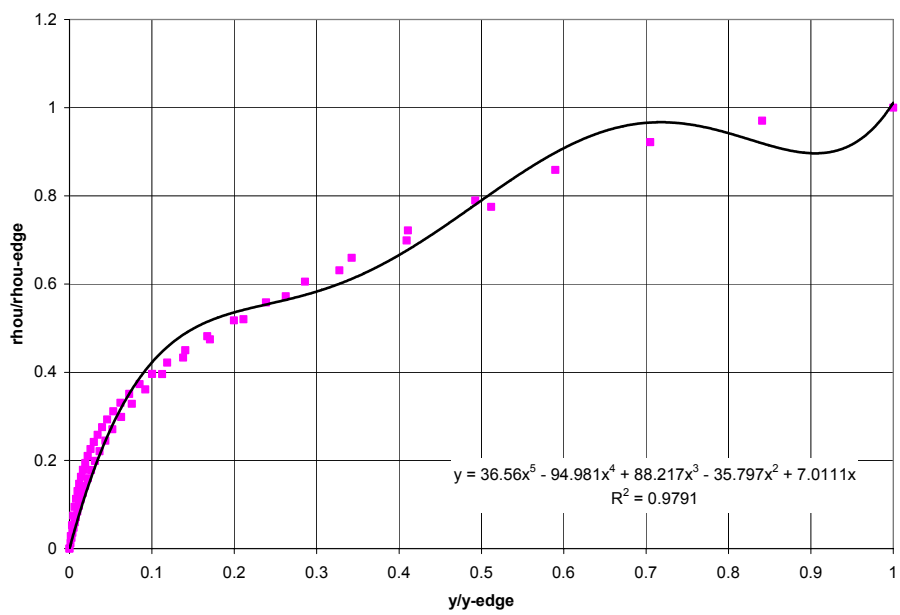

Figure 5.3.2-3 Boundary-layer Mass Flux, $\frac{\rho}{\rho_e}\frac{u}{u_e}$, Curve-fit for LE Panel 8.

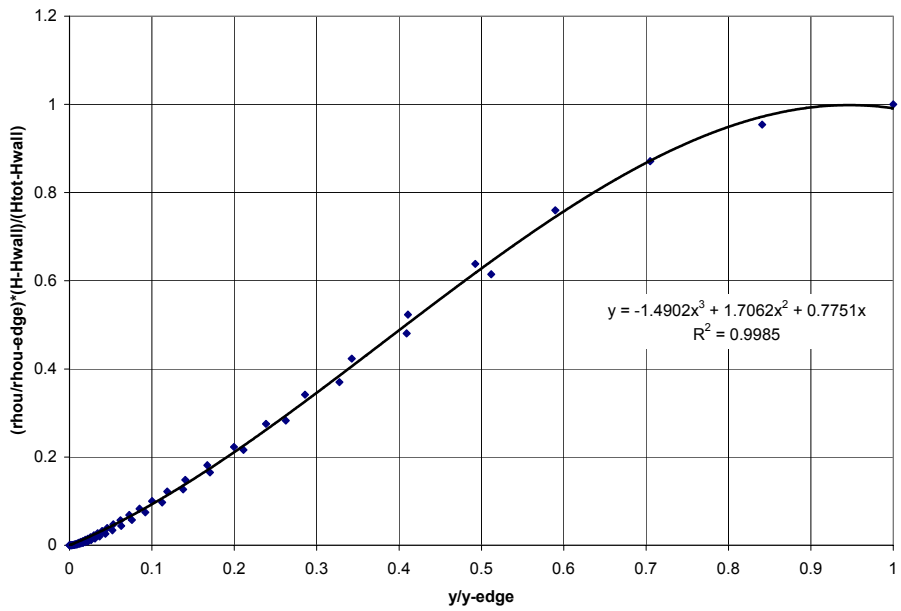

Figure 5.3.2-4 Boundary-layer Energy, $\frac{\rho}{\rho_e}\frac{u}{u_e}\frac{(H-H_{wall})}{(H_e-H_{wall})}$, Curve-fit for LE Panel 8

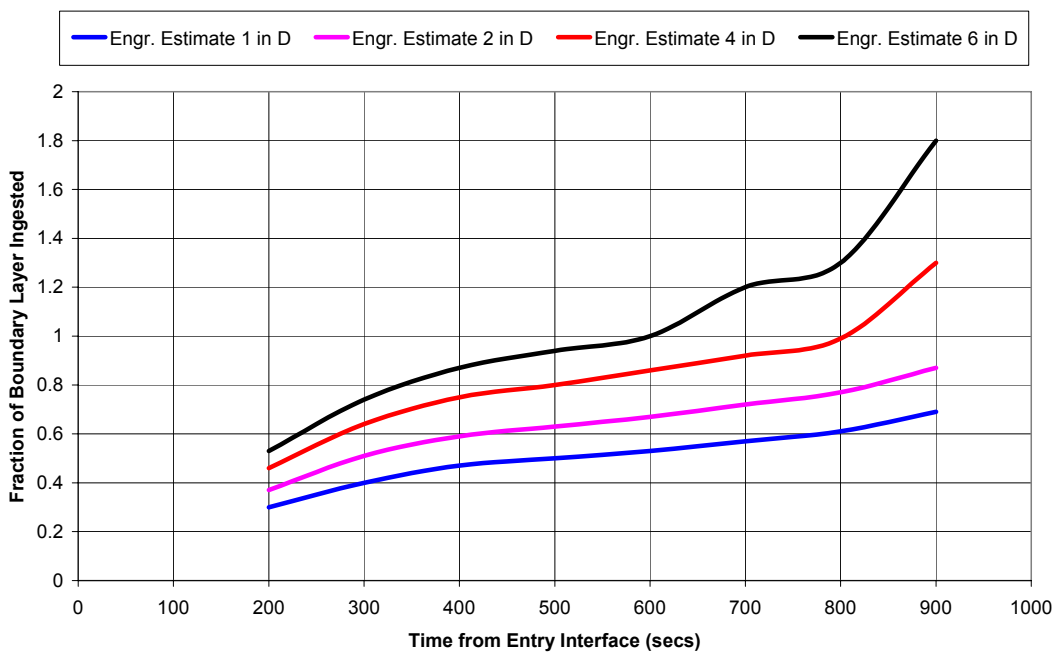

Figure 5.3.2-5 Predicted Fraction of Boundary-layer Thickness of Gas Ingested into Hole in LE Panel 6.

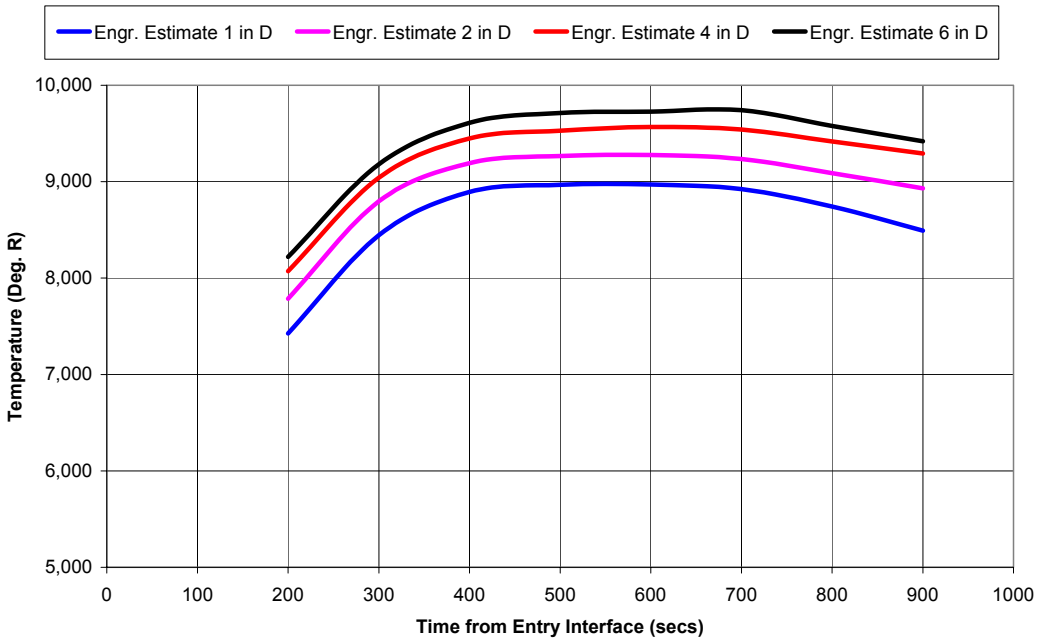

Figure 5.3.2-6 Predicted Bulk Temperature of Gas Ingested into Hole in LE Panel 6.

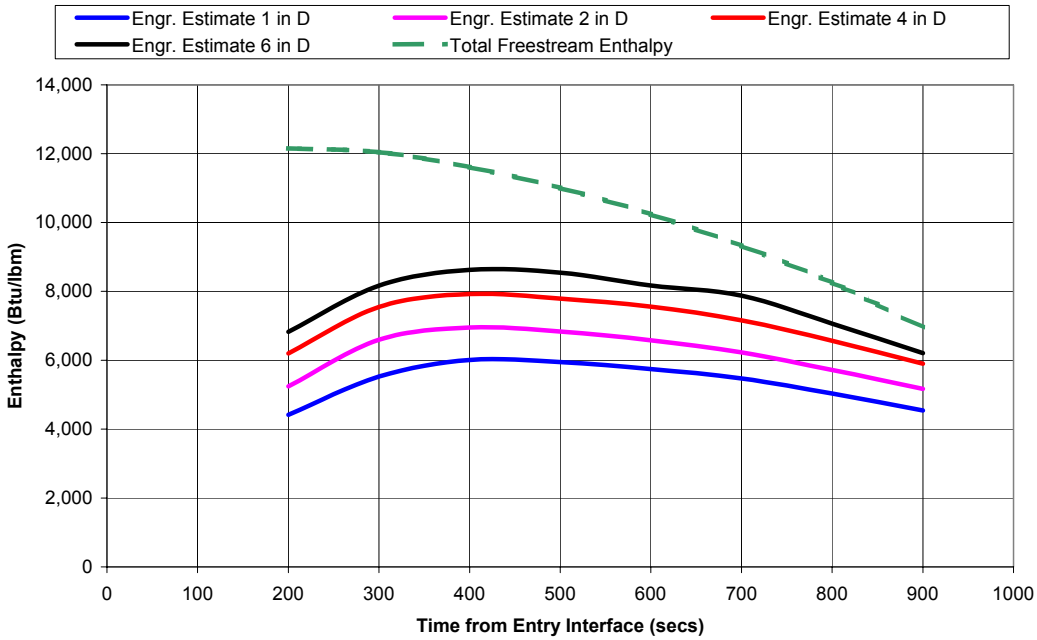

Figure 5.3.2-7 Predicted Bulk Enthalpy of Gas Ingested into Hole in LE Panel 6.

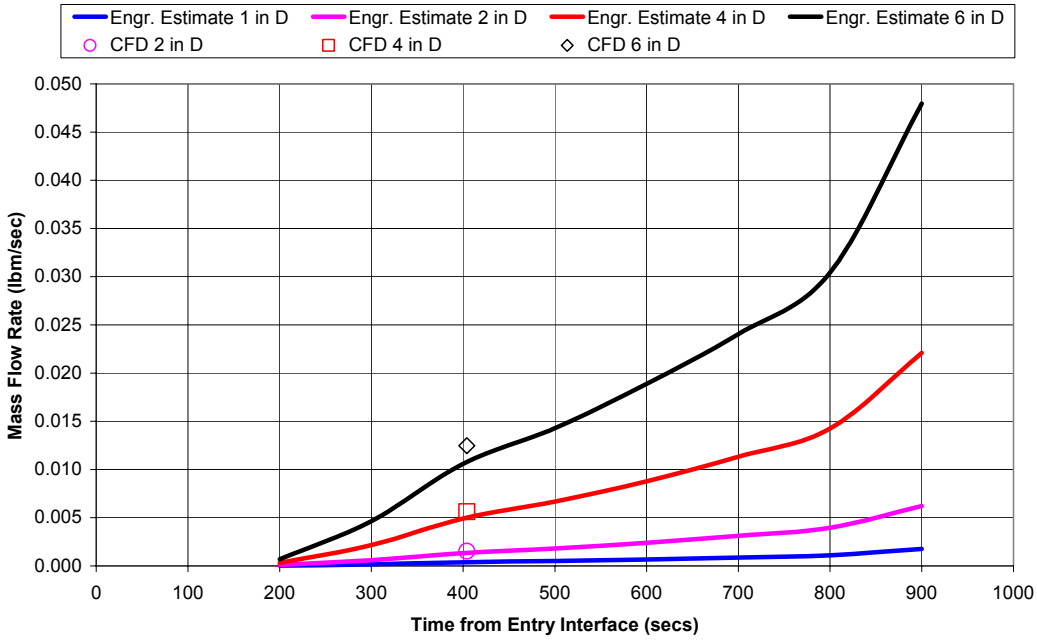

Figure 5.3.2-8 Predicted Mass Flow Rate of Gas into Hole in LE Panel 6.

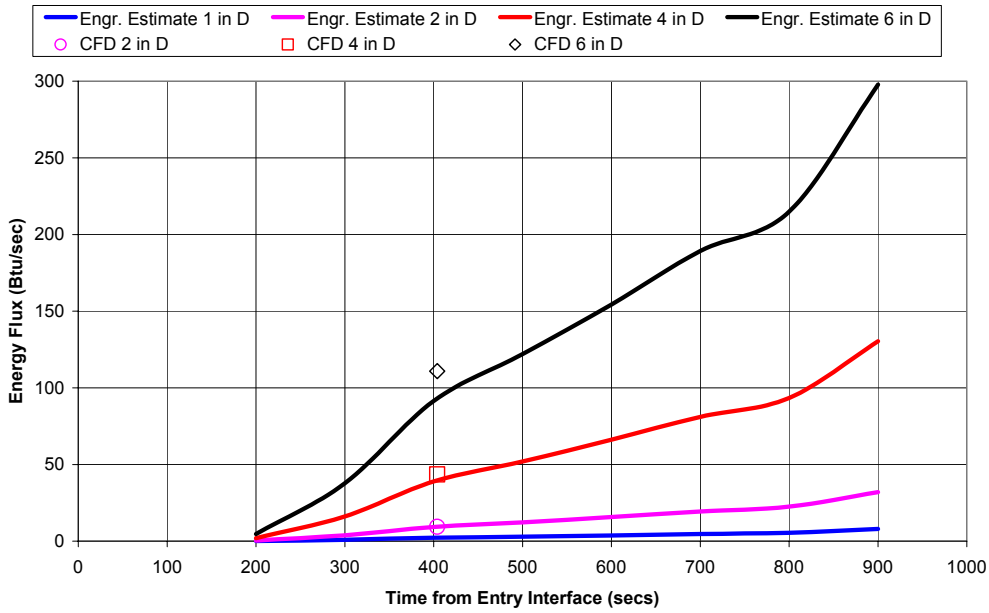

Figure 5.3.2-9 Predicted Mass Flow Rate of Gas into Hole in LE Panel 6.

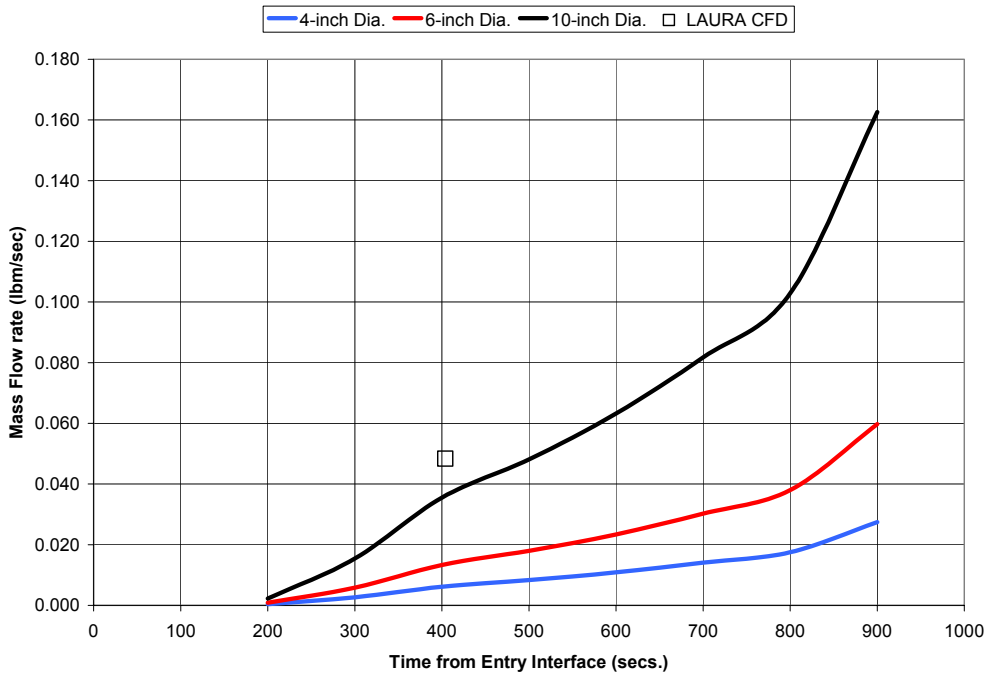

Figure 5.3.2-10 Predicted Mass Flow Rate of Gas into Holes in LE Panel 8.

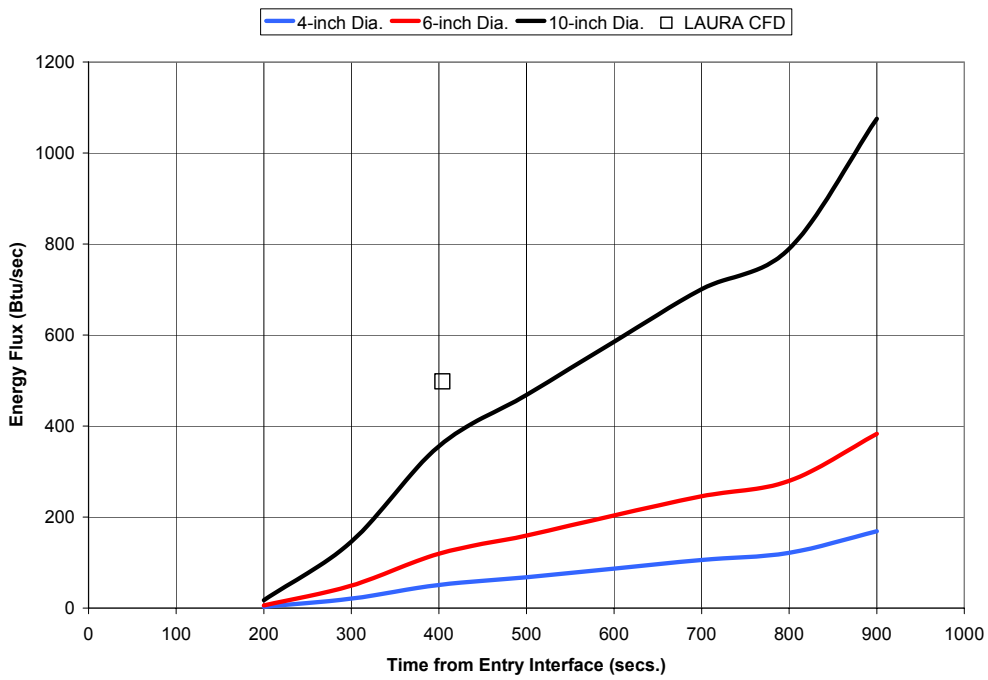

Figure 5.3.2-11 Predicted Energy Flux of Gas into Holes in LE Panel 8.

5.3.3 Plume Model Development

Engineering models of internal jet impingement heating are necessary to assess localized heating in the primary impingement zone for burn through and structural failure analysis. Heating distributions are produced based on:

1) Assumed hole diameter and shape
2) Assumed hole location
3) Freestream conditions
4) Internal pressure
5) Internal geometry
6) External boundary layer properties

The results must be in a form suitable for thermal analysis, typically closed form functions or tables that may be linearly interpolated. Computational results are very expensive to obtain and are only available at discreet points in the trajectory. Engineering models, though, if properly setup, allow for parametric studies in order to match flight data in terms of hole diameter, location, and jet direction. Such studies will be presented in the thermal analysis portion of the report. The following two sections describe the development of an engineering model to predict internal plume impingement values for circular holes, while the model developed to assess missing T-seal segments in described in Section 5.3.3.6.

5.3.3.1 Basic internal plume physics and impingement issues

The nature and structure of a free jet issuing into the Orbiter interior through a breach in the thermal protection system is dictated by the total pressure difference across the surface, the hole diameter, boundary layer properties, and local boundary layer edge Mach number. For small orifices, on the order of one inch, the jet may be assumed to enter normal to the internal surface with a sonic condition. For such a case the governing parameter that dictates shock structure and mixing of the jet is the ratio of external driving pressure to internal pressure. Bulk fluid properties are a function of the percentage of external boundary layer drawn off into the hole. For very small hole, the properties will be near wall conditions, whereas larger holes can produce internal flows with enthalpy levels approaching free stream total values. As the high-speed gas enters the cavity, it immediately starts mixing with the ambient fluid at the boundaries of the jet. This mixing zone gets larger as the jet progresses, until finally the core portion of the jet has been consumed and the jet has reached a fully developed condition. Depending on the conditions driving the jet, this may not occur until ten's of diameters downstream. In the highly under-expanded state, the jet shock structure is dominated by a normal shock downstream of the initial expansion called the Mach disk. Immediately downstream of the Mach disk the flow is subsonic, though it may re-expand to supersonic flow. Figure 5.3.3-1 displays variations in free-jet structure and with varying pressure ratios. Figure 5.3.3-2 shows the impact of pressure ratios in the range expected for Orbiter penetrations on computed flow structure.

Larger hole diameters display significant departure from this relatively simple structure as larger percentages of the highly energetic boundary layer are ingested and increased transverse momentum bends the jet over in the direction of the boundary layer edge flow. This effect was discovered with the first fully coupled, internal/exterior flow solution performed for a two-inch breach into RCC panel 6. Complete results are presented in Section 5.3.6.1.4. Larger diameter penetrations tend to carry highly supersonic, high temperature gases directly to the interior surfaces and produce highly complex shock/impingement structures that can significantly impact local heat transfer rates.

Two dimensional jet structure differs from that of the axisymmetric jet, primarily due to conservation constraints. The three-dimensional source flow falls off as $(1/r^2)$ versus $(1/r \ln r)$. The effect of this can be seen in Figure 5.3.3-3 where the two-dimensional flow structure is quite different and maintains the first shock cell considerably further downstream.

Also, of note in predicting internal jet flow fields is the importance of modeling chemistry correctly. Jet structure and spreading are strongly a function of the ratio of specific heats of the gas. Additional considerations of chemistry are the energies absorbed in chemical reactions and the net energy transfer to the surface. This study will focus equilibrium chemistry options in internal flow computations in order to provide the most reasonable predictions of plume heating with sufficient conservatism.

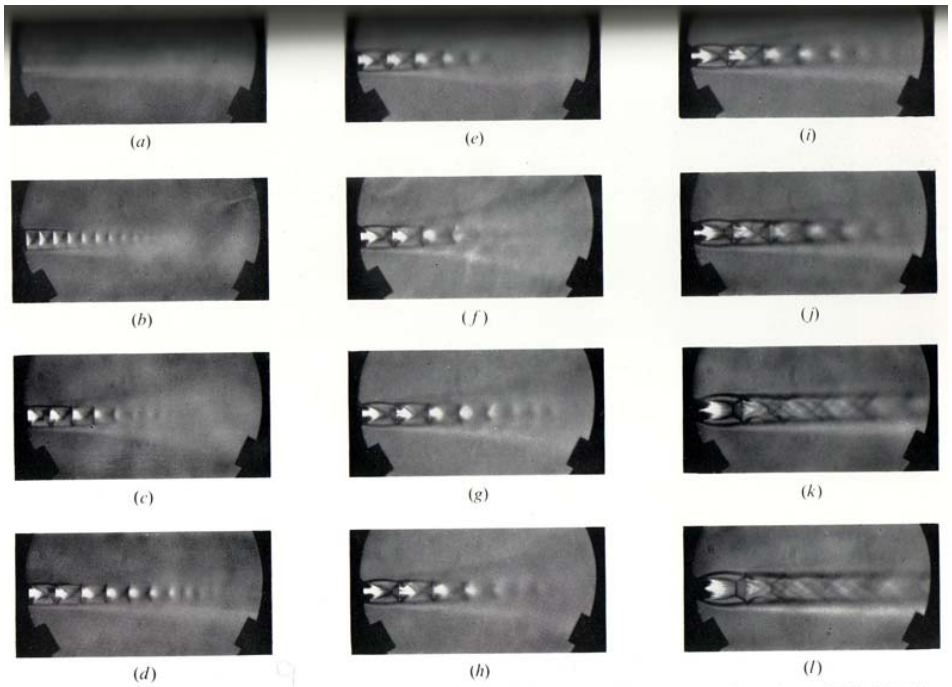

FIGURE 8. Free jet from convergent nozzle photographed with double-pass schlieren system. (a) $p_1/p_\infty = 1{\cdot}00$ (subsonic). (b) $p_1/p_\infty = 1{\cdot}15$. (c) $p_1/p_\infty = 1{\cdot}42$. (d) $p_1/p_\infty = 1{\cdot}59$. (e) $p_1/p_\infty = 1{\cdot}71$. (f) $p_1/p_\infty = 1{\cdot}84$. (g) $p_1/p_\infty = 2{\cdot}00$. (h) $p_1/p_\infty = 2{\cdot}13$. (i) $p_1/p_\infty = 2{\cdot}31$. (j) $p_1/p_\infty = 2{\cdot}59$. (k) $p_1/p_\infty = 3{\cdot}57$. (l) $p_1/p_\infty = 4{\cdot}09$.

Figure 5.3.3-1 Free jet mixing and structure with pressure ratio

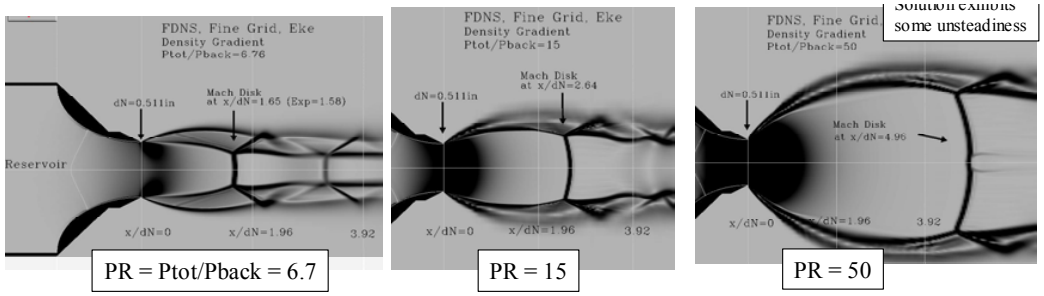

Figure 5.3.3-2 Computed pressure ratio effect on near orifice flow

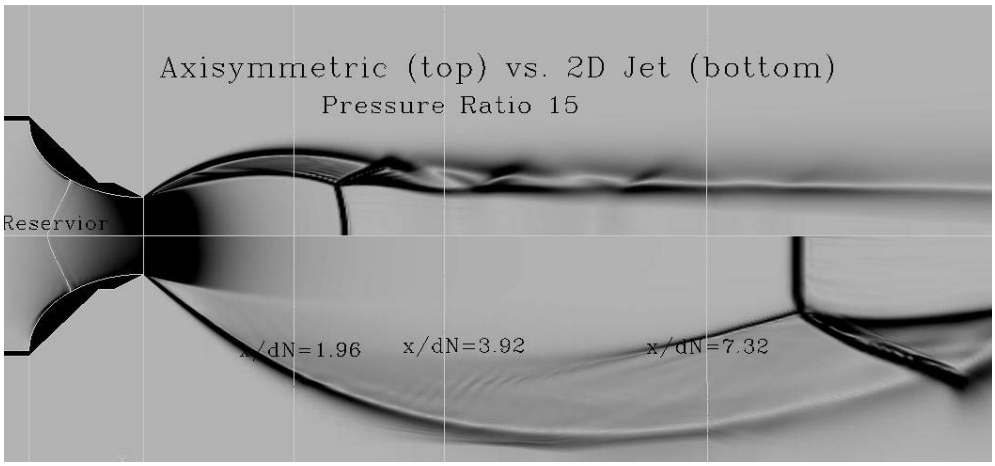

Figure 5.3.3-3 Axisymmetric vs. 2D Jet structure

5.3.3.2 1-D Axisymmetric Equilibrium Plume Heating Model

5.3.3.2.1 History

The plume model used to support the STS-107 accident investigation is a version of that originally developed to support Space Shuttle mission risk definition due to micrometeoroid and orbital debris hazards. The study objective, prompting the original model development, was to define levels of on-orbit impact damage that subsequently results in catastrophic loss of vehicle during entry. Under these conditions, on-orbit penetrations of the OML would result in ingestion of high enthalpy gas during reentry due to the pressure differential across the penetration. Heating environments due to this internal flow were required for thermal and structural analysis of the affected structure. As a result, a simplified internal jet flow model was developed to conservatively estimate time-dependent internal heating environments required for this study. During the course of this work, the analysis methodology and results were presented in 1997 to the National Research Council Review on Shuttle Meteoroid Risk Management.

For the STS-107 investigation, this model was employed for scenario feasibility and screening assessments.

5.3.3.2.2 Development

To provide the required time-dependent environments throughout an entry trajectory, it was desirable to develop a simplified method using closed form expressions to obtain characteristics of such internal flows, primarily impingement heating. The development of this method is described in this section.

5.3.3.2.3 Assumptions/limitations

- Due to the nature of the on-orbit impact hazard, the penetrations analyzed were limited to small holes of 1 inch diameter or less
- As a result, internal flow was modeled as an axisymmetric free jet issuing from a sonic orifice normal to the vehicle OML at the penetration location.
- Jet decay characteristics are based on empirical relations for properly expanded jets
- To maintain a conservative approach, internal heating levels were based on normal impingement angles for surfaces within the jet flow field

5.3.3.2.4 Theoretical Description of the Jet and Impingement Regions

To analyze the impinging jet, four distinct regions of flow are considered. First, a zone of flow establishment extends from the orifice to the apex of the potential core along the centerline of the jet. Within this core the velocity of the jet remains constant. It is surrounded by a region in which mixing occurs between the jet and ambient gas. In the second region, established flow in the direction of the jet beyond the apex of the potential core is characterized by a dissipation of the centerline jet velocity and temperature, and by a spreading of the

jet in the transverse direction. At this point, usually several nozzle diameters downstream from the orifice, the mixing region has spread inward enough to reach the centerline. Beyond this point the mixing region continues to spread as the velocity decays at a rate required to conserve axial momentum. These first two flow regions are shown in Figure 5.3.3-4. A third region is characterized by deflection of the jet from the axial direction at the impingement surface. At this point, local flow conditions on the jet centerline, including the effects of an impingement shock if present, are used to compute a stagnation heating level to a desired surface geometry, either a flat plate or cylinder in crossflow. In the final region of the jet the redirected flow increases in thickness as the boundary layer builds up along the solid impinged surface. Convective heating continues on these surfaces although at levels that progressively drop from the maximum achieved at the stagnation point at the jet centerline.

5.3.3.2.5 Analysis Methodology

Properties of the external flow ingested through the damaged OML are based on a bulk gas enthalpy defined by the method described in Section 5.3.2.1 and the local surface pressure at the hole. With the internal pressure within the RCC cavity controlled by the local pressure at the passive vent located on the upper surface of the wing, a small penetration in the RCC is expected to act as a choked sonic orifice. Flow at the exit of the orifice is based on the 1-D nozzle equation:

$$\text{mdot} = \rho_j U_j A_{hole} C_D$$
$$= p_s (1+((\gamma-1)/2)M_j^2)^{-(1+\gamma)/2(\gamma-1)} M_j (\gamma g /(zRT))^{0.5} A_{hole} C_D$$

where $M_j = 1$ when $P_s/P_a \geq ((1+\gamma)/2)^{\gamma/(\gamma-1)}$, and P_a is the internal pressure within the RCC cavity.

Isentropically expanding this sonic flow to the required internal pressure produces an initial supersonic condition in the flow that is accompanied by a strong normal shock, or Mach disc, in highly underexpanded flows. A calculation procedure conserving mass, momentum and energy fluxes across a normal shock are used to account for the total pressure loss in the jet core due to this shock. High temperature equilibrium air properties are used in all flow property calculations.

A continued expansion to the established internal cavity pressure defines the conditions within the jet core downstream of the Mach disc. Although experimental values of potential core length reported in the literature vary from 4.7 to 7.7, a value of 6.5 orifice diameters was used in this analysis, close to the median reported in the literature. Beyond that point, decaying values of centerline velocity and temperature are given by:

$$U_{cl}/U_c = 6.5 / (X / D_{orifice})$$

$$T_{cl} = T_{ambient} + 0.722 (T_c - T_{ambient}) U_{cl}/U_c .$$

As illustrated in Figure 5.3.3-5, flow conditions approaching the impingement point represent the upstream properties for a normal shock solution, if required, to provide local and total flow properties downstream of the impingement shock. Based on the experimental work in the literature, post-shock properties are used in the calculation of laminar stagnation heat flux:

$$q_{fp} = 0.763\, g\, Pr^{-0.6} (\rho_s\mu_s U_{cl} / r_5)^{0.5} (\rho_w\mu_w / \rho_s\mu_s)^{0.1} (H_s - H_w)$$

$$q_{cyl} = 0.763\, g\, 2^{-0.5}(Pr)^{-0.6} (\rho_s\mu_s)^{0.4} (\rho_w\mu_w)^{0.1} (du/dx)^{0.5} (H_s - H_w)$$

where $du/dx = R_{cyl}^{-1} [2 (p_s - p_j) / \rho_s]^{0.5}$

The stagnation point velocity gradient for the flat plate is experimentally derived as reported in the literature, while that for the cylinder is based on modified Newtonian flow.

5.3.3.2.6 Results Summary

Early in the investigation, impingement heating levels were computed parametrically for various hole sizes on RCC panel 9, several impingement distances and two surface geometries, flat plate and cylinder. The results

of these calculations are shown in Figure 5.3.3-6. Stagnation heating values for ingested flow through large diameter holes in RCC panel 8 were also provided later in the investigation in support of the Working Scenario. Table 5.3.7.2-1 lists these heating values.

As described in Section 5.3.7, these values were used to create internal heating distributions within the RCC cavity.

5.3.3.2.7 Validation/Verfication

To gauge the usefulness of this simplified model, comparisons were made with available CFD solutions discussed in Section 5.3.3.4. Figure 5.3.3-7 shows the results of this comparison and indicates the simplified model off-axis heating profiles generally envelope CFD results and have much smaller rate of decay in radial direction.

Nomenclature

A	Hole area
C_D	Discharge coefficient
D	Hole diameter
H	Enthalpy
M	Mach no.
P	Pressure
Pr	Prandtl no.
q	Heat flux
r_5	Radial distance from jet centerline at $U=U_{cl}/2$
R	Gas constant, Geometric radius
T	Temperature
U	Jet axial velocity
z	Gas compressibility
γ	Ratio of specific heats
ρ	Gas density
μ	Gas viscosity

Subscripts

c	Core
cl	Center line
cyl	Cylinder
fp	Flat plate
j	jet
s	stagnation
w	wall

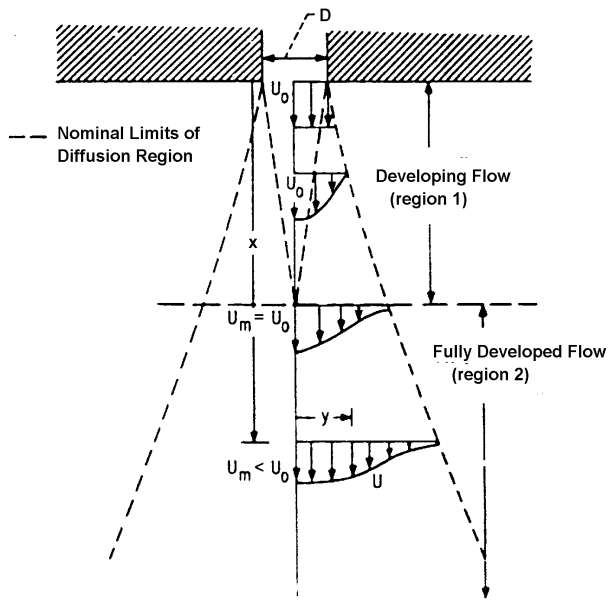

Figure 5.3.3-4 Flow Regions in Free Jet

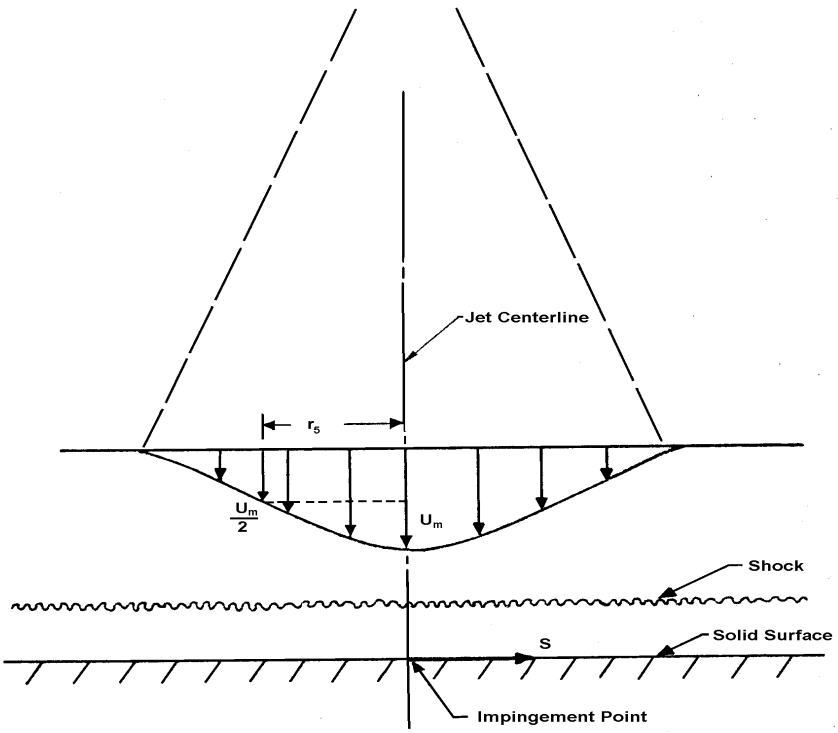

Figure 5.3.3-5 Jet Impingement Within Developed Flow Region

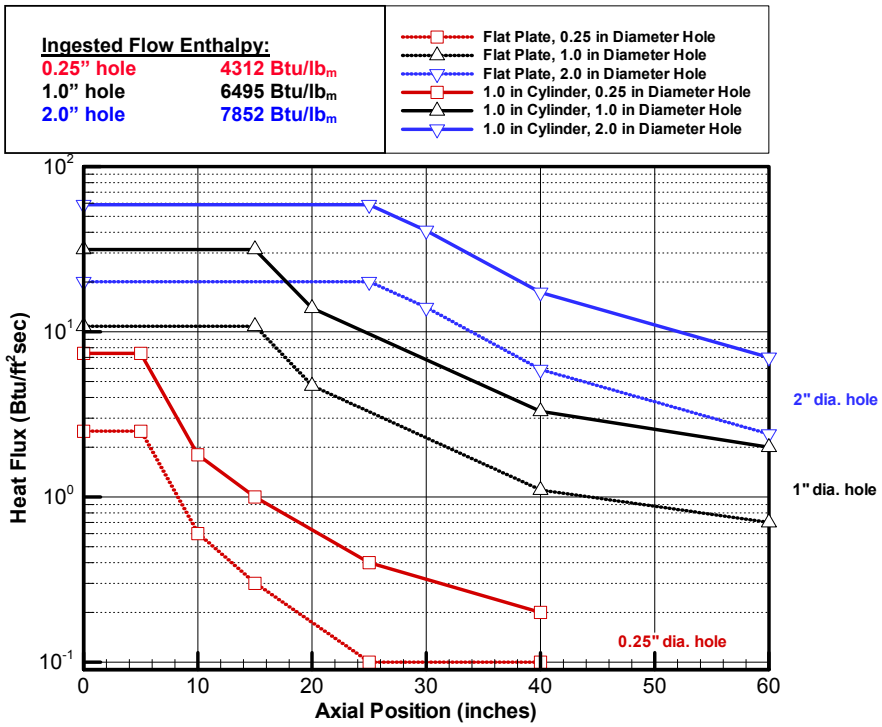

Figure 5.3.3-6 Simplified Plume Model Heating Results at 491 seconds After EI

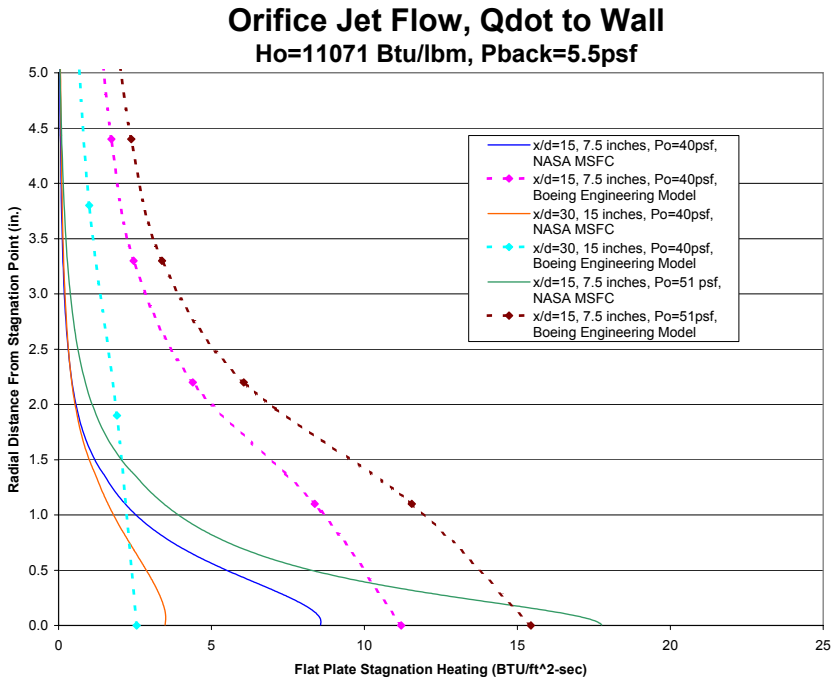

Figure 5.3.3-7 Comparison of Simplified Plume Model Results With NASA MSFC CFD Results

5.3.3.3 Engineering Corrections to Plume Model to Produce Heating Histories

The methodology of 5.3.3.2 allows the computation of stagnation heating to a flat plate, or cylinder, located along the axis of the jet, for fixed total conditions and a specified hole size. Early in the investigation process, the thermal community wanted a set of relations that would allow the assessment of heating distributions to flat plates and cylinders at arbitrary orientations to the jet orifice. The following analytical corrections allow the use of the data from Figure 5.3.3-6 for the assessment of burn-through times and hole sizes required to burn through in a specified time.

5.3.3.3.1 Radial coordinate correction

Axis values for stagnation heating are corrected for radial distance variation based on measured turbulent jet impingement heating characteristics with the distance to 50% of centerline velocity, r_5, as the similarity variable. r_5 is initially equal to the orifice exit radius, r_e, throughout the length of the undisturbed core and then slowly grows to reflect the entrainment and mixing with ambient air in the internal volume. Values from Table 5.3.3.3-1 are linearly interpolated to arrive at the ratio of local heating to centerline heating as a function of distance downstream, x.

r/r_5	$qdot/(qdot)_0$
0	1
1	0.748
2	0.392
3	0.219
4	0.154
5	0.119
6	0.1
7	0.0808
8	0.0615
9	0.0423

$$r_5 = r_e \qquad \text{for } x \le 7.0 r_e$$

$$r_5 = r_e + x \tan\left(\frac{\pi}{30}\right) \qquad \text{for } x > 7.0 r_e$$

Table 5.3.3.3-1 Radial Jet Heating Correction

5.3.3.3.2 Trajectory condition correction

Jet impingement heating values are directly dependent on the effective reservoir conditions driving the development of the plume. Figure 5.3.3-6 reflects the impingement heating values for 491 seconds from entry interface. In order to complete a thermal analysis, complete time histories of heating values must be computed. In order to do so, it is assumed that the internal heating scales with freestream dynamic pressure and the square of freestream velocity. This is equivalent to fixing the local Stanton number and scaling with mass flow through the hole (dynamic pressure) and enthalpy (velocity squared). The necessary equation is

$$\dot{q}(x,r,t,d_{hole}) = \dot{q}(x,0,491\sec,d_{hole}) \times \frac{\overline{q}(t)}{\overline{q}(491)} \times \frac{V_\infty^{\,2}(t)}{V^2{}_\infty(491)} \times \frac{\dot{q}(r)}{\dot{q}(r=0)}$$

5.3.3.3.3 Flat plate and cylinder attitude corrections

It is highly unlikely, given the geometry involved, that the jet will strike the impinged surface at a 90-degree angle. Therefore, corrections to the heating are required in order to reflect the known relationship between pressure and heating for more grazing angles. Using Newtonian theory for local pressures, the heating may be corrected by

$$q(x,r,t,d_{hole},\alpha) = q(x,r,t,d_{hole}) * \sin(\alpha)$$

For wire burn-through analysis, this equation takes the form of

$$q(x,r,t,d_{hole},\Lambda) = q(x,r,t,d_{hole}) * \cos(\Lambda)$$

where Λ is the sweep angle of the wire to the jet axis and is the complement to α, the local angle of attack.

5.3.3.3.4 Hole diameter effects

Holes greater than the two-inch diameter originally simulated can now be assessed for thermal effects through application of curve fit results for the 0.25, 1.0, and 2.0 inch holes. Notice that the exponent is not 2.0, which would be the case for area correction only. The larger exponent results from larger holes pulling off larger and larger portions of the boundary layer and much closer to the free stream total enthalpy.

$$q_{d_{hole}>2.0''} = q_{d_{hole}=2.0''} \times \left(\frac{d_{hole}}{2.0''}\right)^{2.6}$$

5.3.3.4 CFD Supporting the 1-D Axisymmetric Plume Model

CFD analysis was used to verify the Plume Model's (section 5.3.3.2.1) predicted heat transfer. The CFD tools were used to estimate axisymmetric plume impingement heating rates to a cold wall perpendicular to the plume axis. To facilitate the quick development of the Plume Model, the CFD analyses were set up based on past experience for what was required to produce accurate estimates of heat transfer. The CFD codes were not specifically benchmarked for conditions at which they were run. However, two CFD codes were run independently to develop confidence in the results.

5.3.3.4.1 General Boundary Conditions

The Plume Model support CFD analysis was done at conditions derived from the External CFD trajectory point #1, or EI +404 sec. These plume analyses assumed a reservoir condition which decoupled the plume flow from the external flow. Specifics of the boundary conditions for each case are given in the results section. Different chemistry models: frozen, finite rate and chemical equilibrium, were applied as needed. Two sets of plume CFD analyses were performed. The first was for a ½ inch orifice impinging on a flat plate 7.5 and 15 inches downstream from the orifice. The second set was for a six-inch orifice impinging on a plate 30 and 60 inches downstream. In all cases the downstream wall temperature was held at 540° R and was non-catalytic.

5.3.3.4.2 Laminar Flow

A key question about the plumes was whether the flow laminar or turbulent. This was important for two reasons. The first is that the heating rate of a turbulent plume would be higher than of a laminar plume. The second is that turbulent plumes are self-similar. That is, a solution for a plume from a small orifice, with the proper scaling, could be used to assess plume heating for other size orifices.

Mr. W. Dahm, NASA/MSFC, re-produced the Figure 5.3.3-8 from the literature. Although this chart maps plume characteristics for large pressure ratios (P_{total}/P_{back}) it was still useful for the relatively low pressure ratio plume calculations performed to support the Plume Model. The mapping of the plume character is done with Re_L, a Reynolds number based on the location of the plume Mach disk. It can be approximated by the orifice Reynolds number multiplied by the square root of the inverse of the total to static pressure ratio (equation shown in Figure 5.3.3-8).

The CFD plume heating calculations had orifice Reynolds numbers between 100 and 700 (Re_L between approximately 50 and 250) and pressure ratios of 5 to 15 and fell in the lower left had side of the graph. Reviewing Figure 5.3.3-9 the first observation is that for Re_L of 100 to 1000 the plume flow is laminar. The second observation is that the region of interest for the wing penetration was outside those regions in which the plumes would be self-similar. Two conclusions were made. One, the CFD analyses would be run laminar, and two, because the combinations of orifice Re and pressure ratio of interest were outside the regions of self similarity, the CFD results for one orifice size should not be scaled to other orifice sizes.

The three following calculations of a free jet (non-impinging) demonstrate the significant differences in plume structure due to different Re_L. The same total conditions were run for three different orifice sizes to assess the mixing characteristics of the resultant plumes. The orifices sizes were one-half, one and two inches

corresponding to Re_L of approximately 47, 86 and 178, respectively. As can be seen from the Mach number contours in Figure 5.3.3-9, the plume expanded to Mach 3.6 for the two-inch orifice, but only Mach 2.7 for the half-inch orifice. Additionally, the progression to fully developed flow took much longer (x=24") for the two-inch orifice than for the half-inch orifice (x=4").

5.3.3.4.3 Results

Two sets of plume heating rate calculations were performed. The first was done for a half-inch orifice with the freestream total conditions corresponding to a pressure coefficient of 1.5 at EI +404s. These conditions were, H_{total} =11071 Btu/lbm, P_{total} = 37 lbf/ft^2, T_{total}=10400 R. The back pressure was assumed to be 5.5 lbf/ft^2 resulting in a pressure ratio of 6.7.

Both NASA/MSFC and Sandia National Laboratory (SNL) personnel calculated heating rates for these conditions using the FDNS and the SACCARA codes, respectively.

This first set of heating calculations assumed frozen chemistry. The low density and rapid expansion of the gas from the orifice was the basis for this assumption. It was subsequently verified by a DSMC analysis at SNL, that few reactions occurred in these plumes. The gas was modeled as a single specie of average gas properties derived from the constituents of the disassociated gas at the total conditions. At these total conditions the equilibrium mole fractions of the constituents were N_2=0.2, N=0.55, O=0.25. The single specie molecular weight was 17.334 and the ratio of specific heats of was 1.59. Laminar flow was prescribed. Figure 5.3.3-10 shows a representative plume solution from FDNS.

Figure 5.3.3-11 shows the SACCARA and FDNS results for a subset of the cases run. For the half-inch orifice impinging on a plate 7.5 inches downstream the heating to the wall agreed within 20% between the two codes (comparing the solid blue line on the left with the solid red line on the right). Although the total conditions were slightly different, the conclusion drawn from this comparison was that the CFD codes were sufficiently accurate to provide verification for the Plume Model for a half-inch orifice.

The second set of CFD cases were run using the FDNS code. This set nominally modeled a six-inch hole in an RCC panel at EI +404s. The total conditions were based on average gas properties entering a six-inch hole in RCC panel 6 as calculated by a coupled external CFD solution (Section 5.3.6.1.3). Averaged properties of the flow entering the six-inch hole were used as total conditions. They were, H_{total} = 9004 Btu/lbm, P_{total} = 28 lbf/ft^2, T_{total} = 9796 R. At these conditions the equilibrium mole fractions were NO=0.0090, N=0.4151, O=0.2743, N_2=0.3097. The back pressure was set to 4.4 lbf/ft^2 based on the venting analysis (Section 5.3.5) for this size hole at this point in the trajectory. Frozen, finite rate and equilibrium chemistry models were run. The impinged plate was at 30 and 60 inches downstream from the orifice. Figure 5.3.3-12 shows a representative solution for these cases. Figure 5.3.3-13 shows the heating rates for the four calculations. Note that the equilibrium cases had significantly higher heating to the wall. This was a result of the full recombination of the species at the wall. Also note that the finite rate solution and frozen solution heating rates were essentially the same. The shape of the heating distribution indicates that the jet was not yet fully developed and possessed a large subsonic bubble on the axis at the impinged plate. Off axis peaks are the result of relatively high total pressure flow that has been processed through oblique shocks. Of particular interest is the comparison with engineering predictions under the same conditions. Here the model would predict that both the 30" and the 60" locations are still in the underdeveloped core region and hence have the same heating value - 30 Btu/ft^2sec. These results compare well with the peaks observed for both distances.

Nomenclature

x	axial station
d_N	Nozzle Diameter
H	Enthalpy
P	Pressure
Re	Reynolds Number
T	Temperature

Subscripts

L	Length to Mach Disk
total	total conditions

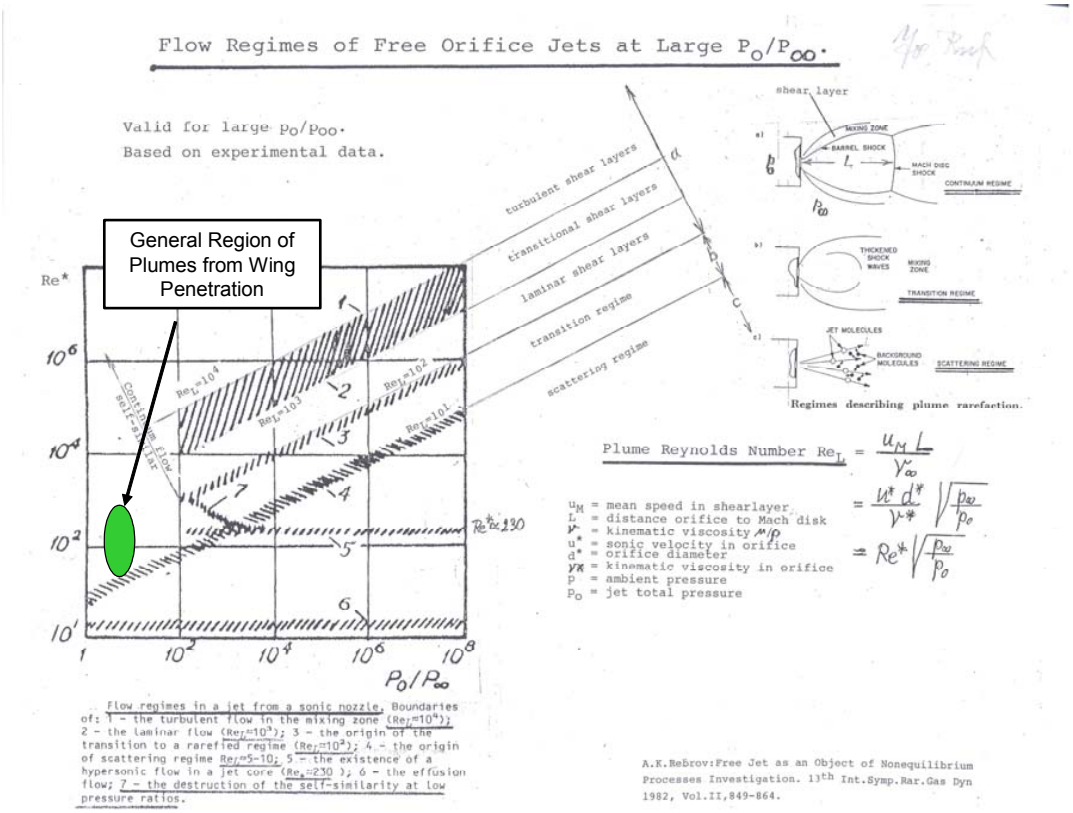

Figure 5.3.3-8 Flow Regimes of Free Jets from an Orifice.

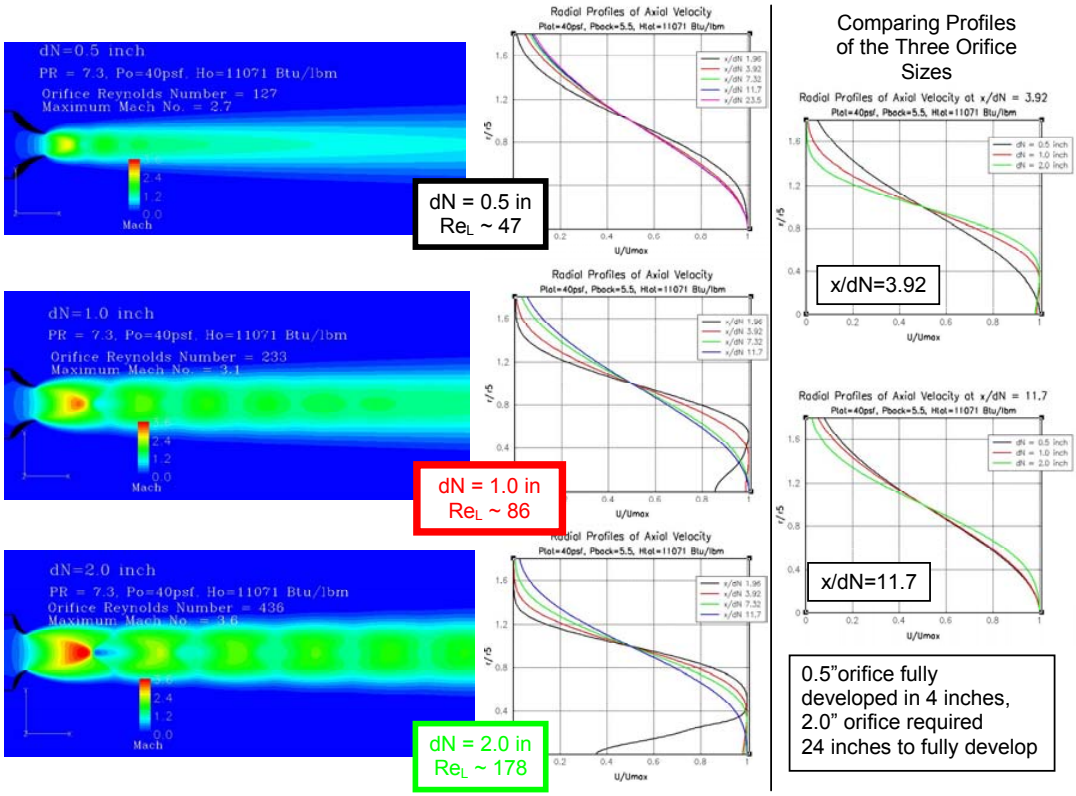

Figure 5.3.3-9 CFD Analysis of a Free Jet at Flight-like Total Conditions for Three Orifice Sizes.

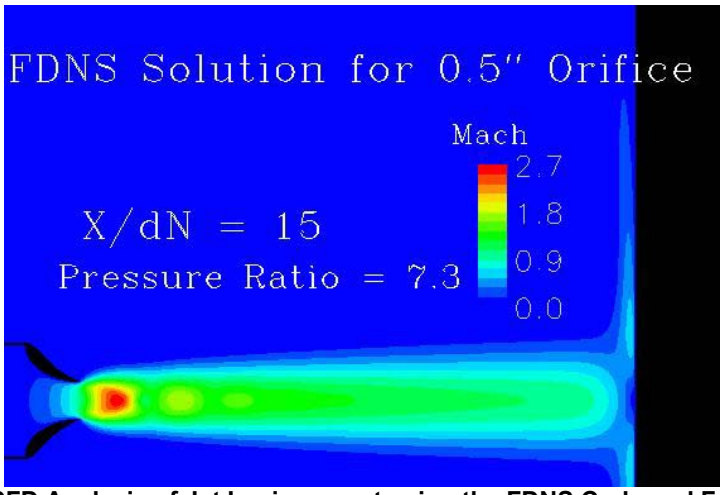

Figure 5.3.3-10 CFD Analysis of Jet Impingement using the FDNS Code and Frozen Chemistry.

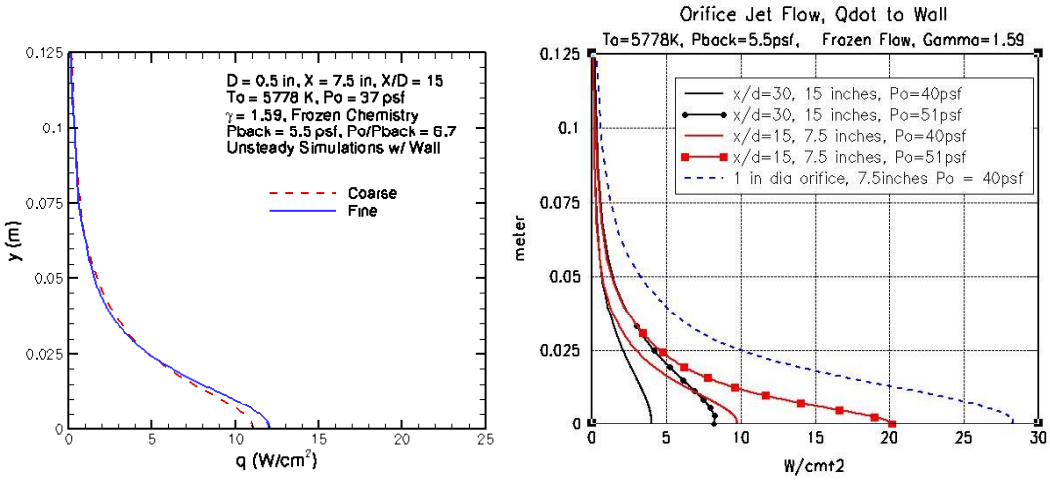

Figure 5.3.3-11 Heat Transfer for Half-Inch Orifice from SACCARA (left) and FDNS (right).

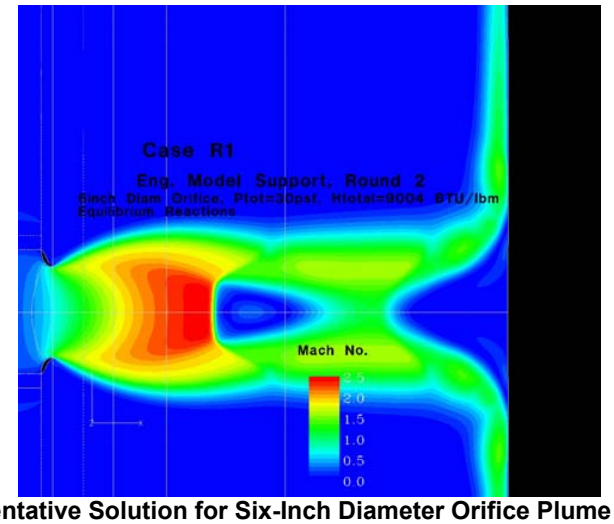

Figure 5.3.3-12 Representative Solution for Six-Inch Diameter Orifice Plume Impinging on a Plate 30 Inches Downstream.

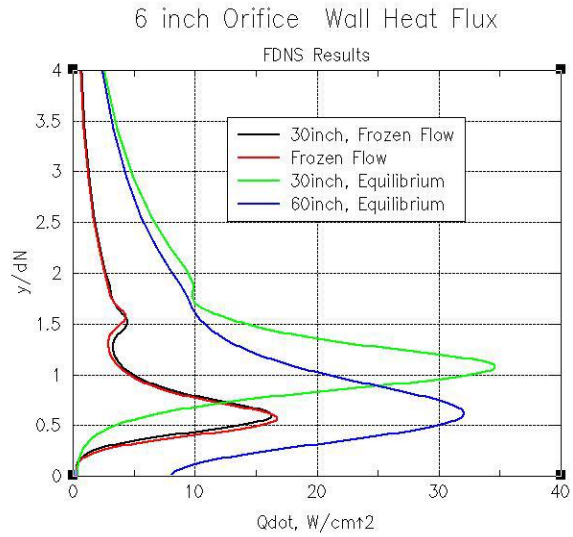

Figure 5.3.3-13 CFD Calculated Heating Rates for Six Inch Diameter Orifice Plume.

5.3.3.5 Arc-jet Test Data for Plume Heating Verification

5.3.3.5.1 Test Description

As described in Section 6.4, arc-jet tests were conducted in the NASA JSC facility to support the evaluation of effects of a breach hole in the Orbiter aeroshell. The test fixture, as sketched in Figure 5.3.3-14, was a rectangular cross-section box that was inserted into the flow exiting the arc-jet nozzle. Figure 5.3.3-15 shows the box with a hole in the front face and the location of test articles in the box downstream of the hole. Tests were conducted with a 1-inch and a 2-inch diameter hole in the front face. At the 15-inch test article location, pitot-probes, heat flux sensors and an instrumented cylinder were used to obtain data to verify the plume heating models.

Arc-jet test conditions were selected to be representative of those in flight by using total enthalpy and stagnation pressure as the simulation parameters. Figure 5.3.3-16 presents the STS-107 history of total enthalpy plotted as a function of the stagnation pressure. These values were derived from the STS-107 EOM3 trajectory simulation. A box is indicated on the plot that is labeled 'Zone of Interest' that corresponds to the range of total enthalpy and stagnation pressure for the time span of 300 to 600 seconds from entry interface. The two symbols on the plot indicate the total enthalpy and stagnation pressures that correspond to the two test conditions at which data were obtained. The arc-jet stagnation pressure was obtained from measurements of the pressure on the front face of the test fixture during runs. The arc-jet total enthalpy was derived from a combination of the stagnation pressure and the measured heat flux on a flat-face 1-inch diameter heat flux probe inserted into the arc-jet flow field at the same location at which the test fixture was located during runs. The following relation documented in Hiester and Clark was used with the measurements to obtain an estimate of the total enthalpy in the arc-jet flow field just upstream of the hole in the test fixture.

$$H_{total} = 24\dot{q}_{stag}\sqrt{\frac{R_{eff}}{P_{stag}}}$$

In this relation, R_{eff}, is the effective radius and is obtained by multiplying the flat-face cylindrical radius by a factor of 3.3, as recommended by Hiester and Clark.

The following table provides a summary of the two test conditions.

Test Configuration	Air Flow Rate (lb_m/sec)	Arc-jet Current (amps)	P_{stag} (psf)	q_{stag} (Btu/ft^2-sec)	H_{total} (Btu/lb_m)
1-inch Dia. Hole	0.3	1200	27	154	12,200
2-inch Dia. Hole	0.4	1200	35	139	9,700

5.3.3.5.2 Results

For the purpose of verifying plume-heating models, the most significant data obtained from this test series were pitot-pressure measurements and heat flux data on a 1.75-inch diameter cylinder at the 15-inch location downstream of the hole. The measured and predicted values are presented in the following table:

Test Configuration	P_{stag} (psf)	H_{total} (Btu/lb_m)	P_{box} (psf)	$P_{pitot\text{-}X=15"}$ (psf)	Measured q_{cyl} (Btu/ft^2-sec)	Predicted q_{cyl} (Btu/ft^2-sec)
1-inch Dia. Hole	27	12,200	0.88	2.02	4.7	21.1
2-inch Dia. Hole	35	9,700	0.68	3.18	12.1	39.3

The predicted values were obtained using the plume-impingement heating model described in Sec. 5.3.3.1. The test fixture stagnation pressures, P_{stag}, the box internal pressures, P_{box}, and a reduced total enthalpy were used as input to these predictions. It was assumed that the total enthalpy in the gas ingested through the test fixture hole was 84% of the arc-jet centerline total enthalpy, H_{total}, for the 1-inch hole case and 93% for the 2-inch hole case. These values were based upon mean temperature estimates for entry-length ducts, as described by Kays and Crawford. Clearly, the predicted values are significantly larger than those measured. It is believed that the test fixture box interfered with the free-jet flow field emanating from the hole and created shock waves inside the box. The simple plume impingement model was not created to predict heating in this type of flow field.

5.3.3.5.3 CFD Computation for Arc-jet Test Setup

At the time of report release, JSC was in the process of running CFD solutions for arc-jet conditions and the test hardware mockup. Preliminary results indicated that the test box walls constrained the plume expansion and created compression shocks that changed the plume flow field.

5.3.3.5.4 Conclusions

The breach hole arc-jet test provided valuable data about hole growth in aluminum plates and about the demise of flight-like instrumentation cable bundles. However, questions about the flow field inside the box prevent the impingement heating data to be used for verifying the plume impingement heating model.

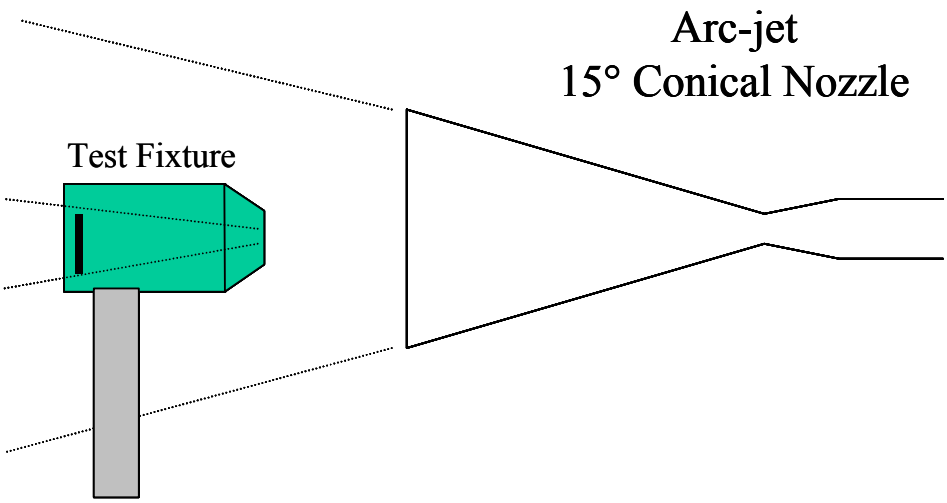

Figure 5.3.3-14 Sketch of Breach Hole Arc-jet Test Setup.

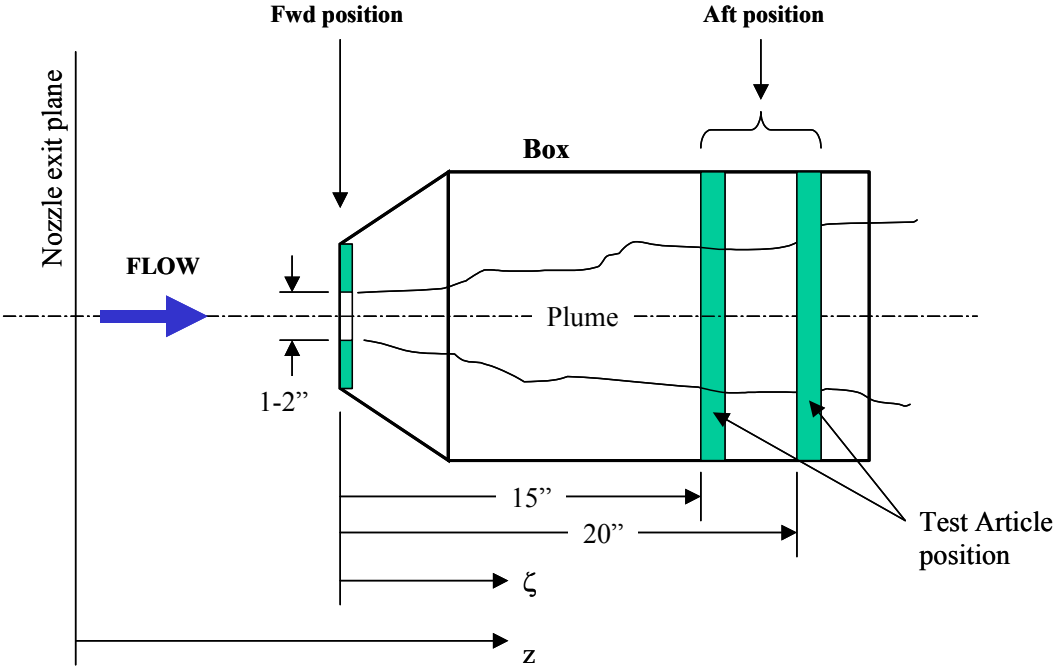

Figure 5.3.3-15 Sketch of Test Fixture and Locations of Test Articles

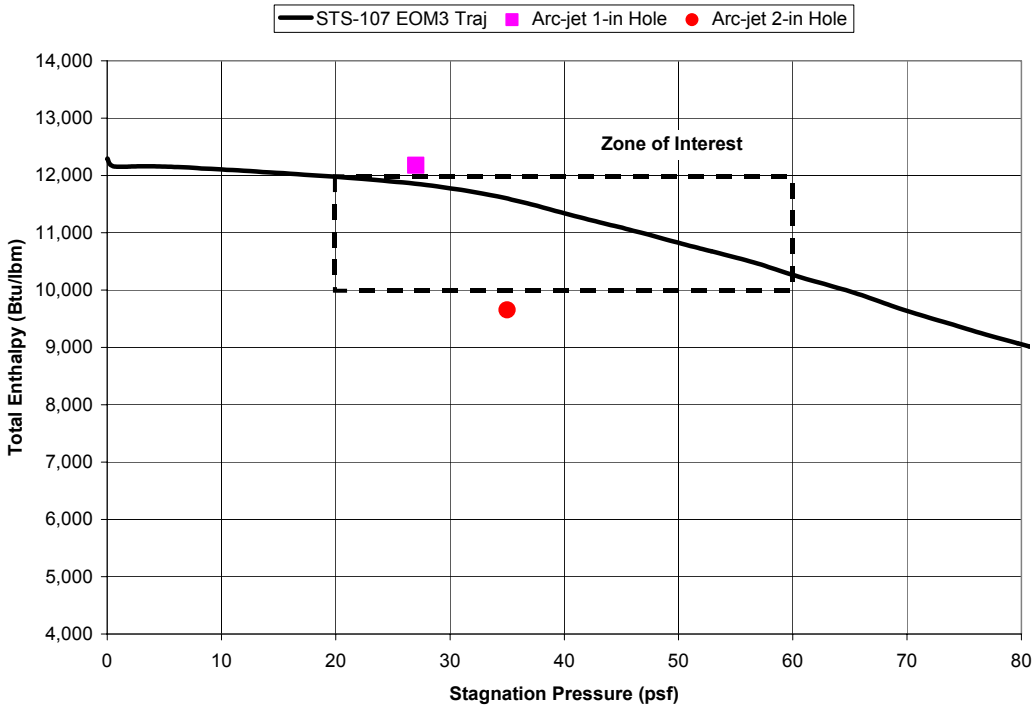

Figure 5.3.3-16 Comparison of STS-107 Flight Conditions and Arc-jet Test Conditions.

5.3.3.6 Slot Jet Heating Model (Missing Panel 8/9 T-seal)

5.3.3.6.1 Scenario Description

One of the damage scenarios evaluated was that the T-seal between leading edge panels 8 and 9 was damaged and missing at the beginning of the STS-107 reentry. In this instance it was postulated that only the lower portion of the T-seal between the apex and the beginning of the internal earmuff insulation was missing. Figure 5.3.3-17 provides a sketch of the geometry for this case. Panel 8 has been removed to permit a view of the internal structure.

5.3.3.6.2 CFD Predictions of Heating to Internal Hardware

Two sets of CFD solutions were used as the basis for developing the transient heating distribution to the earmuff insulation as a result of a missing T-seal between Panels 8 and 9. A 3-D Navier-Stokes CFD solution of the flow through the gap between panel 8 and 9 ribs for a missing 8-inch segment of T-seal has been provided by Boeing-Huntington Beach (see Sec. 5.3.6.2.3) for CFD Point 1:

> CFD Point 1: EI+404 secs.; Mach =24.9; Altitude = 243,000 ft; Angle-of-attack = 40 degs.; Dynamic pressure = 22.0 psf.

The heat flux distribution on the earmuff and spar insulation predicted by this solution is presented in Figure 5.3.3-18. The heat fluxes are for a wall temperature of 460° R. Note that the highest heating is concentrated at the edge of the earmuff closest to the rib channel outlet and quickly drops by a factor of ten on the rest of the earmuff front face. Heating to the earmuff sides and spar insulation is on the order of another factor of ten lower – less than 0.3 Btu/ft^2-sec.

Several 2-D Navier-Stokes CFD solutions were generated for the same flight conditions and for the perpendicular impingement of the flow emanating from the rib channel onto the earmuff insulation (see Sec. 5.3.6.2.1). Figure 5.3.3-19 shows the Mach number contours for the 2-D solution for a 5-inch distance between the rib outlet and the front face of the earmuff insulation. Cases were also run for 2-inch, 11-inch and 21-inch distances between the ribs and the earmuff. The resultant heat flux distributions predicted are presented in Figure 5.3.3-20 for a 1500° F wall temperature. The predicted heat fluxes on the edge of the earmuff are probably high due to a smaller than actual edge radius (0.25" modeled versus a 1.0" actual) used in these solutions. In order to apply the 2-D results to the actual hardware, lines perpendicular to the rib outer edge were projected to the earmuff front face centerline as shown in Figure 5.3.3-21. The radial distances between the rib and the earmuff were selected to approximate the perpendicular distances used in the 2-D CFD cases and the angles between the radial rays and the earmuff centerline were obtained. The 2-D CFD centerline heat flux values were then corrected by the cosine of the impingement angle. The resultant centerline heat fluxes are presented in the table below as a function of distance from the lower edge of the earmuff insulation.

Earmuff Location (inches)	Distance from Rib (inches)	Impingement Angle (degs)	CFD Prediction (Btu/ft^2-s)	Angle Corrected Heat Flux (Btu/ft^2-s)
2	2	70	46.7	15.9
6.5	5	70	17.5	6.0
12	11	65	7.1	3.0
20	18	55	3.1*	1.8

*Value derived by curve-fit since actual data were available for 2, 5, 11, and 21 inches.

5.3.3.6.3 Development of Engineering Model for Earmuff Insulation Heating

The CFD solutions provide heat flux predictions for a single flight condition – CFD Point 1. In order to conduct a thermal analysis and determine the response of the hardware, heat fluxes are needed as a function of time (varying flight conditions) and as a function of the surface temperature. Furthermore, the 3-D CFD solution was modeled with only an 8-inch length of the T-seal missing. Therefore, engineering judgment had to be used to estimate the effect of having a longer length of T-seal missing. The first step in the process of developing the engineering model was to assume that a majority of the heating was on the front face of the earmuff and then to establish the heating along the centerline of the earmuff in a local coordinate system. Figure 5.3.3-22 presents a sketch of the local coordinate system with an origin at the center lower edge of the earmuff and with the x-axis lying along the earmuff centerline from the lower to the upper edge. The z-axis is perpendicular to the earmuff front face.

The earmuff centerline heat fluxes in the local coordinate system are presented in Figure 5.3.3-23. Both the 3-D and corrected 2-D CFD values are shown. A best-estimate curve-fit is also provided that uses a reference maximum heating rate of 55 Btu/ft^2-sec at X_{local}= 0.25 inches.

$$q_{CL}(x) = \frac{0.412 q_{CL}(x = 0.25")}{x^{0.64}}$$

This curve-fit provided the basis for the earmuff centerline cold-wall heating distribution. In order to account for wall temperature effects and the energy available to heat the earmuff, the cold-wall heat fluxes were used to obtain enthalpy-based heat transfer coefficients. The final engineering model provides heat transfer coefficient and bulk enthalpy histories to use in calculating the transient heat flux to the earmuff.

$$q(x, y, t) = h(x, y, t)(H_{bulk}(t) - H_{wall}(T_{wall}))$$

In this relation, h, the heat transfer coefficient is a function of the location (x,y) and the time, t; H_{bulk} is the ingested bulk enthalpy of the flow through the rib channel as a function of time; and H_{wall} is the enthalpy of the gas at the wall temperature. Therefore, the centerline heat flux is defined by

$$q(x,0,t) = h(x,0,t)(H_{bulk}(t) - H_{wall}(T_{wall}))$$

with

$$h_{CL}(x,0,t) = \frac{0.412 h_{CL}(0.25",0,t)}{x^{0.64}}$$

The heat transfer coefficient at the reference point, $h_{CL}(0.25",0,t)$ was obtained for t=EI+404 secs. from the peak cold-wall heat flux value of 55 Btu/ft^2-sec estimated from the CFD solutions and using a bulk enthalpy estimated from the 2-D CFD solutions.

$$h_{CL}(0.25",0,404\,\text{sec.}) = \frac{(5366 Btu/lbm) - H_{wall}(460R))}{55 Btu/ft^2 - \text{sec}} = 0.0105 lbm/ft^2 - \text{sec}$$

To obtain time dependent, and therefore flight condition dependent, values of the heat transfer coefficient at x=0.25" it was assumed that the heating varied as the square-root of the free-stream dynamic pressure. The rationale for this assumption is that impingement heating is proportional to the square root of the impingement pressure. In addition, the impingement pressure on the earmuff is driven by the wing leading edge external pressure which is a function of the dynamic pressure.

The variation of the bulk enthalpy with flight conditions was obtained by using the engineering analysis procedures discussed in Sec. 5.3.2. The effective gap width of the ingested flow was varied until the bulk enthalpy predicted by the engineering analysis matched that estimated from the 2-D CFD solution for t=404 seconds. The resultant bulk enthalpy history and the predicted maximum earmuff heating rate history are presented in Figure 5.3.3-24. The table below also presents the transient values.

EI Time (secs.)	**Ingested Enthalpy (Btu/lbm)**	**Dynamic Pressure (psf)**	$\sqrt{\frac{P_{dyn}}{P_{dyn,t=400s}}}$	**q_{CL}(x=0.25") Tw=460 R (Btu/ft^2-s)**	**h_{CL}(x=0.25") (lbm/ft^2-s)**
200	3781	1	0.23	8.81	0.0024
300	4861	8	0.65	32.26	0.0068
400	5366	19	1.00	55.00	0.0105
500	5387	25	1.15	63.34	0.0120
600	5273	33	1.32	71.20	0.0138
700	5095	41	1.47	76.63	0.0154
800	4741	48	1.59	77.02	0.0166
900	4334	69	1.91	84.23	0.0199

With the centerline heat transfer coefficients and bulk enthalpy values defined as a function of time, the lateral distribution of heat transfer on the earmuff was defined as a function of the centerline values using the results from the 3-D CFD solution. The non-dimensionalized values are presented in Figure 5.3.3-25 for five axial stations – x=0.25, 1, 2, 4, and 8 inches. Beyond 8 inches it was assumed that the distribution was the same as that for the 8-inch station.

Figure 5.3.3-26 presents a comparison of the cold-wall heat flux distribution on the earmuff front face from the 3-D CFD solution and that resulting from the engineering model. The acreage heating provided by the engineering model tends to be greater than that predicted by the CFD and that was done to provide an estimate of the effect of the increased length of the T-seal missing.

Heating to the sides of the earmuff and the spar insulation was assumed to be low and estimated to be below 0.5 But/ft2-sec at EI+404 seconds. Using this value a heat transfer coefficient of 0.0001 was estimated and the heat flux was then computed using the following relation:

$$q = 0.0001\sqrt{\frac{P_{dyn}}{P_{dyn,t=400s}}}(H_{ingested}(t) - H_{wall}(Tw))$$

5.3.3.6.4 Reduction of Heating with Distance from Rib Channel Outlet

In order to estimate the heating to hardware behind the earmuff after the earmuff is removed a relation was derived from the 2-D CFD solutions that provides an indication of the reduction in heating as a function of distance from the rib channel outlet. The relation is presented in Figure 5.3.3-27 and was obtained by curve-fitting the centerline heat flux predictions from the 2-D CFD solutions for a normal impingement.

This curve-fit was used to estimate the heating to a 1.75-inch diameter cylinder located 13 inches from the rib outlet. The cylinder represents an instrumentation cable bundle that would be located at the closest 13 inches from the rib channel outlet. Using the curve-fit from Figure 5.3.3-27, the heating to the front face of the earmuff would be approximately 4.7 Btu/ft^2-sec. However, the earmuff has a blunt front face with a width of 9 inches. To correct the heating for the difference in geometries between the earmuff and the cylinder the square root of the ratio of effective radii is used.

$$q_{cyl} = q_{earmuff-CL}\sqrt{\frac{R_{eff-earmuff}}{R_{eff-cyl}}}$$

The effective radius of the cylinder is half the diameter or 0.875 inches. With the blunt front face of the earmuff the effective radius is estimated to be 3 times the half-width or 13.5 inches. The estimated heat flux to the 1.75-inch cylinder would be 18 Btu/ft^2-sec. The factor of three is a typical ratio for scaling a flat-faced cylinder to an equivalent hemisphere as reported by Hiester and Clark.

This heating value was verified by extracting flow field properties from the 2-D CFD solution at a point 13 inches downstream of the rib channel outlet, and using a stagnation point relation also provided by Hiester and Clark to compute the heating.

$$q_{cyl} = \frac{H_{total}}{24}\sqrt{\frac{P_{stag}}{2R_{eff-cyl}}}$$

The factor of 2 in the relation is used for stagnation heating to cylinders. From the 2-D CFD solution the value of total enthalpy at 13 inches from the rib channel outlet was 5654 Btu/lb$_m$ and the stagnation pressure was determined to be 1.9 psf. Using these values, in the appropriate units, also results in a cold-wall heat flux on the cylinder of 18 Btu/ft^2-sec. This value contrasts with the results of section 6.0 in assessing the heating rate required to match the wire demise rate observed from flight of 89.6 Btu/ft^2-sec.

5.3.3.6.5 Heating to the Panel 8/9 Rib Channel with T-seal Removed

A 2-D CFD solution was also generated by Boeing-Rocketdyne for the detailed 2-D geometry of the channel between leading edge panels 8 and 9 for the CFD Point 1 flight conditions (see Sec. 5.3.6.2.2) with the T-seal removed. Figure 5.3.3-28 presents contours of the gas static temperature predicted by this solution. Three flow field regions were identified from these results – 1) separation region; 2) stagnation region; and 3) duct region. The flow along the Orbiter leading edge consists of a supersonic boundary layer that flows from inboard to outboard. When the flow encounters an open rib channel, the flow locally separates from the surface and then impinges on the downstream edge of the outboard rib. Some portion of the flow is turned inward and flows through the parallel ribs creating a flow similar to a two-dimensional duct. Using the characteristics of these flow regions and the heating distributions predicted by the 2-D CFD solution, an engineering model was developed to predict the local heat flux history in the rib channel for the STS-107 reentry trajectory.

The 2-D CFD solution provided heat flux distributions on the upstream and downstream rib surfaces in a local coordinate system shown in Figure 5.3.3-29. The CFD heat flux distributions for a wall temperature of 2900 R

were used to obtain enthalpy-based heat transfer coefficients, h, referenced to the heat transfer coefficient, h_{ref}, on the external surface of the leading edge.

$$\frac{h(s,t)}{h_{ref}(t)} = \frac{\dfrac{q(T_{wall} = 2900R)}{(H_{rec} - H_{wall}(T_{wall} = 2900R))}}{\dfrac{q_{ref}(T_{wall} = 2900R)}{(H_{fs-total} - H_{wall}(T_{wall} = 2900R))}}$$

To obtain the value h_{ref} the free stream total enthalpy, $H_{fs\text{-}total}$, was used. For the heat transfer coefficients inside the rib channel, the recovery enthalpy, H_{rec}, varied by the flow region. For the stagnation region, the recovery enthalpy was assumed to be equal to the free stream total enthalpy. For the separation and duct regions, the recovery enthalpy was assumed to be equal to the ingested bulk enthalpy found by the methods discussed in Sec. 5.3.2. The heat transfer coefficient distributions for the upstream and downstream surfaces were defined with linear segments based upon the local coordinate, s. A comparison of the heat fluxes derived from the engineering model with those provided by the CFD solution is presented in Figure 5.3.3-30. In order to obtain the transient variation of heat flux within the rib channel, values of the ingested enthalpy were provided as a function of time and it was recommended that the heat flux for BP 5505 on the leading edge of Panel 9 be used for the reference heat flux, q_{ref}. The resultant cold-wall heat flux histories for three locations in the rib channel are presented in Figure 5.3.3-31. These heat fluxes are very high since they use the high leading-edge heating associated with BP 5505 on Panel 9 (see Sec. 5.2.2).

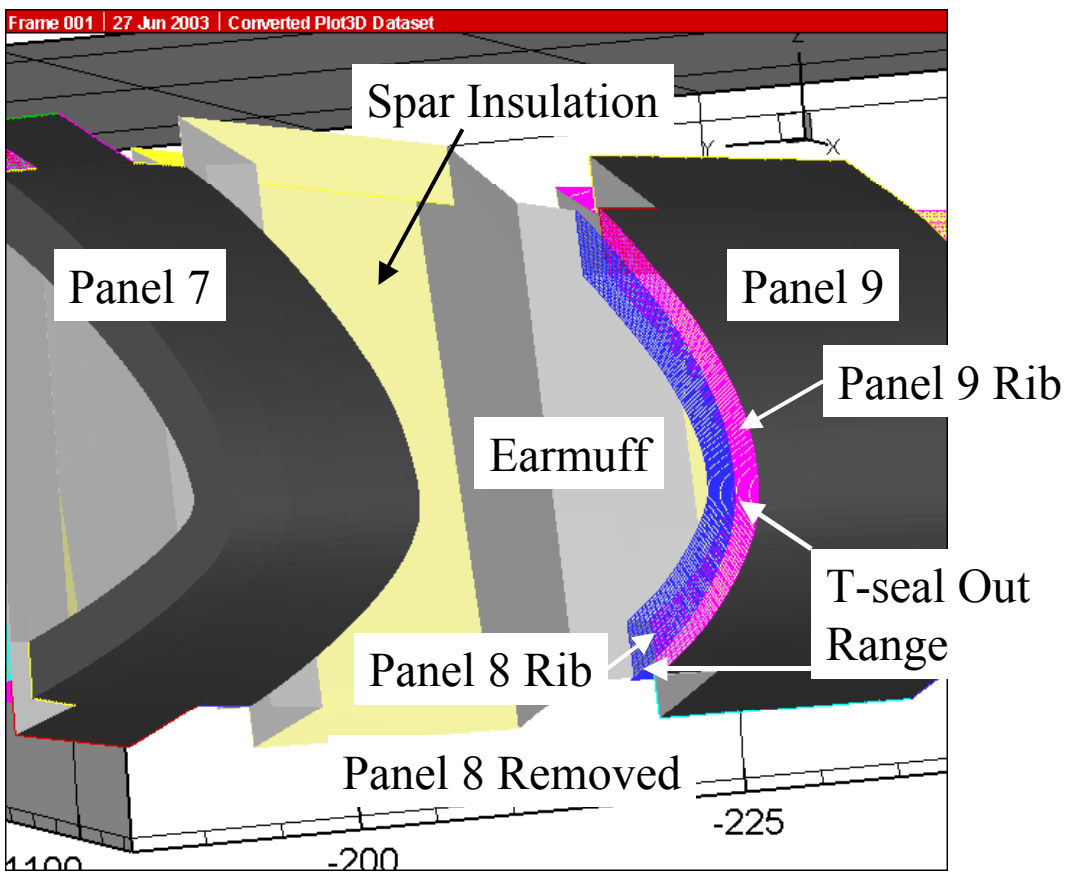

Figure 5.3.3-17 Sketch of Leading Edge Region for Panels 7, 8 and 9.

317

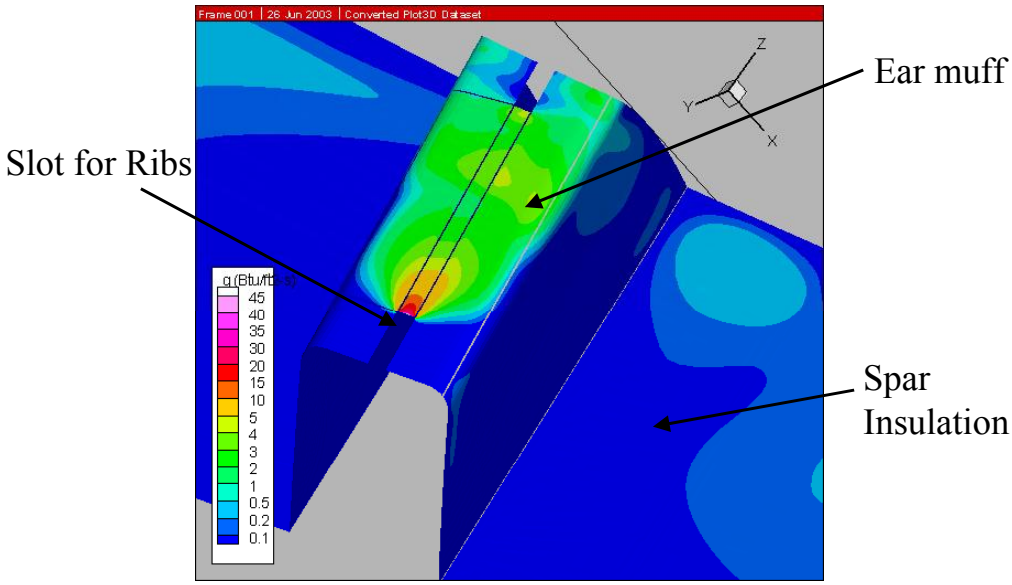

Figure 5.3.3-18 Earmuff and Spar Insulation Heating Predictions for CFD Point 1 from the Boeing-HB CFD Solution – Twall=460 R.

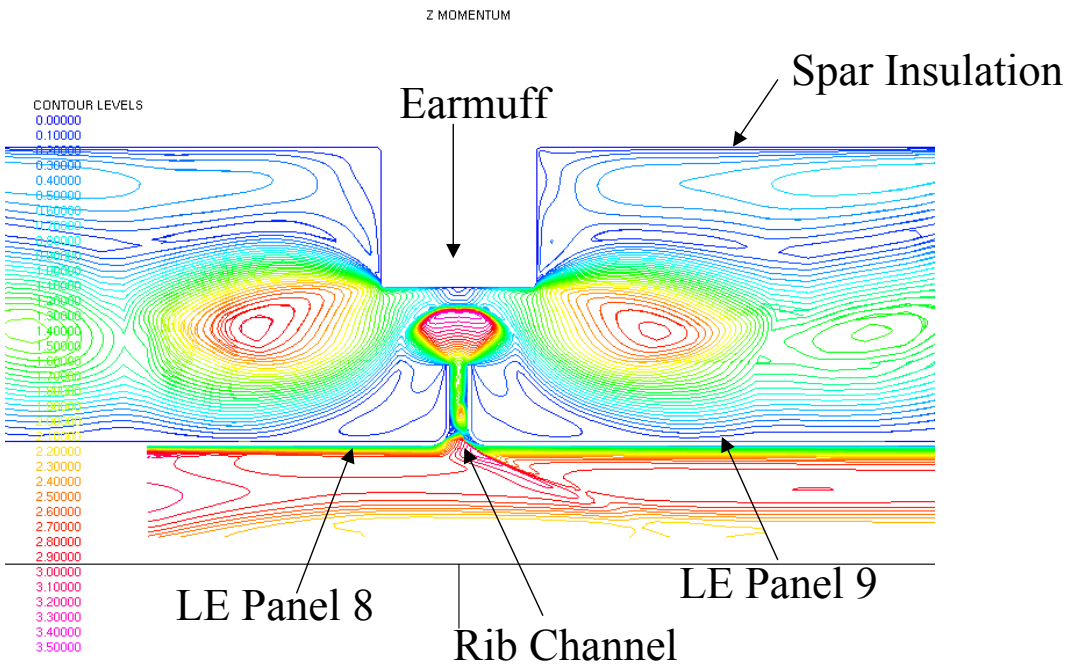

Figure 5.3.3-19 Mach Number Contours for 2-D flow impingement onto Earmuff and Spar Insulation – 5-inch Distance between Rib Channel Outlet and Earmuff.

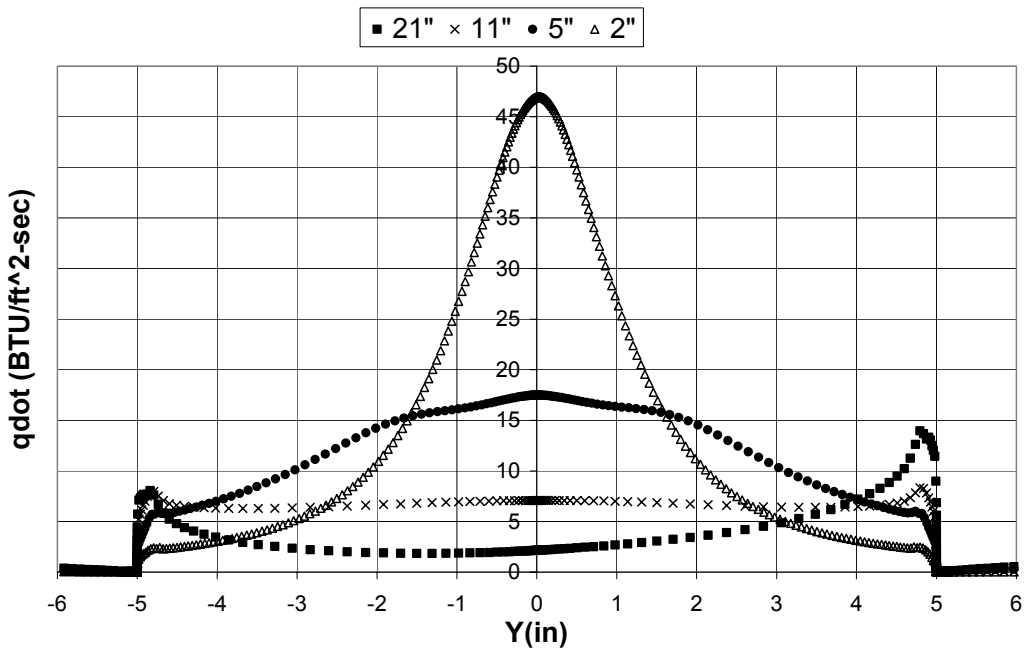

Figure 5.3.3-20 – Earmuff Heat Flux Distributions Predicted by the NASA JSC 2-D GASP CFD Solutions CFD Point 1.

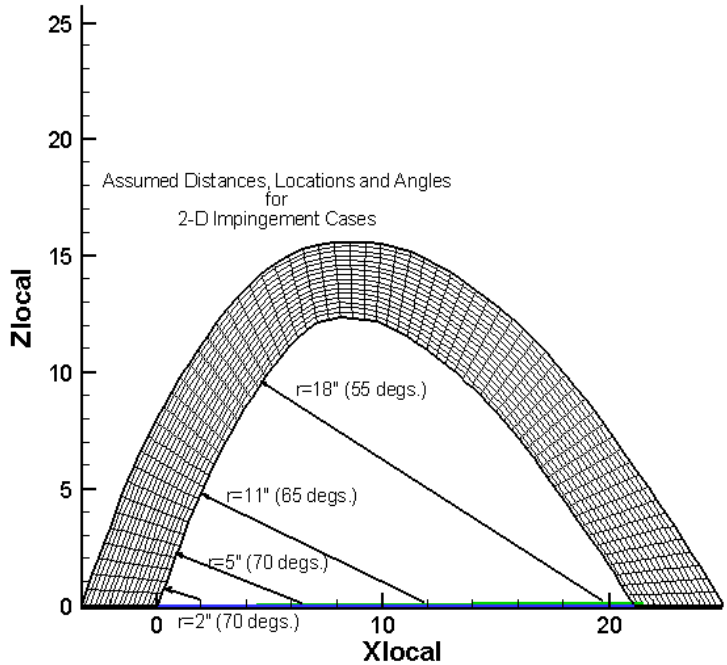

Figure 5.3.3-21 Application of 2-D CFD Solutions to the Actual Hardware

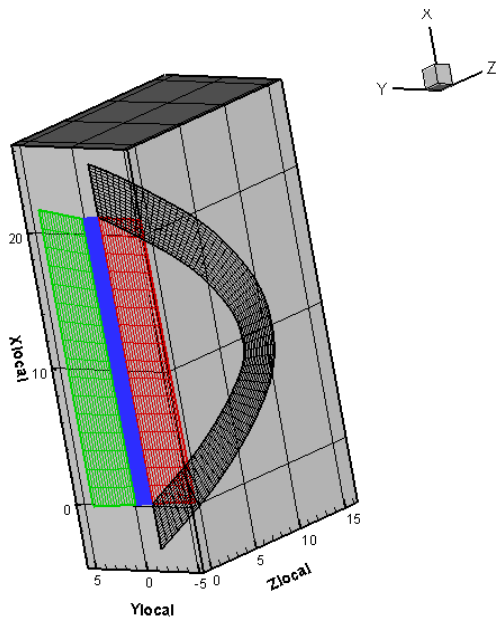

Figure 5.3.3-22 Local Earmuff Coordinate System
Figure 6 – Local Earmuff Coordinate System.

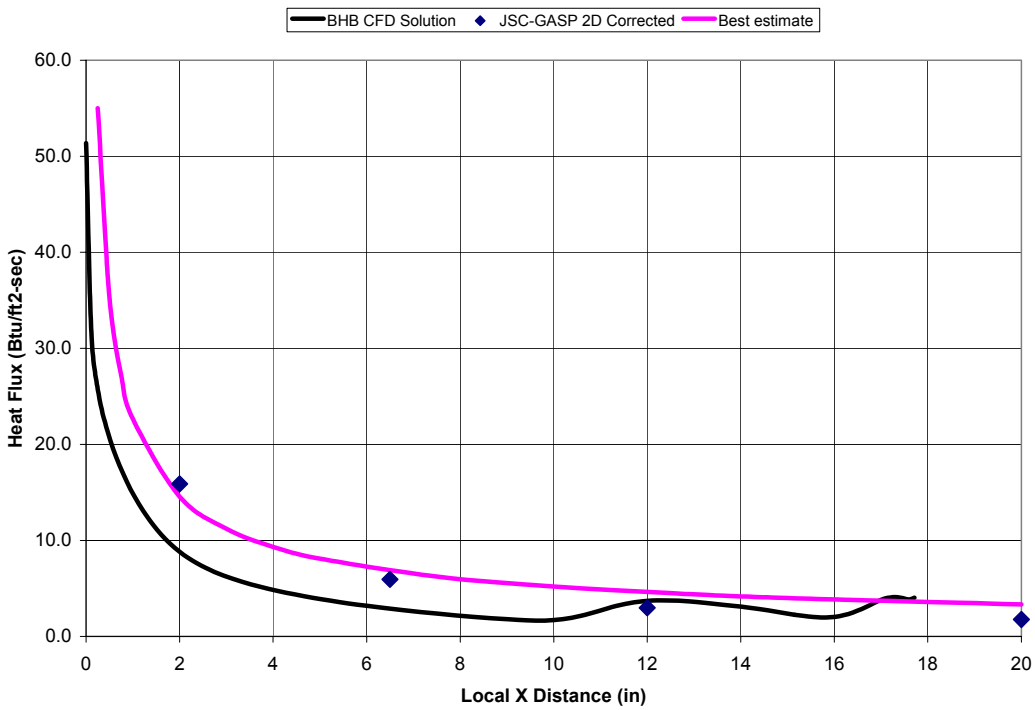

Figure 5.3.3-23 Comparison of Predicted Heat Fluxes on the Earmuff Centerline for CFD Point 1

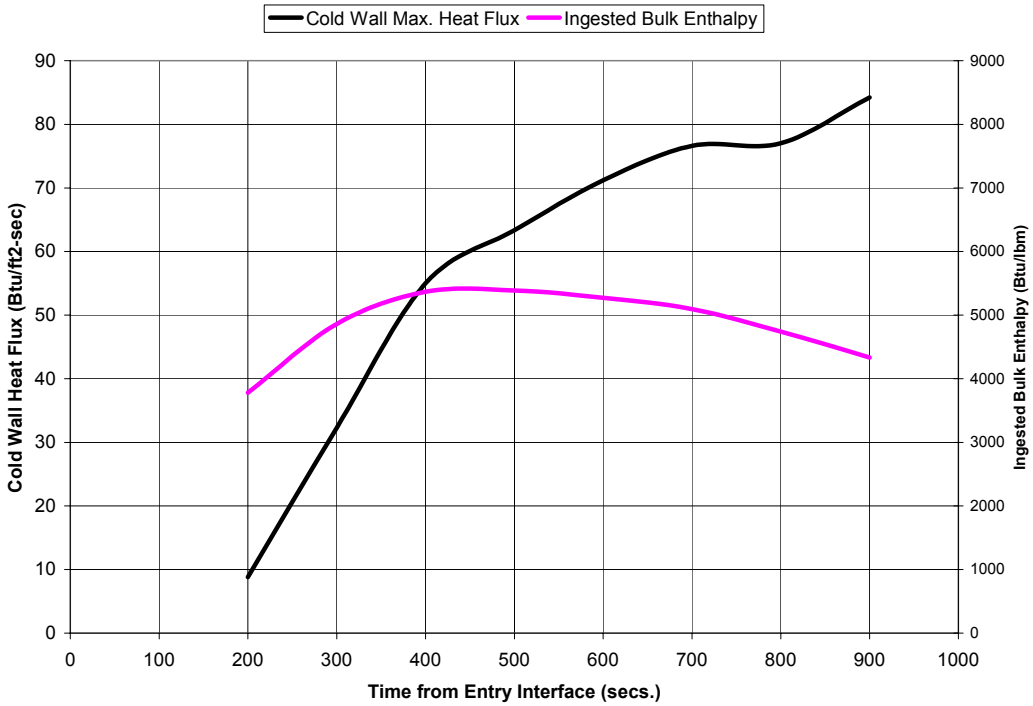

Figure 5.3.3-24 Predicted Maximum Cold-wall Heat Flux and Ingested Bulk Enthalpy Histories.

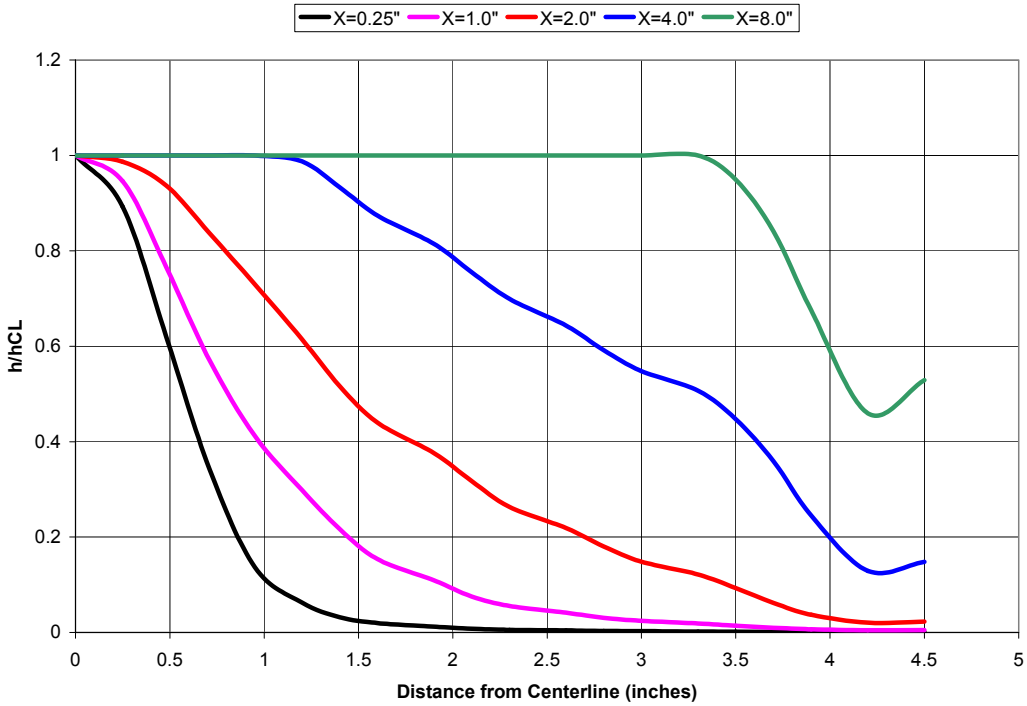

Figure 5.3.3-25 Predicted Maximum Cold-wall Heat Flux and Ingested Bulk Enthalpy Histories.

Twall=460 R

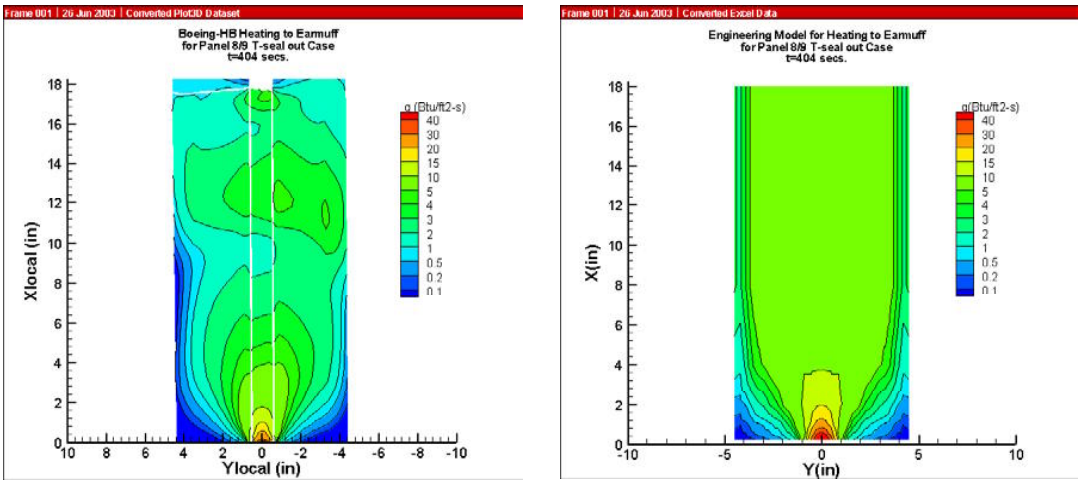

BHB 3-D CFD Results
8-inch T-seal out

Engr. Model Results

Figure 5.3.3-26 Earmuff Front-face Heating Comparison for EI+400 seconds. (Assumed results for 400 and 404 seconds are same.)

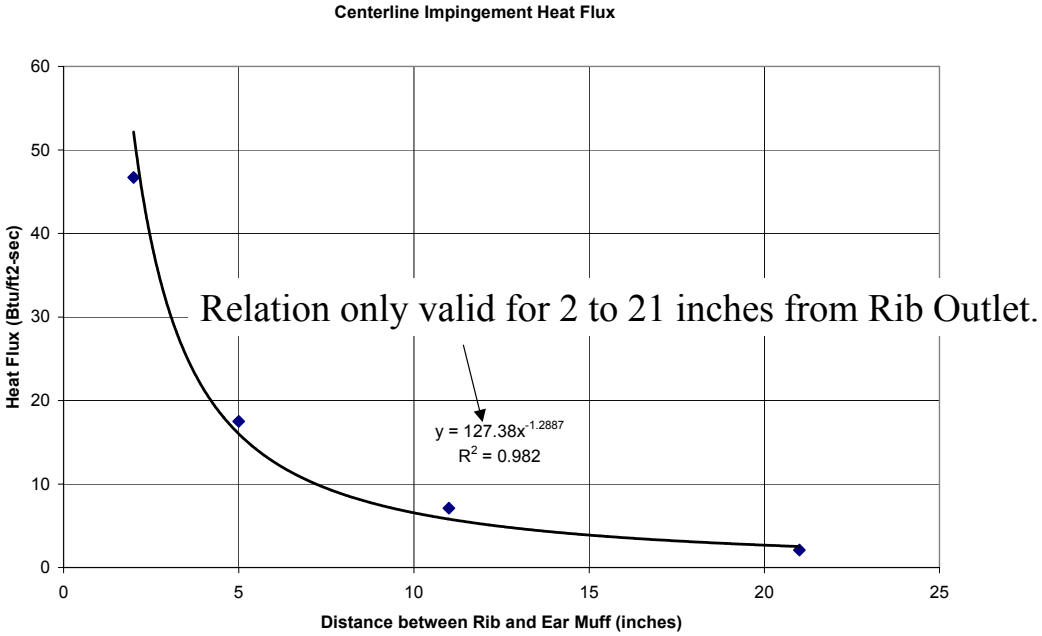

Figure 5.3.3-27 Relation for Estimating Reduction in Heating with Distance from Rib Channel Outlet.

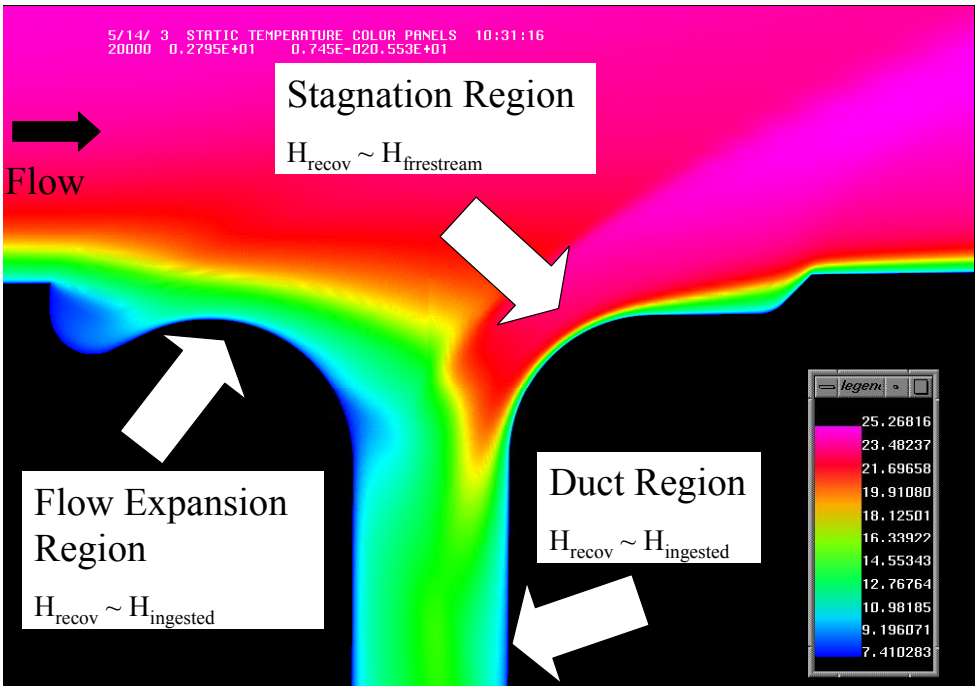

Figure 5.3.3-28 Regions of the Flow field in the T-seal Out Rib Channel.

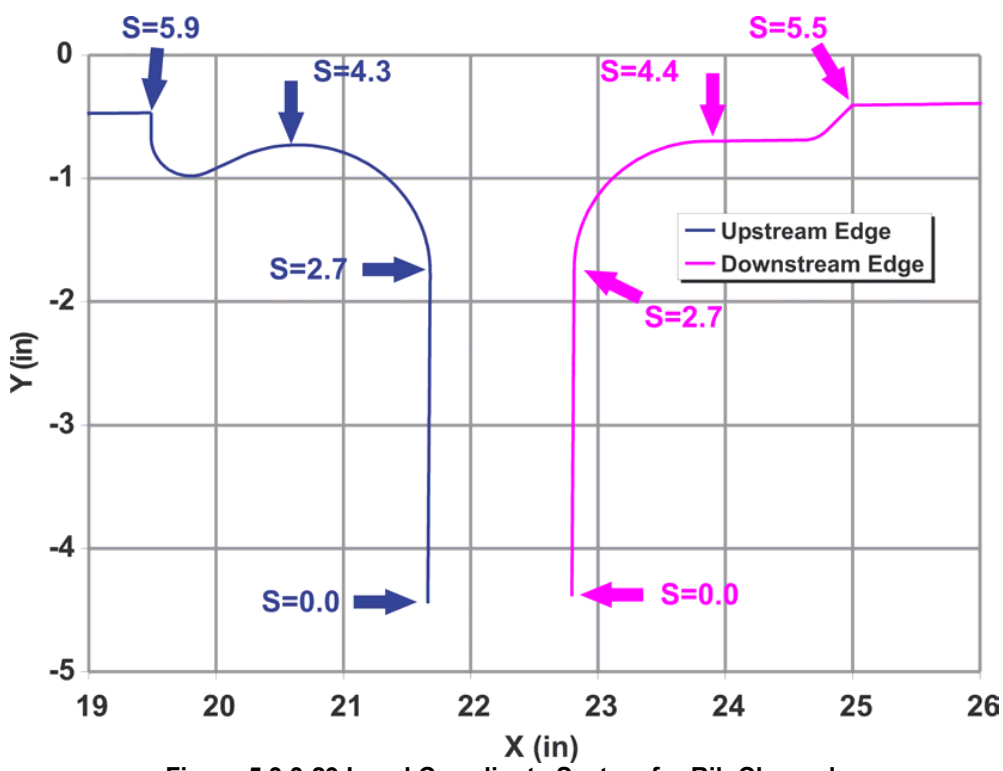

Figure 5.3.3-29 Local Coordinate System for Rib Channel.

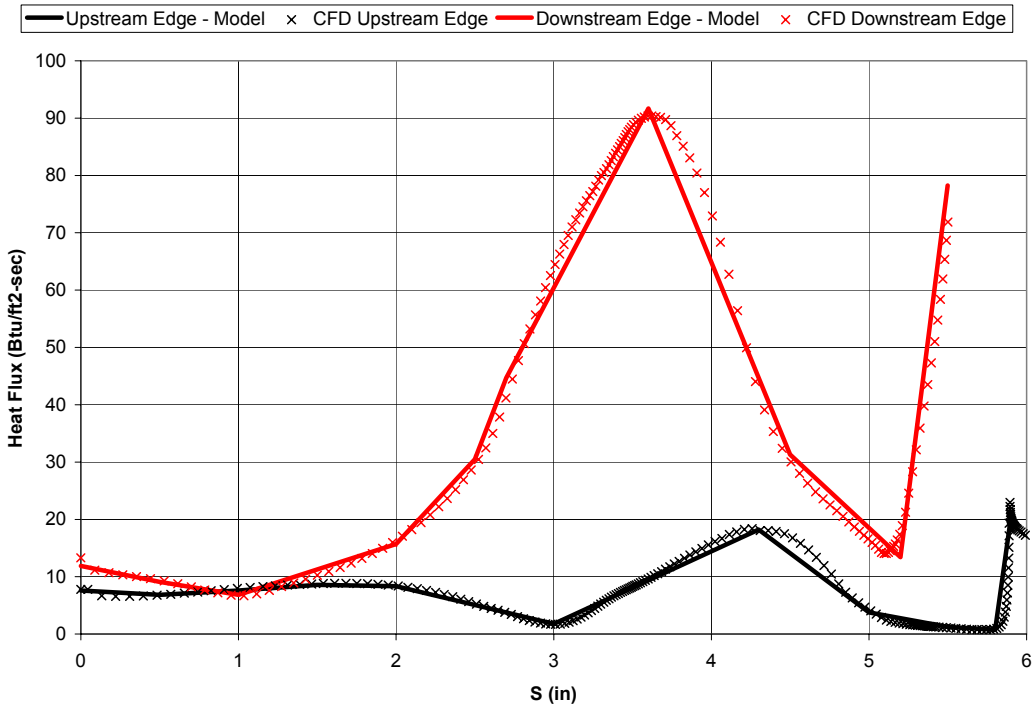

Figure 5.3.3-30 Comparison of Engineering Model Heat Fluxes with CFD Results.

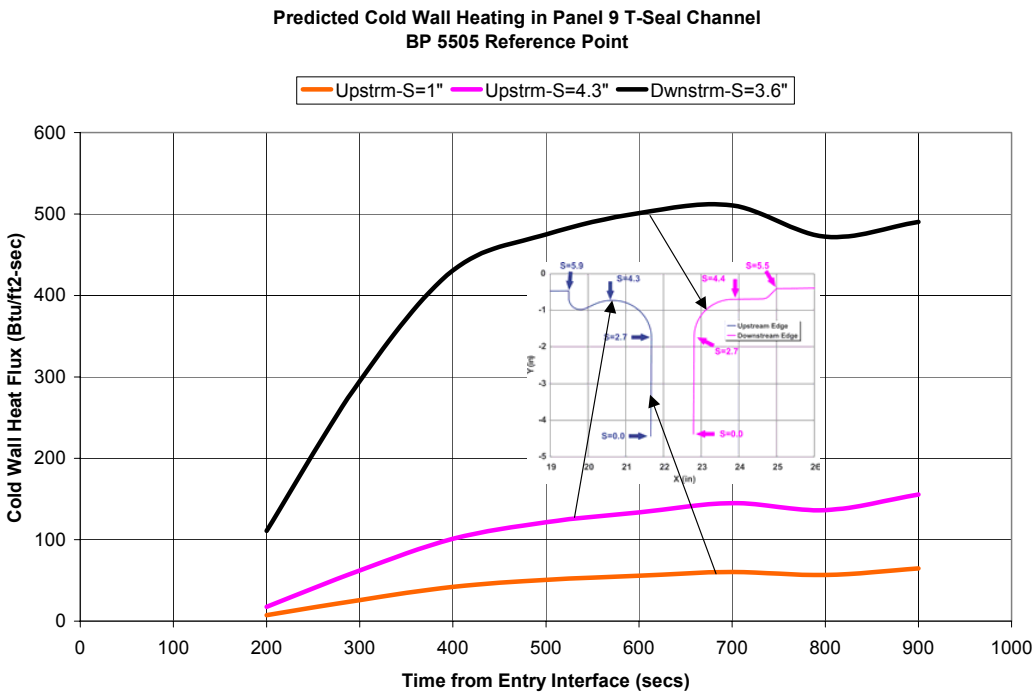

Figure 5.3.3-31 Predicted Cold-wall Heat Flux History for Locations in the Panel 8/9 Rib Channel

5.3.4 Effects of Burning Aluminum

In order to evaluate the effects of aluminum combustion on the STS-107 accident, a team was formed that included the following personnel:

NASA JSC Engineering Directorate Personnel (EG and ES Divisions)
NASA White Sands Test Facility Personnel
Boeing Huntington Beach Engineering Personnel
Lockheed Martin Space Operations Personnel
Sandia National Laboratories Personnel
Princeton – Dr. I. Glassman
Stanford – Dr. J. Jeffries
CalTech – Dr. P. Dimotakis

First, this team reviewed the aerothermodynamic environments associated with the STS-107 reentry. These environments are summarized in the following section. After reviewing these environments it was recognized that there was very limited experience with the exposure of aluminum to the high-temperature and low-pressure air resulting from a breach during reentry. Therefore, an air/aluminum chemical analysis that would determine the key reactions that would occur for the pressure and temperature range of the reentry gases was deemed necessary. Based upon the results of this analysis the heats of formations of the key reactions would be used to determine the additional energy available for propagating damage within the structure of the Columbia wing. A pictorial of the damage propagation process is provided in Figure 5.3.4-1.

5.3.4.1 Overview of STS-107 Aerothermal Environments

During the STS-107 reentry the total free stream energy of the gas surrounding the Columbia varies from about 12,000 Btu/lb_m-air in the early part of the reentry to about 7,000 Btu/lb_m-air at the time the vehicle was lost. Over this same time frame, pressures acting on the vehicle vary from near vacuum to less than 0.1 atmospheres. The resultant gas temperatures range from 6,000 R to over 10,000 R. A breach into the aeroshell exposes the aluminum structure to air at these pressures and temperatures. A more complete description of the STS-107 aerothermal environments is provided in Section 5.2.3.4.

5.3.4.2 Air/Aluminum Chemistry Analysis

5.3.4.2.1 Approach

The NASA Glenn Research Center's computer program for calculation of complex chemical equilibrium compositions and applications developed by S. Gordon and B. J. McBride was used to determine the chemical reactions that occur when aluminum is exposed to high-temperature air. This program was used to determine if the aluminum-oxygen reaction dominates the process or if aluminum-nitrogen reactions are prevalent enough to require consideration and was used to determine the appropriate heat of reaction to use in the plume energy calculations.

Several iterations of the Gordon-McBride program were run in which aluminum and air were present in stoichiometric proportions (phi=1), in fuel-lean proportions (phi=0.5), and in fuel-rich proportions (phi=2). For each fuel/oxidizer ratio a temperature-pressure problem was run in which the final temperature of the reactants were fixed at various temperatures ranging from 8000 to 520 R and the pressure was varied to represent the stagnation pressure at 8 points during re-entry (1.0, 5.1, 15.2, 35.5, 47.6, 76.0, 88.2, and 131.7 psf). More than 50 species were considered in this system including aluminum, oxygen, atomic oxygen, ozone, nitrogen, atomic nitrogen, aluminum oxide (various forms and states), and aluminum nitride (various forms and states).

Next, for each fuel/oxidizer ratio an enthalpy-pressure problem was run in which the initial temperature was input and the enthalpy was held constant for each of the 8 pressures. This calculation provided the adiabatic flame temperature of the reactants. This calculation was performed to provide a value to compare to the literature value of adiabatic flame temperature and thus provide a "sanity check" for the results.

5.3.4.2.2 Results and Conclusions

The results for the stoichiometric case (phi=1) indicate that the primary product of the reaction is Al_2O_3. Figure 5.3.4-2 presents the mole fractions for the 15.2 psf case. Figure 5.3.4-3 presents the enthalpy (energy) required to maintain the mixture at the specified temperatures. Note that for temperatures above ~5000 R energy is required to be input into the mixture to maintain the state and no aluminum oxide is formed. Below ~5000 R aluminum oxide is formed and energy is released.

These results were also confirmed in the fuel-lean case (phi=0.5). In the fuel-rich case (phi=2), aluminum nitride did appear, but it was observed that the presence of aluminum nitride did not significantly affect the calculated heat of reaction. Therefore, it was agreed by the team to use the heat of reaction of Al_2O_3 (1589 Btu/mole-Al_2O_3 (1676 kJ/mole-Al_2O_3) for subsequent calculations (see Glassman's text).

The calculated adiabatic flame temperatures in all cases compared favorably with the adiabatic flame temperatures provided by Glassman and were observed to be below the dissociation temperature of Al_2O_3 (6840 R (3800 K)). Figure 5.3.4-4 presents the flame temperatures for the stoichiometric case.

5.3.4.2.3 Additional notes

It was agreed by the team that aluminum burns if it is directly subjected to the ingested high-temperature 'plume' gases, but structural elements not directly impinged by the plume or not very near the plume will not necessarily sustain combustion. It is necessary to expose those aluminum structures to extreme heating conditions in order to get them to burn. Therefore, while the burning of aluminum contributes to the development of the breach hole and the propagation of damage inside the wing, it is not tangible for the entire wing structure to develop self-sustained burning simply as a result of that single, localized plume. It is important to realize that there are many conditions in which aluminum structural parts will not support self-sustained combustion. Factors that will hinder self-sustained burning of structural aluminum are as follows:

1) Thermal diffusivity: The thermal diffusivity of aluminum is very high enabling aluminum to rapidly conduct heat away from the burning region.
2) Radiative heat transfer: The energy radiated from a plume of hot air with burning aluminum is being distributed to a very large surface area at significant distances from the plume.
3) Fluid dynamics: The flow velocities of the plume are high. In such cases the molten and vaporized and burning aluminum will be rapidly blown downstream carrying much of the heat away from the high-temperature zone of the hole.
4) Protective oxide coating: In cases where the protective Al_2O_3 layer is not forcibly removed or penetrated, the ignition temperature of aluminum increases from the melting point of aluminum (1679 R (933 K)) to the point where the Al_2O_3 layer is breached. For systems with no mechanical disruption of the layer this is usually associated with the melting point of the oxide (4172 R (2318 K)) (see Werley et al).
5) Experience Base: WSTF has significant experience with the burning of structural aluminum and has many examples where aluminum did not support self-sustained combustion even in pure oxygen environments (see Newton and Stradling). The quenching of self-sustained combustion in these cases was clearly a function of heat transfer away from the burning region of the material.

5.3.4.3 Energy Comparison

Given the conclusion that the formation of aluminum oxide was the dominant reaction that would occur due to the exposure of aluminum structure to the reentry environments, an analysis was conducted to determine the maximum energy released by the reaction and compare that energy to the energy already in the reentry gases entering a breach into the aeroshell. As previously mentioned the heat of formation of aluminum oxide is (1589 Btu/mole-Al_2O_3 (1676 KJ/mole-Al_2O_3). Assuming that the reaction is limited by the available oxygen the energy released can be computed on a per mass of oxygen basis.

$$\left(\frac{1676kJ/mole-Al_2O_3}{48gm-O/mole-Al_2O_3}\right)=\frac{35kJ}{gm-O}\text{ or }14{,}982\frac{Btu}{lb_m-O}$$

326

Using this value and the mass flow of air into a breach hole, the maximum energy flux due to aluminum combustion can be computed and compared to the energy flux associated with the high-temperature air. Of course this assumes that sufficient aluminum is available to react with all available oxygen. If the reaction is aluminum limited, then the energy released is

$$\left(\frac{1676kJ/mole-Al_2O_3}{54gm-Al/mole-Al_2O_3}\right)=\frac{31kJ}{gm-Al}\text{ or }13{,}340\frac{Btu}{lb_m-Al}$$

Assuming a 6-inch diameter hole into the leading edge spar, a quantitative comparison between the air energy flux and the aluminum combustion energy flux limited by the available oxygen is presented as a function time during the STS-107 trajectory in Figure 5.3.4-5. It is readily noted that the energy of the high-temperature air entering the breach hole is much greater than the energy released by the combustion of aluminum. At 600 seconds from entry interface, the reentry gas has a total enthalpy of 10,286 Btu/lb_m and flows into the 6-inch diameter hole at a rate of 0.038 lb_m/sec which results in an energy flux of 389 Btu/sec. Assuming that air is approximately 23% oxygen by mass, the energy flux associated with aluminum combustion is 133 Btu/sec or approximately one-third of the energy in the reentry gas. In order to compute the total energy available to heat wing internal structure due to a breach, the specific quantity of aluminum being heated must be considered since the energy required to raise the aluminum to the temperature at which it will begin to combust must be subtracted from the reentry gas energy.

5.3.4.4 Conclusions

Based upon this study several conclusions can be made. First, the ingestion of high-temperature reentry gases into the Columbia wing can result in the vaporization and subsequent combustion of aluminum with the primary reaction being the formation of aluminum oxide, Al_2O_3. Second, the energy released from this reaction is limited by the available amount of oxygen flowing into the wing. The aluminum combustion energy is approximately one-third of the energy already in the ingested reentry gas for the early portion of the reentry (less than 600 secs. from entry interface). Third, aluminum combustion occurs only for that portion of the wing structure being directly heated by the ingested reentry gases.

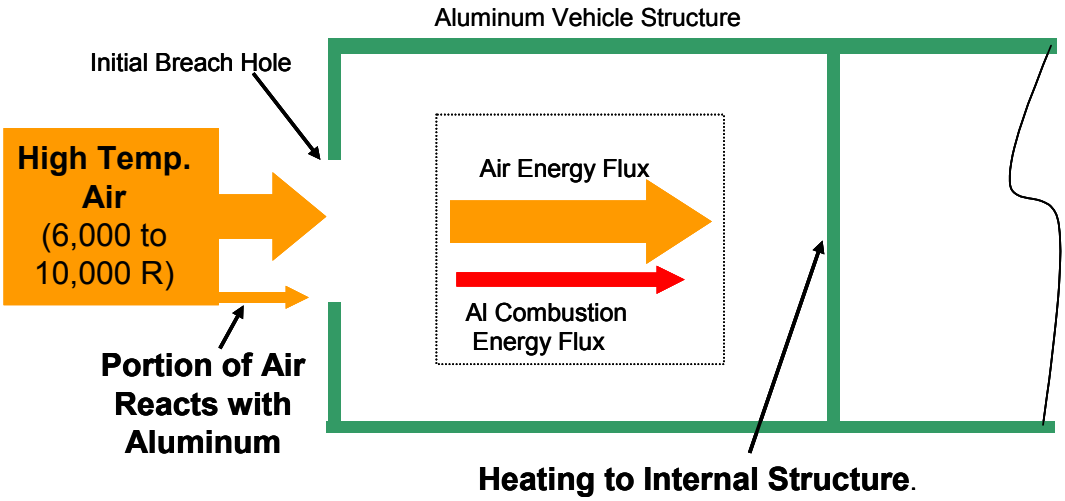

Figure 5.3.4-1 Breach Hole Scenario.

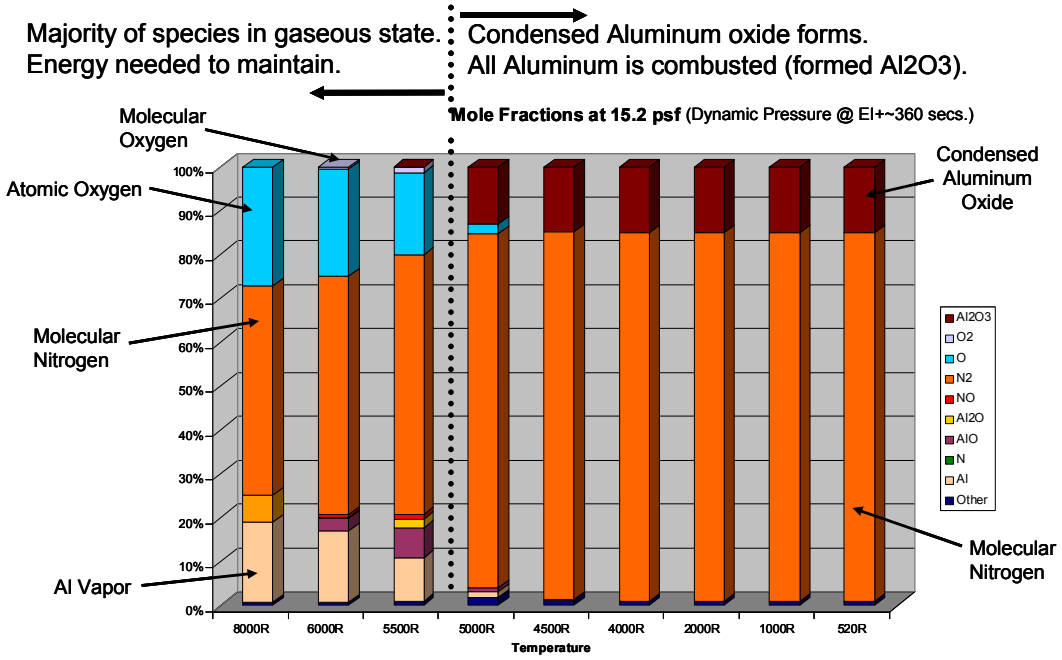

Figure 5.3.4-2 Aluminum/Air Mixture Mole fractions at 15.2 psf for Stoichiometric Conditions.

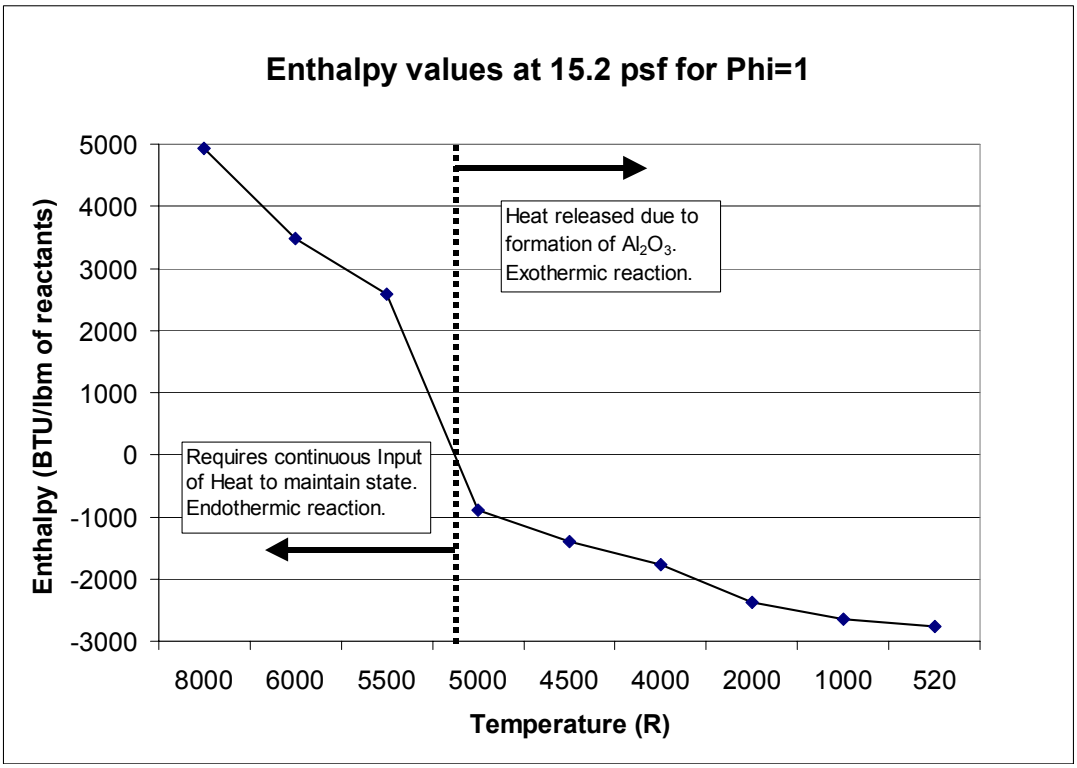

Figure 5.3.4-3 Energy Required to Maintain Air/Aluminum Mixture in Equilibrium State.

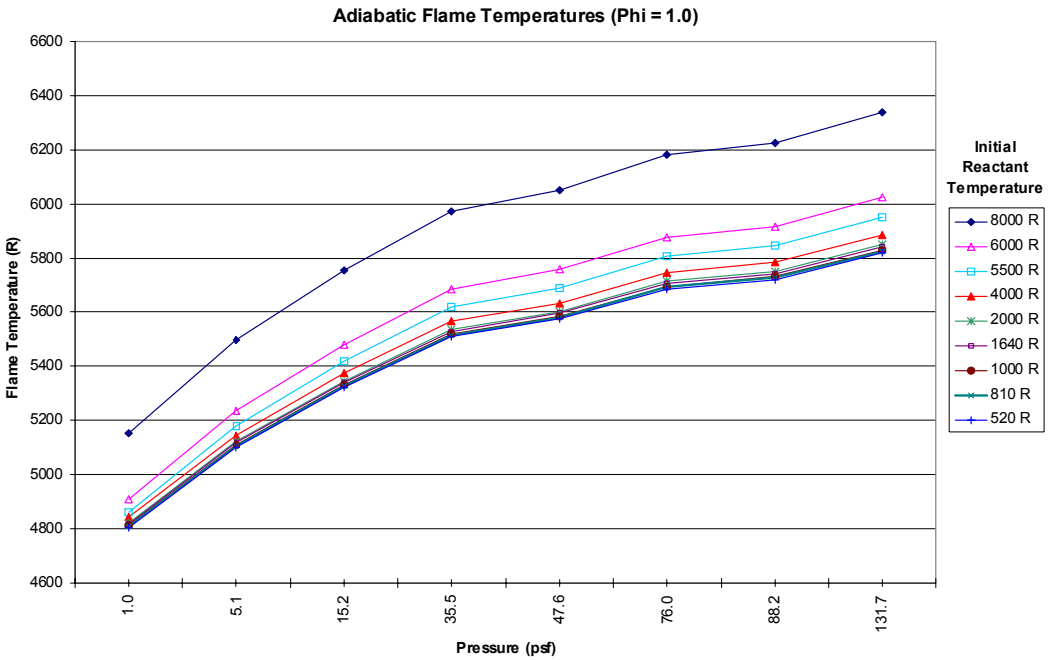

Figure 5.3.4-4 Adiabatic Flame Temperatures of Al Combustion.

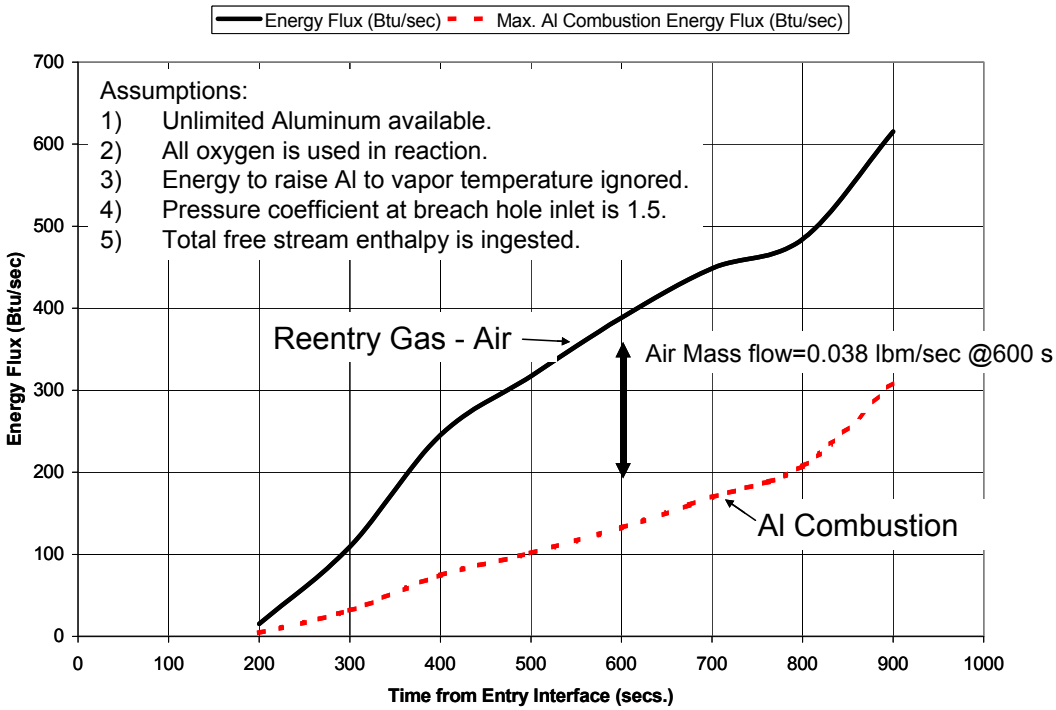

Figure 5.3.4-5 Comparison of Reentry Gas Energy Flux and Al Combustion Energy Flux for 6-inch Diameter Breach Hole in Leading Edge.

5.3.5 Coupled Venting and Thermal Model of Wing

5.3.5.1 Introduction

The objective of this analytical effort was to develop a tool capable of analyzing bulk flow in the STS-107 port wing for various breach scenarios. The intent was to utilize this transient modeling capability to provide pressure and flow rate boundary conditions to steady-state detailed CFD modeling and to screen the case matrix to isolate the more probable scenarios and decrease the number of cases for the more time intensive CFD work.

Originally, the scope was to utilize ideal gas venting codes (both CHCHVENT and FLUINT) and combine this venting model with a thermal representation (SINDA) of the wing for a coupled venting/thermal capability. Once preliminary results were achieved, the scope was increased to include the effect of dissociation and ionization of the ingested air, which was done assuming equilibrium air chemistry properties of the air as a function of air pressure and temperature instead of the ideal gas assumption.

5.3.5.2 Modeling Tools-Capabilities And Limitations

5.3.5.2.1 CHCHVent Program

Program CHCHVENT (see documentation by Fay) models the flow of a mixture of ideal gases with constant specific heats in the continuum flow regime between compartments arbitrarily connected by vents. It is primarily used to model launch vehicle compartment and payload venting environments. The program is based on the conservation equations of mass and energy with heat transfer in the chambers modeled as adiabatic, isothermal, or finite rate with a user-specified heat transfer coefficient.

Flow through the vents is assumed one-dimensional, isentropic, and is determined from the following equations (where subscripts U and D denote properties in the upstream and downstream compartments):

$$\dot{m} = C_d A P_U \sqrt{\frac{\gamma}{R T_U}} \frac{M}{\left[1 + \frac{\gamma - 1}{2} M^2\right]^{\frac{\gamma+1}{2(\gamma-1)}}}$$

where

$$M = \sqrt{\frac{2}{\gamma - 1}\left[\left(\frac{P_U}{P_D}\right)^{(\gamma-1)/\gamma} - 1\right]}$$

where:

$\dot{m} =$ Mass Flowrate

$C_d =$ Discharge Coefficient

$A =$ Flow Area

$P =$ Pressure; U=Upstream; D=Downstream

$M =$ Mach Number

$\gamma =$ Ratio of Specific Heats

$R =$ Gas Constant

T_U = Upstream Temperature

If the Mach number (*M*) is calculated to be greater than one, the program sets the Mach number to one (choked flow). A discharge coefficient (C_d) is used to correct the isentropic mass flow rate predicted from the

above equations. The C_d correction options included in CHCHVENT are: constant value, pressure-ratio dependent, and pressure-ratio-and-cross-flow dependent.

The program explicitly advances in time by numerical integration with the user having choices of 1st order Taylor series, 2nd order Modified Euler, 4th order Runge-Kutta and Runge-Kutta-Merson routines. Local pressure coefficients and local Mach numbers (which are specified as functions of free stream Mach number, vehicle angle of attack, and roll angle) and the trajectory parameters can be specified by the user.

The venting simulation is initialized by specifying pressures and temperatures for all chambers in the model. The total mass and internal energy derivatives with respect to time for a particular chamber are determined by summing the contributions from all vents connected to the chamber. These derivatives are used in the numerical routine to determine the chamber mass and internal energy at the next time, from which the remaining chamber properties are determined:

$$\rho = m / Vol \qquad T = U / mC_v \qquad P = \rho RT$$

where:

$\rho =$ Density
$m =$ Mass
$Vol =$ Compartment Volume
$T =$ Temperature
$U =$ Internal Energy
$C_V =$ Constant Volume Specific Heat
$P =$ Pressure
$R =$ Gas Constant

Using these chamber properties, the above procedure is repeated for the next time step.

5.3.5.2.2 SINDA/FLUINT Program

The Simplified Improved Numerical Differencing Analyzer (SINDA) with Fluid Integrator (FLUINT) is a software package, developed under contract to NASA, for solving lumped parameter network representations of heat transfer and fluid flow problems that are governed by conservation equations. For heat transfer problems, the physical system is partitioned into a Resistance-Capacitance (R-C) network that is analogous to an electrical circuit inasmuch as heat flows between nodes of unequal temperature, current flows between nodes of unequal potential (voltage) in an electrical circuit. Nodes within the thermal network represent discretized portions of the physical system and, in a transient simulation, may store or lose energy much like capacitors in an electrical circuit. Similarly, fluid systems are discretized into lumps and connectors where pressure differences between lumps and the resistance of the connectors determine both the magnitude and direction of the flow. The thermal and fluid networks may be seamlessly integrated through convective ties between fluid lumps and thermal nodes. The coupled thermal/fluid network is solved simultaneously by SINDA/FLUINT, thereby increasing stability and temporal accuracy.

Specifying the mass (or capacitance) of the thermal nodes and/or the volume of the fluid lumps permits transient as well as steady state simulations. A semi-implicit 2nd order forward-backward differencing scheme is used to advance the solution in time. The time-step is dynamically determined by the program to ensure stability with a user defined output interval available to provide results. The transient thermal network is solved such that the energy flows between nodes as well as the energy gained or lost by each node balance over the time-step. The transient flow network is solved such that conservation of mass and energy are maintained at each lump while momentum is conserved within each connector. FLUINT can handle compressible and incompressible flows up to the sonic limit (supersonic flows may be computed in special cases) and choked flows are automatically identified and computed by the program.

Connector-device models exist within FLUINT to allow the user to model a wide variety of flows. The orifice device is used almost exclusively in subsequent SINDA/FLUINT based analyses to describe the connectivity between flow compartments in the orbiter wing and associated volumes in the payload bay or fuselage. The orifice device is pictured below with the important input/output parameters noted. The subscripts U, D, and TH denote the upstream, downstream, and throat conditions, respectively. FLUINT automatically determines the direction of flow and the upstream and downstream conditions are derived from the fluid lumps between which the orifice device is connected. The throat conditions are only used in choking calculations and are determined by assuming an isentropic expansion from the upstream conditions. AORI is the actual physical area of the orifice and ATH is the effective area determined from AORI and a user specified discharge coefficient, CDIS. AF is the upstream area (generally intended for pipe flow) and is set to ten times the actual orifice area for the large freely vented volumes of the orbiter wing.

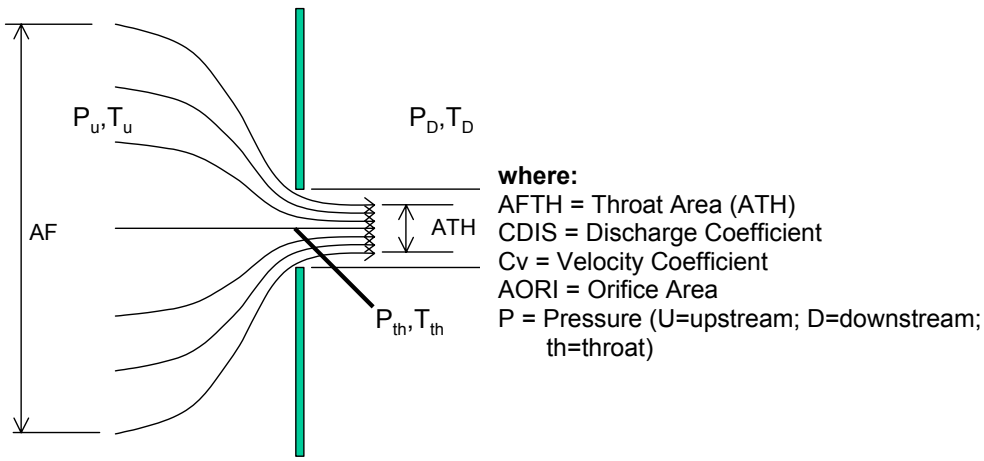

$$AFTH = \frac{CDIS}{C_V} AORI$$

$$C_V = .98$$

The internal algorithm for determining whether the flow-rate through the orifice device is choked is illustrated below. First, isentropic expansion from the upstream conditions and a velocity equal to the speed of sound at the throat are used to determine the critical (choked) flow-rate through the orifice. Next, the actual flow-rate through the orifice is determined from the pressure difference, average density, and a K-factor based upon the geometry of the orifice. Finally, comparing the actual flow-rate to the critical flow-rate yields the correct flow-rate.

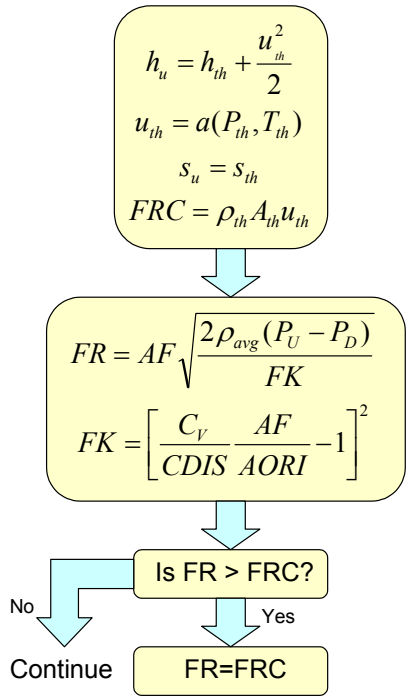

where:
h = enthalpy
u = internal energy
a = speed of sound
s = entropy
FRC = Critical Flowrate (for choking)
AF = Flow Area
FK = loss coefficient
FR = mass flowrate

5.3.5.3 Modeling Assumptions

5.3.5.3.1 Trajectory
The analysis is based on the STS-107 End of Mission 3 (EOM3) trajectory, where time zero corresponds to Orbiter Entry Interface (EI). The pertinent quantities used in the analysis are plotted in Figure 5.3.5-1 and Figure 5.3.5-2.

5.3.5.3.2 Discharge Coefficients
Two orifice discharge coefficient (C_d) corrections were used in the analysis. One is a pressure-ratio dependent C_d for a sharp-edged circular orifice from Shapiro, where C_d is a function only of the pressure ratio across the orifice. The second correction is a pressure-ratio-and-cross-flow dependent C_d for a circular orifice that is from CHCHVENT, which is based on experimental data documented by Haukohl and Forkois. The C_d in this correction is a function of both the pressure ratio across the orifice and the local external Mach number flowing past the orifice. Shapiro's correction is incorporated as a 5th order polynomial curve fit and is depicted in Figure 5.3.5-3. The pressure-ratio-and-cross-flow correction is incorporated as a bi-variant lookup and is depicted in Figure 5.3.5-4. For the high aspect ratio leading edge vents (carrier panel and T-seals), the Haukohl and Forkois data were consulted. Since the leading edge vents are choked for all the cases, the empirical data showed a less than 5% difference compared to the sharp-edged circular orifice correlations, so the circular orifice correlations were used in lieu of computing the family of curves needed to generically account for high aspect ratio vents.

5.3.5.3.3 Local Pressure Coefficients
The local pressure of the flow just outside a vent, leak, or possible penetration is crucial to the venting analysis because it is frequently very different from the freestream pressure. Local pressure coefficients (C_p) computed from LAURA CFD analyses were used as inputs to the venting programs for determining the local external surface pressures. These CFD solutions were completed by Langley Research Center for STS-2, and two solutions (Mach=18.1, angle of attack=41.2 degrees and Mach=24.3, angle of attack=39.4 degrees) were made available by Gnoffo.

In CHCHVENT, the C_p value at a particular location is determined by linearly interpolating between the C_p values for the two Mach numbers, 18.1 and 24.3. Since these C_p values were similar and in an effort to

expedite the process of adding this capability to FLUINT, the C_p values for the two Mach numbers were averaged in the FLUINT models. Also, since the vehicle angle of attack in the EOM3 trajectory is approximately 40 degrees from EI through EI+1000 seconds, the C_p values were considered virtually constant over this range. To validate this assumption, the CHCHVENT model was run with both linearly varying and constant averaged C_p values with negligible change in the results. Contour plots for the windward and leeward sides of the vehicle for the Mach=18.1 solution are depicted in Figure 5.3.5-5 and Figure 5.3.5-6, respectively.

5.3.5.3.4 Breach Boundary Conditions

The derivation for the local boundary conditions for a large breach is based upon the assumption that either all or a sizable fraction of the free stream total enthalpy is ingested at the breach or penetration. The flow through the large breach is modeled by the orifice device (within SINDA/FLUINT) and conditions at the upstream lump (or plenum) are updated each time-step based upon the assumed trajectory.

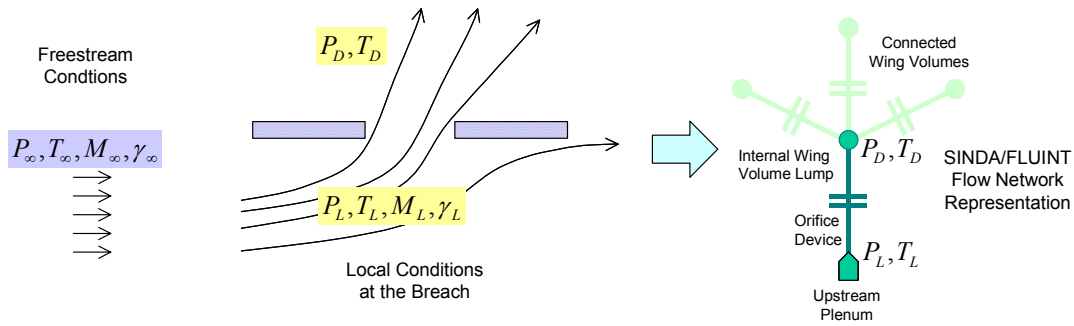

To determine the local conditions for the upstream boundary, the local enthalpy is scaled to the free-stream enthalpy (or taken from the engineering analysis described in Sec. 5.3.2.1) and the local pressure is derived from the free-stream pressure through an externally supplied pressure coefficient. Iteration within the equilibrium air property tables is required to determine the local conditions as a function of enthalpy and pressure for a real gas while a closed form solution exists for a perfect gas. An alternate model was created to more accurately model the period after the internal spar breach, where the local pressure from the jet impinging on the spar is assumed to equal the local external pressure. Also, the bulk enthalpy ingested through the leading edge hole was assumed to be ingested through the spar breach (consistent with jet flow through the breach).

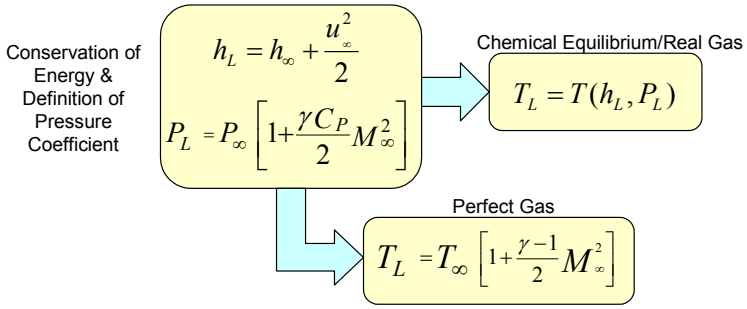

The derivation for the local boundary conditions for a small breach or vent is based upon the assumption that the flow into the small breach or vent is greatly influenced by the surrounding structure which necessitates the use of the local Mach number and the static conditions at the breach.

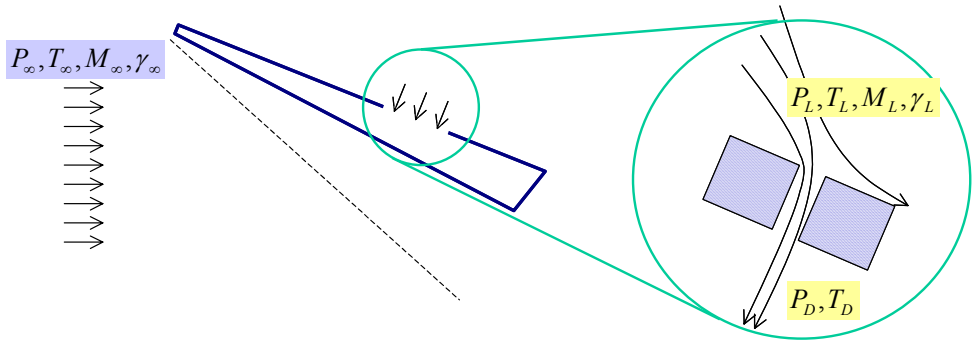

As in the case of the large breach, the local pressure is derived from the free-stream pressure via an externally provided pressure coefficient. The remaining state condition is determined by assuming constant entropy between the free-stream conditions and those locally at the breach or vent. This is not strictly correct if shock waves are present in the flow, but engineering judgement dictates that for wing locations away from the leading edge, the entropy increase through the shock will be largely offset by an entropy decrease due to the non-adiabatic nature of the flow over the wing. Determining the actual energy lost by the non-adiabatic flow to the wing structure is problematic for non-CFD based venting analyses and, for locations away from the leading edge of the wing (such as the windward elevon seals), it is anticipated that only a very small fraction of the free-stream enthalpy would be ingested. As before, a closed form solution exists for an ideal gas while a real gas demands use of the property tables.

Conservation of Energy

$$h_L + \frac{u_L^2}{2} = h_\infty + \frac{u_\infty^2}{2}$$

Definition of Pressure Coefficient

$$P_L = P_\infty \left[1 + \frac{\gamma C_P}{2} M_\infty^2\right]$$

Isentropic

$$s_L = s_\infty$$

Chemical Equilibrium/Real Gas

$$T_L, \rho_L = f(s_\infty, P_L) \Rightarrow h_L = f(P_L, T_L)$$

$$M_L = \frac{\sqrt{2(h_\infty - h_L) + u_\infty^2}}{a(P_L, T_L)}$$

Perfect Gas

$$T_L = T_\infty \frac{\left[1 + \frac{\gamma - 1}{2} M_\infty^2\right]}{\left[1 + \frac{\gamma - 1}{2} M_L^2\right]}, M_L = \sqrt{\frac{2}{\gamma - 1}\left[\frac{\left[1 + \frac{\gamma - 1}{2} M_\infty^2\right]}{\frac{P_L}{P_\infty}^{\frac{\gamma - 1}{\gamma}}} - 1\right]}$$

5.3.5.4 Vent-Only Model Development

5.3.5.4.1 Development/Description

The venting model was developed primarily from Rockwell International's 1994 "Orbiter Entry Venting Substantiation Report" by Wong, and a report documenting an integrated venting model for OV-102, Flight 27, STS-109 by Cline. The models used in the Substantiation Report were based on one-half of the Orbiter; whereas, the geometry was extended to include the complete vehicle to account for the non-symmetric nature of a possible breach in the left wing. The venting model was later modified based on results of a structural leakage test done for this investigation (Cline and Torres), suggested modifications from the JSC Aerothermal Internal Flow team, and estimated leading edge vent areas from Computer Aided Design (CAD) drawings. A graphical representation of the venting model is depicted in Figure 5.3.5-7.

<u>Comparison Of CHCHVENT And FLUINT (Adiabatic/Ideal Gas)</u>

FLUINT did not initially have the capability to calculate local external pressures from pressure coefficients or contain the discharge coefficient models included in CHCHVENT; therefore, these capabilities were added to FLUINT and comparisons between CHCHVENT and FLUINT were made for validation purposes. A typical plot from the comparisons is shown is Figure 5.3.5-8, where the predicted net rate of change of mass in the

left main gear wheel well assuming a 20 in^2 breach into the left wing front glove compartment (section between bulkheads 807 and 1040) is shown. This comparison was made assuming the air as an ideal gas with constant specific heats in both CHCHVENT and FLUINT. In addition, the boundary-condition temperatures used in the comparison cases only were calculated from isentropic equations. For the breach, the local ingested gas temperature was assumed to be the free-stream stagnation temperature and calculated from:

$$\frac{T_{local}}{T_{freestream}} = \left[1 + \frac{\gamma - 1}{2} M^2_{freestream}\right] \text{ (Ideal Gas Case Only – Not used in Final Results)}$$

For all other locations where gas could be ingested (i.e. lower elevon seals, wheel doors, etc.) the following equation was used for the ingested gas temperature:

$$\frac{T_{local}}{T_{freestream}} = \frac{\left[1 + \frac{\gamma - 1}{2} M^2_{freestream}\right]}{\left[1 + \frac{\gamma - 1}{2} M^2_{local}\right]} \text{ (Ideal Gas Case Only – Not used in Final Results)}$$

5.3.5.5 Chemical Equilibrium Air Properties

SINDA/FLUINT Property (FPROP) tables were generated using FORTRAN 90 property routines for chemical equilibrium air obtained from the NASA Langley Research Center (LaRC). Six property tables (all as a function of pressure and temperature) were generated from the property routines: specific volume, enthalpy, speed of sound, entropy, absolute viscosity, and thermal conductivity. Entropy was obtained by numerically integrating the enthalpy tables at constant pressure.

SINDA/FLUINT requires entropy as a function of pressure and temperature for choking calculations in real gas simulations. Entropy tables were generated from the LaRC routines by numerically integrating the relevant *Tds* equation along lines of constant pressure:

$$Tds = dh - vdP$$

$$\int_1^2 ds = \int_1^2 \frac{dh}{T} - \int_1^2 \frac{v}{T} dP$$

$$P = const$$

$$s_2 = \frac{T_1 + T_2}{2T_1T_2}\left[h_2 - h_1\right] + s_1$$

An arbitrary reference entropy of 10,000 J/kg-K (2.39 Btu/lb$_m$-R) was chosen for the pressure equal to 0.001 Pa (9.9e-09 atms) and temperature equal to 200 K (360 R). Initial conditions for the integration were based upon ideal gas estimates of the entropy at 200 K and for a pressure range of 0.002 Pa (1.97e-08 atms) through 101325 Pa (1 atm). The trapezoidal integration was performed row-by-row with each succeeding entropy numerically integrated from the previous row's entropy at the same pressure. The real gas properties of air are markedly different from those of a perfect gas as evidenced by the entropy versus temperature plot shown in Figure 5.3.5-9. The almost cyclical changes in entropy with increasing temperature indicate a pattern of dissociation/ionization as new species are continually formed.

Also to aid choking calculations, a frozen speed of sound was computed from the specific heat ratio and an effective gas constant (R_{EFF}=P/ρT). SINDA/FLUINT utilizes internal routines to provide fluid properties either by direct interpolation or by iteration if not requested as a function of pressure and temperature (i.e. T=T[s,P]).

Several of the interpolation/integration routines were rewritten to remove any dependency on ideal gas assumptions and/or to remove the additional logic present for two-phase fluids.
The property tables were generated over a range of 200 K (360 R) to 9100 K (16,380 R) and from 0.001 Pa (9.9e-09 atms) to 101325 Pa (1 atm). At very low density (due to extreme temperature or low pressure), the LaRC property routines issued cautions. Some thermal conductivity and viscosity data were discarded and replaced with data obtained from the routines at a higher pressure (this is assumed reasonable given the range of pressure profiles expected in this analysis).

5.3.5.6 Thermal Model Development

Thermal representation of the main structure comprising the port wing was developed in order to determine the thermal coupling effects of the structure on the venting model. The model was developed in SINDA/FLUINT format with geometric modeling being performed in Thermal Desktop. The stand-alone thermal model was initially set up utilizing STS-5 re-entry environments (Hartung and Throckmorton) and compared to results from the Dryden Flight Research Center's STS-5 analyses (Gong et al). The model was then modified to STS-107 environments and convectively coupled to the vent models.

Configuration details for the SINDA/FLUINT thermal math model of STS-107 Columbia's left wing were obtained from several sources (Figure 5.3.5-10), Computer Aided Design (CAD) models developed by the STS-107 Accident Investigation Structures Team, Shuttle Drawing System (SDS) – Boeing North America (BNA), Shuttle Operational Data Book on the NASA Human Space Flight website, Space Shuttle Entry Heating Data Book, Volume III – STS-5 (Hartung and Throckmorton), and Dryden Flight Research Center's Space Shuttle SPAR wing model (Gong et al).

5.3.5.6.1 Thermal Model Description

The three-dimensional thermal model consists of six internal wing volumes (sections 1-6) and four wing leading edge volumes (sections 7-10) corresponding to the venting models. Details of the thermal model are shown in Figure 5.3.5-11 and outlined below.

- Wing internal geometry based on CAD model – model includes the wing spars but the struts are omitted.
- Landing gear/wheel assembly derived from CAD model and specifications.
- Spar, fuselage and wheel well closeout panels assumed to be 0.1 inch thick Al-2219.
- Skin Al and Al-honeycomb panel representations are included. Al-honeycomb core is thermally modeled based on X-33 leeward aeroshell skin.
- Leeward honeycomb is 1.15 inches thick including inboard and outboard face-sheets of 0.025 and 0.045 inches, respectively.
- Windward honeycomb is 0.75 inches thick. The face-sheets are the same thickness as the leeward side. Remaining wing skin was assumed to be 0.1 inch thick Al-2219.
- TPS is represented on both windward and leeward sides. Leeward TPS was assumed to be 0.16 inches of FRSI throughout. (LRSI tiles were not modeled). Windward TPS assumed to be HRSI. Thicknesses averaged for each wing section based on the Dryden model data (Gong et al).
- SIP and RTV layers are included.
- Internal radiation is included (Optical properties from Dryden model or estimated from material.)
- Leading edge geometry based on vent volumes in venting models and the spar geometry from the CAD model.
- STS-107 wing leading edge, windward and leeward heat rates for STS-107 End of Mission (EOM) 3 trajectory were supplied by Boeing-Houston.
- Material properties taken from (in order of preference) NASA RP-1193 or TPSX database (NASA ARC).
- Time dependent pressure arrays (required to interpolate pressure and temperature dependent property arrays) estimated from STS-107 EOM3 trajectory profiles, STS-2 LAURA windward and leeward C_p profiles.

5.3.5.6.2 Fluid/Structure Coupling

The lumps representing the air in each of the compartment volumes in the vent models were tied convectively to the internal wing structural nodes in the thermal model. Convection coefficients for each tie were derived from laminar flow, flat plate Nusselt Number correlations (Incropera & Dewitt) utilizing the total flow entering each compartment, the cross-sectional area at the centroid of each volume (roughly normal to the perceived main flow direction), the path length through the centroid (along the perceived main flow direction) and the fluid properties (evaluated at the average of the wall and lump temperatures). The thermal model was later modified to include convective coupling between the leakage into the wheel-well area through the MLG door seal and the door structure. Also, convective coefficients for compartment 3 were later derived from FLUENT CFD modeling of this flow (Sec. 5.3.6.3). A correction factor was derived between the flat-plate Nusselt relation and the CFD at time point 404-sec after entry interface and used for correcting the Nusselt relation for the remainder of the transient simulation.

5.3.5.7 Thermal/Venting Results

The results in this section were generated over several weeks as the modeling assumptions were evolving. The following matrix summarizes the cases for which results are presented in this report with the major assumptions at the time of that modeling effort. Many additional cases were generated, but are not included for brevity, but are available upon request.

Case #	Assumptions	Purpose
1	10”, 6” and 4” diameter RCC Breach hole with Cp=1.46 6” diameter internal Spar Breach hole at 490-sec after EI Ingested Enthalpy = 76% of freestream (based on Gnoffo CFD at 404-s) Local Pressure at Spar Breach calculated based on bulk compartment 8 pressure response. Flat Plate empirical Nusselt correlation for internal heat transfer	Assess leading edge pressure history for CFD boundary conditions and internal wing temperature response
2	10” diameter RCC Breach hole with Cp=1.46 10” diameter internal Spar Breach hole at 487-sec after EI Ingested Enthalpy based on Sec. 5.3.2 calculations. No heat transfer to leading edge structure – all ingested into spar breach. Local Pressure at Spar Breach assumed equal to external pressure (Cp=1.46). Flat plate empirical Nusselt correlation for internal heat transfer except for compartment 3, which uses FLUENT CFD heat transfer coefficient factor from Sec. 5.3.7.	Assess leading edge pressure history for CFD boundary conditions and internal wing temperature response
3	10” & 6” diameter RCC Breach Hole Cases with Cp=1.46 Ingested Enthalpy based on Sec. 5.3.2 calculations No internal Spar Breach	Provide pressure differential across leading edge spar for structural loads failure analyses.

5.3.5.7.1 Leading Edge Pressure Profiles

<u>Case 1</u>

The leading edge compartment pressures were of general use to providing CFD boundary conditions for various breach analyses. The Case 1 results are shown in Figure 5.3.5-12 for the three breach hole diameters. Prior to the EI+490-sec internal spar breach, the pressures represent the balance of flow coming in via the breach and the outflow from the T-seal and Carrier Panel vents of the leading edge. The pressure drop after the spar breach is due to flow into the low pressure compartment 3 volume.

<u>Case 2</u>

For Case 2, the leading edge was not modeled, but rather the spar breach local pressure was set equal to the external RCC pressure (assumed equal to jet impingement pressure). This approach results in a much higher local pressure to the spar breach as shown in Figure 5.3.5-13.

Case 3
The intent of Case 3 was to provide bulk pressure differentials across the leading edge spar, so the jet impingement local pressure to the spar was not appropriate. Therefore, this case models the leading edge bulk compartments (same as Case 1 except no internal spar breach). The pressure differentials for a 6" diameter and 10" diameter RCC hole are shown in Figure 5.3.5-14.

5.3.5.7.2 Internal Volume Pressure Profiles
The internal wing pressures are largely uninfluenced by the leading edge breach since there is only a very small nominal leak around the leading edge spar, but these pressures are dramatically increased by the subsequent internal spar breach at 487-seconds as shown in Figure 5.3.5-15 for both Case 1 and 2. The Case 2 post-spar breach pressures are much higher due to the larger local pressure and the 10" diameter spar breach instead of the 6" diameter breach in Case 1. The bulk of the wing is freely vented, but the forward wing-glove and wheel well compartments are slightly lower due to the large venting through the Payload Bay vent in the wing-glove as illustrated by the close-up of the Case 2 pressures in Figure 5.3.5-16.

5.3.5.7.3 Leading Edge Air Temperature Profiles

Case 1
The leading edge compartment temperatures are shown in Figure 5.3.5-17 for Case 1. Compartment 8 is the hottest due to the breach inflow and the other compartments are lower in temperature due primarily to the energy lost to structure (i.e., the RCC and leading edge spar insulation) and outflow from the leeside vents.

Case 2
As previously stated, Case 2 does not include the full representation of the leading edge, but rather just Compartment 8 treated as a plenum of local conditions for the spar breach. The air temperature for this plenum is illustrated in Figure 5.3.5-18. This is much higher than Case 1, which included the loss of energy to structure, where Case 2 assumes the jet energy carries through the internal spar breach. Therefore, the compartment 8 temperature represents the assumed bulk temperature of the flow entering the wing through the spar.

5.3.5.7.4 Internal Wing Air Temperature Profiles

Case 1
The internal wing compartment air temperatures are shown in Figure 5.3.5-19 for Case 1. The temperatures remain low until the leading edge spar breach at 490-seconds. Compartment 3 has the highest values since this is the compartment that the spar breach flows into directly. Temperatures in the other compartments are lower due to loss of energy to the wing structure. Compartment 1 has the next highest temperatures which is consistent with the mass flow and spar structural temperature results presented later.

Case 2
The internal wing compartment air temperatures for Case 2 are shown in Figure 5.3.5-20. These values are much higher than those for Case 1 due to the larger breach hole and much higher ingested enthalpy. The wheel well (Compartment 2) shows an elevation in temperature prior to the spar breach. This is due to an inflow from the payload bay, which is also at elevated temperature. This is an artificial effect since the standard leaks causing the elevated payload bay temperature would in reality lose energy to structure through those leaks, which the vent-only modeling does not capture. This effect is not a factor after the spar breach because the wheel well pressurizes with respect to the payload bay shortly thereafter.

5.3.5.7.5 Leading Edge Mass Flow Rate and Energy Rate In/Out
The leading edge RCC breach mass flow rate history is plotted in Figure 5.3.5-21 for Case 1. The Case 1 carrier panel and T-seal vent mass outflow is shown in Figure 5.3.5-22. The corresponding energy flux into the breach and out of the vents as well as heat transfer to the RCC and Cerachrome insulation is shown in

Figure 5.3.5-23. The mass flow through the spar breach for both Case 1 and 2 is compared in Figure 5.3.5-24 and the corresponding energy inflow is shown in Figure 5.3.5-25. The Case 2 mass and energy inflow are much higher due to the larger 10" hole instead of the 6" diameter and since energy is not transferred to structure before flowing through the spar breach in Case 1 as was shown in Figure 5.3.5-23.

5.3.5.7.6 Internal Wing Mass Flow Rate and Energy Rate In/Out

The forward and aft Compartment 3 vents (at Xo=1040 and Xo=1191) and wheel well forward Xo=1040 vent mass flow rates are plotted in Figure 5.3.5-26. The corresponding energy rates are shown in Figure 5.3.5-27.

The wheel well is of particular interest based on the flight data. The energy rates in/out from various vents/leaks for Case 1 is shown in Figure 5.3.5-28 and for Case 2 in Figure 5.3.5-29. Note the addition of energy into the wheel well prior to spar breach from the main landing gear door juncture leakage for Case 1. This energy is significant for Case 1 but not for Case 2 due to the much higher energy flux entering the wing for Case 2. Also, Case 2 reveals a brief inflow through the forward vent after the breach, but then the flow begins to outflow almost immediately. This transient is most likely due to the rapid pressurization of the wheel well from Compartment 1.

5.3.5.7.7 Leading Edge and Internal Wing Mach Number Histories

The RCC breach hole, the leading edge vents and the internal spar breach hole are almost immediately choked for all cases, so the plots of Mach Number are not presented. The Case 1 vent Mach Numbers for the Xo=1040, Xo=1191 and wheel well forward vents are plotted in Figure 5.3.5-30. The Case 2 results are shown in Figure 5.3.5-31.

5.3.5.7.8 Internal Wing Heat Transfer Coefficient Histories

Case 1 and 2

The heat transfer coefficients in Compartment 3 for Cases 1 and 2 are shown in Figure 5.3.5-32 and Figure 5.3.5-33, respectively. Case 2 includes the FLUENT CFD-based correction factors on these values. The wheel well (Compartment 2) Case 1 and 2 heat transfer coefficients are plotted in Figure 5.3.5-34 and Figure 5.3.5-35. The Case 2 values are higher primarily due to higher velocity flow rates.

Solid Wall Temperature Histories for the Leading Edge

The leading edge spar is insulated with Cerachrome that has a thin outer layer of Inconel. The Inconel temperature for Case 1 is plotted in Figure 5.3.5-36. Local heating effects caused by the leading-edge breach jet impinging on the insulation are not modeled and therefore the resultant temperatures for Compartment 8 are lower than what would be expected. However, for compartments away from the breach (7, 9, and 10) the predicted Inconel temperatures are considered realistic and indicate that the insulation would remain intact. The spar behind this insulation is plotted in Figure 5.3.5-37 and shows that the insulation performs very well.

Solid Wall Temperature Histories for Internal to the Wing

The Compartment 3 wall skin temperatures are shown in Figure 5.3.5-38 and Figure 5.3.5-39 for Cases 1 and 2, respectively. The wheel well wall temperatures are plotted in Figure 5.3.5-40 and Figure 5.3.5-41 for Cases 1 and 2, respectively. Case 2 temperatures are dramatically higher due to the larger hole in the spar, and the much higher ingested enthalpy. Note that the Case 2 temperatures exceed the aluminum melting point for many of the areas, which is known not to be the case from the telemetry data. This indicates that the Case 2 includes too much energy flowing into the wing (as compared to actual) due to either too large a size of the breach holes or the ingested enthalpy with local pressure assumptions being too high. The actual results are somewhere between the Case 1 and Case 2 predictions.

The spar temperatures for the remaining wing compartments are compared to Compartment 3 in Figure 5.3.5-42. The results indicate that heat is removed from the flow as it passes through the wing and that Compartment 1 structural temperatures are the next highest compared to Compartment 3. This trend is consistent with the higher flow rates through the 1140 vent into Compartment 1.

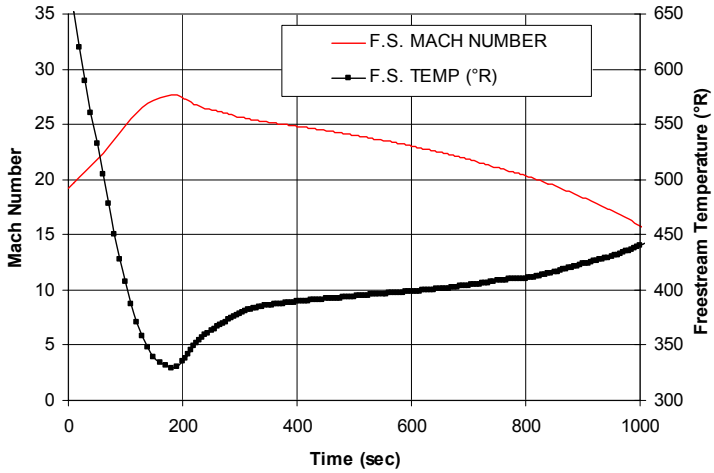

Figure 5.3.5-1 EOM3 Trajectory – Free-stream Mach Number and Temperature History.

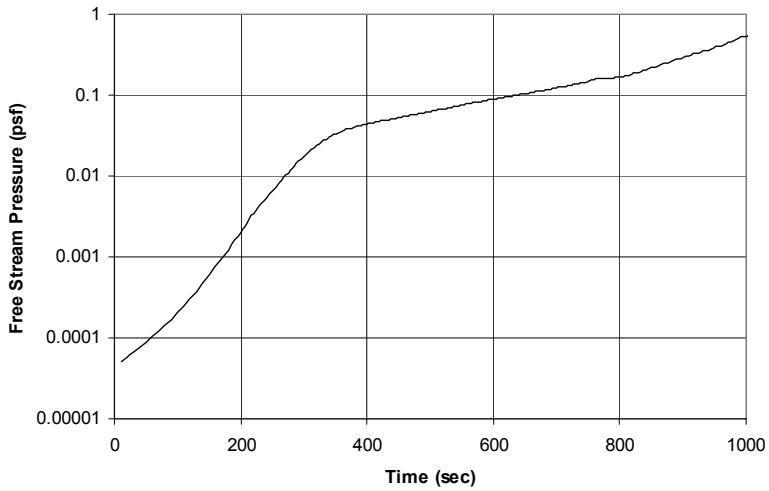

Figure 5.3.5-2 EOM3 Trajectory – Free-stream Pressure History.

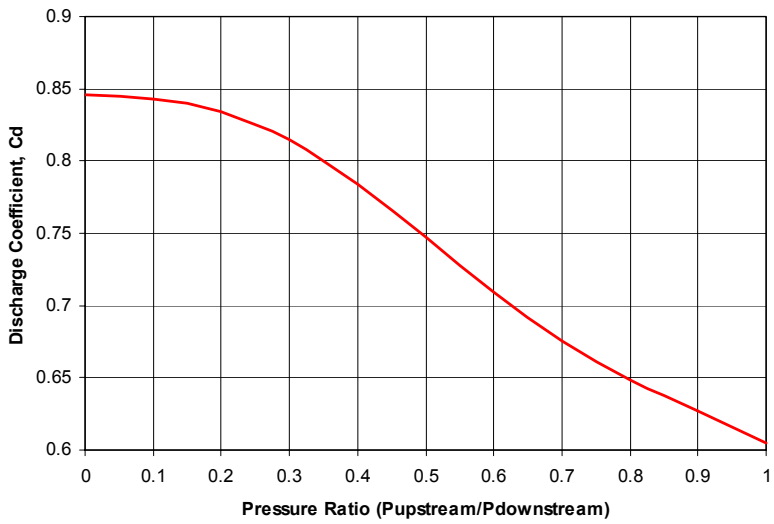

Figure 5.3.5-3 Pressure-Ratio Dependent Sharp Edge Orifice Discharge Coefficient .

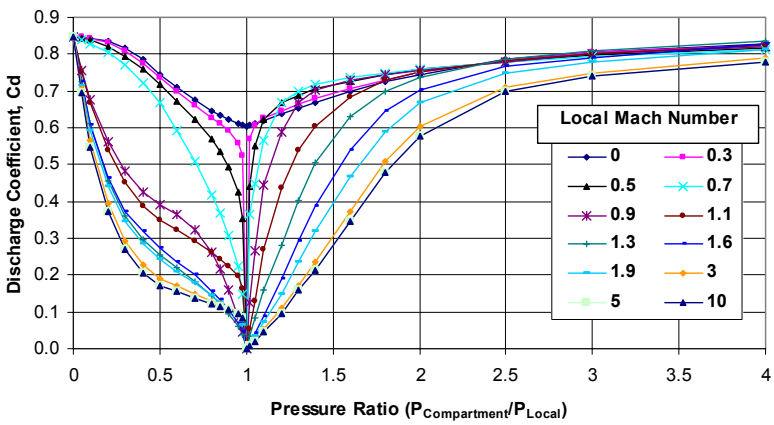

Figure 5.3.5-4 Pressure-Ratio-and-Cross-Flow Dependent Discharge Coefficient.

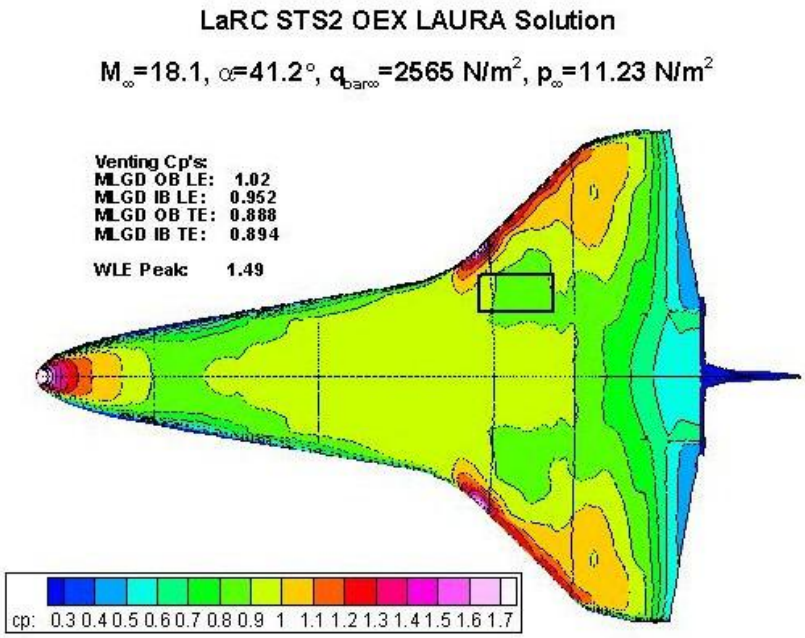

Figure 5.3.5-5 Windward LAURA Solution (STS-2, Mach 18) Surface Pressure Coefficient Contours.

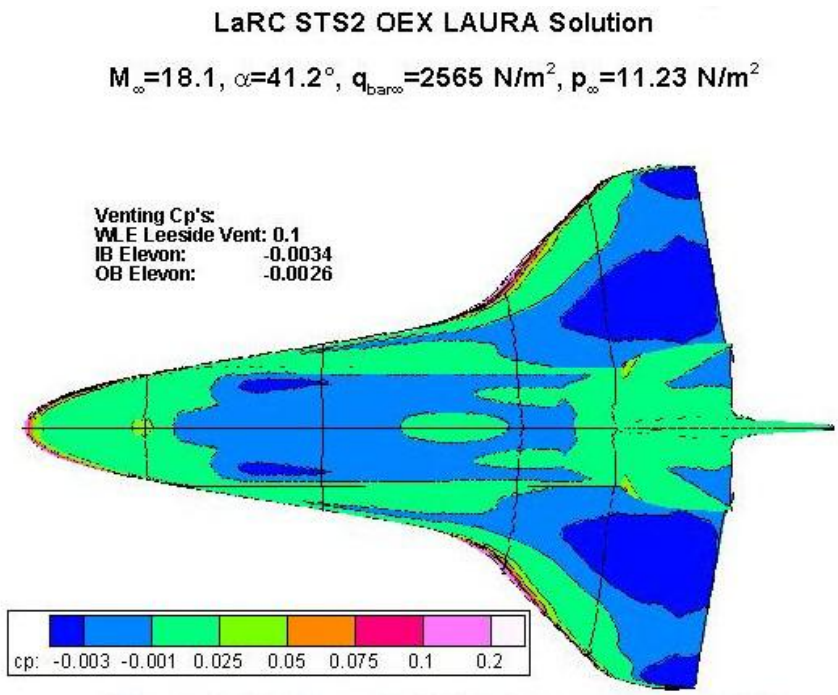

Figure 5.3.5-6Leeward LAURA Solution (STS-2, Mach 18) Surface Pressure Coefficient Contours.

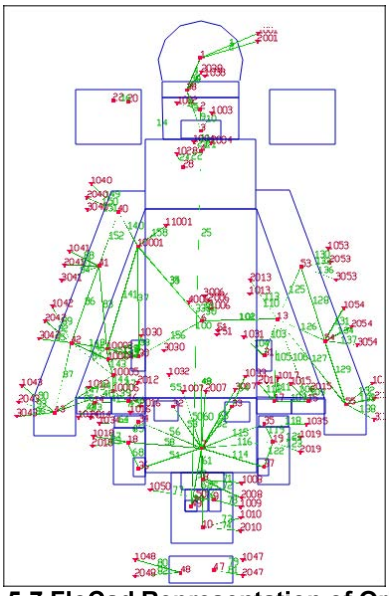

Figure 5.3.5-7 FloCad Representation of Orbiter Venting Model.

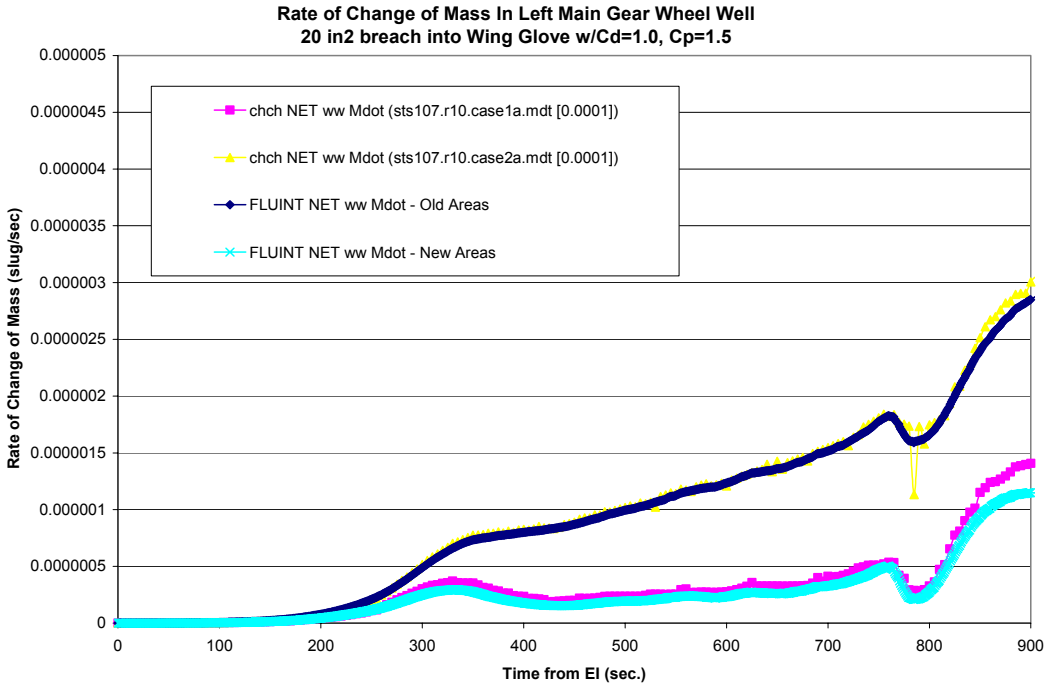

Figure 5.3.5-8 CHCHVENT and FLUINT Venting Comparison.

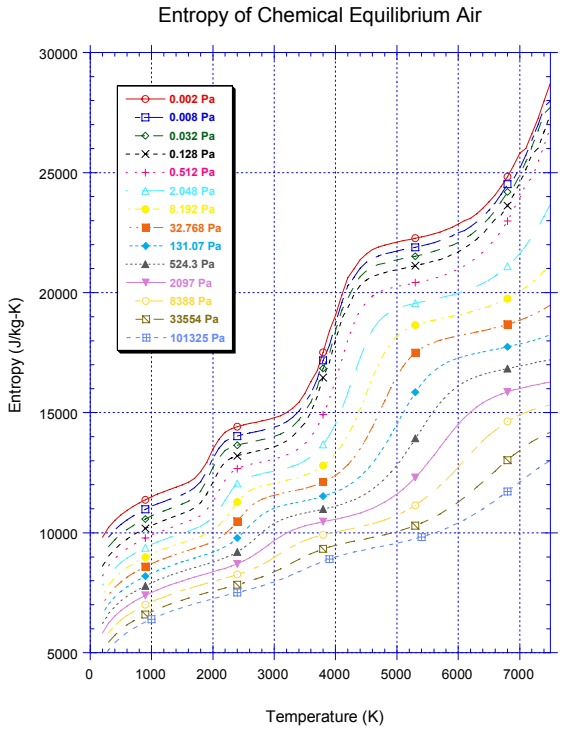

Figure 5.3.5-9 Equilibrium Air Entropy Variation with Temperature.

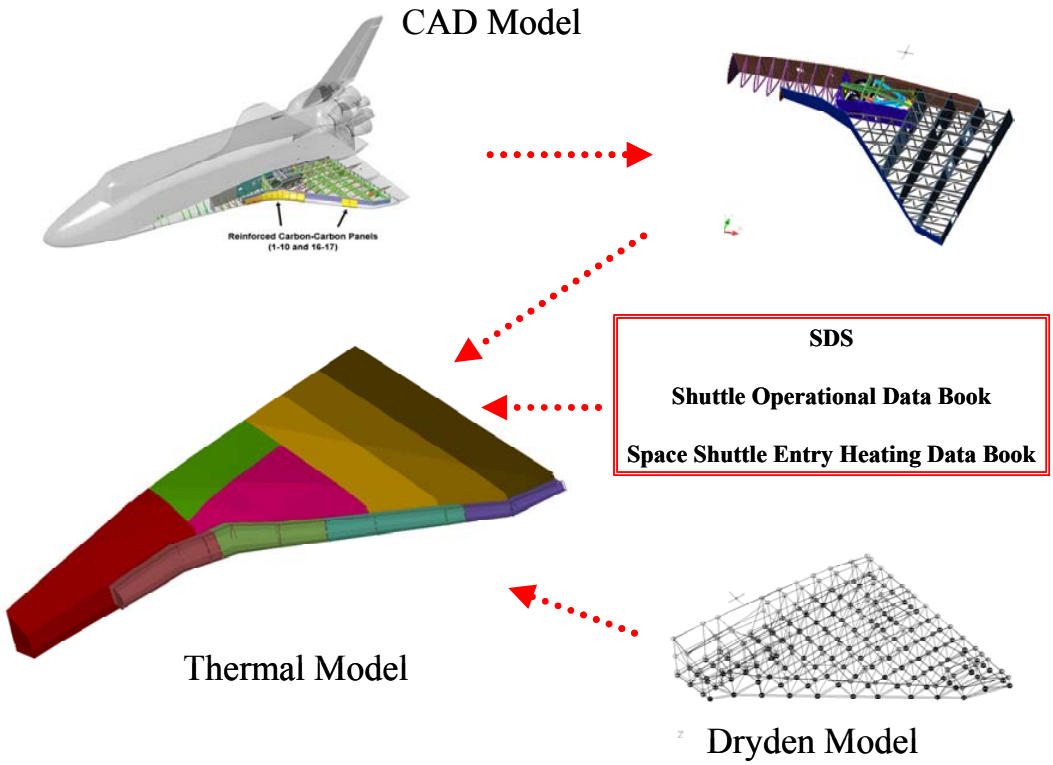

Figure 5.3.5-10 Orbiter Thermal Model Development Heritage.

RCC Leading Edge

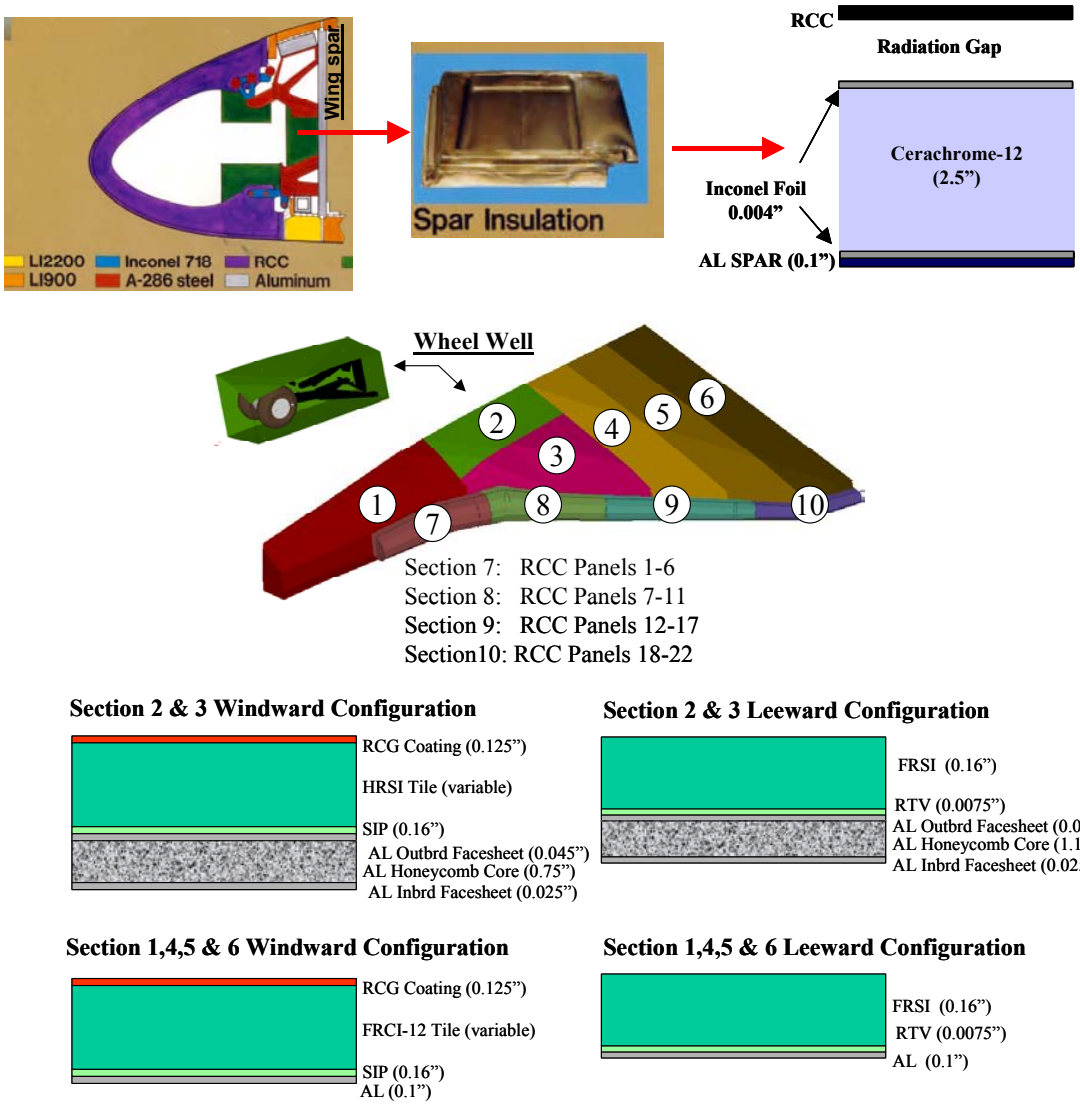

Figure 5.3.5-11 Thermal Model Configuration Details.

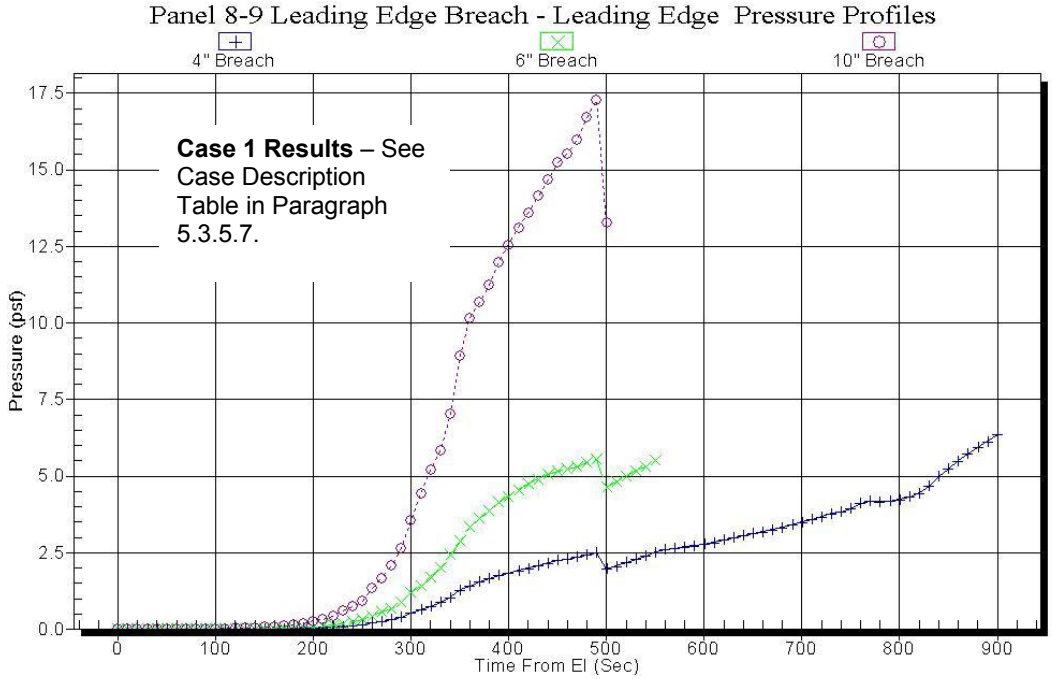

Figure 5.3.5-12 Case 1 Leading Edge Pressure History Plot for 4", 6" & 10" Diameter Breach

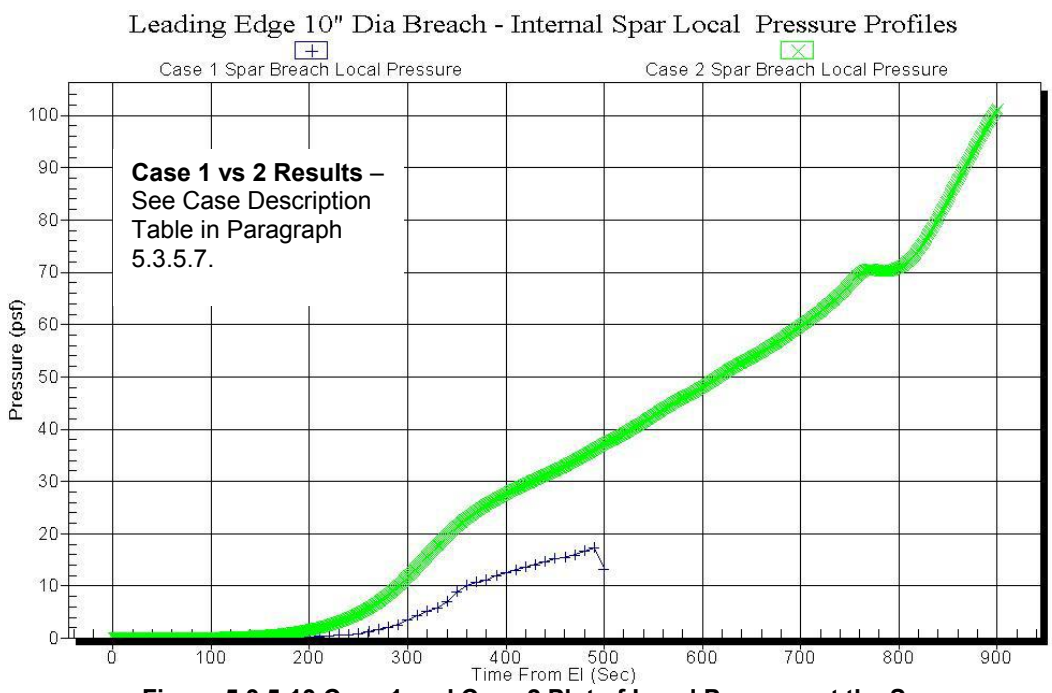

Figure 5.3.5-13 Case 1 and Case 2 Plot of Local Pressure at the Spar

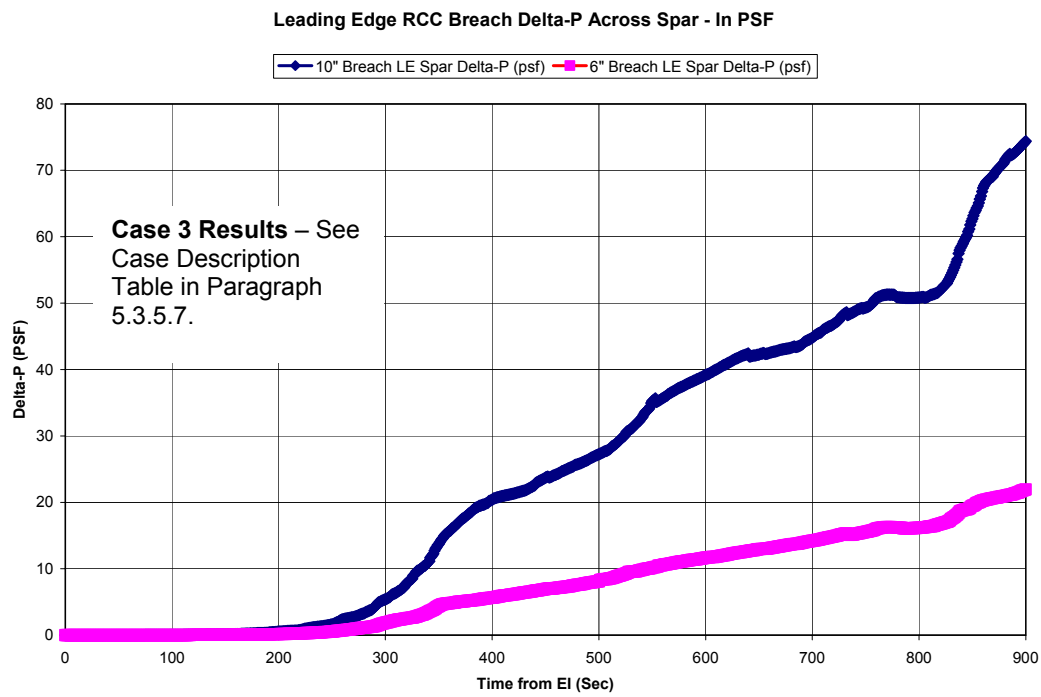

Figure 5.3.5-14 Case 3 Plot of Differential Pressure Across Leading Edge Spar for 6" and 10" Diameter Breach

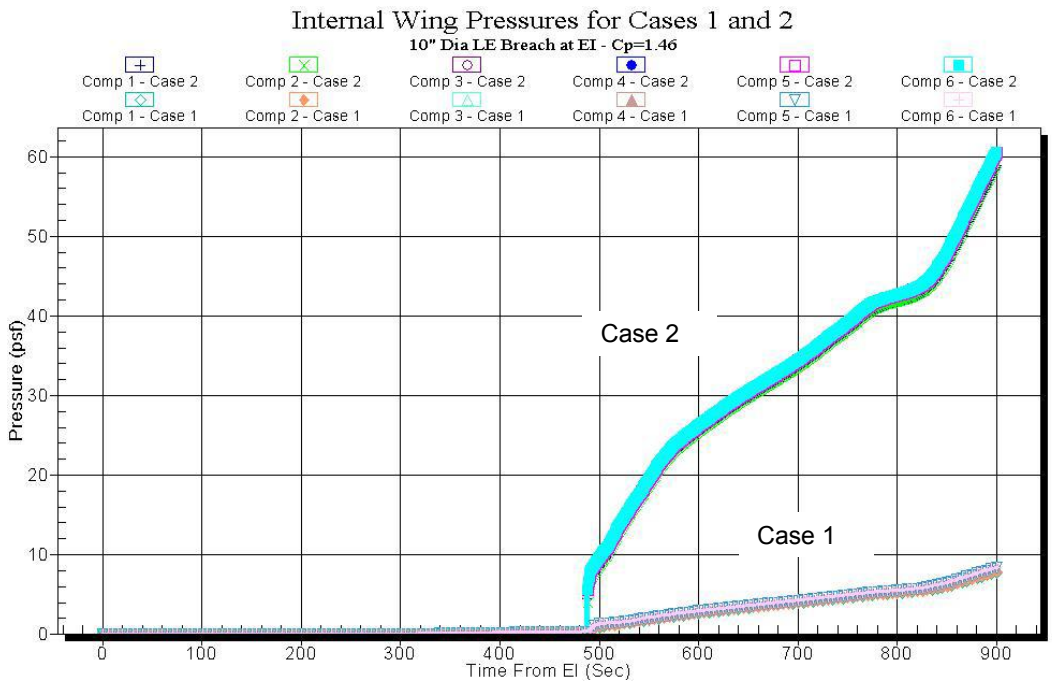

Figure 5.3.5-15 Internal Wing Pressure Histories for Cases 1 and 2

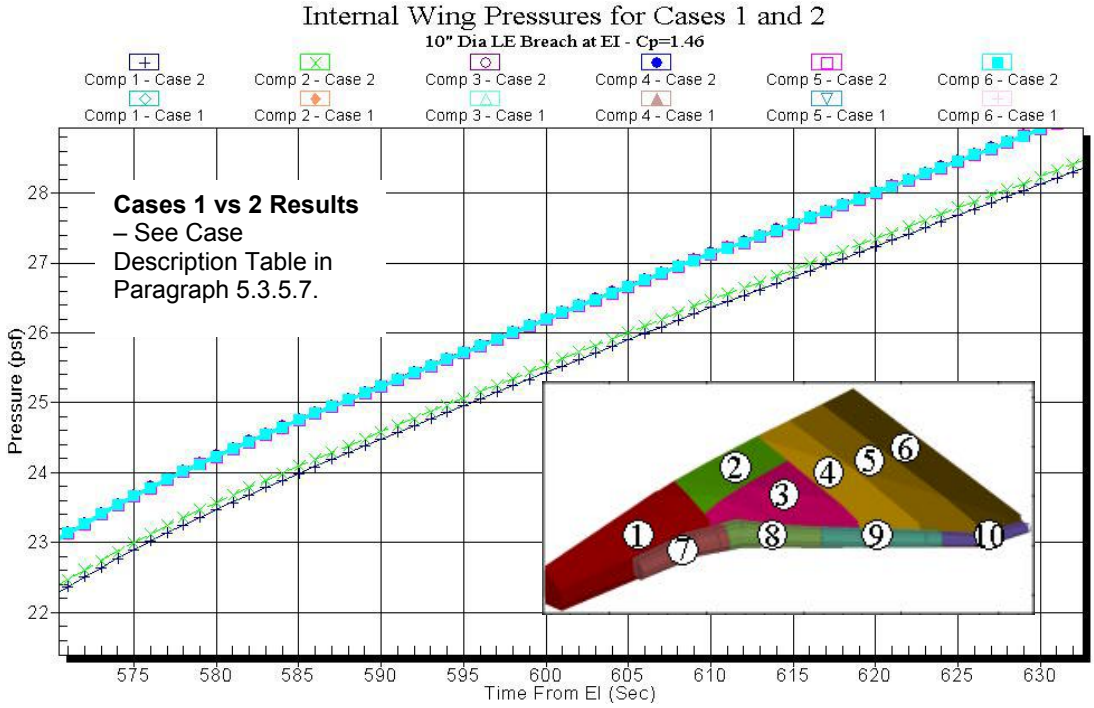

Figure 5.3.5-16 Detail Time-slice of Internal Wing Pressure Histories for Case 2

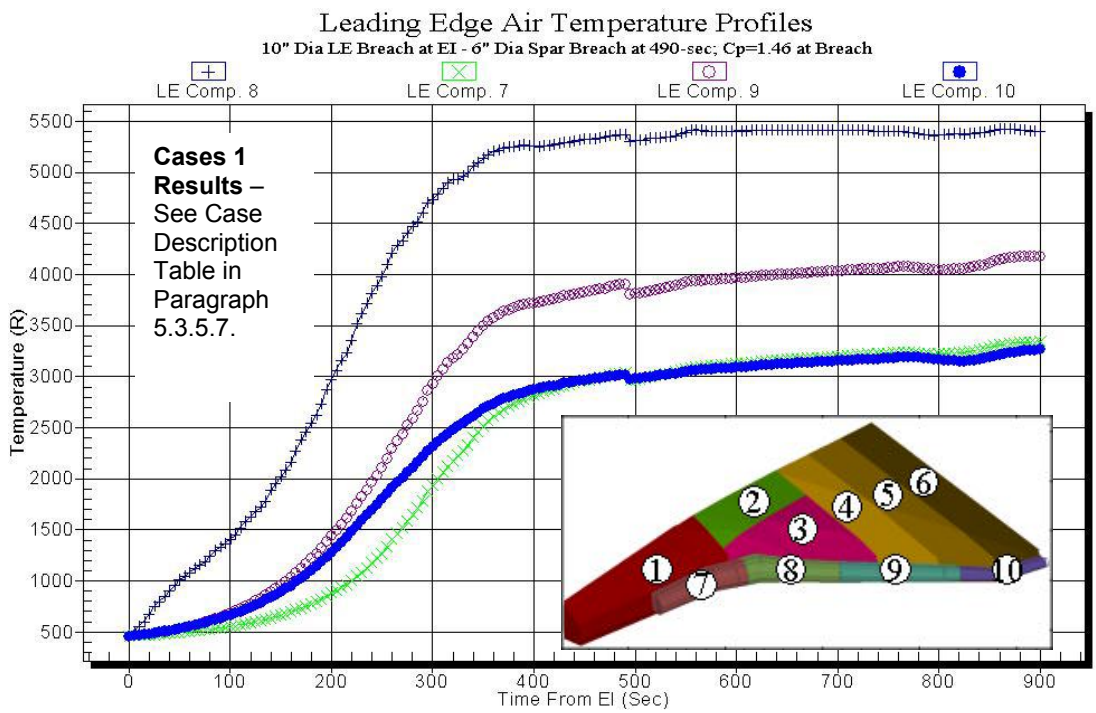

Figure 5.3.5-17 Leading Edge Air Temperature Histories for Case 1

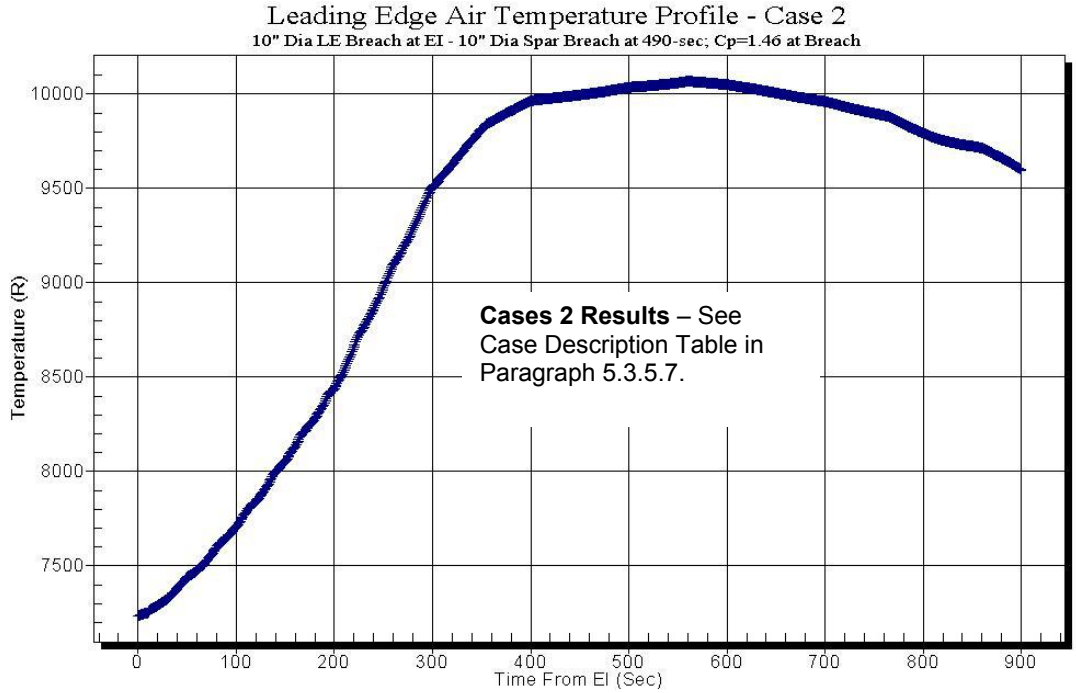

Figure 5.3.5-18 Leading Edge Air Temperature Histories for Case 2

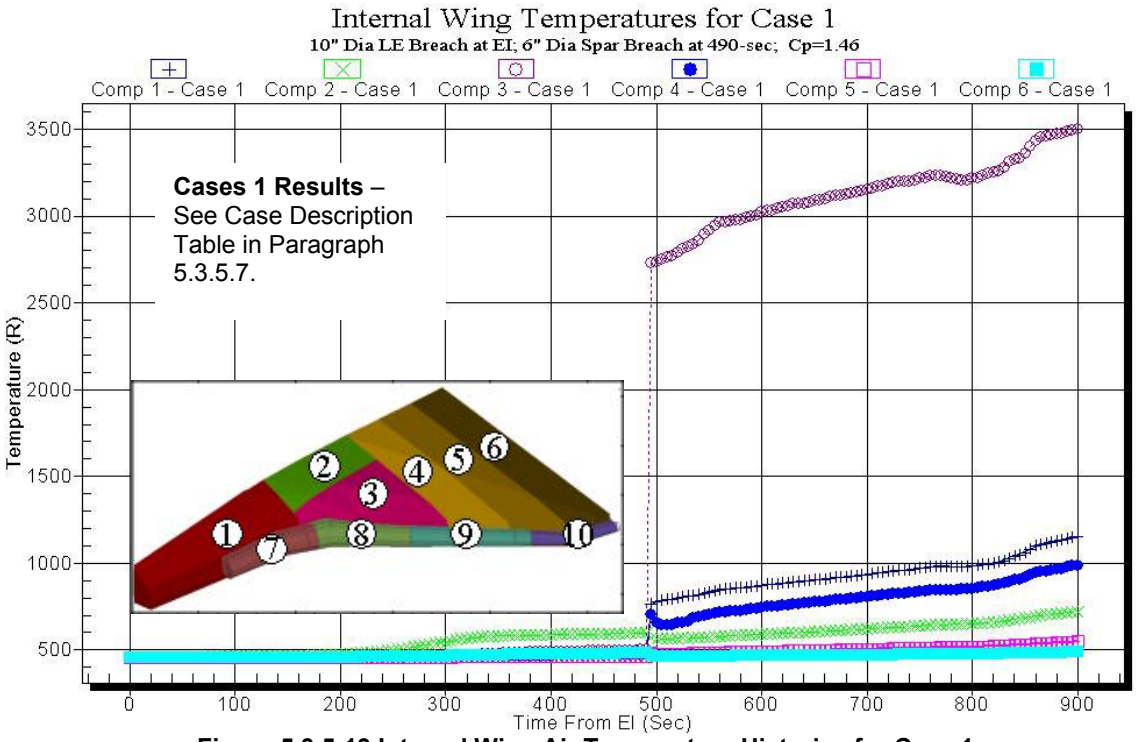

Figure 5.3.5-19 Internal Wing Air Temperature Histories for Case 1

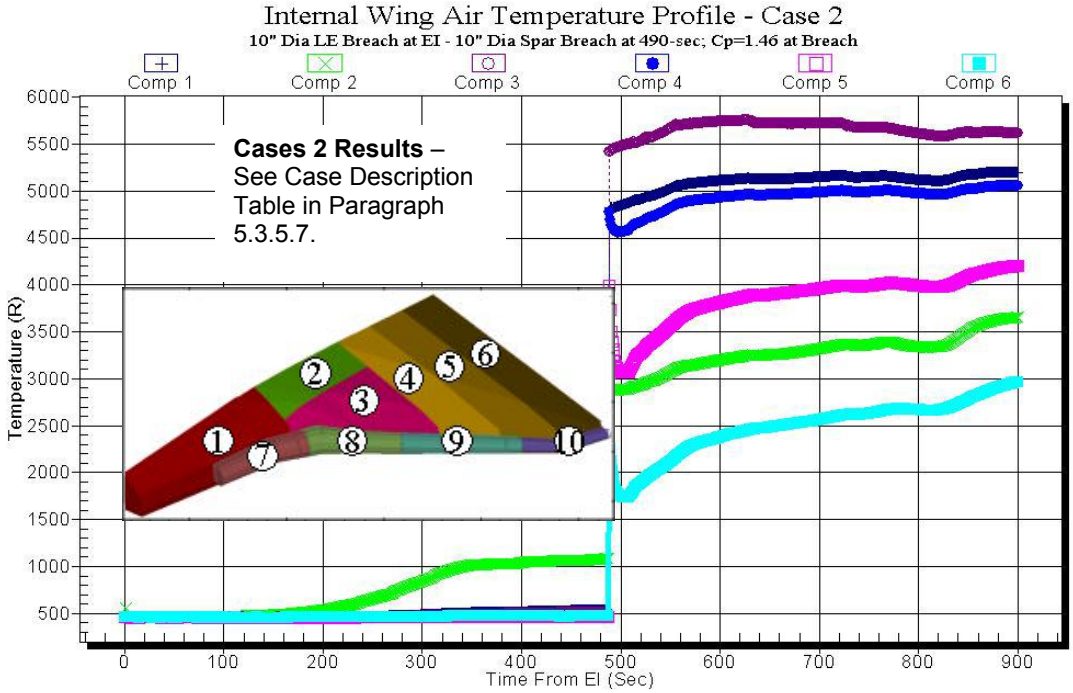

Figure 5.3.5-20 Internal Wing Air Temperature Histories for Case 2

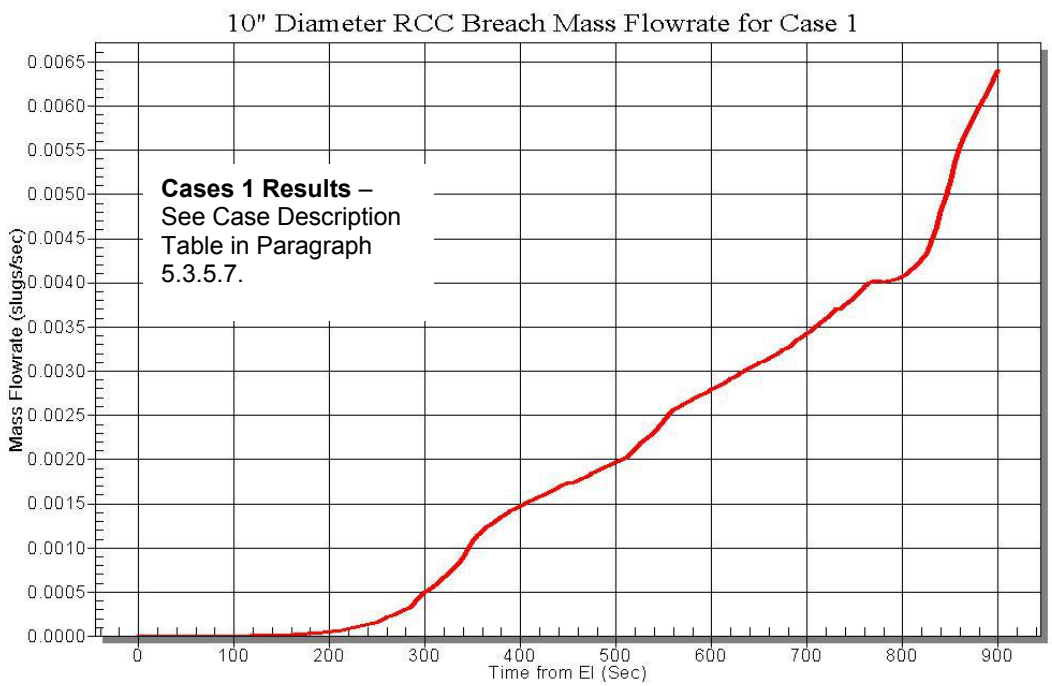

Figure 5.3.5-21 Leading Edge Breach Mass Flowrate for Case 1

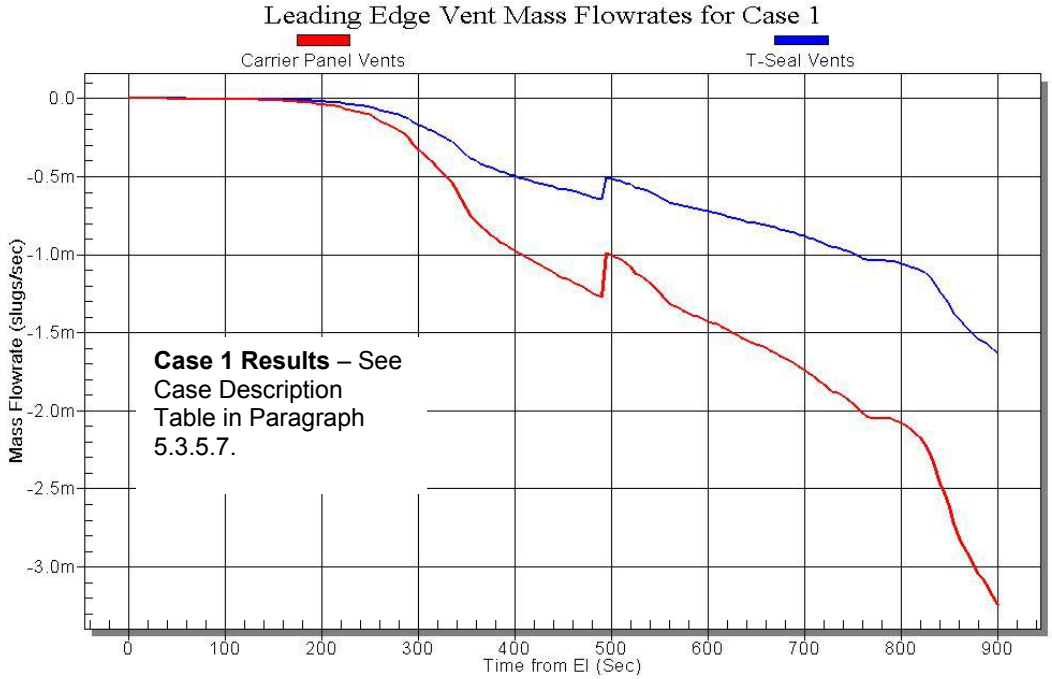

Figure 5.3.5-22 Leading Edge Vent Mass Flowrates for Case 1

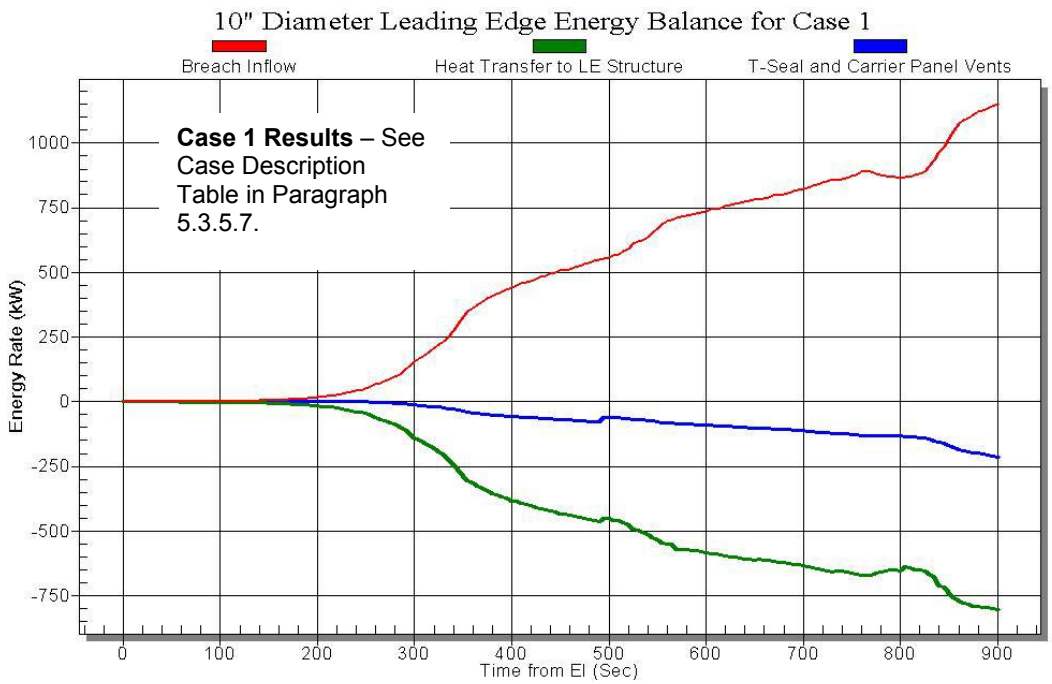

Figure 5.3.5-23 Leading Edge Breach Energy Inflow and Vent Outflow for Case 1

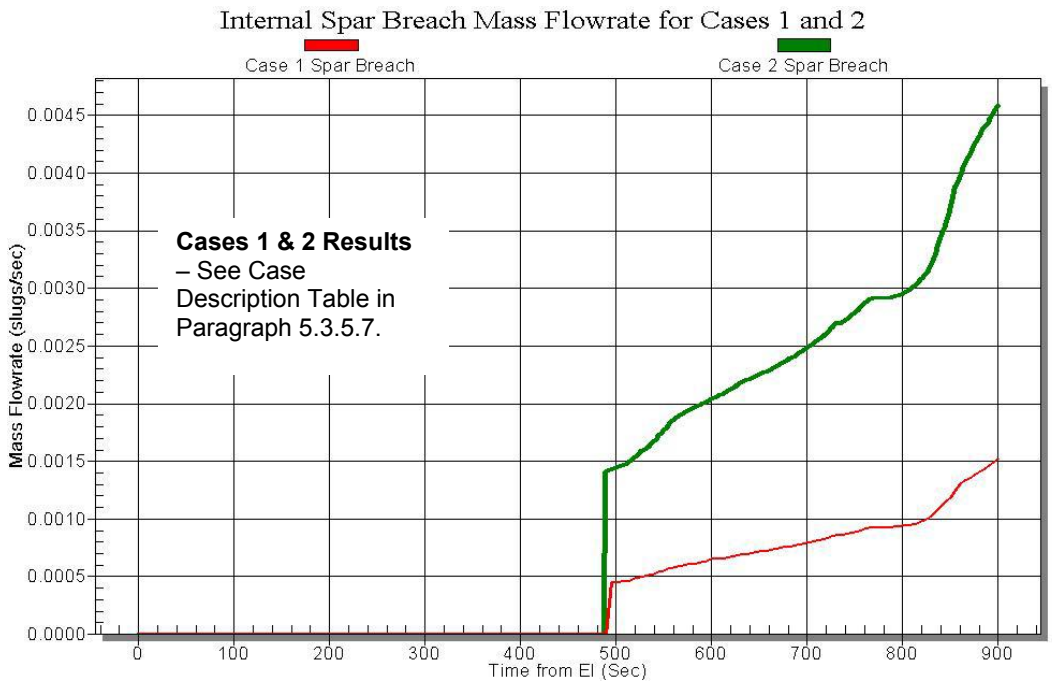

Figure 5.3.5-24 Spar Breach Mass Flowrate Comparison Between Case 1 and 2

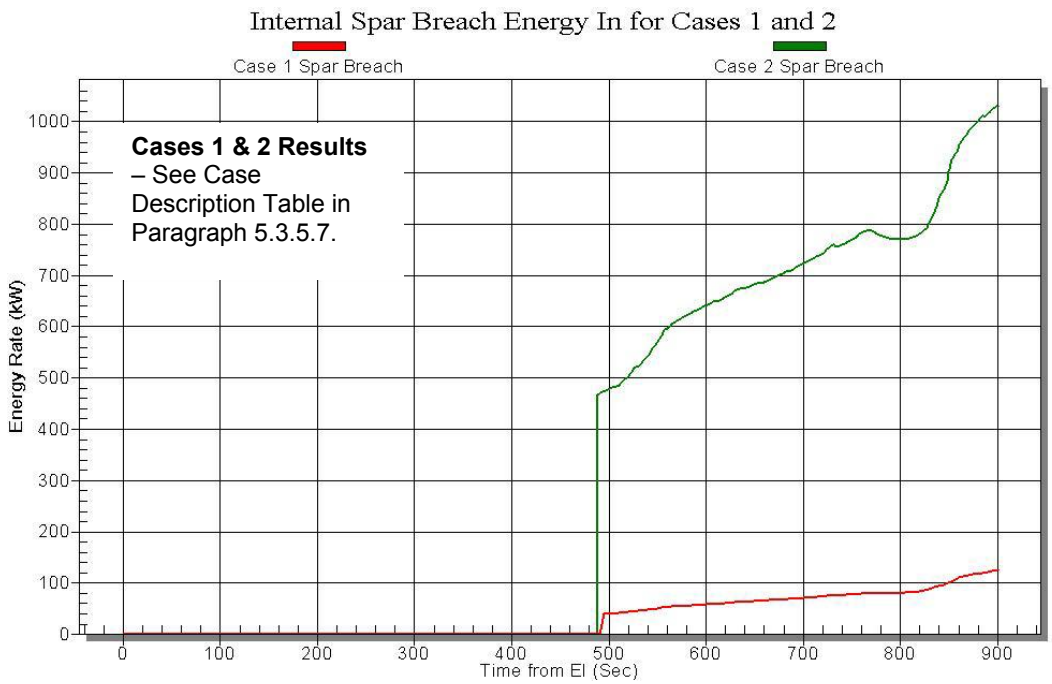

Figure 5.3.5-25 Spar Breach Energy Inflow Comparison Between Case 1 and 2

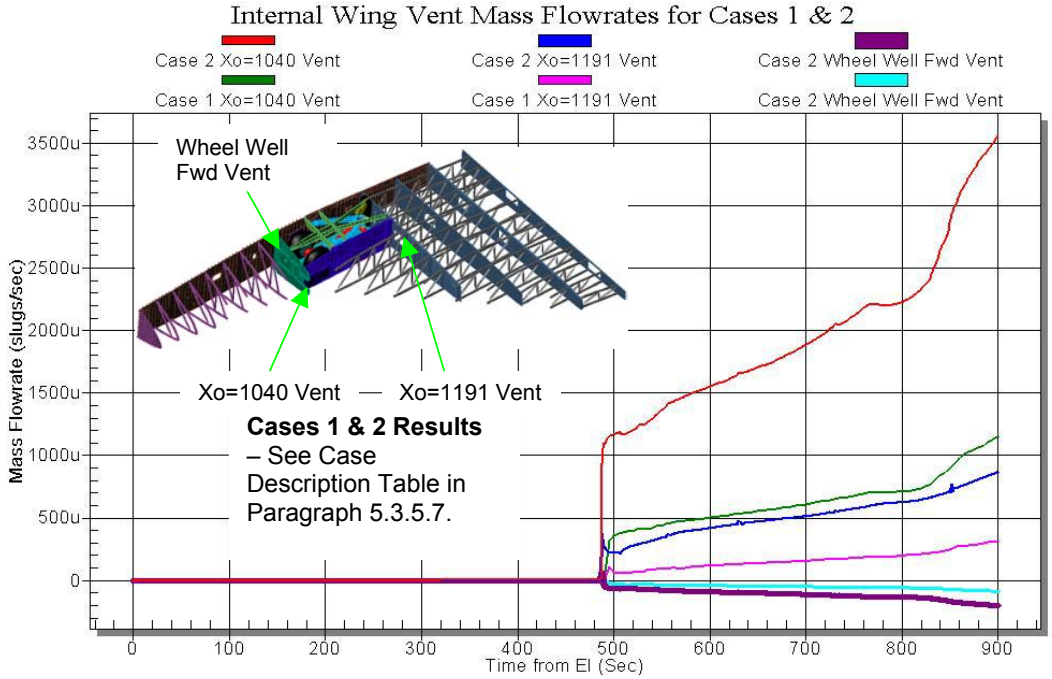

Figure 5.3.5-26 Internal Wing Vent Mass Flowrates for Cases 1 and 2

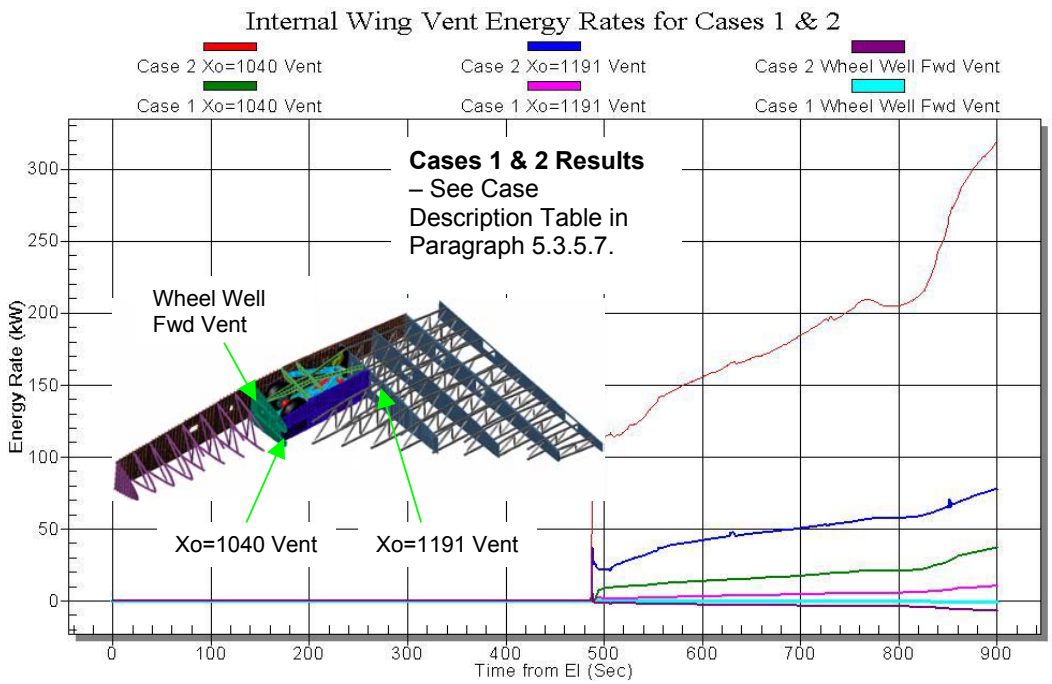

Figure 5.3.5-27 Internal Wing Vent Energy Inflows for Cases 1 and 2

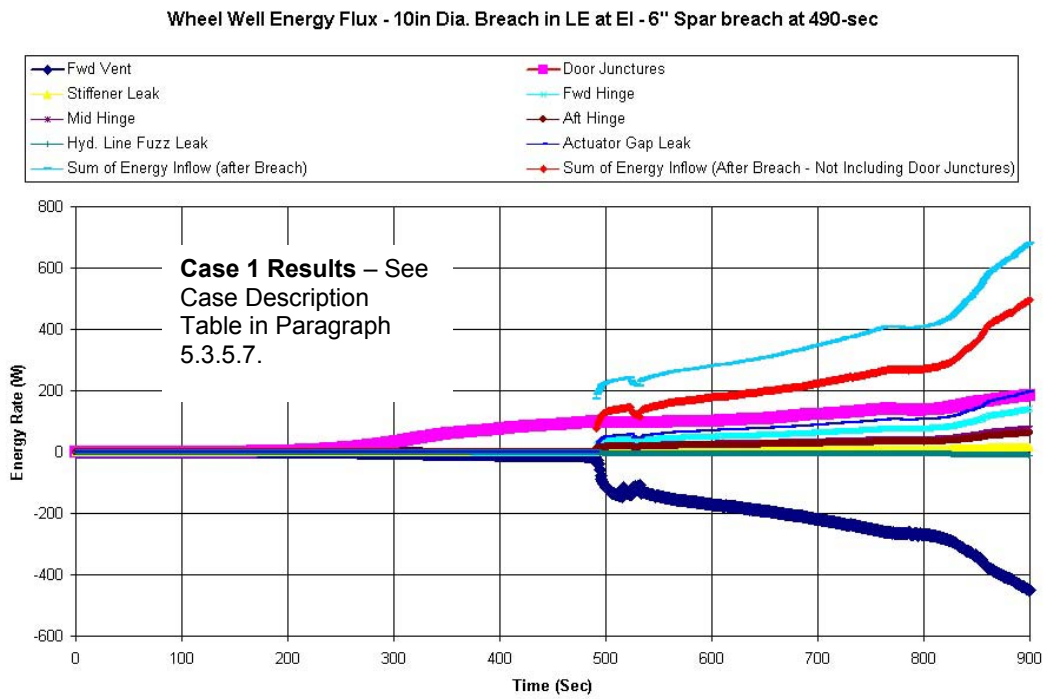

Figure 5.3.5-28 Wheel Well Energy Inflows for Case 1

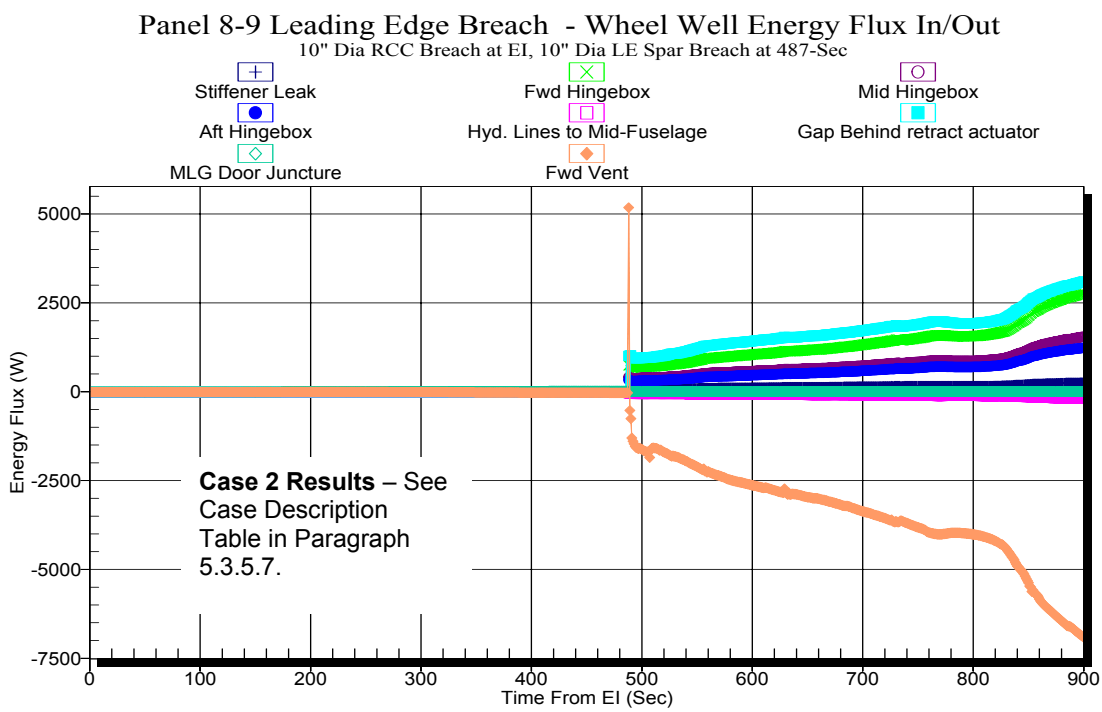

Figure 5.3.5-29 Wheel Well Energy Inflows for Case 2

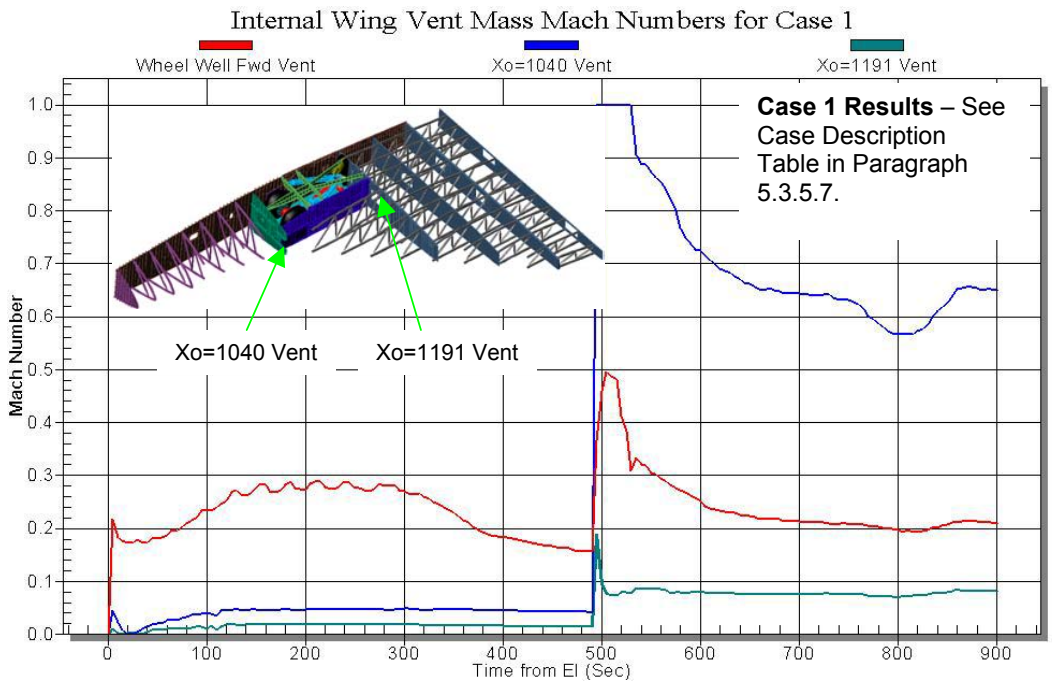

Figure 5.3.5-30 Internal Vent Mach Numbers for Case 1

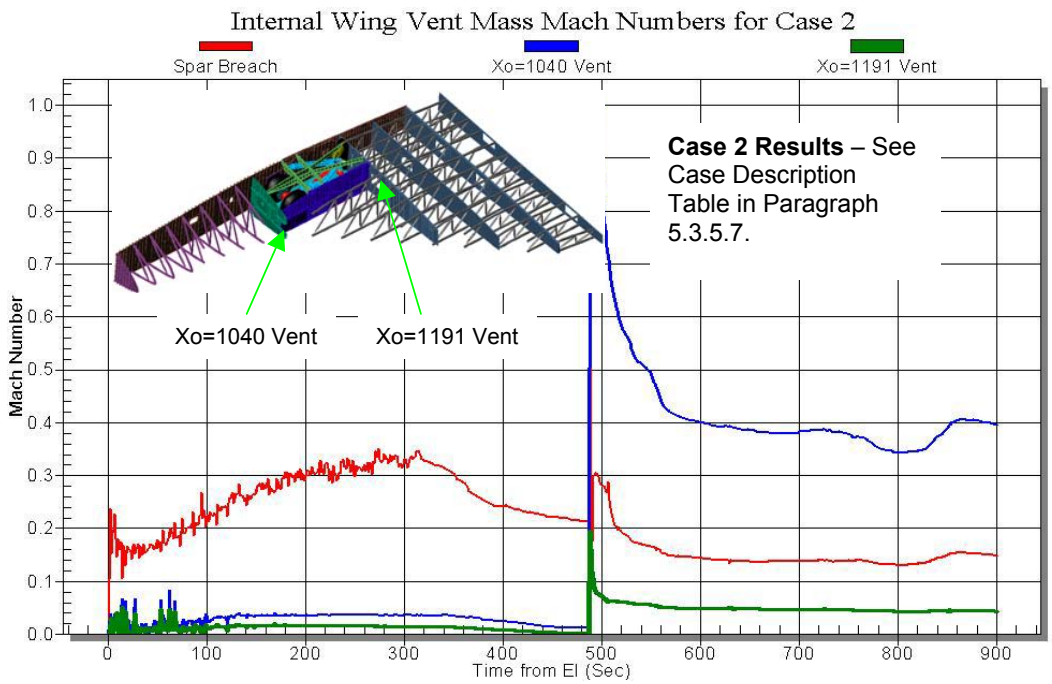

Figure 5.3.5-31 Internal Vent Mach Numbers for Case 2

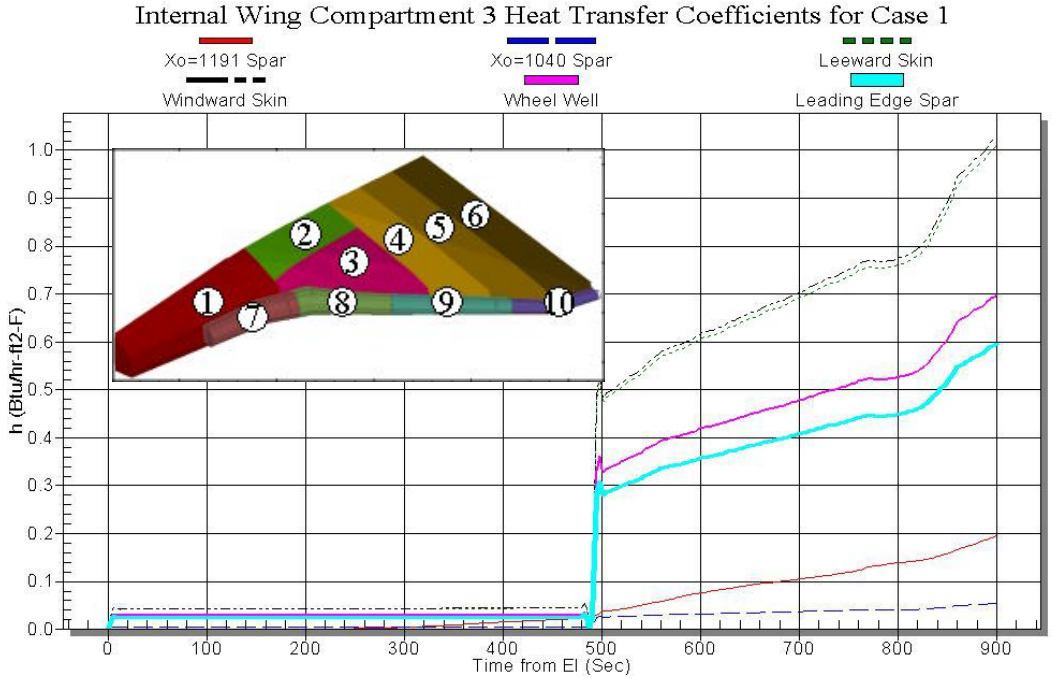

Figure 5.3.5-32 Compartment 3 Heat Transfer Coefficients for Case 1

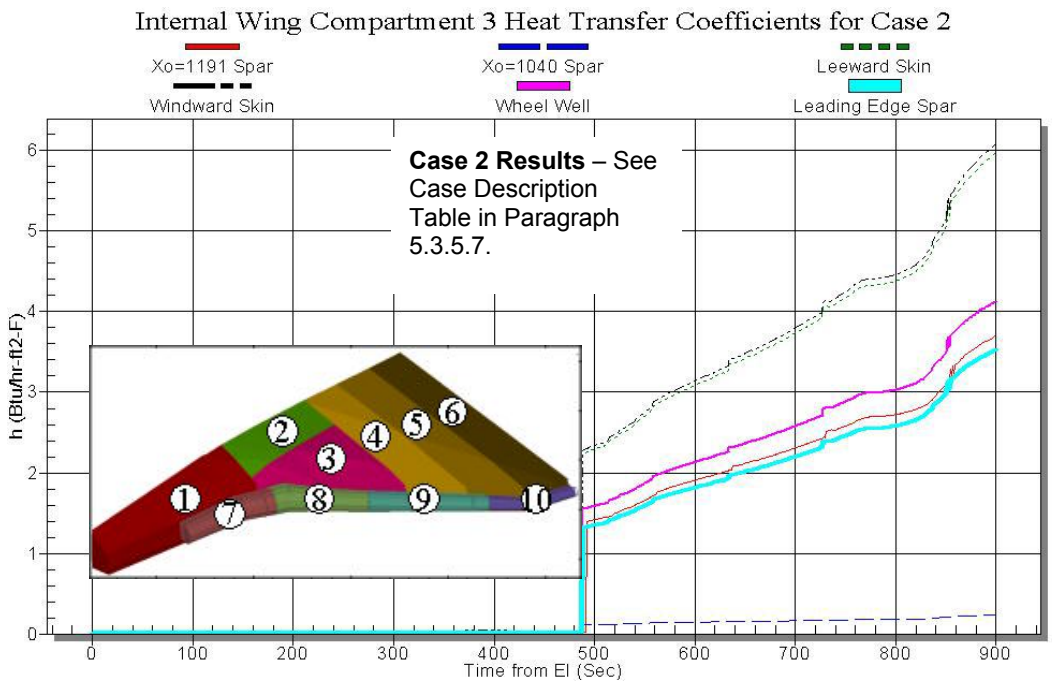

Figure 5.3.5-33 Compartment 3 Heat Transfer Coefficients for Case 2

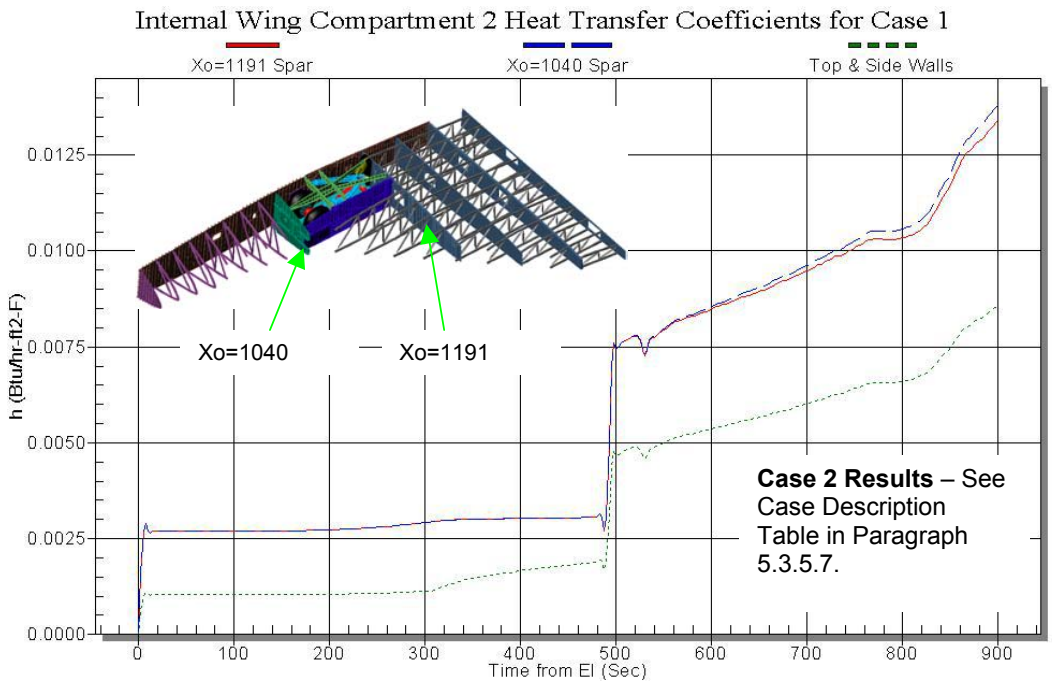

Figure 5.3.5-34 Wheel Well Heat Transfer Coefficients for Case 1

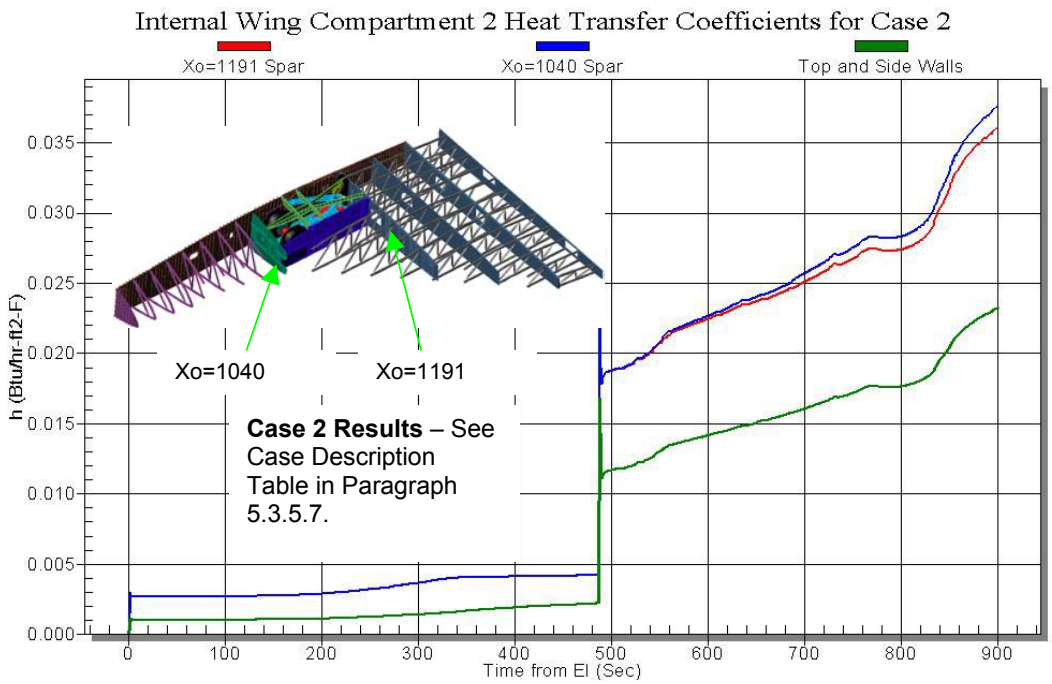

Figure 5.3.5-35 Wheel Well Heat Transfer Coefficients for Case 2

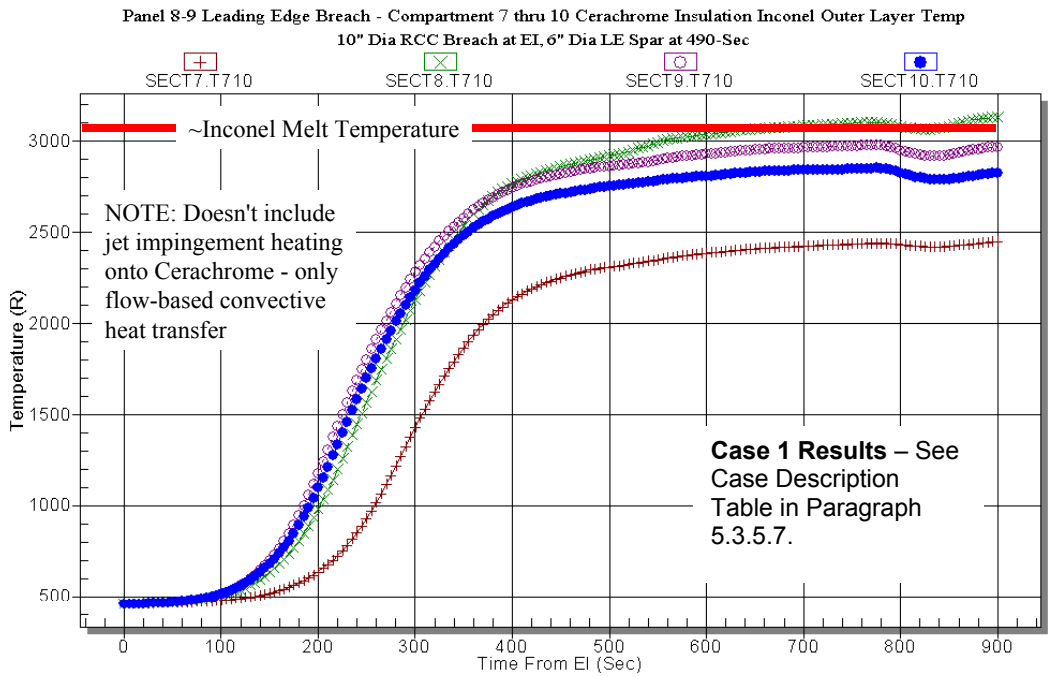

Figure 5.3.5-36 Leading Edge Cerachrome Insulation Inconel Outer Layer Temperature

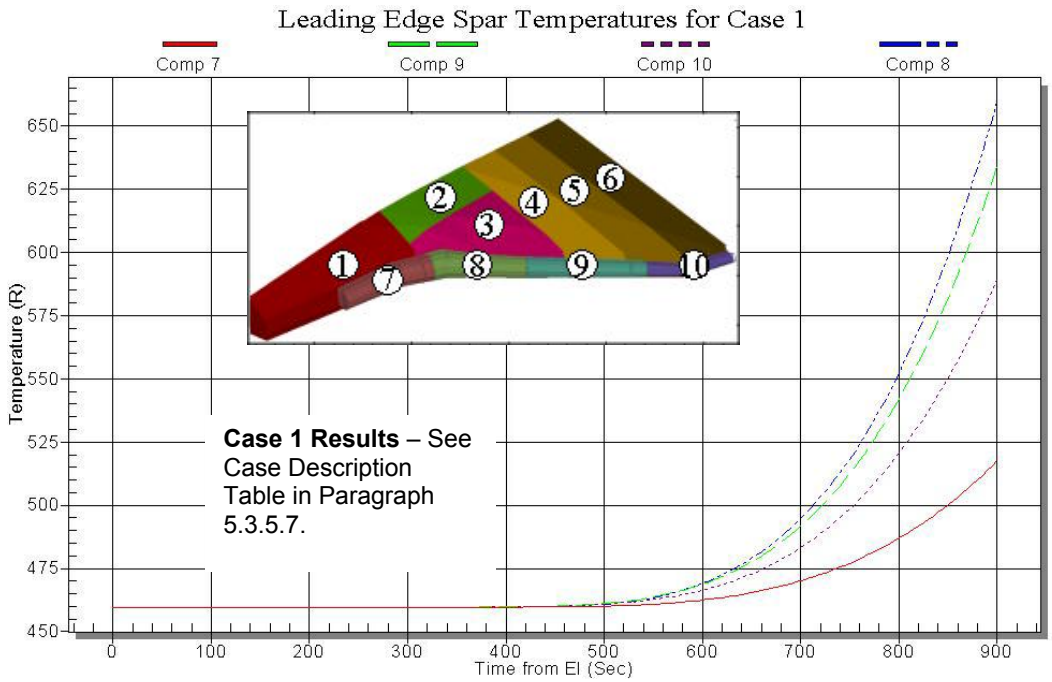

Figure 5.3.5-37 Leading Edge Structural Spar Temperature

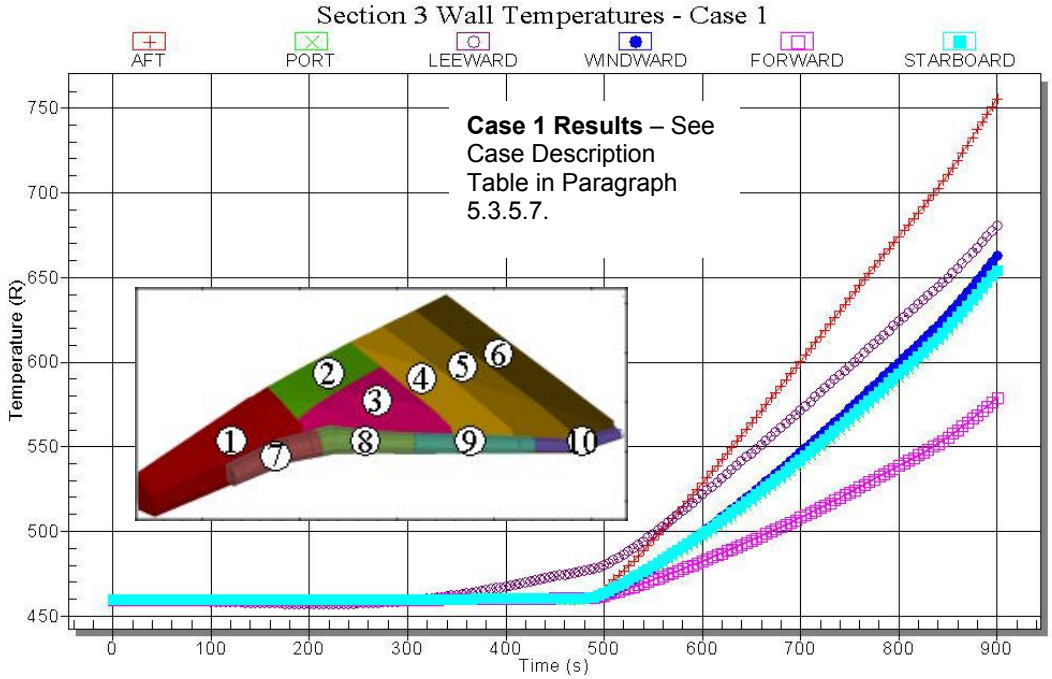

Figure 5.3.5-38 Compartment 3 Spar and Wall Skin Temperatures for Case 1

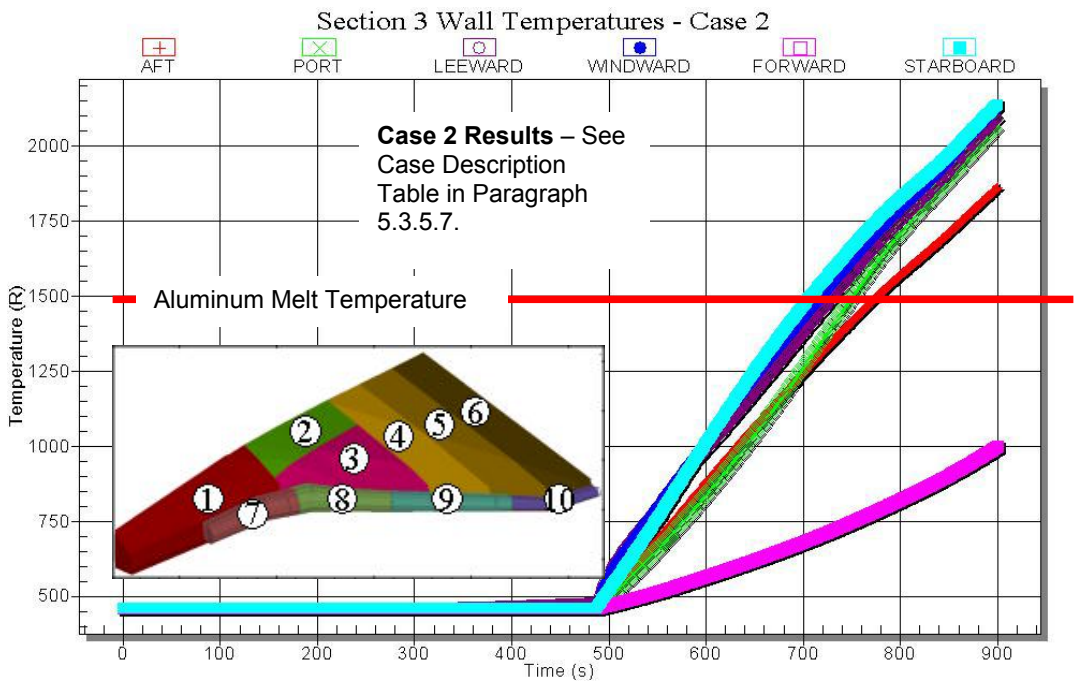

Figure 5.3.5-39 Compartment 3 Spar and Wall Skin Temperatures for Case 2

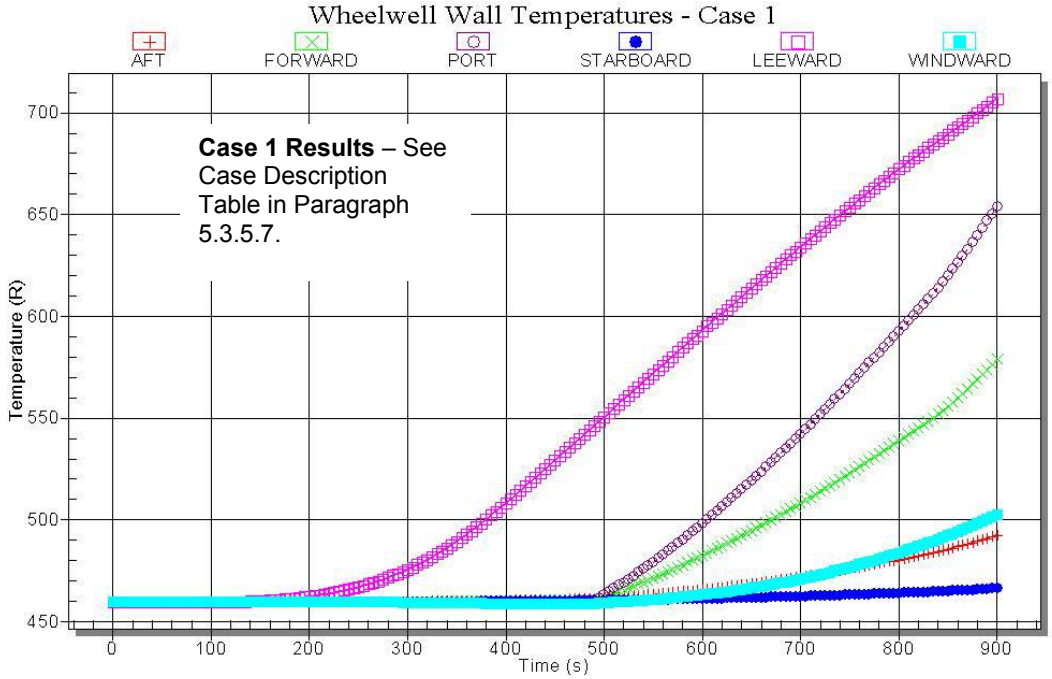

Figure 5.3.5-40 Compartment 2 Spar and Wall Skin Temperatures for Case 1

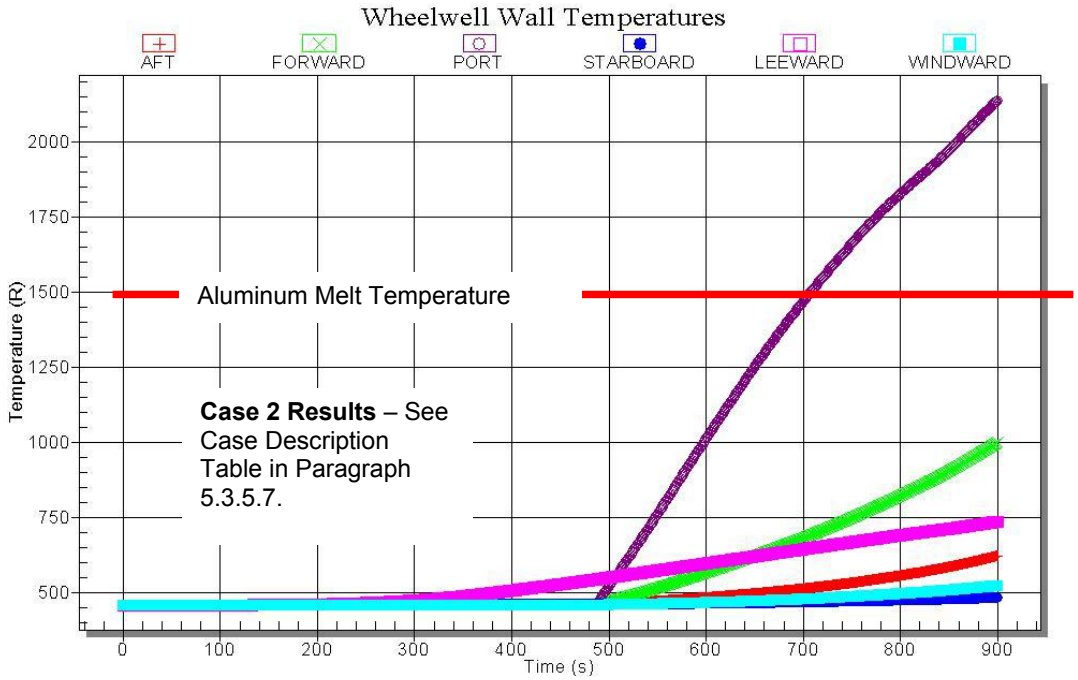

Figure 5.3.5-41 Compartment 2 Spar and Wall Skin Temperatures for Case 2

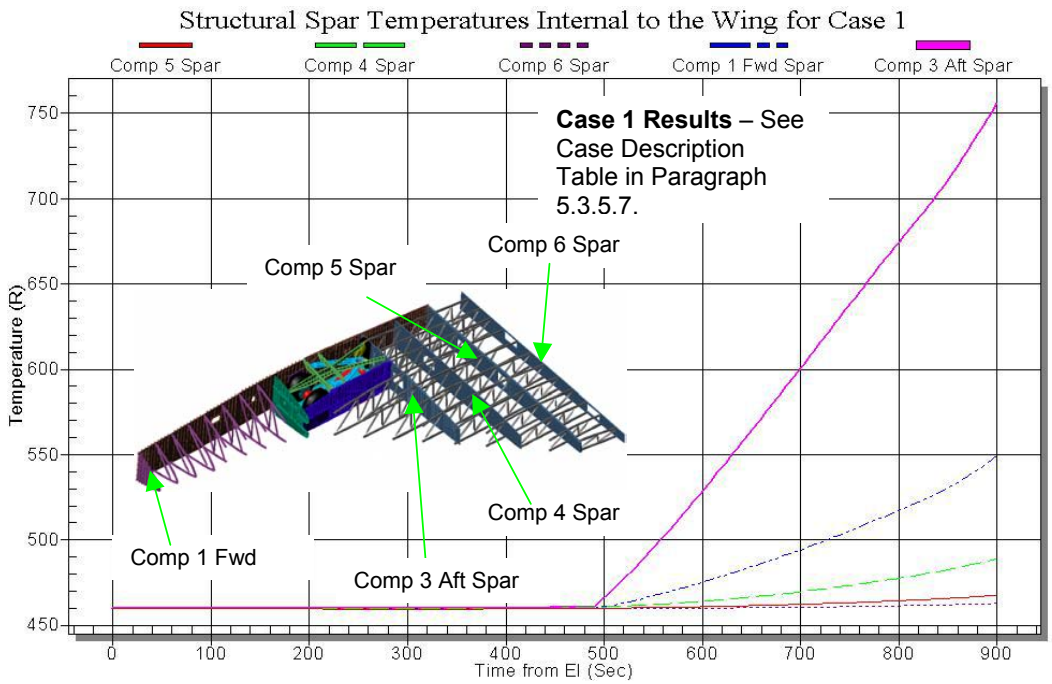

Figure 5.3.5-42 Internal Wing Spar Temperatures for Case 1

5.3.6 3D CFD & DSMC of Wing Leading Edge Cavity

5.3.6.1 CFD of RCC Panel Acreage Damage

5.3.6.1.1 Panel 7 6" Hole Decoupled Solution

5.3.6.1.1.1 Case description

This effort focused on a 6" diameter hole in RCC Panel 7 located on the attachment line at the panel midpoint (X = 1048 in, Y = -217 in, Z = 291.6 in). The attachment line location was determined from nominal geometry hypersonic Navier-Stokes solutions at approximately 40 degrees angle of attack. This study was conducted in two stages using the Unified Solution Algorithm (USA) flow solver with equilibrium air chemistry. The grid models were generated using ICEM/Hexa software. The first stage of the simulation involved a computational domain limited to the hole inlet and a section of the RCC channel from Panels 5-9, and is referred to as the decoupled internal flow case. Coupled external/internal flow simulations were performed next in the second stage. This decoupled internal flow simulation provided initial jet plume flow field information and convective heating environments to internal structure in the leading edge volume.

5.3.6.1.1.2 Geometry and Grid Definition

The CFD grid model used in this simulation included the ribs on both sides of Panel 7. Figure 5.3.6-1 show the surface grid. For the volume grid the wall spacing is 0.0005 inch to ensure a cell-Reynolds number of 1 or less. Rectangular openings to simulate the T-seal vent gaps were modeled on the leeside between Panels 5 and 6; Panels 6 and 7; Panels 7 and 8; and Panels 8 and 9. The respective areas of these vents are 0.5556, 0.642, 0.7704 and 0.642 square inches. These leeside rectangular vents of 0.2 inch width were modeled between the RCC panels in a chordwise orientation 2 inches ahead of upper carrier panels. To account for the vents in Panels 1-4, a circular vent of area 22.03 square inches was modeled at the inboard end of the Panels 5-9 channel. Similarly, another circular vent of area 55.29 square inches was modeled on the outboard end of the Panels 5-9 channel to account for the vents on Panels 10-22. The total vent area of about 80 square inches was purposely made to be about 20% larger than 66.4 square inches of all the documented spanwise vents in front of the upper carrier panels and the chordwise vents between RCC Panels just ahead of upper carrier panels.

5.3.6.1.1.3 Boundary Conditions

For the decoupled internal flow simulation the total conditions at the hole inlet were obtained from the Orbiter nominal geometry Navier-Stokes solutions for STS-107 CFD Point 2 flight condition (491.4 sec from Entry Interface). In this laminar simulation with equilibrium air chemistry, a pressure of 38.6 psf and temperature of 18,375° R were specified as the reservoir conditions at the hole inlet. This results in a total enthalpy of 27,500 Btu/lbm whereas the actual total enthalpy is 11,175 Btu/lbm for the flight condition at 491.4 sec after EI. The interior surfaces were kept at 0° F. A back-pressure of 0.5 psf was specified at the vents for the simulation.

5.3.6.1.1.4 Results

Figure 5.3.6-3 shows Mach contours of the jet plume with the corresponding jet pressure contours illustrated in Figure 5.3.6-4. The total enthalpy contours are shown in Figure 5.3.6-5. The pressure results on the RCC channel and the front spar are shown in Figure 5.3.6-6 and Figure 5.3.6-7, respectively. Similarly, Figure 5.3.6-8 and Figure 5.3.6-9 illustrate the heating on the RCC channel surfaces and on the front spar, respectively. The results discussed thus far in this section were obtained with a 2 million-cell grid model. Another simulation with a denser grid model of about 15 million cells was also conducted to evaluate grid convergence effects. Figure 5.3.6-10 and Figure 5.3.6-11 show the surface pressure and heating distributions, respectively, on the front spar and the RCC cavity from the 15 million-cell model simulation. The heating results are as high as twice the results from the 2 million-cell model simulation. The jet plume is probably better resolved as seen in the flow field Mach and pressure distributions illustrated in Figure 5.3.6-12 and Figure 5.3.6-13, respectively. The decoupled internal flow CFD heating results are higher than predictions from engineering models calculated at the same conditions. Nevertheless, the decoupled internal flow simulation provided a lead-in to the coupled external/internal flow simulations.

5.3.6.1.2 Panel 7 6" Hole Coupled External/Internal Flow Solution

5.3.6.1.2.1 Case description

Two coupled external/internal flow simulations were conducted during the second stage of this study for a 6-inch diameter hole in leading edge panel 7 using the freestream flow conditions from flight at 404 sec after EI. The first simulation used a finer grid but did not model the internal earmuff insulation between Panels 7 and 8. The second simulation used a coarser grid but the earmuff insulation between both panels 7/8 and panels 8/9 was modeled.

5.3.6.1.2.2 Geometry and Grid Definition

The grid models used for the coupled simulation included the RCC channel, vents and the 6" hole, as well as the Orbiter external flow grid in order to generate coupled external/internal flow solutions. In addition, the grid model used in the first coupled external/internal flow simulation included the ribs on both sides of RCC Panel 7 and Panel 8, along with the earmuff insulation between Panels 8 and 9. The far and close-up views of the surface grid of the external and internal flow regimes are shown in Figure 5.3.6-14 and Figure 5.3.6-15, respectively. Figure 5.3.6-16 and Figure 5.3.6-17 illustrate further the details of the geometry inside the RCC cavity, whereas a cross-section of the grid is shown in Figure 5.3.6-18. The wall spacing is 0.0005 inch to ensure the cell-Reynolds number of 1 or less on the surface.

5.3.6.1.2.3 Boundary Conditions

In this equilibrium air chemistry simulation, the RCC interior surfaces were kept at 0° F, whereas the Orbiter exterior surfaces were specified with radiative equilibrium temperature boundary condition. The vent areas and pressure boundary conditions used in the decoupled simulation were also applied to these simulations.

5.3.6.1.2.4 Results

Figure 5.3.6-19 and Figure 5.3.6-20 show the Mach and Pressure contours, respectively, in the jet plume for a planar cut through the leading edge cavity. Figure 5.3.6-21 illustrates the pressure contours in the flow field whereas the Mach contours in flow field are shown in Figure 5.3.6-22 and Figure 5.3.6-23 for a constant-z cut. The surface pressure distributions are shown in Figure 5.3.6-24 and Figure 5.3.6-25 on the RCC channel and the front spar, respectively. Similarly, the heating results are illustrated in Figure 5.3.6-26 and Figure 5.3.6-27 for the RCC channel and the front spar, respectively. These results are from a dense grid model with about 15 million cells. The heating environment inside the RCC cavity is converged, except on the front spar where there are some small variations. The secondary impingement of

the jet on the front spar is probably not a steady-state phenomenon, but the level of heating on the spar is not very high. The earmuff insulation between Panels 7 and 8 were not modeled in this simulation, because the jet was thought to be going straight toward the earmuff between RCC Panels 8 and 9. This simulation however showed that the jet hits primarily the outboard rib of RCC Panel 7 and the rib redirects the jet toward the region of the earmuff insulation between RCC Panels 7 and 8. The second coupled external/internal flow simulation in this study conducted included the earmuff insulation between RCC Panels 7 and 8.

Figure 5.3.6-28 and Figure 5.3.6-29 illustrate the external flow grid model for this simulation whereas the internal flow grid model is shown in Figure 5.3.6-30, Figure 5.3.6-31 and Figure 5.3.6-32. The results for this simulation using a grid model of about 2 million cells are discussed below. Figure 5.3.6-33, Figure 5.3.6-34 and Figure 5.3.6-35 show pressure distributions on the RCC channel, whereas similar heating distributions are illustrated in Figure 5.3.6-36, Figure 5.3.6-37 and Figure 5.3.6-38. Also, pressure contours in flow field are shown in Figure 5.3.6-39 and Figure 5.3.6-40, whereas Figure 5.3.6-41 and Figure 5.3.6-42 illustrate Mach contours in the flow field. The jet hits the outboard rib of Panel 7, then the outboard edge of the earmuff insulation between RCC Panels 7 and 8, and then the front spar behind RCC Panel 8.

• RCC Panels 5-9 with leeside vents modeled. (Side vents represent vents for other panels either side).

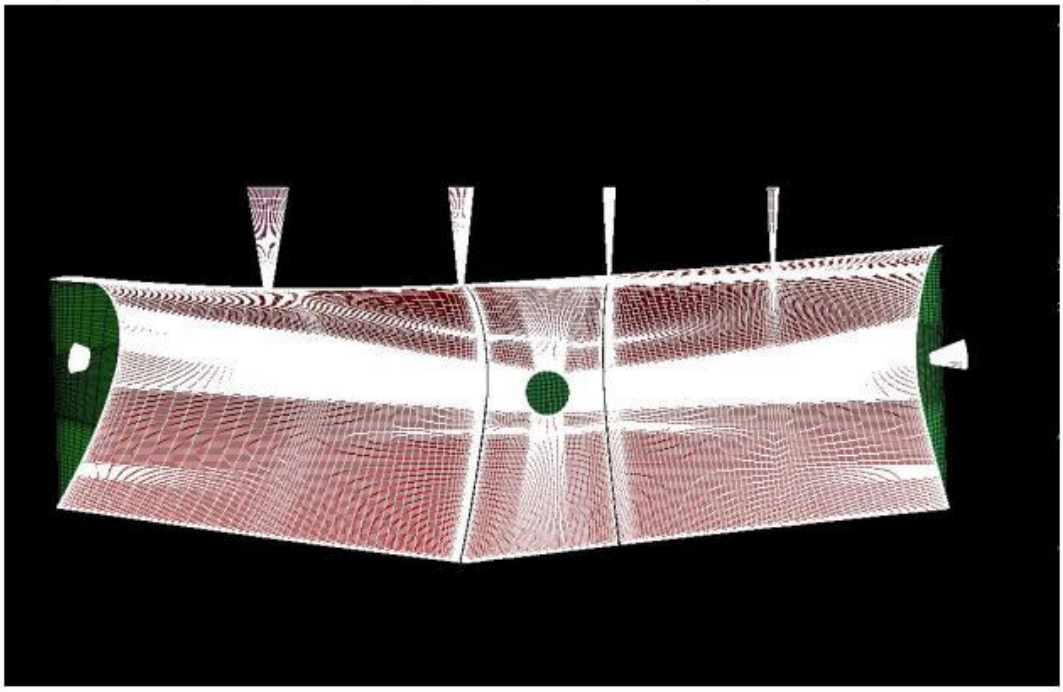

Figure 5.3.6-1 Grid Model for Panel 7 Hole Internal Flow Simulation

• Vents are connected to a fictitious dump chamber where back-pressure from leeside specified. (Brackets modeled either side of Panel 7)

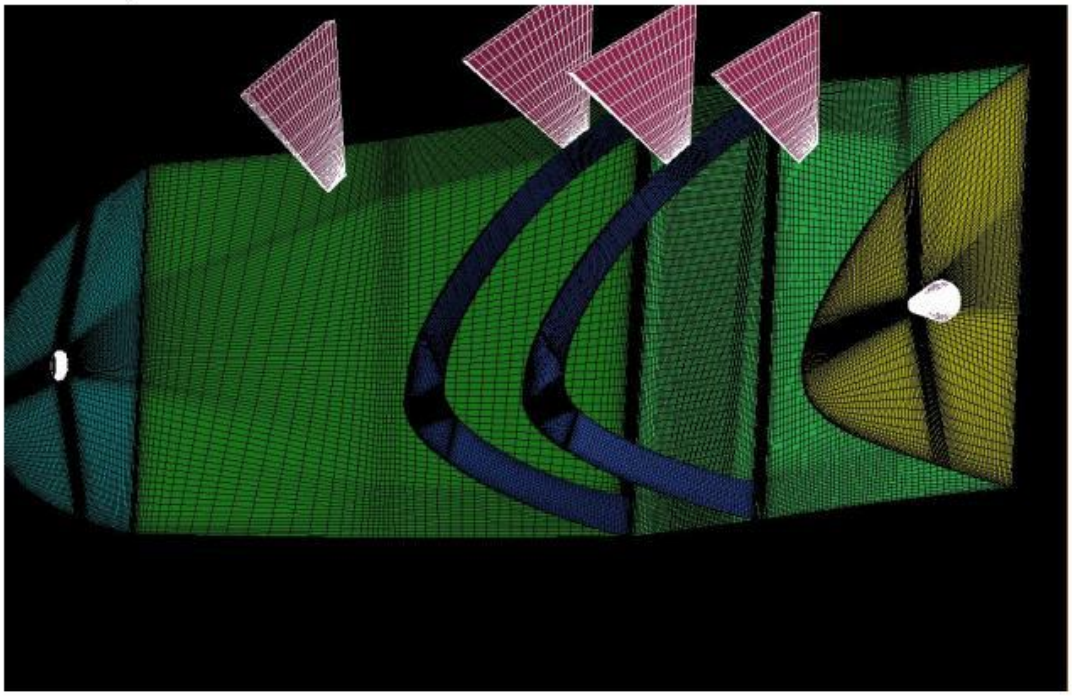

Figure 5.3.6-2 Grid Model for Panel 7 Hole Internal Flow Simulation

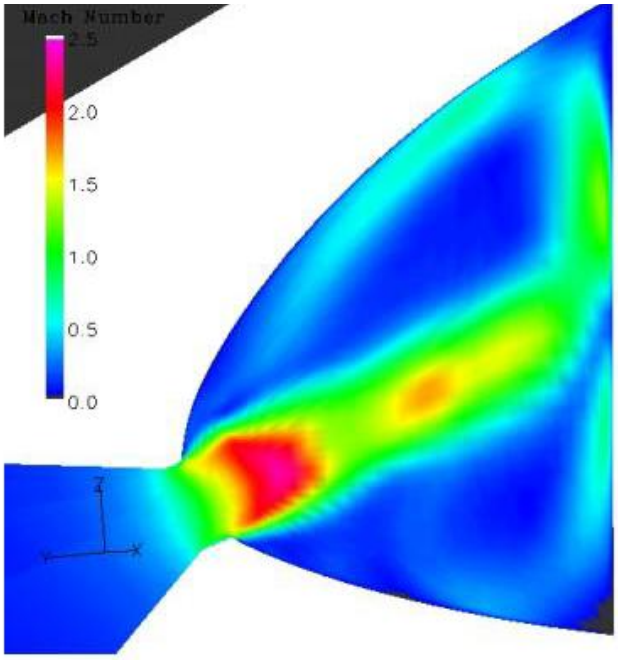

Figure 5.3.6-3 Mach Contours for Panel 7 Hole Internal Flow Simulation with 2 million-cell Model

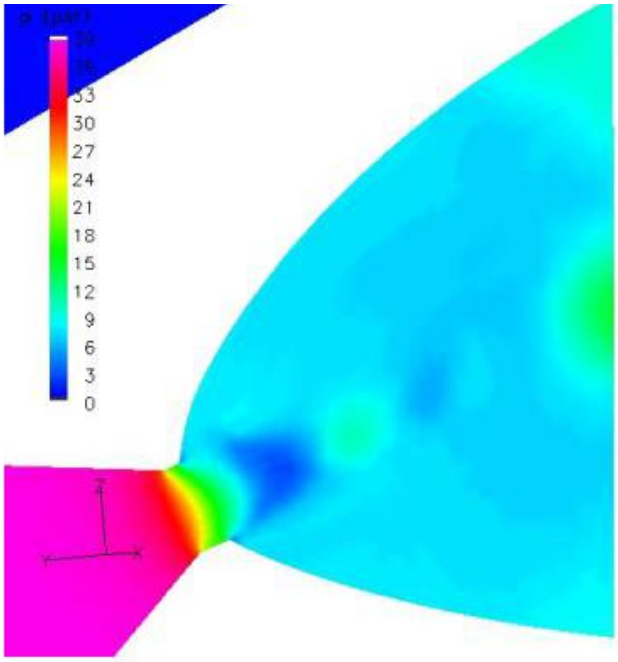

Figure 5.3.6-4 Pressure Contours for Panel 7 Hole Internal Flow Simulation with 2 million-cell Model

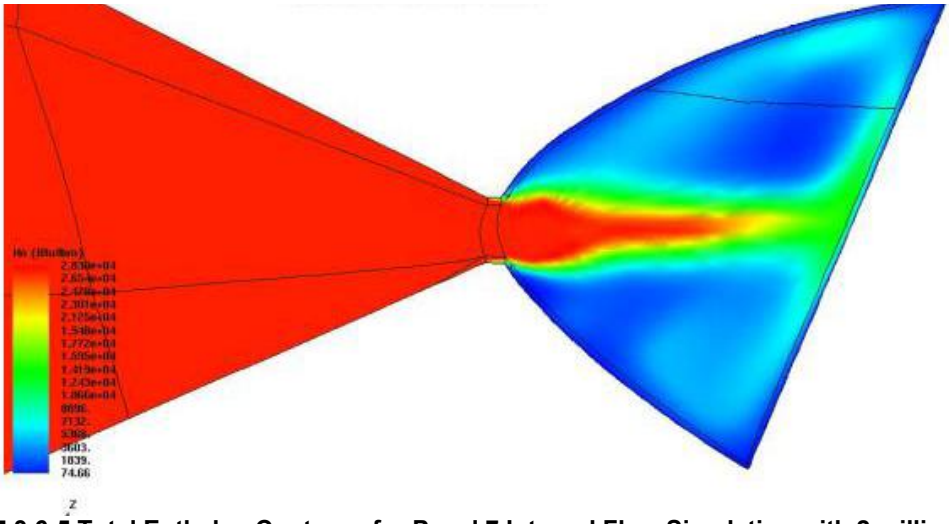

Figure 5.3.6-5 Total Enthalpy Contours for Panel 7 Internal Flow Simulation with 2 million-cell Model

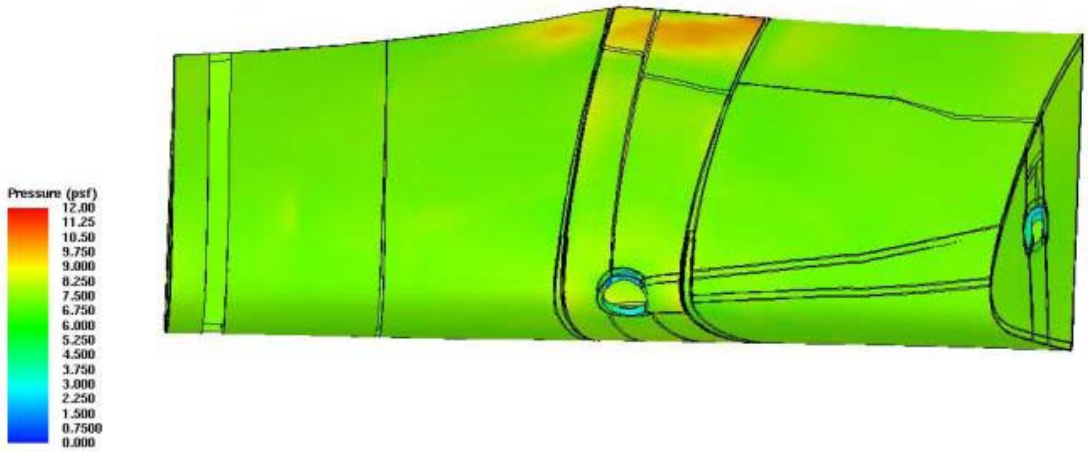

Figure 5.3.6-6 Pressure Contours on RCC Channel from Panel 7 Hole Internal Flow Simulation with 2 million-cell Model

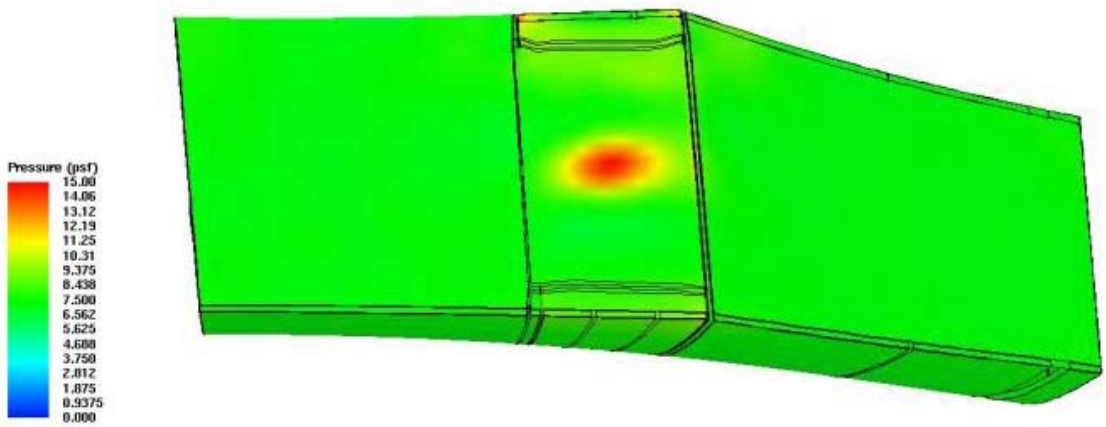

Figure 5.3.6-7 Pressure Contours on Front Spar from Panel 7 Hole Internal Flow Simulation with 2 million-cell Model

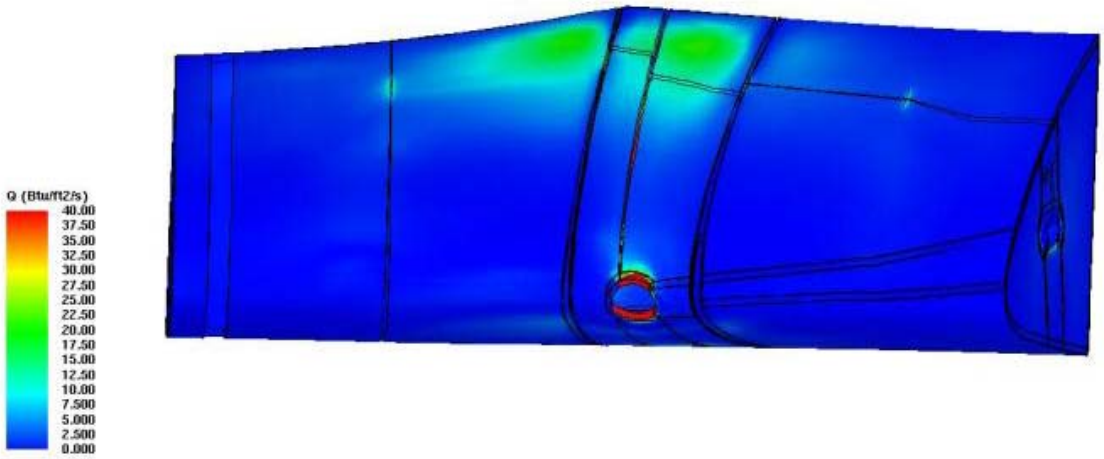

Figure 5.3.6-8 Heating Contours on RCC Channel from Panel 7 Hole Internal Flow Simulation with 2 million-cell Model

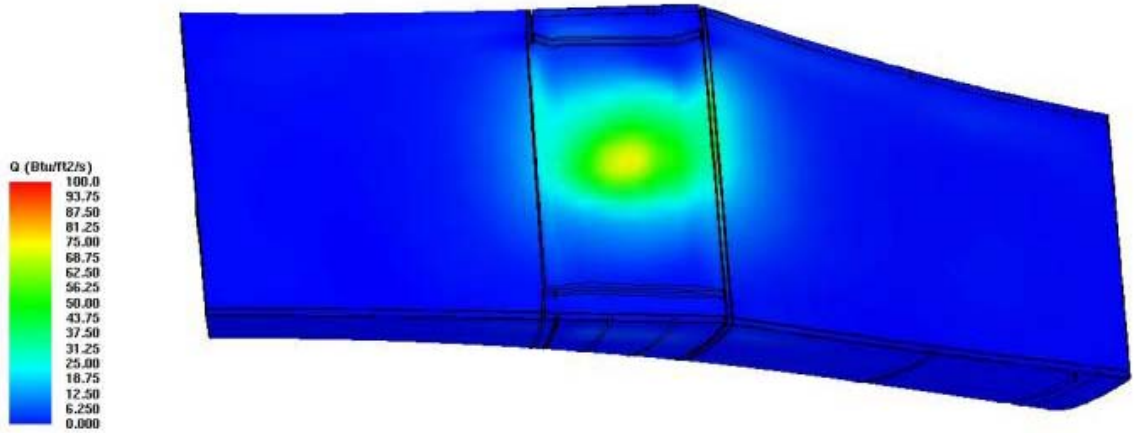

Figure 5.3.6-9 Heating Contours on Front Spar from Panel 7 Hole Internal Flow Simulation with 2 million-cell Model

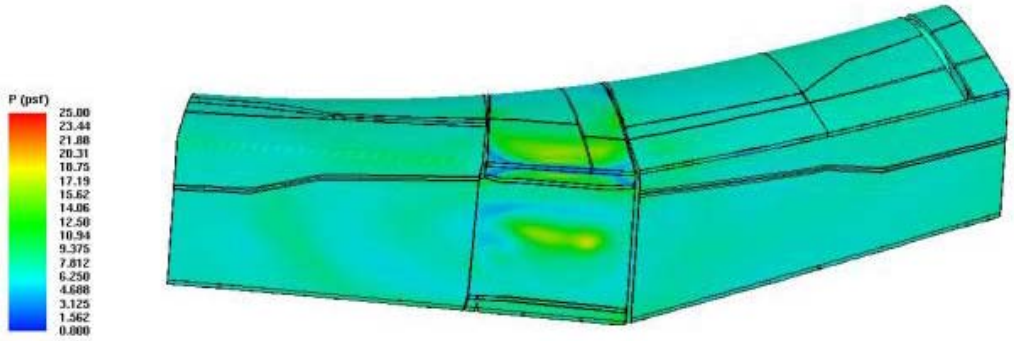

Figure 5.3.6-10 Pressure Contours on Front Spar and RCC Cavity from Panel 7 Hole Internal Flow Simulation with 15 million-cell Model

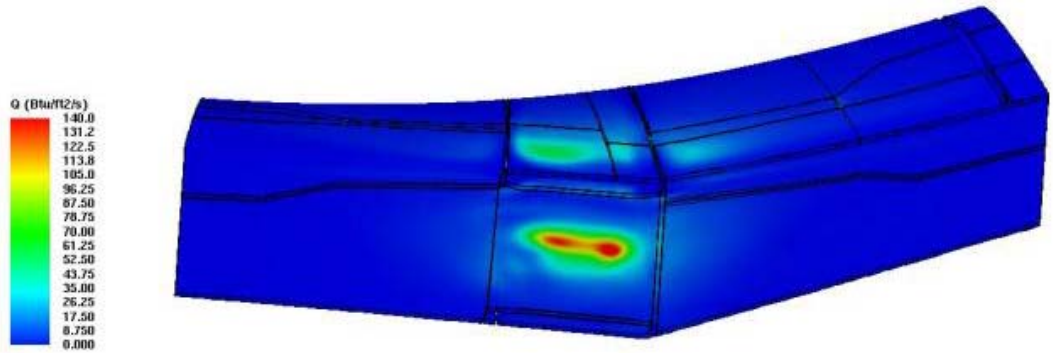

Figure 5.3.6-11 Heating Contours on Front Spar and RCC Cavity from Panel 7 Hole Internal Flow Simulation with 15 million-cell Model

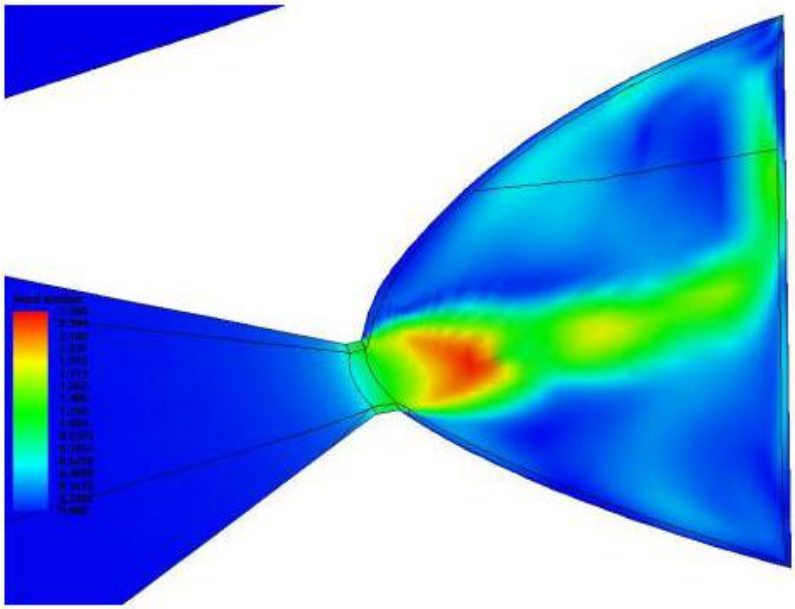

Figure 5.3.6-12 Mach Contours for Panel 7 Hole Internal Flow Simulation with 15 million-cell Model (Post-processed with every other points)

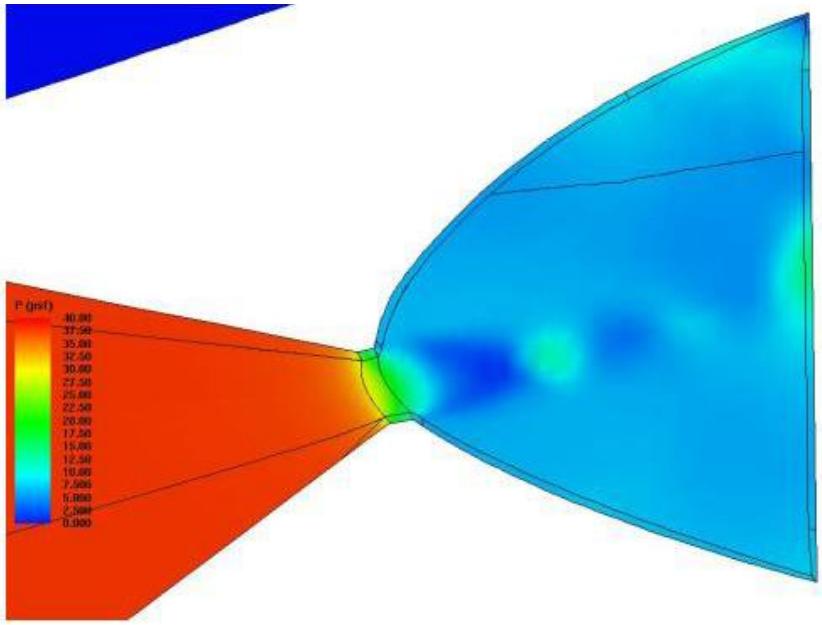

Figure 5.3.6-13 Pressure Contours for Panel 7 Hole Internal Flow Simulation with 15 million-cell Model (Post-processed with every other points)

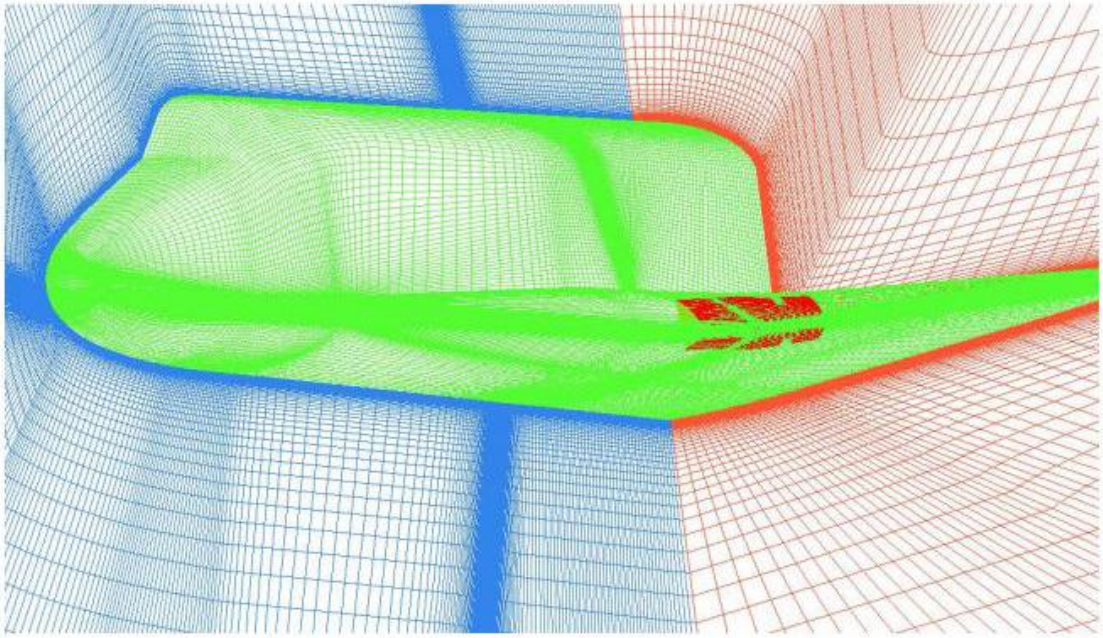

Figure 5.3.6-14 Grid Model for Panel 7 Hole Coupled External/Internal Flow Simulation I

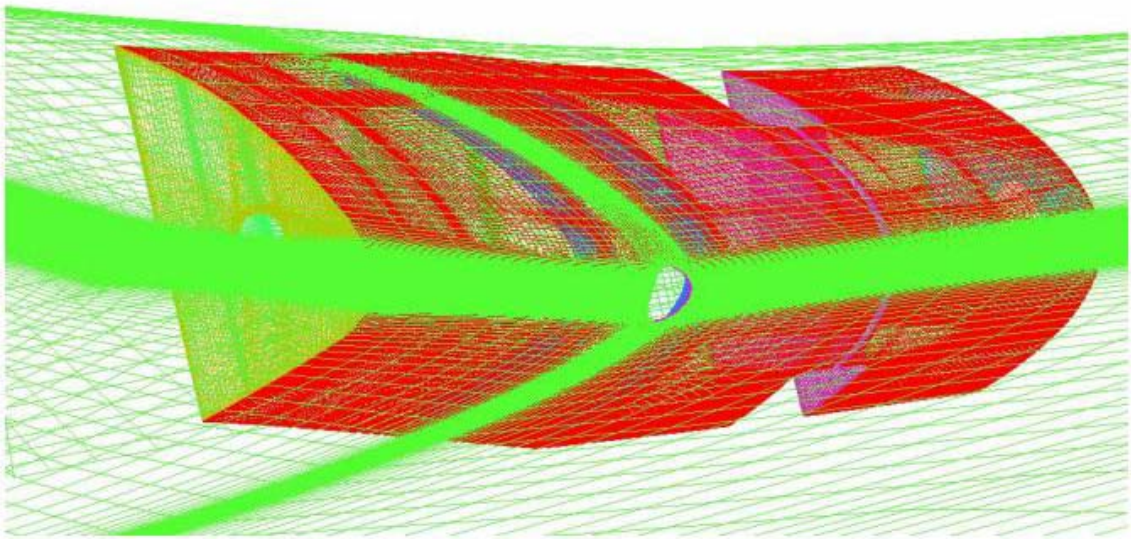

Figure 5.3.6-15 Grid Model for Panel 7 Hole Coupled External/Internal Flow Simulation I

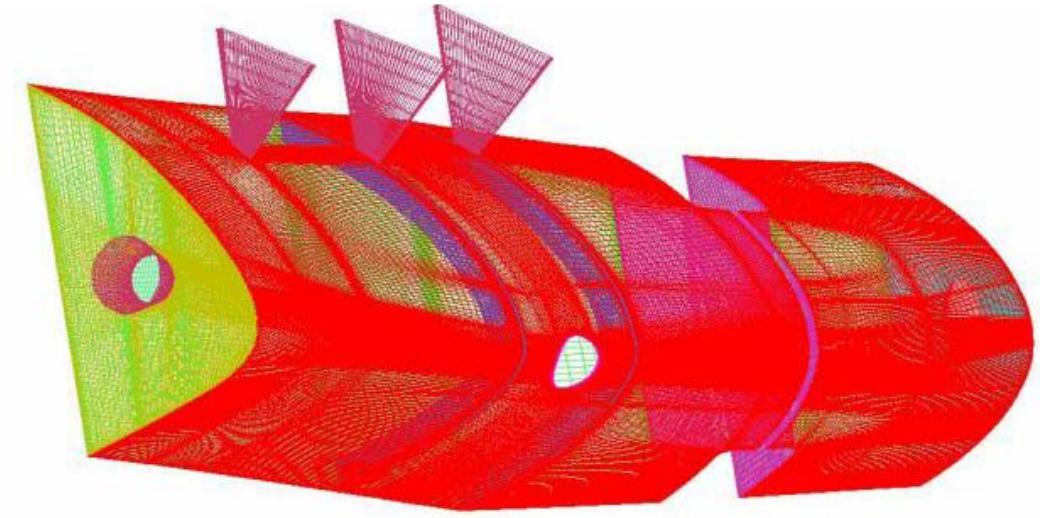

Figure 5.3.6-16 Grid Model for Panel 7 Hole Coupled External/Internal Flow Simulation I

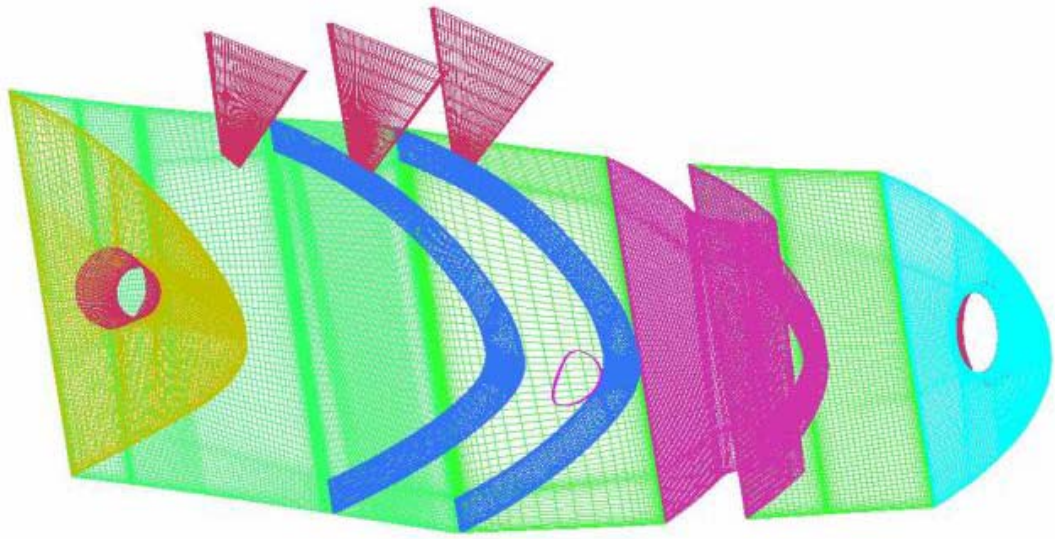

Figure 5.3.6-17 Grid Model for Panel 7 Hole Coupled External/Internal Flow Simulation I

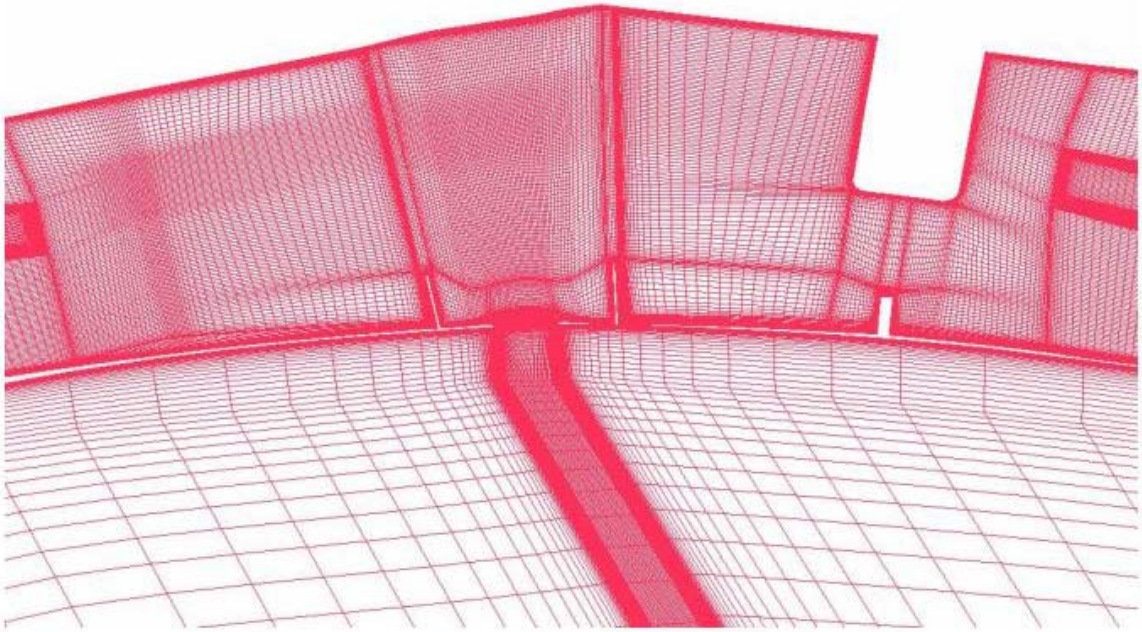

Figure 5.3.6-18 Grid Model for Panel 7 Hole Coupled External/Internal Flow Simulation I

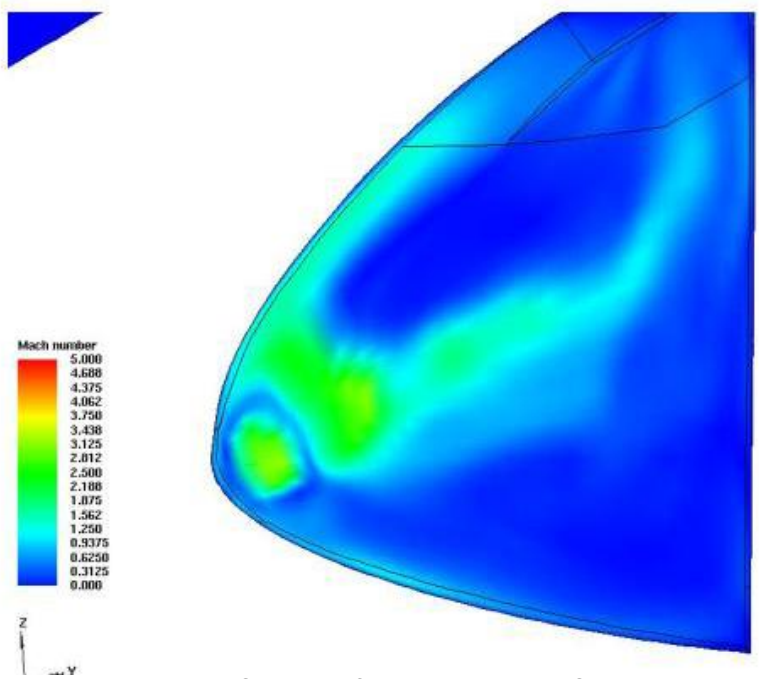

Figure 5.3.6-19 Mach Contours from Panel 7 Hole Coupled External/Internal Flow Simulation I (Postprocessed using every other points)

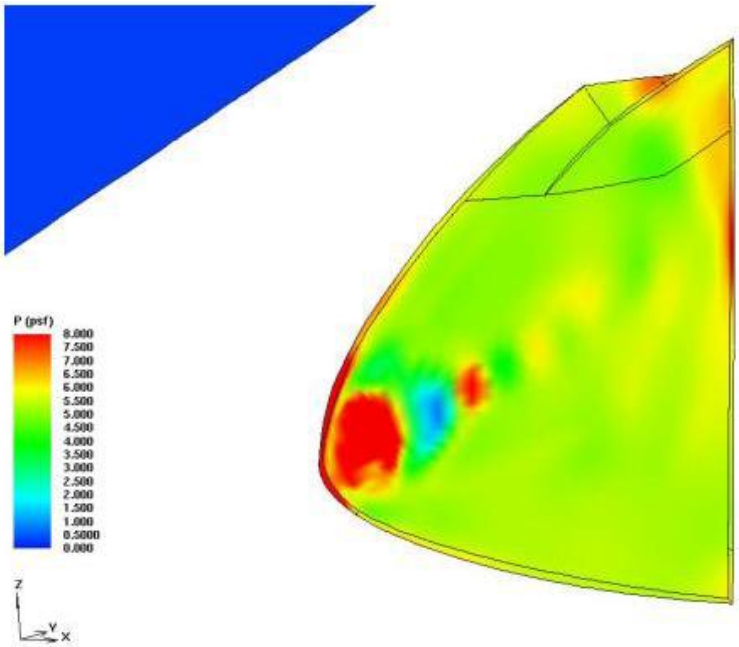

Figure 5.3.6-20 Pressure Contours from Panel 7 Hole Coupled External/Internal Flow Simulation I (Postprocessed using every other points)

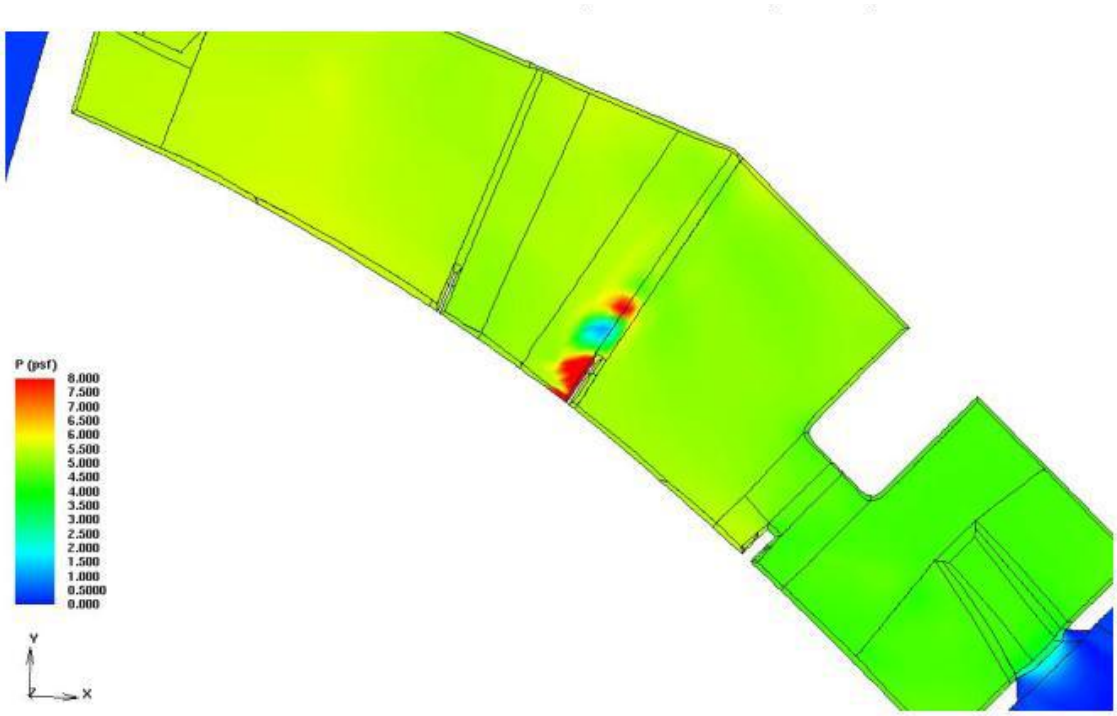

Figure 5.3.6-21 Pressure Contours from Panel 7 Hole Coupled External/Internal Flow Simulation I (Z=297.3; Postprocessed using every other points)

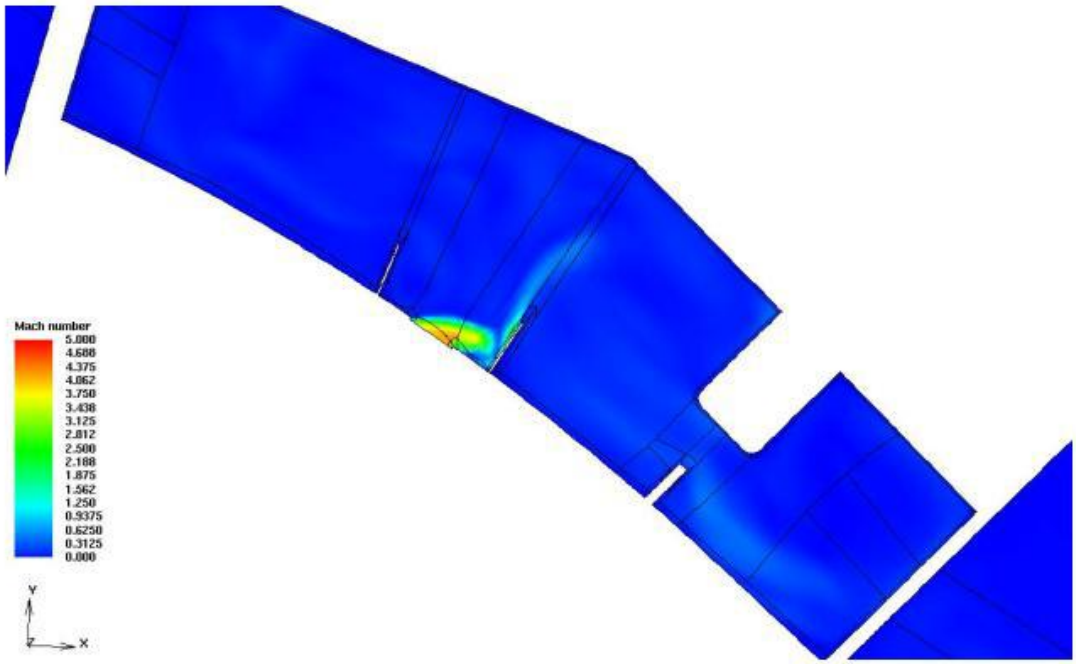

Figure 5.3.6-22 Mach Contours from Panel 7 Hole Coupled External/Internal Flow Simulation I (Z=291.6; Postprocessed using every other point)

Figure 5.3.6-23 Mach Contours from Panel 7 Hole Coupled External/Internal Flow Simulation I (Z=301.6; Postprocessed using every other point)

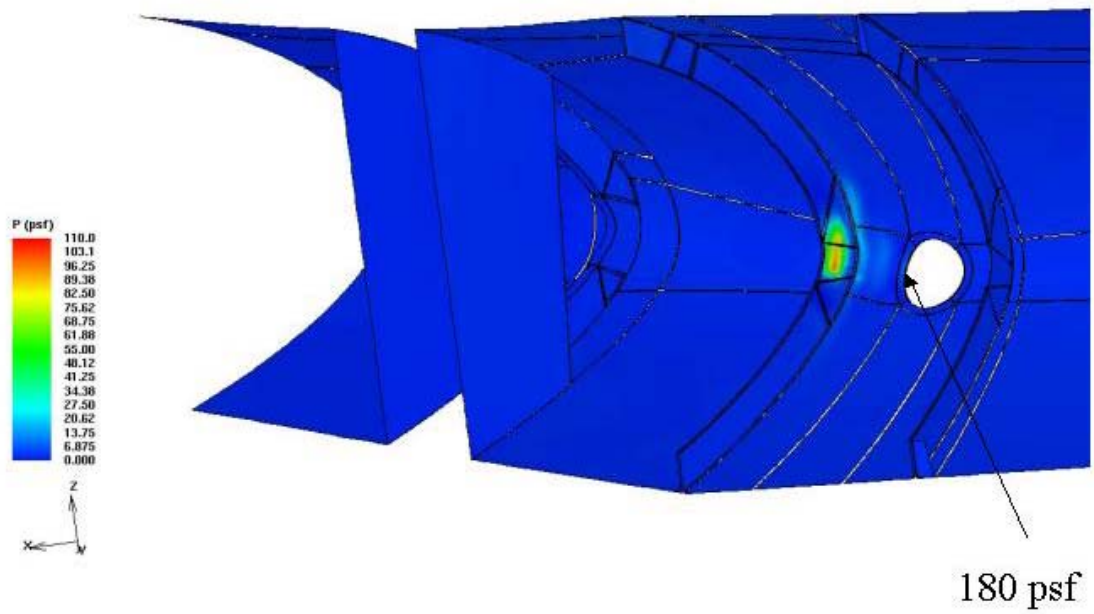

Figure 5.3.6-24 Pressure Contours on RCC Channel from Panel 7 Hole Coupled External/Internal Flow Simulation I

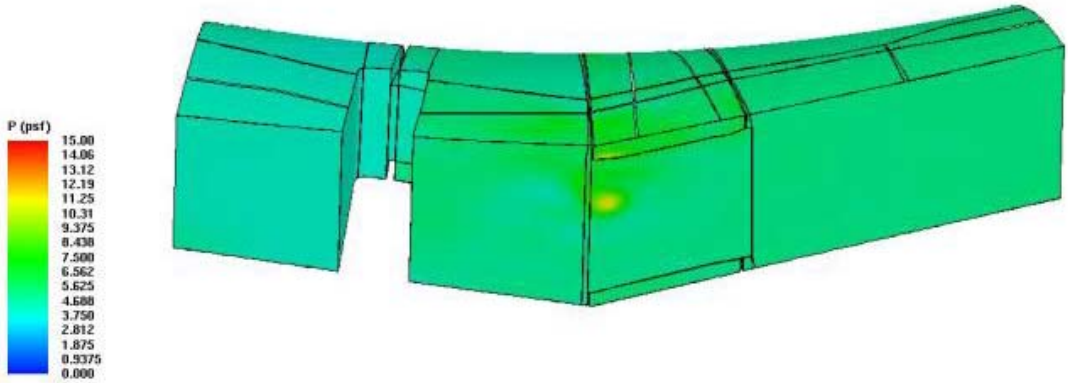

Figure 5.3.6-25 Pressure Contours on Front Spar from Panel 7 Hole Coupled External/Internal Flow Simulation I

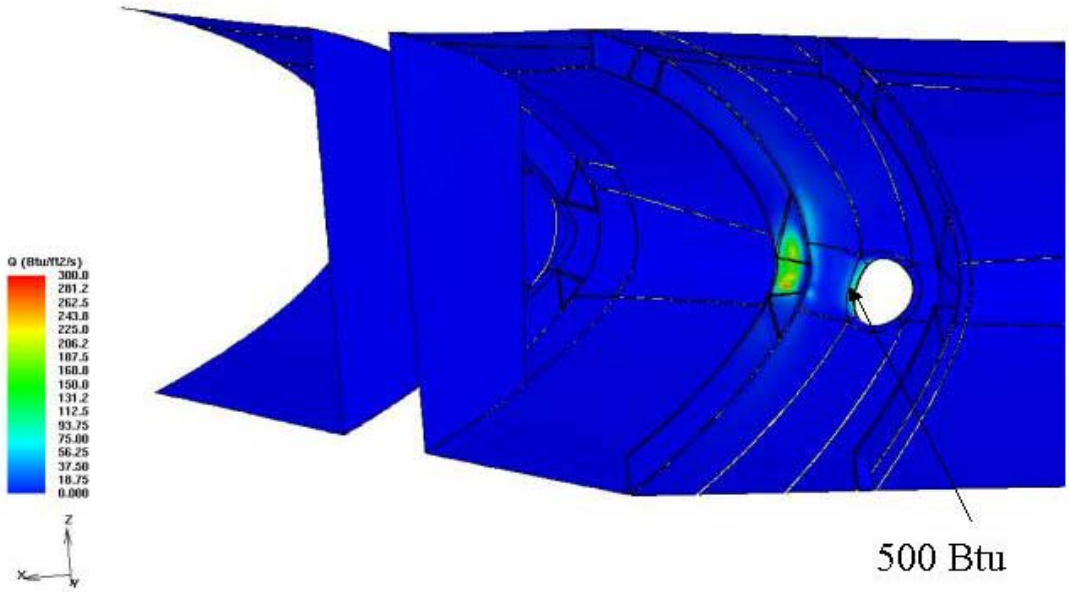

Figure 5.3.6-26 Heating Contours on RCC Channel from Panel 7 Hole Coupled External/Internal Flow Simulation I

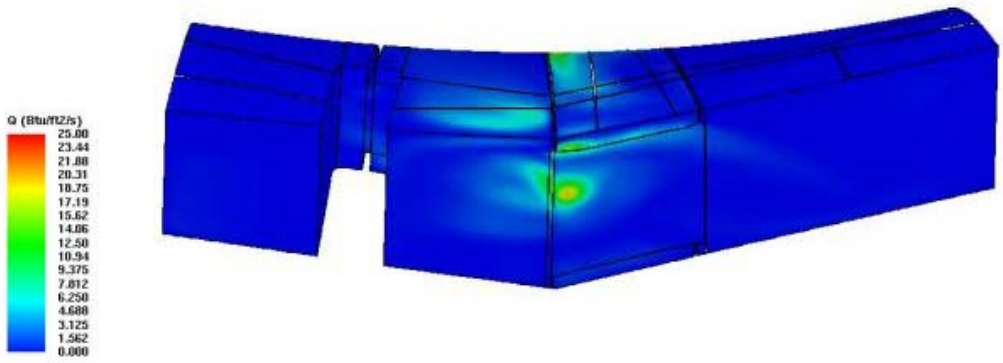

Figure 5.3.6-27 Heating Contours on Front Spar from Panel 7 Hole Coupled External/Internal Flow Simulation I

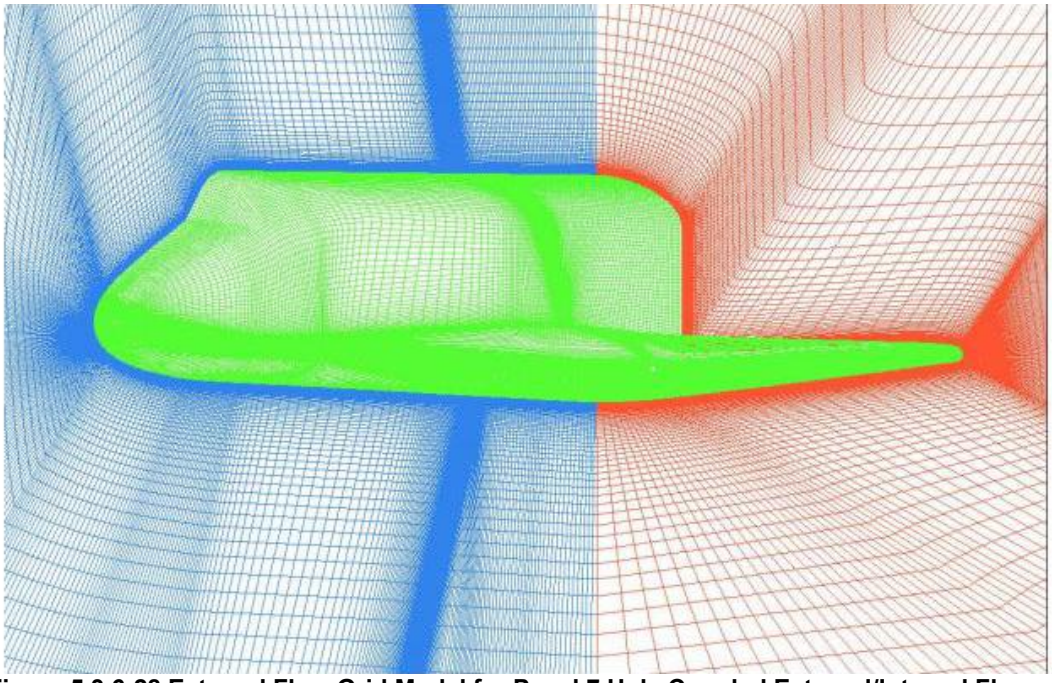

Figure 5.3.6-28 External Flow Grid Model for Panel 7 Hole Coupled External/Internal Flow Simulation II

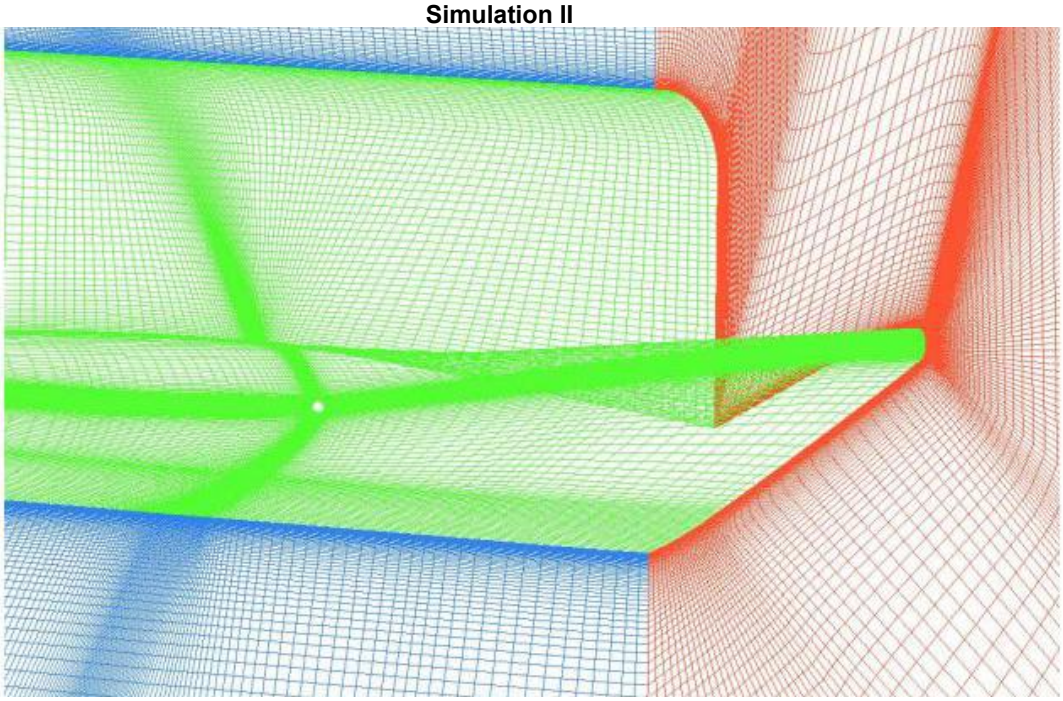

Figure 5.3.6-29 External Flow Grid Model for Panel 7 Hole Coupled External/Internal Flow Simulation II

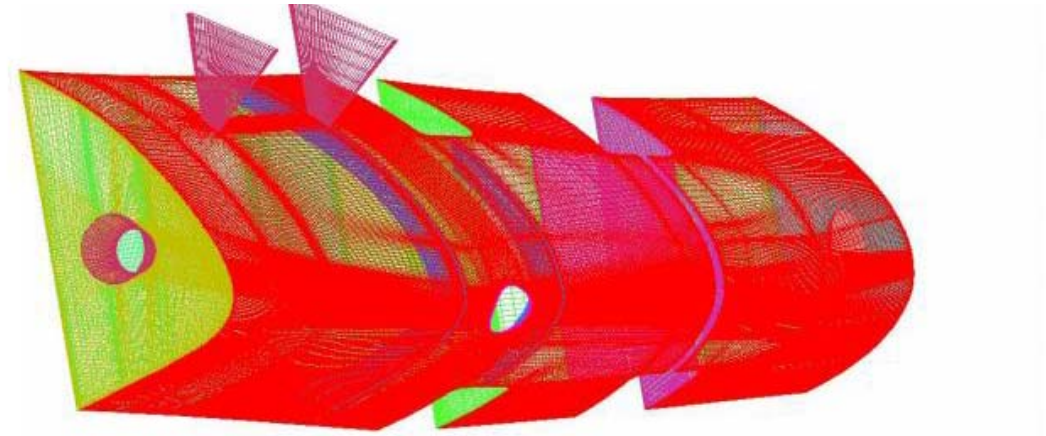

Figure 5.3.6-30 Internal Flow Grid Model for Panel 7 Hole Coupled External/Internal Flow Simulation II

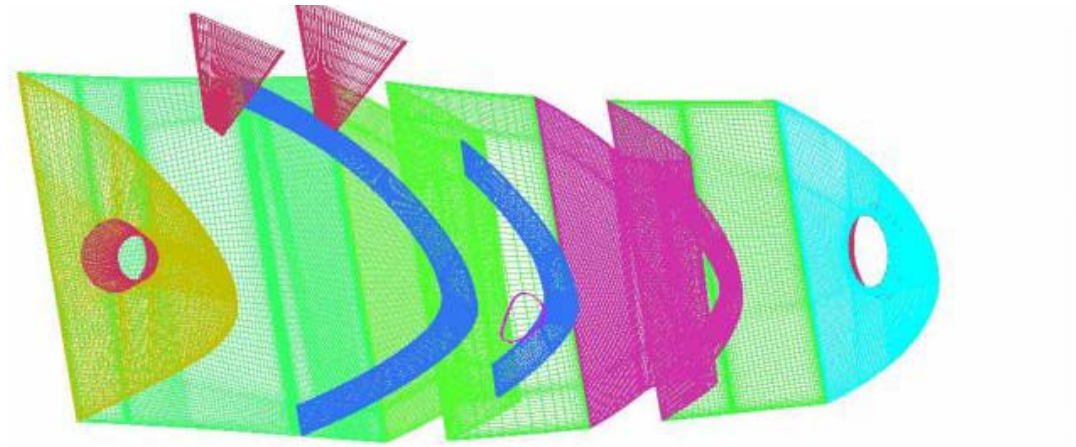

Figure 5.3.6-31 Internal Flow Grid Model for Panel 7 Hole Coupled External/Internal Flow Simulation II

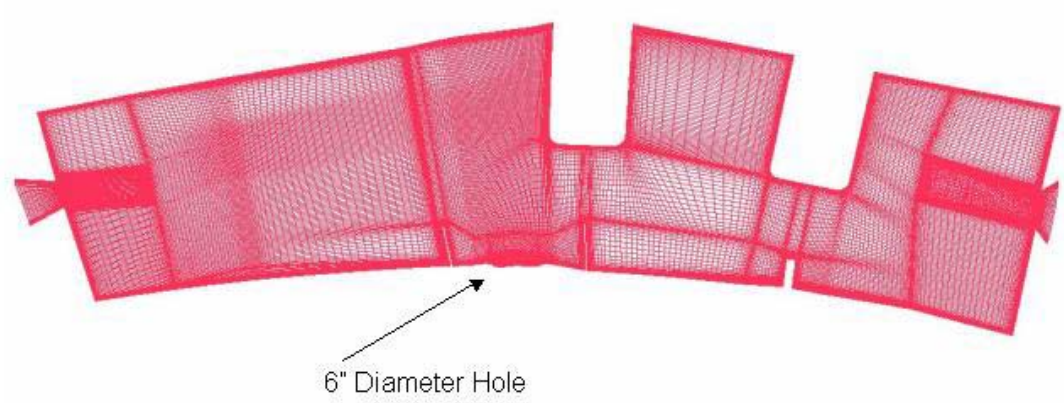

Figure 5.3.6-32 Internal Flow Grid Model for Panel 7 Hole Coupled External/Internal Flow Simulation II

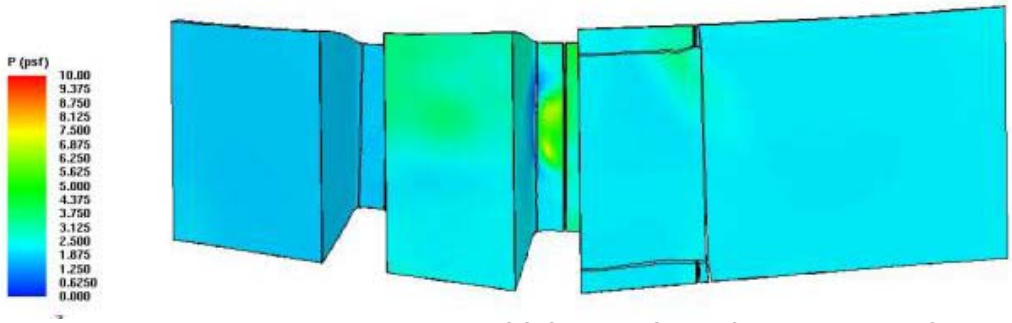

Figure 5.3.6-33 Pressure Distribution on RCC Channel Cavity for Panel 7 Hole Coupled External/Internal Flow Simulation II

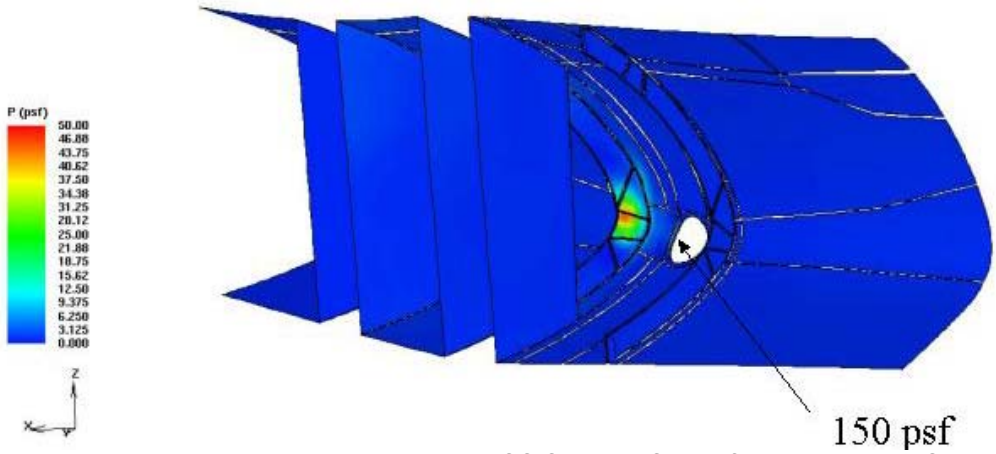

Figure 5.3.6-34 Pressure Distribution on RCC Channel Cavity for Panel 7 Hole Coupled External/Internal Flow Simulation II

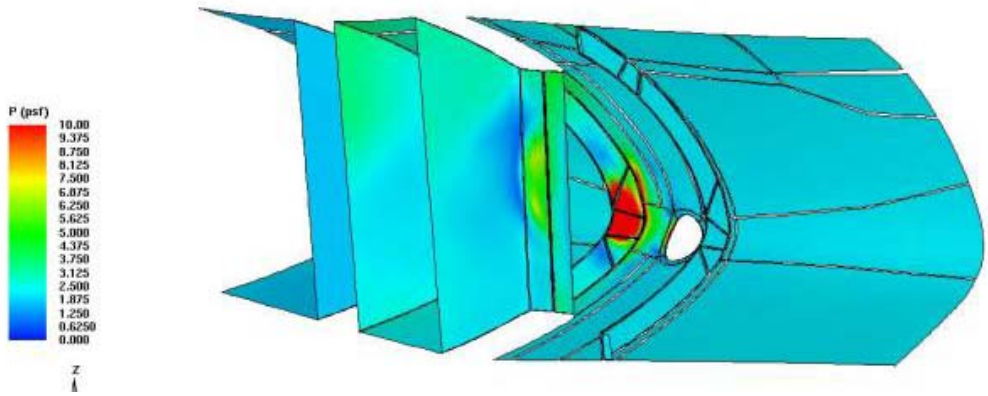

Figure 5.3.6-35 Pressure Distribution on RCC Channel Cavity for Panel 7 Hole Coupled External/Internal Flow Simulation II

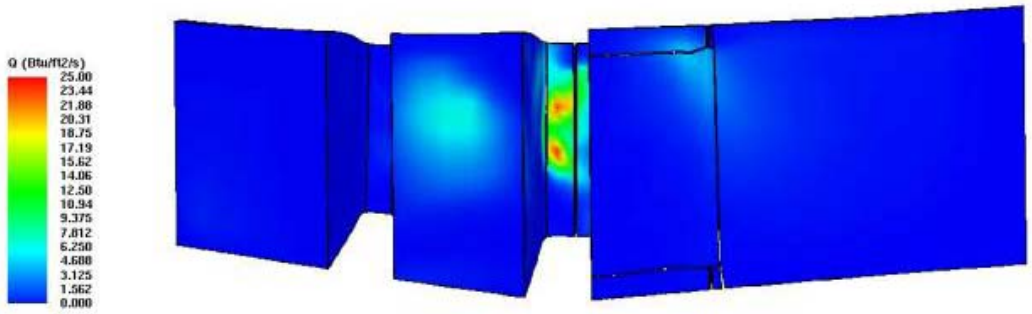

Figure 5.3.6-36 Heating Distribution on RCC Channel Cavity for Panel 7 Hole Coupled External/Internal Flow Simulation II

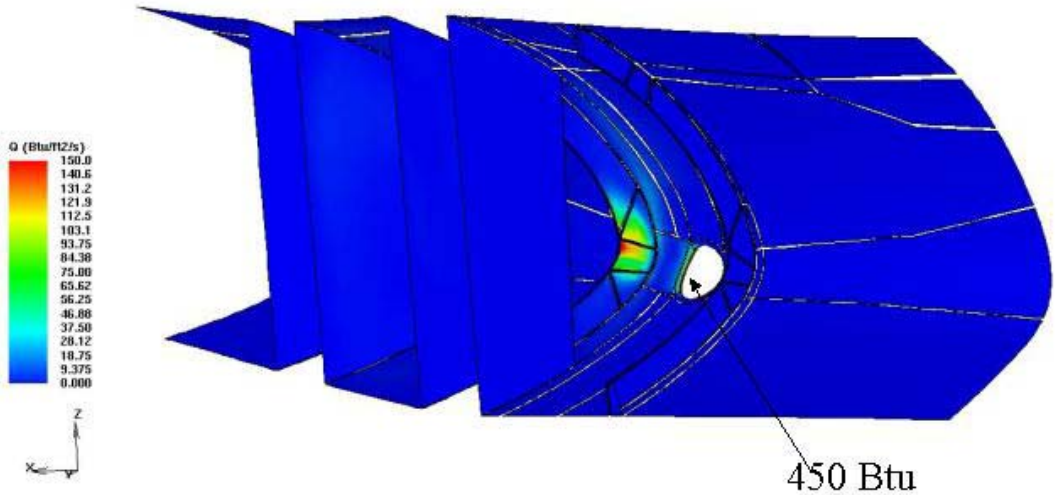

Figure 5.3.6-37 Heating Distribution on RCC Channel Cavity for Panel 7 Hole Coupled External/Internal Flow Simulation II

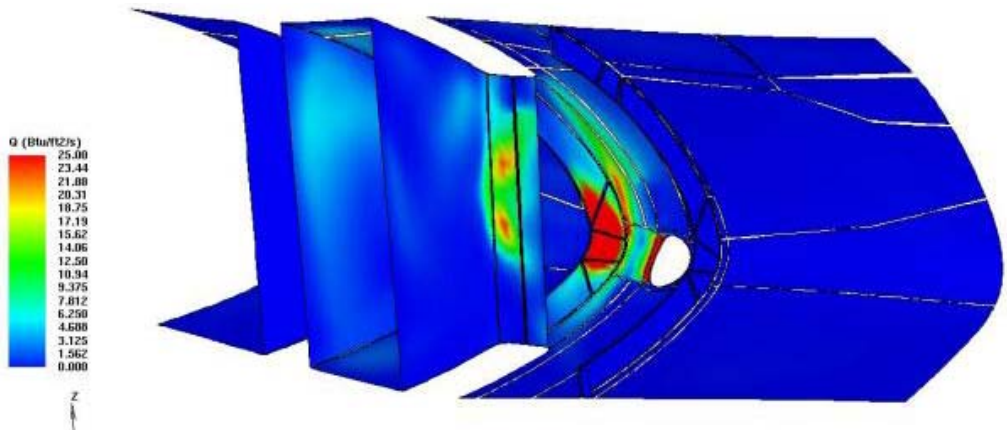

Figure 5.3.6-38 Heating Distribution on RCC Channel Cavity for Panel 7 Hole Coupled External/Internal Flow Simulation II

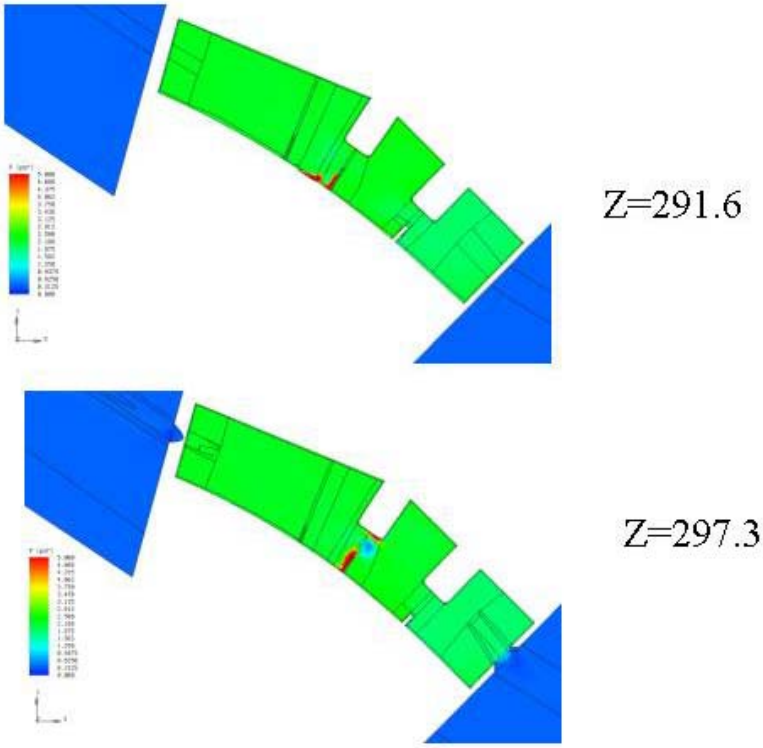

Figure 5.3.6-39 Pressure Contours in flow field for Panel 7 Hole Coupled External/Internal Flow Simulation II

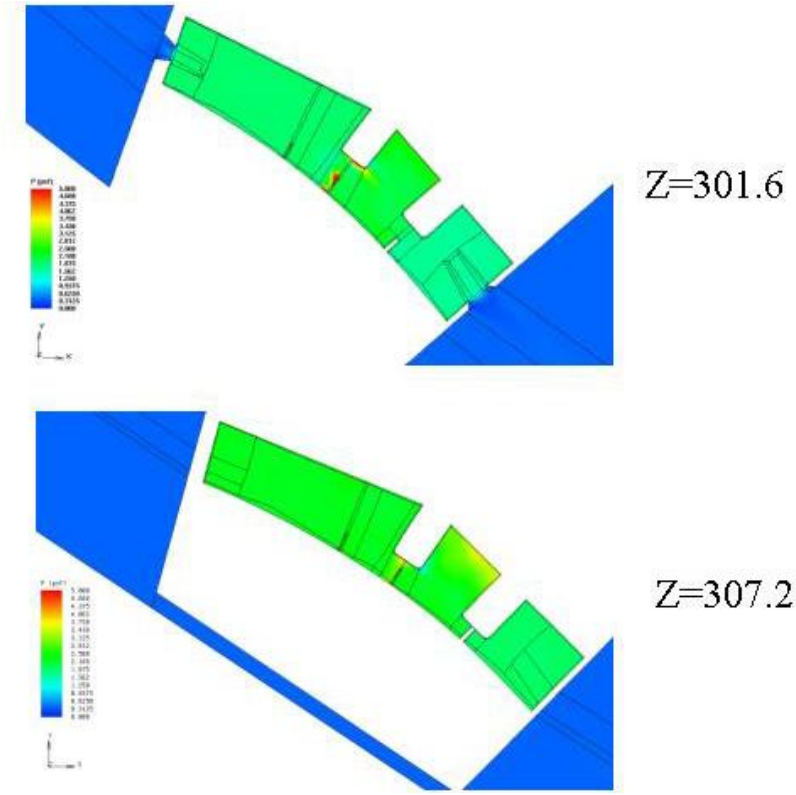

Figure 5.3.6-40 Pressure Contours in flow field for Panel 7 Hole Coupled External/Internal Flow Simulation II

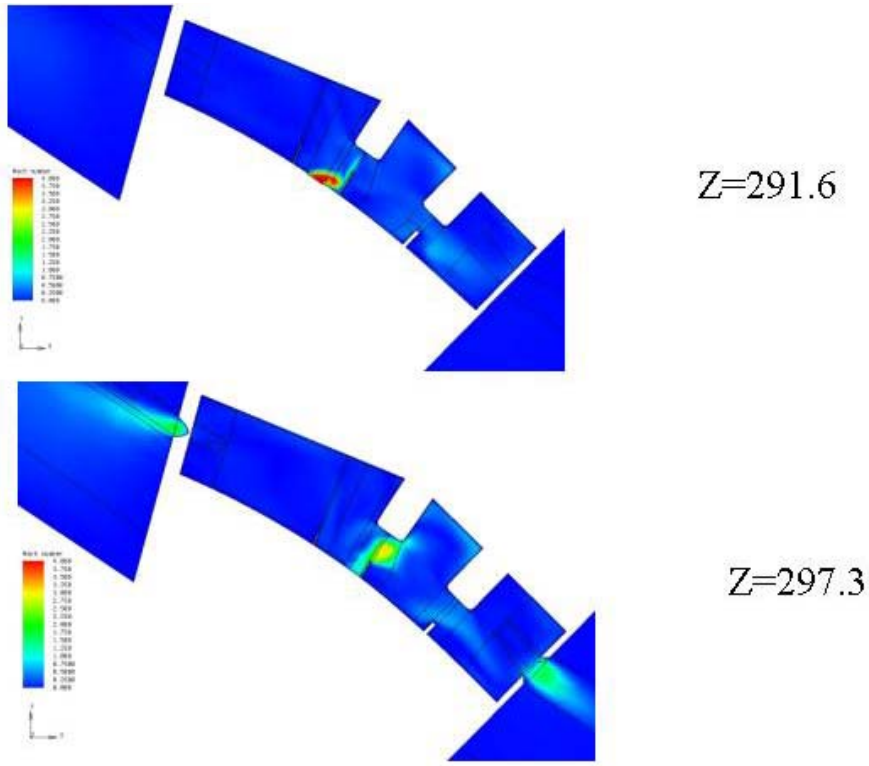

Figure 5.3.6-41 Mach Contours in flow field for Panel 7 Hole Coupled External/Internal Flow Simulation II

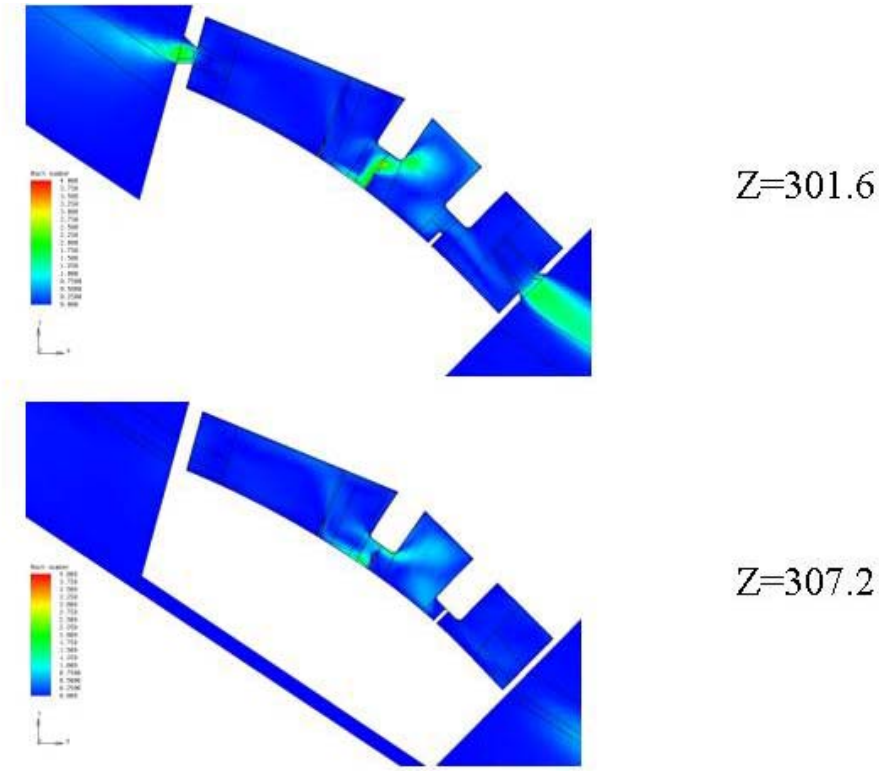

Figure 5.3.6-42 Mach Contours in flow field for Panel 7 Hole Coupled External/Internal Flow Simulation II

5.3.6.1.3 RCC Panel 8 10" - Boeing Rocketdyne

5.3.6.1.3.1 Case Description

The objective of this analysis was to compute convective heating rates on the Leading Edge Structural Subsystem (LESS) cavity internal surfaces. The intended application of the data was to enhance the engineering heat transfer models and to improve understanding of this flow field structure.

A 10 inch diameter hole was located at coordinates X=1066.00, Y=-214.75, Z=234.6 as shown in Figure 5.3.6-43. Also shown is a jet penetration analysis by NASA JSC based on a NASA LaRC LAURA external flow solution. This indicates that impingement will occur on the inboard side of the RCC 8/9 spanner beam insulators (earmuffs) given a hole at this location. These results were used as a guide for grid clustering in this analysis.

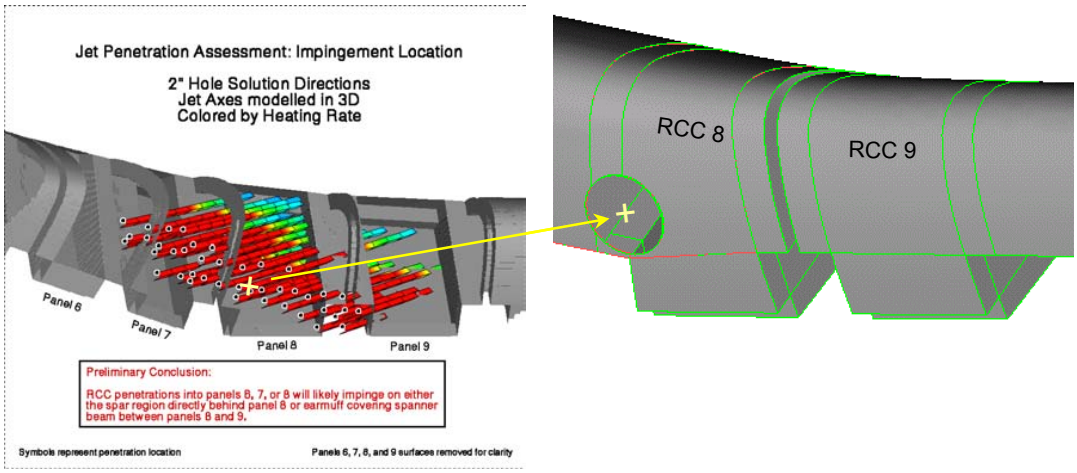

Figure 5.3.6-43 - 10 inch Hole Location Compared to Jet Penetration Analysis

5.3.6.1.3.2 *Grid/Solution Development*

The JSC model mentioned above was selected as the internal surface geometry for this analysis. This model had the benefits of possessing the RCC 7/8, 8/9, 9/10 earmuffs and the forward spar insulators (hot tubs) in between them. The hot tubs had been specifically requested for this analysis, while all three earmuffs were deemed desirable based on the anticipated flow field in this region. The negative aspects were that all of the edges are sharp, which conflicted with other models and photographs. Dimensions of key components, such as the earmuffs and hot tubs, were also somewhat uncertain since the JSC dimensions conflicted with a model used by Boeing Huntington Beach and some photographs. Due to time constraints however, the JSC model was employed while a more accurate model of the LESS was started using the Pro/Engineer CAD system. Extruded "dump" regions were added on either side of RCC 8 and 9 to enable the application of constant pressure outflow boundary conditions. The dimensions of these regions were based on the results of the 2-D T-Seal analysis (Section 5.3.6.2.2). Previous analyses had shown that a high degree of coupling existed between the internal and external flow fields. For a hole of this size, the external flow is capable of negotiating the opening while remaining supersonic. The LAURA external solution was used to provide the necessary coupling, but only a small two-zone (37 and 38) portion of it. This was carefully selected to reduce the size of the model while preserving the external solution in the region of interest (Figure 5.3.6-44).

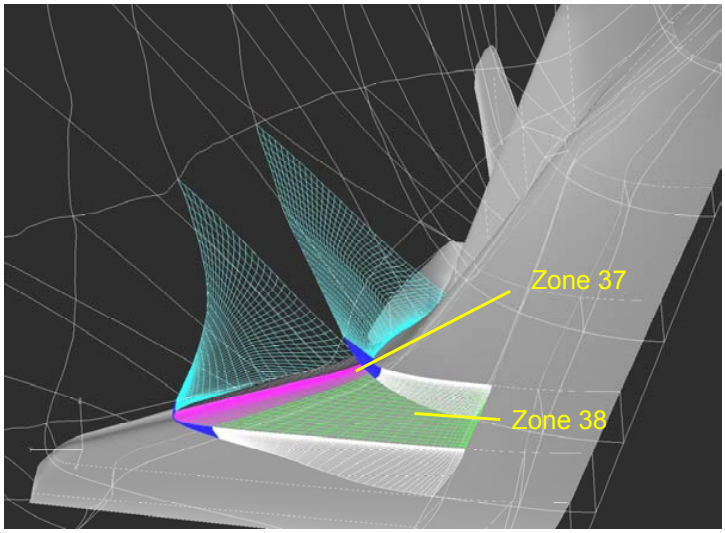

Figure 5.3.6-44 - LAURA Solution Zones Used as External Domain

The Boeing APPT system was used to generate the hybrid viscous unstructured computational grid. The unstructured approach greatly reduces the time required to generate the grid and eliminates wasted clustering cells in complex internal regions. After a number of revisions, final grids (Figure 5.3.6-45) were produced containing 4.1M elements with a wall spacing of $1.0e^{-4}$ inches (medium grid), and 4.9M elements with a wall spacing of $1.0e^{-5}$ inches (fine grid). The solutions were obtained using the Boeing ICAT code. Fully laminar flow was assumed based on the extremely low Reynolds numbers present. Liu-Vinokur equilibrium air thermochemistry and Tannehill transport properties were used. The convergence criteria were to drive net fluxes to an initial steady-state and also to drive integrated heat load in key areas to steady-state. Contours of heat flux in key areas were also plotted at different time steps.

The CFD Condition 1 trajectory point was used to define the freestream conditions. All wall temperatures were set to 3,000ºR. This corresponds to the melting temperature for the Inconel 601 outer layer of the Dynaflex surfaces such as the earmuffs and hot tubs. The pressures on the cavity outflow surfaces were established from the venting analysis (Section 5.3.5) and are presented in Table 5.3.6.1-1.

Cavity Outflow Pressure					
Cp	P/Pinf	*psf*	*psia*	*N/m^2 (Pa)*	
0.188	82.198	4.177	0.0290	200	Boeing Huntington Beach RCC7 6 inch hole
0.567	246.593	12.531	0.0870	600	This analysis

Table 5.3.6.1-1 – RCC Cavity Outflow Boundary Pressure

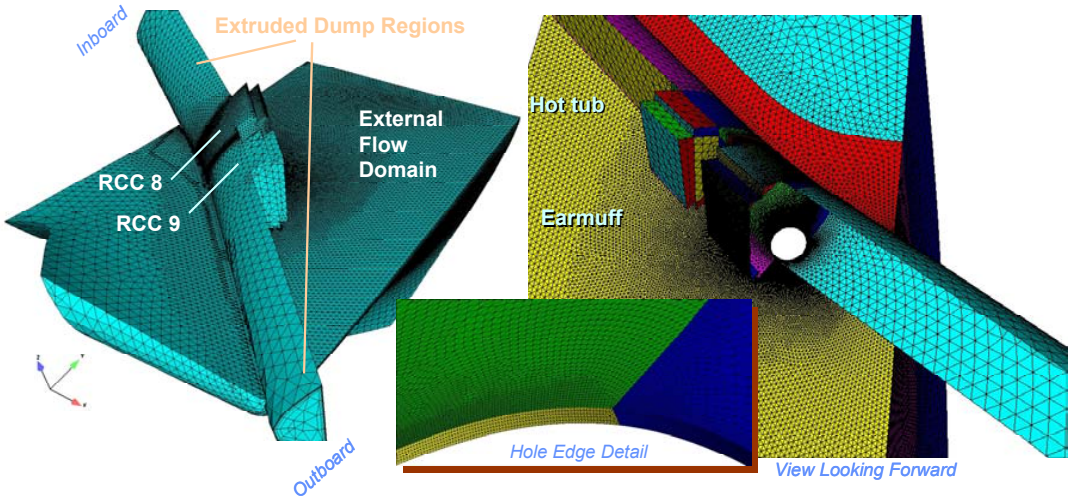

Figure 5.3.6-45 - Hybrid Viscous Unstructured Grid

5.3.6.1.3.3 Results

Major flow-structure comments

Figure 5.3.6-46 shows the flow inside the LESS cavity. The walls are colored by static pressure and the streamtubes are colored by Mach number. The primary jet issuing from the hole impinges on the inboard side of the RCC 8/9 earmuff. The jet makes a near constant-pressure turn (as observed by the small change in Mach number) and splits into two supersonic tails. This behavior was consistently observed in the T-Seal 2-D solutions (Section 5.3.6.2.2). The weaker tail (#2) impinges in upper corner of hot tub, while the stronger tail (#1) impinges in lower corner of hot tub. The latter impingement creates a transonic "re-tail" that impingements on RCC 7/8 earmuff outboard surface then shocks down to subsonic conditions. Entrainment of a subsonic vortex by the primary jet creates small supersonic impingement on RCC 8 rib. These features account for all of the supersonic flow inside the LESS cavity, and hence all of the high pressure and heat flux areas. Once subsonic, the flow twists into complex vortical patterns and makes its way to the outflow boundaries.

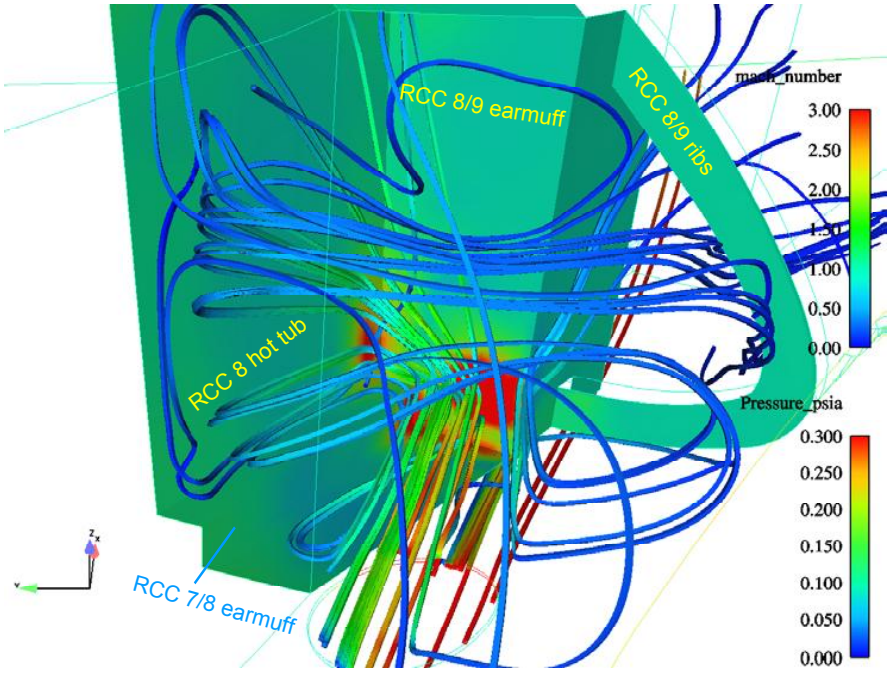

Figure 5.3.6-46 – Mach-colored Streamtubes and Wall Static Pressure Viewed from in Front of Leading Edge

Figure 5.3.6-47 shows static pressure on the walls and Mach number on a cutting plane. The cutting plane includes the internal and external flow fields. The external flow captured by the hole includes all of the wing boundary layer and some of the local freestream. Recall that the local freestream has been processed through the vehicle shock envelope that is oblique in this area. The captured flow expands through a 10° turn into the hole and forms the primary jet. The jet expansion is small internally since the pressure ratio due to the turn is only about 1.9. The primary jet then encounters a near-normal (80°) impingement onto the RCC 8/9 earmuff. The resulting stagnation pressure exceeds freestream-normal shock pressure due to recompression by oblique vehicle shock. Supersonic tail #2 is observed moving vertically along the earmuff.

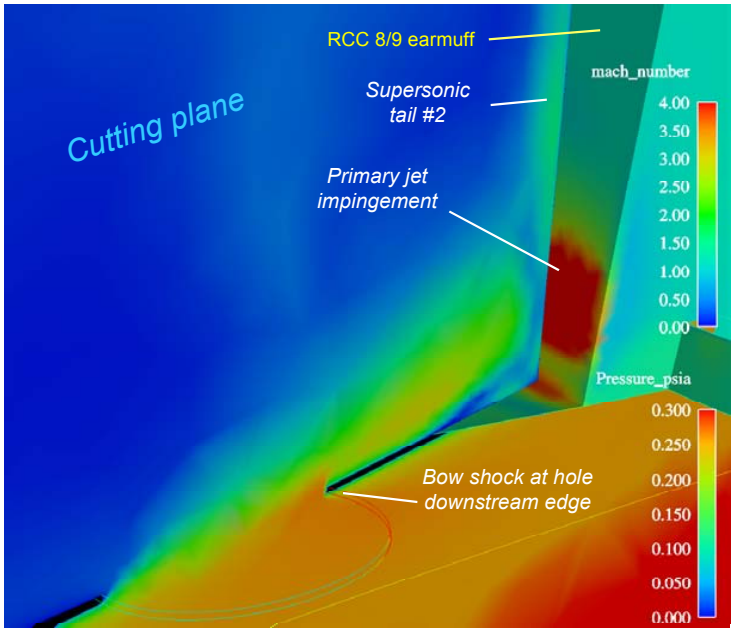

Figure 5.3.6-47 - Mach-colored Cutting Plane and Wall Static Pressure Detail View From in Front of Leading Edge

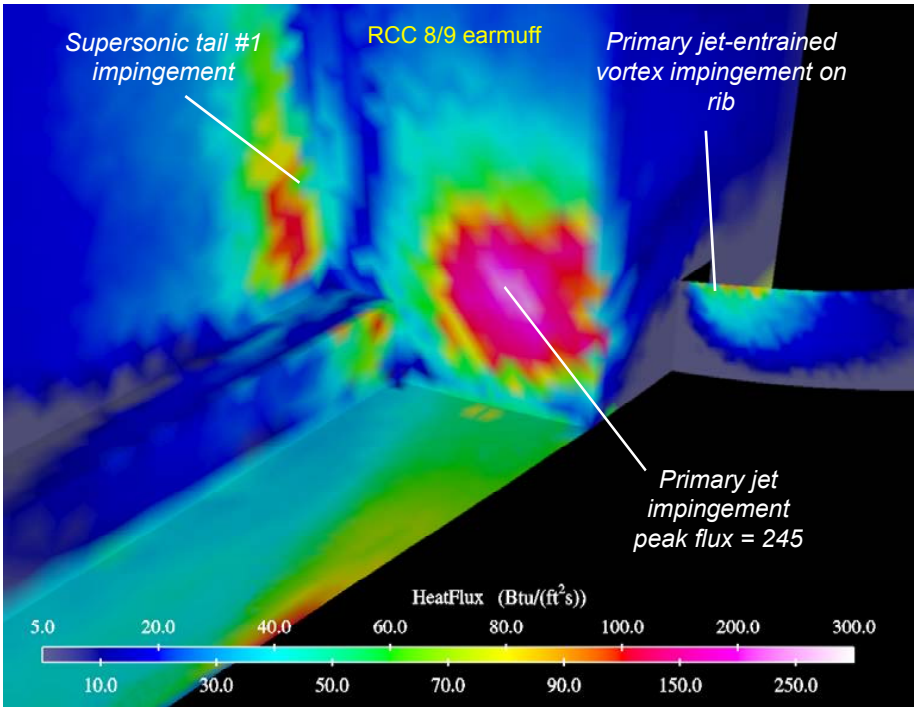

Figure 5.3.6-48 – Surface Heat Flux Detail View From in Front of Leading Edge – Medium Grid Solution

Surface heating and pressure comments

Figure 5.3.6-48 shows surface heat flux for the medium grid solution in the region where the RCC 8/9 earmuff and the RCC 8 hot tub intersect. This is the area of highest heating, as would be expected based on the pressure and Mach fields observed. The primary jet impingement produces the highest heating, while supersonic tail #1 produces the second highest. The tail flow has lost some total pressure due to shock waves encountered in the turning process that created it (Figure 5.3.6-48) so its stagnation pressure

and heat flux are lower. The RCC 8 rib encounters some heating do to the impingement of vortical flow that was reaccelerated to supersonic velocity via entrainment in the primary jet. Flow field animations were used to reveal this phenomenon as the source of that heating.

The fine grid solution is shown in Figure 5.3.6-49. The peak heat flux is 14% lower, however this occurs at a single surface cell. The integrated heat load in the regions of interest differs by only 2.3% with the fine grid solution having the lower value. Based on the proximity of these results, grid independence can be claimed. The medium grid solution was run a total of 30,000 time steps, while the fine grid solution was run a total of 32,000 time steps. Both were monitored periodically using flow visualization. No indication of unsteady flow was found, however there is still a possibility that this could occur. Many more time steps would be needed to be certain.

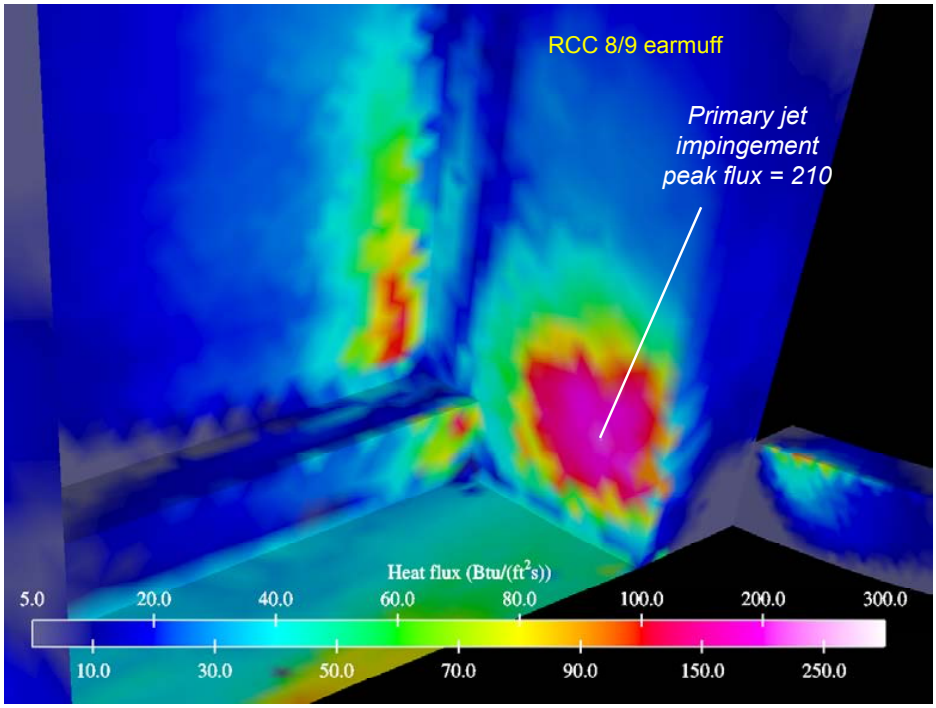

Figure 5.3.6-49 – Surface Heat Flux Detail View From in Front of Leading Edge – Fire Grid Solution

An equilibrium thermochemistry model was employed for computational efficiency based on the historical equivalence of surface heat flux from solutions using equilibrium air and those using finite-rate chemistry with a fully catalytic wall. The Dynaflex material covering the earmuff and hot tub surfaces has a 0.004" thick Inconel 601 foil. Figure 5.3.6-50 from Goulard shows that metals are highly catalytic under these conditions. The actual catalycity of the Inconel 601 and underlying materials under these conditions is not known at this time, however. Actual heat fluxes can range from 25%-80% less than the fully catalytic value if the materials have a lower catalycity.

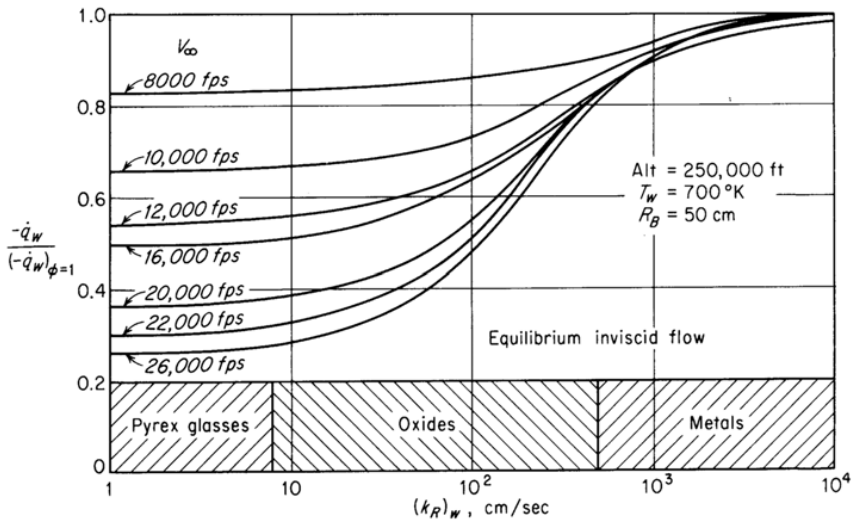

Figure 5.3.6-50 - Effect of Wall Material on Heat Flux (Goulard)

5.3.6.1.4 LaRC Solutions of Various Hole Size and Locations

The Langley Aerothermodynamic Upwind Relaxation Algorithm (LAURA) [NASA TM 4674, NASA TP 2867] was applied to external and internal flow simulations for the Columbia investigation. LAURA is a high fidelity analysis tool, specialized for hypersonic re-entry physics, utilizing state-of-art algorithms for computational fluid dynamic (CFD) simulations. Previous simulations of STS 1,2 and 5 with LAURA to resolve questions of a pitching moment anomaly (STS 1) and to validate heating predictions were published in the AIAA Journal of Spacecraft and Rockets in 1994 [JSR Vol. 31 No. 3]. All of the current simulations specify laminar flow of air in chemical nonequilibrium (N, O, N_2, O_2, NO) and thermal equilibrium. Only CFD point 1 is simulated with freestream conditions: V_∞ = 24,116 fps (7350.6 m/s), ρ_∞ = 7.5681 x 10^{-8} slugs/ft^3 (3.9005 x 10^{-5} kg/m^3), T_∞ = 391.2° R (217.3 K), α = 40.1681 deg., and time = 13.50.53.0 GMT. The external flow simulations are implemented on the shared, baseline grid developed for the External Environments Team. The baseline grid is modified to allow coupling of the external flow with flow through a breach in the wing entering a vented cavity.

The simulations described in this section were generated relatively quickly and early in the investigation on the NAS Cray SV1 because simplifications were made to the leading edge cavity geometry. These simplifications enabled (1) a very quick grid generation procedure; and (2) high fidelity corroboration of jet physics with internal surface impingements ensuing from a breach through the leading edge, fully coupled to the external shock layer flow at flight conditions.

5.3.6.1.4.1 Holes in Panel 6

The following material is the first application of LAURA to flow in a vented cavity. Consequently, geometric complexity was incrementally added to better understand ensuing flow physics and effects of boundary condition specification.

Initially, quarter inch deep holes with varying diameters were inserted into the baseline, external flow solution at Panel 6. (See Figure 5.3.6-51.) The boundary condition at the bottom of the hole used a zero-order extrapolation from interior points for density and velocity and a specified reservoir pressure equal to

2 p_∞ (approximately 0.1 psf). The flow through this boundary evolved to be substantially supersonic for hole-sizes greater than two inches. The vent backpressure is sufficiently low to maintain at least sonic conditions through the vent and is characteristic of leeside levels.

The two-inch-hole simulation was then expanded to include an internal cavity extruded from the backside of panel 6. The cavity was roughly 1ft x 1ft x 1ft but its shape evolved from an ad-hoc grid generation process. A two-inch vent hole was included at the far end of the cavity. Flow through the breach is fully coupled to the external flow and the vent boundary condition was transferred to its new location.

Methodology
An in-house utility to insert structured grids defining Reaction Control System (RCS) jets through the outer mold lines (OML) of hypersonic vehicles was modified to define a quarter-inch deep, circular hole through the leading edge of shuttle orbiter wing. The modified surface grid blends smoothly with the baseline external grid as shown in Figure 5.3.6-52. A detail of the surface grid defining the hole is shown in Figure 5.3.6-53.

Taking the inserted, rectangular domain surrounding the breach shown in Figure 5.3.6-52 and creating a quarter-inch offset orthogonal to the OML produced the near wall of the cavity. This surface was extruded into the interior in a direction defined by the axis of the hole. An initial cell size taken from the external flow domain was applied. A constant growth factor (1.20) grows the grid off the wall for 32 cells and then an inverse factor is applied for another 32 cells to resolve a boundary layer on the opposite wall. Sidewall boundary-layer resolution is achieved with a similar procedure in which additional points are added in directions defined by an extrapolated coordinate line. A view of this extruded cavity is shown in Figure 5.3.6-54.

Immediate vent (No internal cavity)
These simulations provided early evidence that the flow through a two-inch diameter (or larger) breach entered the cavity with significant retention of external flow directionality. A normal jet into the cavity was not an appropriate model for these conditions at CFD Point 1 (Mach 24). The breach diameters were of the same order or larger than the local, external boundary-layer thickness. High impingement heating and pressures on the downstream lip of the breach are computed. It is likely that hole shape would evolve as a slot cut in the direction of the external streamlines as shown in Figure 5.3.6-51. In the case of the six-inch diameter breach the boundary layer is fully ingested. Summary of results follow.

Two-inch hole
The contour plot of total enthalpy in Figure 5.3.6-55 shows the boundary edge as the transition from orange to red color. The total enthalpy above the boundary layer edge, outside of viscous dissipation effects, is a constant. The boundary layer thickness is roughly ¾ of the hole diameter. The pressure field and streamlines entering the breach (Figure 5.3.6-56) indicate significant retention of streamwise momentum after processing by a Prandtl-Meyer expansion emanating from the sonic line in the boundary layer. Surface heating rates exceed 264 Btu/ft^2-sec (300 W/cm^2) (Figure 5.3.6-57) and surface temperatures approach 5400° R (3000 K) (Figure 5.3.6-58) at the downstream lip of the breach where impingement is strongest. Ingested mass and energy rates are 0.00152 lb_m/s (0.000689 kg/s) and 9.4 Btu/s (9.92 kW), respectively. Boundary conditions (radiative equilibrium, finite catalytic wall) and examination of near surface grid quality (Re_{cell} of order 10 at impingement) suggest this heating rate is a lower bound. More data on grid convergence tests will be provided in the Panel 8 results to follow.

Four-inch hole
The contour plot of total enthalpy in Figure 5.3.6-59 is repeated for the four-inch diameter hole. The boundary layer edge impinges on the downstream lip. The pressure field and streamlines entering the breach (Figure 5.3.6-60) indicate even more retention of streamwise momentum as compared to the previous case for the smaller hole. Surface heating rates again exceed 264 Btu/ft^2-sec (300 W/cm^2) (Figure 5.3.6-61) and surface temperatures exceed 5400° R (3000 K) (Figure 5.3.6-62) at the downstream lip of the breach where impingement is strongest. Ingested mass and energy rates are 0.00562 lb_m/s (0.00255 kg/s) and 43.6 Btu/s (46 kW), respectively.

Six-inch hole
The contour plot of total enthalpy in Figure 5.3.6-63 is repeated for the six-inch diameter hole. The boundary layer edge and some inviscid flow at the maximum freestream total enthalpy above it are

completely ingested. The lip is impacted by streamlines carrying the total freestream enthalpy and a relatively large total pressure. The pressure field and streamlines entering the breach (Figure 5.3.6-64) show the same trends for retention of streamwise momentum as compared to the previous case for the four-inch hole. Surface heating rates again exceed 264 Btu/ft^2-sec (300 W/cm^2) (Figure 5.3.6-65) and surface temperatures exceed 5400° R (3000 K) (Figure 5.3.6-66) at the downstream lip of the breach where impingement is strongest. Of the three hole sizes, the present case should exhibit the largest heating because it is seeing undissipated flow from above the boundary layer edge. Ingested mass and energy rates are 0.0125 lb_m/s (0.00566 kg/s) and 111 Btu/s (117 kW), respectively.

Vented internal box

These simulations allowed the jet to develop naturally within the cavity and to view initial impingement and deflections of flow to other surfaces. Jet orientation is a strong function of hole depth to diameter ratio. Summary of results follow.

Two-inch hole to vented box

Figure 5.3.6-67 shows streamlines entering the breach and the ensuing reflected wave pattern producing compressions and expansions in the jet core. The jet is non-orthogonal to the back plane of the breach. It has a significant directional component defined by the external flow direction. An expansion off the upstream side of the hole overtakes a shock off the downstream side of the hole. The shock forms in response to supersonic flow from the upper portion of the boundary layer and the boundary layer edge impinging on the downstream lip. The Mach number distribution in Figure 5.3.6-68 provides additional detail of the jet entering the cavity. A sonic line sets up behind the inner edge of the breach lip shock indicating a choked condition. The interesting feature here is that the sonic line does not span the back plane of the hole but rather spans a smaller area defined by convergence of the streamlines entering from the circular border. Pressure coefficients in Figure 5.3.6-69 indicate the ambient pressure level in the cavity of approximately (1/8) $\rho_\infty V_\infty^2$. This level is attained at the back plane of the hole. The dependence of cavity ambient pressure on vent hole size has not been explored. It is interesting to note that a specification of the vent pressure immediately behind the back plane of the hole results in approximately the same ambient pressure level in the cell preceding the outflow boundary. Pressures exceeding the external pressure of approximately (1/2) $\rho_\infty V_\infty^2$ ($C_p = 1$) would effectively block ingestion of external flow.

The temperature in the shock over the downstream lip approaches 14,400° R (8000 K) in Figure 5.3.6-70. The corresponding total enthalpy profile is shown in Figure 5.3.6-71 that corresponds to the earlier result in Figure 5.3.6-55 except now the cavity beneath the hole is included. Conditions just below the boundary layer edge impact the lip to drive the large surface heating rates and surface temperatures (Figure 5.3.6-72). The impingement heating on the edge will tend to cut a slot along the surface in the external streamline direction.

The oxygen content of ingested flow is almost fully dissociated as indicated in Figure 5.3.6-73. A strong catalytic heating effect would be expected on metallic cavity walls but the finite catalytic boundary condition on the external surfaces was continued into the cavity. Also, the radiative equilibrium wall boundary condition assumes cavity walls can radiate to free space whereas the actual closed environment would restrict radiative cooling. Conductive cooling through metallic walls is not considered. Given these conditions (expected to produce lower heating rates) the surface temperatures on the cavity walls (Figure 5.3.6-74) exceed the melting point of pure aluminum at the impingement zone. Note that the breach hole through the lower surface is not visible in this figure. The vent hole on the top surface still sees temperatures that would melt aluminum.

Quarter-inch hole to vented box

A quarter-inch diameter hole was simulated to provide reference conditions in which the hole diameter was not larger than the hole depth and all hole dimensions were smaller than the local boundary layer thickness. In this case, the jet develops in an orthogonal direction to the wall as seen in the Mach number contour of Figure 5.3.6-75. Impingement heating and temperatures on the downstream lip are much more benign (Figure 5.3.6-76) because the energy content and total pressure of the impinging streamlines emerging from deep within the boundary layer is significantly dissipated. Temperatures entering the cavity (Figure 5.3.6-77) exceed 1800° R (1000 K).

5.3.6.1.4.2 Ten-inch Hole in Panel 8

These simulations were initiated in mid-May to complement ongoing simulation work on higher fidelity internal grids and to insure that sufficient corroborating data for engineering analyses could be made available as quickly as possible. However, greater fidelity to the internal geometry was requested (as compared to the ad-hoc cavity) so that jet development lengths and splash to adjoining internal surfaces may be better simulated.

A simulation plan was developed to maximize productivity in the limited, remaining time. First, the simulation of a ten-inch hole in Panel 8 into the ad-hoc cavity as described in the previous section was produced. (The grid in this case had to be post-processed by the VGM utility to compensate for problems associated with the larger ratio of local effective radius to hole diameter.) This simple simulation would next be used to initialize the cavity flow in a more realistic "chunnel" geometry generated concurrently. A grid sequencing process is used to complete the simulation and significant sharpening of the jet was observed in the transition from moderate to fine grid. When the jet boundaries sharpened, it was noted that the impingement location was under-resolved. An additional grid-processing step was required to bring a factor ten finer resolution on the wall at impingement.

The chunnel geometry was built off of the ad-hoc cavity and expanded to include the domain behind panels 7-9. The back plane was defined by the actual spar location. Two vent slots with combined area of 66 in^2 were included on the leeside, back surface. An internal core system of blocks was approximately bounded by the inner extent of ribs at the panel interfaces to accommodate possible future extensions of internal complexity. A combination of an O- and C- grid topology was used to accommodate the complex internal structure. The C-grid provides the ability to capture the rib and spar geometry while offering a decoupling of the grid requirements for stretching and clustering at the internal wall surfaces. As shown in Figure 5.3.6-78 and Figure 5.3.6-79, the C-grid easily captures the necessary chunnel features. Within the C-grid, in the bottom block, the hole in the RCC is accommodated by simply replacing the block of the C-grid with an "embedded" O-grid, which enables accurate modeling of the flow entering the chunnel. The O- and C-grid junction enables the accurate modeling of the existing geometry while offering the expandability to increasing geometric complexity without restructuring and regenerating the entire chunnel volume grid.

In the final simulation, the top vents were closed and the side core vents (combined area 79.3 in^2) were opened to enable the splash from an impinging jet to spill over a rib and through a vent. Summary of results follow.

Vented internal box

Mach number and streamlines entering the box through the ten-inch hole in panel 8 are shown in Figure 5.3.6-80. Streamlines exit a ten-inch diameter vent at the top of the box. The flow is strongly supersonic entering this cavity. The most interesting details of this simulation (that remain true for the subsequent chunnel simulations) are the high temperatures and pressures in the shock layer over the downstream lip of the hole. The high temperature (approaching 21,600° R (12000 K) in Figure 5.3.6-81) is easily explained because the lip is bathed in flow that carries the full freestream total enthalpy. The local pressure coefficient (C_p = 10) is higher than the stagnation point because the local streamlines here were processed by an oblique shock so that total pressure losses are less than those experienced in crossing a normal shock. Computed heating rates exceed 704 Btu/ft^2-sec (800 W/cm^2) in this case. When considering the factor of increase in pressure and factor decrease of local radius of curvature relative to the stagnation point one may expect this rate (ignoring ablative cooling) is a lower bound.

Chunnel with slotted leeside vents

Results in this section discuss the solution after adaptation of the finest grid to concentrate more mesh to the jet impingement point. Error norms had dropped to order 0.4 (a five to six order of magnitude decrease from the initial solution off the coarse grid). Some unsteadiness is evident when monitoring the solution but there was insufficient time to gather meaningful statistics on frequency. The jet impingement point has moved very little over about 10000 relaxation steps and it is believed that the basic flow physics presented here are correct.

Details of the jet in the cutting plane through the chunnel are presented in Figure 5.3.6-82 (total enthalpy), Figure 5.3.6-83 (Mach number), and Figure 5.3.6-84 (temperature). A tongue of high enthalpy flow persists up to the impingement point. A high temperature shock layer forms above this location. The jet initially scrapes the surface and then rises above it.

A "strip" of high pressure (Figure 5.3.6-85) and high heating rate (Figure 5.3.6-86) is evident at the relatively narrow impingement location. These figures show the sharpening of the profile associated with refinement from the medium grid to the fine grid (a factor of 2 in the i, j, and k directions). Review of solution metrics at the impingement showed high cell Reynolds number and large jump between imposed wall temperature (900° R (500 K)) and boundary cell center temperature (5184° R (2880 K)). Consequently, a grid adaptation was implemented to provide a target factor of 10 finer grid at the wall (i-direction) using a greater stretching factor for the same number of cells in the near wall blocks. Even with this refinement, the worst-case cell center temperature next to the wall was (2088° R (1160 K)). The convergence of peak impingement heating on these three sequential cases (not located at exactly the same surface mesh point) progressed from 102 Btu/ft^2-sec (116 W/cm^2) (medium grid) to 265 Btu/ft^2-sec (301 W/cm^2) (fine grid) to 635 Btu/ft^2-sec (721 W/cm^2) (adapted fine grid, Figure 5.3.6-87).

Chunnel with side vents

This side vent case (top vents now closed) was initialized from the previous top vent case with the finest grid and adaptation of grid on the impingement boundary.

The error norm for this case jumped about 4 orders of magnitude from the previous converged solution and returned to order 1 values at this "snapshot". An attempt to force the solution to advance more quickly with a constant, large time step eventually diverged. A smaller constant time step was again applied and the solution began to recover but insufficient time remained to drive it to convergence. The solution posted here is thought to have a jet impingement point that will continue to rise toward the side vent. The magnitude of jet oscillations cannot be estimated from the solution generated to date. A representative jet structure is presented in Figure 5.3.6-88 (total enthalpy) and Figure 5.3.6-89 (pressure). The basic structure is very similar to that observed in the previous case. The expansion process to sonic conditions at the side vent is displayed in Figure 5.3.6-90 (pressure) and Figure 5.3.6-91 (Mach number) in the impingement zone.

Top vent versus side vent internal surface pressures are compared in Figure 5.3.6-92. The equivalent heating comparison is presented in Figure 5.3.6-93 and Figure 5.3.6-94. Heating at impingement on the finest grid has remained between 440 and 616 Btu/ft^2-sec (500 and 700 W/cm^2).

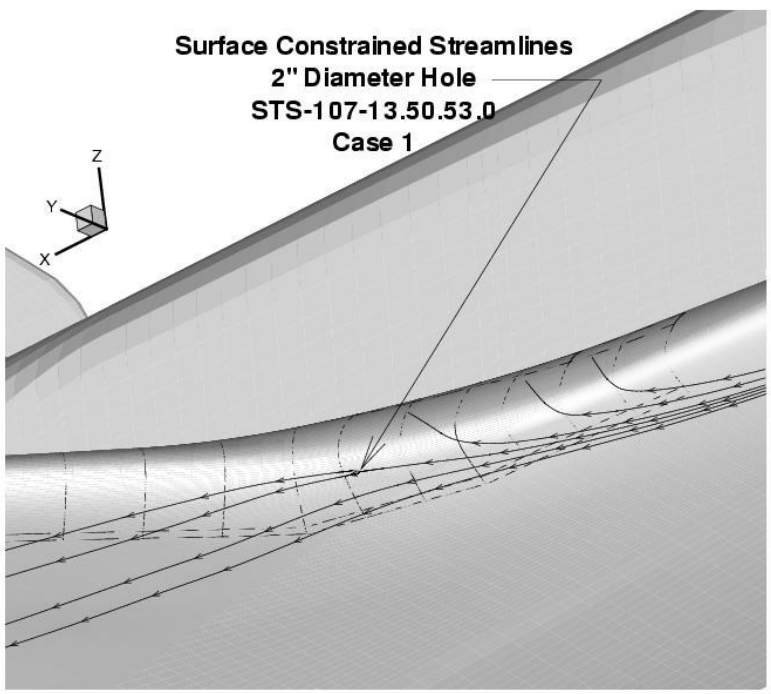

Figure 5.3.6-51 Streamlines over RCC panels on the leading edge and the location of the circular breach through the wing in panel 6.

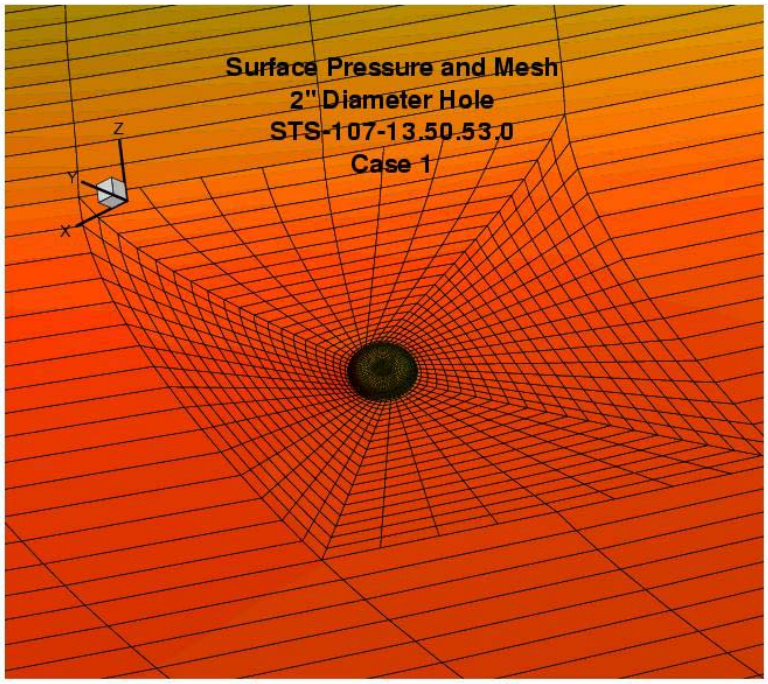

Figure 5.3.6-52: Modified surface grid in the vicinity of the hole.

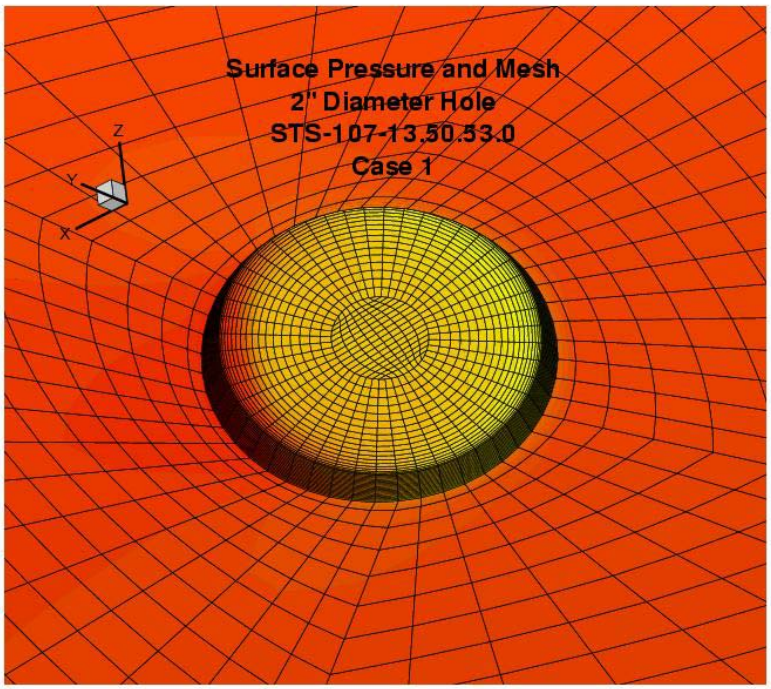

Figure 5.3.6-53: Structured grid within hole, approximately 20 cells deep and 60 cells across.

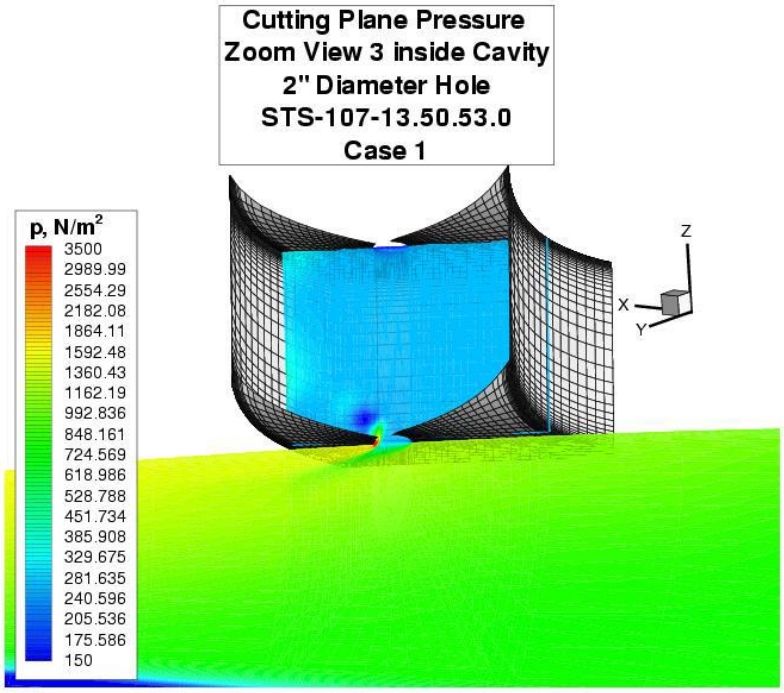

Figure 5.3.6-54: Pressure in cutting plane across breach and view of surface grid defining the vented cavity.

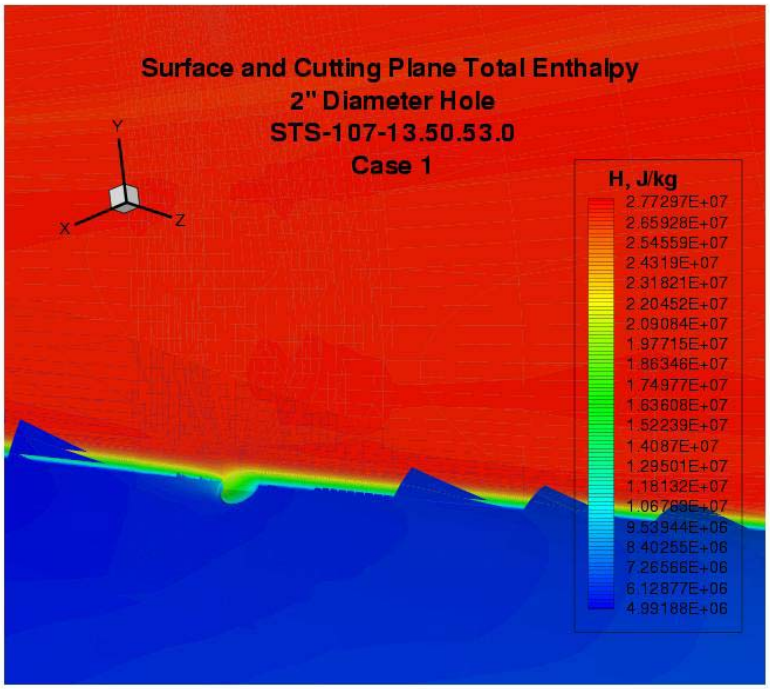

Figure 5.3.6-55: Total enthalpy in cut plane above hole showing partial ingestion of the boundary layer. (Blue jags are artifact of picture format conversion.)

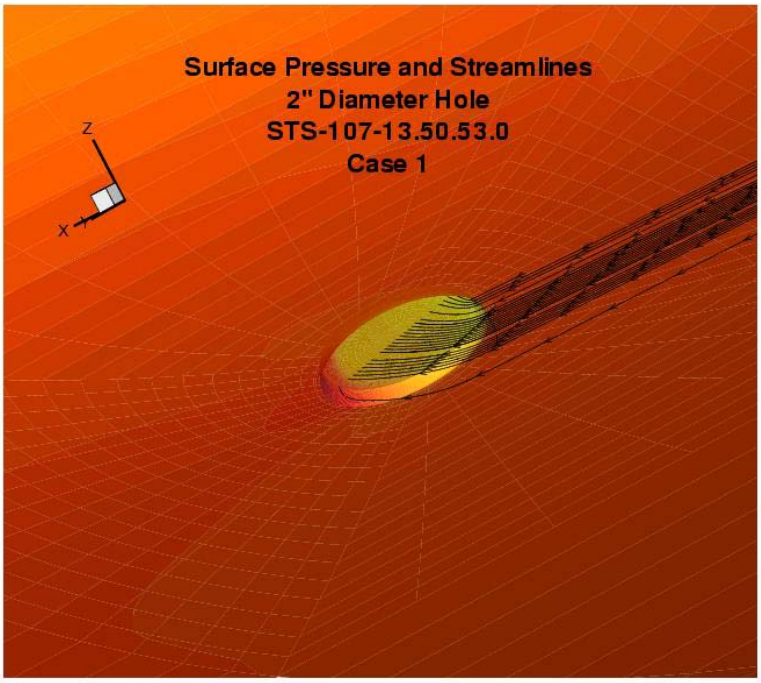

Figure 5.3.6-56: View of streamlines entering breach showing significant retention of external streamwise momentum.

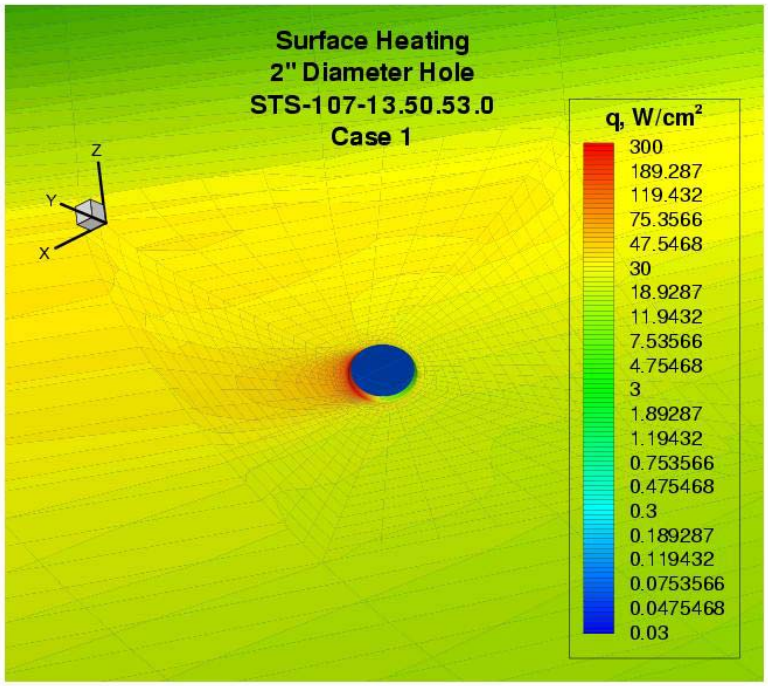

Figure 5.3.6-57: Surface-heating contours in the vicinity of the two-inch hole in Panel 6.

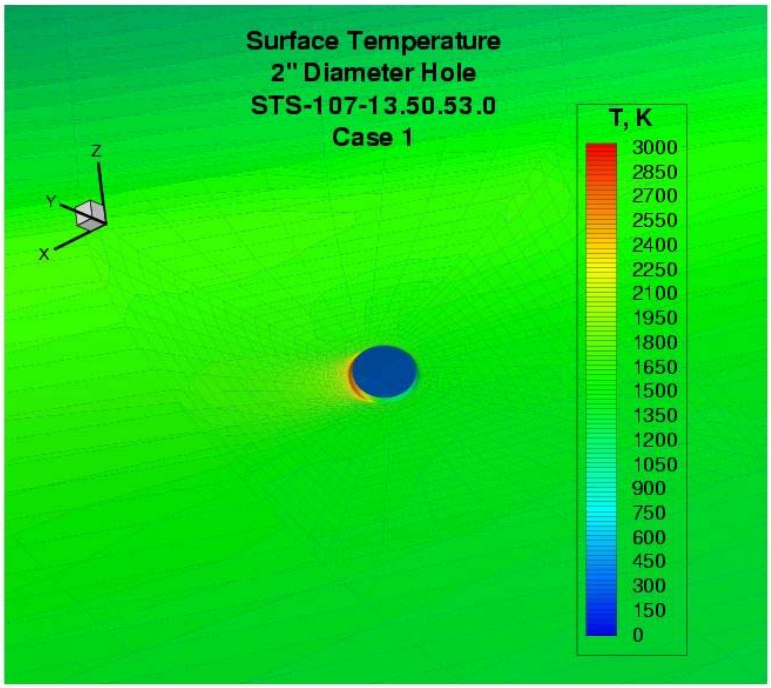

Figure 5.3.6-58: Surface temperature contours in vicinity of the two-inch hole in Panel 6.

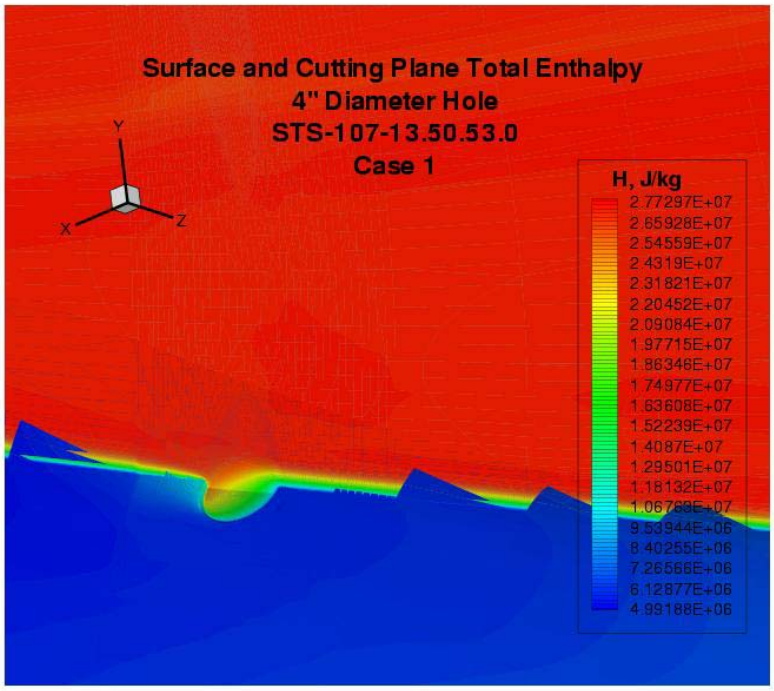

Figure 5.3.6-59: Total enthalpy in cut plane above four inch hole showing significant ingestion of the boundary layer. (Blue jags are artifact of picture format conversion.)

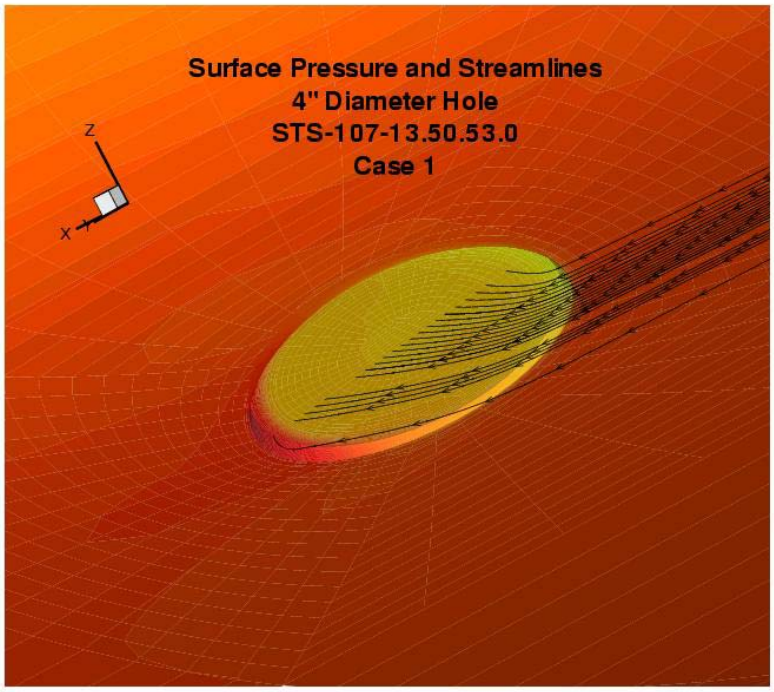

Figure 5.3.6-60: View of streamlines entering four-inch breach showing significant retention of external streamwise momentum.

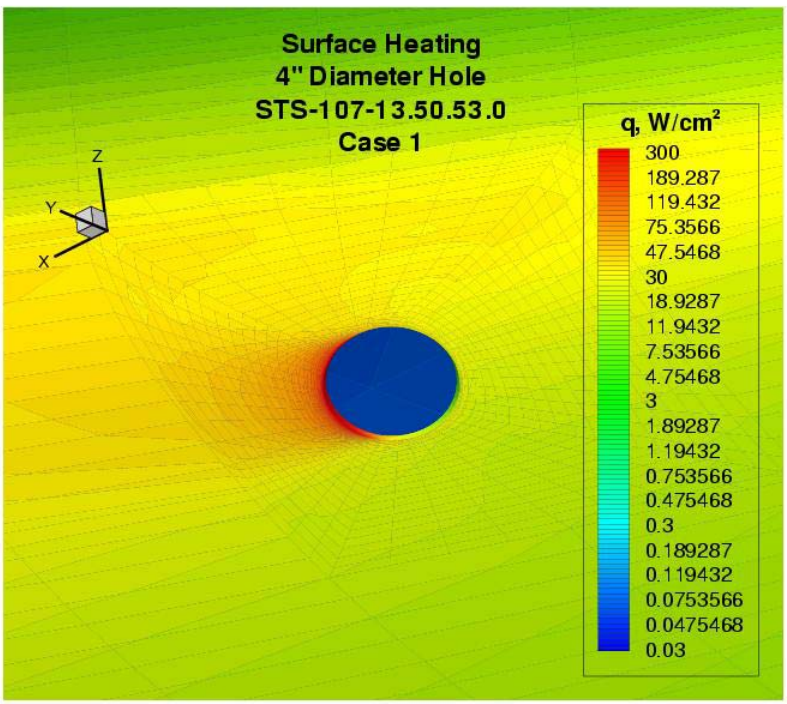

Figure 5.3.6-61: Surface-heating contours in the vicinity of the four-inch hole in Panel 6.

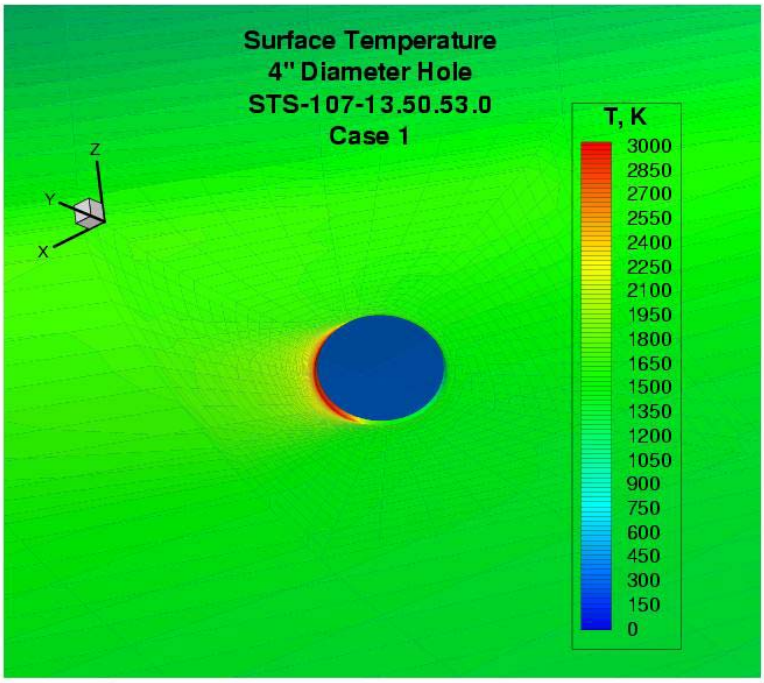

Figure 5.3.6-62: Surface temperature contours in vicinity of the four-inch hole in Panel 6.

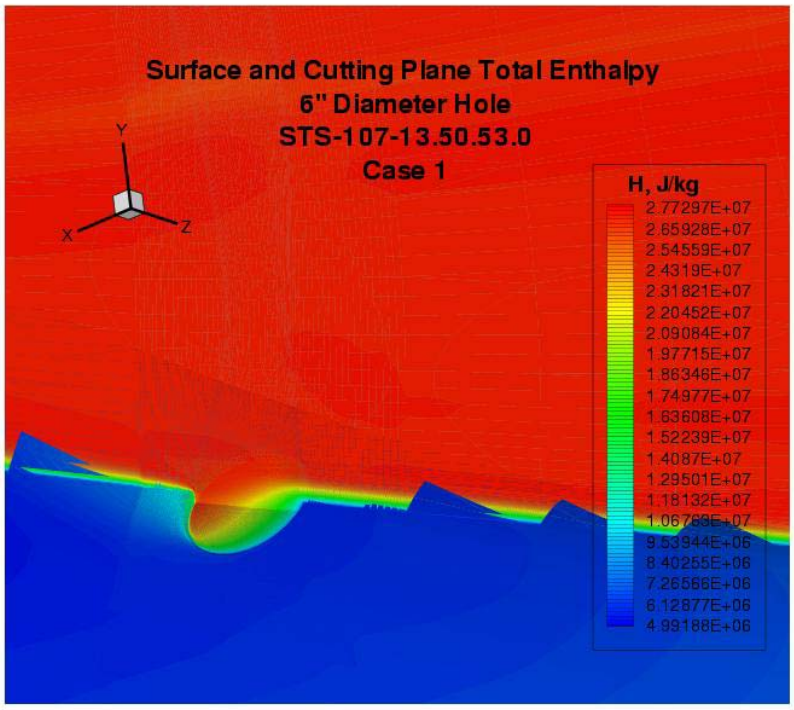

Figure 5.3.6-63: Total enthalpy in cut plane above six inch hole showing complete ingestion of the boundary layer. (Blue jags are artifact of picture format conversion.)

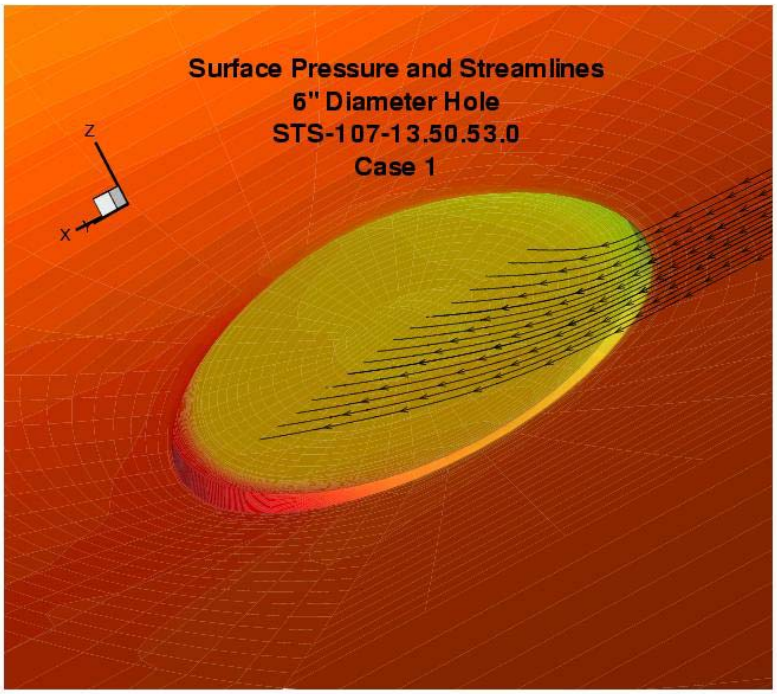

Figure 5.3.6-64: View of streamlines entering six-inch breach showing significant retention of external streamwise momentum.

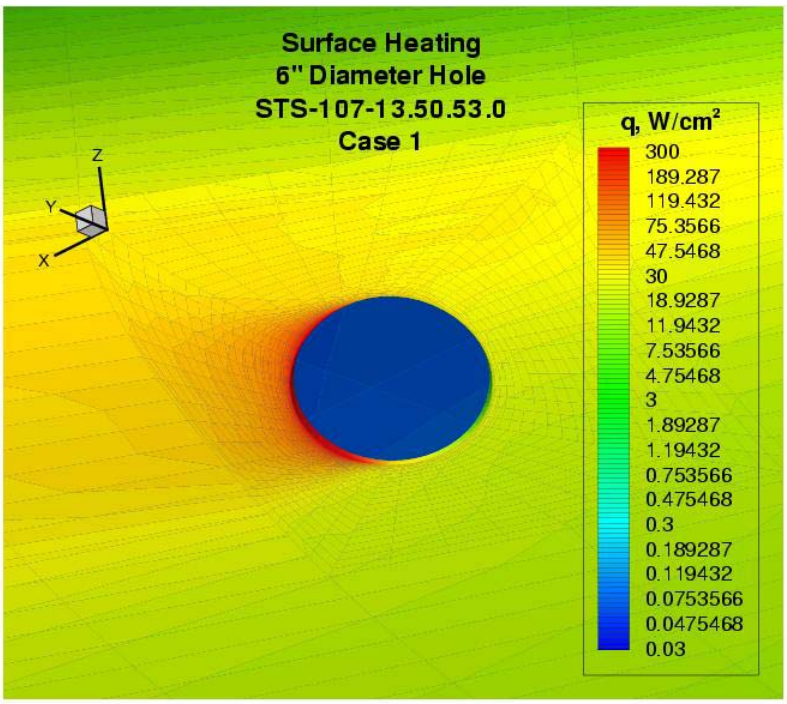

Figure 5.3.6-65: Surface-heating contours in the vicinity of the six-inch hole in Panel 6.

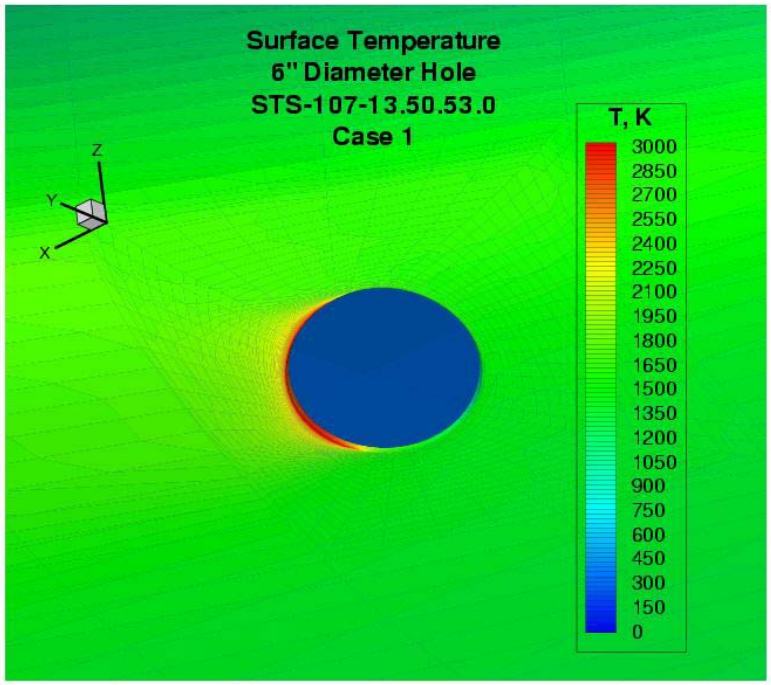

Figure 5.3.6-66: Surface temperature contours in vicinity of the six-inch hole in Panel 6.

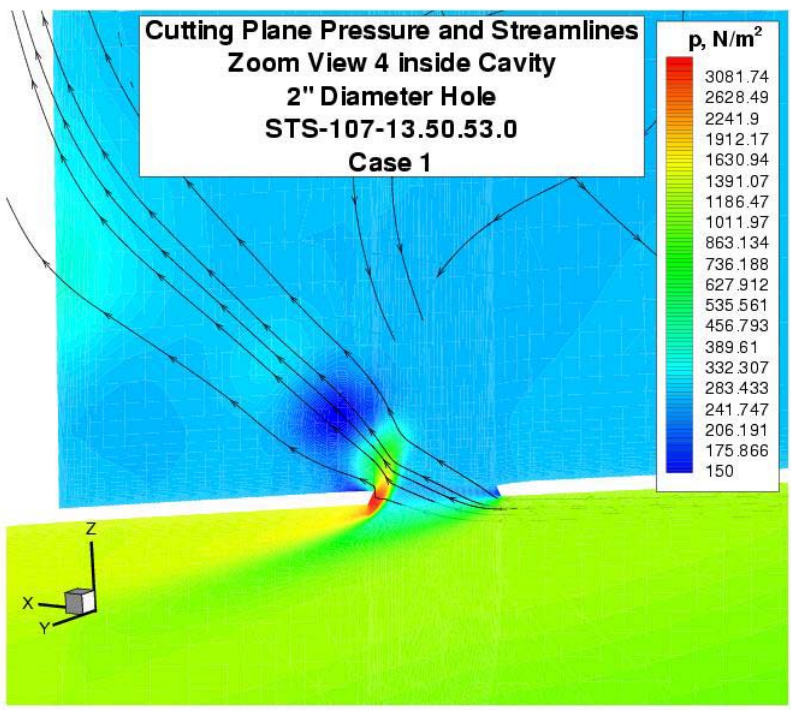

Figure 5.3.6-67: Streamlines entering the breach and pressure levels in the cutting plane. External flow direction is from the right to the left.

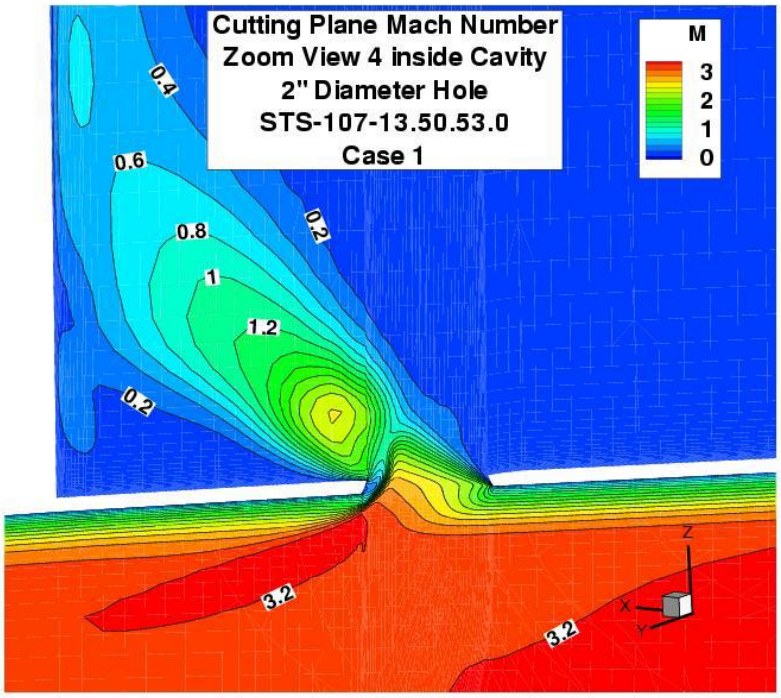

Figure 5.3.6-68: Mach number contours across the breach and in the jet entering the cavity. A sonic, choked condition sets up behind the lip shock over the downstream lip of the breach.

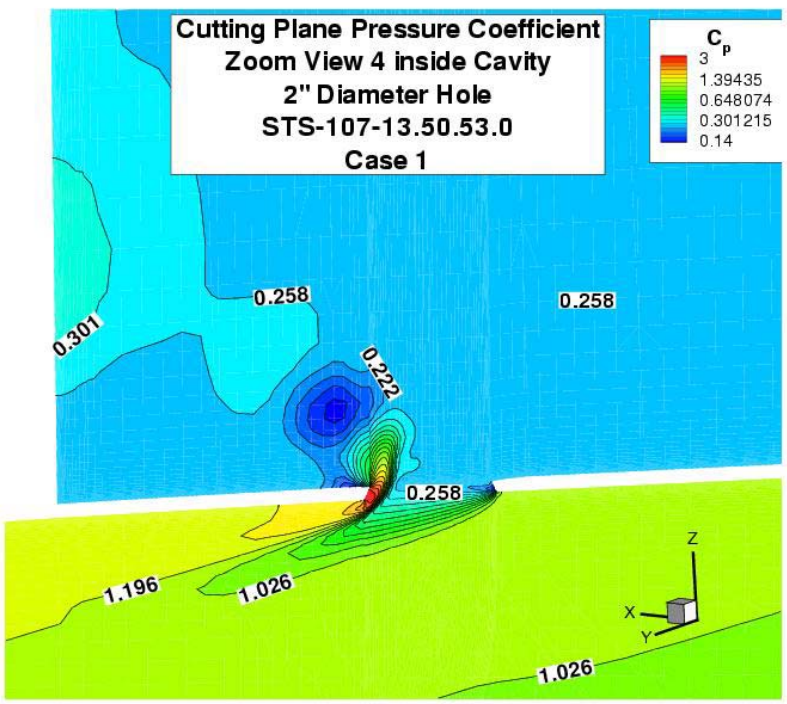

Figure 5.3.6-69: Pressure coefficient in vicinity of the breach.

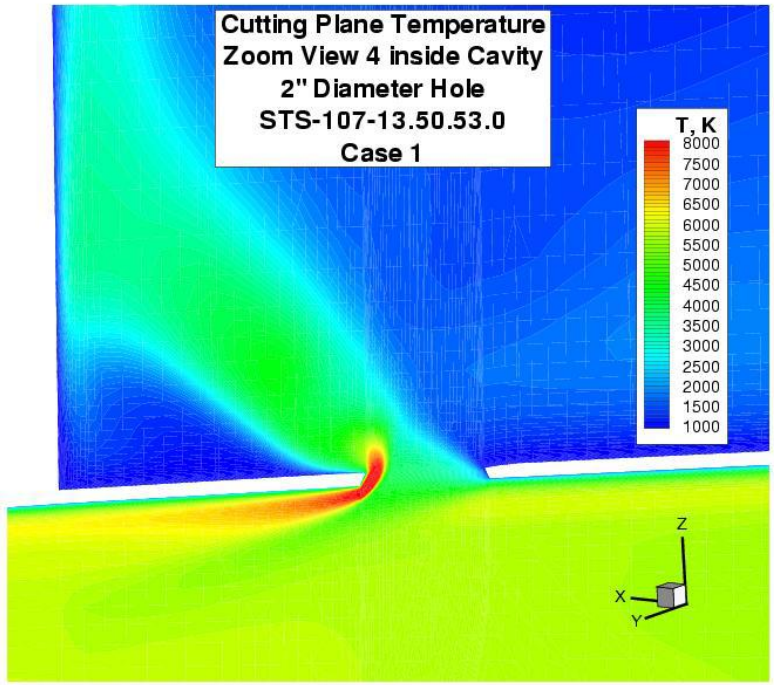

Figure 5.3.6-70: Temperature in vicinity of the breach.

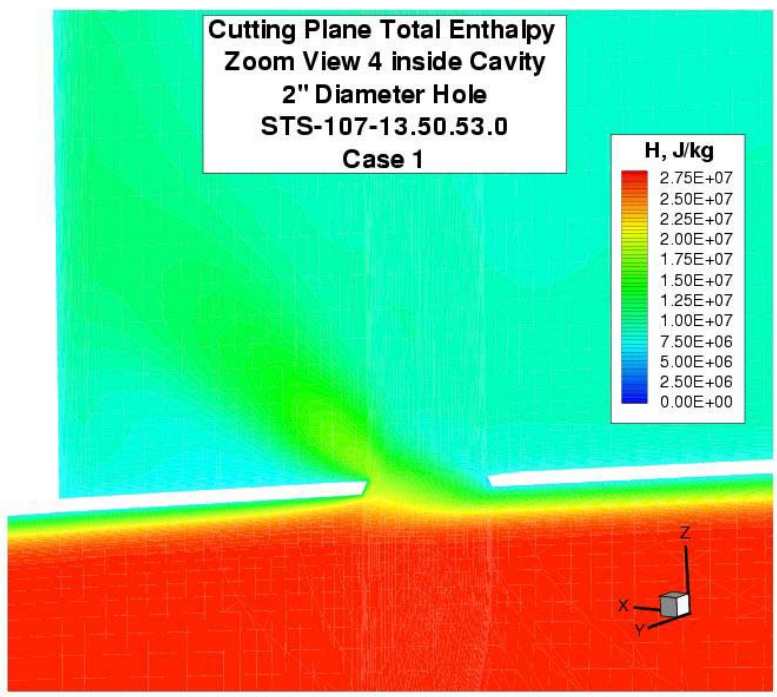

Figure 5.3.6-71: Total enthalpy in vicinity of breach indicating level of ingestion of the external boundary layer.

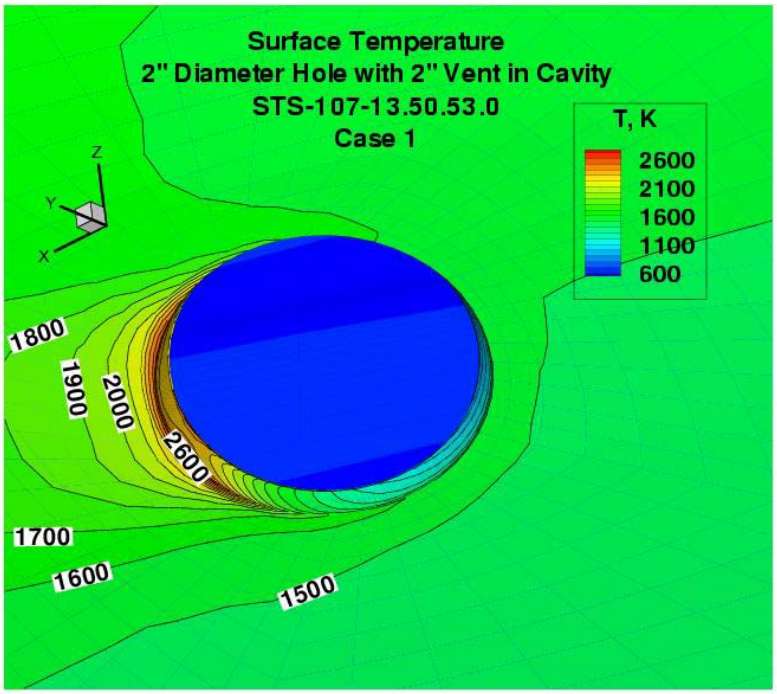

Figure 5.3.6-72: Surface temperatures in vicinity of downstream lip of two-inch hole over cavity.

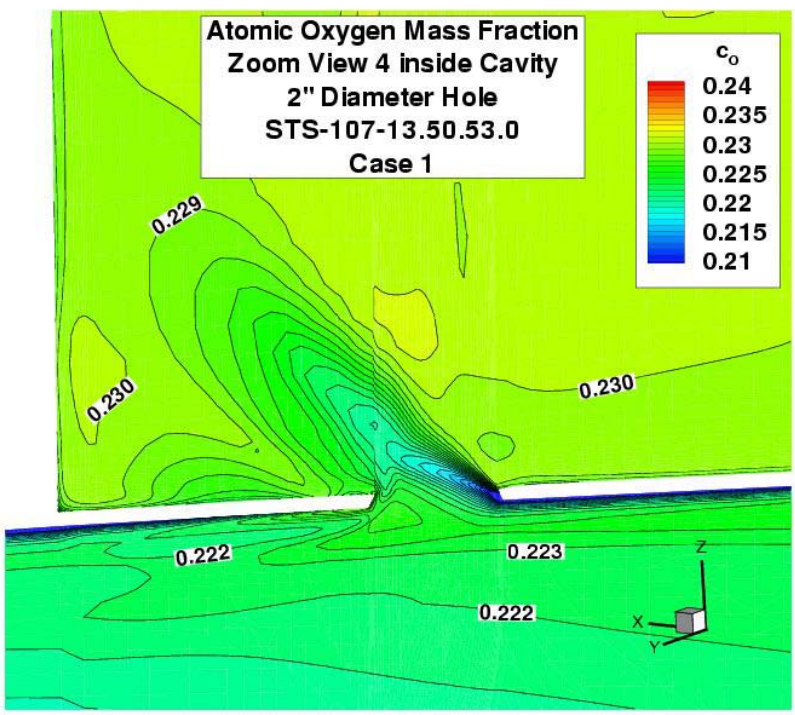

Figure 5.3.6-73: Atomic oxygen mass fraction ingested through breach.

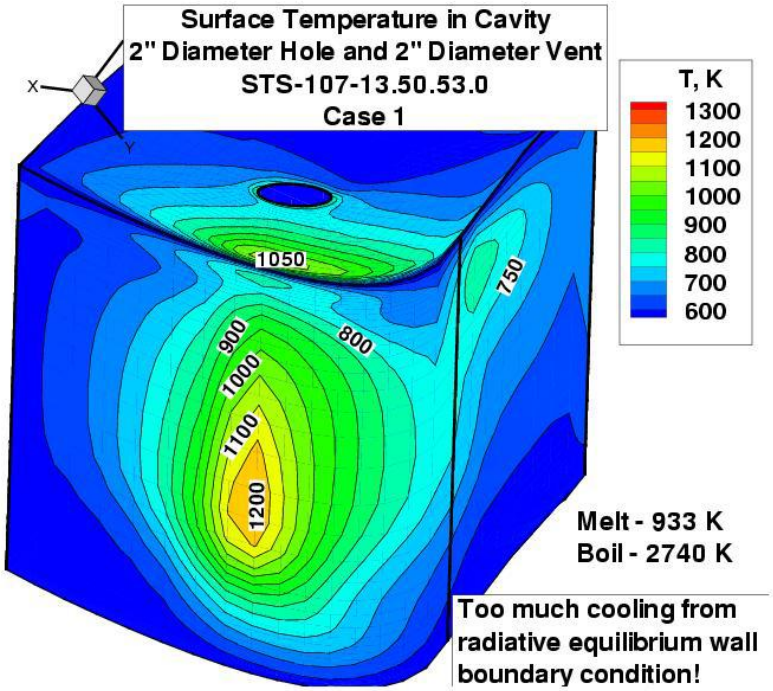

Figure 5.3.6-74: Surface temperature on cavity walls with identical cooling mechanisms as used for external flow.

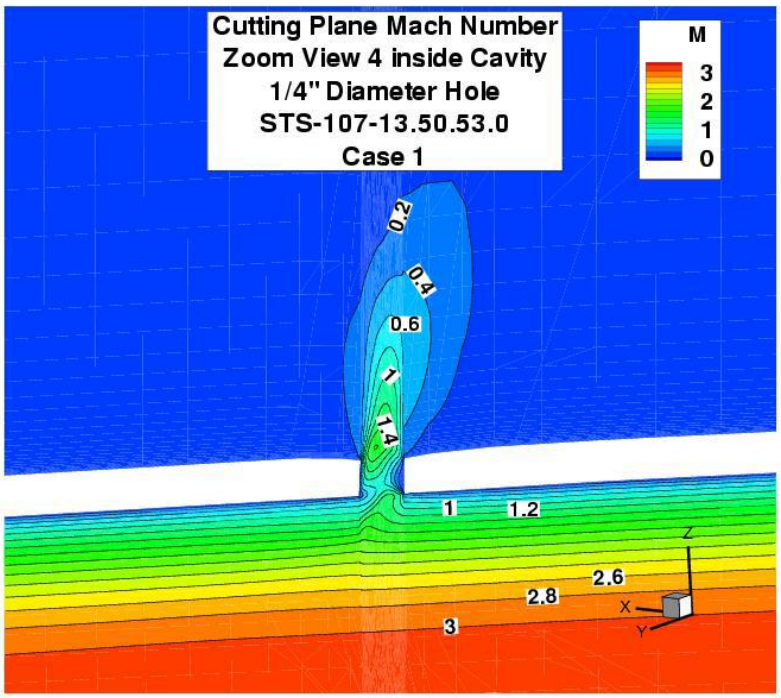

Figure 5.3.6-75: Mach number contours of jet entering cavity through quarter-inch diameter hole.

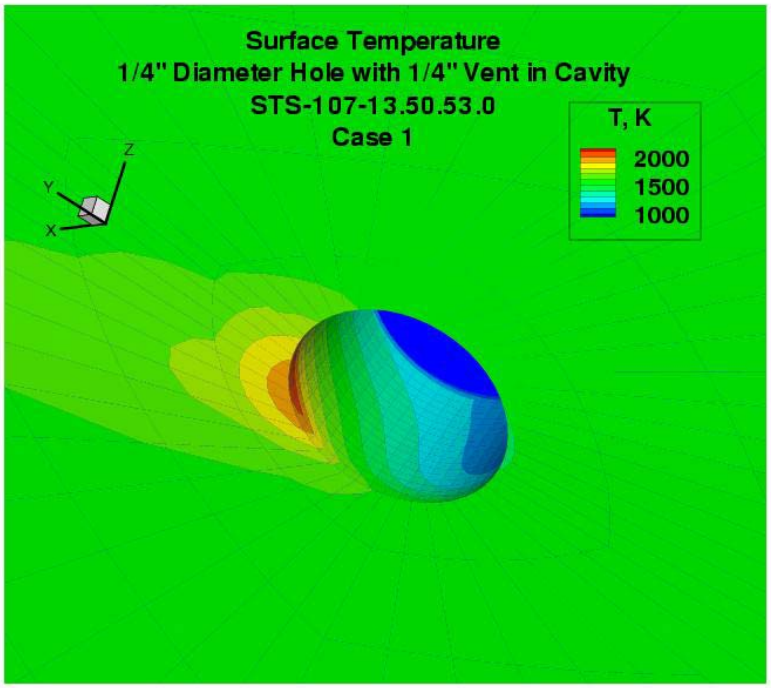

Figure 5.3.6-76: Surface temperatures in vicinity of quarter-inch hole.

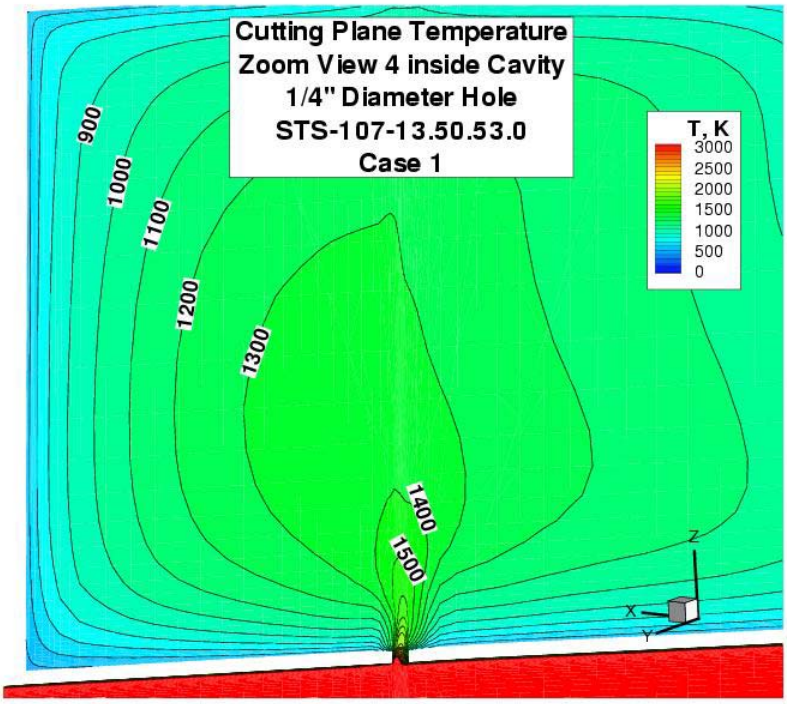

Figure 5.3.6-77: Jet temperatures in cavity bled from bottom of external boundary layer.

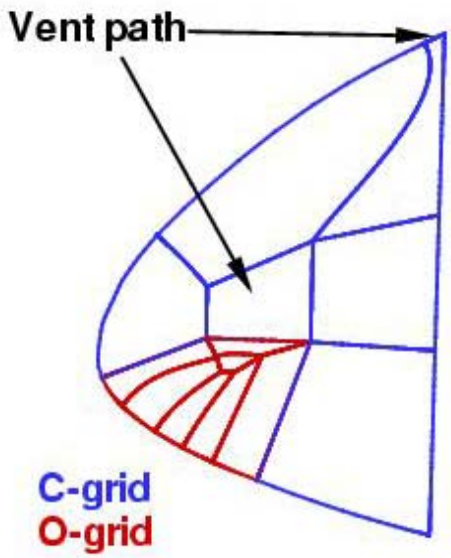

Figure 5.3.6-78: Internal block structure merging ad hoc cavity and chunnel showing relative vent positions.

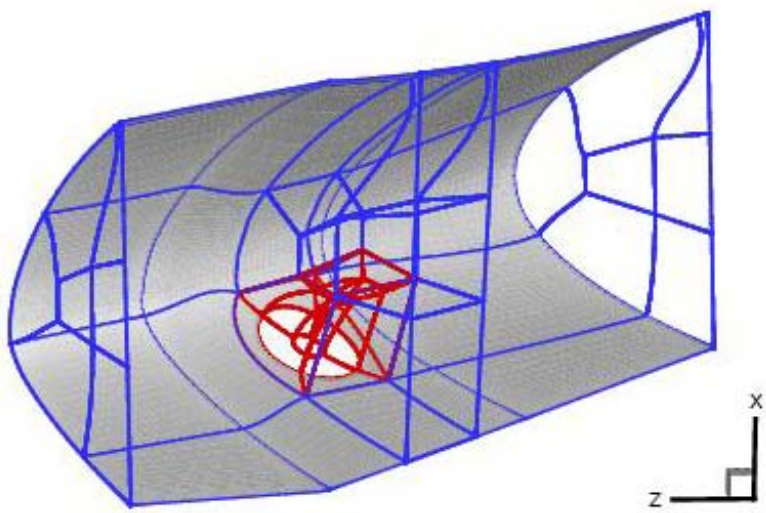

Figure 5.3.6-79: Global view of chunnel block structure.

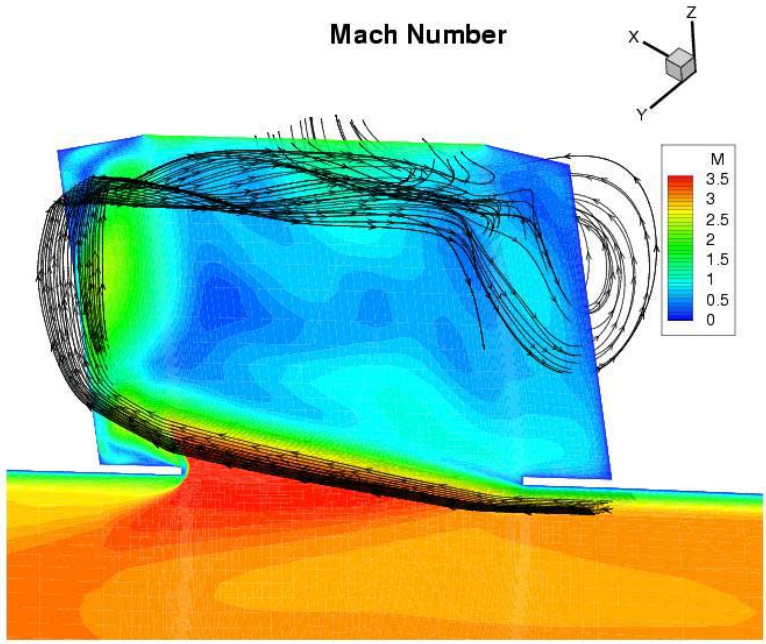

Figure 5.3.6-80: Mach number and streamlines in cavity behind panel 8 with ten-inch diameter hole and ten inch diameter vent.

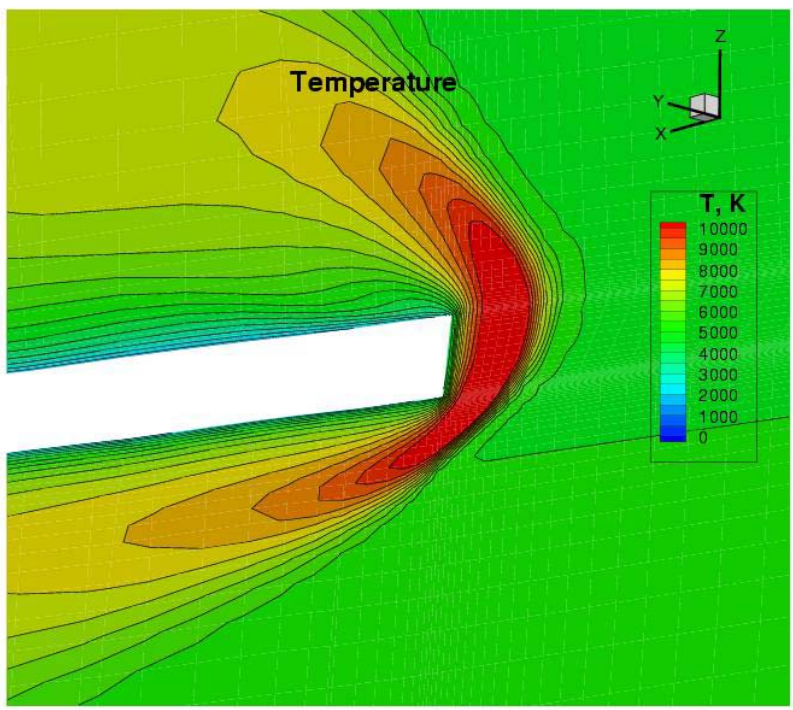

Figure 5.3.6-81: Details of temperature in shock layer over downstream lip with ten-inch breach through panel 8.

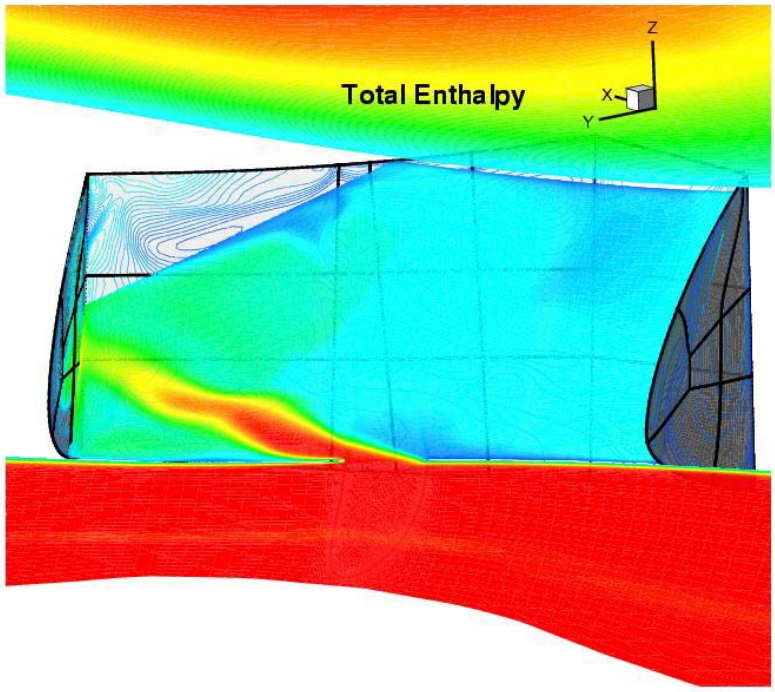

Figure 5.3.6-82: Total enthalpy entering chunnel through Panel 8. Venting is through slots on top of chunnel.

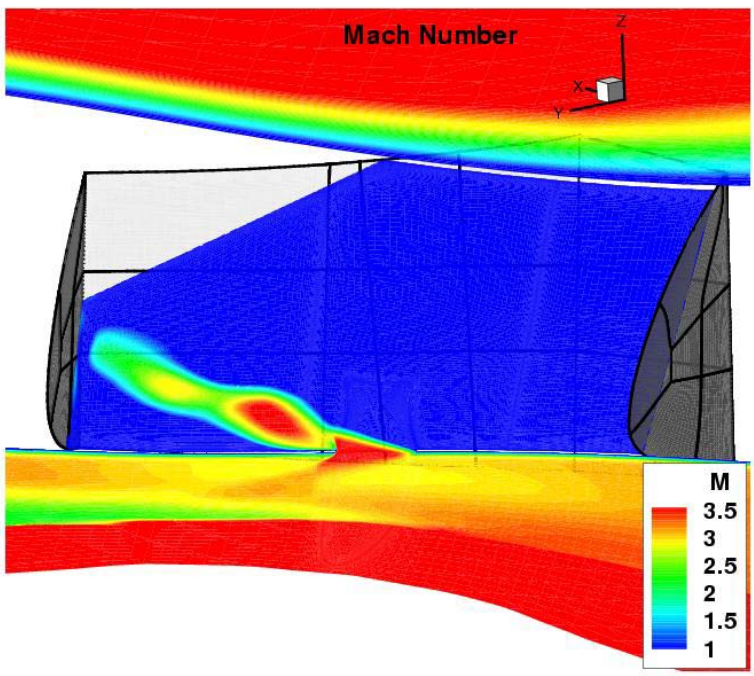

Figure 5.3.6-83: Mach number contours focused on supersonic domain.

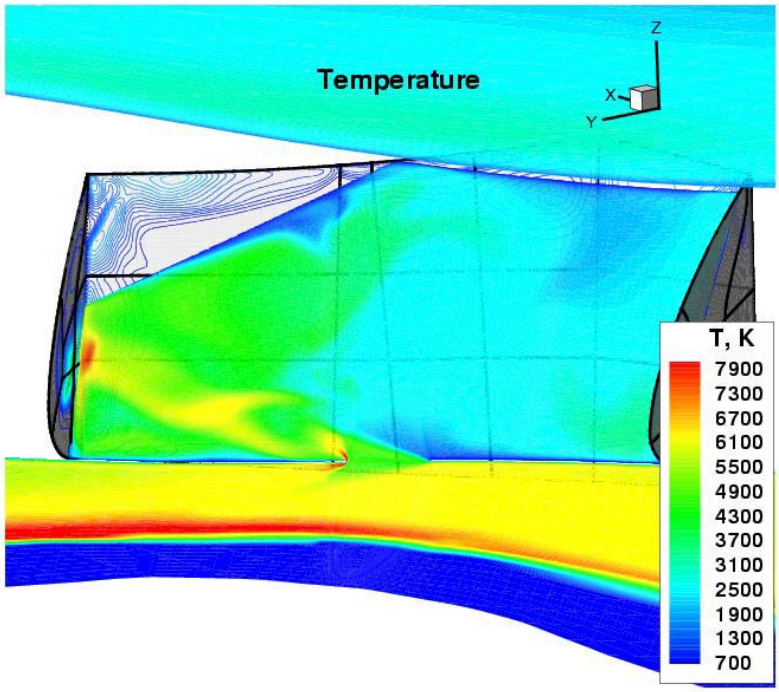

Figure 5.3.6-84: Temperatures in cutting plane through chunnel showing high temperatures at impingement of jet on the side wall.

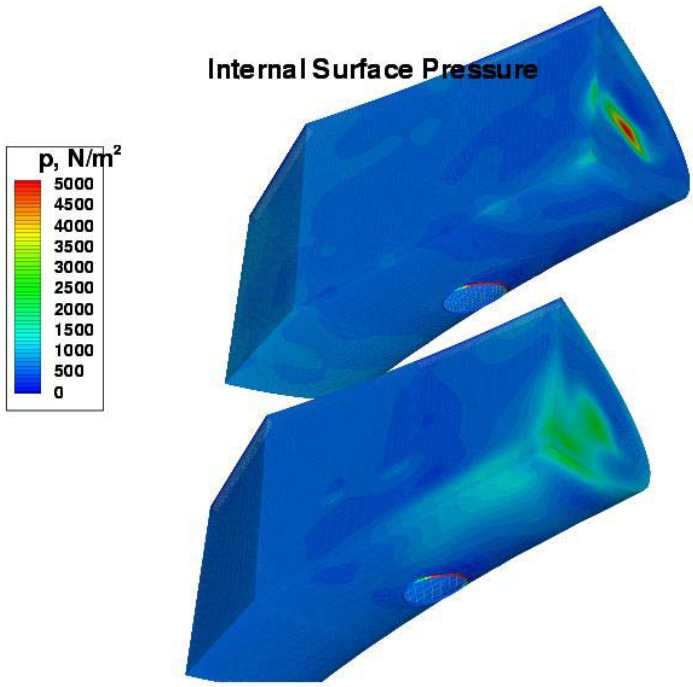

Figure 5.3.6-85: Comparison of chunnel surface pressures from medium grid and unadapted fine grid.

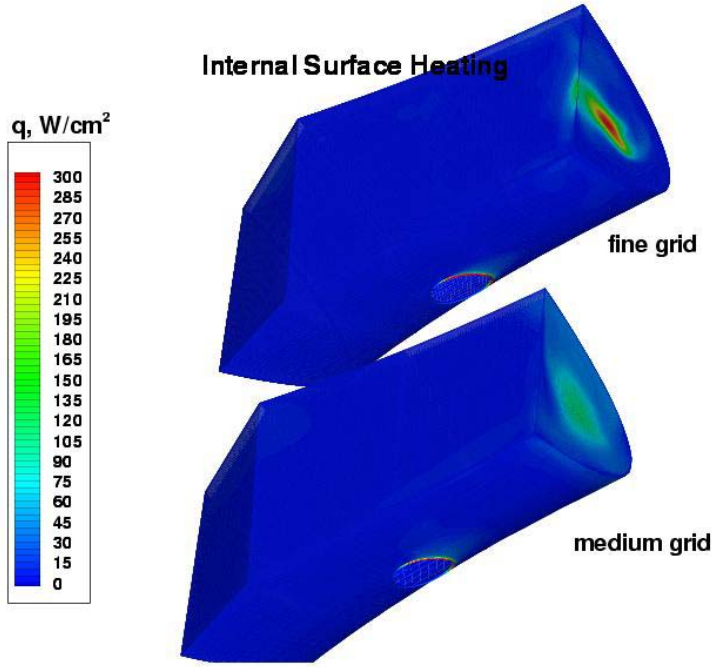

Figure 5.3.6-86: Comparison of chunnel surface heating from medium grid and unadapted fine grid.

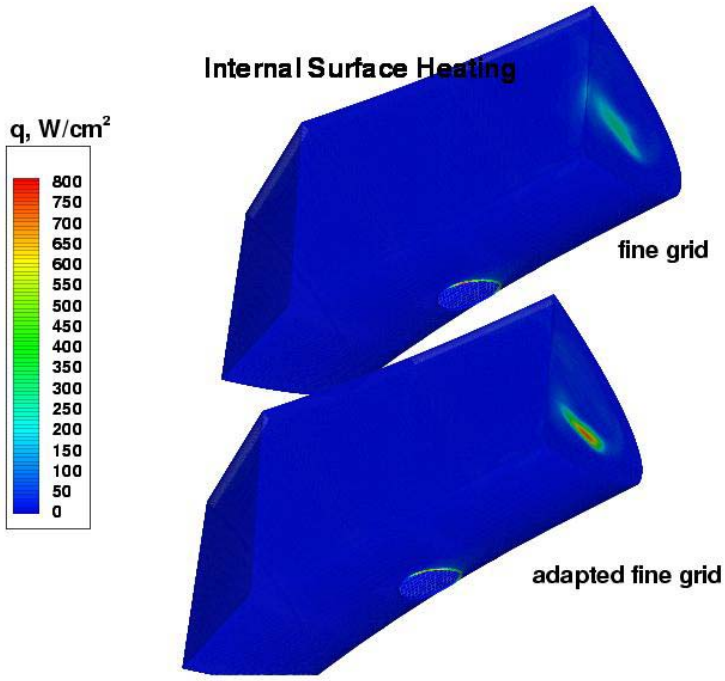

Figure 5.3.6-87: Comparison of chunnel surface heating from unadapted fine grid and adapted fine grid on impingement surface.

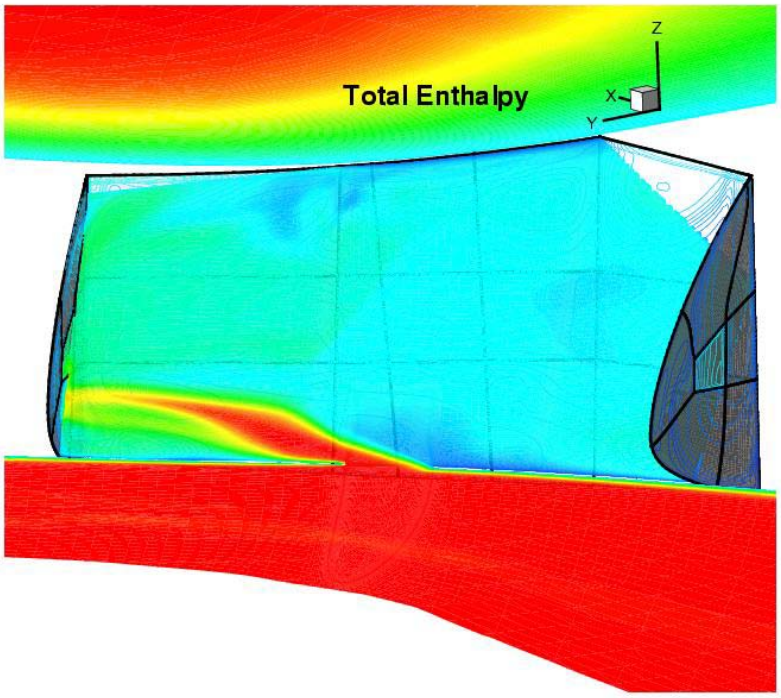

Figure 5.3.6-88: Total enthalpy in chunnel with side vents.

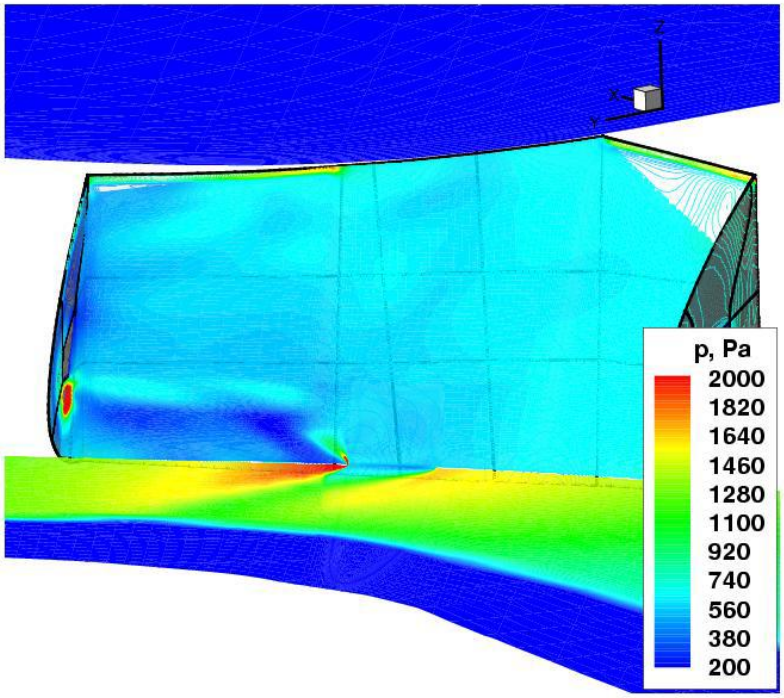

Figure 5.3.6-89: Pressures in chunnel with side vents.

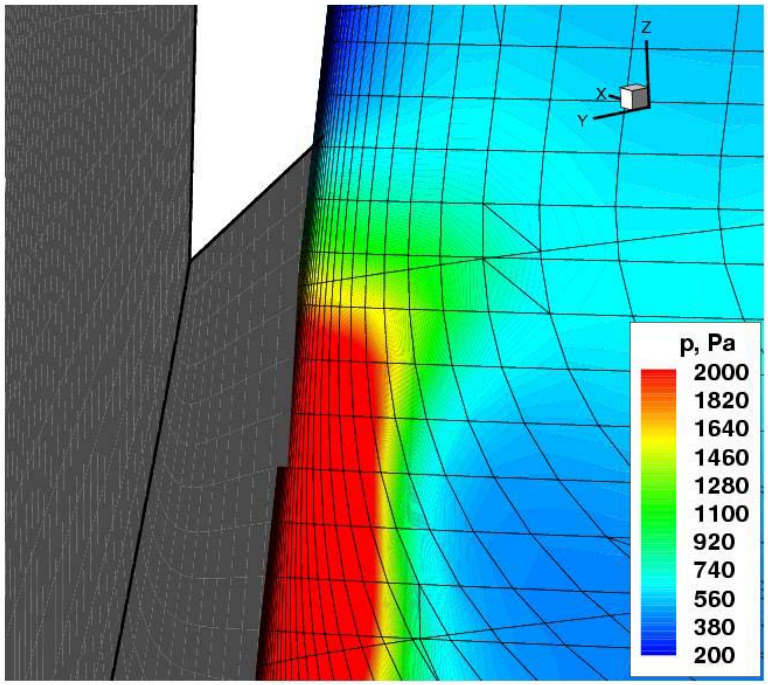

Figure 5.3.6-90: Detail of pressure at impingement location below side vent with supporting grid in the cut plane.

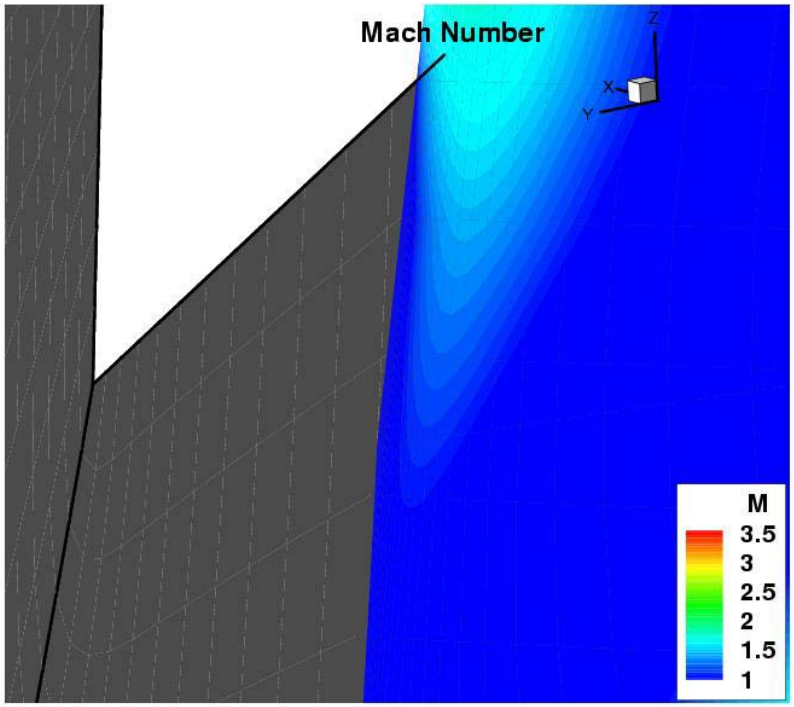

Figure 5.3.6-91: Magnified view of Mach number expanding to sonic condition at side vent.

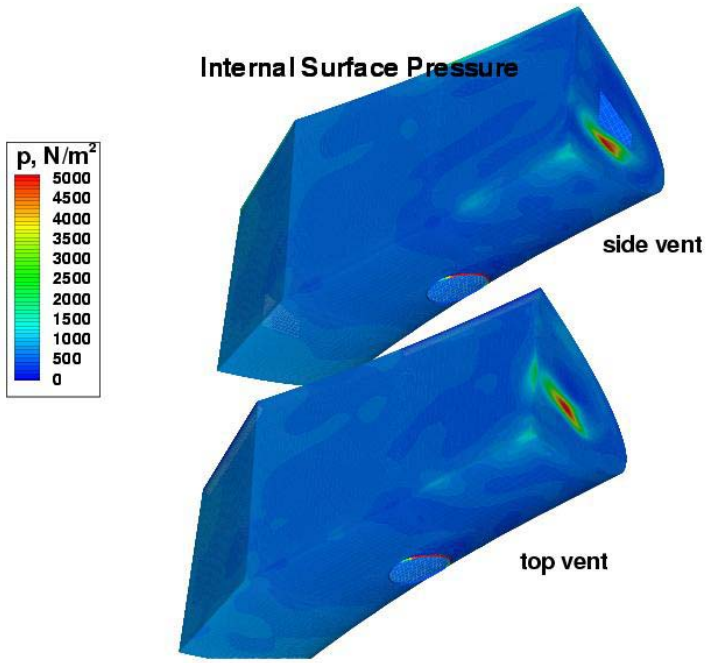

Figure 5.3.6-92: Comparison of chunnel surface pressures with top and side vents.

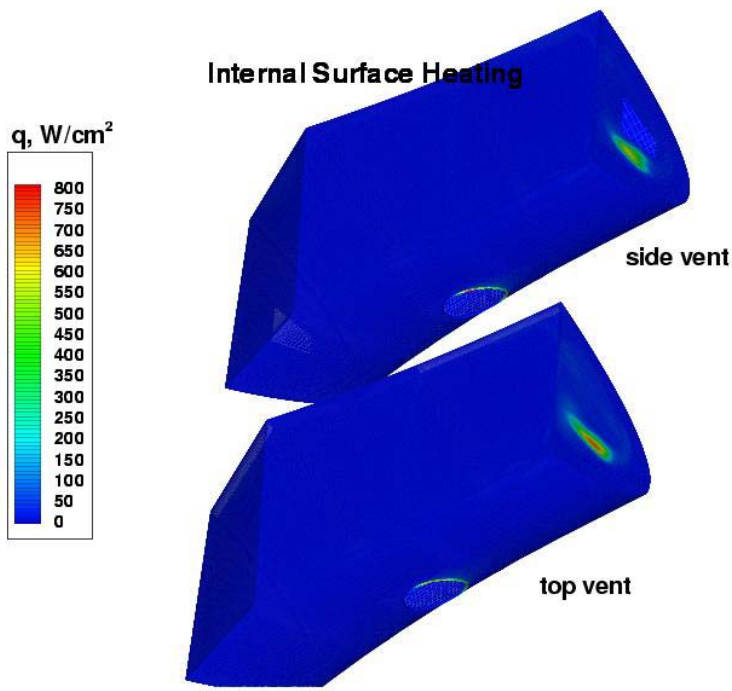

Figure 5.3.6-93: Comparison of chunnel surface heating with top and side vents.

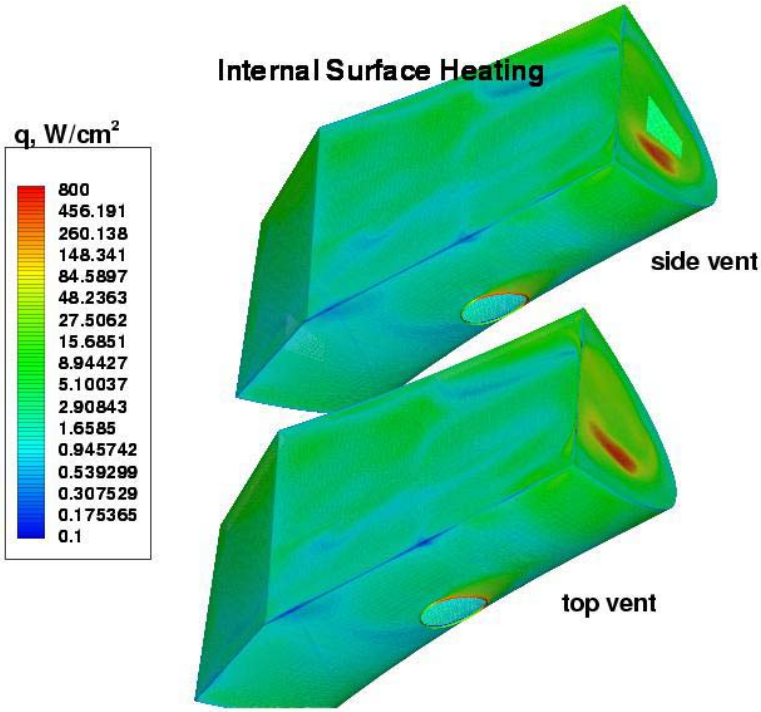

Figure 5.3.6-94: Logarithmic scaling of surface heating.

5.3.6.1.5 DSMC – Panel 8 10" Hole

5.3.6.1.5.1 Case Description

Using the DSMC Analysis Code, a DSMC case was run to simulate internal flow behind RCC panels 7, 8, and 9 due to a 10-inch hole in RCC panel 8. In this case, inflow boundary conditions were extracted from the previously run DSMC external flow solutions at an altitude of 350,274 and 300,000 feet. Vents were also applied to each side of the geometry with a total area equivalent to 66 inches squared.

5.3.6.1.5.2 Grid Development

Surface Grid
A heritage CAD definition for the RCC cavity was obtained from Jim Greathouse (NASA-JSC). This definition includes wing geometry from the leading edge back to the wing spar and includes a definition for the earmuffs between panels. The geometry used in this case was developed using the GridGen grid generation tool. After importing the CAD into GridGen, a 10-inch hole was generated in RCC panel 8 at a location of X = 1065 inches, Y = -219 inches, and Z = 286 inches in the orbiter coordinate system. Vent holes were included on each side of the geometry. It was assumed that the RCC thickness was uniform at ¼ inch, so the 10-inch hole in RCC panel 8 was given a thickness of approximately ¼ inch.

Since a DSMC solution had already been obtained for a nominal case at an altitude of 350,274 feet, it was felt that it was not necessary for a full-length shuttle case to be run for this failure scenario (1). Instead, an external flow field box-like "geometry" was created that connected to the hole from the external flow side. Great care was taken to create an external flow field geometry large enough so that the hole geometry would not significantly affect the flow at the upstream boundary, but small enough so that the case would run in a timely manner. The external flow field geometry was created to connect to a corresponding

portion of the outer RCC surface, which in turn, connected to the surface representing the thickness of the hole. Two different views of the surface geometry are displayed in Figure 5.3.6-95 and Figure 5.3.6-96.

In DAC, the surface geometry is represented as a collection of unstructured triangular elements and the entire surface geometry must be created to be "watertight" and possess continuous connectivity among triangles. In this case, the surface geometry contained approximately 53,000 surface triangles. Each individual surface triangle has specific boundary conditions associated with it. The triangles representing the surfaces of the wing were given the "solid wall" boundary condition, which means that no molecules are produced at the wall and none pass through. The triangles representing the vents were given the "outflow" boundary condition, which means that any molecules that hit the surface will disappear. Finally, the triangles representing the external flow field surface were given the "inflow" boundary condition. An inflow boundary creates molecules on the flow field side of the triangle, but any molecules that hit the surface will disappear.

Flow field Grid
The computational domain was specified to encompass the surface geometry created in this case and the boundary conditions of the computational domain were specified as vacuum. For the 350 kft case the internal flow field was discretized with Level-I Cartesian cells and each cell was specified to have a length of 1.18 inches (0.03 meters). The flow field grid was refined to the mean free path resolution though an adaptation process. After the adaptation process, the total number of cells in the computational domain was approximately 0.86 million cells. For the 300 kft case the Level I discretization employed cells of 0.059 inches (0.0015 meters). The total number of cells after the adaptation was approximately 40 million.

5.3.6.1.5.3 Input Parameters

The solution was run fully diffuse and the surface wall temperature was assumed to be 540° R (300 Kelvin). A chemistry model for high temperature reacting air was used that contained six molecular species – O_2, N_2, O, N, NO, and Argon. The mole fractions of these species were obtained from the 1976 Standard Atmosphere Model[1]. Number density, velocity, and freestream temperature were obtained from STS-107 flight data. To obtain the inflow boundary conditions from the full-length shuttle case already run at an altitude of 350,274 feet, the Surface Tools Plus (STP) DAC utility code was used to interpolate flow field properties onto the inflow geometry.

5.3.6.1.5.4 Results

Figure 5.3.6-98 and Figure 5.3.6-99 display a Y-slice of the flow field number density for the 350kft and 300 kft cases respectively. Due to the fact that the SLICE code (the DAC post-processing code that extracts the flow field properties of a certain plane) only has the capability to extract properties in a constant x, y, or z plane, Figure 5.3.6-97 was included to display a visual picture of the Y-direction cutting plane chosen. In Figure 5.3.6-98 and Figure 5.3.6-99, the streamlines shown depict the movement of the flow as it enters the hole in panel 8 and begins re-circulating inside the cavity. Figure 5.3.6-100 through Figure 5.3.6-103 (front and back view for the 350 and 300 kft cases, respectively) show the heating distribution in the RCC cavity while and Figure 5.3.6-104 through Figure 5.3.6-107show the corresponding pressure distribution. For the 350 kft case both the heating and pressure values shown in the legends on the right side of the figures have been normalized by reference heating and pressure values chosen from a point near the hole in panel 8 on the upstream RCC external surface. For the 300 kft case the heating and pressure were normalized by the free stream values at 300 kft. From these figures, it is evident that the area of highest pressure and heating due to the breach is near the earmuff between panels 8 and 9. In Figure 5.3.6-100 through Figure 5.3.6-103, a splash effect is shown on the panel 8 spar surface. As the flow hits the corner of the earmuff, a shock is formed and the flow is seen to splash onto the spar. Elevated heating levels are also seen near the earmuff between panels 7 and 8.

As was mentioned previously, mean free path resolution was obtained in the flow field grid for the 350 kft case. Historically, solutions that have reached mean free path resolution in their flow field grids have compared well with experimental data. The 300 kft case proved more challenging and although the available computational resources were exhausted mean free path resolution was not achieved throughout the domain. (That would have required a total number of cells in excess of 100 million). However, most cells were concentrated near the walls to capture the surface properties as accurately as possible.

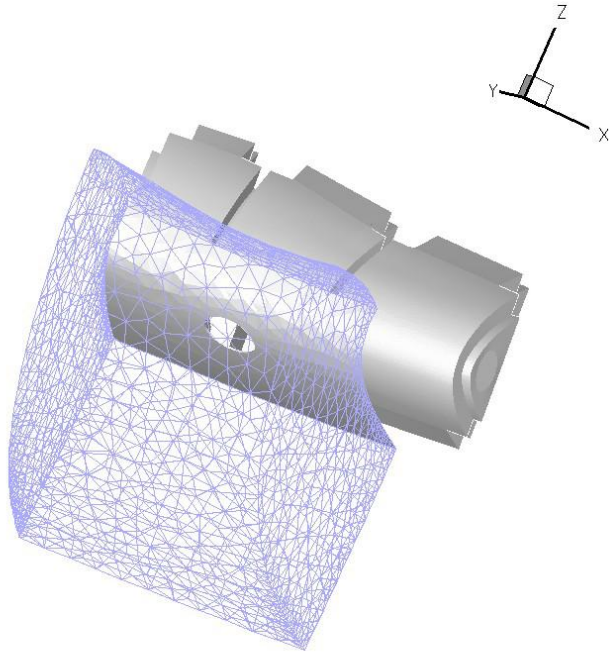

Figure 5.3.6-95 External (Triangulated) and Internal (Solid) Computational Domains – Front View

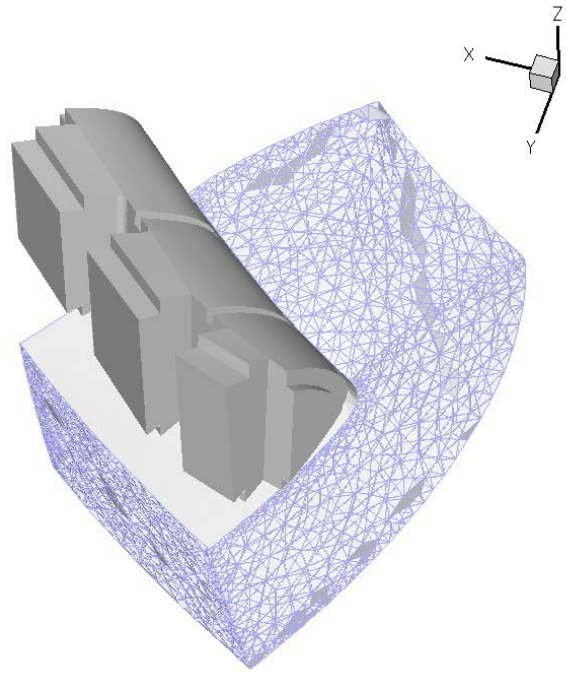

Figure 5.3.6-96 External (Triangulated) and Internal (Solid) Computational Domains – Back View

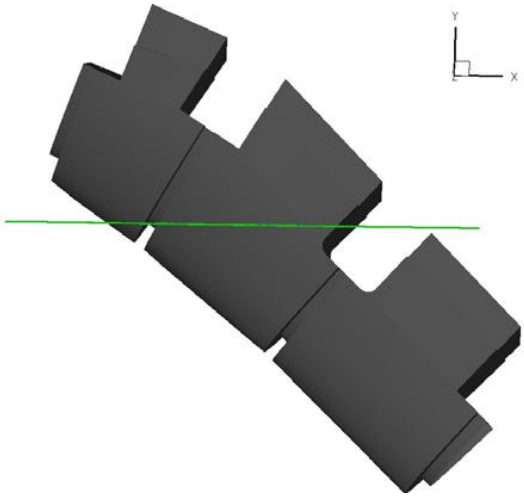

Figure 5.3.6-97 Visual of Cutting Place Chosen for Figure 5.3.6-98 and Figure 5.3.6-99

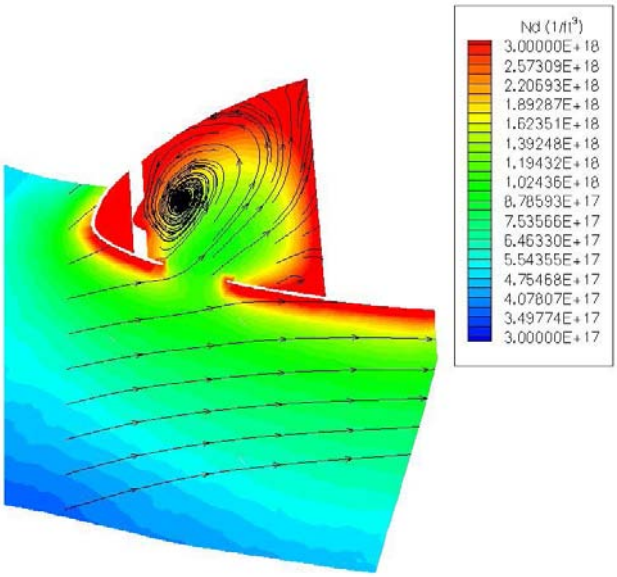

Figure 5.3.6-98 350kft Case-Number Density in Flowfield with Streamlines (Slice in Y-Direction)

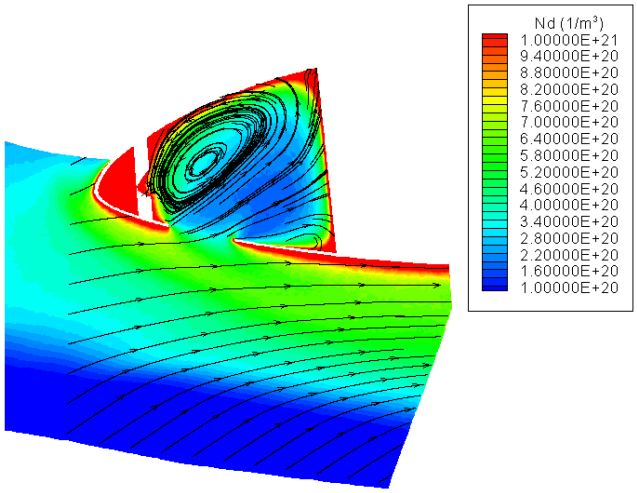

Figure 5.3.6-99 300kft Case-Number Density in Flowfield with Streamlines (Slice in Y-Direction)

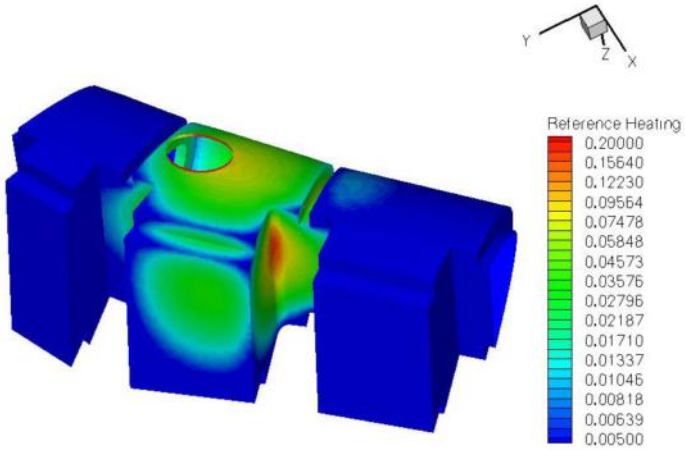

Figure 5.3.6-100 350kft Case-Reference Heating Distribution in RCC Cavity - Front View

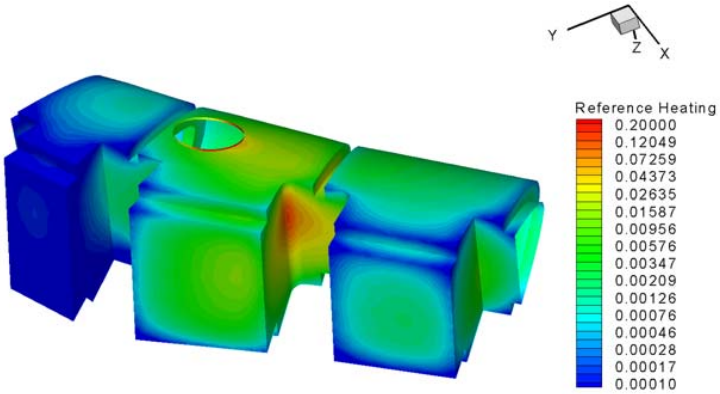

Figure 5.3.6-101 300kft Case-Reference Heating Distribution in RCC Cavity - Front View

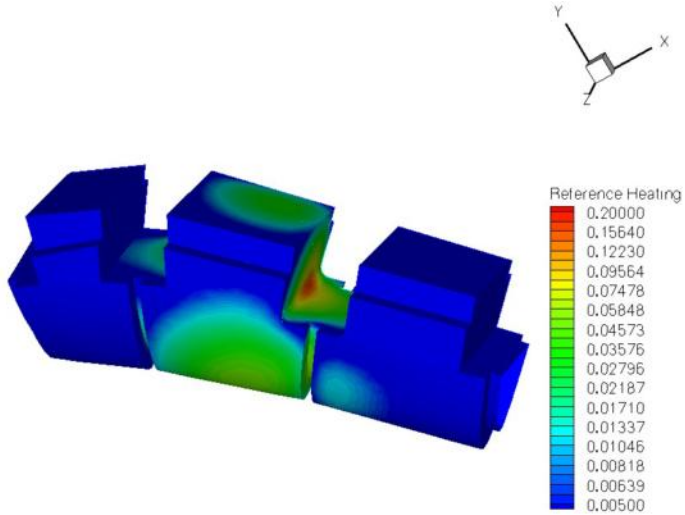

Figure 5.3.6-102 350kft Case-Reference Heating Distribution in RCC Cavity – Back View

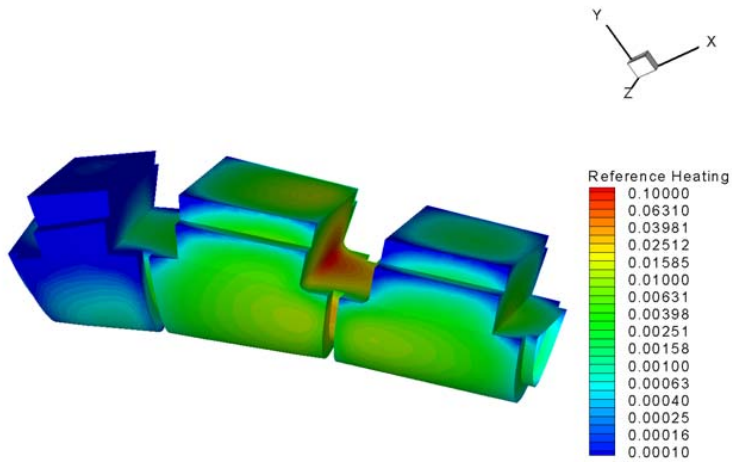

Figure 5.3.6-103 300kft Case-Reference Heating Distribution in RCC Cavity – Back View

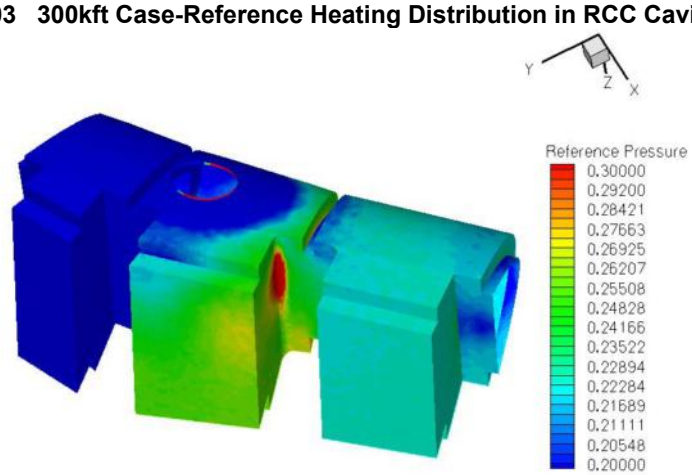

Figure 5.3.6-104 350kft Case-Reference Pressure Distribution in RCC Cavity – Front View

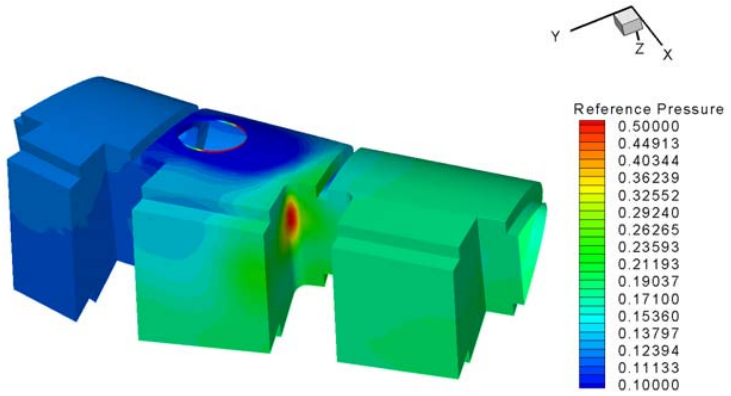

Figure 5.3.6-105 300kft Case-Reference Pressure Distribution in RCC Cavity – Front View

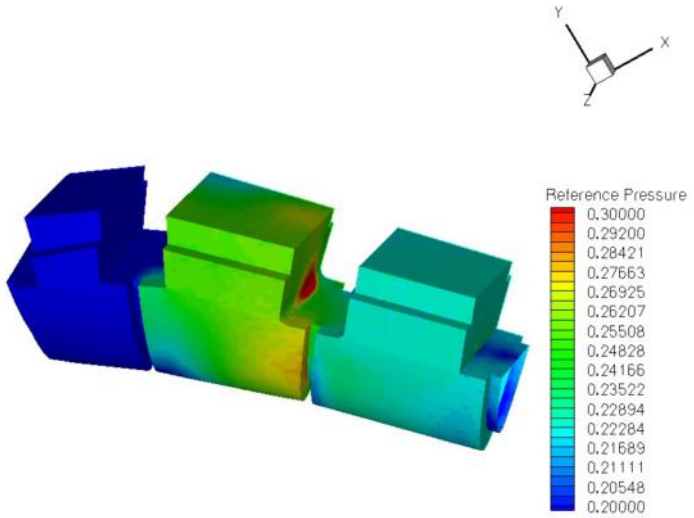

Figure 5.3.6-106 350kft Case-Reference Pressure Distribution in RCC Cavity – Back View

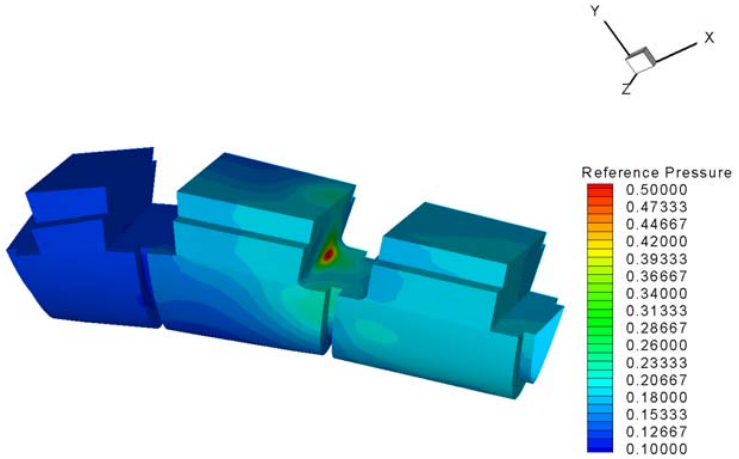

Figure 5.3.6-107 300kft Case-Reference Pressure Distribution in RCC Cavity – Back View

Footnotes

1. The value of the Knudsen number (a ratio of the molecular mean free path to a reference length) is often used as an indicator of rarefied flow. A Knudsen number of 0.01 or less is typically used to describe continuum flow, whereas higher Knudsen numbers indicate more rarefied flow. In this case, the Knudsen number is an order of magnitude larger when simulating only the portion of the flow field near the leading edge of the wing, than when simulating the entire flow field around the full-length vehicle. This corresponds to fewer computational resources needed due to fewer flow field molecules simulated.

5.3.6.2 CFD of RCC T-Seal Damage (Missing Portion of T-Seal)

5.3.6.2.1 JSC GASP 2D Solutions

5.3.6.2.1.1 Brief CFD Intro / Application Description

Two-dimensional simulations were done with GASP to model the internal wing flow field around the earmuff with a T-seal missing. Figure 5.3.6-108 is a representation of this simplified geometry. The true wall contour on the windward surface was not modeled in the GASP simulations. Instead, the windward surface was just a straight wall (black line instead of blue line in Figure 5.3.6-108).

GASP 4.1 with the overset grid option was used to expedite grid generation. Figure 5.3.6-109 shows the grid system. Sixteen grids were used with no overlap on the viscous surfaces. The upstream boundary was obtained by interpolating from a solution provided by the LAURA code from CFD point 1. The exact point to interpolate the boundary layer profile from was found by locating the attachment line on the wing leading edge and then locating the point between panels 8 and 9 that interested the attachment line. Figure 5.3.6-110 shows streamlines across the wing leading edge. The center of the red square is where the boundary layer profile was interpolated.

The interpolated boundary layer profile was in 3-D coordinate space, which was not the same coordinate system as the two-dimensional model problem. To transform the profile to the two-dimensional coordinate system the three-dimensional vector was dotted with the surface normal (along the attachment line) to get the x-component of the 2-D profile and dotted with the surface normal at the interpolation point to get the y-component of the 2-D profile. Figure 5.3.6-111 shows the boundary layer profile by components.

The out of page component is the velocity that would be out of the page in the 2-D simulation. It is small in comparison for the entire profile so it was ignored. The Mach number was used to limit the height of the profile that was used. The computational domain was limited to about 6.3 inches (0.16 meters) above the windward surface. Beyond that, the shock affected the Mach number profile.

5.3.6.2.1.2 Case Definition

The inlet to the simulation, as stated above, was a boundary layer profile from the LAURA code (CFD point 1). The internal back pressure was taken to be 0.835 psf (40 Pa). This was the leeside pressure above the leading edge from the same LAURA simulation (where the actual wing venting occurred). The internal wall temperature (on the earmuff) was held at 1500° F (fully catalytic surface). The external wall used the wall temperature from the LAURA solution (2794° F, partially catalytic surface).

5.3.6.2.1.3 Configurations Analyzed

The original geometry called for the internal surface to be 45” away from the windward surface of the wing. This made the distance from the earmuff to the T-seal exit to be 31” in the simulation. Four other cases were ran, with the distance from the earmuff to the T-seal exit being 21”, 11”, 5”, and 2”. The purpose for the fives cases was to create an earmuff heating model that varied as a function of distance from the T-seal exit to the earmuff. To speed up the running of the extra 4 cases, the original 31” solution was interpolated to each of the new grid systems (21”, 11”, 5”, and 2”) and the solution was ran from there. This saved the time of the flow setting up into the T-seal inlet. This was a legitimate way of running the cases because the flow out of the T-seal exit was supersonic thus the flow through the T-seal inlet never changed even when the earmuff was moved closer.

5.3.6.2.1.4 Heating Results

The heating distribution on the earmuff is shown in Figure 5.3.6-112. As the earmuff approaches the T-seal exit, the jet expands less, thus the heating on the earmuff is more localized and the peak heating is

much higher. The heating on the corners of the earmuff seems to increase slightly as the earmuff gets further from the T-seal exit.

5.3.6.2.1.5 Observations and Conclusions

The distance from the T-seal exit to the earmuff surface largely affects the plume structure. Figure 5.3.6-113 shows Mach contours for the 31" case. Figure 5.3.6-114 shows the mach contours for the 5" case. The maximum Mach number in the plume is at least 25% lower for the 5" case than the 31" case. Figure 5.3.6-115 shows the T-seal inlet flow structure. As the plume passes through the nozzle created by the missing T-seal, the flow directionality of the freestream is mostly washed away. This is evident by the symmetric flow at the exit of the T-seal.

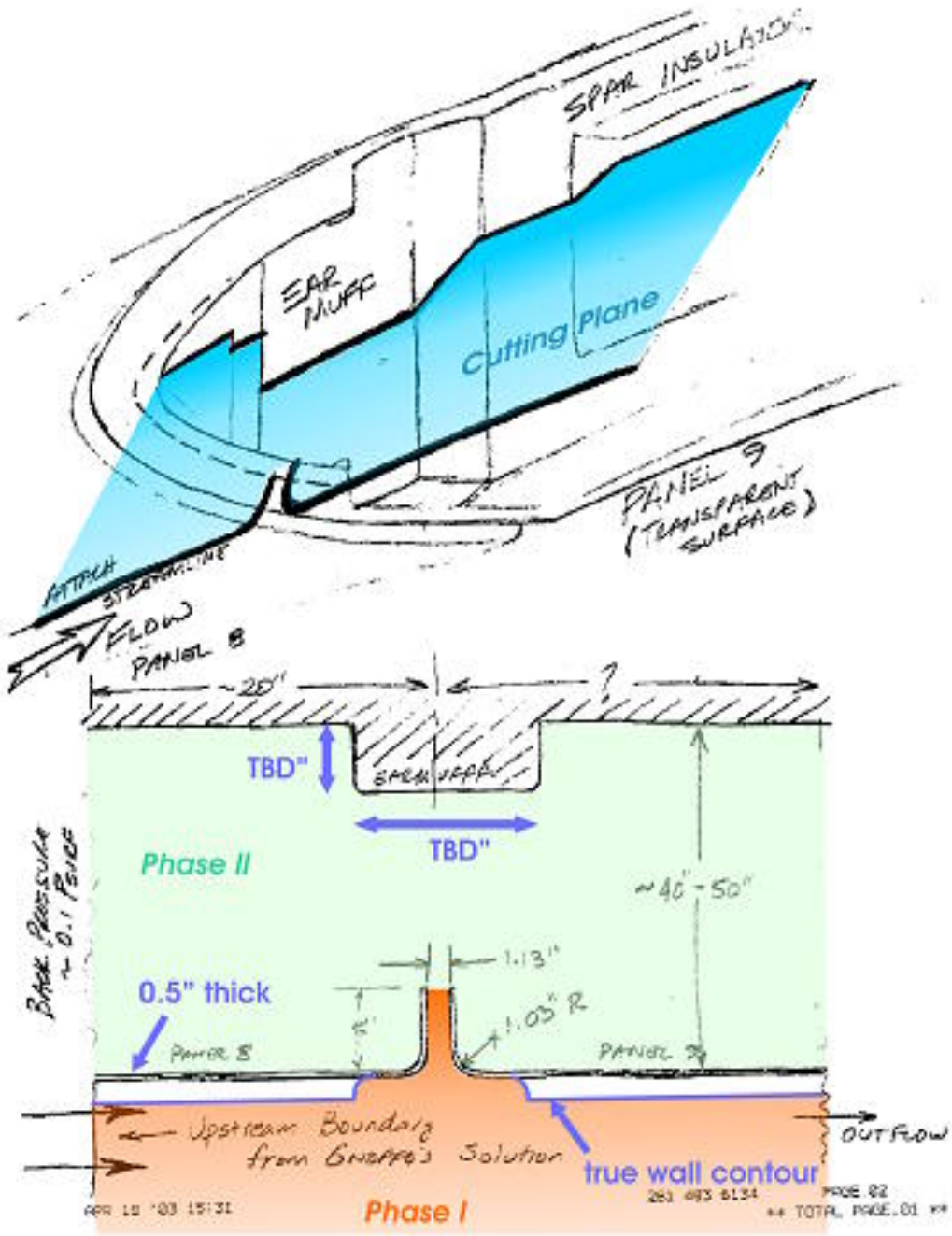

Figure 5.3.6-108 Representative T-seal geometry

a) Overview of Grid System

427

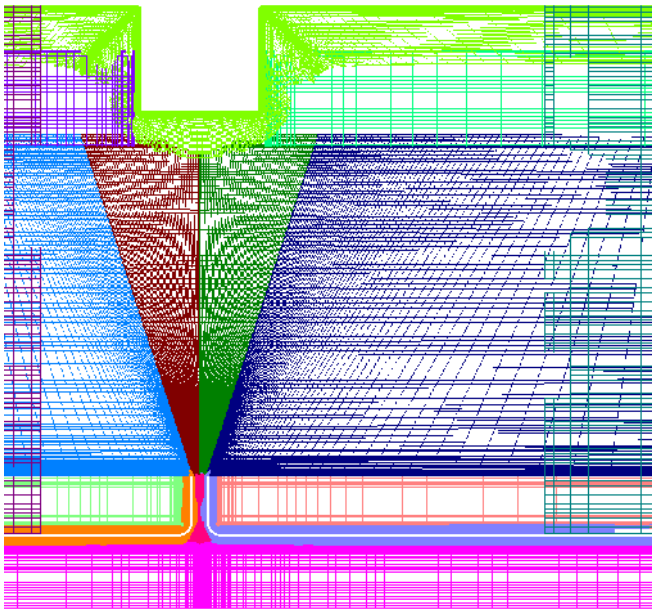

b) Close up of Earmuff Region

Figure 5.3.6-109 T-Seal Grid System

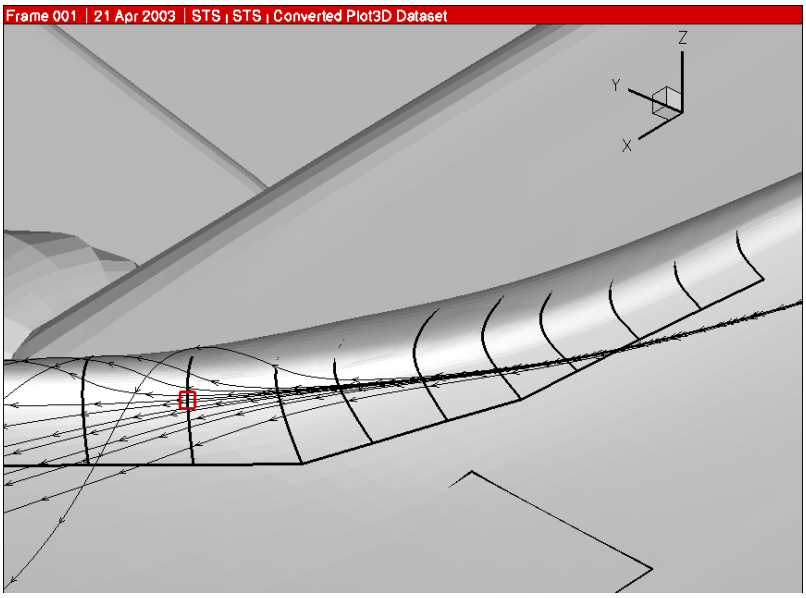

Figure 5.3.6-110 Panel 8 Attachment Line

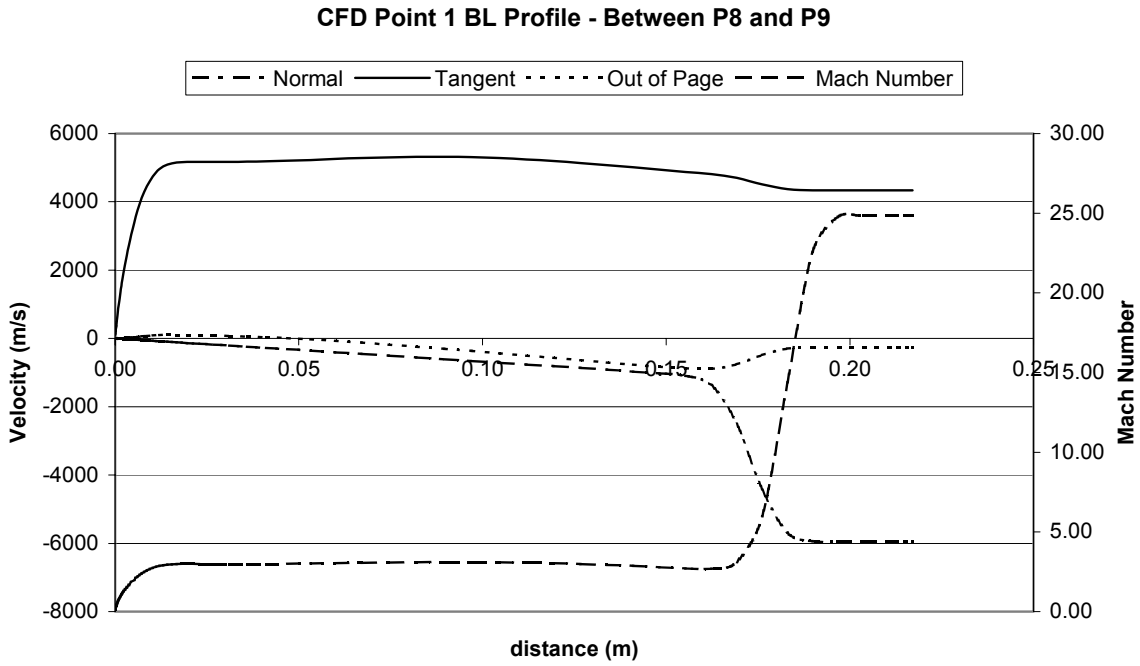

Figure 5.3.6-111 Transformed Boundary Layer Profile

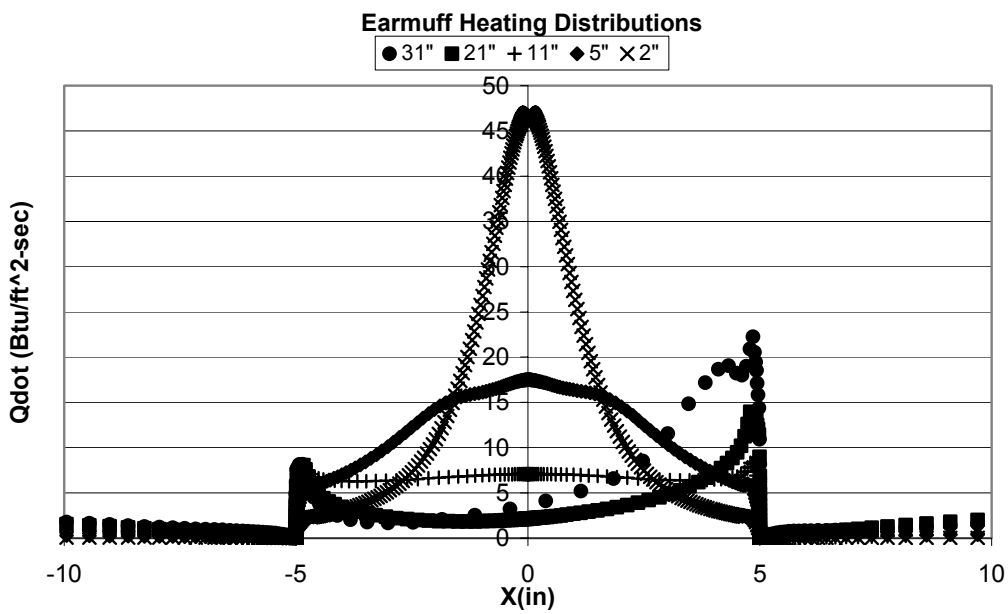

Figure 5.3.6-112 Earmuff Heating Distributions for Varying Distances

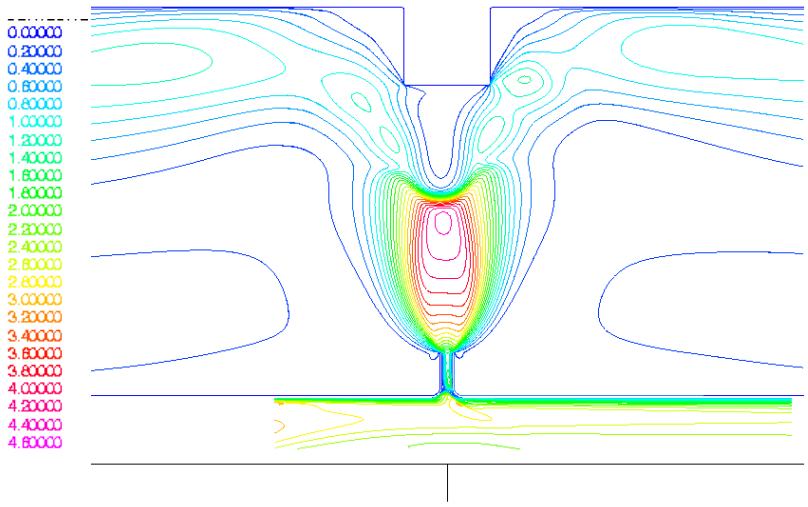

Figure 5.3.6-113 Mach contours for the 31" separation case

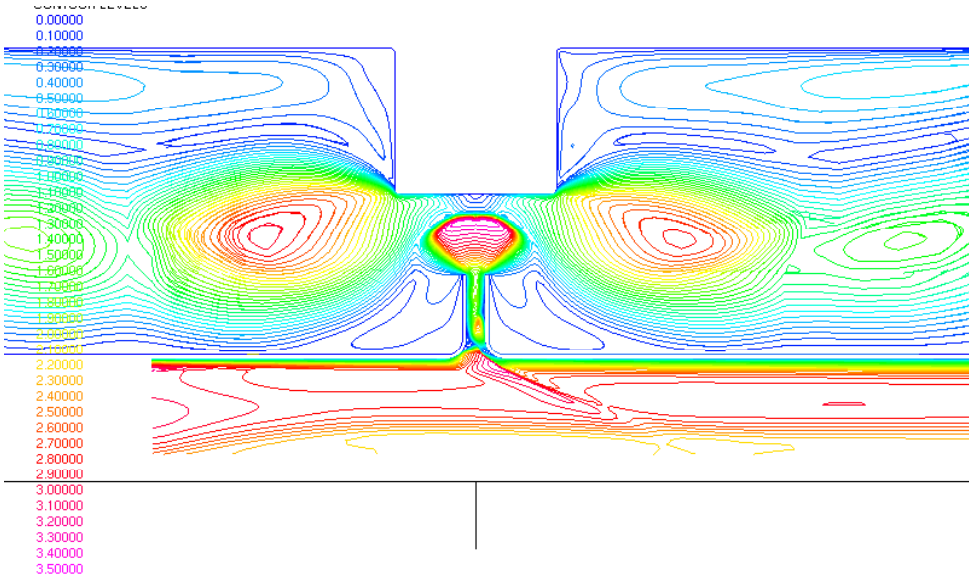

Figure 5.3.6-114 Mach contours for the 5" separation case

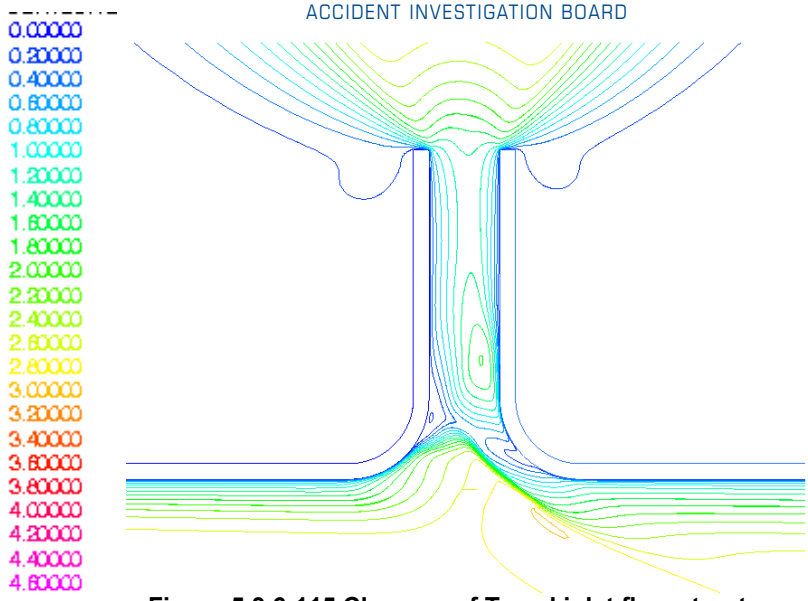

Figure 5.3.6-115 Close up of T-seal inlet flow structure

5.3.6.2.2 Rocketdyne 2-D T-Seal solution

5.3.6.2.2.1 Case description

The objective of the Rocketdyne 2-D CFD analyses was to compute convective heating rates on the RCC T-seal cavity and rib channel areas as well as on the spanner beam insulation directly behind the T-seal (RCC 8/9 "earmuff"). The motivation for these analyses was to create a "bridge" between the unit physics validation problems and the full 3-D failure scenario simulations. The experience obtained from these analyses was intended to improve the understanding of the flow field and heat transfer mechanisms applicable within the T-seal cavity and on the earmuff. The experience gained would be directly applied to constructing the models for 3-D failure scenarios. In order to obtain solutions in a timely manner and break down the complexity of the problem further, a two-phase approach was implemented for the 2-D analyses. The first phase examined only the external surface, T-seal cavity, and rib channel flow fields and heat fluxes. The second phase expanded upon the first phase to examine the flow field inside the RCC panel cavities and the heat fluxes the earmuff would be subjected to.

5.3.6.2.2.2 Grid/Solution development

A planar cut of the RCC T-seal cavity on the underside of the wing provided the geometry used to generate the grid. The cut was made through a Pro-E subassembly of RCC panels 8 and 9. A sketch of the flow domain and subassembly are shown below in Figure 5.3.6-116. External LAURA CFD solutions helped determine the appropriate placement of the planar cut to ensure that the flow was mostly perpendicular to the edge of the T-seal.

The grids for both phases were block structured and created using the Boeing APPT system. In the first phase, a dummy "dump" zone was added to the grid at the end of the T-seal rib channel to improve convergence time. The wall spacing used was 1.0e-4 in., and the grid was "wrapped" around the external surfaces and T-Seal cavity to maintain a consistent grid clustering normal to the walls. The phase I grid consisted of four zones, contained 38, 788 cells, and is shown in Figure 5.3.6-117.

The second phase grid was more or less identical to the first phase grid over the external region, T-Seal cavity, and rib channel, but several zones were created to replace the dump zone with a representation of the RCC panel internal geometry. Dimensions for the earmuff and some other geometrical information were extracted from the sketch in Figure 5.3.6-116 as well as the 2-D grid discussed in Sec. 5.3.6.2.1. Consequently, the representation of the wing leading edge internal geometry is not exact. Furthermore, the earmuff is modeled with sharp corners. This does not correspond to the actual geometry and does have an appreciable affect on the heat transfer as discussed in the results section below. The geometry, however, is good enough to provide a feel for the flow field and heat transfer. The outflow areas of the grid for phase II were expanded to include "dump" regions to allow the application of constant pressure boundary conditions. The wall spacing used was 1.0e-4 in. It should also be noted that the grid

coordinate system for phase II was different from that of phase I although this has no effect on the results. The phase II grid consisted of seven zones, contained 115,355 cells, and is shown in Figure 5.3.6-118.

For both phases of the 2-D analyses, solutions were obtained using the USA structured solver. Fully laminar flow was assumed based on the extremely low Reynolds numbers present. In phase I, Liu-Vinokur equilibrium air thermochemistry and Tannehill transport properties were used. In phase II, a finite rate thermochemistry model with five species and seventeen reactions was used and fully catalytic walls were assumed. The transport properties were determined using Sutherland's law. Additionally, a laminar Schmidt number of 0.52 was used. Also, for both phases of the 2-D analyses, the CFD Condition 1 trajectory point data provided the freestream conditions, and the external LAURA flow solution established the external flow boundary conditions. Three different wall temperature boundary conditions for the RCC external walls (2900° R – STS-5 nose temperature, 3523° R – approximate RCC coating loss temperature, and 5273° R – approximate RCC oxidation temperature) were run in both the first and second phases to obtain a "database" of wall heat fluxes versus temperature and wall location. In the second phase, a 3000°R boundary condition was applied to the earmuff wall. This specific temperature was chosen because it was assumed there was enough heating on the earmuff surface to melt the material and that insulation material has an external layer of Inconel, which has a melting point of 3000° R. The "databases" created by these analyses were intended to aid any subsequent radiation analyses. Furthermore, three different cavity backpressure values were set at the end of the extended outflow region (Cp = 0.02, Cp = 0.06, and Cp = 0.10) for phase II, while the phase I outflow condition was set to be supersonic outflow. In phase I, the convergence criterion was to drive the net fluxes to steady state. Phase II retained that same criterion, but also added another – steady state heat flux on the earmuff windward surface.

5.3.6.2.2.3 Results

5.3.6.2.2.3.1 Major flow structure comments

Figure 5.3.6-119 shows all the major flow structure features of interest from the phase I solutions. The image is for the 2900° R solution – all the other flow fields are similar in nature so only data from the 2900° R solution is presented. There are changes to the flow field with temperature, but the effects are negligible. There is a high degree of internal/external flow coupling and all of the captured flow is from the external boundary layer. Large recirculation regions exist in the T-Seal cavity corners, as is expected for laminar flow. There is also a "bow shock" on the downstream side of the T-Seal cavity as the flow in the boundary layer turns and hits the T-Seal rib cavity walls. Of particular interest is the aerodynamic throat in the T-Seal channel that is formed by this bow shock and the separation area on the upstream side of the rib channel. This aerodynamic throat chokes the incoming flow and leads to expanding supersonic flow leaving the rib channel. This, in turn, affects the heat transfer environment inside the RCC cavity.

In phase II of the 2-D analyses, the external flow field changes very little from that obtained in the phase I 2-D analyses. The internal RCC panel flow field structure, however, varies significantly depending upon the backpressure boundary condition chosen. The flow is not, however, particularly sensitive to external or internal wall temperatures. As a result, most of the following discussion focuses on the changes in flow structure arising from different backpressure boundary conditions.

In phase I, it was clearly established that the flow exiting the rib channel would be supersonic based upon an assumed low backpressure within the cavity. The pressure differential between the flow reaching the cavity exit and the RCC cavity backpressure would provide more than enough energy to accelerate the flow to supersonic speeds. Given such circumstances (a backpressure such that Cp <= 0.10), the rib channel flow becomes a supersonic jet fired into the RCC panel cavity, and some sort of plume expansion expected. The results of the phase II analyses showed that the amount of plume expansion in the cavity is closely tied to the cavity backpressure. Consequently, the higher the backpressure, the more mass flow that impinges on the "earmuff" and the larger the expected heat flux on the earmuff windward surface (given that the incoming jet flow does not unchoke). The following six figures (Figure 5.3.6-120 through Figure 5.3.6-125) clearly show the differences in the plume and shock structures of the RCC cavity jet flow as the backpressure varies. All three backpressures exhibit very large-scale separated regions resulting in large-scale constant pressure regions. Such separated regions are, again, expected because of the laminar nature of the flow. Similarly, all three backpressures have a canted stagnation streamline due to the asymmetric flow in the rib channel. In addition, supersonic "tails" develop in the interior of the RCC panel cavity. How those tails impinge upon the interior surfaces changes with the backpressure in a minor

way. Furthermore, those tails turn almost 90° while staying supersonic due to the constant pressure recirculation regions they see on either side of the earmuff.

Figure 5.3.6-120 and Figure 5.3.6-121 demonstrate that low backpressures (Cp = 0.02) result in a large plume expansion. Most of the incoming jet does not impinge on the earmuff, and the normal shock occurs at a considerable distance from the earmuff surface.

Similarly, Figure 5.3.6-122 and Figure 5.3.6-123 show that a slightly higher backpressure (Cp = 0.06) results in as much as a third of the incoming jet impinging on the surface. Furthermore, a complicated shock pattern develops and the normal shock is much closer to the earmuff surface. Unfortunately, the solution on the earmuff seems unsteady and goes through cycles. This adds uncertainty to the validity of any heat flux information that may be extracted. See the discussion in the section below for more detail.

Finally, in Figure 5.3.6-124 and Figure 5.3.6-125 when the highest backpressure is run (Cp = 0.10), all of the incoming jet impinges on the surface. Once again, there is a complicated shock pattern that develops and the standoff distance of the normal shock from the earmuff surface is at a minimum leading one to expect a higher temperature gradient and thus a larger heat flux.

5.3.6.2.2.3.2 Surface heating and pressure comments

The heart of these 2-D analyses is to help determine the heating environments on various internal structures of the orbiter wing and aid the heat transfer analysts by providing them insight into the flow field and heat transfer mechanisms. In the simplest terms, the largest heat fluxes occur where the largest temperature gradients reside. Most often, the largest temperature gradients occur at the geometrical features with the smallest radii (sharp corners, etc.) because more often than not such features thin or destroy the thermal and viscous boundary layers. This trend is observed in both the phase I and phase II results. As mentioned in Section 5.3.6.2, some parts of the geometry were modeled as having sharp corners even though pictures of the actual hardware indicated that the corners are actually rounded. One would expect to over-predict the heat flux at those corners, and indeed, large localized spikes in heat flux do occur in both the phase I and phase II solutions at any geometrical corner or feature with a small radius. Figure 5.3.6-126 shows the arc length coordinate system that is used to describe the positional heat flux along the walls of interest while Figure 5.3.6-127 shows the actual heat flux values along the T-Seal cavity from the Phase I solutions and Figure 5.3.6-128 shows a comparison of the phase I and phase II solutions on the external and T-Seal cavity surfaces. The heat flux predicted in phase II is quite a bit less almost over the entire length of the external, T-Seal cavity and rib channel walls, roughly 55% of the phase I solution. More importantly, except for at the sharp corners and other geometrical features with small radii, it is a consistent. The explanation for most of this difference lies in the different thermochemical and transport models used.

Figure 5.3.6-129 presents the heat flux predictions on the surface of the earmuff. Note the sharp spikes in heat flux at the sharp corners of either side of the top surface of the earmuff due to the thinning of the thermal boundary layer. There was a problem, however with the data obtained on the earmuff windward surface. For a backpressure of Cp = 0.06 (and probably Cp = 0.10), even though the solution seemed to have converged, there was a slow oscillation in the position and magnitude of the peak heat flux and pressures on the earmuff surface. In order to explain this discrepancy, the solver was allowed to run through twenty cycles (800 time steps each) of this oscillation. The data from the twentieth such cycle is shown in Figure 5.3.6-130. As is easily visible, the oscillation is not trivial and leads to a great deal of uncertainty in the results for Cp $\geq$ 0.06. Even more unsettling is the fact that there is 13-fold change in the peak heat flux during the oscillations. This behavior points to unsteady behavior in the flow.

In summary, the Phase I and Phase II bridging problems provided a wealth of useful information and helped troubleshoot the CFD process for implementing full 3-D failure scenarios.

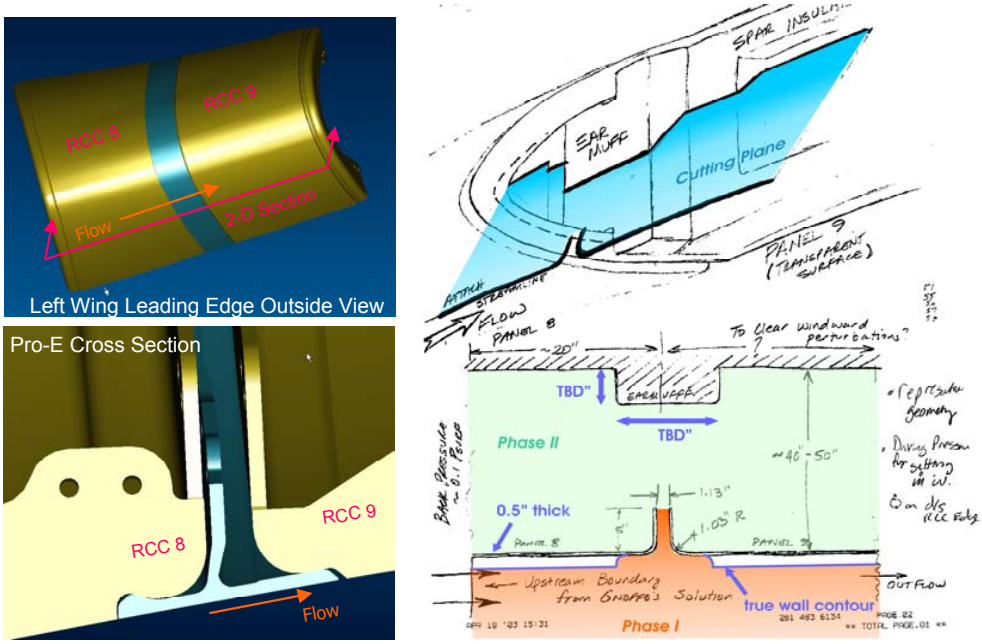

Figure 5.3.6-116 Assumed geometry and 3-D Pro/E subassembly

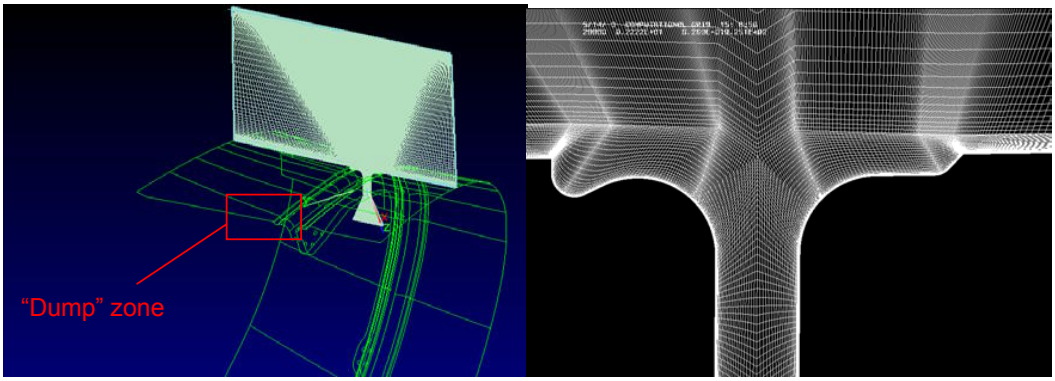

Figure 5.3.6-117 Phase I grid

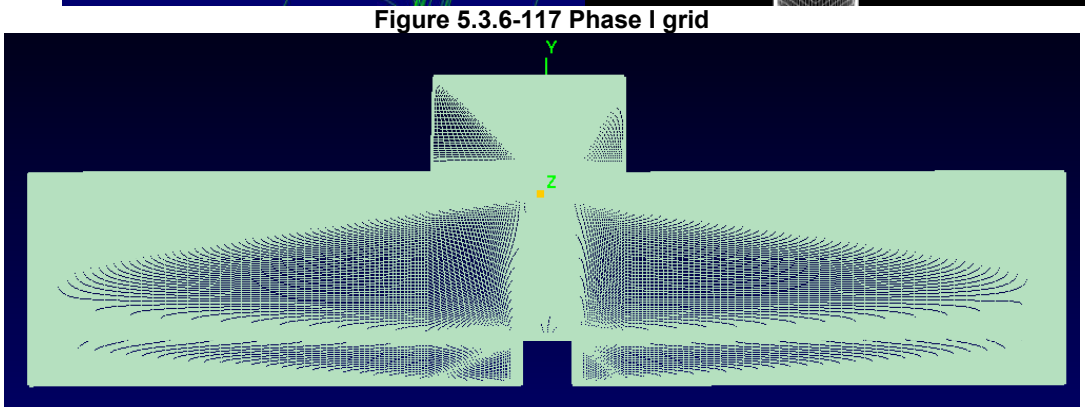

Figure 5.3.6-118 Phase II Grid

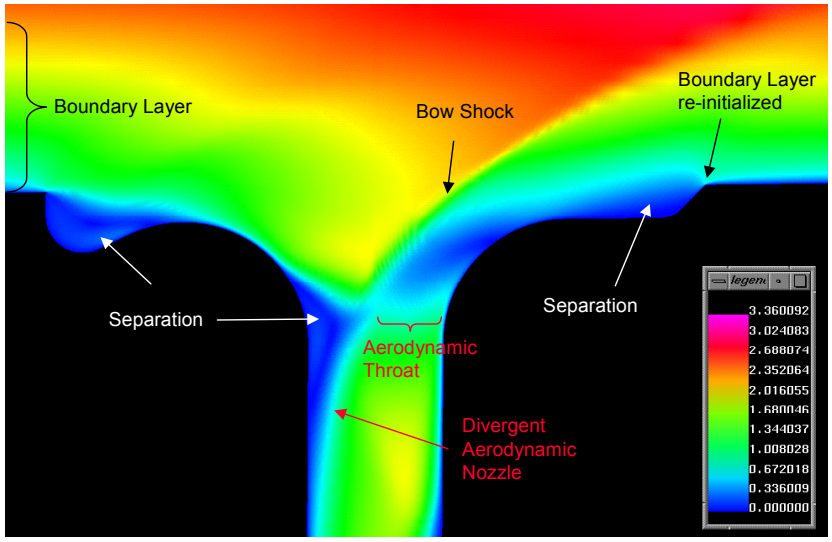

Figure 5.3.6-119 Mach Contours for T = 2900°R, phase I

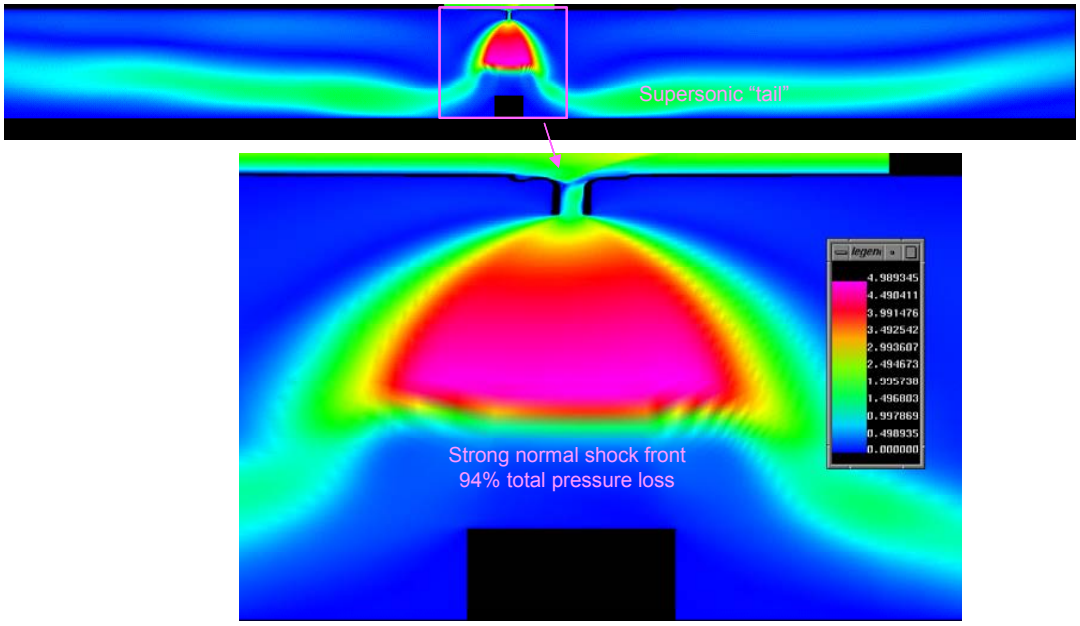

Figure 5.3.6-120 – Mach Contours for T = 2900°R and Cp = 0.02, phase II

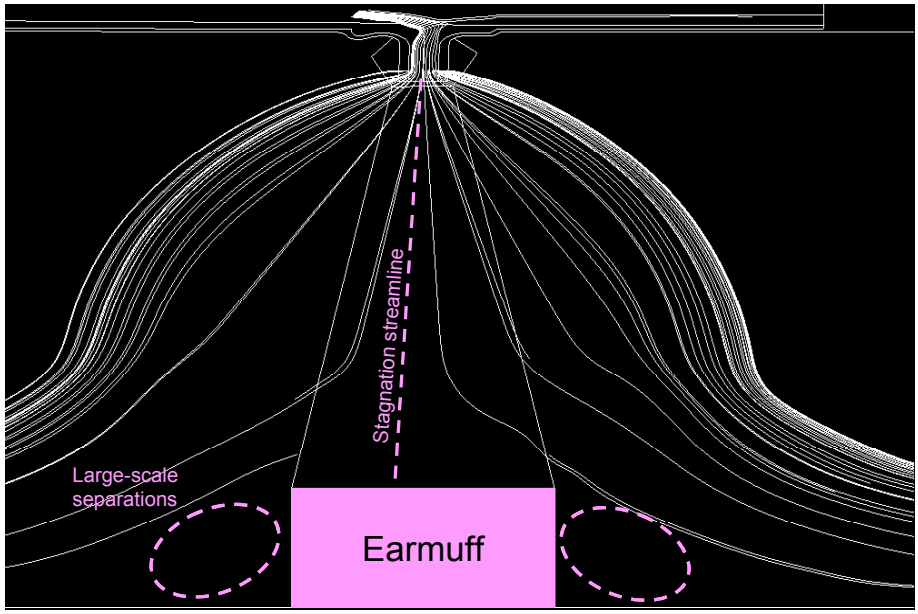

Figure 5.3.6-121 Streamlines for T = 2900°R and Cp = 0.02, phase II

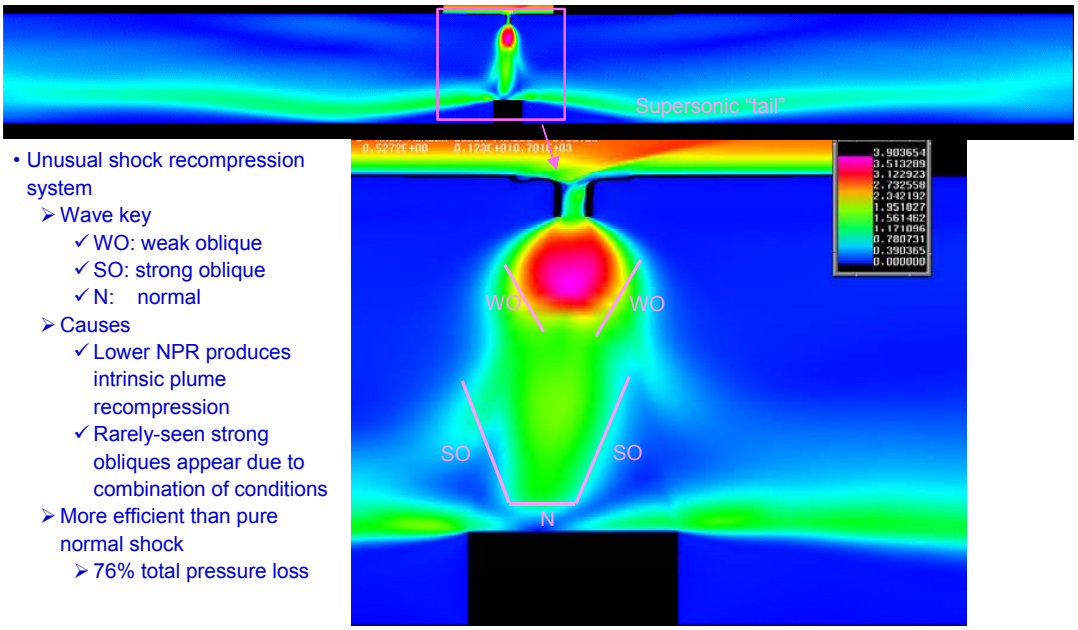

Figure 5.3.6-122 – Mach contours for T = 2900°R and Cp = 0.06, phase II

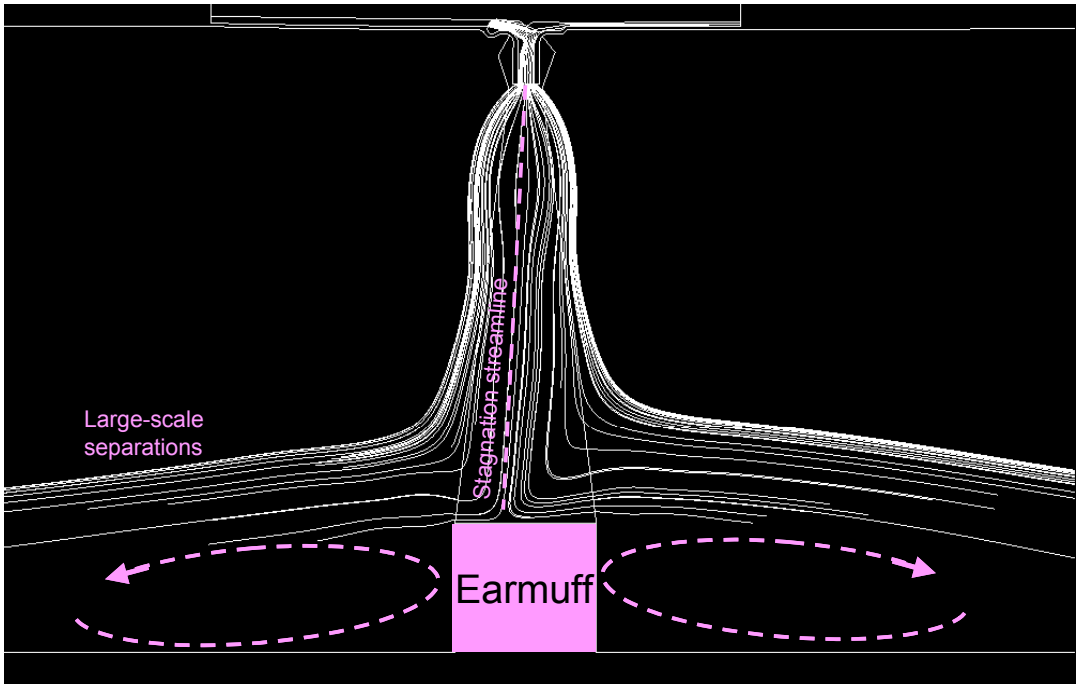

Figure 5.3.6-123 Streamlines for T = 2900°R and Cp = 0.06, phase II

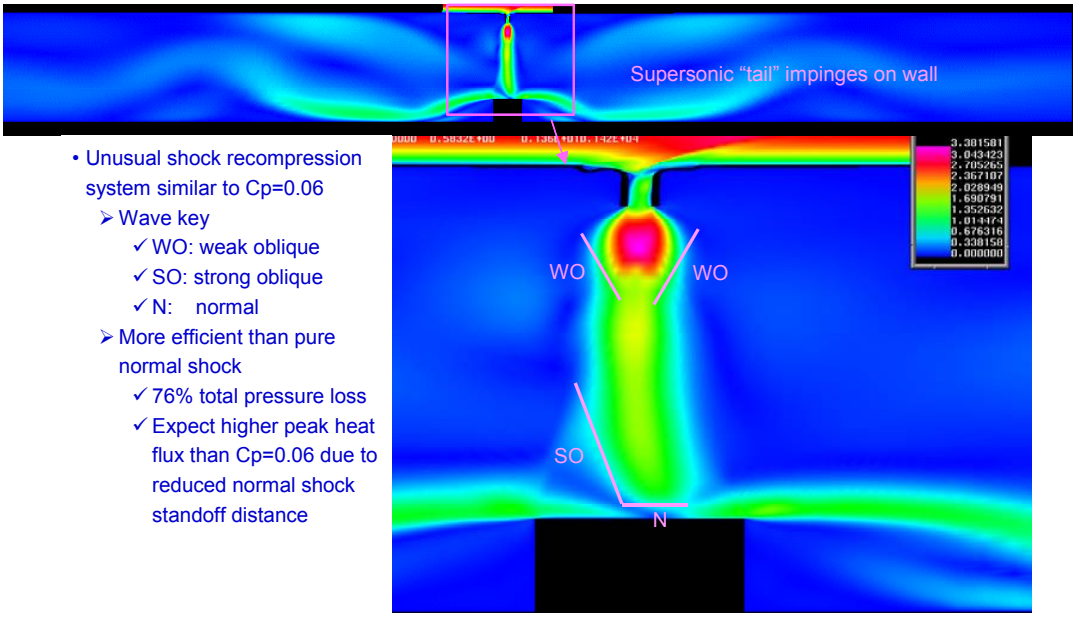

Figure 5.3.6-124 Mach contours for T = 2900°R and Cp = 0.10, phase II

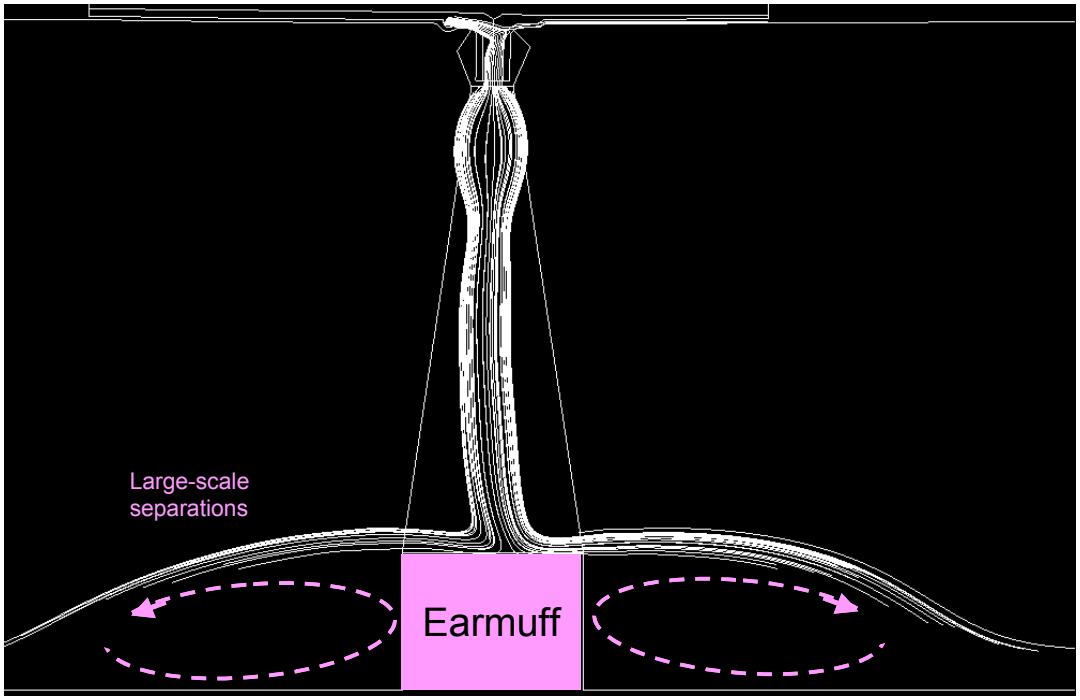

Figure 5.3.6-125 streamlines for T = 2900°R and Cp = 0.10, phase II

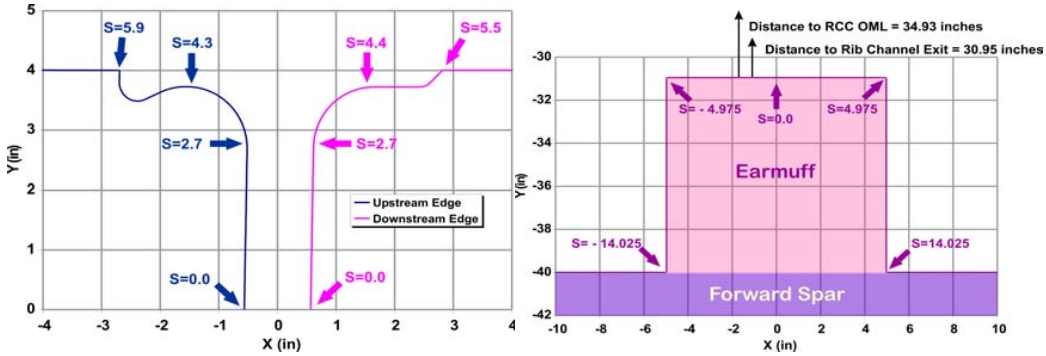

Figure 5.3.6-126 Arc length coordinate systems, phase I & II

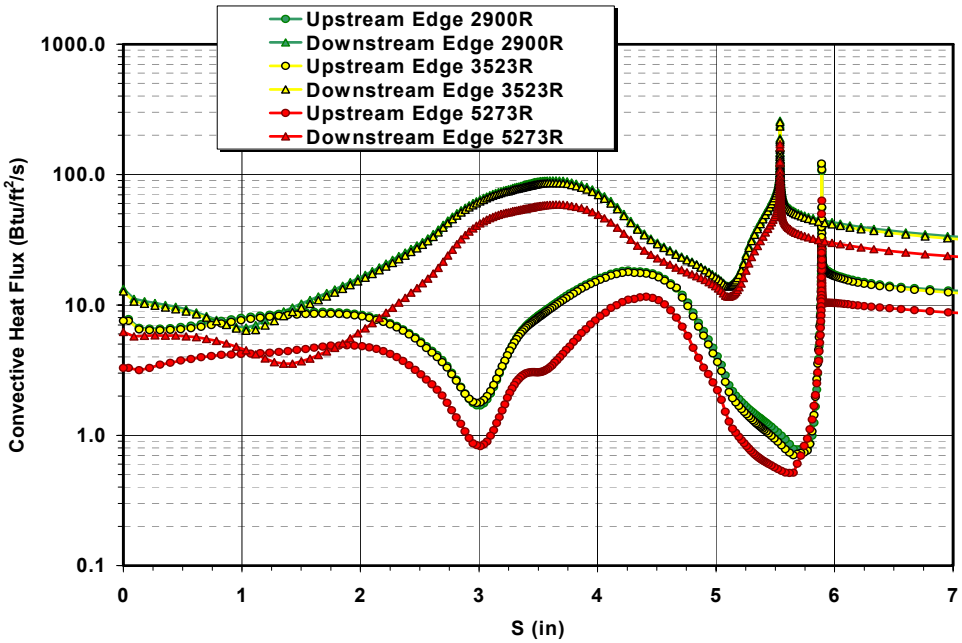

Figure 5.3.6-127 Convective heat flux on T-seal Cavity Surfaces, phase I & II

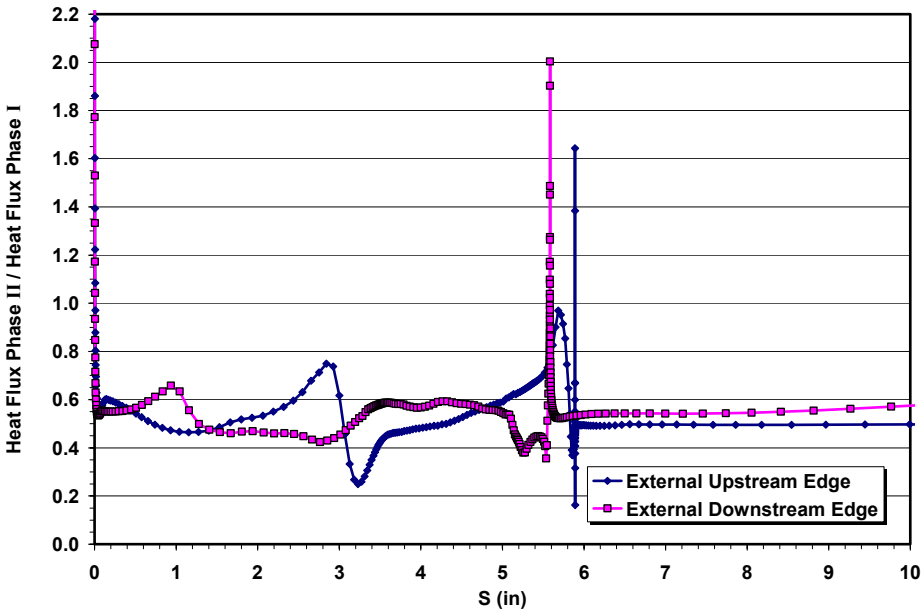

Figure 5.3.6-128 Phase I and phase II Comparison of T-seal Cavity Convective heat flux, T = 2900°R

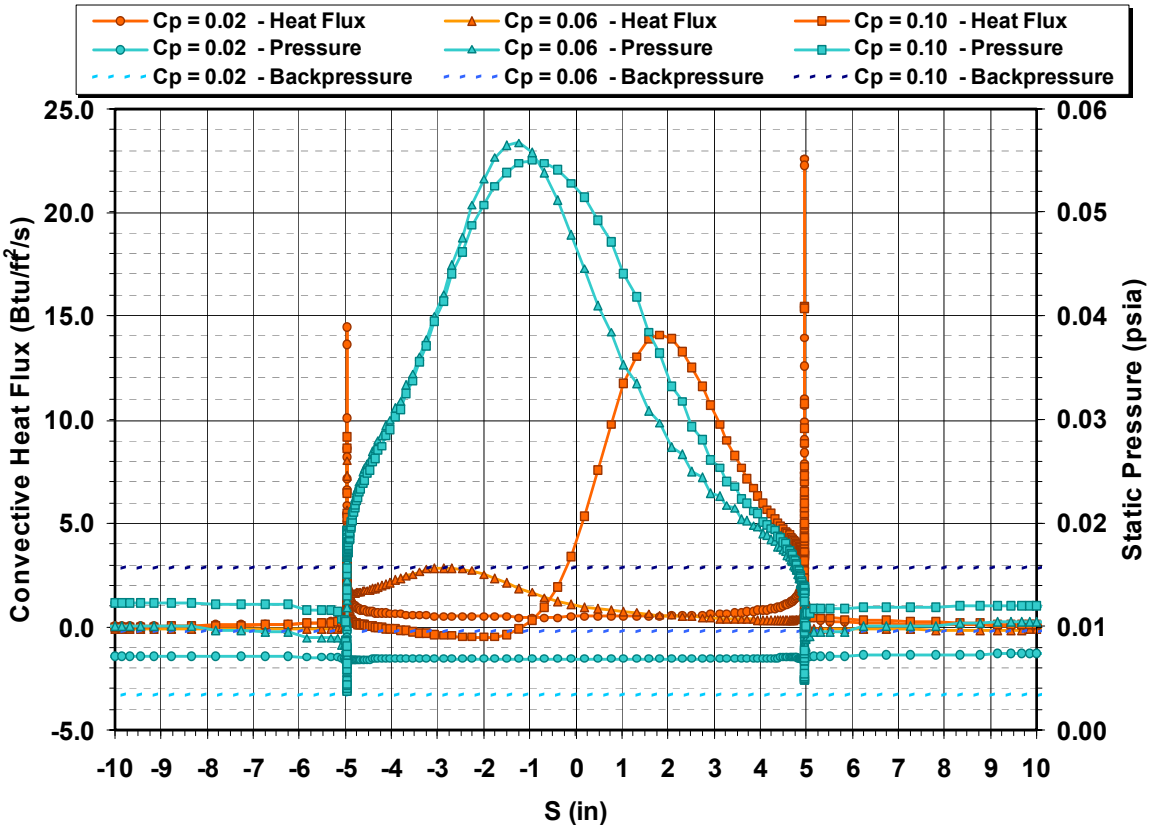

Figure 5.3.6-129 Earmuff Convective heat flux for T = 3000°R and Back-pressures, Phase II

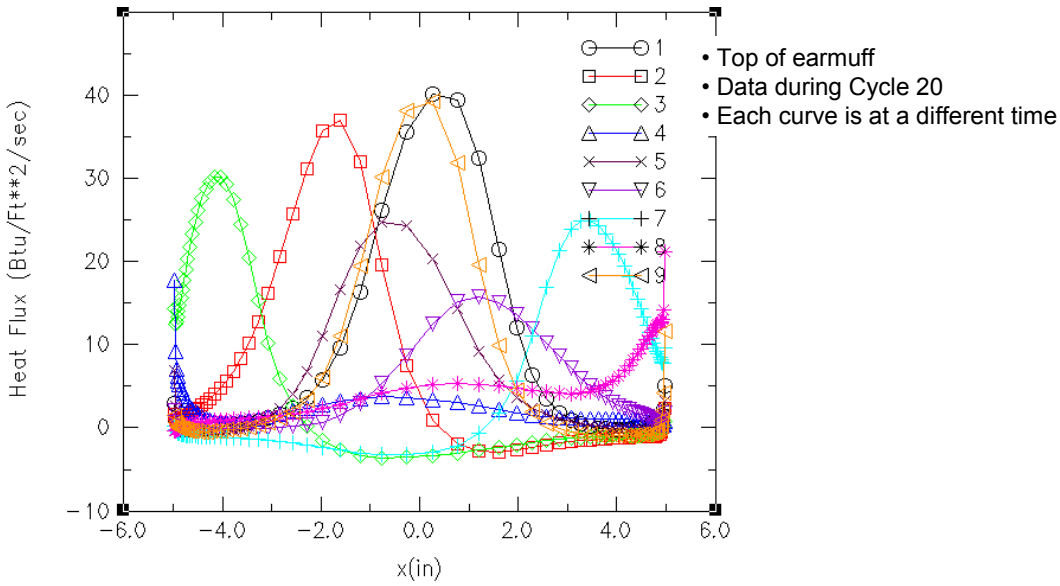

Figure 5.3.6-130 Earmuff Heat Flux Distribution Unsteadiness, phase II

5.3.6.2.3 BHB 3-D Panel 8/9 T-seal Damage

5.3.6.2.3.1 Case Description

T-seal damage between RCC Panels 8 and 9 was also one of the scenarios considered. This numerical study conducted with the USA flow solver at Boeing, Huntington Beach modeled a rectangular opening of 8" by 1.13" between the ribs of RCC Panels 8 and 9 on the windward side approximately 8" from the aft end of the lower carrier panel. This simulation included the ribs and the earmuff insulation between RCC Panels 8 and 9.

5.3.6.2.3.2 Geometry and Grid Definition

The external surface grid is illustrated in Figure 5.3.6-131, Figure 5.3.6-132 and Figure 5.3.6-133. Figure 5.3.6-134 and Figure 5.3.6-135 show the surface grid for the internal leading edge cavity. The volume grid was generated such that the wall spacing is 0.0005 inch to ensure the cell-Reynolds number of 1 or less near the surface. Solutions with both 2 and 15 million grid cells were generated.

5.3.6.2.3.3 Boundary Conditions

This equilibrium air chemistry simulation was conducted at the CFD Point 1 flight condition corresponding to 404 seconds after entry interface. The RCC interior surfaces were kept at 0° F, whereas for the Orbiter exterior surfaces a radiation equilibrium temperature boundary condition was applied.

5.3.6.2.3.4 Results

The flow field pressures are shown in Figure 5.3.6-136 and Figure 5.3.6-137 for chordwise and spanwise vertical cuts, respectively, through the T-seal damage. The corresponding Mach number distributions are illustrated in Figure 5.3.6-138 and Figure 5.3.6-139. The surface pressure and heating on the earmuff and the ribs in the vicinity of the T-seal damage are illustrated in Figure 5.3.6-140 and Figure 5.3.6-141 for the 2 million-cell model simulation. Similarly, Figure 5.3.6-142 and Figure 5.3.6-143 present the pressure and heating distributions for the 15 million-cell model simulation. The 15-million cell model results show as high as twice the heating levels, compared to the 2 million-cell model. The jet in this case acts like a wall-jet right next to the earmuffs.

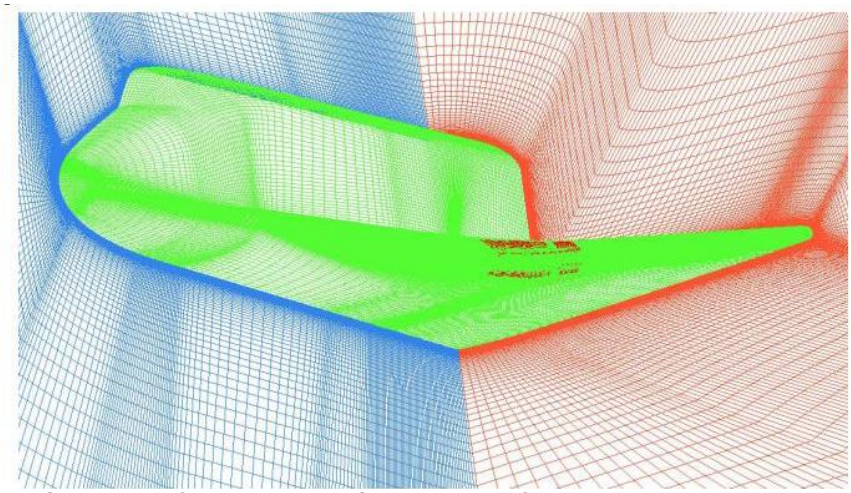

Figure 5.3.6-131 Grid Model for Panel 8/9 T-Seal Damage Coupled External/Internal Flow Simulation

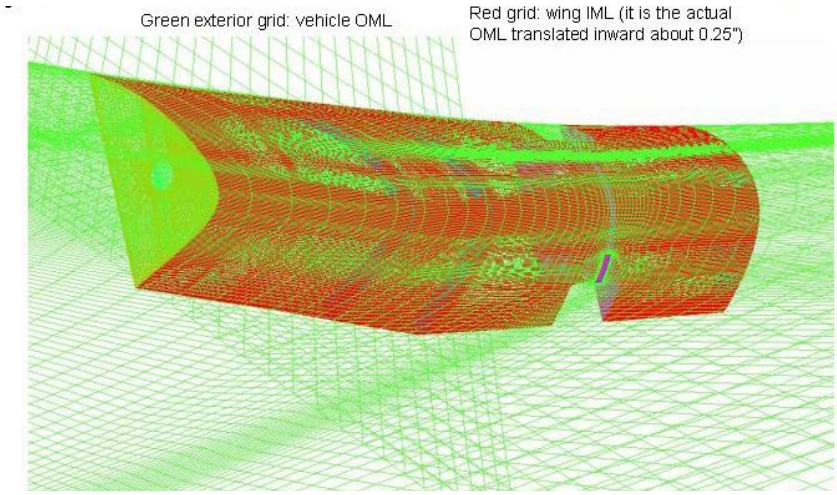

Figure 5.3.6-132 Grid Model for Panel 8/9 T-Seal Damage Coupled External/Internal Flow Simulation

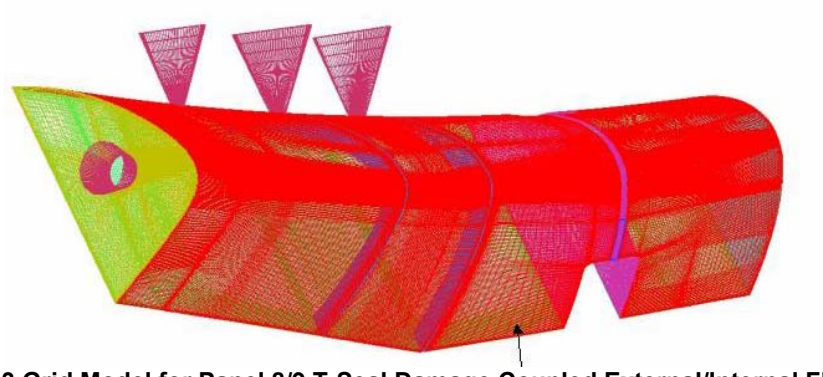

Figure 5.3.6-133 Grid Model for Panel 8/9 T-Seal Damage Coupled External/Internal Flow Simulation

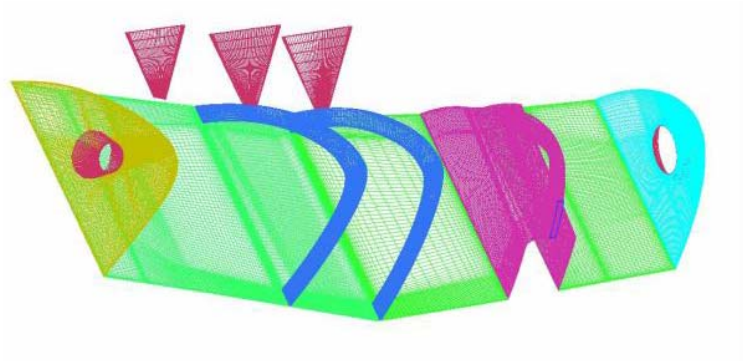

Figure 5.3.6-134 Grid Model for Panel 8/9 T-Seal Damage Coupled External/Internal Flow Simulation

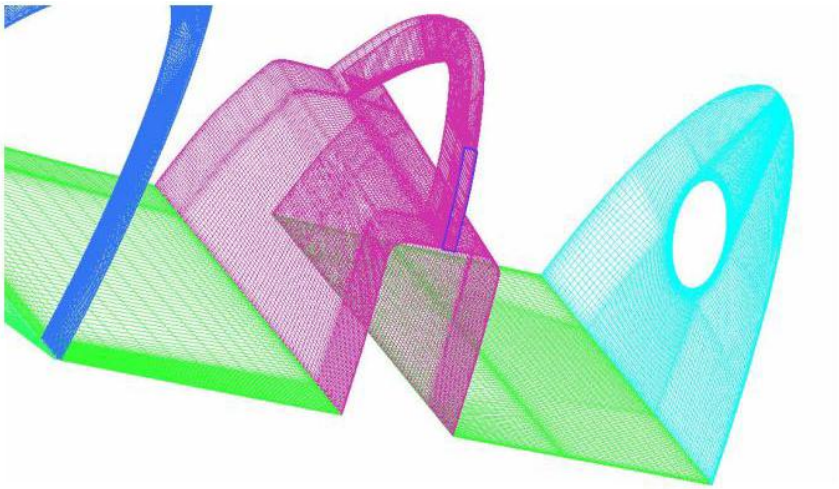

Figure 5.3.6-135 Grid Model for Panel 8/9 T-Seal Damage Coupled External/Internal Flow Simulation

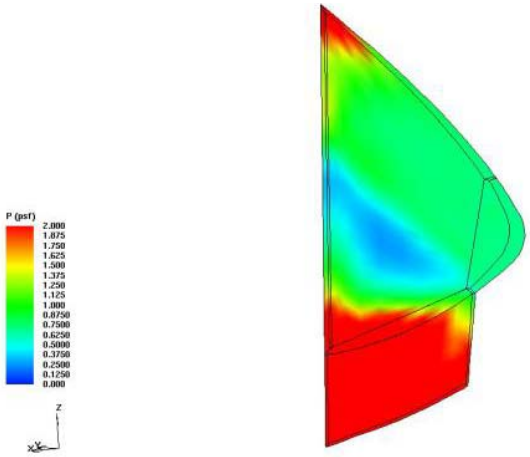

Figure 5.3.6-136 Pressure Contours from Panel 8/9 T-Seal Damage Coupled External/Internal Flow Simulation (15 million-cell Model; Postprocessed using every other points)

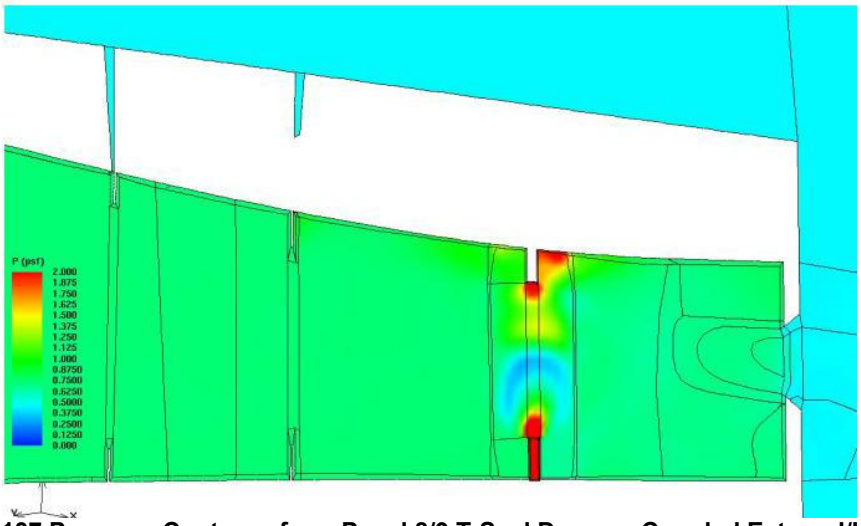

Figure 5.3.6-137 Pressure Contours from Panel 8/9 T-Seal Damage Coupled External/Internal Flow Simulation (15 million-cell Model; Postprocessed using every other points)